The Processing and Characterization of Porous Ni/YSZ and NiO/YSZ Composites used in Solid Oxide Fuel Cell Applications

by

Ryan Michael Christian Clemmer

A thesis
presented to the University of Waterloo
in fulfillment of the
thesis requirement for the degree of
Doctor of Philosophy
in
Mechanical Engineering

Waterloo, Ontario, Canada, 2006

I hereby declare that I am the sole author of this thesis. This is a true copy of the thesis, including any required final revisions, as accepted by my examiners.

I understand that my thesis may be made electronically available to the public.

Abstract

A solid oxide fuel cell (SOFC) is an energy conversion device that has the potential to efficiently generate electricity in an environmentally-friendly manner. In general, a SOFC operates between 750°C and 1000°C utilizing hydrogen or hydrocarbons as fuel and air as an oxidant. The three major components comprising a fuel cell are the electrolyte, the cathode, and the anode. At present, the state-of-the-art SOFC is made from a dense yttria-stabilized zirconia (YSZ) electrolyte, a porous lanthanum manganite cathode, and a porous nickel/YSZ composite anode. With the advent of the anode-supported SOFC and the increased interest in using a wider range of fuels, such as those containing sulphur, knowledge of the anode properties is becoming more important.

The properties of the current anodes are limited due to the narrow range of nickel loadings imposed by the minimum nickel content for electrical conductivity and the maximum allowable nickel loading to avoid thermal mismatch with the YSZ electrolyte. In addition, there is little research presented in the literature regarding the use of nickel metal as a starting anode material, rather than the traditional nickel oxide powder, and how porosity may affect the anode properties.

The purpose of this investigation is to determine the influence nickel morphology and porosity distribution have on the processing and properties of tape cast Ni/YSZ composites. Specifically, the sintering characteristics, electrical conductivity, and thermal expansion behaviour of tape cast composites created from YSZ, nickel, nickel oxide (NiO), nickel coated graphite (NiGr), and/or graphite (Gr) powders are investigated. In addition to samples made from 100% YSZ, 100% Ni, and 100% NiO powders, five composite types were created for this investigation: NiO/YSZ, NiO&Gr/YSZ, Ni/YSZ, NiGr/YSZ, and Ni&Gr/YSZ each with nickel loadings varying between 4 vol% Ni of total solids and 77 vol% Ni of total solids. Another set of composites with a fixed nickel loading of 27 vol% Ni and 47 vol% Ni of total solids and varying graphite loadings were also created.

During the burnout stage, the composites made from nickel oxide powder shrink slightly while the composites made from nickel metal expand due to nickel oxidation. Graphite additions below 20 vol% of the green volume do not alter the dimensional changes of the composites during burnout, but graphite loadings greater than 25 vol% of the green volume cause significant expansion in the thickness of the composites.

After sintering, the amount of volumetric sintering shrinkage decreases with higher nickel loadings and is greater for the composites made with nickel oxide compared to the composites made from nickel metal. The porosity generated in the composites containing graphite is slightly higher than the volume of graphite added to the composite and is much greater than the porosity contained in the graphite-free composites.

Dimensional changes of the porous Ni/YSZ and NiO/YSZ composites during both burnout and sintering were analysed based on concepts of constrained sintering of composite powder mixtures. In some cases constrained sintering was evident, while in others, a more simple rule of mixtures behaviour for shrinkage as a function of YSZ content was observed.

When nickel oxide is reduced to nickel metal during the reduction stage there is essentially no change in the composite volume for the composites containing YSZ because the YSZ prevents the composites from shrinking. After reduction the additional porosity generated in the composites is equivalent to the change in volume due to the reduction of nickel oxide to nickel metal.

When measuring the electrical conductivity, each composite type demonstrated classic percolation behaviour. The NiGr/YSZ composites had the lowest percolation threshold, followed by the Ni/YSZ and NiO/YSZ composites. When graphite was added with a nickel coating, the added porosity did not

disrupt the nickel percolation network and allowed the nickel to occupy a larger effective volume compared to a composite made with similar sized solid nickel particles. When graphite was added to the composites, the electrical conductivity was reduced and the percolation threshold increased.

Generally, the coefficient of thermal expansion (CTE) for Ni/YSZ composites are expected to follow the rule of mixtures prediction since the elastic properties for nickel and YSZ are similar. However when porosity is distributed unevenly between the YSZ and nickel phases, the CTE prediction will deviate from the rule of mixtures. When cornstarch was added to the NiGr/YSZ composites, the CTE increased as the amount of porosity in the YSZ phase increased. The CTE of the NiGr/YSZ composites followed the rule of mixtures indicating that the porosity was evenly distributed between the nickel and YSZ phases. For the other composite types, the measured CTE was higher than the rule of mixtures prediction suggesting that more porosity was contained within the YSZ phase.

Acknowledgements

It is my honour to thank the many people who have contributed to the development of this thesis and its author.

First and foremost, I would like to thank my thesis supervisor, Dr. Stephen Corbin, for giving me the opportunity to pursue graduate studies in a field I have long held an interest in. I have valued the freedom you've given me to grow as a researcher, your willingness to provide the necessary time and resources to further this research, and your genuine concern for me as a person. I have also enjoyed the many discussions we've shared over a cup of coffee (or juice) and the many valuable insights you have provided that have led to a deeper understanding of my research.

I am also grateful for the expertise and assistance of my Doctoral Thesis Committee: Dr. Fowler, Dr. Li, Dr. Plumtree, and Dr. Sarkar. Thank you for your interest in my research, your support towards my many scholarship applications, and the time you've committed toward me completing this milestone. May our paths cross again in the future.

It is with pleasure that I thank the many individuals who helped me complete my research and contributed to a rewarding research environment. In particular, I'd like to acknowledge the assistance of Matthew Birkett, Yuquan Ding, Brian Ellis, Michael Kuntz, Dennis Turriff and Mark Whitney. Without your help I would still be finishing my experiments.

I also want to acknowledge the financial support (which is very much appreciated) given to me by NSERC, OGS, and the University of Waterloo.

Finally, I must thank my family for their support and patience over the past many months as I finished writing. To my parents: Ruth and Richard, you encouraged me to pursue my dreams and you provided me a firm foundation to build my life upon. To my wife: Kristine, you are an inspiration to me. Your love and encouragement has been incredible, particularly when the finish line seemed so far away. To you, my family, I dedicate this thesis.

Table of Contents

List of Tables

List of Figures

CHAPTER 1:
INTRODUCTION

A fuel cell is an energy conversion device, like a battery, that generates electricity directly from fuel and oxygen through a series of electrochemical reactions [1]. However, unlike a battery, a fuel cell will continue to generate electricity provided there is sufficient fuel available. Since fuel cells convert chemical energy directly into electricity, they offer many advantages over traditional power sources such as improved efficiency, greater fuel diversity, high scalability, and have a lower impact on the environment [2,3,4].

One particular type of fuel cell, the solid oxide fuel cell (SOFC), operates between 750ºC and 1000°C using air as an oxidant and hydrogen as fuel, although internally reformed hydrocarbons may also be used for fuel. The ability to use fuels other than hydrogen is unique to SOFCs and is a result of its higher operating temperature. Unfortunately, the high operating temperatures also create many technical and materials related challenges that must be overcome before the use of SOFCs is wide spread.

1.1 PRINCIPLES OF SOFC OPERATION

1.1.1 Electrochemical Reactions

In its simplest form, a single fuel cell consists of an anode, a cathode and an electrolyte. A fourth component, called the interconnect, is used to stack multiple cells together in order to increase the amount of power generated. To generate electricity, fuel is fed to the anode and an oxidant is fed to the cathode, as illustrated in Figure 1-1. For solid oxide fuel cells, hydrogen and carbon monoxide can be used as fuel, an advantage over other fuel cell types, and pure oxygen or air are used as oxidants.

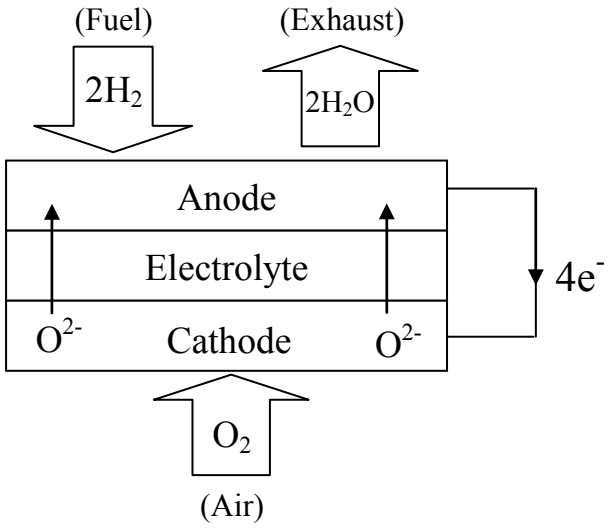

Figure 1-1: Schematic diagram depicting the operation of a fuel cell [3].

At the anode, the hydrogen fuel reacts with oxygen ions to form water and electrons, as indicated by the anode half cell reaction of Equation (1-1). The electrons travel from the anode to the cathode, due to the voltage difference between the two electrodes, through an external circuit creating an electric current. Meanwhile, at the cathode, the electrons transfer their charge to oxygen molecules at the cathode/electrolyte interface to form oxygen ions, as given by the cathode half cell reaction of Equation (1-1). To complete the circuit, the oxygen ions diffuse through the electrolyte to the anode/electrolyte interface to combine with hydrogen to form water given by the overall electrochemical reaction of Equation (1-1) [3].

$$\begin{aligned} &Anode: H_2 + O^{2-} \rightarrow H_2O + 2e^- \\ &Cathode: \frac{1}{2}O_2 + 2e^- \rightarrow O^{2-} \\ \hline &Total: H_2 + \frac{1}{2}O_2 \rightarrow H_2O \end{aligned}$$

(1-1)

When carbon monoxide is used as fuel, rather than hydrogen, the reaction by-product becomes carbon dioxide, as shown in Equation (1-2). Similarly, it is possible to internally reform hydrocarbons, such as methane, within a SOFC by the reaction given in Equation (1-3) [1].

$$CO + \frac{1}{2}O_2 \rightarrow CO_2$$

(1-2)

$$CH_4 + H_2O \rightarrow CO + 3H_2$$

(1-3)

After reforming the methane, the resultant hydrogen and carbon monoxide gases are consumed as fuel in order to generate power as before. If there is insufficient steam for reforming the hydrocarbons then carbon may deposit on the surface of the anode through the following reactions [1]:

$$2CO \rightarrow CO_2 + C$$

(1-4)

$$CH_4 \rightarrow 2H_2 + C$$

(1-5)

Carbon deposition should be avoided to minimize the deleterious effect on the performance of the fuel cell as a result of carbon occupying active reaction sites and blocking gas flow within the pores.

Regardless of the fuels used, an electrochemical reaction takes place where there is a means of transporting fuel and oxygen to active reaction sites, and transporting the reaction products and excess electrons away. Consequently, reaction sites are only electrochemically active at the triple phase

boundary (TPB) between the electrode, electrolyte, and porosity [5,6,7,8]. By increasing the TPB area in each electrode, the electrochemical performance of the fuel cell is improved.

1.1.2 Chemical Thermodynamics

1.1.2.1 Reversible Cell Potential

The maximum amount of work, W_{max}, a fuel cell can perform is related to the Gibb's free energy change, ΔG, associated with the electrochemical reactions taking place [9]. That is:

$$W_{\max} = -\Delta G \tag{1-6}$$

The corresponding electrochemical potential, E, at equilibrium is also associated with the change in free energy by the following fundamental relationship:

$$\Delta G = -nFE \tag{1-7}$$

where n is the number of moles of electrons exchanged in the reaction, and F is Faraday's constant equal to 96,500 coulombs per mole of electrons [10]. By definition, a spontaneous chemical reaction ($-\Delta G$) will produce a reversible potential, E_r, (i.e. a positive electrochemical potential) at equilibrium. Hence, at 25°C and atmospheric pressure, the combination of hydrogen and oxygen to form water (i.e. Equation (1-1)) yields a reversible potential of 1.229 volts.

1.1.2.2 Temperature and Pressure Effects

In addition to being dependent on the electrochemical reaction, the reversible potential, E_r, is also affected by temperature and pressure as follows:

$$\left(\frac{\partial E_r}{\partial T}\right)_P = \frac{\Delta S}{nF} \tag{1-8}$$

$$\left(\frac{\partial E_r}{\partial P}\right)_T = \frac{-\Delta V}{nF} \tag{1-9}$$

where ΔS is the change in entropy, and ΔV is the volume change associated with a change in temperature and pressure respectively. For the formation of water reaction, the change in entropy is negative at higher temperatures causing a decrease in reversible potential. Conversely, an increase in pressure results in a negative volume change thereby increasing the reversible potential [1]. As a result, the reversible potential for a SOFC using hydrogen and oxygen as fuel while operating at 750ºC and 1000ºC is 0.997 V and 0.924 V respectively [1].

1.1.2.3 Concentration Effects

The reversible potential calculated in Equations (1-7) to (1-9) assumes that the reactants participating in the reaction are 100% pure. However, this is typically not the case under normal SOFC operating conditions. The fuels used in a SOFC may consist of a mixture of hydrocarbons, hydrogen, carbon monoxide, and water, while air is commonly used as the oxidant. As a result, the reversible potential, E_r, will change according to the general Nernst equation [3,9]:

$$E_r = E_0 - \frac{RT}{nF}\ell nK \tag{1-10}$$

where E_o is the equilibrium potential, R is the universal gas constant, and K is the equilibrium constant calculated from the activity, *a*, for the individual products and reactants (for the reaction in Equation (1-1)) as follows:

$$K = \frac{a_{products}}{a_{reactants}} = \frac{a_{H_2O}}{a_{H_2} \cdot a_{O_2}^{1/2}} \tag{1-11}$$

where H_2 and O_2 are reactants and H_2O is the product.

In addition, the reversible potential will vary within the cell because of variations in fuel and oxidant compositions entering and leaving the cell. The concentration of reactants will be greatest at the gas inlet and decrease when flowing towards the gas outlet as they are consumed during subsequent reactions. Thus, the maximum potential of the fuel cell will be based on the lowest Nernst potential of the cell since the electrodes, having the same surface potential, are designed to be good electronic conductors.

To prevent the concentration of the reactants from dropping to zero and producing a null Nernst potential, fuel cells are typically operated with more reactant than is necessary. The amount of reactant utilization, Ut, is determined by:

$$Ut = \frac{N_{consumed}}{N_{supplied}} \tag{1-12}$$

where $N_{consumed}$ and $N_{supplied}$ is the mole flow rate of the reactants consumed and supplied respectively. The common fuel utilization is between 80%-85% for fuel and 50% for air [3].

1.1.3 Electrochemical Polarization

In practice, the operating voltage of a fuel cell is a function of the operating conditions and any irreversible losses, called polarization, associated with the electrochemical reactions taking place. That is, the operating voltage, V, of a fuel cell is equal to the reversible potential, E_r, less any polarization losses [4] i.e.:

$$V = E_r - \eta_a - \eta_c - \eta_\Omega$$

(1-13)

where η_a, η_c, and η_Ω, are the three basic types of polarization: activation, concentration, and ohmic respectively. Although polarization cannot be eliminated entirely, it may be minimized by expanding the triple phase boundary area through careful selection of materials and proper cell design [1,4].

1.1.3.1 Activation Polarization

Activation polarization is generally a result of a slow rate-determining step in a series of reactions. All chemical reactions have an activation energy barrier that is overcome before the reaction takes place. Slower reactions have higher activation energy barriers, whereas faster reactions have lower activation energy barriers. In terms of the expected electrochemical reactions in a fuel cell, the slowest reaction may be attributed to the adsorption of a reactant onto the surface of the electrode, charge transfer, or desorption of the product.

There are two methods of overcoming the activation energy barrier in electrochemical reactions. The first method involves increasing the operating temperature and the second method is to apply an extra voltage [11]. Activation polarization, η_A, is the extra voltage required to counteract the slow kinetics of the reaction and is related to current density, *i*, by the Butler-Volmer equation:

$$i = i_0\left[\exp\left(\frac{\alpha n F \eta_A}{RT}\right) - \exp\left(\frac{-(1-\alpha) n F \eta_A}{RT}\right)\right]$$

(1-14)

where i_o is the exchange current density, and α is the transfer coefficient. The exchange current density is equivalent to the equal forward and reverse electrode reaction rates at the equilibrium potential, E_o. The transfer coefficient is defined as the fraction of polarization change that leads to a change in the reaction rate constant [1]. When activation polarization is high, the far right hand term in Equation (1-14) may be neglected to obtain the Tafel equation:

$$\eta_A = \frac{RT}{\alpha n F}\ell n\left(\frac{i}{i_0}\right) \text{ or } \eta_A = \beta \log\left(\frac{i}{i_0}\right)$$

(1-15)

where β is a constant related to the electrode material and type of reaction [1]. Due to the high operating temperatures of SOFCs, the rates of reaction are typically high such that the amount of activation polarization is relatively small.

1.1.3.2 Concentration Polarization

Concentration polarization, η_c, occurs when the electrochemical reactions are hindered by mass transport effects, such as: slow diffusion of the reactant gas to the reaction site, slow diffusion of ions through the electrolyte, or slow removal of the reaction products. To enhance the diffusion of reactants and products to and from the reaction sites, the anode and the cathode should possess an open network of large pores. Furthermore, the extent of concentration polarization will depend on the operating temperature, pressure, concentration, and the physical properties of the electrode. When the fuel cell reactions are completely governed by diffusion, there is a rapid drop in the cell voltage. The current density at which the voltage begins to drop is called the limiting current, i_L, and is calculated by:

$$i_L = \frac{D_z nFC_B}{\delta} \tag{1-16}$$

where D_z is the diffusivity of the reacting species, z, C_B is the uniform bulk concentration, and δ is the thickness of the concentration gradient [10]. For an electrode process free of activation polarization, the concentration polarization can be determined by [1]:

$$\eta_c = \frac{RT}{nF} \ell n\left(1 - \frac{i}{i_L}\right) \tag{1-17}$$

Since concentration polarization is a function of the concentration of the reactant gases, the degree of polarization increases as the conversion rate of the reactant increases. However, by increasing the limiting current, the significance of concentration polarization can be minimized.

1.1.3.3 Ohmic Polarization

Ohmic polarization, η_Ω, is a function of the resistance to ion conduction in the electrolyte, the electrical resistivity of the electrodes, and the contact resistance at the electrode/electrolyte interface and is calculated by:

$$\eta_\Omega = iR_i \tag{1-18}$$

where R_i represents the total cell resistance, and i the resultant electric current. For SOFCs, the low ionic conductivity of the electrolyte is the largest contributor to ohmic polarization. To overcome this problem, higher operating temperatures are used to improve the ionic conductivity of the electrolyte. As a result, early SOFC cells were operated at much higher temperatures because they were constructed from thick electrolyte layers (100-200 μm) that supported the cell. More recent designs implement an anode-supported cell with a thin electrolyte layer (10-20 μm) in order to reduce the degree of ohmic polarization and allow for lower operating temperatures [12].

1.2 SOFC DESIGN

Optimal fuel cell performance may be achieved through the appropriate cell design and material selection, such that the chemical thermodynamics are maximized and the electrochemical polarization losses are minimized.

1.2.1 SOFC Cell Design

Although there are many possible methods of constructing a solid oxide fuel cell, the two most common cell designs are the tubular and planar design configurations [13].

1.2.1.1 Tubular Design

The tubular design, first proposed in 1980, is the most mature SOFC design with many cells having successfully operated for tens of thousands of hours with excellent and stable performance [1,2,3]. As illustrated in Figure 1-2, the cell foundation is a 30% porous calcia-stabilized zirconia ($CaO\text{-}ZrO_2$) support tube which is closed at one end. The support tube is typically 1.5 cm in diameter, 1.5 mm thick, and 2 m in length. The thin 35% porous $LaMnO_3$ cathode layer is deposited directly onto the support tube through a slurry coating and then sintered in air. Using electrochemical vapour deposition (EVD), a 9 mm wide dense $MgO\text{-}LaCrO_3$ interconnect layer is placed on the cathode. A dense electrolyte layer is then deposited on the remaining cathode area again using EVD. Finally, the 40% porous Ni/YSZ anode layer is applied to the electrolyte by dipping the cell in a nickel slurry and then adding YSZ to the nickel matrix through EVD.

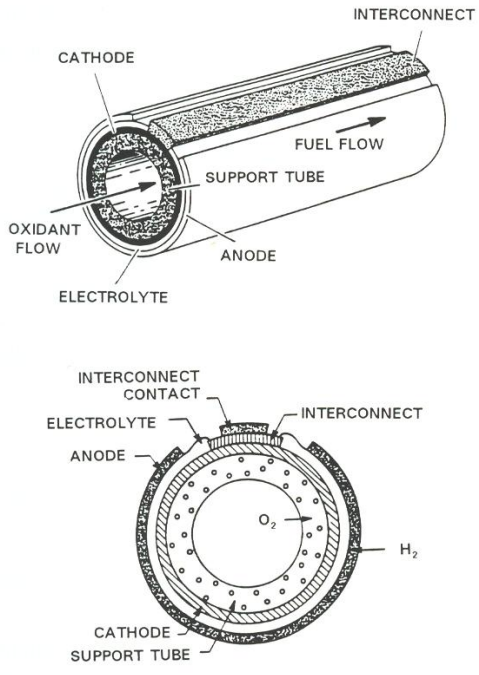

Figure 1-2: Tubular SOFC design [1]

During operation, air enters the inside of the cell through an injector tube, while the fuel is passed over the outside of the tube. With this configuration gas-tight seals are not required, a significant advantage over other cell designs, and electrical connections are less complex because they are made in a reducing atmosphere. As a result, multi-kilowatt stacks may be constructed by connecting individual cells in series and parallel using nickel felt. Unfortunately, tubular cells do not perform as well as other cell designs since they tend to have long current paths that contribute to higher ohmic losses while the support tube slows gas diffusion to the cathode causing lower cell efficiencies and power densities [1,2].

1.2.1.2 Planar Design

The planar cell also known as the flat-plate design is gaining popularity because of its simple geometry and fabrication flexibility. A single cell is composed of thin layers of each component stacked on top of each other, as illustrated in Figure 1-3 [1]. Unlike the tubular cell, a planar cell may be co-fired in one step or many steps. For example, the electrolyte and interconnect may be sintered separately so that their respective sintering processes are optimized for densification. The anode and cathode may then be added through tape casting, slurry coating, screen printing, plasma spraying, or other deposition techniques [1,3]. Typically, each layer is formed through tape casting and then laminated together. Depending on the design, the cell is supported either by the electrolyte or the electrode with each design having its own merits.

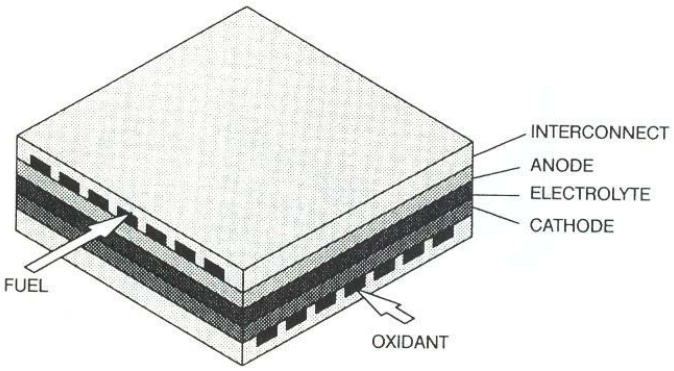

Figure 1-3: Planar SOFC design [1]

The planar design offers improved performance and higher power density compared to the tubular design. First, the internal resistance of the cell is minimized by keeping the component layers thin. Consequently, current travels through the thickness of the cell, rather than along the plane. This makes the internal cell resistance independent of the cell area, but also susceptible to high contact resistances that may develop between component layers if they are not properly joined together. By using a planar cell configuration, gas manifolding is less complicated because of the flexibility in designing the geometry of the cell. Unfortunately, gas tight and electrically insulating seals are required to separate the interior of the manifold and the outside environment. Therefore, sealing becomes quite difficult, especially at the high temperatures and the extreme operating conditions of a SOFC [1,2].

1.2.2 Component Design

Having selected an appropriate cell configuration, it is important to select the proper materials before the cell is built. The three main components of a solid oxide fuel cell are the electrolyte, cathode, and anode, and each require its own specific material requirements.

1.2.2.1 SOFC Electrolytes

The electrolyte has two important functions. First, it separates the anode and cathode to avoid unwanted mixing of the fuel and oxidant gases. Second, the electrolyte acts as an ionic conductor while simultaneously preventing electron cross-over which can lead to a reduction in the power generated by the fuel cell. To meet these requirements, the electrolyte must be fully dense, have high ionic conductivity, negligible electrical conductivity, and be physically and chemically stable in both the reducing and oxidizing environments in the anode and cathode during processing and operation.

One possible electrolyte material is derived from zirconia (ZrO_2). However, in its pure form, zirconia is a poor ionic conductor and undergoes a large volume change when it transforms from a monoclinic structure to a tetragonal structure at 1170ºC and a cubic structure above 2370ºC. On its own, ZrO_2 is an unsuitable electrolyte material, but the cubic zirconia structure can be made stable from room temperature to its melting point through the additions of other oxide materials such as CaO, MgO, Y_2O_3, and Sc_2O_3.

As an added benefit, the ionic conductivity of the newly stabilized zirconia increases with the addition of stabilizing oxides. To achieve the maximum ionic conductivity, the lowest amount of oxide required for stabilizing the zirconia should be added. For yttria-stabilized zirconia, the minimum amount of yttria required is 8-mole% [1]. Beyond this minimum oxide loading, the ionic conductivity decreases with increasing oxide content because of defect ordering, vacancy clustering, and/or electrostatic interaction [2].

Although higher conductivities are possible with other oxide additions, yttria-stabilized zirconia (YSZ) is currently the most common electrolyte material used in SOFC because of its availability and cost. It possesses an adequate ionic conductivity over the required operating range of oxygen partial pressures and is stable physically and chemically in both the reducing and oxidizing environments.

Ceria (CeO_2) is another potential electrolyte material having a higher ionic conductivity compared to YSZ, but is less stable under the reducing conditions at the anode [3,14]. Under reducing conditions at higher temperatures, ceria develops higher electrical conductivities that diminish the fuel cell potential and energy conversion efficiencies. For this reason, ceria is used primarily in low temperature (500°C) SOFC applications.

1.2.2.2 SOFC Cathode Design

The purpose of the SOFC cathode is to convert oxygen molecules into mobile ions for use in electrochemical reactions within the anode. A good cathode has high ionic and electronic conductivities, an open network of pores, a coefficient of thermal expansion that matches the other cell components, and physical and chemical stability in oxidizing environments.

One of the most common cathode materials is lanthanum manganite ($LaMnO_3$) which has an acceptable coefficient of thermal expansion of 11.2×10^{-6} cm/cm·K and an adequate electrical conductivity of 10 S/cm at 1000°C. Unfortunately, it has a very low ionic conductivity of 10^{-7} S/cm at the same 1000°C temperature [15].

Another drawback to using $LaMnO_3$ is the high mobility of manganese above 1000°C. During cell fabrication, manganese can easily diffuse into the electrolyte causing lanthanum excess in the cathode. In the absence of manganese, the lanthanum forms a highly reactive oxide, La_2O_3 [16]. This oxide then combines with the zirconia in the electrolyte to form a highly resistive second phase, lanthanum zirconate ($La_2Zr_2O_7$). This new second phase zirconate has an electrical conductivity three orders of magnitude less than yttria-stabilized zirconia, which is already a poor electron conductor at 0.1 S/cm [5,17]. Fortunately, maintaining a non-stoichiometric lanthanum deficiency of approximately 10% can minimize this formation of lanthanum zirconate [1].

Strontium and calcium doping is the most common method to increase the electrical conductivity of lanthanum manganite, but there is a penalty associated with increasing the electrical conductivity in the form of a higher coefficient of thermal expansion. For example, the coefficient of thermal expansion increases from 10.1 to 11.4 x 10^{-6} 1/K for a calcium content ranging from 10 to 50 mol% [1]. Doping also has the added benefit of limiting the formation of high resistance second phases like lanthanum zirconate. At lower temperatures, small amounts of dopant suppress the migration of manganese atoms to the electrolyte interface; thus, the lanthanum excess that would react with the yttria-stabilized zirconia to form the zirconate does not develop.

Lanthanum cobaltite ($LaCoO_3$) is another common cathode material. One of the major benefits to using $LaCoO_3$ is its high electrical and ionic conductivities of 1000 S/cm at 1000°C and 0.1 S/cm at 900°C respectively [17]. Unlike $LaMnO_3$ however, $LaCoO_3$ has a coefficient of thermal expansion of 21.5 x 10^{-6} 1/·K, which is unacceptable [17]. Although it is possible to reduce the coefficient of thermal expansion somewhat, the reduced thermal expansion comes with a severe reduction in electrical conductivity [18]. $LaCoO_3$ also readily forms lanthanum zirconate at temperatures above 1100°C making it difficult to fabricate this type of cathode with the electrolyte [1].

1.2.2.3 SOFC Anodes

As research focuses on lowering the operating temperature of the SOFC through the reduction of the electrolyte layer thickness, particularly for planar cell designs, the fuel cell performance becomes increasingly dependent on the characteristics of the electrodes [19]. With a thin electrolyte layer, the anode or the cathode must be thickened in order to support the cell. Since the electrochemical performance of the anode is nearly independent of its thickness, unlike the cathode, the anode supported cell is the preferred planar cell construction [20].

The purpose of the anode is to facilitate the conversion of fuel into useable electric current. To achieve this aim, the anode should possess: 1) high electrochemical or catalytic activity; 2) a large triple phase boundary where pores, electrode, and electrolyte are in contact within the microstructure; 3) a high degree of porosity to supply fuel and remove reaction products such as water; 4) a high electrical conductivity; 5) a coefficient of thermal expansion (CTE) that matches the other cell components; and 6) suitable mechanical strength in order to support the other cell components.

The degree of electrochemical and catalytic activity is highly dependent on the anode materials chosen. When the catalytic activity and electrical conductivity of the anode is high, the activation and ohmic polarization losses can be minimized. Under the reducing conditions in the anode it is possible to use metals, which generally have high catalytic activity and electrical conductivity, as an anode material instead of more complex mixed ionic and electronic conducting oxides.

Suitable metals capable of withstanding the more oxidizing conditions at the fuel exit during operation include: nickel, copper, cobalt, ruthenium and other noble metals. Nickel is excellent for its hydrogen catalytic activity and steam reforming of methane; however, it also tends to enhance the

catalytic cracking of higher hydrocarbons which can lead to excessive carbon formation [21,22,23]. Consequently, copper has been proposed as a replacement for nickel to alleviate the problems of carbon deposition when operating a SOFC with common hydrocarbon based fuels [21]. Alternatively, cobalt offers improved tolerance to sulphur impurities but is relatively expensive, while ruthenium has good resistance to sintering and has high reforming activity. Despite these differences, nickel is the metal of choice because of its satisfactory properties and significantly lower cost [2,23].

While a pure nickel anode may be used as an anode material, it has a tendency to sinter easily at the typical SOFC operating temperatures. As a result, small nickel particles coalesce during operation, reducing the triple phase boundary area, and cause a decrease in the performance of the SOFC over time. In addition, nickel has a much higher coefficient of thermal expansion (CTE) of 16.3×10^{-6} 1/K compared to the CTE of YSZ which is 10.2×10^{-6} 1/K [24]. This discrepancy between the CTEs can cause large thermal stresses which result in severe cracking and delamination during the fabrication and operation of the fuel cell [2].

To combat this problem, yttria-stabilized zirconia is combined with the nickel metal to form a composite anode. By doing so, there are three major improvements to the properties of the anode. First, adding YSZ to the anode creates a mixed conducting composite with increased ionic conductivity and extends the triple phase boundary area into the 3-D network of the anode structure from the two-dimensional anode/electrolyte interface. This improves the electrochemical performance of the fuel cell by increasing the triple phase boundary area and lowering the activation polarization losses [12]. Second, YSZ inhibits the sintering of nickel during operation which is a significant factor in the deterioration of SOFC performance over time [25,26]. Finally, YSZ lowers the coefficient of thermal expansion of the anode thereby improving the reliability of the cell.

Lastly, an anode must possess a high degree of porosity. If the network of pores present in the anode is closed, too fine, or too tortuous, the electrochemical performance of the anode will suffer due to increased concentration polarization losses. Conversely, if there is too much porosity, the anode will lack the necessary strength to support the fuel cell and may negatively affect the electrical conduction path. The ideal amount of porosity lies between the two extremes, where there is sufficient porosity to freely move fuel and reaction products into and out of the anode while simultaneously maintaining a reasonable strength.

CHAPTER 2:
LITERATURE REVIEW & RESEARCH OBJECTIVES

Many researchers have studied various aspects of solid oxide fuel cell technology. For instance, several articles have been published in the literature relating to solid oxide fuel cell research in general [1,2,13,26,27], while reviews by Zhu and Deevi [4], Jiang and Chan [19], and Atkinson et al. [21] have examined the status of materials research specifically relating to SOFC anodes. The majority of the literature has focused on some aspect of the electrochemical performance of an SOFC, usually made from unique materials or fabrication processes; although some researchers have examined the processing and properties (electrical conductivity, thermal expansion, etc) of SOFC anodes.

2.1 ANODE PROCESSING

Many different fabrication techniques have been utilized to construct a number of anode structures. Typically, commercial NiO and YSZ powders are used when forming the anode, however, spray pyrolysis [28], gel-precipitation [29], "mechanochemical" surface fusion [30], and "coat-mix" particle agglomeration [31] processes have also been used to create composite NiO/YSZ particles. Electrochemical vapour deposition [32], plasma spraying [13], and electrophoretic deposition [33] have been successfully used to create tubular cells, while more traditional powder processing techniques have been implemented when building planar cells. Common powder processing methods include: mechanical milling and dry pressing [29], screen printing [30,34,35], and tape casting [20,31,36,37,38,39].

2.1.1 Tape Casting

Tape casting is the preferred method of forming thin and flat ceramic parts which are well suited for planar SOFC applications. Typically, tapes are cast with dried thicknesses ranging from 0.025 mm to 1.27 mm while tapes as thin as 5 μm have been successfully cast [40]. Dry pressing, roll compaction, and extrusion are other possible techniques to create thin parts. These processes, however, are much more difficult to control, especially at smaller thicknesses [40,41]. For SOFC applications, the key advantage to tape casting is the ability to produce thin tapes with controlled thicknesses that may be laminated to other component layers quite easily. These multilayered structures are then co-sintered together to form a single cohesive structure.

At first glance, tape casting is a very simple process, as illustrated in Figure 2-1 [40,41]. A slurry consisting of solid ceramic and/or metallic powders, solvents, dispersants, binders, and plasticizers is poured into a casting block with a "doctor blade." From the casting block, the doctor blade meters out the slurry deposited on the carrier film and controls the thickness of the tape with an adjustment of the doctor blade height. Although the width of the tape is determined by the width of the casting block, the length of the tape can be controlled by the amount of slurry available for casting. For this reason, tape casting may be used as a continuous casting operation.

For small scale tape casting operations, the doctor blade moves across a stationary carrier film. Conversely, larger scale operations will use an automatic tape-casting machine that moves the carrier film and fixes the doctor blade. The larger casting machines are often equipped with heaters to assist with evaporating the solvent while drying the tape [40,41]. Once dry, the strong flexible tape may be cut into various shapes and/or laminated to other pieces before firing.

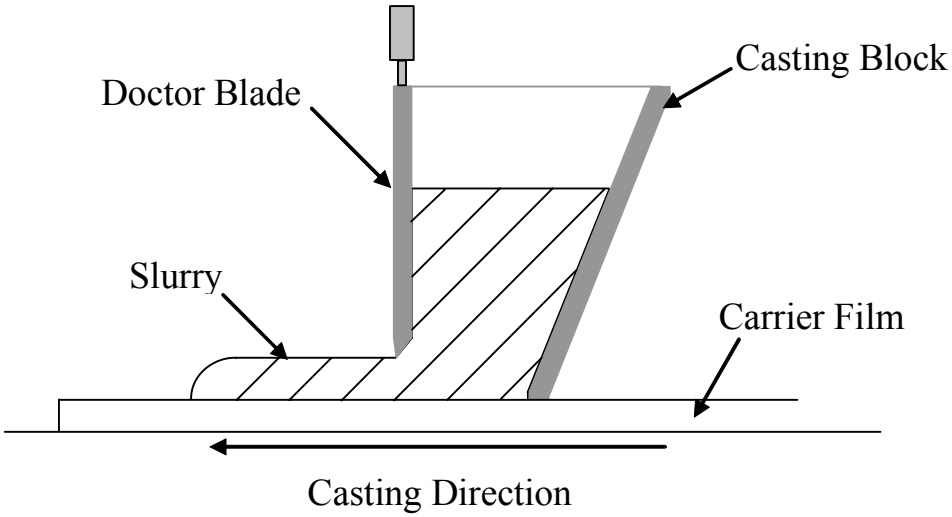

Figure 2-1: Schematic diagram showing the tape casting process

The challenge in tape casting is selecting the proper materials as the quality of the dried tape greatly affects the quality of the finished sintered product. Powders with high surface area are generally used because of their superior sintering characteristics, but tend to clump together to form large clusters called agglomerates. When agglomerates are present, sintering is non-uniform and may cause warping or excessive porosity in the final product.

After selecting the desired solid material to tape cast, the most important consideration is the choice of the binder/plasticizer/dispersant system [42]. Binders give the tape its strength and bind the solids together after the solvents have evaporated, while dispersants improve the solid material loading and keep the powders in a stable suspension. Solvents are added to dissolve the dispersant, binder, and plasticizer and to distribute the materials evenly throughout the slurry.

Good binders will form a tough, flexible film when dried, burn cleanly with little residual ash, remain stable during storage, and dissolve easily in inexpensive, volatile, non-flammable solvents. Common binders include: polyvinyl acetate, polyvinyl chloride, polystyrene, and polyvinyl butyral. For tapes thicker than 0.25 mm, polyvinyl butyral with alcohols and toluene are commonly used while more volatile solvents, like acetone, are necessary for thinner tapes. Plasticizers are added to improve the flexibility and toughness of the dried tape but they may also reduce its strength [41,43,44].

A dispersant, such as Menhaden fish oil, is typically a moderately long-chained organic molecule that is slightly polar in nature. During ball milling powder agglomerates are broken up, and one end of the polar dispersant molecule is attracted to the powder surface and attaches itself there. In this way, the dispersant physically separates the powders and prevents the powders from re-agglomerating. With dispersants added, the viscosity of the slurry is lowered through increased mixing of the solid powders and leads to better tape casts.

Having selected the appropriate materials, slurries are prepared by mixing the solvents and dispersant first. Then the solid powder material is added to a jar mill before milling for 4 to 24 hours. The milling assists with the break up of hard particles and agglomerates and ensures that the powder and dispersant are well mixed.

After dispersion milling, the plasticizer followed by the binder are added to the slurry. The binder and plasticizer should be added separately from the dispersant to avoid competition for the solid powders which could lead to a reduction in the dispersion of the powder agglomerates and poor slurry mixing. To aid mixing, the binder and plasticizer are sometimes pre-dissolved before being added to the slurry. Regardless, the slurry is milled for another 12 to 24 hours.

Once milling is complete, any entrapped air which negatively affects the quality of the dried tape is removed by slow rotation of the jar mill or by stirring the slurry under a vacuum. After de-airing, the slurry is ready to be cast. A filtration step may be added to remove any milling media debris, undissolved binder or larger agglomerates for thin defect free tapes [41].

2.1.2 Use of Pore Forming Agents

The idea of adding pore forming agents to generate porosity in ceramics and metal/ceramic particles is relatively new. Corbin et al. [45,46] examined how adding corn starch, graphite and polyethylene particles to tape casting slurries of YSZ affected the porosity and sintering behaviour of YSZ. In general, the volumetric sintering shrinkage was not affected by the addition of pore forming agents and the amount of porosity generated was equivalent to the volume of pore forming agent material added. Corbin et al. [39] also studied the sintering behaviour, electrical conductivity, and thermal expansion behaviour of Ni/YSZ composites made from nickel coated graphite particles. The results from this body of research are discussed in more detail in the following sections.

Other researchers have explored how pore forming agents affect various properties and the electrochemical performance of the anodes. Lee et al. [47] looked at the influence graphite pore formers have on the electrical conductivity of Ni/YSZ composites, while Haslam et al. [48] determined that adding rice starch was effective in reducing polarization losses and the optimal rice starch loading was approximately 20 wt%. Another pore forming technique was developed by Moon et al. [49] where water based slurries were freeze-dried to produce radially aligned pore channels in a tubular Ni/YSZ anode.

2.1.3 Sintering Characteristics

In order to build a useful anode from powder materials, it is necessary to sinter the powders together to give the anode strength. Sintering by definition is a process in which a powder compact is made strong and dense through heating to high temperatures [44]. While a few studies have examined how sintering temperature affects the properties and electrochemical performance of the anode [19,28,50], very little research explicitly investigating the sintering characteristics of Ni/YSZ composites is presented in the literature. One study by Matsushima et al. [51] examines the sintering characteristics of NiO/YSZ composites made from commercial NiO and YSZ powder and pre-calcined YSZ powder. NiO/YSZ composites with weight fractions of NiO ranging from 30 wt% NiO to 60 wt% NiO were sintered in a dilatometer by heating to 1500°C at 15°C/min. While the relative particle sizes of each of the powders used was not given, the composites shrunk less with increasing NiO loadings. Pure YSZ samples were found to linearly shrink approximately 27% while the pure NiO samples had linear sintering shrinkages of 16%.

Another study, by Marinsek et al. [29], examined the densification and linear sintering shrinkage of NiO/YSZ anodes made from NiO/YSZ composite powders developed through a gel-precipitation method. Dry pressed anode samples, with NiO loadings ranging from 100% NiO to 100% YSZ, were sintered in air by heating to 1300°C and holding for two hours. Unlike the study by Matsushima, the composites with the highest NiO loadings also had the highest linear sintering shrinkage. For

example, the 100% NiO samples were found to shrink the most with a linear sintering shrinkage of 19% while the 100% YSZ samples had the lowest linear sintering shrinkage at 10%. The reason for the discrepancy in the sintering shrinkage data may be attributed to the change in density during sintering. The 100% NiO samples reached a relative density of 96% after sintering from a green density of 51% compared to the 100% YSZ samples which only achieved a relative density of 63% after sintering from a green density of 45%. The linear sintering shrinkage of the 100% YSZ samples could have been higher had they sintered to full density like the 100% NiO. Similarly, the composite anodes made with higher NiO loadings also achieved higher relative densities after sintering. The linear sintering shrinkages for the NiO/YSZ composites ranged from 15.7% for the lowest NiO loading (18 wt% NiO) with a relative density of 90% to 18.8% for the highest NiO loading (94 wt% NiO) with a relative density of 96%. It is not clear why the relative density of each of the samples is so different, but it may be a result of the inconsistent processing methods used to create the various anode samples. For instance, some samples were prepared at a temperature of 10°C with methanol while others were prepared at 97°C using water.

Lastly, Corbin et al. [39] examined the properties, including the sintering characteristics, of tape cast Ni/YSZ composites made from nickel coated graphite particles. In this study, a series of Ni/YSZ composites with varying nickel and graphite loadings (9 vol% Ni to 49 vol% Ni of total solids) were sintered in air for two hours at 1475°C. By increasing the nickel content (and subsequently the graphite loading) in the composite, the volumetric and linear sintering shrinkages decreased from 57% to 35% and 17% to 10% respectively. Conversely, when uncoated graphite was added to pure YSZ, the sintering shrinkage did not change. The decrease in sintering shrinkage was attributed to the nickel coating on the graphite particle since plain graphite did not affect the sintering behaviour.

2.2 ELECTRICAL CONDUCTIVITY MEASUREMENTS

Many researchers have measured the electrical conductivity of NiO/YSZ composites made with varying amounts of nickel oxide powder at different temperatures [2,19,39,52,53,54]. Dees et al. determined that the minimum nickel oxide loading in the composite for sustained electrical conductivity is 30 vol% NiO of total solids for tape cast NiO/YSZ anodes as expected based on percolation theory [52]. According to percolation theory, below a critical volume fraction of nickel, the electrical conductivity of a NiO/YSZ composite will be similar to the electrical conductivity of YSZ, while above the critical volume fraction of nickel the composite will have electrical conductivities that are closer to that of nickel. A more detailed discussion relating to percolation theory is given in the next section (Section 2.2.1).

Most electrical conductivity measurements presented in the literature were taken at elevated temperatures where the electrical conductivity is much lower than at room temperature. In general, a Ni/YSZ composite made from nickel oxide powder has an electrical conductivity ranging between 500 S/cm and 1000 S/cm at 1000°C [1,55]. Although not as common, electrical conductivity data measured at room temperature is given in the literature. For example, Simwonis et al. created a composite (56 wt% NiO, unknown porosity) that has an electrical conductivity of 3900 S/cm at 25°C and 650 S/cm at 900°C [53].

In experiments conducted by Corbin et al. the electrical conductivity of tape cast composites made from nickel coated graphite particles with varying nickel loadings was measured. The room temperature electrical conductivity for the NiGr-29 composite (29 vol% Ni of total solids) and the NiGr-49 composite (49 vol% Ni of total solids) are 2747 S/cm and 11,034 S/cm respectively [39]. Compared to other Ni/YSZ composites, the NiGr/YSZ composites showed a lower nickel critical

percolation threshold due to a larger "effective" nickel volume due to the removal of graphite during processing.

Other unique Ni/YSZ composite anodes were created from nickel coated YSZ particles by Hu et al. using a powder metallurgy technique [56]. The electrical conductivity of the composites, having a wide range of nickel loadings, was measured at room temperature. The composites with nickel loadings of 14 vol% Ni, 26 vol% Ni, and 49 vol% Ni of total solids, and porosities ranging from 20-30%, exhibited electrical conductivities of 57 S/cm, 2382 S/cm, and 16,900 S/cm respectively.

In a study that examines the role pore forming agents have on the electrical conductivity of porous Ni/YSZ composites, Lee et al. [57] investigated the impact anisotropic NiO/YSZ composite microstructures have on the electrical conductivity of the composite. Two sets of composites were created, one method involved mixing NiO and YSZ powders prepared by spray drying and adding plate graphite particles, while a liquid condensation process was implemented to create another more uniform composite microstructure. After measuring the electrical conductivity of the composites in two orthogonal directions (perpendicular and parallel to the anode surface) it was determined that the composites with graphite additions had electrical conductivities that were dependent on the direction measured. The electrical conductivity ranged from 500 S/cm to 600 S/cm at elevated temperatures (600°C to 1000°C) in the direction perpendicular to the composite surface, and only 100 S/cm parallel to the composite surface. The difference in the electrical conductivity was associated with the higher porosity and poor nickel-to-nickel contacts in the parallel direction due to the graphite additions. Conversely, the composite created from the liquid condensation method showed higher electrical conductivities (1900 S/cm to 1400 S/cm from 600°C to 1000°C) that were independent of the direction measured.

2.2.1 Percolation Theory

Percolation theory is a mathematical model used to describe the formation of long-range interconnected networks within a very large system [58,59,60]. In terms of electrical conductivity, percolation theory may be used to describe the transition from an insulating network to a conducting network within a composite material when a lattice of insulating particles is randomly replaced by conducting particles. Percolation theory is important when determining the electrical conductivity of particulate composites since the amount and distribution of the conducting phase within an insulating matrix will greatly influence the electrical conductivity of the composite.

A powder compact of particles can be approximated by a regular array of particles at particular lattice sites, as shown in Figure 2-2. The probability, p, that a lattice site is occupied by a conducting particle increases as the number of conducting particles in the lattice increases. A cluster of conducting particles forms when more than two adjacent lattice sites are occupied by conducting particles. Eventually enough conducting particles will combine to form a cluster large enough to span the entire lattice, called the percolation threshold, p_c. The percolation threshold indicates the emergence of this lattice spanning percolation cluster which corresponds to the transition from an insulating network to a conducting network.

The formation of a percolated network is shown in Figure 2-2 where the probability of a conducting particle occupying a site (heavy dots) increases from p = 0.25 to 0.5 to 0.75. Although not shown in the figure, initially the entire lattice is blank and without heavy dots to represent a lattice free of conducting particles. As more and more conducting particles replace insulating particles, the lattice begins to fill with heavy dots (Figure 2-2a). Clusters begin to form and grow with further increases in the number of conducting particles because the number of adjacent conducting particles rises (Figure 2-2b). Eventually, at a probability of p = 0.75 a spanning percolating cluster is visible (Figure 2-2c).

In fact, the percolation threshold for this particular example in Figure 2-2 is p = 0.59, corresponding to site percolation on a square lattice in two dimensions as calculated analytically [58]. As the probability of an occupied site increases to p = 1, the entire lattice depicted in Figure 2-2 will ultimately consist of heavy connected dots representing a lattice containing only conducting particles.

Despite the formation of a conducting network at the percolation threshold, the electrical conductivity of the composite network is still quite low. This low conductivity is a result of some of the conducting particles forming "dead-ends" and not contributing to the conductivity of the composite even though they are connected to the spanning cluster. For example, in Figure 2-2c, sites in the bottom left and right corners and the centre sites at the top of the lattice will not conduct electricity because they are not part of a closed conducting loop. When more lattice sites become occupied, the electrical conductivity of the network dramatically increases as some of the previous dead-end clusters are now able to conduct electricity.

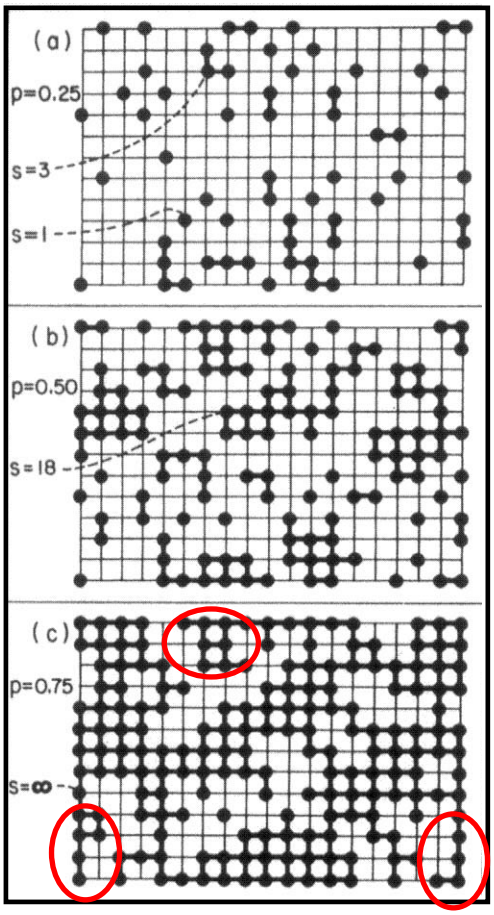

Figure 2-2: The formation of a percolating network when the probability of a lattice site containing a high conducting material (heavy dots) changes from a) 25%, b) 50%, to c) 75%. Heavy lines represent a bond to an adjacent conducting lattice site, and "s" indicates the cluster size with the percolating cluster having infinite size [58]

Although percolation theory is primarily derived from regular lattice structures, it can also be applied to a random continuum material. The percolation threshold can be determined by the following equation [58,59]:

$$\phi_c = \nu p_c \tag{2-1}$$

where ϕ_c is the critical volume fraction representing the fraction of total space occupied by the conducting material, ν is the filling factor of the lattice corresponding to the packing of equal, touching, non-overlapping spheres centred on lattice sites, and p_c represents the percolation threshold. The critical volume fraction is approximately independent of the lattice structure and varies depending on the dimensions of the system. For instance, the critical volume fraction for a two dimensional random continuum material is 0.45 and 0.16 for a three dimensional random continuum material with equal sized spherical particles.

Equation (2-1) has been used to predict the percolation threshold of a random closed packed system, such as a beaker filled with similar sized spheres of conducting and non-conducting material. In this illustration, varying ratios of conducting (aluminum) to non-conducting (glass) spheres are randomly placed within a glass beaker simulating a random close-packed structure. (See Figure 2-3.) At the top and bottom of the beaker are two aluminum foil electrodes that are connected to a power source and an ammeter. If there is a sufficient number of conducting spheres then a current will be measured. The percolation threshold is observed when the fewest number of conducting spheres begin to conduct electricity.

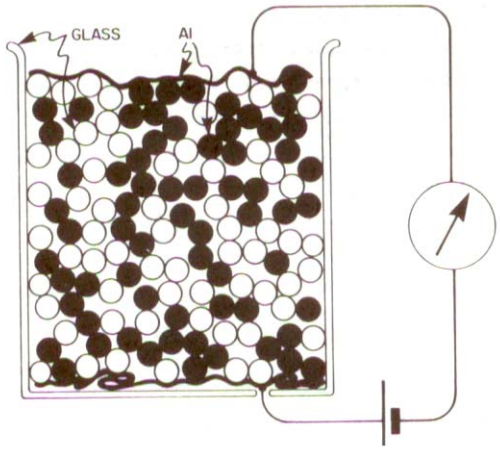

Figure 2-3: Example of Percolation in a Random Close-packed structure [59]

Using the critical volume fraction corresponding to a three-dimensional space (ϕ_c = 0.16), and the approximate packing factor of ν = 0.6 for a random closed packed structure, the percolation threshold is found to be 0.27 from Equation (2-1). This means that 27% of the solid volume contained in a beaker must be made of the conducting spheres in order for the system to posses a measurable electrical conductivity [58].

Nevertheless, the percolation threshold can be altered significantly by modifying the shape and size of the conducting particles. For instance, critical volume fractions (ϕ_c) of 1% and 60% were measured experimentally for several composite materials [61,62]. The percolation threshold changes because the size and the shape of the particles will affect the distribution and the packing of each phase within the composite. When the size of the conducting particles decreases relative to the size of the insulating particles the percolation threshold decreases because the smaller conducting particles tend to fill the voids between the larger insulating particles [61,63]. The lowest percolation threshold is achieved when the conducting particles are sufficiently small to form a coating on the insulating particles as shown in Figure 2-4a. As a coating, the conducting phase completely isolates the insulating phase and is free to form a percolating network. In this case, the critical volume fraction is approximately 3% [62].

By the same argument, the percolation threshold of a composite can be dramatically increased if the conducting particles are much larger than the insulating particles. In this scenario, the insulating particles can form a coating on the conducting particles thereby isolating the conducting particles from one another as shown in Figure 2-4b. When the conducting particles are completely isolated then there is no percolating path and the composite no longer conducts electricity.

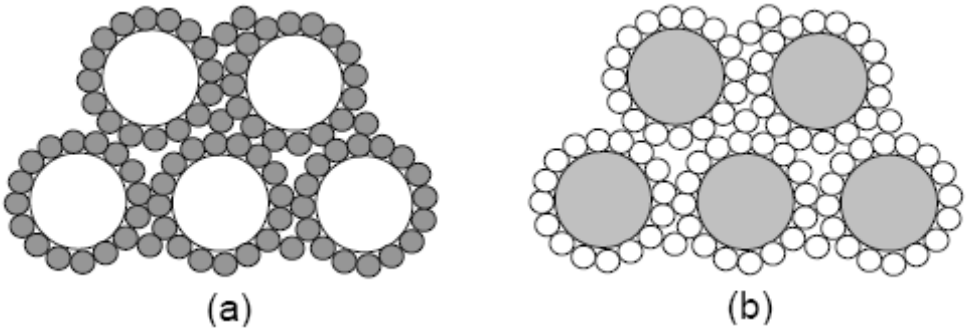

Figure 2-4: Distribution of particles when the conducting particles (grey) are a) smaller and b) larger than the insulating particles (white)

The determination of the percolation threshold is further complicated when the shape of the constituent particles is non-spherical. Particles with an elongated geometry, such as long conducting fibres, feathery particles, or other geometries that improve the particle to particle contact within the conducting phase will also reduce the percolation threshold [61]. Elongated particles can sweep out a larger volume compared to a spherical particle thus increasing the probability of contacting another particle. For example, Carmona et al. investigated the electrical conductivity of carbon-polymer composites made with carbon particles and carbon fibres. They found that the critical volume fraction for electrical conductivity is 15.5% for the composites made with carbon particles and 0.24% to 1.1% for composites made with carbon fibre [64].

2.3 THERMAL EXPANSION BEHAVIOUR

Compared to the number of investigations relating to the electrical conductivity of composite Ni/YSZ anodes, there are few investigations of the thermal expansion behaviour of these composites. Since nickel has a higher coefficient of thermal expansion than YSZ, it is generally accepted that the coefficient of thermal expansion of the composite increases with increasing nickel loading [2,65,66].

In two different studies, Mori et al. [65] and Muller et al. [67] investigated the thermal expansion behaviour of oxidized and reduced Ni/YSZ composites. Mori et al. prepared NiO/YSZ composites with varying nickel loadings by die pressing ball milled powders and sintering them in air for 5 hours at 1500°C. After measuring the coefficient of thermal expansion of the composites with nickel oxide, the composites were reduced in a humidified hydrogen atmosphere. The measured coefficient of thermal expansion from 50°C to 1000°C for Ni/YSZ composites with a nickel loading of 30 vol% Ni and 50 vol% Ni of total solids was 11 x 10^{-6}/°C and 12 x 10^{-6}/°C respectively. In addition, the measured thermal expansion of pure nickel was 16.9 x 10^{-6}/°C. In the study by Muller et al., anodes with nickel loadings of 36 – 73 vol% Ni of total solids were prepared by die pressing NiO and YSZ powders with various particle size ratios and then sintering the compacts in air at 1300°C and 1400°C for 5 hours. The coefficient of thermal expansion was measured using a Netzsch 402C dilatometer in both air and a reducing atmosphere consisting of 6% hydrogen and the balance nitrogen. While a minimum coefficient of thermal expansion of the oxidized composites was achieved when the NiO to YSZ particle size ratio was 3:2, there was no clear relation between particle size ratio and the coefficient of thermal expansion after the composites were reduced. In fact, due to an unspecified variability in the measurements, the reduced composites samples with a nickel content of 73 vol% Ni had a CTE (temperature range not specified) greater than 13.7 x 10^{-6}/°C and the composite samples with a lower nickel loading had a CTE less than 12.8 x 10^{-6}/°C. Muller et al. also found that the composite samples sintered at 1400°C had a slightly higher CTE compared to the composites sintered at 1300°C.

The thermal expansion behaviour of composites made with unique nickel particles was also investigated by Corbin et al. [39] and Hu et al. [66]. Corbin et al. studied the thermal expansion behaviour of tape cast composites made from nickel coated graphite particles. The measured CTE (25°C to 1000°C in nitrogen-5% hydrogen atmosphere) for a NiGr/YSZ composite with a nickel loading of 29 vol% Ni and 49 vol% Ni of total solids is 11.64 x 10^{-6}/°C and 11.87 x 10^{-6}/°C respectively, which is higher than the CTE predicted by the rule of mixtures,. The higher CTE values for the NiGr/YSZ composites were attributed to the "lower constraint imposed on the nickel by the YSZ due to the porous nature of the composite." That is, the nickel phase was permitted to expand more freely because of the degree of porosity contained in the YSZ matrix.

In the investigation by Hu et al. the coefficient of thermal expansion of Ni/YSZ composites, with a wide range of nickel loadings were created from nickel coated YSZ particles, was measured from room temperature to 950°C in a dilatometer. Since the atmosphere used to measure the thermal expansion behaviour is not given, it is difficult to determine if the thermal expansion data is for the oxidized or reduced Ni/YSZ composites. The estimated CTE from 13.5°C to 950°C for Ni/YSZ composites with a nickel loading of 26.2 vol% Ni, 49.5 vol% Ni, and 72.3 vol% Ni is 12.05 x 10^{-6} 1/K, 12.35 x 10^{-6} 1/K, and 12.65 x 10^{-6} 1/K respectively. The measured CTE of pure nickel from 13.5°C to 950°C by Hu et al. is 13.0 x 10^{-6} 1/K which is lower than the published CTE value for nickel (16.3 x 10^{-6} 1/K from 20°C to 900°C) [24] and nickel oxide (14.2 x 10^{-6} 1/K from 50°C to 1000°C)

[65]. In addition, equations used to fit the thermal expansion data over a range of temperatures predict CTE values that are about 3 orders of magnitude greater than the published values.

In the only studies found examining the influence porosity has on the CTE of metal/ceramic composites, Shen modeled the thermal expansion behaviour of Al/SiC composites with and without voids [68,69]. While the thermal expansion behaviour of Al/SiC composites is expected to be quite different than the thermal expansion behaviour of porous Ni/YSZ composites due to the very different elastic properties of each phase, the study does offer some insights into the effect porosity has on the CTE of a metal/ceramic composite. When aluminum was assumed to be a continuous rectangular fibre embedded into a silicon carbide matrix, the composites contracted more during cooling when the aluminum phase was pore free compared to the composites with pores located in the concave corners. It was reasoned that the presence of pores reduced the local constraint on the aluminum phase and enhanced local deformation [68]. In contrast, when silicon carbide fibres with a cross shaped cross-section was embedded into an aluminum matrix, the presence of pores had little effect on the thermal expansion of the composite since the aluminum was constrained less by the silicon carbide [68].

2.4 CURRENT STATE-OF-THE-ART ANODE

The current state-of-the-art anode is typically tape cast and prepared from nickel oxide and yttria-stabilized zirconia powders with an approximate nickel loading of 30 to 35 vol% Ni to total solids. Porosity in the conventional anode is controlled by the amount of sintering and the transformation of nickel oxide to nickel after reduction. Since nickel oxide is less dense than nickel metal, the volume of space occupied by the nickel will be lower leading to the formation of 20% to 40% porosity. In addition, the electrical conductivity of an anode containing 30 vol% Ni and 30 vol% porosity is approximately 500 S/cm at 1000ºC while the coefficient of thermal expansion of a similar anode is around 12.5 x 10^{-6} 1/K [1]. Finally, the microstructure of a conventional anode is given in Figure 2-5 where the white, light grey, and dark regions are Ni, YSZ, and porosity respectively.

While the current anode construction gives acceptable properties and performance, there are a few drawbacks associated with using Ni/YSZ composite anodes. The most significant disadvantage to using nickel as an anode material is its tendency to coarsen and agglomerate with time, leading to a reduction in fuel cell performance [19,25]. The agglomeration of nickel can also impact the ability of the anode to withstand multiple oxidation and reduction cycles of the nickel phase. Since nickel expands when oxidized, the larger nickel agglomerates may significantly damage the cell if the anode were to oxidize due to disruptions to the fuel supply [38]. Resistance to thermal cycling is another important consideration especially when powering up and shutting down the fuel cell stack. Also, nickel is an excellent catalyst for cracking hydrocarbons. During operation of a SOFC using hydrocarbon based fuels, carbon deposits can form on the nickel reducing the cell performance and eventually destroying the nickel microstructure [21].

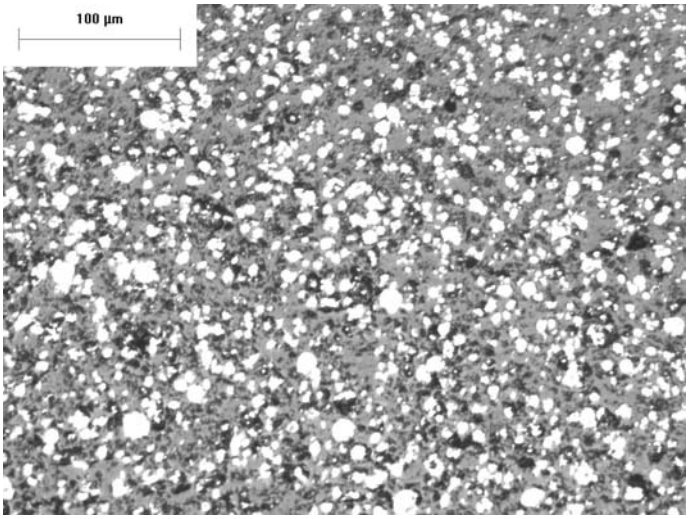

Figure 2-5: Sintered & reduced conventional anode microstructure made from NiO and YSZ powders

2.5 RESEARCH OBJECTIVES

The current Ni/YSZ anode research has focussed almost exclusively on nickel oxide and YSZ based composites with a very narrow range of nickel loadings. The nickel content of the anodes has been limited because a minimum nickel loading is required for sufficient electrical conductivity while, too high a nickel loading will yield an adverse coefficient of thermal expansion. Similarly, the formation of porosity has been restricted to controlling the degree of sintering in the composite and the reduction of nickel oxide to nickel metal.

Given that alternatives to the Ni/YSZ composite anode are still in development, it is worthwhile to investigate methods of improving the existing technology. Through the use of different nickel morphologies, it may be possible to lower the nickel percolation threshold thereby reducing the minimum amount of nickel required. Similarly, introducing pore forming agents to engineer porosity into the composite could lead to improved electrochemical performance. In order to construct working cells with a new anode technology it is also important to understand how changing the starting materials can affect the processing characteristics of the composite anode.

Despite all the research relating to the development of Ni/YSZ composite anodes, there are still some areas that can be improved upon. Specifically, there have been few researchers that have developed Ni/YSZ composite anodes from non-nickel oxide based materials. In fact, not one study was found where regular nickel metal powder was used to form the anode and since nickel powders with unique morphologies are commercially available, the feasibility of their use in SOFC applications is important to explore [70]. Furthermore, the literature fails to provide a clear understanding of how nickel loading affects the sintering characteristics of Ni/YSZ composite anodes. Finally, little research has been conducted to determine how adding pore forming agents, such as graphite, will affect the processing and properties of the anode. Therefore, the objective of this research is to systematically study the sintering characteristics, electrical conductivity, and thermal expansion behaviour of tape cast Ni/YSZ composite anodes created with nickel oxide, nickel metal, or nickel coated graphite particles with varying amounts graphite added as a pore forming agent.

CHAPTER 3:
EXPERIMENTAL METHODS

3.1 TYPES OF COMPOSITE NI/YSZ ANODES

Several different composites were created with varying nickel and graphite loadings in order to determine the effect that porosity and nickel distribution have on the sintering characteristics, electrical conductivity, and thermal expansion behaviour of nickel/YSZ composites. In this investigation there were five basic types of composites made from:

1) Nickel and YSZ powders	(Ni/YSZ)
2) Nickel coated graphite and YSZ powders	(NiGr/YSZ)
3) Nickel, graphite, and YSZ powders	(Ni&Gr/YSZ)
4) Nickel oxide and YSZ powders	(NiO/YSZ)
5) Nickel oxide, graphite, and YSZ powders	(NiO&Gr/YSZ)

The various nickel and graphite loadings for each of the nickel based composites are shown in Figure 3-1. The first composite type consists entirely of nickel and yttria-stabilized zirconia powders with no graphite additions. The nickel loadings vary from 4 vol% Ni of total solids to 77 vol% Ni of total solids and appear on Ni/YSZ axis only. When nickel coated graphite particles are used to create the composites, the nickel loading and graphite loading increase simultaneously with a fixed Ni:Gr volume ratio of 24:76, as indicated in Figure 3-1. To compare the effects of the nickel coating on the properties of the composites, another series of composites made from separate nickel and graphite particles with the same nickel and graphite loadings was created. Since the nickel and graphite loadings are the same as the NiGr/YSZ composites, the Ni&Gr/YSZ composites appear on the same line as the NiGr/YSZ composites in Figure 3-1. While not shown in Figure 3-1, the nickel loadings for the composites made with nickel oxide powder, after the nickel oxide has been reduced, are the same as the composites made from nickel powder. Therefore, the NiO/YSZ and NiO&Gr/YSZ composites have the same composition as the Ni/YSZ and Ni&Gr/YSZ composites respectively.

To further understand the effects graphite may have on the processing and properties of the anode, another set of composites were created with a fixed nickel loading and varying graphite content. These composites were made from:

1) Nickel, graphite, and YSZ powders with a nickel loading of 27 vol% Ni of total solids - (Ni&Gr-27/YSZ)
2) Nickel, graphite, and YSZ powders with a nickel loading of 47 vol% Ni of total solids - (Ni&Gr-47/YSZ)
3) Nickel oxide, graphite, and YSZ powders with a nickel loading of 27 vol% Ni of total solids - (NiO&Gr-27/YSZ)
4) Nickel, graphite, and YSZ powders with a nickel loading of 47 vol% Ni of total solids - (NiO&Gr-47/YSZ)

Again, the nickel and graphite loadings of the various nickel based composites are shown in Figure 3-1, with the nickel oxide based composites having similar nickel and graphite loadings. For the Ni&Gr-27/YSZ composites, the nickel to YSZ volume fraction was fixed at 27:73. The amount of separate graphite powder added to create the composites was a fraction of the amount of graphite used to create the NiGr/YSZ and Ni&Gr/YSZ composites at the same nickel loading. The amount of graphite added to the Ni&Gr-27/YSZ composite ranged from 30 wt% to 90 wt% of the graphite added to create the Ni&Gr/YSZ composite. Similarly, the Ni&Gr-47/YSZ composites had varying amounts of graphite added; however, the nickel to YSZ volume ratio was fixed at 47:53.

To summarize, the different composites created will allow comparisons to be made between nickel based and nickel oxide based composites to determine how starting with nickel powder affects the processing and properties of the anode. The effect of adding nickel coated graphite particles may be ascertained by comparing the NiGr/YSZ composite properties to composites with similar uncoated graphite loadings. Finally, the effect graphite additions have on the properties of the composite may be more clearly understood when the nickel loading of the composites is fixed.

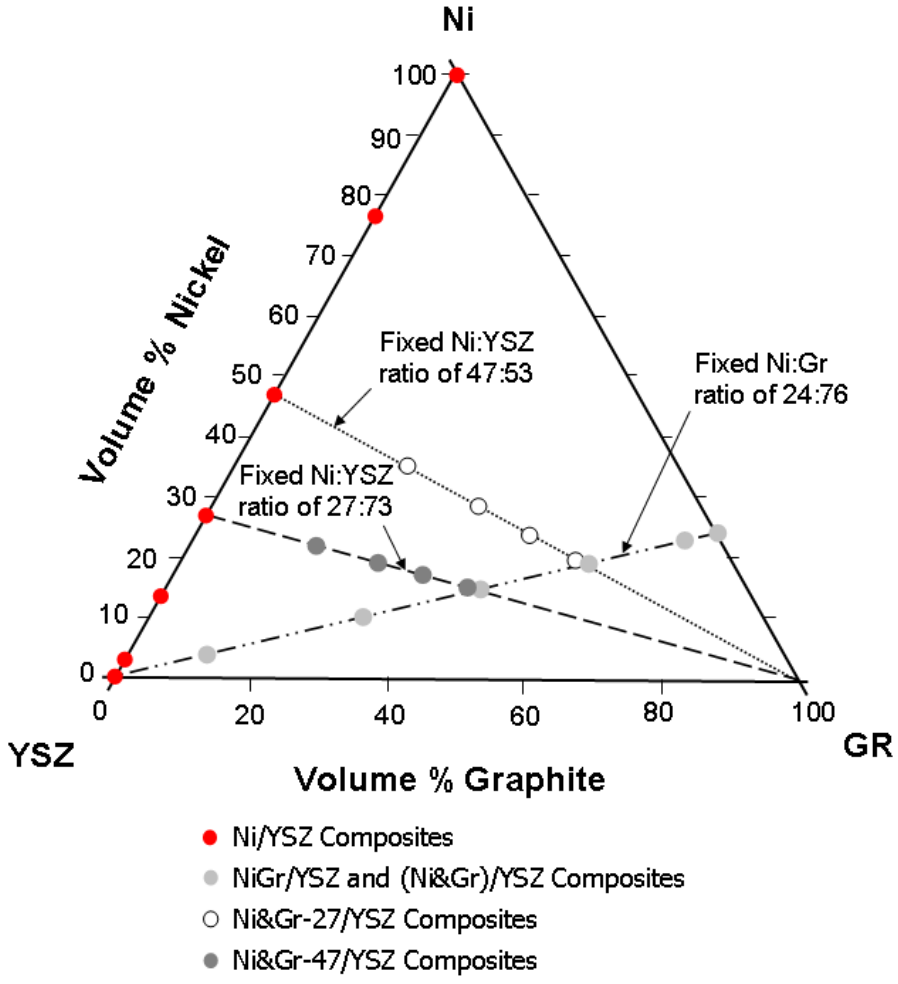

Figure 3-1: Schematic ternary plot depicting the compositions of the various Ni/YSZ composites investigated [71]

3.2 COMPOSITE FABRICATION/PROCESSING

There are a number of steps required to prepare the desired composites before any property measurements can be done, as shown in Figure 3-2. First, the appropriate tape casting slurries are to be prepared before the composites are tape cast. After casting, samples are prepared by laminating several layers together and then heated through a burnout, sintering and reduction stage. Once the samples are sintered and reduced, the electrical conductivity and coefficient of thermal expansion may be measured.

3.2.1 Composite Tape Casting Formulations

The powders that were used to create the composite samples are: 8-mole% yttria-stabilized zirconia (YSZ), nickel metal powder (Ni), graphite powder (Gr), nickel coated graphite powder (NiGr), and/or green nickel oxide (NiO) powder. These powders were then mixed with polyvinyl butyral, butyl benzyl phthalate S-160 Type I plasticizer, Menhaden fish oil, ethanol and toluene to form tape casting slurries. The properties of the solid material and organic constituents are shown in Table 3-1 and Table 3-2 respectively. All composite formulations were prepared such that each composite type (i.e. Ni/YSZ, NiGr/YSZ, Ni&Gr/YSZ, NiO/YSZ, and NiO&Gr/YSZ) would have identical nickel loadings as a fraction of the total solids (i.e. Ni and YSZ) in the final sintered and reduced state.

For tape casting to be successful, several ratios between the ingredients must be considered. For example, the amount of solvent added must be sufficient to produce slurries with viscosities that are neither too low nor too high. If the viscosity of the slurry is too low, the cast tape will not hold its shape and flow freely on the carrier film. Conversely, if the slurry viscosity is too high, it will not easily flow from the ball milling jar into the casting block resulting in a poorly shaped tape. Other proportions, such as the ratio of dispersant to solid material, the ratio of solid material to organic material, and the binder to plasticizer ratio must also be carefully controlled.

Table 3-1: Solid material used for each composite type during tape casting

Material	Description	Supplier	Density (g/cm^3)	Nominal Average Particle Size* (µm)
YSZ	8-mole% yttria stabilized zirconia	Tosoh	6.1	1.74
Ni	Nickel metal powder	Alpha Aesar	8.9	17.7
Gr	Graphite, natural briquetting	Alpha Aesar	2.25	77
NiGr	Nickel coated graphite (55 wt% Ni)	INCO	3.82	133
NiO	Green nickel oxide powder, Type A	Novamet	6.8	15.4

*Particle size analysis data is presented in Appendix A

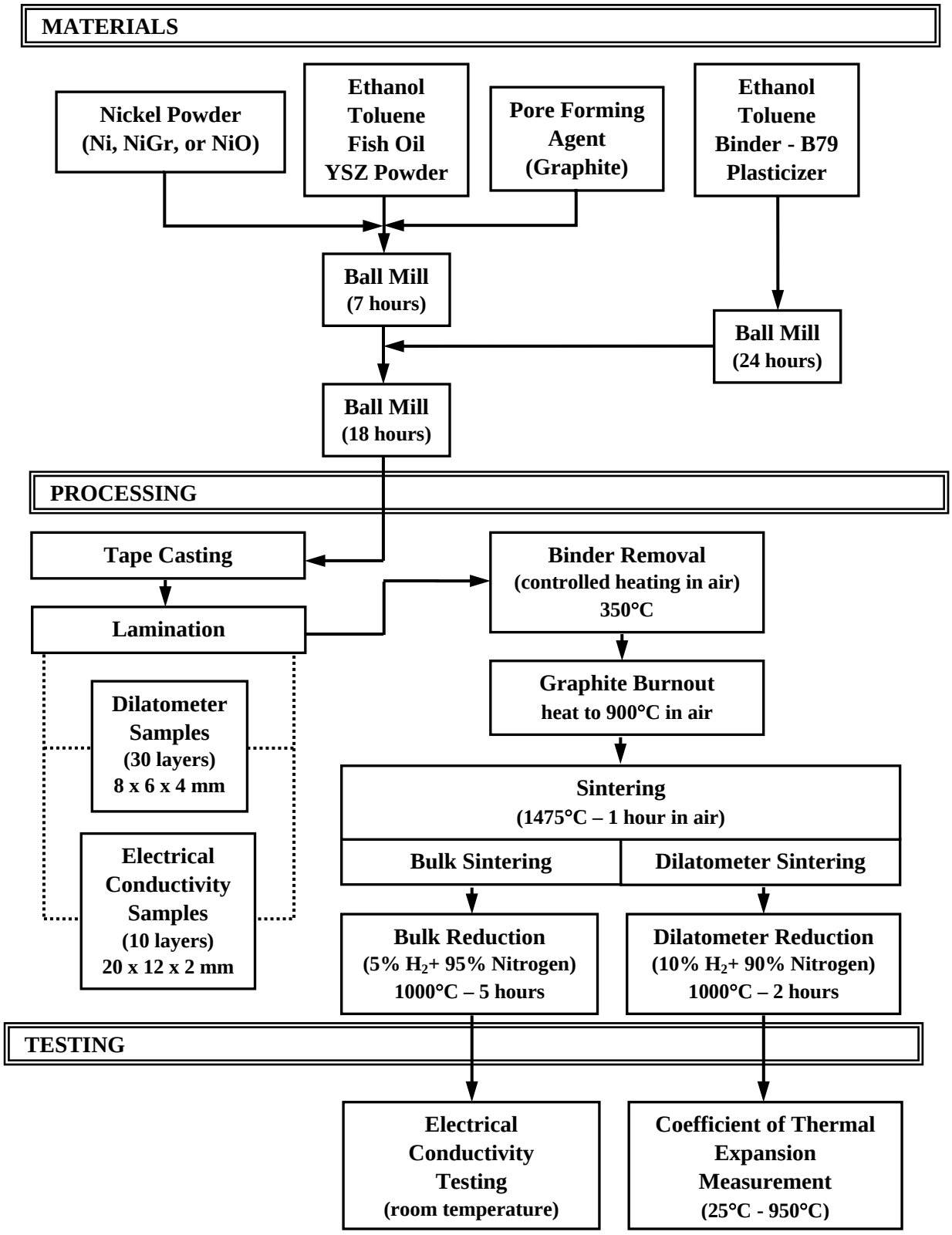

Figure 3-2: Sample preparation sequence

Table 3-2: Organic material used for tape casting

Material	Description	Supplier	Density (g/cm^3)
Ethanol	Bulk ethanol	UW Chem Stores	0.79
Toluene	Bulk toluene	UW Chem Stores	0.87
Fish Oil	Z3 Blown Menhaden Fish Oil	Richard Mistler Inc.	1.00
Polyvinyl Butyral (B79)	Polyvinyl butyral, grade B79	Richard Mistler Inc.	1.10
Santicizer 160	Butyl Benzyl Phthalate S-160 Type I Plasticizer	Richard Mistler Inc.	1.12

3.2.1.1 Monolithic Tapes

A 100% YSZ tape was the first created because, based on previous experiments, it was the most difficult to cast into a high quality tape as early formulations yielded dried tapes that were severely cracked. Through much iteration and many small scale trials, the formulation for a high quality 100% YSZ tape was finally developed as listed in Table 3-3. To achieve a high quality tape, the amount of solvent, dispersant, and polymer material was altered so that the slurry was neither too viscous (difficult to pour) or too thin (slurry would not maintain cast shape). In addition, the formula was adjusted to ensure that the dried tape was defect free (no cracks or pinholes), had sufficient strength for cutting and handling samples, and that the tapes held their shape after laminating several layers together. During the development of the 100% YSZ tape cast formulation, it was discovered that pre-dissolving the binder and plasticizer separately before adding it to the slurry dramatically improved the quality of the final tape by reducing the number of tape defects after drying. The composition of the pre-dissolved polymer solution consisting of binder, plasticizer, ethanol, and toluene used in making the 100% YSZ slurry is shown in Table 3-4.

With the 100% YSZ formulation as a guide, other tape casting slurry formulations for 100% nickel, 100% nickel oxide, 100% nickel coated graphite, nickel & graphite only, and nickel oxide & graphite only were created as a starting point for making other composite tapes. Again, the formulation for each new slurry was adjusted for proper slurry viscosity, minimal dried tape defects, good tape strength, and reasonable lamination characteristics. Each of the formulations, given in Table 3-3, produced a high quality defect-free dried green tape. More than one trial was needed for each new monolithic tape since the different starting powders dramatically changed the characteristics of the slurry. For instance, the graphite powder was considerably less dense compared to the nickel powder, thus requiring significantly more solvent to obtain an appropriate Ni&Gr slurry. Likewise, the amount of dispersant, and polymer material was adjusted depending on the type and volume of material added.

Table 3-3: Slurry Formulations for Selected Anode Types

Monolithic Tape	Mass of Component (g)								
	YSZ	Ni	NiO	NiGr	Graphite	Ethanol	Toluene	Fish Oil	Polymer Solution*
100% YSZ	45.75	-	-	-	-	7.02	10.29	1.00	18.70
100% Ni	-	45.75	-	-	-	3.51	5.14	0.50	4.67
100% NiO	-	-	45.75	-	-	5.27	7.73	0.75	7.00
100% NiGr	-	-	-	45.75	-	6.32	9.26	0.90	24.93
Ni & Gr Only	-	25.16	-	-	20.59	14.04	20.58	2.00	14.03
NiO & Gr Only	-	-	27.86	-	17.89	14.04	20.58	2.00	14.03

*The composition of the polymer solution is shown in Table 3-4

Table 3-4: Formulation for Polymer Solution used for Tape Casting

Material	Polyvinyl Butyral (B79)	Santicizer 160	Ethanol	Toluene
Mass (g)	43.80	81.96	38.40	60.36

3.2.1.2 Composite Tapes

Once the tape cast formulations for the high quality monolithic tapes were established, new composite tapes were easy to prepare. The composite tape cast formulations were created by using a by weight rule of mixtures with the 100% YSZ tape cast formulation and the desired nickel based formulation. For example, in order to make a Ni/YSZ composite containing 70% Ni and 30% YSZ by weight, 70% of the pure Ni monolithic tape cast formulation was mixed with 30% of the pure YSZ monolithic tape cast formulation to get the desired composite. Similarly, the other basic composite types were created by combining the 100% YSZ tape cast formulation with the 100% NiGr, Ni&Gr, 100% NiO, and NiO&Gr formulations.

To cover a wide range of composite structures for testing, five different nickel loadings were used for each of the basic composite types, ranging from 4 vol% to 77 vol% Ni based on total solids in the sintered and reduced state. The tape cast formulation for each composite was adjusted so that every composite type had the same final nickel loading in the sintered & reduced state in addition to having the same total weight of solid material added to the slurry. Therefore, the proportions of the nickel and YSZ were adjusted to accommodate any graphite additions and any extra weight associated with the presence of oxygen contained within the nickel oxide powders. Furthermore, the volume fractions of the constituent materials in the green state may be different for each composite type since the tape cast formulations for each composite required varying amounts of solvent and polymer material to ensure high quality dried tapes. The tape cast formulations for each of the composites investigated are shown in Appendix B.

The NiO&Gr-27/YSZ composites were prepared by combining the tape cast formulation for the NiO/YSZ composite with a nickel loading of 27 vol% Ni and the formulation for the NiO&Gr/YSZ composite at the same nickel loading. These additional composites were created by taking 30%, 50%,

70%, and 90% of the graphite loading used for the NiO&Gr/YSZ tape cast formulation. Thus, six composites with the same nickel oxide loading and varying graphite content were made. Likewise, six composites with varying graphite content were produced from the Ni&Gr/YSZ composites with a nickel loading of 27 vol% Ni and 47 vol% Ni, and the NiO&Gr/YSZ composites with a nickel loading of 47 vol% Ni of total solids. The tape cast formulations for the composites with varying graphite loading are also shown in Appendix B.

3.2.2 Composite Sample Preparation

Once the tape cast formulation for every composite was established, several additional steps were necessary to form the final composite structure. The composite sample preparation sequence is illustrated in Figure 3-2 with the details of each step discussed in the following sections.

3.2.2.1 Tape Casting

Well established colloidal processing techniques were used to prepare a number of tape casting slurries with varying nickel and graphite loadings. To prepare the tape casting slurries, ethanol, toluene, and fish oil were added to a 125 ml nalgene bottle filled one third with 6 mm diameter zirconia milling material. The bottle was then shaken until the fish oil was completely dissolved in the solvents. After the solid material was added, the bottle was shaken again to aid mixing of the slurry and then ball milled for 7 hours at 120 rpm (25% power setting) using a US Stoneware ball mill (model 755RM4). Premixed polymer and solvent solution were added to the slurry, after initial milling, and milled an additional 18 hours at the same speed. Upon completion of milling, the ball mill was turned to the lowest setting (28 rpm) for 2 minutes to de-air the slurry. The 100% YSZ slurries were further de-aired under a fume hood for another 2 minutes.

Before tape casting, a silicone coated mylar sheet was taped to the automatic tape casting belt (Richard Mistler Inc.). A 60 mm casting block, with a doctor blade gap set to 0.5 mm, was placed upon the mylar sheet. Once ready to cast, the casting speed for the automatic tape caster was set to 0.36 m/min (a setting of 60 on the tape caster dial) and the slurry was poured directly into the casting block. When 100% YSZ tapes were produced the slurry was poured into a sieve to filter the slurry before entering the casting block. The filtering step is used to remove any large undissolved polymer, agglomerates, and any entrapped air in order to ensure that the YSZ sinters to full density more readily. After casting, four weights were placed around the tape to prevent curling while the tape dried for a minimum of 16 hours.

3.2.2.2 Lamination

In preparing the composite samples for high temperature dilatometry experiments, 30 rectangular pieces approximately 5 mm x 7 mm were cut from the dried green tape with the length of each piece cut parallel to the casting direction. Similarly, 10 rectangular pieces measuring 10 mm x 18 mm were cut from the green tape to form samples for the electrical conductivity experiments. The cut pieces were then laminated in a die at room temperature with a loading of 5000 lb for the dilatometer samples and 11,000 lb for the electrical conductivity samples using a hydraulic press (Carver Laboratory Press – Model ‘C’). To prevent the laminated pieces from sticking to the die, a small piece of silicone coated Mylar sheet was placed on each die face. After lamination, the dilatometer samples were in a shape of a cube with nominal dimensions of 8 mm x 6 mm and 3 to 5 mm thick, whereas the electrical conductivity samples formed a wafer with nominal dimensions of 12 mm x 20 mm and 2 to 3 mm thick, as shown in Figure 3-3. Each sample was then weighed and its dimensions measured.

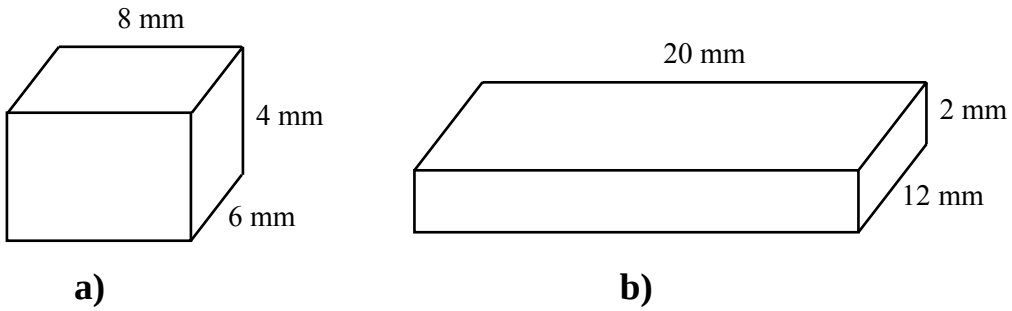

Figure 3-3: Schematic diagram showing the dimensions of a) samples for dilatometer experiments and b) samples for electrical conductivity experiments.

3.2.2.3 Burnout

After lamination, each sample was heated in air with a Thermolyne 6000 Furnace to a temperature of 350˚C in order to remove the organic binder, plasticizer, and fish oil. Heating had to be carefully controlled to prevent blistering, cracking, and delamination caused by the resultant exit gases [39]. The heating schedule used during the first burnout stage is shown in Table 3-5. A second burnout stage was added to remove any graphite, which pyrolyzes in air above 850˚C, and to improve the strength of the samples by pre-sintering them. The heating schedule for the second burnout stage is shown in Table 3-6. After the second burnout stage, each sample was weighed and its dimensions measured.

Table 3-5: Heating profile for the first burnout stage

Segment	Ramp Rate (˚C/min)	Temperature (˚C)	Hold Time (min)
1	2	142	90
2	1	161	90
3	1	190	90
4	1	231	90
5	1	270	90
6	1	310	90
7	1	350	90
8	End: Furnace cool to room temperature		

Table 3-6: Heating profile for the second burnout stage

Segment	Ramp Rate (˚C/min)	Temperature (˚C)	Hold Time (min)
1	10	350	10
2	2	665	15
3	2	900	120
4	End: Furnace cool to room temperature		

3.2.2.4 Bulk Sintering

Bulk sintering runs of several composite samples, placed on alumina foam plates, were carried out in a high temperature box furnace (CM Furnaces). The heating schedule given in Table 3-7, developed from previous investigations, was used because it could achieve a high sintered density in the YSZ phase [39,45,46]. Again, after sintering, each composite sample was weighed and its dimensions measured.

Table 3-7 Heating Profile for Bulk Sintering

Segment	Ramp Rate (˚C/min)	Temperature (˚C)	Hold Time (min)
1	20	900	0
2	5	1475	60
3	20	25	60

3.2.2.5 Bulk Reduction

Since nickel metal oxidizes during the sintering process, a reduction step is required to convert the nickel oxide back into nickel metal if the composites are to act as useable anodes. Bulk reduction runs were carried out in a Thermcraft 3-zone split tube furnace (model 22-20-3ZH) by heating samples to 1000°C for 5 hours in a 7% hydrogen and 93% nitrogen reducing atmosphere. Initially, samples were held at 1000°C for only 2 hours but this did not completely reduce the samples as determined by visual inspection (see below). Consequently, the samples were heated to 1000°C and held for an additional 3 hours which resulted in the complete reduction of the nickel oxide.

For reduction, composite samples were placed in an alumina combustion boat and then placed within a quartz tube inside the tube furnace. Before heating, air was purged from the quartz tube by the hydrogen and nitrogen gas mixture. After purging for several minutes, the samples were heated to 1000°C by setting the furnace controller to 960°C [72]. Heating to 1000°C took approximately 90 minutes and after holding at 1000°C for 5 hours the furnace was turned off by returning the furnace controller to zero. While cooling, the quartz tube could be safely removed from the furnace at about 400°C and allowed to cool to room temperature. Once the quartz tube had completely cooled, the reducing gas was shut off, and the samples were removed. Upon completion of the reduction stage, each composite sample was weighed and its dimensions were measured.

The success of the reduction stage may be quickly assessed through visual inspection. Nickel oxide is green and nickel metal has a dull silver/grey appearance. Before reduction, the anode composites are varying shades of green depending on the nickel oxide content. After reduction, the anodes are varying shades of grey due to the existence of nickel and the darkening of the YSZ. Anodes that are still green or are light grey are not fully reduced. Figure 3-4 depicts some composite samples in the sintered and the sintered & reduced states.

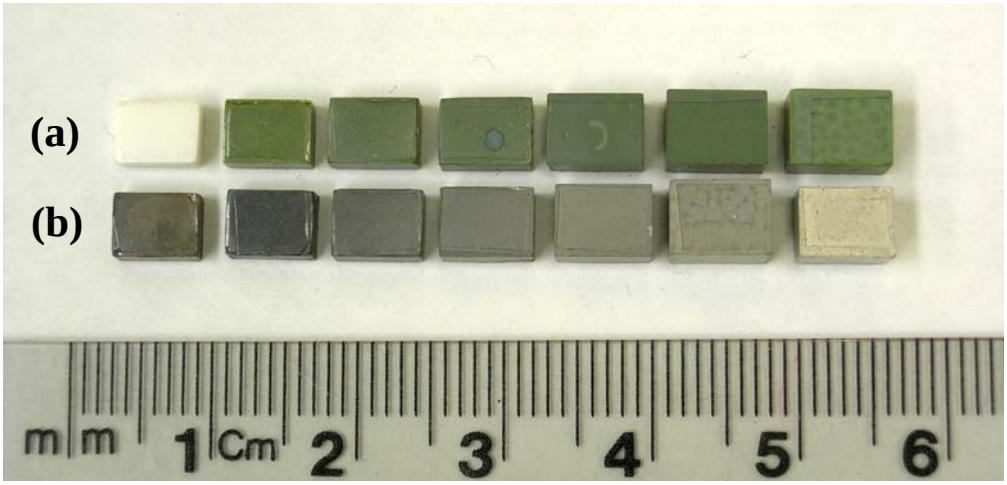

Figure 3-4: Images of NiO/YSZ composite samples in the a) sintered and b) sintered & reduced states. The nickel content increases from 0 vol% Ni (i.e. 100% YSZ) on the left to 100 vol% Ni on the right.

A quantitative estimate of the degree of nickel reduction may also be calculated by:

$$\%\ Reduction = \frac{Theoretical\ Reduced\ Mass}{Sample\ Reduced\ Mass} \times 100\% \tag{3-1}$$

where the sample reduced mass (SRM) is the measured reduced mass for each sample after sintering and reduction, while the theoretical reduced mass (TRM) is given as:

$$Theoretical\ Reduced\ Mass = Pressed\ Green\ Sample\ Mass \times (wt\%\ YSZ + wt\%\ Ni) \tag{3-2}$$

where the pressed green sample mass is the measured weight of the sample in the pressed green state, while the wt% YSZ and wt% Ni are the weight fractions of YSZ and nickel in the green state respectively according to the tape casting formulations of Appendix B. For the composites made from nickel oxide powder, the weight fraction of NiO in the green state was converted into a nickel weight fraction in order to determine the theoretical reduced mass.

When a sample is not fully reduced, the excess oxygen associated with the residual nickel oxide makes the SRM greater than the TRM. As a result, the %-reduction for samples that are not fully reduced will be less than 100%. A %-reduction value that is greater than 100% indicates that the SRM is less than the TRM. The lower SRM may be associated with some material loss during processing, excess polymer material in the green state, or measurement variability.

3.2.2.6 Error Discussion for Sample Weights and Dimensions

After each processing stage, the dimensions and weights of each composite sample were measured using 6" digital vernier callipers (STM - 3 Button Digital Calliper) and a digital scale (Denver Instrument Company - TR-203) with each instrument having a measurement precision of ±0.01 mm and ±0.001 grams respectively. To measure the sample dimensions, several measurements were taken at different locations along the length, width, and thickness of the samples and then averaged. Care was taken to use consistent pressure for each measurement to ensure good contact with the sample while avoiding any significant deformation.

Variability in the measurements can introduce measurement errors, particularly when comparing the weights and dimensions of the samples after each of the processing stages. When the quantities measured are large, they are not affected by the variability in the measurements as greatly as the smaller quantities. For example, with the given calliper tolerances, if the sample has a known length of 8.00 mm, the percent difference between the measured sample and the true length with the given tolerance (i.e. sample measurements of 8.01 and 7.99 mm) is 0.25%. However, if the known length is 2.00 mm, then the percent difference between the measured sample and the true length becomes 1%. Similarly, when a known weight of 1.000 g is measured, the percent difference between the measured sample and the known weight is 0.2%, while the percent difference becomes 0.8% when a standard with a known weight of 0.250 g is measured. Given the range of the sample dimensions and weights measured, the average measurement error associated with both dimensional and weight measurements is approximately 0.5%.

3.3 METALLOGRAPHY/MICROSTRUCTURAL STUDIES

3.3.1 Mounting and Polishing

Metallographic specimens were prepared by placing composite samples in mounting cups and then covering them with a room temperature cold mount epoxy (Struers Specifix-20). To ensure that the epoxy penetrates the porous samples, each mounting cup was placed under a vacuum in a Struers Epovac for 15 minutes. Once the samples cured overnight (~16 hours), they were removed from the mounting cups and ground using silicon carbide grit paper (220 to 600 grit American Standard). Lastly, the samples were polished using a 6 μm permanent diamond suspension followed by a 1 μm alumina slurry. No chemical etching was used to enhance the composite microstructures.

3.3.2 Optical Microscopy

An optical microscope (Olympus – BH2-UMA with Roper Scientific – Photometrics digital camera) was used to examine the polished microstructures of selected composite samples after each processing stage and in the final sintered & reduced state. The microscope is capable of magnifying images between 5 times and 1000 times (IC5 to IC100). Microstructure images were captured through a digital camera and processed using an image analysis software package called Image Pro 4.5 (Media Cybernetics, USA).

The Image Pro software was used to calculate the area fractions of the composite phases in order to estimate the volume fractions of nickel and porosity in the sintered & reduced state. Area fractions were determined from the areas associated with a range of pixels in the picture. White portions of the image had a pixel value of 255, while black portions were assigned a value of 0. Since the nickel

phase in the sintered & reduced state is white, the range of pixels associated with the nickel was typically between 200 and 255 depending on the image. Conversely, porosity in each image was generally black, so the range of pixels associated with porosity was typically between 0 and 100.

A feature of Image Pro allows the user to see what areas are assigned to a particular range of pixels by colouring that range with a single colour. The precise range of pixels associated with each of the composite phases could be adjusted depending on the image quality and verified by observing the coloured areas. Due to the varying shades of grey in the image, it was sometimes difficult to distinctly determine what areas were nickel, YSZ, and porosity. As a result, only the desired phase was measured as a fraction of the total area.

To determine how sensitive the area fractions of a particular phase were to adjustments in the pixel threshold, the range of the pixel values used to calculate the area fractions was adjusted upwards and downwards by five. For example, an image of a Ni/YSZ composite sample with a nickel loading of 14 vol% of total solids showed a porosity area fraction of 20.9% when the pixel threshold was between 0 and 75. However, when the threshold was increased by five to 80, the new porosity area fraction was 24.9%, representing a change of nearly 20%, and typical for the other composite samples. The large variation in area fractions can be attributed to the low contrast between the phases. When the contrast of the image is low, it is more difficult to distinguish between the various phases and the area fractions are more sensitive to variations in the pixel threshold. Conversely, when the contrast is high, there is a narrow range of pixels that correspond to a particular phase making the area fractions less sensitive to variations in the pixel threshold.

3.3.3 Scanning Electron Microscopy

A scanning electron microscope (SEM) gives higher magnification and resolution compared to an optical microscope. Generally, the SEM was used in creating back scatter electron images for estimating the bulk porosity of the sintered & reduced composite samples. The higher detailed images were obtained using an SEM (JEOL – JSM – 6460) and energy-dispersive x-ray spectrometer (Oxford Instruments – INCA).

3.4 ELECTRICAL CONDUCTIVITY MEASUREMENTS

After sintering and reduction, three electrical conductivity samples for each composite type were placed individually into a simple test jig in order to measure their electrical conductivity, as shown in Figure 3-5. To reduce the amount of contact resistance between the samples and the copper terminal blocks, the ends of the composite samples were lightly sanded to create a smooth, flat surface before being clamped into the test jig. The clamps had sufficient adjustability to accommodate composite samples with non-parallel ends and provide better contact with the terminal blocks. The sample was secured into position by tightening two bolts on each clamp.

After mounting the composite sample, a 1 ampere current was applied to the sample through the terminal blocks with a constant current DC power source (BK Precision DC Power Supply 1611). The voltage drop across a previously marked distance of 10 mm in the centre of the sample was then measured by a voltmeter (HP -34401A and Micronta 22-179A). For each sample two voltage readings were taken by the two voltmeters and recorded.

The two voltmeters were used to measure the voltage drop across the sample to ensure that an accurate reading was taken. The HP voltmeter was capable of measuring μV (0.0001 mV) but did not produce a stable reading at that precision. Conversely, the Micronta voltmeter was only capable of

measuring as low as 0.1 mV but the readings were quite stable and did not fluctuate greatly. For the measured electrical conductivities of the composites tested, the two voltmeters showed readings (up to 3 significant figures) in very good agreement with each other.

Using the dimensions of the sample, the voltage drop, and applied current, the electrical conductivity, σ, may be calculated with the following equation:

$$\sigma = \frac{Il}{VA} \tag{3-3}$$

where I is the applied current, V is the measured voltage drop, A is the cross-sectional area (i.e. the sample width multiplied by the sample thickness) and l is the distance between the voltmeter probes.

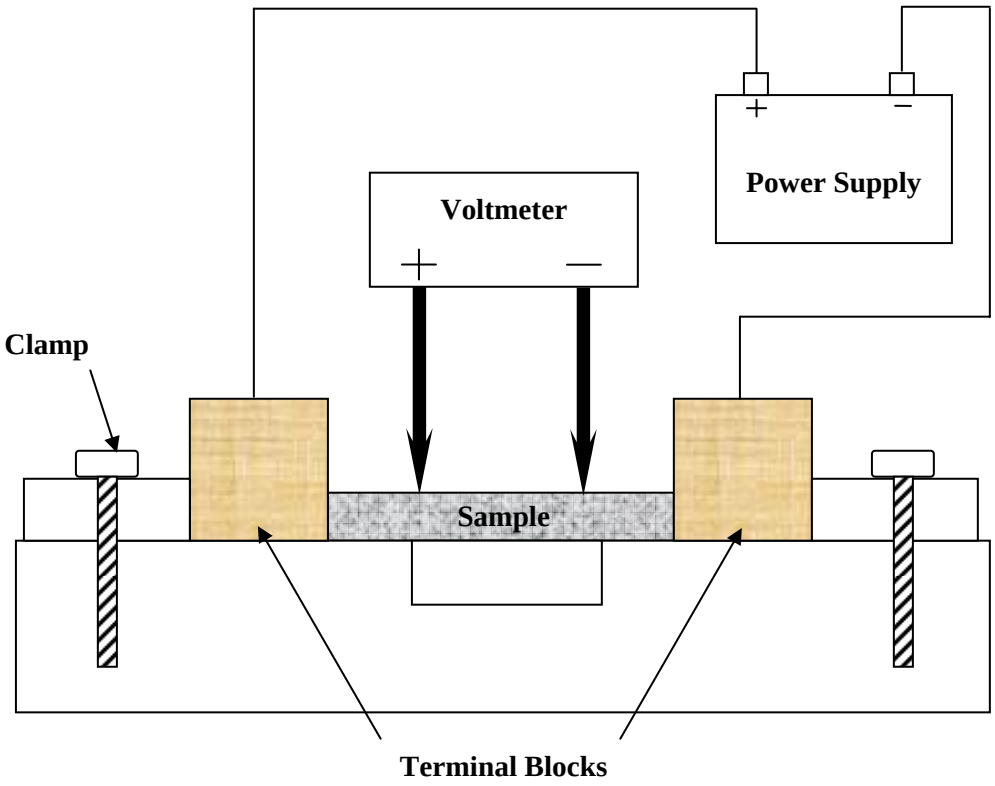

Figure 3-5: Electrical Conductivity Test Set-up

3.4.1 Error Discussion for Electrical Conductivity Experiments

The electrical conductivity of a pure nickel (99.5%) sample and a pure silicon (99.999%) sample, each purchased from Alpha Aesar, was measured in order to determine the effectiveness of the electrical conductivity test set-up shown in Figure 3-5. The nickel sample, measuring 15 mm x 11.5 mm x 6 mm, had an electrical conductivity of 142,500 S/cm and the silicon sample, measuring 25 mm x 25 mm x 6 mm, had an electrical conductivity of 0.049 S/cm. The measured electrical conductivities of both samples were within ±2% of the published electrical conductivities of 146,000 S/cm and 0.05 S/cm for nickel and silicon respectively [73].

The electrical conductivity measurements are sensitive to measurement variations associated with the placement of the voltmeter probes, and therefore care must be taken to ensure accurate results. The measured electrical conductivity for each composite may vary approximately ±10% for a 0.5 mm deviation from the 10 mm markings on the sample.

3.5 HIGH TEMPERATURE DILATOMETRY

High temperature dilatometry is a technique for measuring the dimensional changes of a sample with respect to time and temperature. Common applications include measuring sintering and densification characteristics, thermal expansion, and monitoring phase transformations. Changes in dimension are detected by a push rod that is in contact with the sample to be measured. A small force, approximately 0.35 N, is applied to ensure good contact with the sample but is low enough to prevent interfering with the sample expansion. Through the push rod, changes in length are transferred from the sample to a linear variable displacement transducer which converts the displacement to a signal that is recorded by a computer. Dimensional changes of up to ±2.5 mm may be recorded with a sensitivity of 1.25 nm/1 digit. The computer is also used to program the temperature and heating rate of the horizontal tube furnace.

The Netzsch 402C dilatometer [74] used in this investigation was equipped with alumina and fused silica sample holders. The alumina sample holder could withstand a maximum temperature of 1500˚C while the fused silica sample holder was limited to a temperature of 950˚C. Consequently, the alumina holder was used for the sintering and reduction measurements while the fused silica sample holder was used to determine the coefficient of thermal expansion (CTE) of the composite samples. The fused silica holder was used for CTE measurements due to its better stability and lower coefficient of thermal expansion compared to the alumina holder. With this particular dilatometer, the atmospheric conditions could also be altered by supplying a purging gas or evacuating the test chamber. Measurements were taken in air during the sintering operation and in reducing atmospheres of 10% hydrogen and 90% nitrogen gas during the reduction and CTE measurement stages.

During testing, the dilatometer components experience thermal expansion and thermal contraction depending on the heating schedule used. To compensate for the expansion of the dilatometer components, a “correction” file is created by heating an alumina standard under the same test conditions as the samples to be measured. When the dilatometer data is collected for the measured sample, the data can be “corrected” by removing the effects of dilatometer components from the raw measurement data, thus isolating the true dimensional change of the sample.

3.5.1 Sintering Measurements

To measure sintering shrinkage, the sintering process was performed in a dilatometer using the heating schedule given in Table 3-8. To prevent contamination of the push rod (as nickel oxide reacts with alumina to form a spinel) an alumina disk and platinum foil were placed between the push rod and the sample. The sample was also placed against another piece of platinum foil adjacent to the alumina slide at the end of the dilatometer. A schematic diagram of the set up is shown in Figure 3-6.

The heating schedule used for the sintering stage, given in Table 3-8, is the same heating schedule used during the bulk sintering operation. The dilatometer tube furnace cools more slowly than the programmed heating schedule (i.e. the furnace only cools to about 200°C when the heating program finishes). A one hour hold at room temperature is programmed into the heating schedule to ensure that the dimensional changes of the sample are recorded while the composite sample cools to room temperature.

Table 3-8: Heating Profile for Sintering Stage

Segment	Ramp Rate (˚C/min)	Temperature (˚C)	Hold Time (min)
1	20	1000	0
2	5	1475	60
3	20	25	60

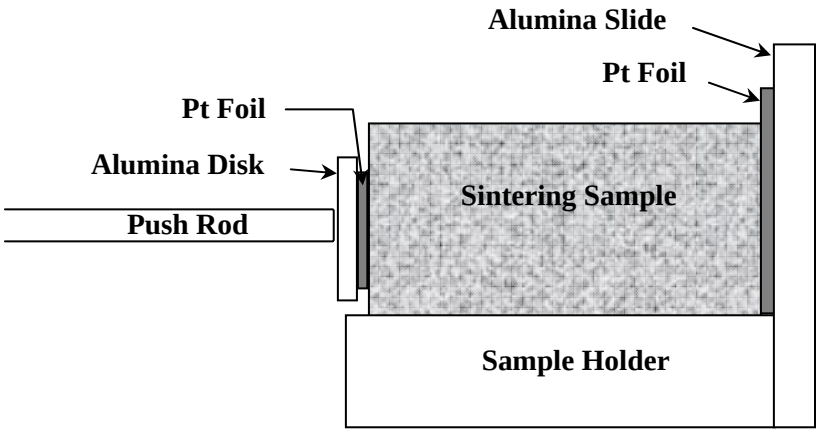

Figure 3-6: Schematic diagram depicting the set-up used to sinter samples in a dilatometer

3.5.2 Reduction Measurements

Reduction measurements were carried out in a dilatometer by heating a single composite sample to 1000°C under reducing atmospheric conditions with a 10% hydrogen and 90% nitrogen gas mixture following the heating schedule of Table 3-9. It is believed that this heating schedule will sufficiently reduce the composite samples as Corbin et al. verified, using XRD, that heating similar NiGr/YSZ composites to 800°C and holding for two hours in a 5% hydrogen and 95% nitrogen atmosphere was sufficient to fully reduce the samples [39]. Again, a hold time at room temperature is required to

ensure that the dilatometer furnace cools fully to room temperature before the reducing gas is turned off. As was the case for the sintered samples, the samples to be reduced were placed between two platinum foils to prevent contamination of the alumina push rod.

Table 3-9 Heating Profile for Reduction stage

Segment	Ramp Rate (˚C/min)	Temperature (˚C)	Hold Time (min)
1	15	1000	120
2	15	25	60

3.5.3 Thermal Expansion

The coefficient of thermal expansion was measured by heating a sintered & reduced composite sample in a dilatometer under the same reducing conditions used in the reduction stage described in Section 3.5.2 while using the heating schedule listed in Table 3-10. A hold time of 45 minutes ensured that thermal contraction data was collected and the reducing conditions remained until the composite samples cooled to room temperature. For better precision, the alumina push rod and sample holder was replaced with a silica push rod and silica sample holder.

To ensure an accurate CTE measurement, several heating cycles were repeated until the last CTE measurement curve matched the previous CTE measurement curve. This required at least three trials as the first CTE measurement was typically lower than the subsequent CTE measurements. The reason for the lower CTE measurement after the first trial was attributed to system settling and skewed sample seating. It usually required at least one trial before the system stabilized and the sample was properly seated.

Table 3-10: Heating Profile for Measuring Coefficient of Thermal Expansion

Segment	Ramp Rate (˚C/min)	Temperature (˚C)	Hold Time (min)
1	10	950	0
2	10	20	45

3.5.4 Error Analysis for High Temperature Dilatometry Experiments

In order to estimate the accuracy of the dilatometer measurements, the measured coefficient of thermal expansion data for an alumina standard was compared to the published coefficient of thermal expansion for alumina. To calculate the coefficient of thermal expansion, an alumina standard was heated in air to 1475°C at 10°C/min and then cooled to room temperature in an alumina sample holder. Once the thermal expansion behaviour of the alumina standard was recorded, the raw data was corrected so that the expansion of the alumina sample holder was accounted for. The measured and published coefficient of thermal expansion data for the alumina standard is shown in Table 3-11 [24]. Note that seven heating cycles were used to ensure an accurate thermal expansion reading. Ultimately, the difference in the coefficient of thermal expansion between the measured and published values at lower temperatures is less than 6%. As the temperature increases, the degree of accuracy decreases as

the difference between the measured and published coefficient of thermal expansion rises to 11.1% at 1400°C.

Table 3-11: Measured and Published Coefficient of Thermal Expansion Data for an Alumina Standard using an Alumina Sample Holder

Temperature °C	Alumina Standard CTE 10^{-6} 1/K	Published CTE [24] 10^{-6} 1/K	Percent Difference
500	7.16 ± 0.12	7.6	-5.8%
1000	9.16 ± 0.09	8.5	7.7%
1400	10.11 ± 0.07	9.1	11.1%

CHAPTER 4:
SINTERING THEORY

Most often, materials are formed into a desired shape by softening or melting them first. Unfortunately, most ceramic materials cannot be formed in this traditional manner because of their very high melting temperatures. As a result, ceramics are formed into useful shapes by other powder processing techniques and sintering. There are several types of sintering, such as liquid phase sintering, and pressure assisted sintering, but only solid-state sintering will be discussed in detail here.

Solid-state sintering, by definition, is a process in which a powder compact is made strong and dense through heating to high temperatures in the absence of liquid and external pressure [75]. The high temperatures required to initiate sintering vary for each material but are usually between half and two-thirds of the material's melting temperature [76].

Sintering will take place during heating if there is a mechanism to transport material from one area to another to reduce the total energy of the system. The five major transport mechanisms for solid-state sintering include: evaporation-condensation, surface diffusion, volume diffusion, grain boundary diffusion, and viscous flow. In addition to requiring a material transport mechanism, there must also be an energy source to activate it, which is typically heat [44].

With active transport mechanisms, the macroscopic driving force for sintering is the reduction of the free energy, ΔG_T, associated with the volume (ΔG_v), boundaries (ΔG_b), and surfaces (ΔG_s) of the grains within the compact as shown in Equation (4-1) [76].

$$\Delta G_T = \Delta G_v + \Delta G_b + \Delta G_s \tag{4-1}$$

Since the majority of the free energy of a powder compact is associated with its surface energy, the primary driving force for sintering is the reduction of the internal surface area. When powder compacts are formed using small diameter particles, the total internal surface area is greater and therefore yields a greater driving force for sintering. Likewise, when large diameter particles are used the driving force for sintering is lowered because of its lower internal surface area.

Before sintering, the internal surface area of the powder compact is at a maximum as the particles are just simply in contact with each other. In order to reduce the total internal surface area, the particles begin to fuse together through the growth of the contact area, called a neck. Also forming at the point of contact is a grain boundary separating the two particles. As the neck grows in diameter, the grain boundary area between the two particles also grows. To illustrate, the formation of necks and grain boundaries between three copper particles sintered together is shown in Figure 4-1.

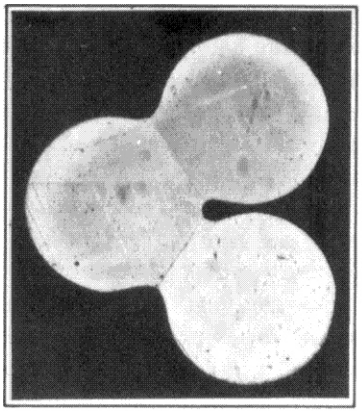

Figure 4-1: Micrograph depicting the sintering of three copper particles after 8 h at 1025°C. Note the grain boundary formation within the particle necks [77].

The process of neck growth between two contacting particles by surface diffusion is illustrated in Figure 4-2a. Neck growth is propelled by the smoothing of the variation in curvature between the top of the particles and the neck [75]. Atoms on a convex surface are less tightly bound and have a tendency to travel to concave surfaces where there is a high concentration of vacancies to be filled. As the atoms move from the convex surfaces to the concave surface, the difference in surface curvature lessens. If the atoms move from the top surface of the particle to the neck, the neck increases but the particle centres remain the same distance apart. As a result, the particles merely change shape to decrease the surface area but no densification or pore removal occurs. When surface diffusion is the source of atoms moving to the neck, the neck grows without densification.

Conversely, densification and pore removal will take place if material is transported from the grain boundary to the neck surface, as shown in Figure 4-2b. In essence, material is removed from the surface of the particle at the grain boundary and relocated at the neck. As more material is transported along the grain boundary to the neck, the curvature of the neck decreases. Furthermore, with less material separating the particles at the grain boundary, the particle centres move closer together thereby decreasing the amount of porosity within the compact. Pores between particles will continue to be removed as long as they remain very close to the grain boundary and the energy conditions are favourable [77].

As a result of neck growth, the surface energy decreases but there is also a corresponding increase in the grain boundary energy. For sintering to continue, the increase in grain boundary energy must be less than the amount of free energy lost because of the reduction in the internal surface area. The grain boundary energy, γ_{gb}, is related to the surface tension, γ_{sv}, by the following equation:

$$\gamma_{gb} = 2\gamma_{sv} \cos\left(\frac{\phi}{2}\right) \qquad \textbf{(4-2)}$$

where ϕ is the dihedral angle representing the angle of intersection of a pore at the pore-grain boundary interface as indicated in Figure 4-3. Neck growth should occur when $\gamma_{gb} < \sqrt{3}\gamma_s$.

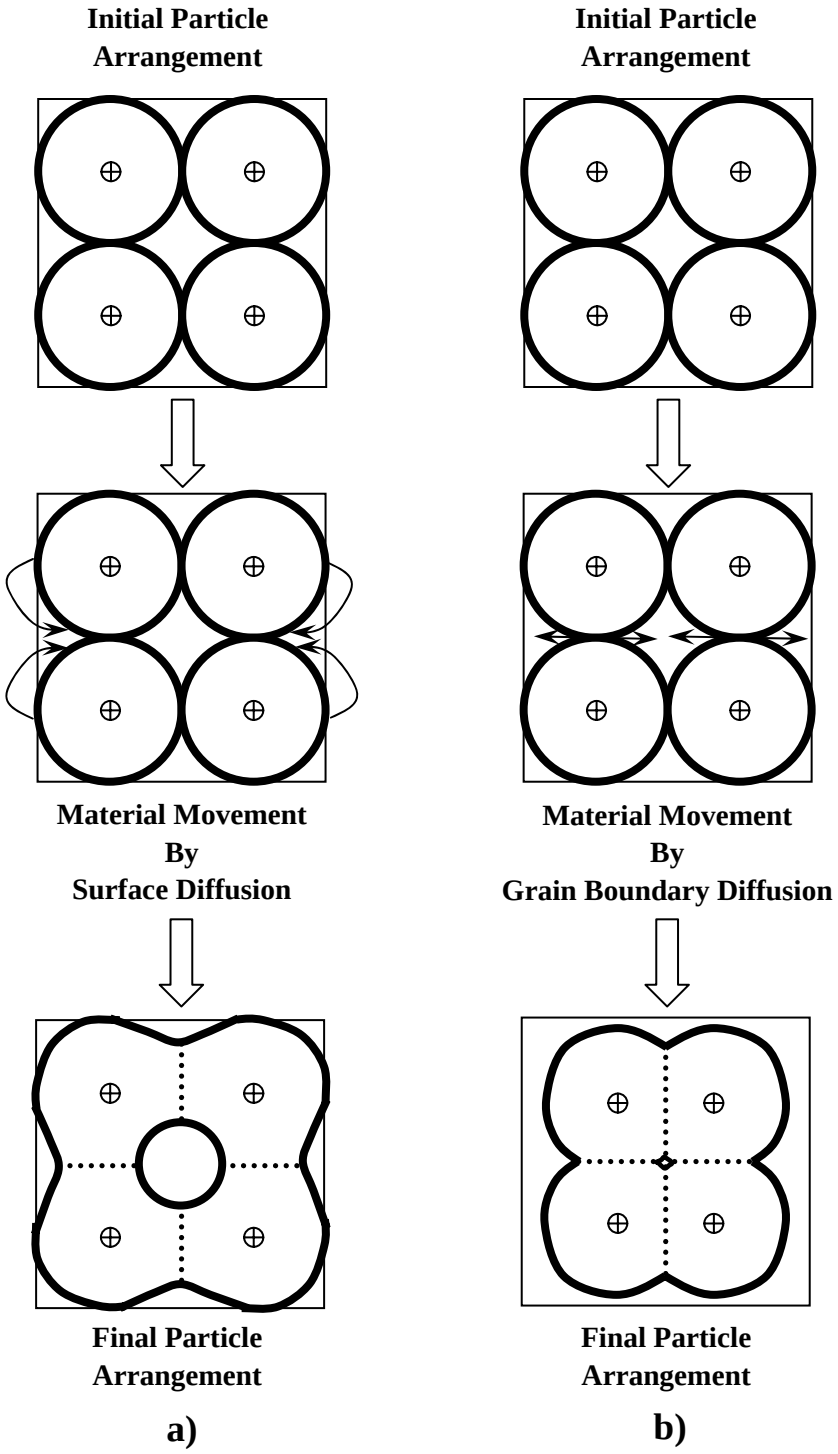

Figure 4-2: Cartoon depicting the changes in particle shape caused by a) surface diffusion and b) grain boundary diffusion

For most oxide systems, $\gamma_{gb} \approx \gamma_s$ resulting in a dihedral angle of 120°, while in metallic systems γ_{gb} is approximately 2 to 4 times smaller than γ_s [75, 76]. If γ_{gb} is too high or ϕ too large, neck growth and thus pore elimination will cease. This can cause the formation of round thermodynamically stable pores within the interior of a grain that are nearly impossible to remove through further sintering. For some systems that are difficult to sinter, a dopant may be added to reduce the grain boundary energy thereby improving densification.

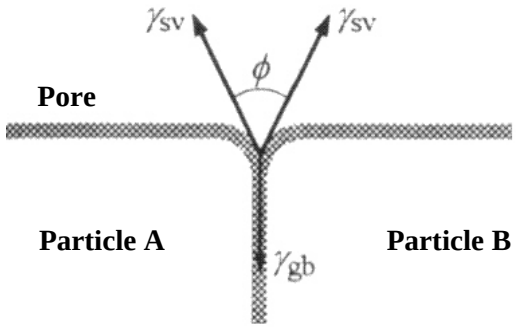

Figure 4-3: Equilibrium dihedral angle at the pore-grain boundary interface [75]

The change in energy associated with neck growth and densification may also be regarded as a "sintering stress". This sintering stress is proportional to the driving force for sintering and when applied to the powder compact, it causes densification by forcing the particle centres to move together. In physical terms, the sintering stress is equivalent to the stress required to compress the initial powder compact into its final fully dense form. Therefore, powder compacts created from small diameter particles have a high internal surface area resulting in a greater sintering driving force and a higher sintering stress.

4.1 STAGES OF SOLID STATE SINTERING

To describe the sintering process, three stages of sintering: initial, intermediate, and final are used. An illustration of the microstructural changes that happen during sintering is shown in Figure 4-4.

4.1.1 Initial Stage

In the initial stage of sintering, particles rearrange themselves to maximize the number of particle-to-particle contacts. Necks begin to form where the surface energy is highest and material can be transported. Since surface diffusion has the lowest activation energy, it is most active at the low temperatures during the early stages of sintering. As the sintering temperature increases, more significant material transport occurs as grain boundary diffusion and then lattice diffusion becomes more active. Until that time, neck growth resulting from surface diffusion increases the contact area between particles, but does not significantly change the degree of porosity. At this stage, the powder compact only experiences a modest increase in density [75].

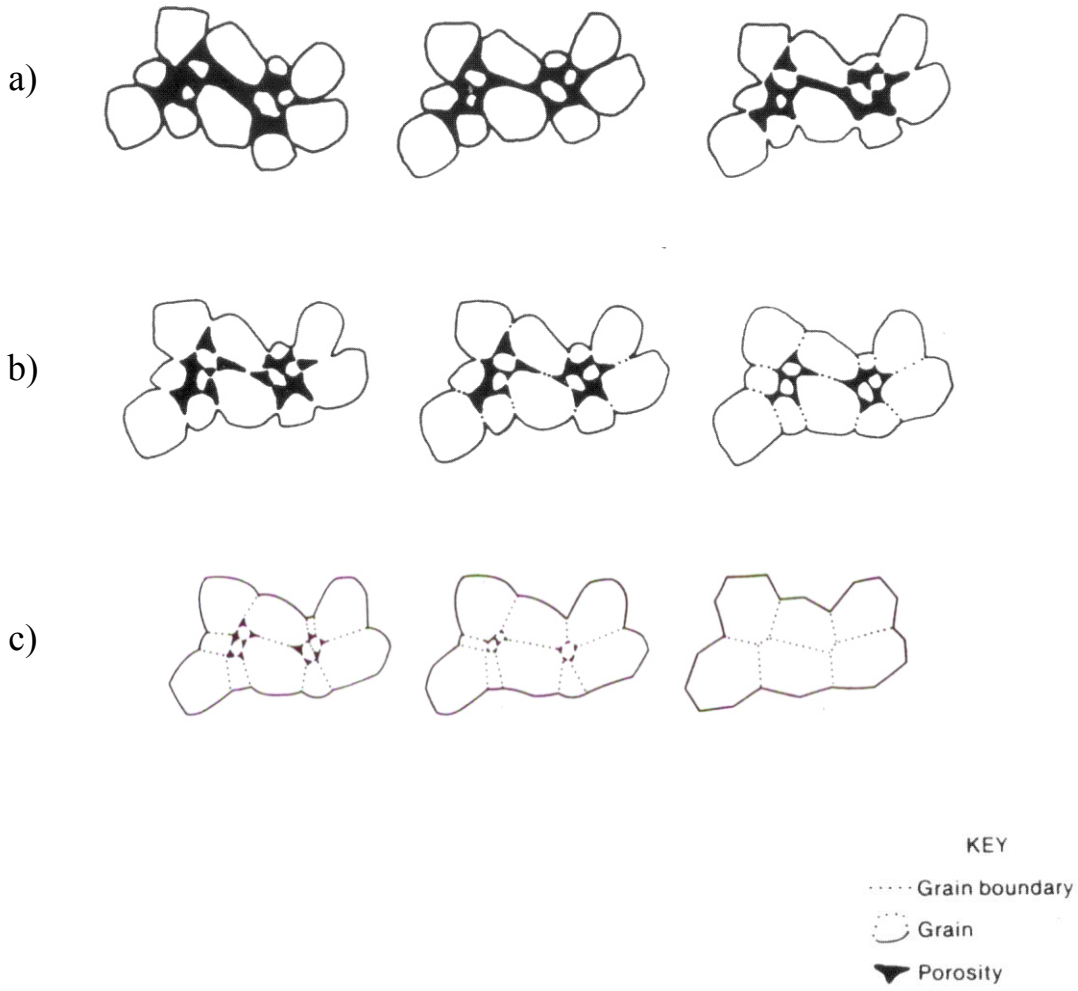

Figure 4-4: Microstructural changes that occur during the a) initial, b) intermediate, and c) final stages of sintering. During the initial stage, particles rearrange and necks grow. In the intermediate stage, necks continue to grow, the grain boundary length increases, and the volume decreases. Lastly, the final stage results in grain growth and porosity elimination [44].

Typically, sintered parts undergo dimensional shrinkage as a result of densification. The sintering shrinkage, $\Delta L/L_o$, in the initial stage of sintering may be modelled by [76]:

$$\frac{\Delta L}{L_o} = \left[\frac{K D_v \gamma_s V_v t}{k_B T d^n} \right]^m \tag{4-3}$$

where D_v is the diffusivity of the vacancies with volume V_v, γ_s is the surface energy, t is time, k_B is the Boltzmann constant, T is temperature, and d is the particle diameter. The particles used in this model are assumed to be spherical, and of the same dimensions, although an average particle size may be

assigned to characterize a mixture of particles with different sizes [78]. The constant, K, is dependent on the geometry of the system, while the exponent, n, is commonly close to 3, and the exponent, m, is generally between 0.3 and 0.5.

There are some limitations associated with the model presented above. First, the model assumes that the particles used are identical spheres. However, in practise powders take many shapes and sizes. In fact, much of the difficulty in developing sintering models lies in predicting the complex geometry of the green body [79]. Second, only one diffusion mechanism is assumed to be dominant during sintering; however, more than one transport mechanism may be active depending on the temperature. For example, if lattice diffusion is active it will most likely take place in conjunction with grain boundary diffusion and surface diffusion. Further complicating the model is the use of complex parameters. Accurate experiments are required to obtain the activation energies associated with the bulk transport mechanisms and surface energies. Finally, heating the component to the sintering temperature will result in some sintering that will not be accounted for by the model.

Despite its limited practical use, the model presented in Equation (4-3) gives a good indication of the key influences on sintering. It is evident that sintering shrinkage is greatly influenced by temperature (both directly and in terms of diffusivity), and particle size. Green bodies with smaller particles, which have an increased surface energy, will tend to shrink more than bodies with larger sized particles.

4.1.2 Intermediate stage

The intermediate stage starts after the initial neck growth and ends when the particle compact reaches approximately 90% of the theoretical density. In this stage, necks and grain boundaries continue to grow, particles move closer together, and pores shrink resulting in volumetric shrinkage. It is during the intermediate stage where the majority of densification takes place [44,75,79].

Again, modeling of the sintering shrinkage during the intermediate stage is very difficult. Sintering in this stage is still dependent on the same parameters associated with Equation (4-3) but further complicating matters are the multiple active diffusion mechanisms, grain growth, and difficulty in predicting the size, shape, and packing of the particles [76]. In order to reduce the total grain boundary energy, grain growth is significant as smaller grains are consumed by larger grains. With increased densification, the shrinking network of open pores becomes so long and thin, it is no longer stable and transforms into smaller spherical pores. This transition to closed porosity (small non-continuous pores) from open porosity marks the end of the intermediate stage.

4.1.3 Final Stage

The final stage of sintering marks the eventual elimination of pores and is accompanied by grain growth. To reach full density, grain boundary movement (i.e. grain growth) must be carefully controlled since pores are eliminated by the annihilation of vacancies at the grain boundary. If the small pores remain at the grain boundary, vacancies diffuse easily and the pores are eliminated. Sintering aids are often added to slow the grain boundary movement and allow enough time for pore removal. If however, grain growth is too rapid, the pores may detach from the grain boundary and become surrounded by the grain. When this happens, the diffusion distances for the vacancies to the grain boundary are quite large making the removal of pores within a grain very difficult. Once a pore becomes isolated within a grain, it becomes nearly impossible to reach the full theoretical density [44].

4.2 FACTORS THAT AFFECT SINTERING

As suggested earlier, there are several factors that can affect the sintering process. The most significant factor affecting solid state sintering is temperature. Since diffusion is temperature dependent, increasing the sintering temperature will greatly enhance sintering kinetics. Rapidly heating to a higher temperature can minimize surface diffusion while enhancing bulk diffusion leading to greater densification. Likewise, longer hold times at the desired sintering temperature will allow more time for diffusion resulting in greater densification and grain growth. Generally, rapid heating with the minimal isothermal hold time at the maximum sintering temperature can lead to fully dense compacts with minimal grain growth [76]. Lastly, controlled heating and cooling is necessary to avoid uneven temperature distributions and residual stresses.

The size of the particles is another important consideration. Smaller particles will have a larger surface area thereby increasing the driving force for densification. Nevertheless, too fine of particles may cause agglomeration, where the fine particles quickly sinter together to form larger particles. These larger agglomerated particles lead to a decrease in sintering and the creation of large pores between the particles.

Larger particles can also lead to exaggerated grain growth whereby a few grains grow quickly into very large grains contributing to poor densification. Fortunately, this phenomenon can be avoided when the powder compact is made from particles with a narrow particle size distribution. Unfortunately, uniformly packing particles with a narrow size distribution is more difficult, which can lead to large pore formations that are difficult to remove [44,75].

The green density and microstructure also affect the resultant sintered microstructure. The densification of a compact is related to both the starting density and linear sintering shrinkage as follows:

$$\rho_s = \frac{\rho_g}{\left(1 - \frac{\Delta L}{L_o}\right)^3} = \frac{\rho_g}{\left(1 - \frac{\Delta V}{V_o}\right)} \qquad \textbf{(4-4)}$$

where ρ_s is the sintered sample density, ρ_g is the green density, $\Delta L/L_o$ is the linear shrinkage, and $\Delta V/V_o$ is the volumetric shrinkage [80]. A higher green density results in a higher final density because there is less pore volume to remove during sintering. This is an important consideration when tape casting since increasing the polymer content of a tape cast green body results in lower green densities and thus a higher sintering shrinkage. In fact, altering the polymer content of the green body is an effective means of changing the sintering shrinkage of the material [39]. Lastly, a uniform green microstructure also means that there are fewer agglomerates that can adversely affect the sintered microstructure and cause non-uniform densification.

Sintering may be improved if additives are added to the green compact, as sintering aids, in order to enhance diffusion or suppress coarsening and grain growth. Additives concentrated at the grain boundary can also enhance sintering by reducing the grain boundary energy or slowing grain boundary movement. By slowing down the movement of grain boundaries, more time is available for pore elimination which leads to better densification.

Finally, the sintering atmosphere will also affect the final microstructure. Unwanted oxidation and reduction reactions can be avoided by using an appropriate atmosphere. The proper atmosphere can

enhance diffusion while a poorly selected atmosphere may actually hinder sintering through increased coarsening. The gas used in the atmosphere should also be soluble in the solid so that the gas can dissolve into the material as the pores shrink during densification [75]

4.3 COARSENING VERSUS DENSIFICATION

As mentioned, the driving force for sintering is the reduction of the free energy associated with the volume, grain boundary, and surface energy of the particles within a powder compact (i.e. Equation (4-1)). There are two processes that result in the reduction of the free energy of the system: densification and coarsening. Densification will occur while pores are eliminated when bulk diffusion mechanisms, such as grain boundary diffusion and lattice diffusion, are the dominant material transport mechanisms. However, if surface diffusion dominates, grains grow too rapidly, or pores coalesce, the free energy of the compact is reduced but no densification occurs meaning the microstructure has coarsened. Coarsening is enhanced when the sintering temperature is too low, the grain boundary energy is too high, or pore geometry is thermodynamically stable. In order for the powder compact to become fully dense, coarsening must be suppressed until the majority of the shrinkage has occurred [75].

Densification can be easily monitored by measuring the change in density or sintering shrinkage with time using a dilatometer. Since coarsening results in very little shrinkage, it is better to monitor coarsening through changes in grain size. A plot of grain size versus density, shown in Figure 4-5, illustrates the difference between coarsening and densification. To reach full density, coarsening must be suppressed until the latter stages of sintering (curve z). If coarsening dominates, grains grow but there is little densification (curve x). Typically, densification and coarsening occur simultaneously resulting in some densification and grain growth (curve y) [75,81].

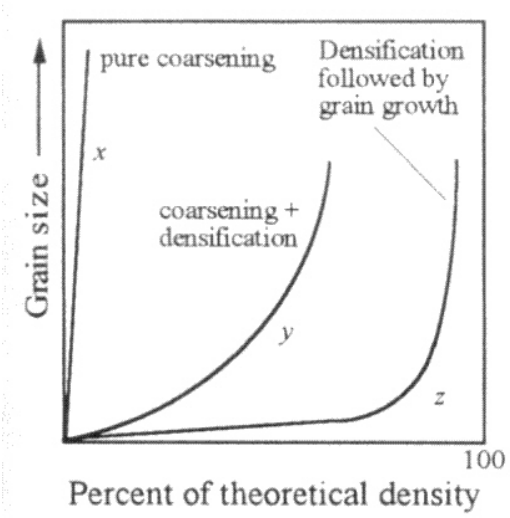

Figure 4-5: Grain size versus density plot showing densification followed by grain growth (curve z), pure coarsening (curve x), and simultaneous densification and coarsening (curve y) [75]

4.4 COMPOSITE SINTERING

The sintering behaviour of a composite may be quite different from the constituent materials when two materials with different sintering characteristics are combined together. Constrained sintering is said to occur when one composite phase impedes the sintering of another. Since ceramic particulate composites can offer advantages over single phase materials, many researchers have investigated the effect rigid inclusions have on the sintering behaviour of glass and fine grained polycrystalline ceramic composites [73,82,83,84,85,86,87].

The effect rigid inclusions have on the sintering behaviour of a composite material is best described in terms of hydrostatic sintering stresses. The maximum compressive sintering stress occurs when the pure matrix material is free of inclusions and is allowed to sinter to full density under ideal conditions. If, however, rigid inclusions are present in the matrix, the material will contain residual porosity and therefore not sinter to full density. The lack of densification is a result of tensile "back stresses" that impede the densification of the matrix by counteracting the sintering stress, as shown in Figure 4-6 [83]. These tensile forces essentially lower the amount of densification by pushing the matrix particles apart. As a result of the tensile back stresses, the grain boundary energy may rise thereby reducing neck growth and pore elimination (i.e. Equation (4-2)). The inclusions can also hamper the packing of the matrix particles in the green state resulting in a lower green density and ultimately lower densification.

Generally, the presence of non-sintering, rigid inclusions impedes the densification of the matrix because of the dissimilar sintering shrinkages of the constituent materials. However, there are other factors, in addition to hydrostatic back stresses, that can cause reduced densification of a composite material. For instance these factors include, "sintering damage" such as cracks and voids that form between the matrix and inclusions, the formation of a continuous network of rigid inclusions, varying densification due to a random distribution of inclusion particles, microstructural anisotropy in the matrix, and coarsening of the matrix [82].

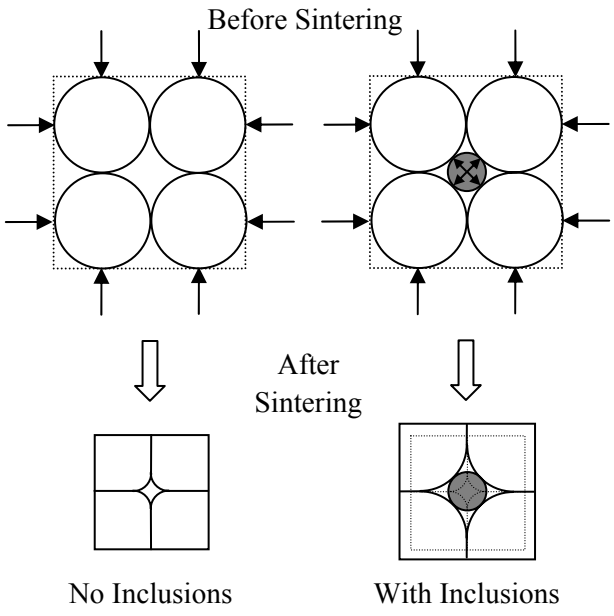

Figure 4-6: The effect of inclusions on the densification during sintering. The dark arrows represent the hydrostatic stresses acting on each particle.

The amount of constrained sintering can be qualitatively shown, as in Figure 4-7, by plotting the change in density from the green state to the sintered state for each inclusion loading ($\Delta\rho$), normalized by the change in density of the pure matrix ($\Delta\rho_{matrix}$), with respect to the inclusion loading (i.e. plotting $\Delta\rho/\Delta\rho_{matrix}$ with respect to the inclusion loading) [83]. If the plot follows the rule of mixtures, constrained sintering is not significant as there is little stress interaction between the inclusions and the matrix. Conversely, if hydrostatic back stresses exist, or a rigid network of inclusions is present, the plot will deviate significantly from the rule of mixtures indicating a constrained sintering effect [83,84,86]. In the example presented in Figure 4-7, the presence of silicon carbide particles causes a substantial deviation from the rule of mixtures suggesting that constrained sintering is significant and densification is hindered greatly. The normalized change in density also deviates from the rule of mixtures when the size and the formation of a rigid network (at approximately 50 vol% SiC) are accounted for.

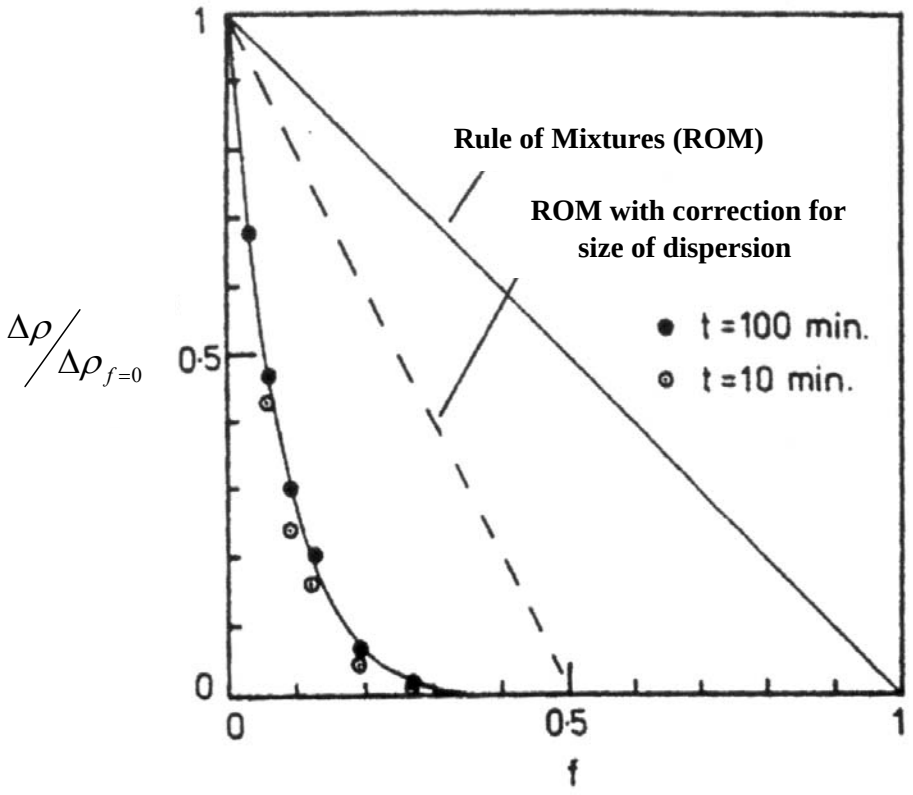

Figure 4-7: Evidence of constrained sintering by plotting the normalized change in density with respect to the volume fraction of SiC inclusions in a ZnO matrix [83].

CHAPTER 5:
SINTERING EXPERIMENTAL RESULTS

5.1 THE PRESSED GREEN STATE

In the green state, each tape consists of evenly distributed solid powder (YSZ, Ni, and/or NiO), graphite (when added), polymer material, and any porosity that may be present as illustrated in Figure 5-1. It is assumed that the solvents used in tape casting have evaporated completely and that the volume fractions of each constituent are consistent throughout the entire tape. That is, a piece of the dried green tape has the same proportion of material as the whole green tape. The volume of each constituent within the dried green tape is calculated by dividing the mass measured during preparation of the tape casting slurry by its density and the total volume of the green tape is calculated by summing the volume of each individual component. Volume fractions for each of the constituent materials in the green state may be calculated as follows:

$$vol\%\, i = \frac{Volume_i}{Total\ Volume\ of\ Dried\ Green\ Tape} = \frac{Mass_i \Big/ \rho_i}{\sum_{j=1}^{n} Mass_j \Big/ \rho_j} \tag{5-1}$$

where i represents the desired constituent from a mixture of n components with a density, ρ_i.

Equation (5-1) can also be used to calculate the volume fractions of the materials as a function of the total solids. For example, composite samples in the sintered & reduced state would consist entirely of nickel and YSZ. As a result, the volume fraction of nickel, as a fraction of total solids, would be equal to:

$$vol\%\ Ni\ of\ Total\ Solids = \frac{Volume\ Ni}{Volume\ of\ Total\ Solids} = \frac{Mass_{Ni} \Big/ \rho_{Ni}}{Mass_{Ni} \Big/ \rho_{Ni} + Mass_{YSZ} \Big/ \rho_{YSZ}} \tag{5-2}$$

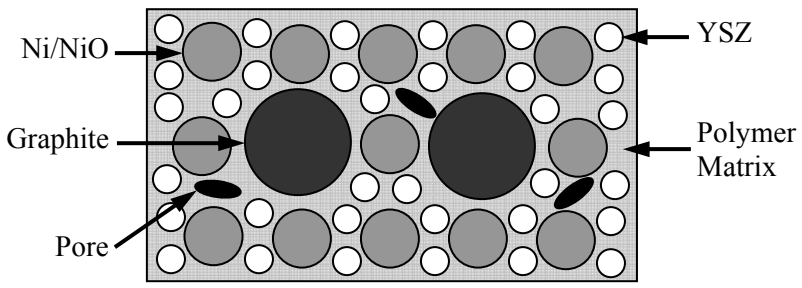

Figure 5-1: Schematic diagram representing the pressed green microstructure

In order to build samples with more useful geometries, several small pieces of green tape are laminated together in a die at room temperature. The pressed green state refers to the condition of each sample after lamination but before polymer burnout and sintering. Three influential green state parameters are the volume fraction of each constituent phase, the polymer content, and the pressed green density, since the properties of the green state can influence the sintering behaviour of a sample.

5.1.1 Nickel Loading

The volume fraction of nickel and nickel oxide with respect to the volume fraction of YSZ for each composite sample is plotted in Figure 5-2. To simplify the comparison between the different composite types, the results are plotted with respect to the YSZ loading because each composite type have similar YSZ loadings in the green state for a given nickel content. In addition, the actual nickel loadings are given as a volume fraction of the dried green tape for the composites made from nickel powder (Ni/YSZ, NiGr/YSZ, and Ni&Gr/YSZ). Likewise, the actual nickel oxide loadings are given for the composites made from nickel oxide powder (NiO/YSZ and NiO&Gr/YSZ).

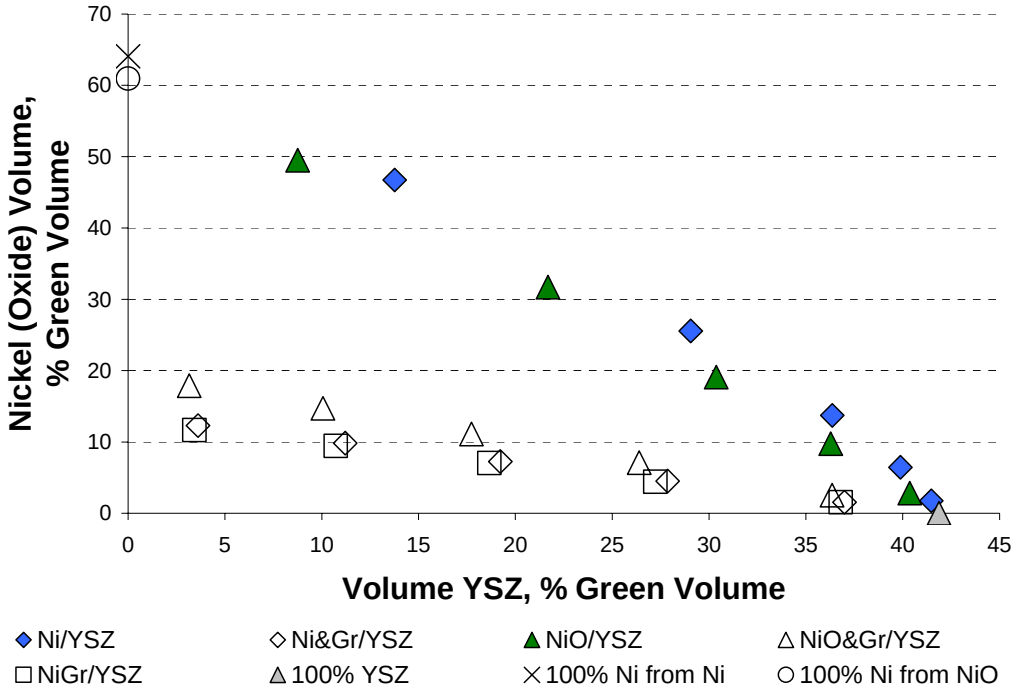

Figure 5-2: Volume fraction of nickel and nickel oxide with respect to YSZ loading for each composite type

From Figure 5-2, it is evident that the composites containing graphite have lower volume fractions of nickel and nickel oxide in the green state compared to the composites without graphite. The lower nickel volume fractions are due to the graphite additions occupying a portion of the green body volume. The Ni&Gr/YSZ and NiGr/YSZ composites have very similar nickel loadings at a given YSZ content, while the NiO&Gr/YSZ composites have slightly higher nickel oxide loadings.

In addition to creating Ni/YSZ composites with increasing nickel loadings, another set of composites were created by fixing the nickel loading and altering the graphite content. Four other

composite types (Ni&Gr-27/YSZ, Ni&Gr-47/YSZ, NiO&Gr-27/YSZ, and NiO&Gr-47/YSZ) were created from nickel and nickel oxide powder with a fixed nickel loading of 27 vol% Ni of total solids and 47 vol% Ni of total solids. The actual measured nickel loading for these composites are plotted with respect to the graphite content in Figure 5-3. The volume of the dried green tape occupied by nickel and nickel oxide decreases with increasing graphite content because more graphite is being added to the composite which then occupies a greater proportion of the green tape.

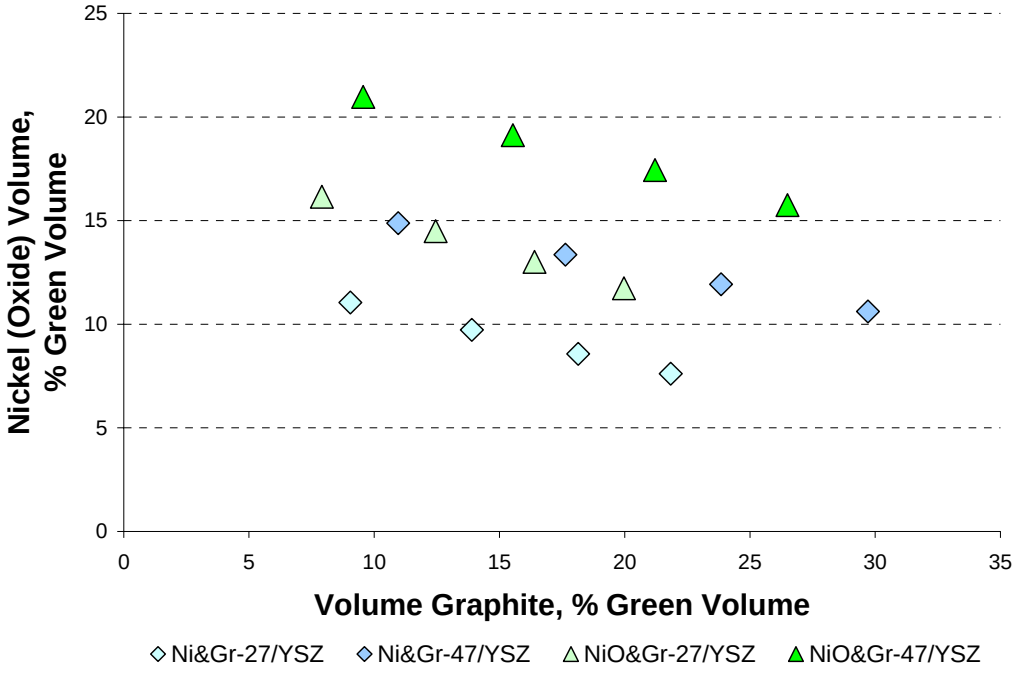

Figure 5-3: Nickel and nickel oxide loadings with respect to graphite loading in the pressed green state for the Ni&Gr-27/YSZ, NiO&Gr-27/YSZ, Ni&Gr-47/YSZ, and NiO&Gr-47/YSZ composites

5.1.2 Graphite Loading

The graphite loading for each composite type in the green state is shown in Figure 5-4. Obviously, the graphite-free composites (Ni/YSZ and NiO/YSZ) do not contain any graphite, while the graphite containing composites (Ni&Gr/YSZ, NiO&Gr/YSZ, and NiGr/YSZ) have similar increasing volume fractions of graphite with decreasing YSZ loadings by design. The Ni&Gr/YSZ and NiO&Gr/YSZ composites are designed to have the same graphite loadings as the NiGr/YSZ composites; so when the volume fraction of nickel increases with additional nickel coated graphite particles, the amount of graphite increases as well.

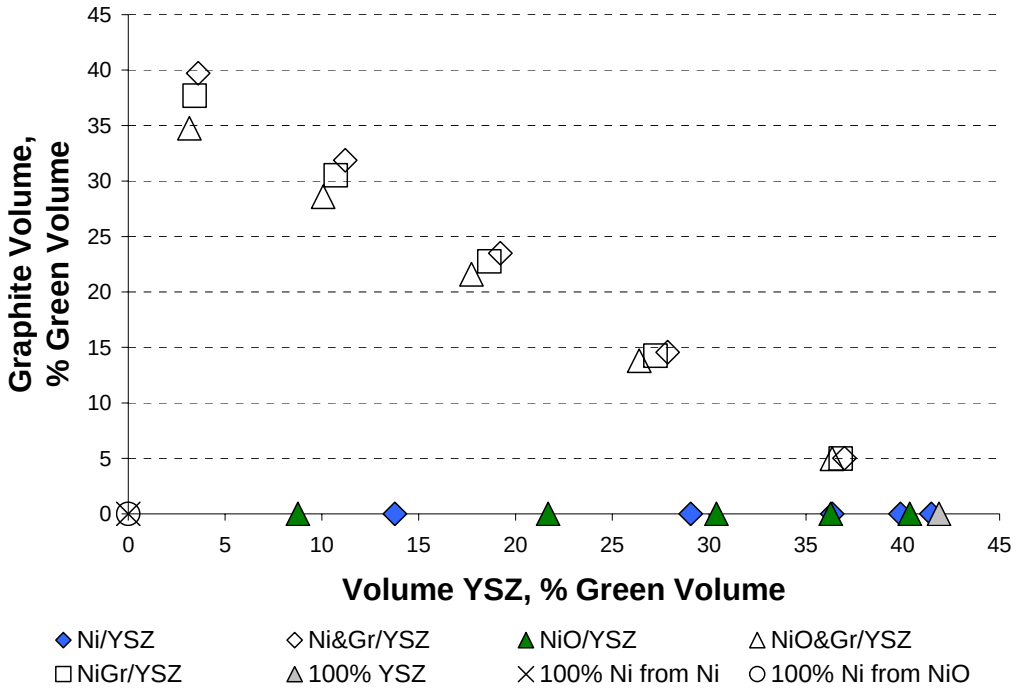

Figure 5-4: Volume fraction of graphite in the green state plotted with respect to YSZ loading for each composite type

5.1.3 Pressed Green Density

When forming the composite samples, several layers of the dried green tape are laminated together to create samples with a reasonable thickness and to improve their sintering behaviour. Materials with higher green densities shrink less than materials with lower green densities. In order to accurately compare the sintering behaviour of the various composites, it is important that they have similar starting green densities based on the theoretical green density. The theoretical density was calculated from the rule of mixtures using the organic and solid material densities based on the tape casting formula for each composite type. From Figure 5-5, it is evident that each composite sample has been pressed to a theoretical density of greater than 90% with the exception of the pure NiO samples which had an average pressed green density of 89%.

After pressing the samples, a small amount of flashing, caused by material flowing between the punch and the die wall, was removed. Usually, the flashing has a similar composition to the bulk sample. However, for the NiGr/YSZ composites, the pressed green densities may be greater than 100% of theoretical because the NiGr particles are much larger than the other powders and may not have fit between the punch and die wall. As a result, the flashing that was removed would not be representative of the bulk composition as it contains a higher proportion of lower density polymer material leading to a higher pressed green density.

It should also be noted that the pressed green density of each of the composites with varying graphite loadings were all greater than 90% of the theoretical density as illustrated in Figure 5-6. The instances where the pressed green density is greater than 100% of the theoretical density may be attributed to variations in measuring the weight and dimensions of the sample which can be on the order of 1%.

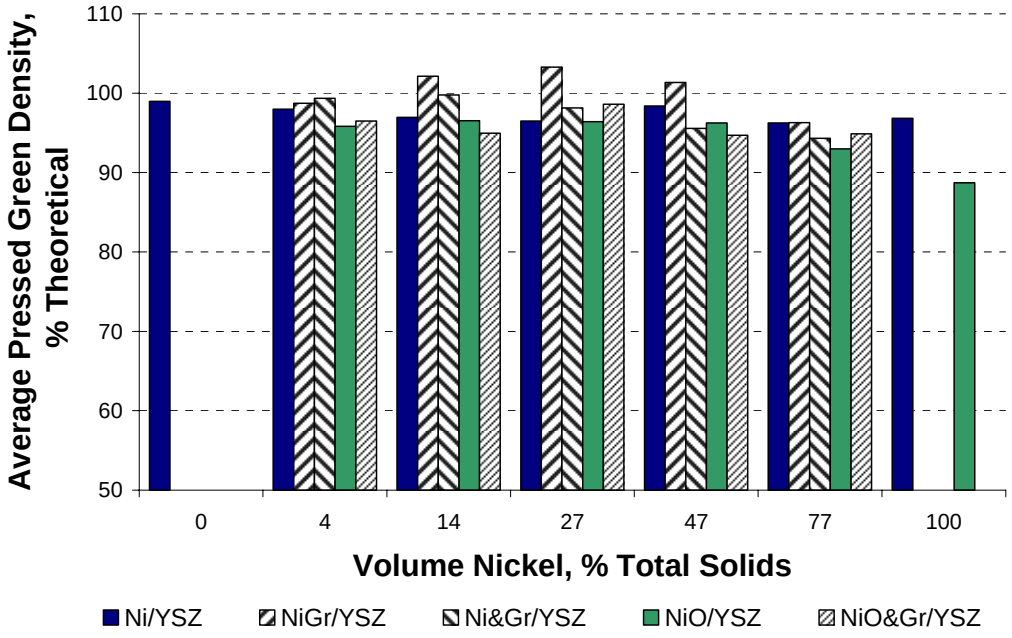

Figure 5-5: Average pressed green density as a percentage of theoretical for samples of each composite type

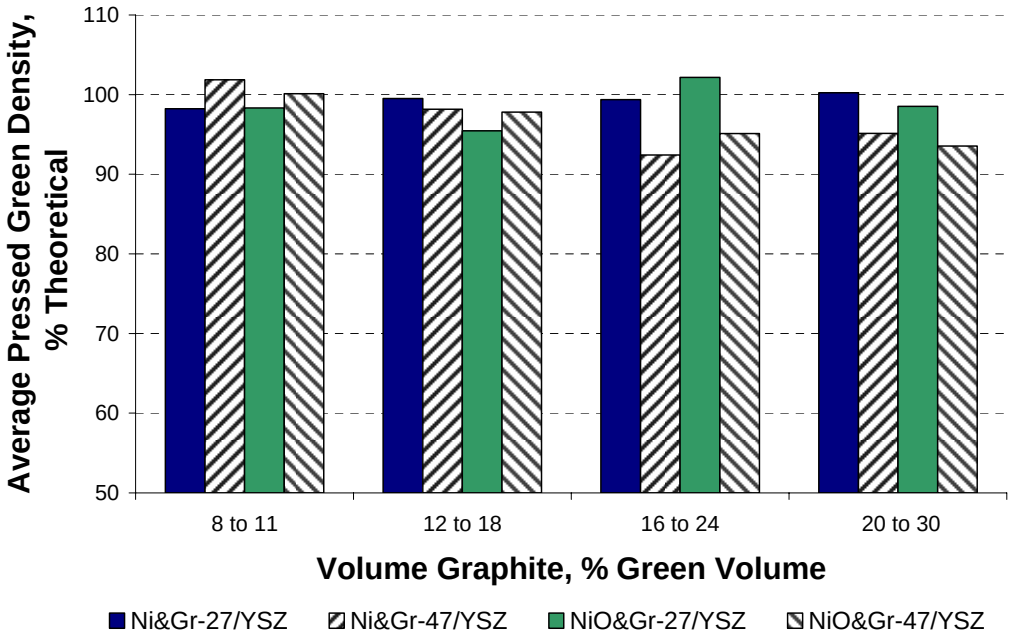

Figure 5-6: Pressed green density as a percentage of theoretical for the Ni&Gr-27/YSZ, NiO&Gr-27/YSZ, Ni&Gr-47/YSZ, and NiO&Gr-47/YSZ composites with varying graphite content

5.1.4 Bulk Packing Density

In addition to achieving a high pressed green density, the packing of the solid particles may influence the sintering behaviour of the green bodies. As described in Section 3.2.2.1, tape casting formulations were developed to produce a high quality tape for each composite type. When graphite or NiGr powders were added, more polymer solution was needed for a quality tape compared to the graphite-free composites. In previous work by Corbin et al. [46], when large pore forming agents (PFA) are added to fine ceramic particles, the extra polymer added is redistributed throughout the fine ceramic powders because of the lower surface area of the large PFA particles, as shown in Figure 5-7. Similarly, in this study the size of the graphite and NiGr powders are much larger than the YSZ and nickel powders and the additional polymer material distributes itself throughout the finer YSZ and nickel powders reducing their bulk packing density in the pressed green tape. This reduced bulk packing density, ρ^b_c, can be calculated as:

$$\rho_c^b = \frac{Volume\ of\ YSZ\ \&\ Ni}{V_T - Volume\ of\ PFA} \times 100\% \qquad \textbf{(5-3)}$$

where V_T is the total pressed green volume of the part measured experimentally and the volumes of the YSZ, Ni and PFA are calculated knowing the weight (and volume) fractions for a particular tape cast formula. In the case where the nickel is added as a coating on the PFA, both the nickel and graphite volumes are included in the volume of PFA term and the YSZ packing factor is the only concern. The results of the bulk packing density calculations for three samples of each composite are presented in Figure 5-8 and Figure 5-9. For comparison, the bulk packing densities of the nickel and YSZ (or NiO and YSZ) without graphite additions are also shown in Figure 5-8.

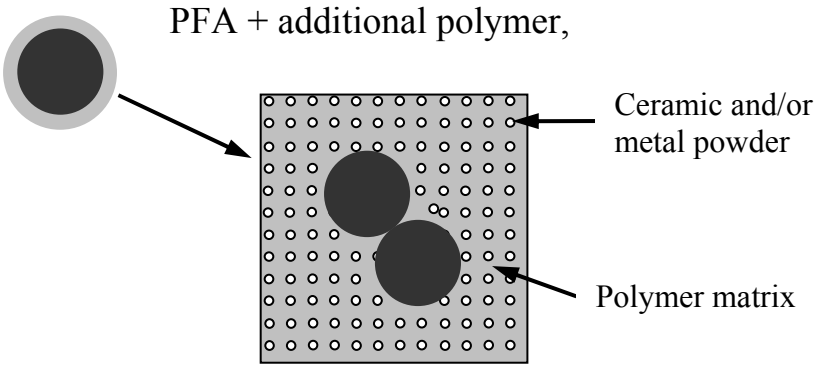

Figure 5-7: Schematic diagram of a unit volume of green tape where the additional polymer is uniformly distributed throughout the green tape [46]

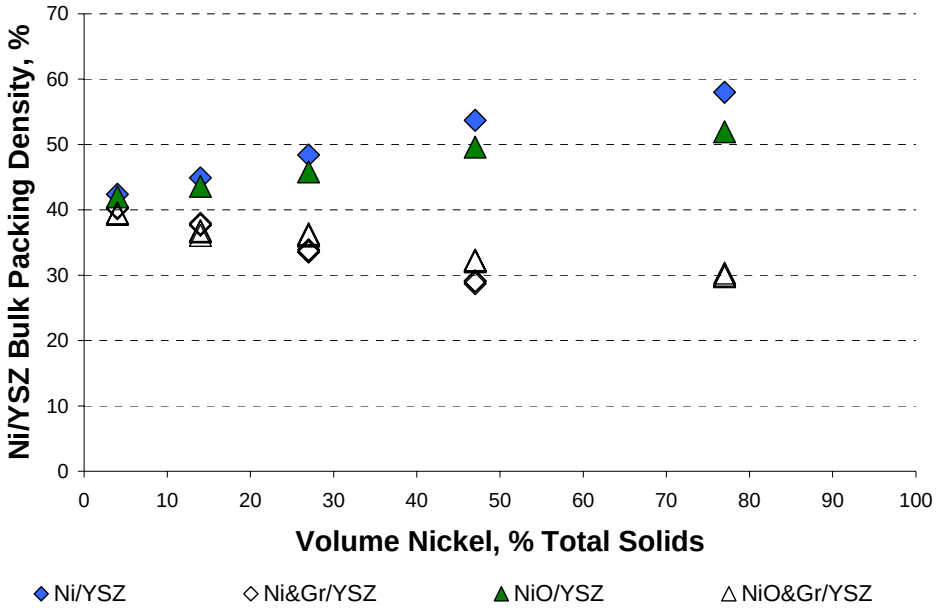

Figure 5-8: Nickel and YSZ packing densities within the green Ni/YSZ, Ni&Gr/YSZ, NiO/YSZ, and NiO&Gr/YSZ composites

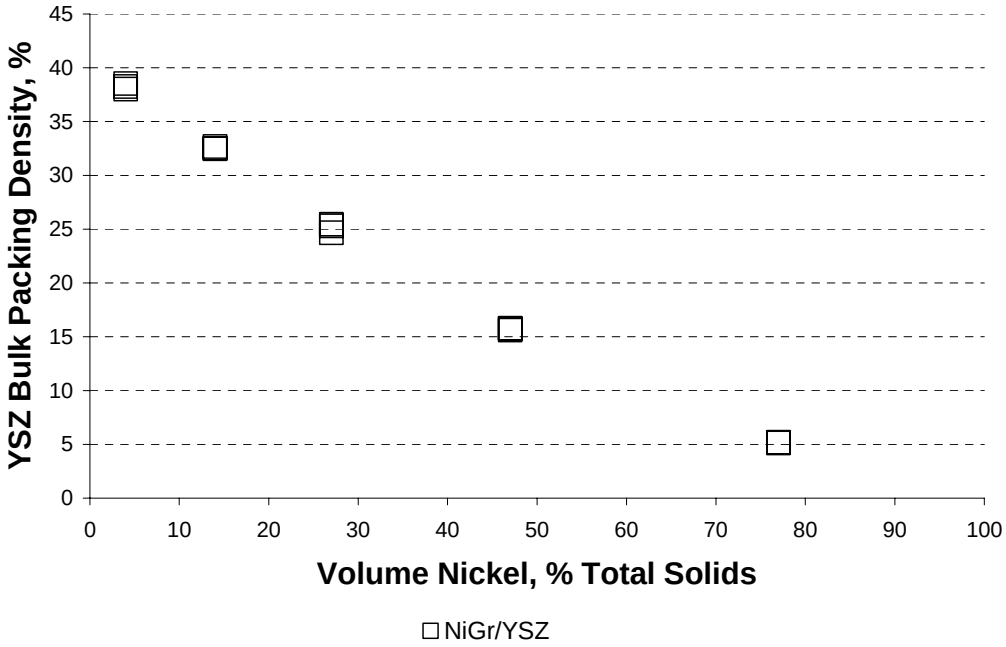

Figure 5-9: YSZ packing densities within the green NiGr/YSZ composites

From Figure 5-8, it is clear that the additional polymer material added to the tape cast slurry along with the graphite powder causes a "dilution" of the nickel and YSZ packing within the green tape from about 40% to 25% at the higher nickel (and therefore graphite) content. In contrast, the graphite-free composites have packing densities that increase with increasing nickel content as less polymer material is added to the tape cast slurry with higher nickel loadings (See Appendix B). For the NiGr/YSZ composites, it is the YSZ packing density alone that is of interest (See Figure 5-9). Again, due to the additional polymer content added along with the NiGr particles the bulk YSZ packing density decreases from about 37% to 5% with higher NiGr loadings. Finally, the packing densities for the Ni&Gr-27/YSZ, Ni&Gr-47/YSZ, NiO&Gr-27/YSZ and NiO&Gr-47/YSZ composites are plotted in Figure 5-10 and Figure 5-11. Like the other graphite containing composites, as the graphite content increases the nickel and YSZ packing densities decrease by about 10%. These effects on packing density may have an influence over sintering and electrical conductivity behaviour as will be discussed in Sections 6.2 and 7.5 to follow.

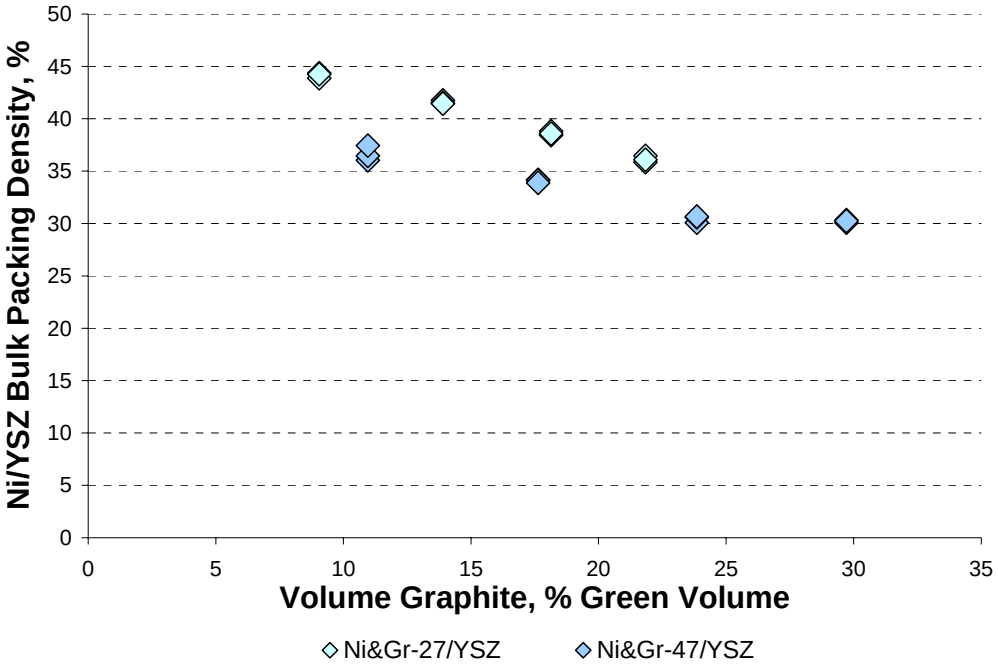

Figure 5-10: Nickel and YSZ packing densities within the green Ni&Gr-27/YSZ and Ni&Gr-47/YSZ composites

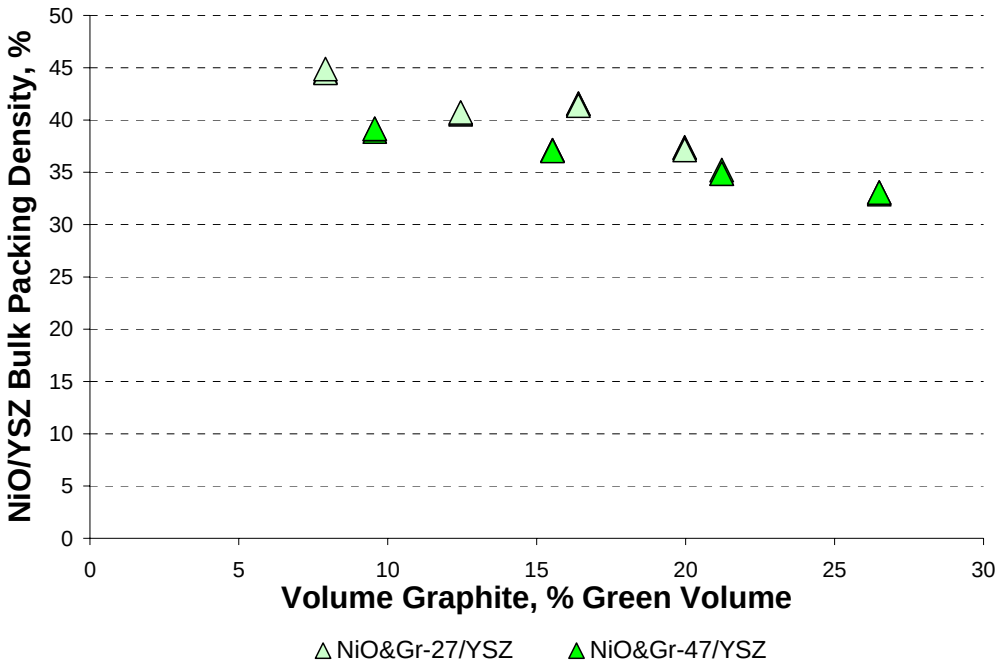

Figure 5-11: Nickel and YSZ packing densities within the green NiO&Gr-27/YSZ and NiO&Gr-47/YSZ composites

5.1.5 Nickel Oxidation

Another factor that may influence the sintering characteristics of the composites containing nickel powder is the change in volume that the nickel experiences during oxidation. Since nickel oxide is less dense than nickel metal (6.81 g/cm^3 and 8.9 g/cm^3 respectively), when nickel oxidizes it experiences an increase in volume of nearly 66%. The volume of nickel oxide, V_{NiO}, formed during nickel oxidation may be calculated as:

$$V_{NiO} = \frac{1.27 \times wt_{Ni}}{\rho_{NiO}} \qquad \textbf{(5-4)}$$

where wt_{Ni} is the weight of the original nickel powder and ρ_{NiO} is the density of nickel oxide.

Given that nickel is expected to oxidize during the burnout and sintering stages, Table 5-1 shows how the volume fractions of nickel oxide in the NiO/YSZ and NiO&Gr/YSZ composites compare to the Ni/YSZ and Ni&Gr/YSZ composites in the green state if the nickel powder within these composites is completely oxidized. Clearly, the Ni&Gr/YSZ and NiO&Gr/YSZ composites show very good agreement between the actual and theoretical nickel oxide loadings. On the other hand, the nickel oxide loadings for the Ni/YSZ and NiO/YSZ composites compare less favourably as the nickel oxide content increases.

Table 5-1: Nickel and nickel oxide green volume fractions for Ni/YSZ, NiO/YSZ, Ni&Gr/YSZ, and NiO&Gr/YSZ composites

Ni/YSZ		*NiO/YSZ*	*Ni&Gr/YSZ*		*NiO&Gr/YSZ*
Ni(O) Volume (% of Green Volume)		**Measured Volume NiO (% of Green Volume)**	**Ni(O) Volume (% of Green Volume)**		**Measured Volume NiO (% of Green Volume)**
Measured Ni Loading	**Theoretical NiO Loading**		**Measured Ni Loading**	**Theoretical NiO Loading**	
1.74	2.86	2.81	1.55	2.54	2.53
6.45	10.3	9.76	4.50	7.26	7.09
13.7	20.9	19.1	7.25	11.5	11.1
25.6	36.3	31.7	9.84	15.3	14.7
46.7	59.3	49.5	12.3	18.9	17.9
64.1	74.8	61.0			

The differences in the nickel oxide loadings, given in Table 5-1, can be attributed to the differences in the amount of polymer contained in each of the original composite tapes. For the graphite containing composites, the relative amounts of nickel oxide, YSZ, graphite, and polymer material are similar between the composites made from nickel oxide powder and nickel powder once the oxidation of nickel is accounted for, as shown in Figure 5-12b and Figure 5-13. Since the polymer loadings are similar and there is a lower volume fraction of nickel (due to the graphite additions), the differences in the volume fraction of the oxidized nickel and the volume fraction of nickel oxide powder is small.

On the other hand, the Ni/YSZ composites show a greater difference in oxidized nickel loadings because the Ni/YSZ composites contain less polymer material than the NiO/YSZ composites. With less polymer added, and no graphite, the oxidized nickel occupies a greater proportion of the green volume in the Ni/YSZ composites. This difference in nickel oxide loading could alter the sintering behaviour of the Ni/YSZ composites because the relative density of these composites will be higher after the polymer material is burned away compared to the NiO/YSZ composites.

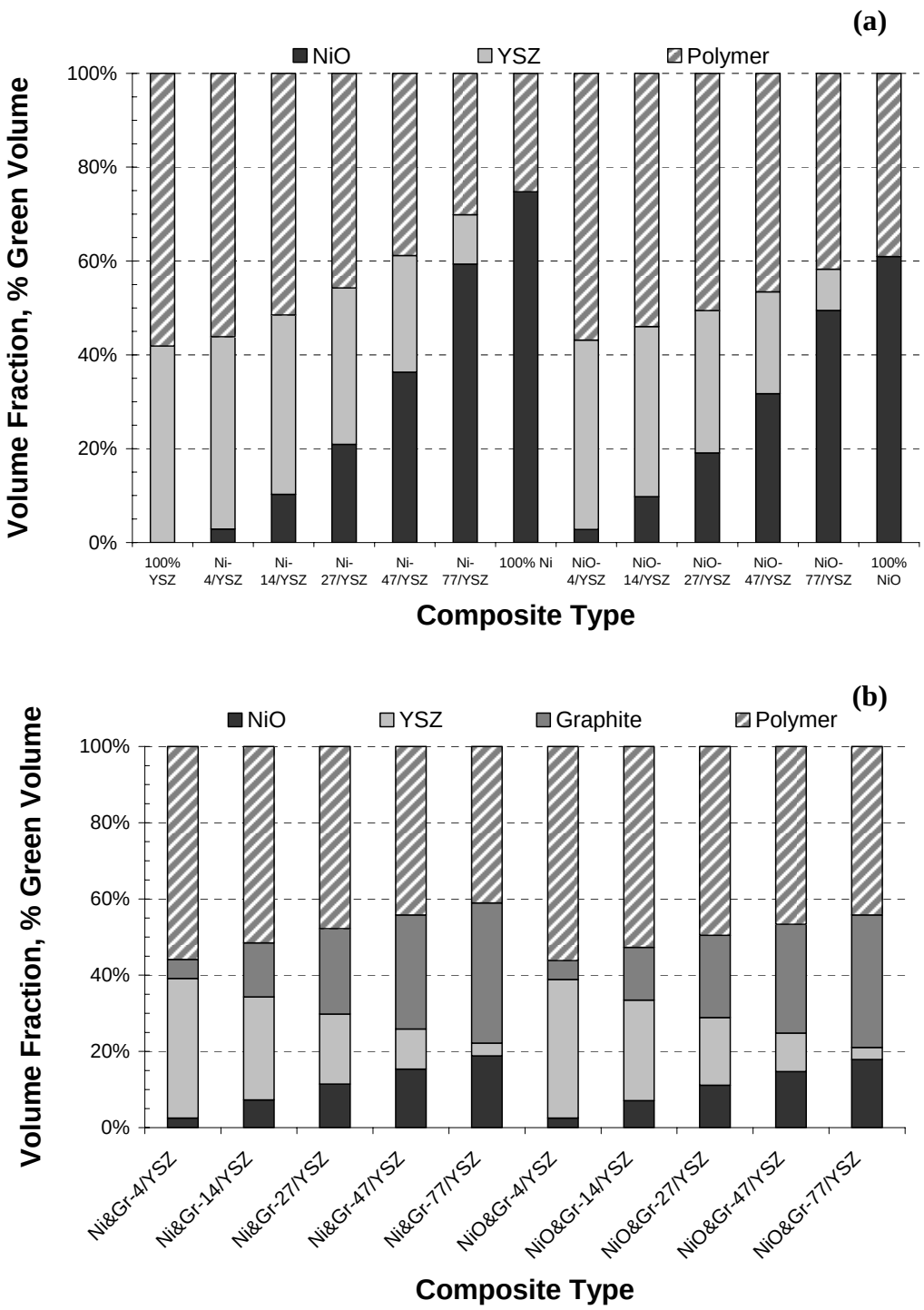

Figure 5-12: Volume fractions of the polymer, the YSZ, and the actual and theoretical nickel oxide phases for a) Ni/YSZ and NiO/YSZ composites, and b) Ni&Gr/YSZ and NiO&Gr/YSZ composites

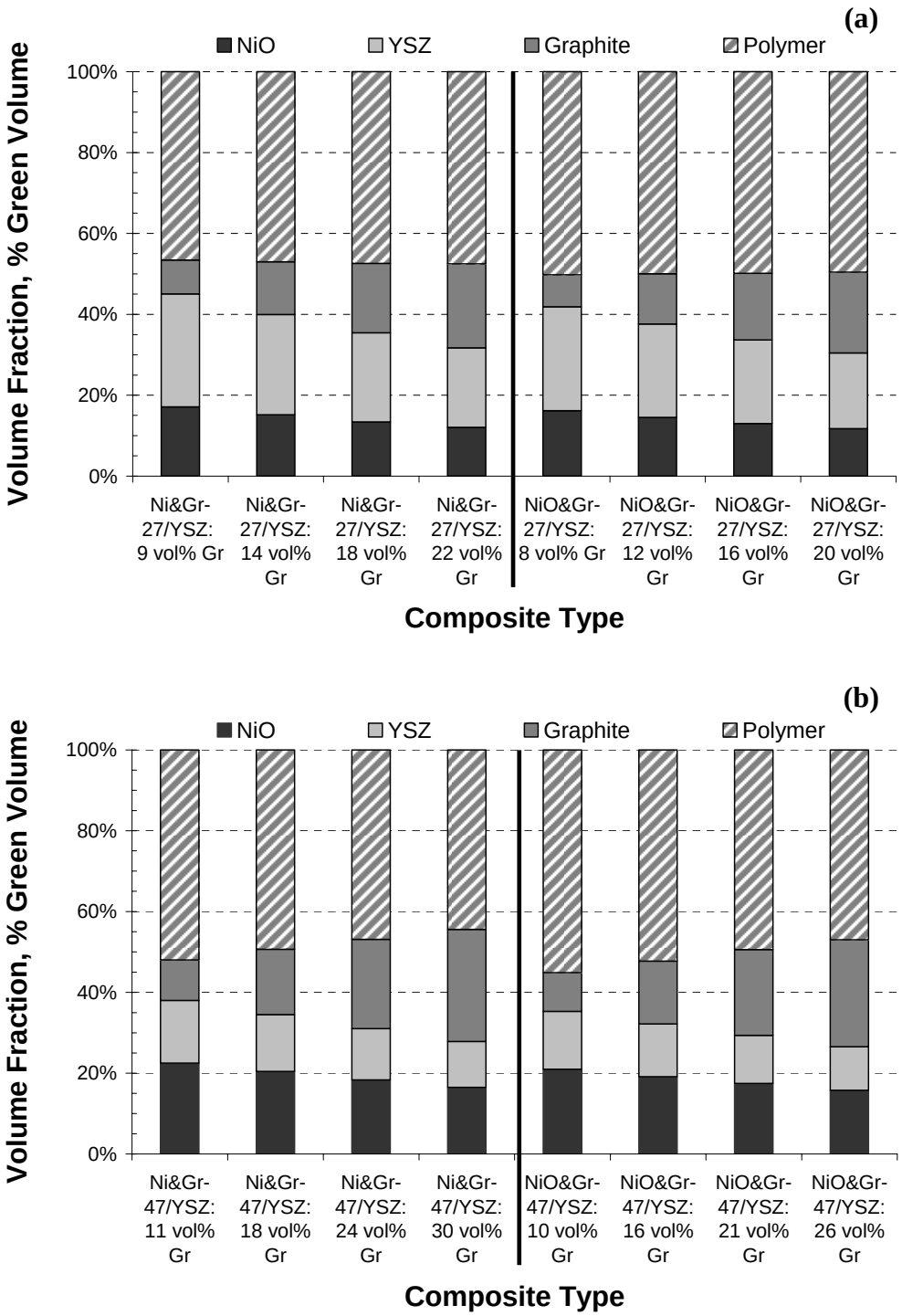

Figure 5-13: Volume fractions of the polymer, the YSZ, and the actual and theoretical nickel oxide phases for a) Ni&Gr-27/YSZ and NiO&Gr-27/YSZ composites, and b) Ni&Gr-47/YSZ and NiO&Gr-47/YSZ composites

5.2 THE BURNOUT STATE

Before sintering, each sample is heated in air in order to burn away any polymer and graphite material present. To remove the polymer material, each sample is slowly heated to 350°C. Following this, the samples are heated to 900°C to remove any existing graphite.

5.2.1 Theoretical Weight Changes

During the graphite burnout stage where temperatures reach 900°C the polymer and graphite are expected to be fully vaporized, while any nickel powder present in the composite is expected to be fully oxidized. The degree of polymer and graphite removal and nickel oxidation can be estimated by comparing the actual sample weight change with the theoretical value. For the nickel oxide containing composites, the weight change during the burnout stage is simply associated with the loss of polymer and graphite since the nickel is already oxidized. The nickel metal containing composites however will experience a weight gain due to the oxidation of nickel coupled with the loss of the polymer and graphite material. The percentage of the theoretical weight change for three samples of each composite type is given in Figure 5-14.

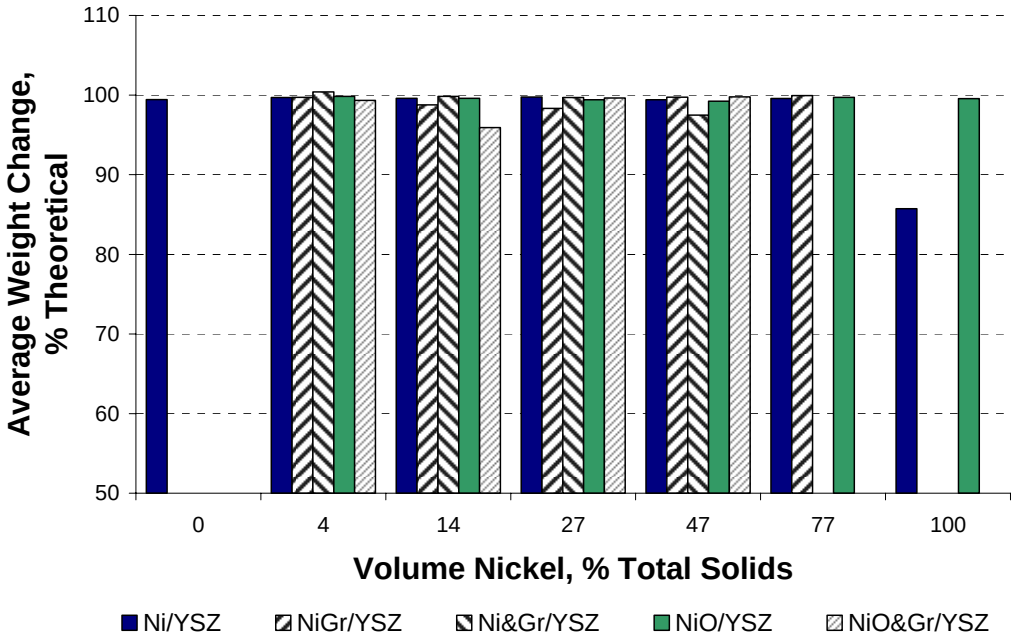

Figure 5-14: The average change in sample weight as a percentage of the theoretical weight change for Ni/YSZ, Ni&Gr/YSZ, NiGr/YSZ, NiO/YSZ, and NiO&Gr/YSZ composite samples

From Figure 5-14, it is clear that nearly all samples have the expected change in weight. Therefore, it is reasonable to assume that all the polymer and graphite material burned away and that all the nickel metal present completely oxidized. One exception is the 100% Ni from Ni samples where the expected weight change averages only 85%. Given that the 100% Ni from Ni samples do not have any graphite additions and the polymer material vaporizes at relatively low temperatures, the lower sample weight is likely a result of the nickel metal not completely oxidizing. In fact, the micrograph depicted in Figure 5-15 shows evidence of some residual nickel metal found in a 100% Ni sample even after

sintering to 1475°C in air for one hour. The bright white areas of the micrograph are areas of nickel metal, while the dark grey areas are the previously oxidized nickel. It is interesting to note that the nickel distribution around the nickel oxide suggests that the remaining nickel melted filled the pores within the nickel oxide structure. This is not surprising since there exists a Ni-NiO eutectic structure that melts at 1440°C and the melting point of pure nickel is 1455°C [88].

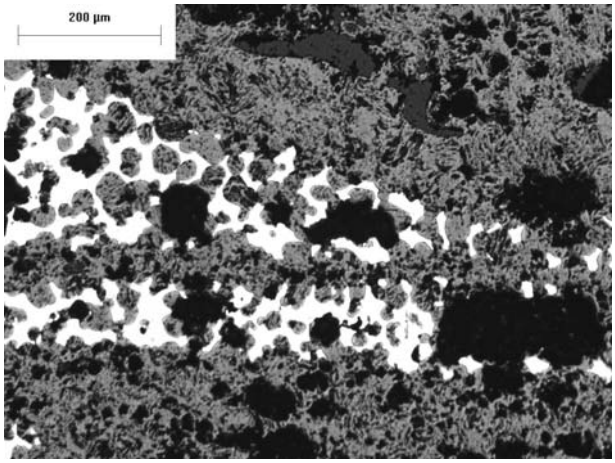

Figure 5-15: Micrograph of a 100% Ni from Ni sample after sintering in air for one hour at 1475°C. The light phase is nickel metal, the grey phase nickel oxide, and the dark regions porosity.

The theoretical weight changes for the composites with varying graphite content are given in Figure 5-16. Again, the results suggest that all the polymer and graphite material has been burned away and all the nickel powder is completely oxidized.

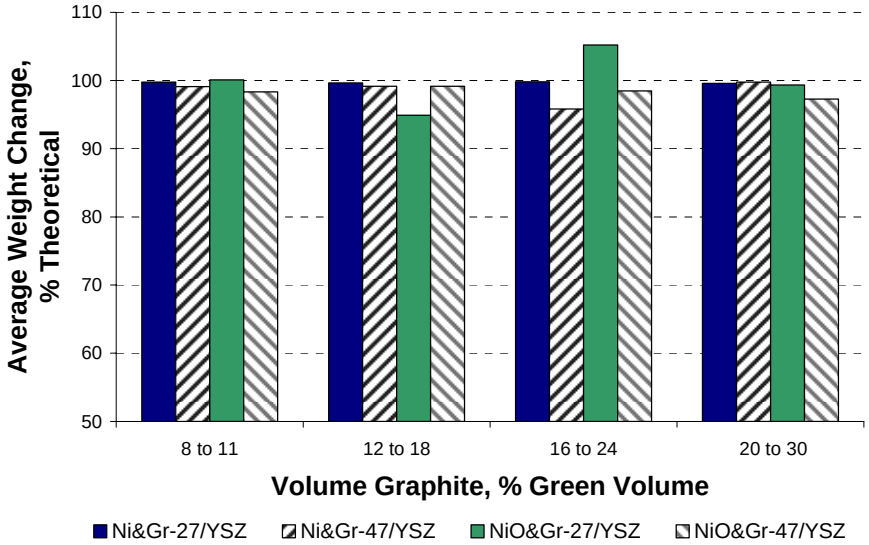

Figure 5-16: The average change in sample weight as a percentage of the theoretical weight change for Ni&Gr-27/YSZ, Ni&Gr-47/YSZ, NiO&Gr-47/YSZ, and NiO&Gr-47/YSZ composite samples. For each composite type, the lowest graphite loading is on the left and progressively increases to the highest graphite loading on the right.

5.2.2 Volumetric Dimensional Changes during Burnout

During the burnout stage, each 8 mm x 6 mm x 3 mm sample, created for dilatometric studies, experience some dimensional change during the burnout stage. The volumetric shrinkage as a result of the polymer and graphite burnout stages may be calculated by taking the difference in the volume between the pressed green sample volume (V_G) and the sample volume after burnout (V_{BO}) and dividing by the sample pressed green volume as follows:

$$Volumetric\ Shrinkage = \frac{V_G - V_{BO}}{V_G} \times 100\% \tag{5-5}$$

By definition of Equation (5-5), positive volumetric shrinkage values represent a reduction in volume (i.e. shrinkage) while negative volumetric shrinkage values represent an increase in volume (i.e. expansion). The calculated volumetric shrinkages for three samples of the Ni/YSZ and NiO/YSZ composites are shown in Figure 5-17, while the volumetric shrinkages for three samples of the Ni/YSZ, NiGr/YSZ, and Ni&Gr/YSZ composites and three samples of the NiO/YSZ and NiO&Gr/YSZ composites are shown in Figure 5-18 and Figure 5-19 respectively.

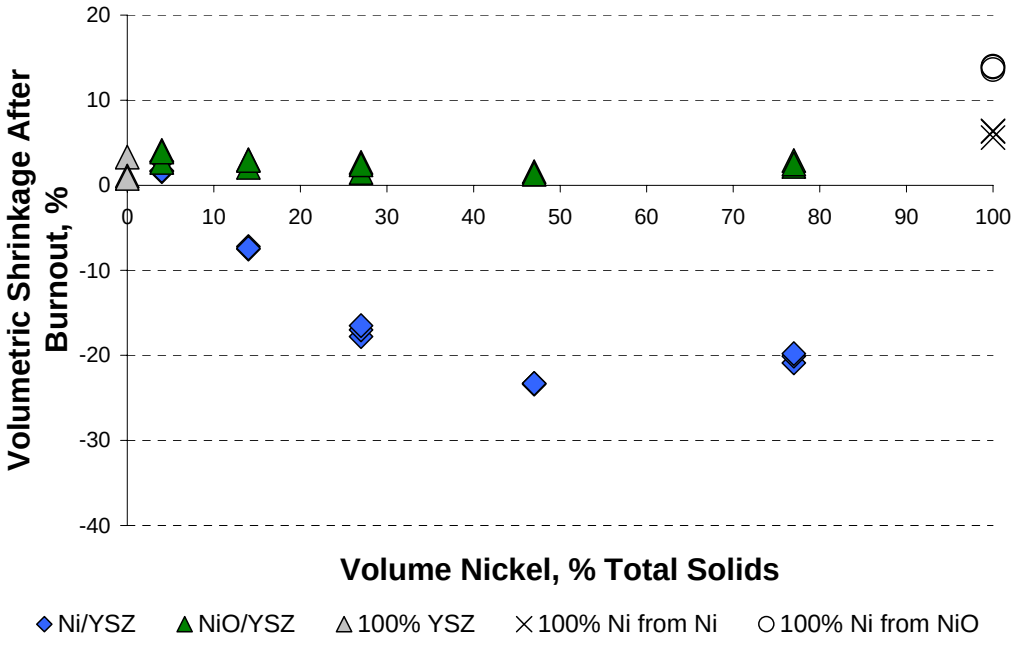

Figure 5-17: Volumetric changes for the Ni/YSZ and NiO/YSZ composites during burnout

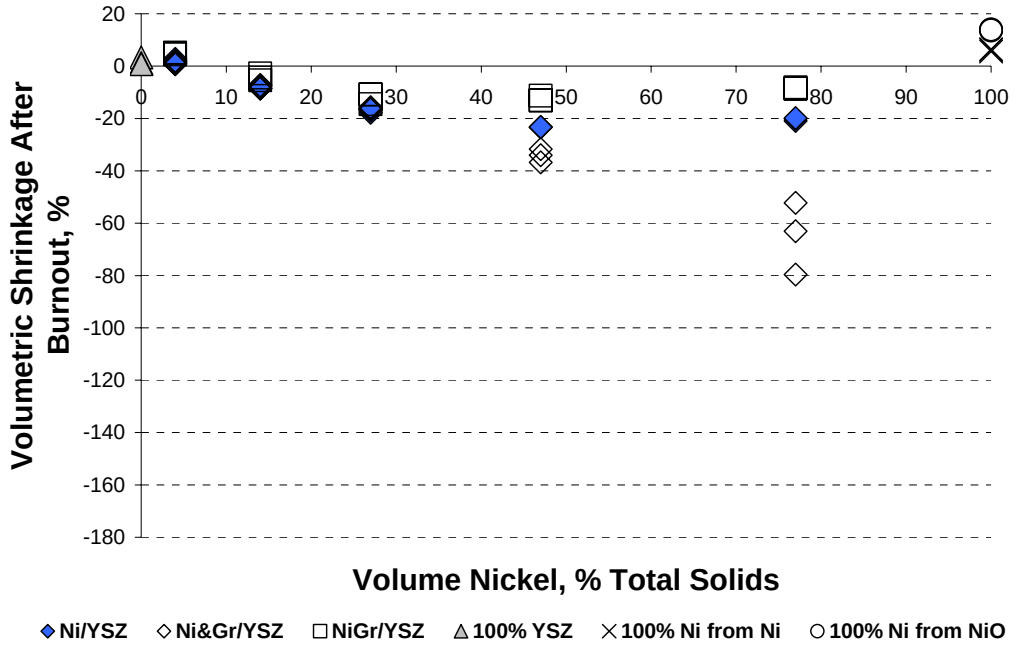

Figure 5-18: Volumetric changes for the Ni/YSZ, NiGr/YSZ, and Ni&Gr/YSZ composites during burnout

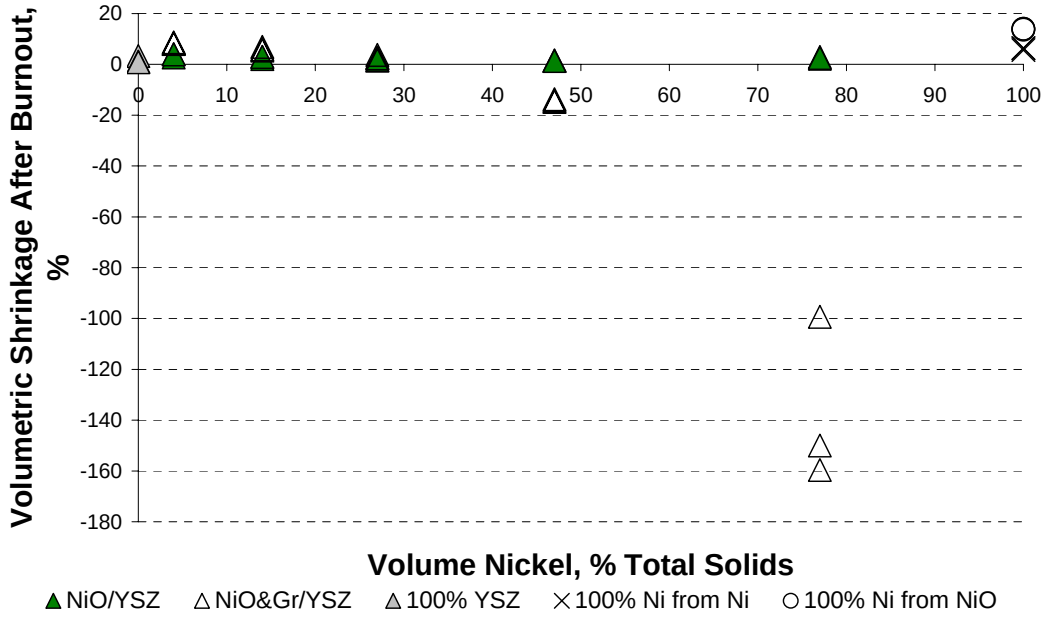

Figure 5-19: Volumetric changes for the NiO/YSZ and NiO&Gr/YSZ composites during burnout

As suggested by the sample weight changes, the nickel powder is expected to be fully oxidized after the burnout stage and cause a volumetric expansion of the nickel phase because nickel oxide is less dense than nickel metal. When examining Figure 5-17, the Ni/YSZ composites experience a significant volume expansion, particularly with higher nickel loadings, with the maximum expansion occurring at 47 vol% Ni of total solids. However, at nickel loadings above 47 vol% Ni the amount of volume expansion begins to decrease. This would suggest that there is a competition between the composites shrinkage due to pre-sintering and expansion due to nickel oxidation.

Interestingly, the 100% Ni sample from Ni powder actually experiences a volumetric shrinkage giving further evidence that the nickel powder is not completely oxidized. Like the pure nickel sample, the 100% Ni from NiO samples experience a significant volumetric shrinkage. While less significant, the nickel oxide composites also shrink slightly, similar to the 100% YSZ samples, at each nickel loading. The volumetric shrinkage for the NiO/YSZ composites appears to reach a minimum however at a nickel loading of 47 vol% Ni of total solids.

The NiGr/YSZ and Ni&Gr/YSZ composite types each show a volumetric expansion, like the Ni/YSZ composites, as shown in Figure 5-18. The NiGr/YSZ composites exhibit an increasing volumetric expansion at low nickel loadings reaching a maximum expansion at 47 vol% Ni of total solids before the volumetric expansion decreases. The Ni&Gr/YSZ composites however, have a steadily increasing volumetric expansion with increasing nickel content until the volumetric expansion becomes quite severe at 77 vol% Ni of total solids.

The variability in the 77 vol% Ni composite sample measurements is a result of the difficulty in accurately measuring the samples. The fragile samples had to be measured with a simple ruler as trying to measure the samples with callipers usually resulted in breakage. Figure 5-20 shows a photograph of the "exploded" Ni&Gr/YSZ and NiO&Gr/YSZ composites with a nickel loading of 77 vol% Ni of total solids after the burnout stage.

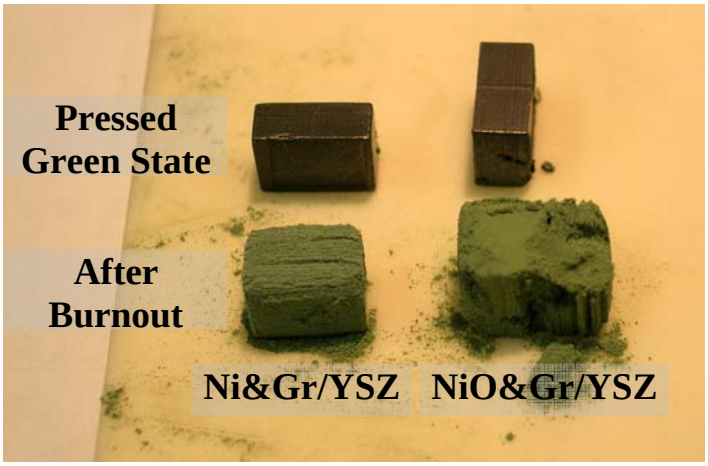

Figure 5-20: Photographs of Ni&Gr/YSZ (left) and NiO&Gr/YSZ (right) composites with a nickel loading of 77 vol% Ni of total solids in the pressed green state shown above the composites after the burnout stage.

The NiO&Gr/YSZ composites, as depicted in Figure 5-19, have similar volumetric changes during the burnout stage when compared with the NiO/YSZ composites up to a nickel content of 47 vol% Ni of total solids. At this nickel loading, the NiO&Gr/YSZ composites begin to expand (~14%) while the volumetric expansion increases dramatically (>100%) at a nickel loading of 77 vol% Ni of total solids. As was the case for the high nickel content Ni&Gr/YSZ composites, the variability in the

measurements of the highest nickel content NiO&Gr/YSZ samples is a result of the difficulty in accurately measuring the samples without breaking them.

Evidence of a critical volume fraction of graphite where the dimensional changes of the graphite containing composites deviates from that of the graphite-free composites is presented in Figure 5-21 with the volumetric changes for the Ni&Gr-27/YSZ, Ni&Gr-47/YSZ, NiO&Gr-27/YSZ, and NiO&Gr-47/YSZ composites. The dimensional changes for the Ni&Gr-27/YSZ and NiO&Gr-27/YSZ composites are independent of the graphite loading in the green composites. However at the higher nickel content of the Ni&Gr-47/YSZ and NiO&Gr-47/YSZ composites, a dramatic increase in volumetric expansion at the higher graphite loadings occurs.

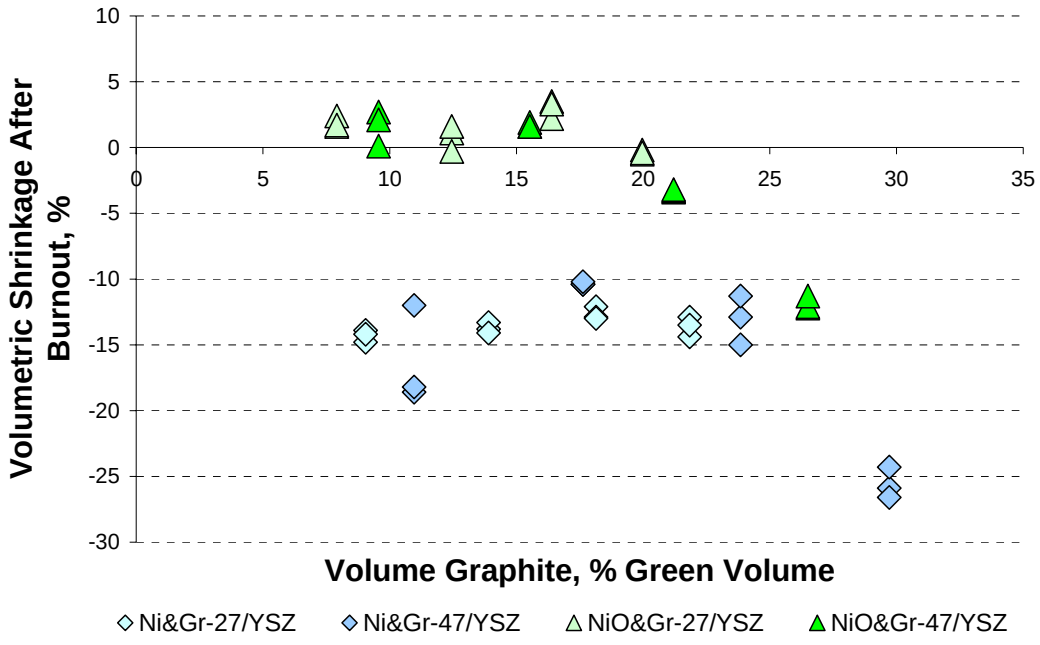

Figure 5-21: Volumetric changes for the Ni&Gr-27/YSZ, Ni&Gr-47/YSZ, NiO&Gr-27/YSZ, and NiO&Gr-47/YSZ composites having a fixed nickel loading and varying graphite content during burnout

5.2.3 Linear Dimensional Changes during Burnout

In addition to quantifying the volumetric changes during burnout, the linear dimensional changes can be calculated for any measured dimension (i.e. length, width, and thickness) by dividing the difference in the dimensions in the pressed green state and after burnout by the dimension in the pressed green state. For instance, the linear dimensional change in the length can be calculated as follows:

$$Dimensional\ Shrinkage = \frac{L_G - L_{BO}}{L_G} \times 100\% \quad \textbf{(5-6)}$$

where L_{BO} is the length after burnout, and L_G is the length of the sample in the pressed green state. As was the case for volumetric shrinkages, positive dimensional shrinkage values represent a linear reduction in dimension. A diagram defining the direction of length, width, and thickness is shown in Figure 5-22. The linear dimensional changes during burnout in the three directions for three samples of each composite type are shown in Figure 5-23 through Figure 5-29.

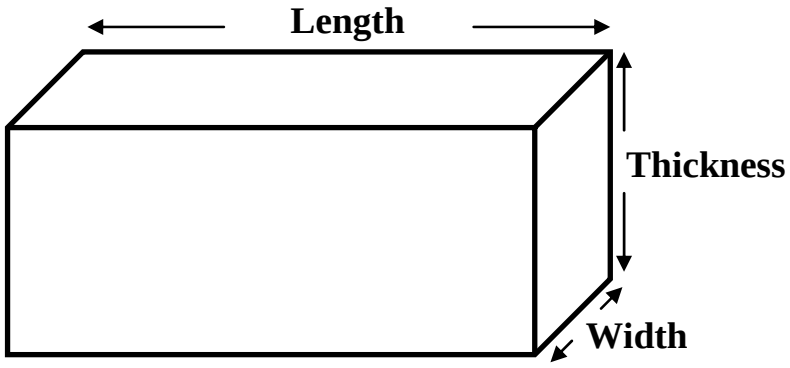

Figure 5-22: Definition of the length, width, and thickness directions for calculating the linear sintering shrinkage of a composite sample. Lamination for each sample took place by pressing individual layers in the thickness direction.

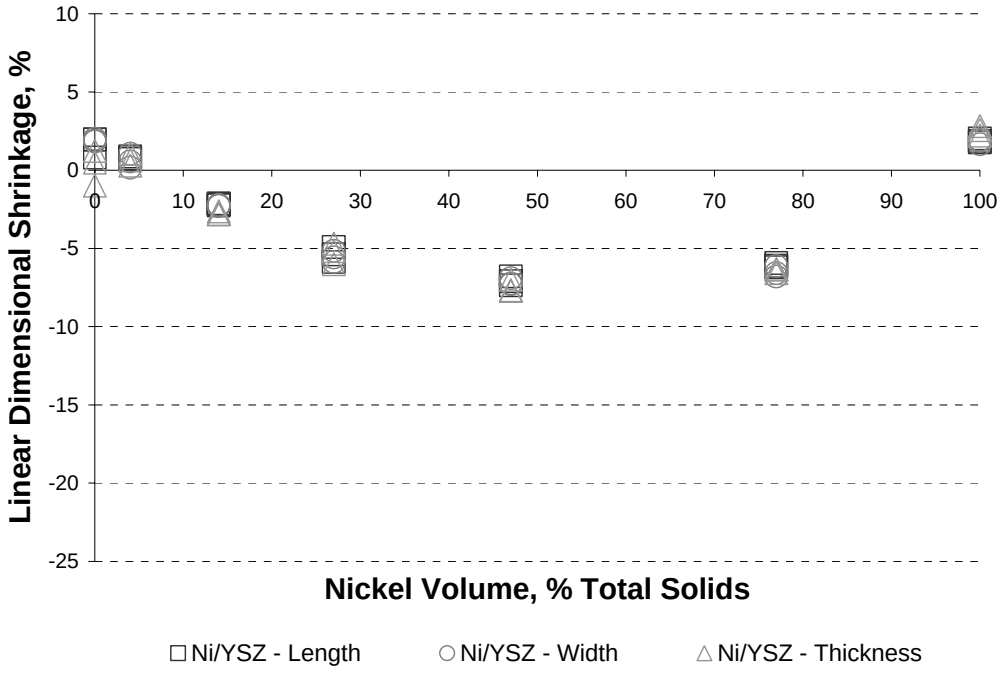

Figure 5-23: Manually measured dimensional changes from the green to burnout state for the length, width, and thickness of Ni/YSZ composite samples

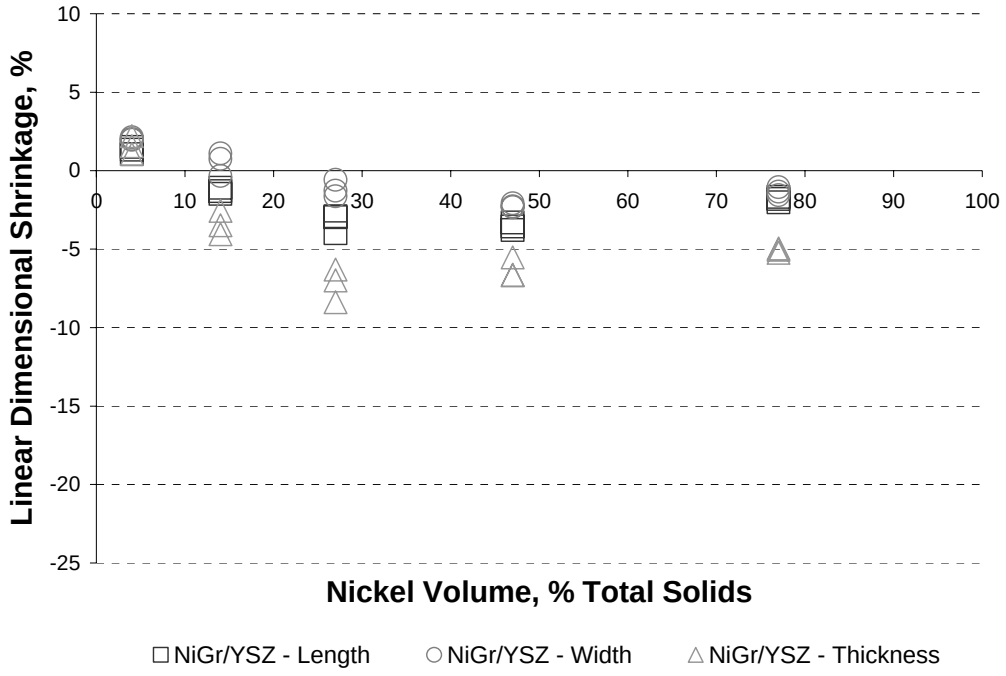

Figure 5-24: Manually measured dimensional changes from the green to burnout state for the length, width, and thickness of NiGr/YSZ composite samples

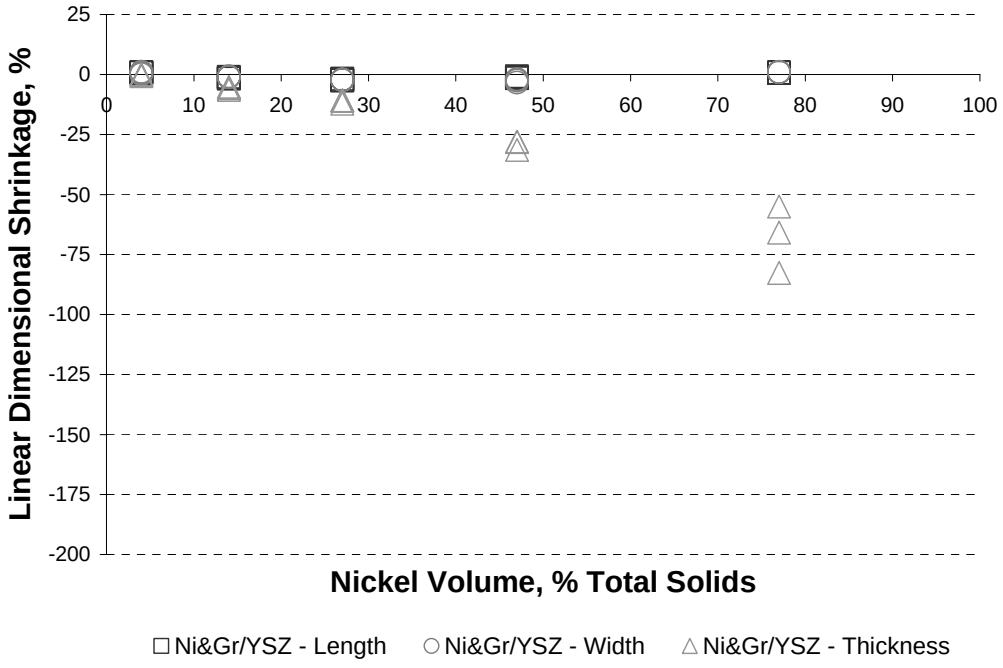

Figure 5-25: Manually measured dimensional changes from the green to burnout state for the length, width, and thickness of Ni&Gr/YSZ composite samples

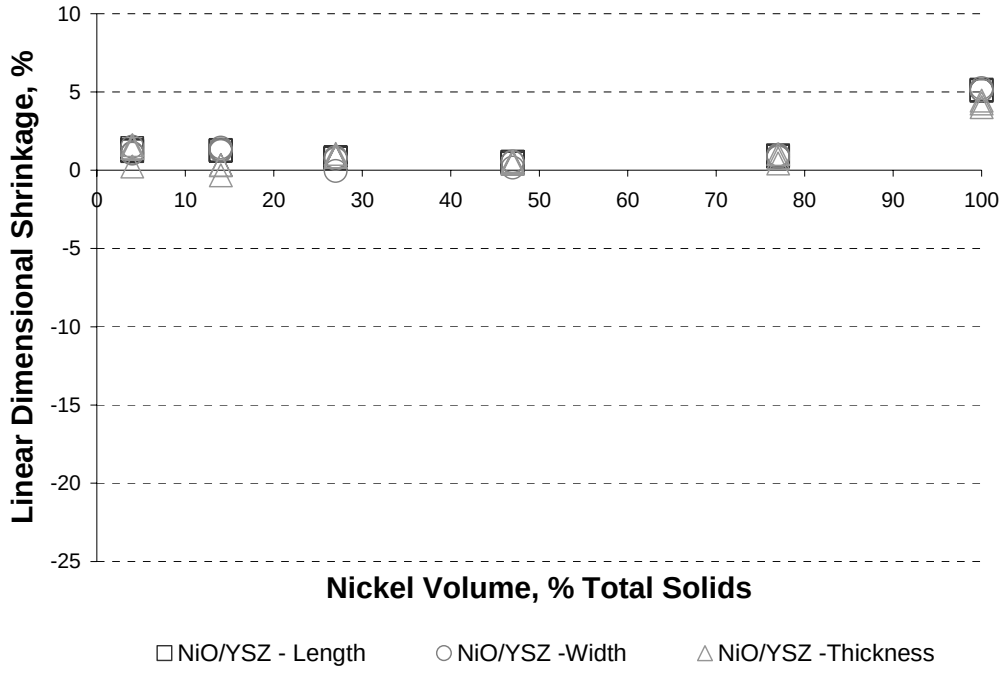

Figure 5-26: Manually measured dimensional changes from the green to burnout state for the length, width, and thickness of NiO/YSZ composite samples

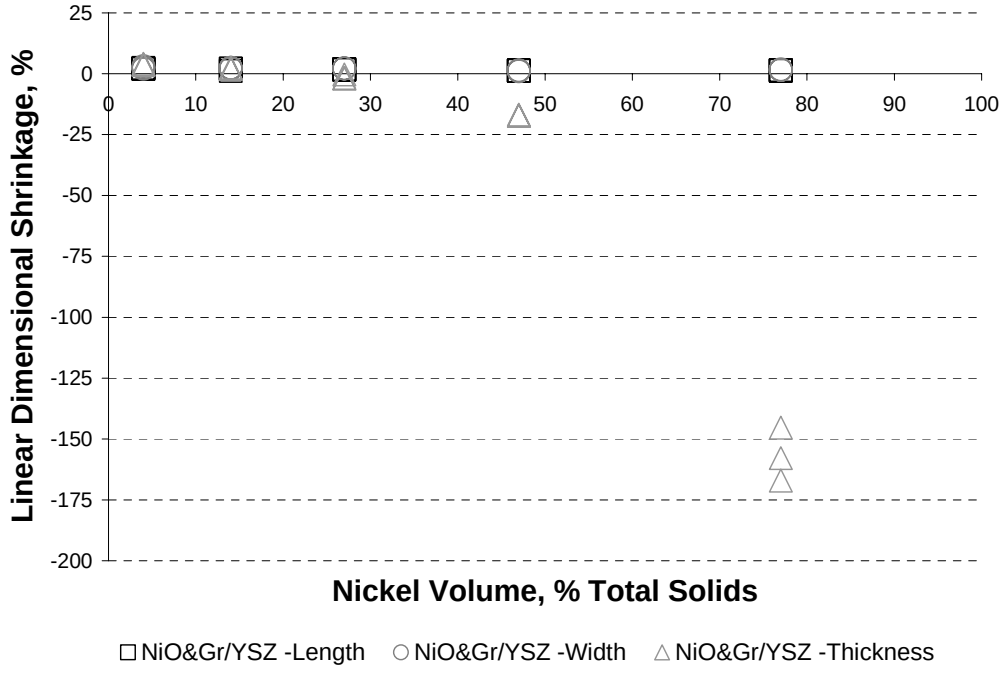

Figure 5-27: Manually measured dimensional changes from the green to burnout state for the length, width, and thickness of NiO&Gr/YSZ composite samples

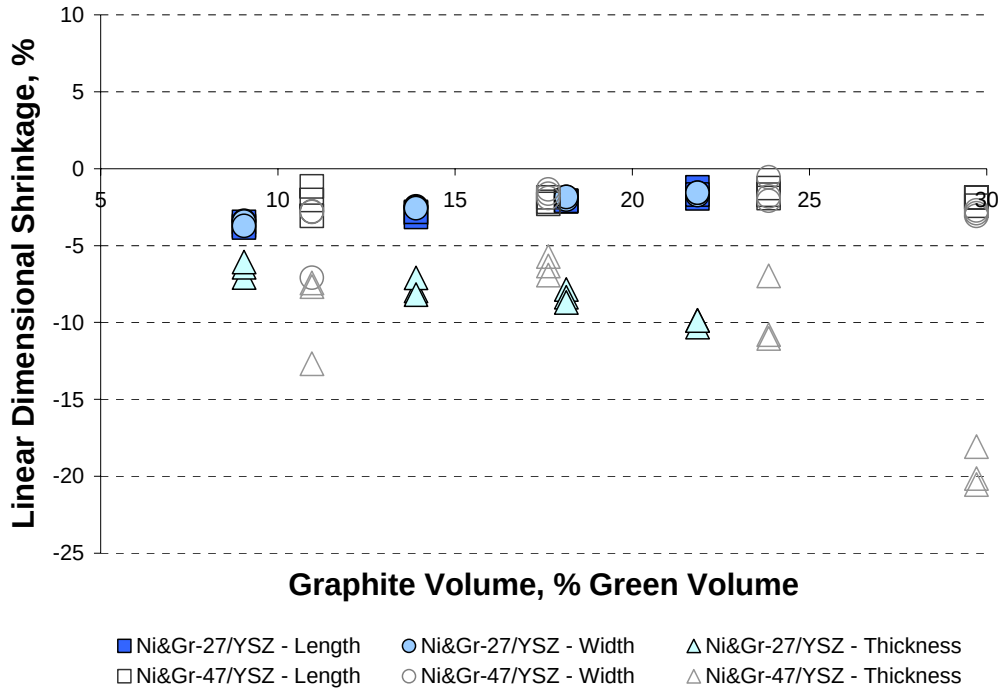

Figure 5-28: Manually measured dimensional changes from the green to burnout state for the length, width, and thickness of Ni&Gr-27/YSZ and Ni&Gr-47/YSZ composite samples

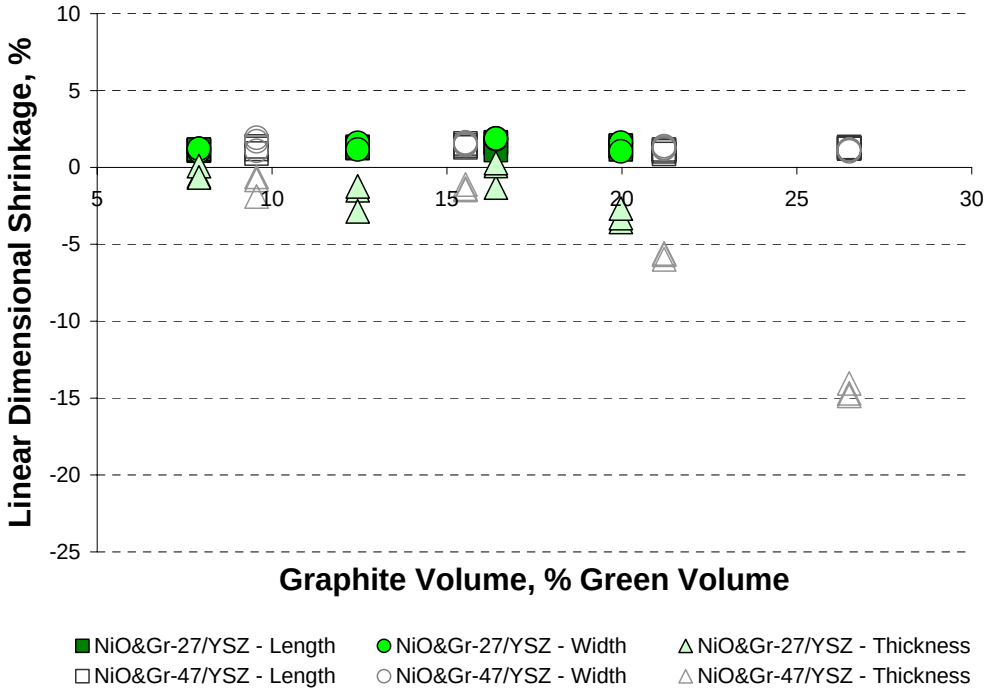

Figure 5-29: Manually measured dimensional changes from the green to burnout state for the length, width, and thickness of NiO&Gr-27/YSZ and NiO&Gr-47/YSZ composite samples

In general, the amount of anisotropy associated with the dimensional changes during burnout is dependent on the composite type. The graphite-free composites (See Figure 5-23 and Figure 5-26) have linear dimensional changes during burnout that are nearly isotropic. That is, the dimensional shrinkage in the length, width, and thickness are almost identical. Since the volumetric shrinkages during burnout are a function of the linear shrinkages, it is not surprising that the Ni/YSZ composites show the same parabolic expansion trend with increasing nickel content with a maximum expansion at a volume fraction of 47 vol% Ni of total solids. Similarly, the NiO/YSZ composites show the same general shrinkage with a minimum shrinkage at the same nickel loading of 47 vol% Ni of total solids.

Conversely, when graphite is added the dimensional shrinkage is no longer isotropic, particularly in the thickness direction. Although the length and width generally experience the same dimensional change for a given composite sample, the thickness tends to change quite differently depending on the graphite loading. For example, the Ni&Gr/YSZ and NiO&Gr/YSZ composite samples, from Figure 5-25 and Figure 5-27 respectively, show the same dimensional shrinkage in the length and width direction when compared with the graphite-free composites, but experience a significant change in the thickness direction as the nickel (and corresponding graphite) content increases. At low nickel volume fractions, the dimensional changes are nearly isotropic. However, at a nickel loading of 27 vol% Ni of total solids the NiO&Gr/YSZ composites begin to expand slightly in the thickness direction and as the nickel content continues to increase, the expansion becomes more severe, particularly at a nickel loading of 77 vol% Ni of total solids.

The influence of graphite on the anisotropy of the dimensional shrinkages is clearer when examining the dimensional shrinkages of the Ni&Gr-27/YSZ, Ni&Gr-47/YSZ, NiO&Gr-27/YSZ, and NiO&Gr-47/YSZ composites with varying graphite loadings, as shown in Figure 5-28 and Figure 5-29. At lower graphite loadings, the spread between the dimensional changes in each of the three directions is relatively small. As the graphite loading increases, the dimensional change in the thickness direction deviates more substantially from the dimensional change in the length and width. For the Ni&Gr-27/YSZ and Ni&Gr-47/YSZ composites, the width and length tend to expand less with increasing graphite, while the thickness tends to expand more. Likewise, the NiO&Gr-47/YSZ composites show a constant dimensional change in the length and width directions and a significant increase in the degree of expansion in the thickness direction. The NiO&Gr-27/YSZ composites, however, do not show any sizable variation in the dimensional changes for any direction as the graphite loading increases.

For completeness, the NiGr/YSZ composites (Figure 5-24) show more dimensional shrinkage anisotropy in all three directions relative to the other composite types. That is, the dimensional shrinkage in the length, width, and thickness directions are dissimilar. The NiGr/YSZ composites tend to show less dimensional expansion in the width direction compared to the length and thickness directions. The degree of anisotropy appears greatest at a nickel loading of 27 vol% Ni of total solids where the range of dimensional expansion is greatest. Above 27 vol% Ni of total solids, the difference between the length and width dimensional expansion decreases and the expansion in the thickness decreases as well.

5.2.3.1 Dilatometer Studies

From Figure 5-23, the Ni/YSZ composite samples appear to reach a maximum linear expansion at a nickel content of 47 vol% Ni of total solids. This suggests that there may be a competition between a shrinking effect due to the sintering of the YSZ and nickel particles and an expansion effect due to the oxidation of nickel. The significant shrinkage of the 100% Ni from Ni and 100% Ni from NiO samples provide evidence that a small amount of sintering is taking place.

To monitor the dimensional changes during the burnout stage, two samples of 100% YSZ, 100% Ni from Ni, 100% Ni from NiO, Ni/YSZ composites with a nickel loading of 47 vol% Ni and 77 vol% Ni of total solids, and NiO/YSZ composites with a nickel loading of 47 vol% Ni of total solids were heated in a dilatometer using the second burnout heating schedule, with the results shown in Figure 5-30. As anticipated, the average linear dimensional change measured by the dilatometer corresponds to the manually measured samples from before.

However, the manner in which the final dimensions are reached is quite interesting. For the 100% YSZ samples, there is very little dimensional change taking place over the course of the second burnout stage after thermal expansion and contraction effects are accounted for. Similarly, the NiO&Gr/YSZ composite samples show very little dimensional change. On the other hand, the 100% Ni from Ni samples show a slightly different behaviour. After about one hour (at ~400°C), the 100% Ni from Ni samples experience a sharp drop in length indicating that some degree of sintering is taking place. One hour later (at ~500°C), the 100% Ni from Ni samples stop shrinking and the dimensional change stabilizes. At the same time (at ~500°C), both the Ni/YSZ composites begin to expand rapidly until the isothermal hold at 900°C where the amount of expansion levels off. The rapid expansion at 500°C suggests this is the temperature where the nickel begins to oxidize. Finally, the 100% Ni from NiO samples begin to sinter after three hours (at ~750°C) and start to shrink continuously for the remainder of the heating cycle.

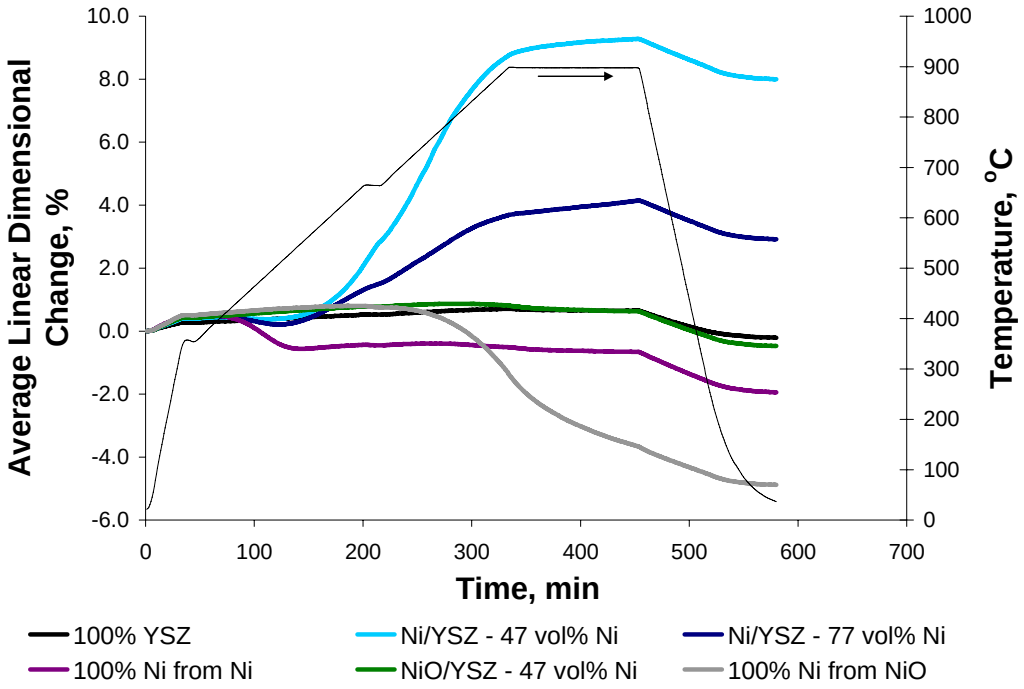

Figure 5-30: Dilatometer plots showing the average linear dimensional change of various Ni/YSZ composites. Samples made from 100% YSZ and 100% Ni are included for reference. The percentages given represent the volume fraction of nickel as a percent of total solids in the sintered and reduced state. The heating cycle used is represented by the dashed line.

To verify that the nickel is indeed oxidizing at 500°C, a sample of a Ni/YSZ composite with a nickel loading of 47 vol% Ni of total solids, and a sample of the 100% Ni from Ni tape were each heated in a thermogravimetric furnace using the same burnout heating cycle (See Table 3-6) after the first polymer burnout stage (See Table 3-5). Upon inspection of Figure 5-31, it is clear that the 100% Ni from Ni sample actually begins to oxidize (i.e. gain weight) around 400°C whereas the Ni/YSZ composite sample starts to oxidize around at 500°C.

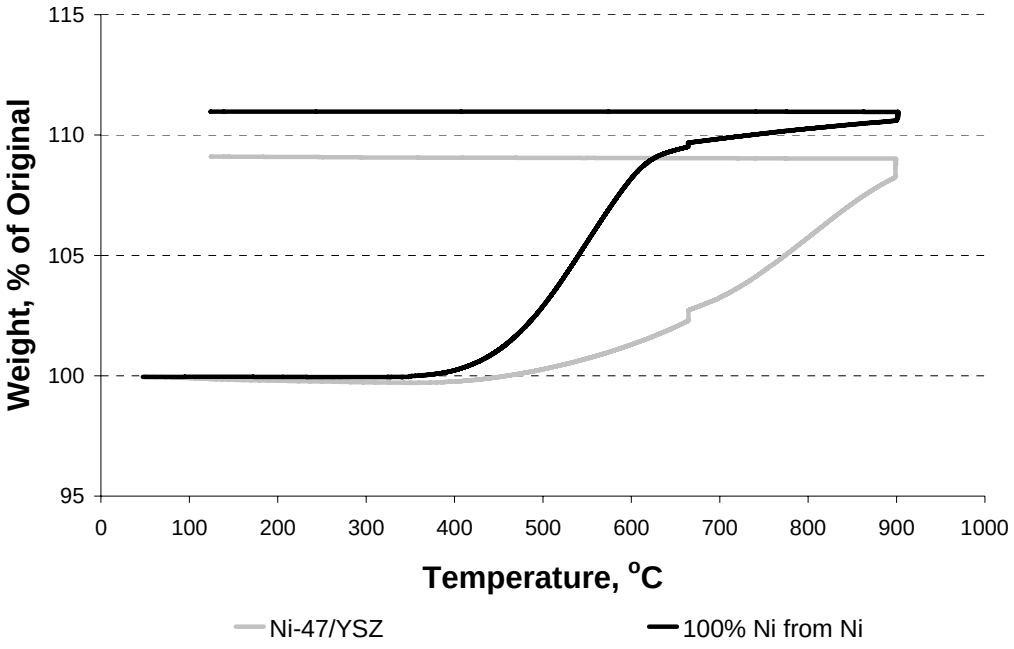

Figure 5-31: Weight gain during burnout of a Ni/YSZ composite sample with a nickel loading of 47 vol% Ni of total solids and a 100% nickel sample

5.2.4 Density Variations during Burnout

Typically, dimensional changes during sintering are accompanied by changes in density. The relative density for three samples of each composite type as a percentage of the theoretical density, assuming that the nickel is completely oxidized during burnout, is shown in Figure 5-32 through Figure 5-34. The change in density during the burnout stage for the Ni&Gr-27/YSZ, NiO&Gr-27/YSZ, Ni&Gr-47/YSZ, and NiO&Gr-47/YSZ composites are shown in Figure 5-35.

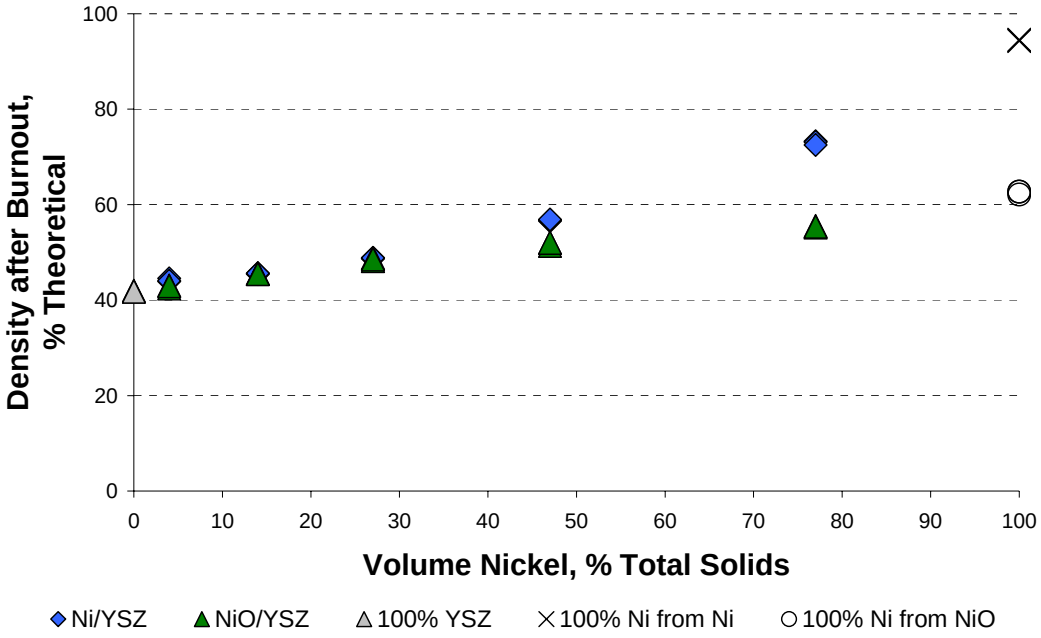

Figure 5-32: Density changes with respect to the theoretical density during the burnout stage for Ni/YSZ and NiO/YSZ composite types. The change in density for the 100% YSZ, 100% Ni from Ni, and 100% Ni from NiO samples are added for reference.

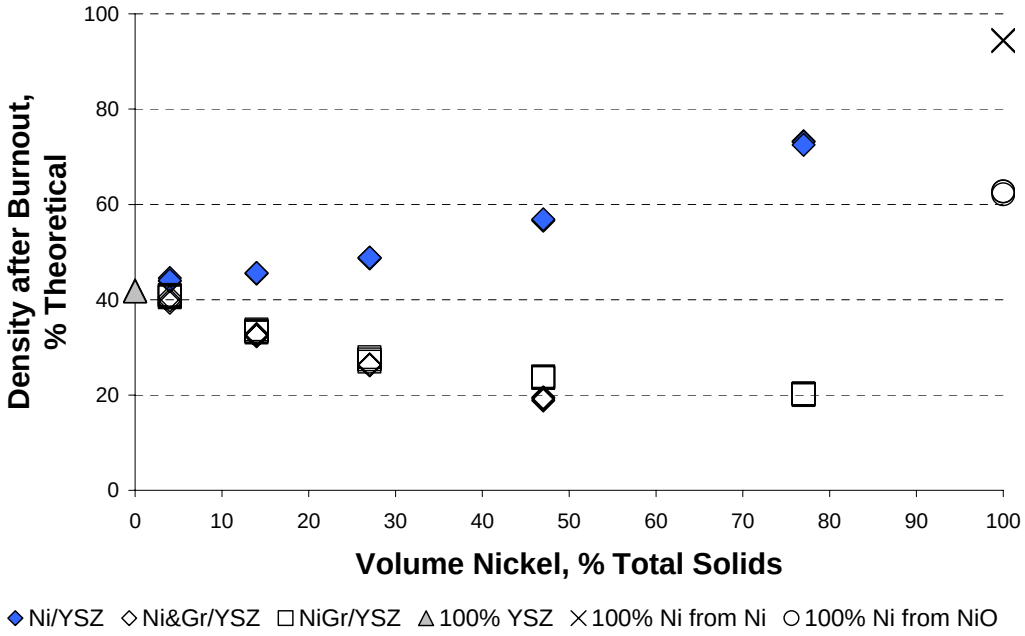

Figure 5-33: Density changes with respect to the theoretical density during the burnout stage for Ni/YSZ, Ni&Gr/YSZ, and NiGr/YSZ composite types. The change in density for the 100% YSZ, 100% Ni from Ni, and 100% Ni from NiO samples are added for reference.

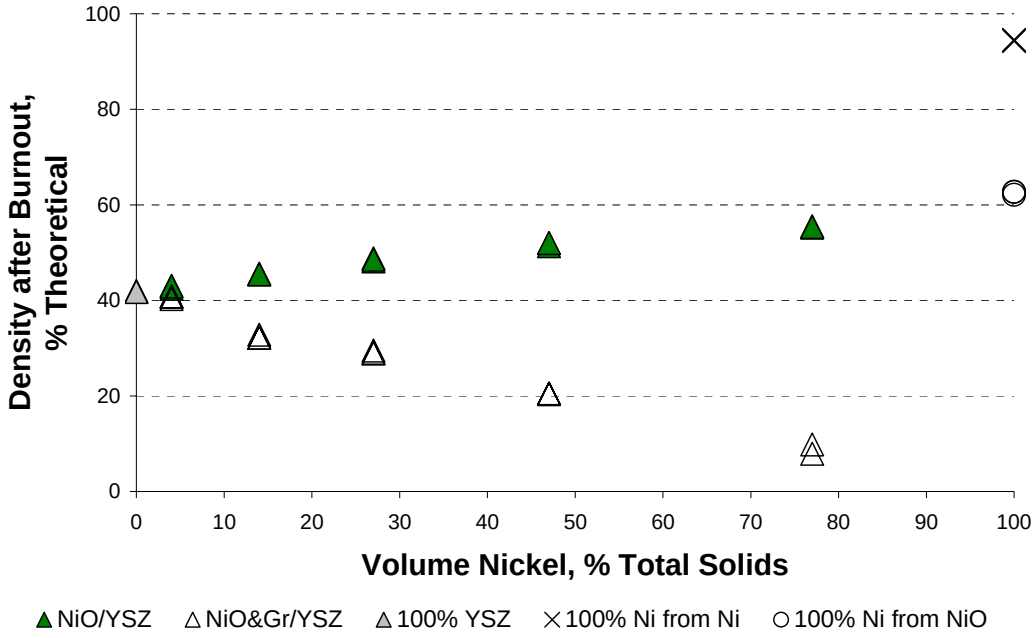

Figure 5-34: Density changes with respect to the theoretical density during the burnout stage for NiO/YSZ and NiO&Gr/YSZ composite types. The change in density for the 100% YSZ, 100% Ni from Ni, and 100% Ni from NiO samples are added for reference.

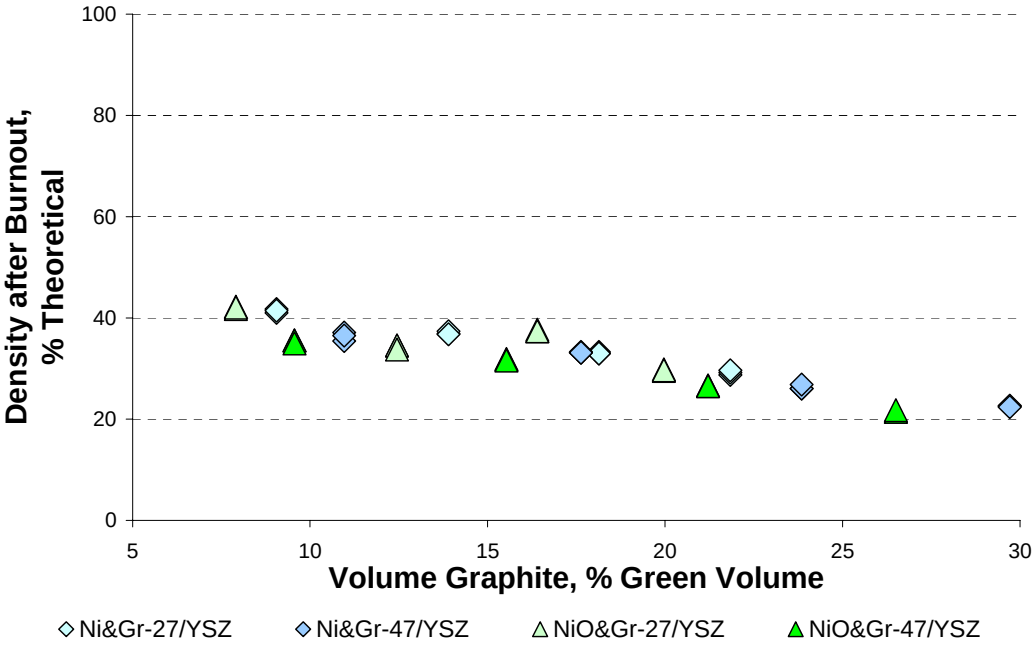

Figure 5-35: Density changes with respect to the theoretical density during the burnout stage for Ni&Gr-27/YSZ, NiO&Gr-27/YSZ, Ni&Gr-47/YSZ, and NiO&Gr-47/YSZ composite types.

Since the pure nickel samples exhibit the highest density, the Ni/YSZ and NiO/YSZ composites have relative densities that increase with the amount of nickel present in the composite. In addition, the densification of the samples with nickel loadings up to 27 vol% of total solids is similar to the densification of the 100% YSZ samples, while the higher nickel content samples have a change in density that is closer to that of the 100% Ni samples.

However, the high relative density of the 100% Ni from Ni samples is misleading since it is not completely oxidized. That is, the 95% theoretical density of the 100% Ni from Ni samples is a function of not only nickel oxide and porosity, but nickel metal as well. The presence of non-oxidized nickel metal, having a density greater than nickel oxide, contributes to a higher sample density compared to the density of pure nickel oxide. The amount of nickel remaining in the 100% Ni from Ni samples after the burnout stage can be determined by dividing the weight of the samples after burnout by the expected weight of the samples if they were completely made of nickel oxide. In this particular instance, only 86% of the nickel was converted to nickel oxide, suggesting that 14% of the nickel remains unoxidized. When the unoxidized nickel is accounted for, the relative density of the 100% Ni from Ni samples becomes 91%.

As expected, the relative density of the composites containing graphite decrease during burnout rather than increase like the graphite-free composites (See Figure 5-33 and Figure 5-34). Since graphite is added to the Ni&Gr/YSZ, NiGr/YSZ, and NiO&Gr/YSZ composites to create porosity, the relative density of the composites should be lower. At the highest nickel loading, graphite additions result in a significant change in density compared with the graphite free composites with a similar nickel loading of 77 vol% Ni of total solids. For the NiGr/YSZ composite samples, the relative density is only 20% compared to a relative density of over 70% for the Ni/YSZ composites. Similarly, the relative density of the NiO&Gr/YSZ composite samples is only 10% compared to a relative density of 55% for the NiO/YSZ composites.

The method of adding graphite, either as a separate particle, or with a nickel coating, does not significantly alter the densification of the samples during burnout. Both the Ni&Gr/YSZ and NiGr/YSZ composites have similar relative densities for a given nickel loading, as illustrated in Figure 5-33. Data for the Ni&Gr/YSZ sample with a nickel loading of 77 vol% nickel of total solids is not presented because of difficulty in measuring the samples without breaking them.

Lastly, the composites with a fixed nickel content and varying graphite loadings show a similar decrease in relative density with increasing graphite content. The relative density of the composites given in Figure 5-35 ranges from approximately 20% to 40% of theoretical with the composites containing the higher graphite loading having the lower relative density.

5.3 THE SINTERED STATE

Three samples of each composite type were prepared for both sintering within a dilatometer and bulk sintering in a box furnace. The following sections present the results of the sintering experiments including linear and volumetric sintering shrinkages and bulk porosity measurements. During sintering, each sample was heated in air to 900°C at 20°C/min, followed by heating to 1475°C at 5°C/min, before holding at 1475°C for one hour, and then cooling to room temperature at 20°C/min.

5.3.1 Dilatometric Studies

5.3.1.1 Dilatometer Measurements

While each individual sample is being sintered, the dilatometer records any dimensional changes in the sample length with time and temperature. For these results, a negative change in dimension represents a linear shrinkage while a positive displacement represents a linear expansion.

The corrected dilatometer plots illustrating the average change in sample length over time during sintering for three individual samples are given in Figure 5-36, Figure 5-37, and Figure 5-38 for the Ni/YSZ, NiGr/YSZ, and NiO/YSZ composites respectively. Also included in each figure is the average dimensional change for samples made with 100% YSZ, 100% nickel powder, and 100% nickel oxide powder. Finally, the heating schedule used for sintering the composite samples is presented as a dashed line within each dilatometer plot.

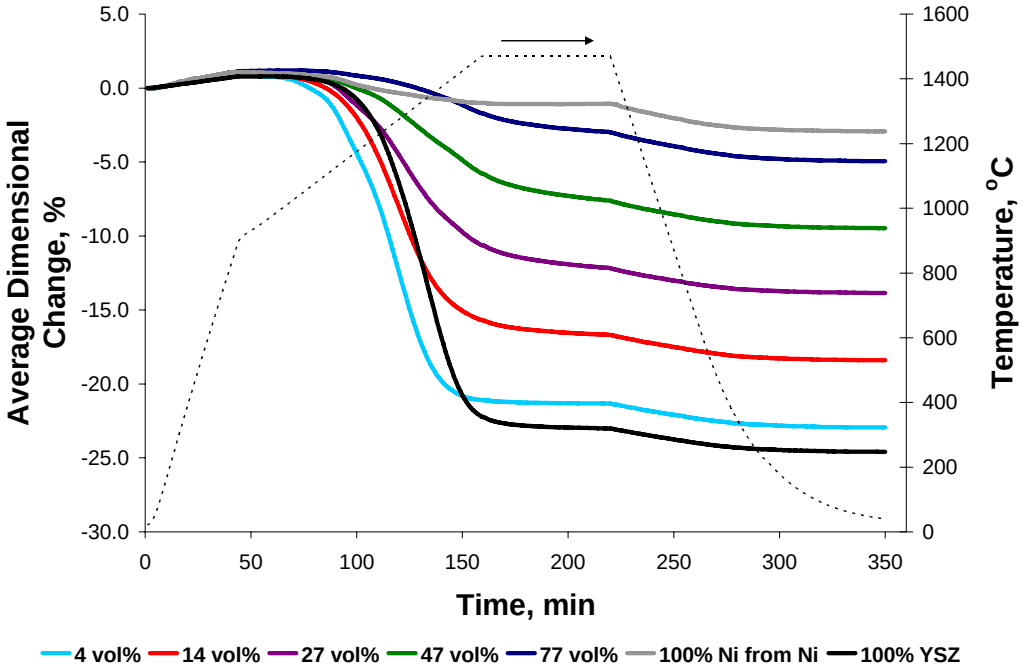

Figure 5-36: Dilatometer plots showing the average sintering shrinkage of various Ni/YSZ composites. Samples made from 100% YSZ and 100% Ni are included for reference. The percentages given represent the volume fraction of nickel as a percent of total solids in the sintered & reduced state.

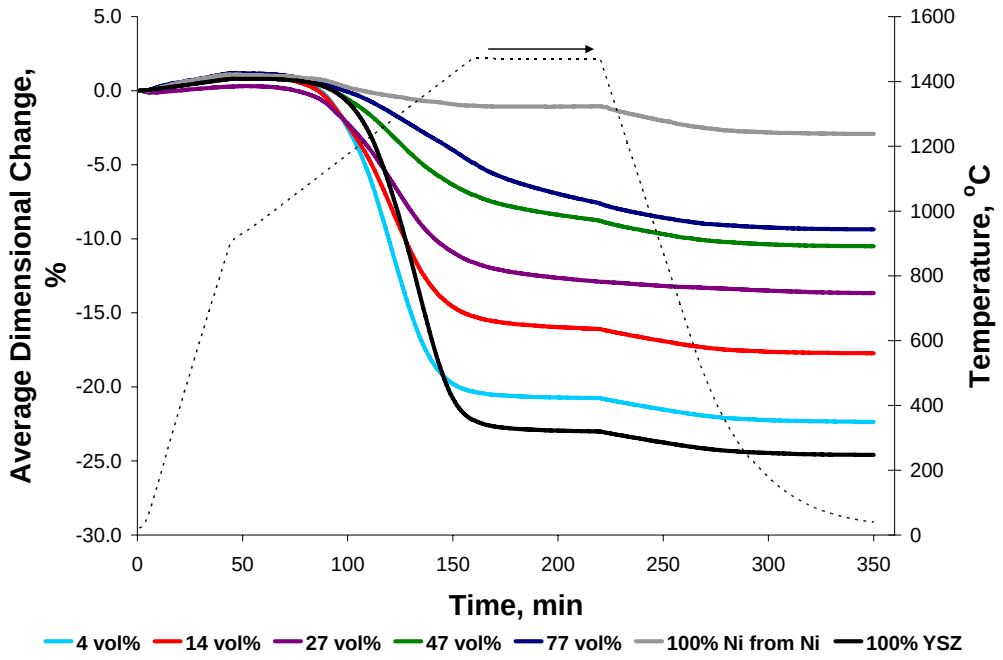

Figure 5-37: Dilatometer plots showing the average sintering shrinkage of various NiGr/YSZ composites. Samples made from 100% YSZ and 100% Ni are included for reference. The percentages given represent the volume fraction of nickel as a percent of total solids in the sintered & reduced state.

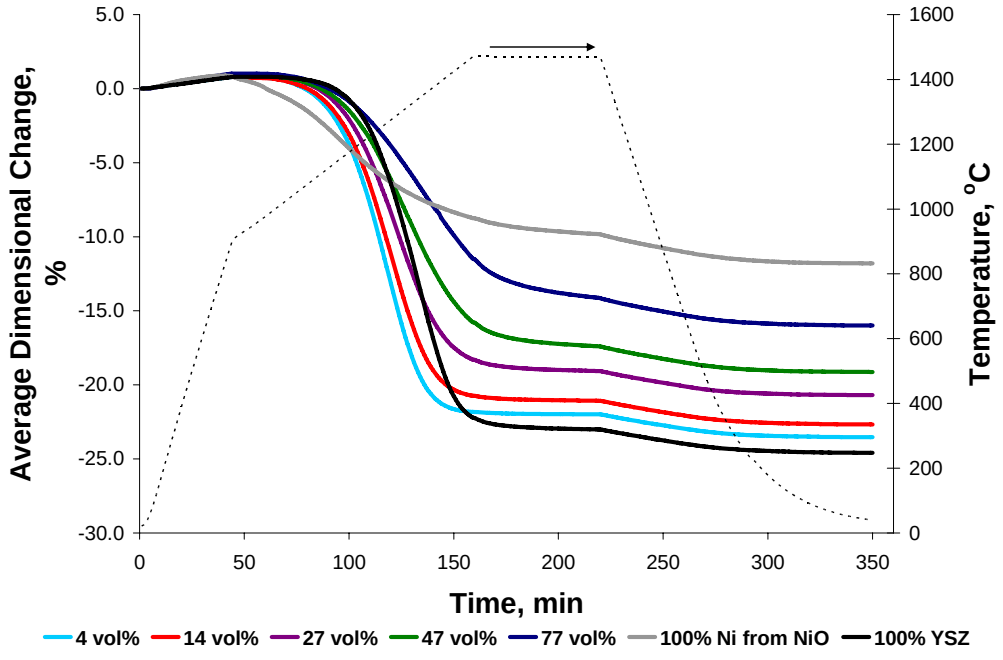

Figure 5-38: Dilatometer plots showing the average sintering shrinkage of various NiO/YSZ composites. Samples made from 100% YSZ and 100% NiO are included for reference. The nickel fractions represent the volume of nickel as a percent of total solids in the sintered & reduced state.

In general, each composite sample experiences the same type of dimensional changes over time, with the extent of the change dependent on the composite type. Initially, each sample experiences a slight thermal expansion before the onset of sintering. After approximately 100 minutes (at ~1175°C), the samples start to shrink significantly and continue to shrink until 150 minutes have elapsed (at ~1425°C). Little change takes place during the one hour hold time at 1475°C, but after this hold time the samples begin to shrink again as they cool to room temperature due to normal thermal contraction. The inflection point in the dilatometer plots after the one hour hold time represents the start of cooling and the corresponding thermal contraction.

From each of the dilatometer plots, it is apparent that the 100% YSZ samples have a very different sintering behaviour compared to the 100% Ni from Ni and 100% Ni from NiO samples. The 100% YSZ samples begin to rapidly shrink at approximately 75 minutes (at ~1050°C) with the majority of the 25% linear shrinkage occurring before the 150 minute mark (at ~1425°C). After 150 minutes, the YSZ samples undergo a modest 1% to 2% decrease in length as the samples cool to room temperature as a result of thermal contraction.

Interestingly, the 100% Ni from Ni and the 100% Ni from NiO samples behave quite differently despite both materials consisting primarily of nickel oxide. Like the 100% YSZ samples, the 100% Ni from NiO samples show a significant sintering shrinkage but at a more gradual rate. Linear sintering shrinkage begins around 50 minutes (at ~925°C) and continues until 150 minutes (at ~1425°C) where the amount of shrinkage essentially plateaus at 11%. The 100% Ni from Ni samples on the other hand, show only a marginal sintering shrinkage of 2%.

When the nickel content increases from pure YSZ to pure nickel, the linear sintering shrinkage decreases for each of the Ni/YSZ, NiGr/YSZ, and NiO/YSZ composites. The composites made initially from nickel powder have shrinkages between that of 100% YSZ and 100% Ni from Ni, with intermediate nickel loadings yielding a steady decrease in sintering shrinkage with increasing nickel content. Similarly, the NiO/YSZ composites show linear sintering shrinkages ranging between the pure 100% YSZ and the 100% Ni from NiO sample shrinkages.

When graphite is added to create porosity, the effect of adding nickel is no longer clear, especially when examining the sintering behaviour of the Ni&Gr/YSZ and NiO&Gr/YSZ composites given in Figure 5-39 and Figure 5-40. The Ni&Gr/YSZ composite samples with nickel loadings between 4 vol% and 27 vol% Ni of total solids show the same decreasing sintering shrinkage with increasing nickel content, like the Ni/YSZ composites, albeit with a greater overall sintering shrinkage. The 47 vol% Ni of total solids samples, however, have a higher than expected sintering shrinkage based on its nickel content as they appear to shrink as much as the 100% YSZ samples.

For the NiO&Gr/YSZ composites, there is little difference in sintering shrinkage regardless of nickel content, although the 47 vol% Ni of total solids sample has a slightly higher sintering shrinkage. Surprisingly, each of the NiO&Gr/YSZ composites have a sintering shrinkage that is greater than or equal to the sintering shrinkage of the 100% YSZ samples.

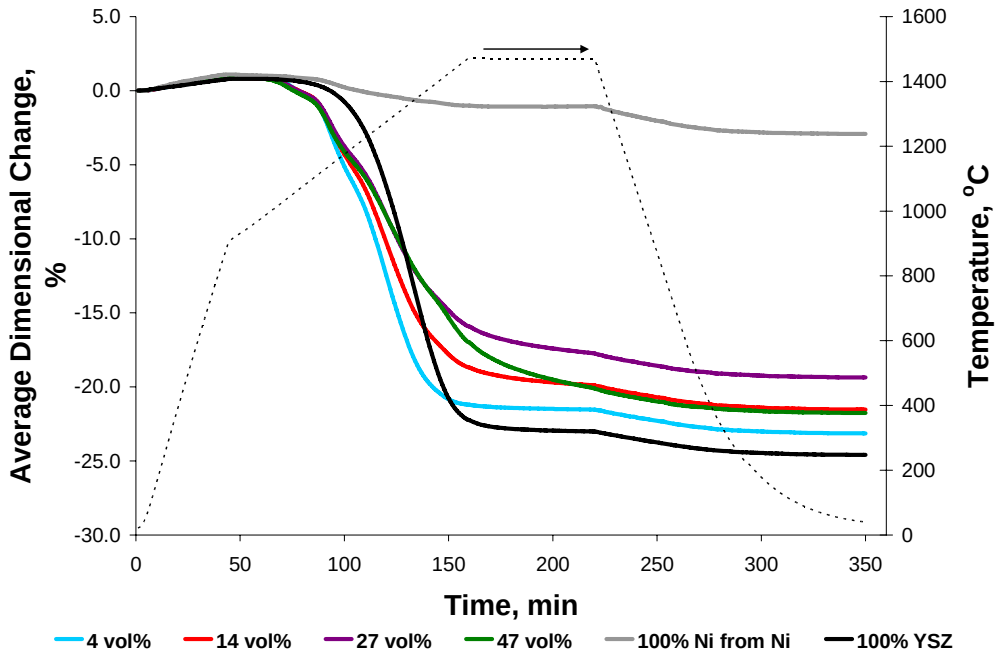

Figure 5-39: Dilatometer plots showing the average sintering shrinkage of various Ni&Gr/YSZ composites. Samples made from 100% YSZ and 100% Ni are included for reference. The nickel fractions represent the volume of nickel as a percent of total solids in the sintered & reduced state.

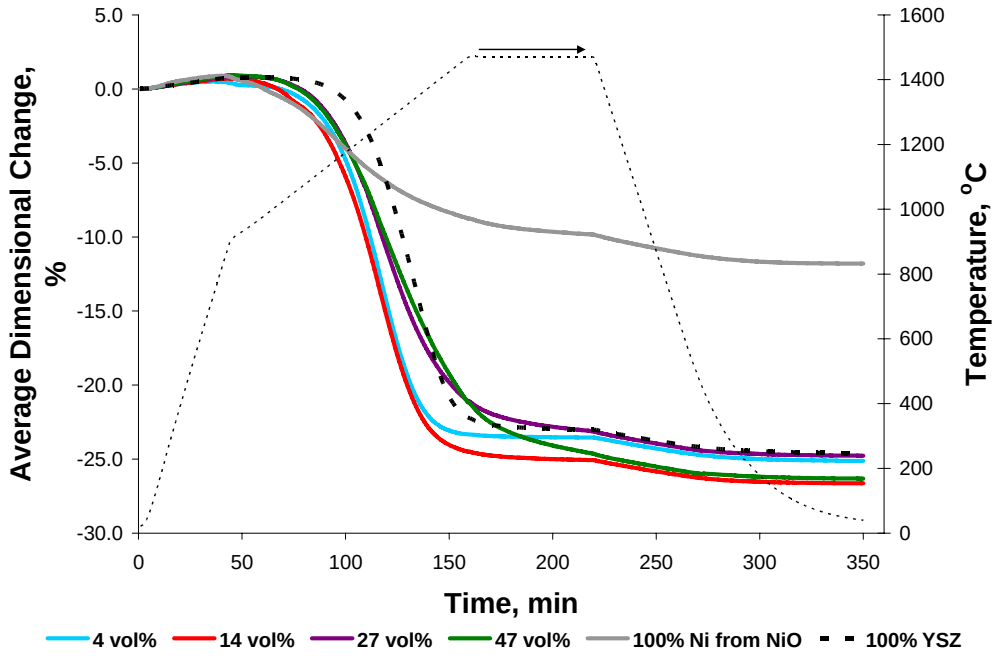

Figure 5-40: Dilatometer plots showing the average sintering shrinkage of various NiO&Gr/YSZ composites. Samples made from 100% YSZ and 100% Ni are included for reference. The nickel fractions represent the volume of nickel as a percent of total solids in the sintered & reduced state.

The sintering behaviour of the Ni&Gr/YSZ and NiO&Gr/YSZ composites with a fixed nickel content may be examined to clarify the effect that porosity, formed through graphite additions, has on the sintering behaviour of these porous nickel/YSZ composites. The linear sintering shrinkage of the Ni&Gr-27/YSZ, NiO&Gr-27/YSZ, Ni&Gr-47/YSZ, and NiO&Gr-47/YSZ composites are shown in Figure 5-41, Figure 5-42, Figure 5-43, and Figure 5-44 respectively. For each composite type with the same nickel loading, based on nickel content as a fraction of total solids, the sintering data for the corresponding graphite-free composite (Ni/YSZ or NiO/YSZ) and highest graphite loading composite (Ni&Gr/YSZ or NiO/YSZ) is also included for reference.

Overall, increasing graphite – and the resultant increased porosity after burnout (See Figure 5-33 to Figure 5-35) – causes a consistent decrease in the linear sintering shrinkage between the graphite-free composite samples and the composite samples with the greatest graphite loading. The NiO&Gr-27/YSZ and Ni&Gr-47/YSZ composite samples show a fairly uniform decrease in sintering shrinkage with increasing graphite loading. The other composite types show a similar trend, despite some compositions having very similar sintering shrinkages at different graphite loadings. For example, the Ni&Gr-27/YSZ composite samples with a graphite loading of 14 vol% of the green volume (63% porosity after burnout), and 18 vol% of the green volume (67% porosity after burnout) have nearly identical sintering shrinkages despite the difference in porosity.

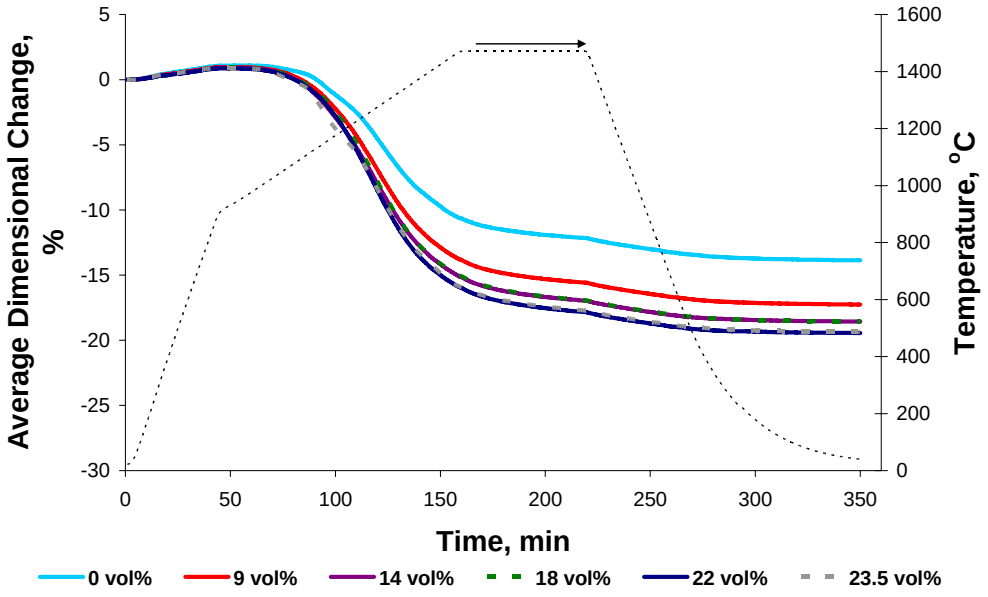

Figure 5-41: Dilatometer plots showing the average sintering shrinkage of Ni&Gr-27/YSZ composites with a fixed nickel content of 27 vol% Ni of total solids and varying graphite loadings. The percentages given represent the volume of graphite as a percent of the dried green volume.

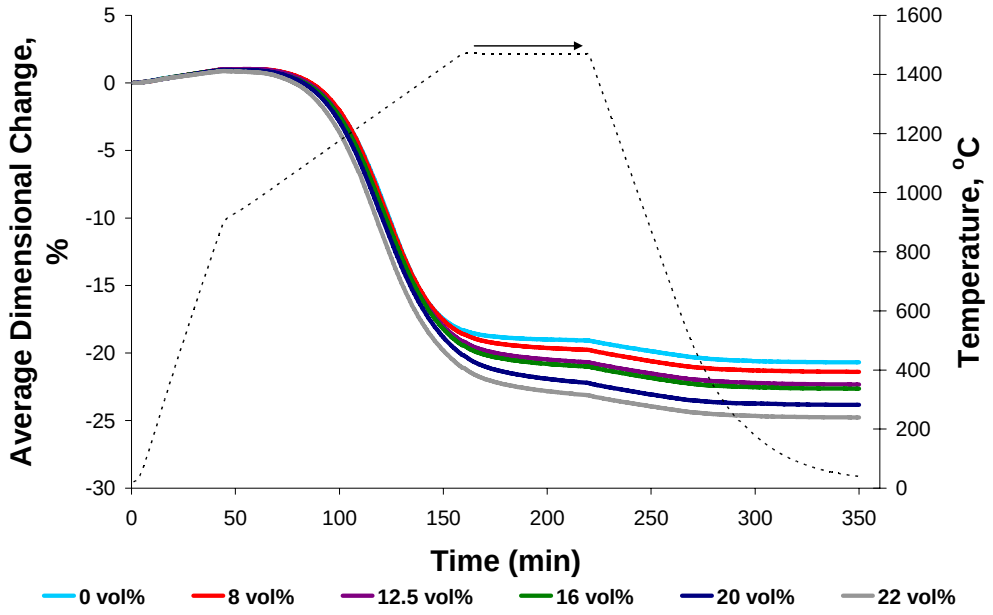

Figure 5-42: Dilatometer plots showing the average sintering shrinkage of NiO&Gr-27/YSZ composites with a fixed nickel content of 27 vol% Ni of total solids and varying graphite loadings. The percentages given represent the volume of graphite as a percent of the dried green volume.

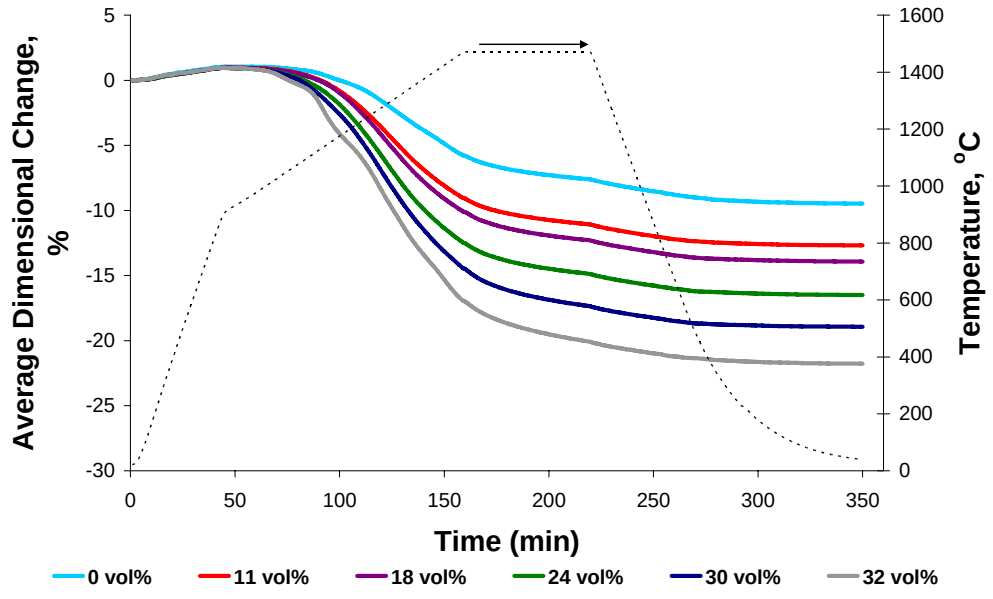

Figure 5-43: Dilatometer plots showing the average sintering shrinkage of Ni&Gr-47/YSZ composites with a fixed nickel content of 47 vol% Ni of total solids and varying graphite loadings. The percentages given represent the volume of graphite as a percent of the dried green volume.

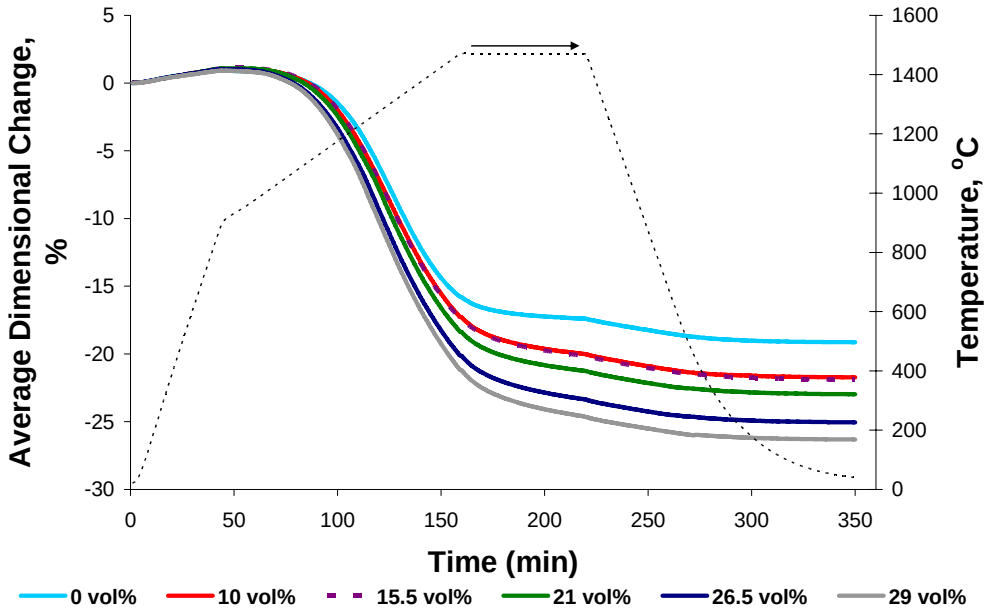

Figure 5-44: Dilatometer plots showing the average sintering shrinkage of NiO&Gr-47/YSZ composites with a fixed nickel content of 47 vol% Ni of total solids and varying graphite loadings. The percentages given represent the volume of graphite as a percent of the dried green volume.

5.3.1.2 Dilatometer Sample Measurements

To measure the accuracy of the in-situ dilatometer measurements, the dimensions of each sample were measured before and after sintering within the dilatometer and compared with the sintering shrinkage measured by the dilatometer. The overall linear sintering shrinkages in the length direction as measured by the dilatometer and manually by hand are shown in Figure 5-45 and Figure 5-46 for Ni/YSZ and NiGr/YSZ composites. The Ni/YSZ composites show the best agreement between the manually measured and dilatometer measured linear sintering shrinkages while the NiGr/YSZ composites show the weakest agreement between the two measurements. The Figures for the other composite types can be found in Appendix C.

In general, the linear sintering shrinkages measured manually and with the dilatometer are consistent for a given composite type and nickel loading. The agreement between the manual measurements and the dilatometer measurements are best for the non-graphite containing composites and the composites made from nickel oxide. Although the manual and dilatometer measurements show the same trends for the NiGr/YSZ and the Ni&Gr/YSZ composites, the manual measurements are consistently lower than the dilatometer measurements. In particular, the Ni&Gr-27/YSZ and Ni&Gr-47/YSZ composites have manual measurements that are approximately 5% less than the dilatometer measurements.

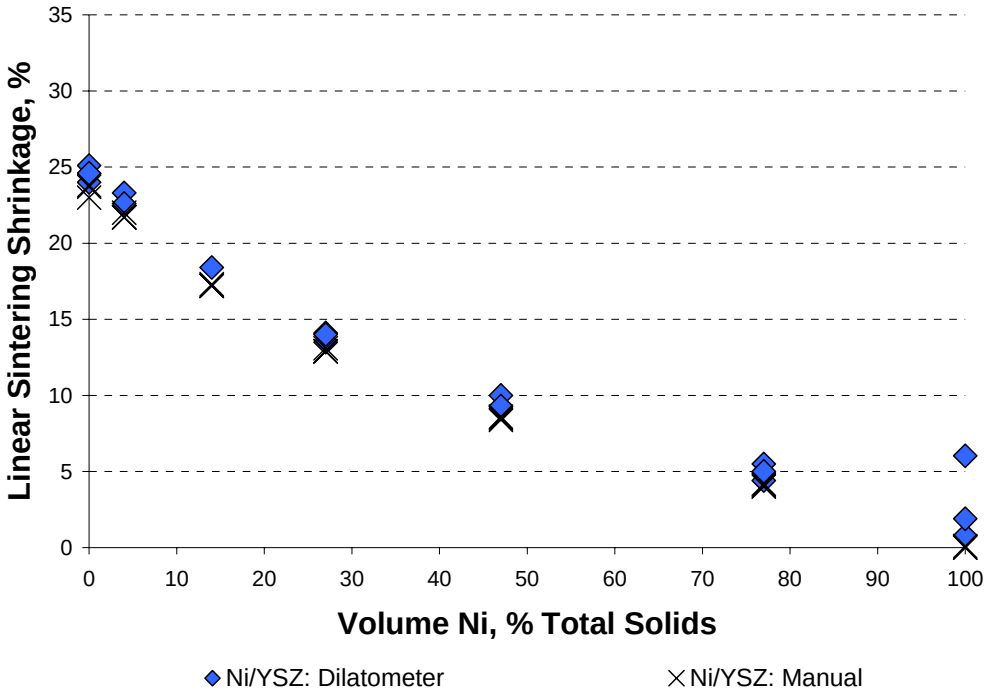

Figure 5-45: Comparison of linear sintering shrinkages as measured manually and with a dilatometer for the Ni/YSZ composites

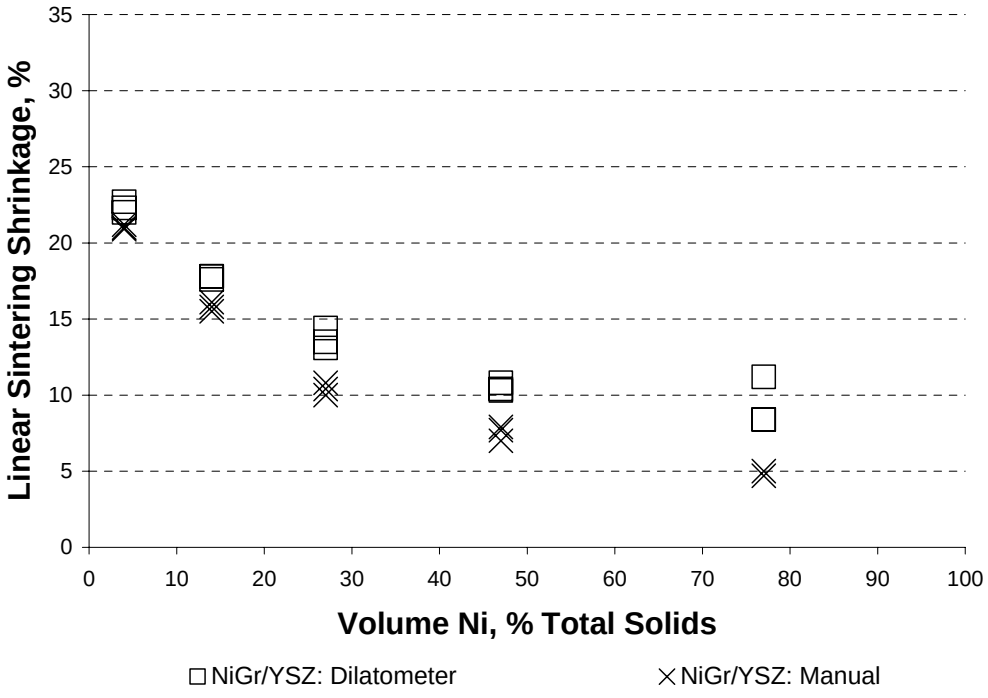

Figure 5-46: Comparison of linear sintering shrinkages as measured manually and with a dilatometer for the NiGr/YSZ composites

The reason for the underestimation of the linear sintering shrinkage is not entirely clear. The discrepancy in the sintering shrinkages may be associated with the difficulty in accurately measuring the length of each sample when the end faces of the sample are not completely flat. The length of each sample is likely to be overestimated through manual measurement when the edges of each sample are higher than the centre due to curvature of the samples. In an effort to minimize this effect, several measurements were taken at different locations.

The nature of the dilatometer measuring technique may also contribute to the difference between the manual and dilatometer measurements. Since the dilatometer push rod is placed near the centre of the sample, any surface curvature that develops during sintering will be measured by the dilatometer but difficult to measure with the callipers. Variations in the correction file and the measured file, along with sample settling may also cause an increase in the linear sintering shrinkage measured compared to the manually measured samples. The true linear sintering shrinkage is likely between the manually measured shrinkage and the shrinkage as measured by the dilatometer.

5.3.1.3 Directional Linear Sintering Shrinkages

The directional linear sintering shrinkage was calculated, like the dimensional changes during burnout in Equation (5-6), for the length, width, and thickness of each sintered sample by dividing the difference in the dimension after burnout and sintering by the dimension after burnout. The linear sintering shrinkage for the length, width, and thickness of three samples for each of the different composite types is shown in Figure 5-47 through Figure 5-51.

Upon inspection of Figure 5-47 through Figure 5-51, the directional linear sintering shrinkage of each of the composites has varying degrees of anisotropy depending on the composite construction. For the non-graphite containing composites, Ni/YSZ (Figure 5-47) and NiO/YSZ (Figure 5-50), the linear sintering shrinkages of the length, width, and thickness are quite similar indicating that the sintering shrinkage is essentially isotropic. For the NiO/YSZ composites, the linear shrinkage of the thickness tends to be slightly lower than the linear shrinkage in the length and width.

The 100% YSZ, 100% Ni from Ni, and 100% Ni from NiO samples (plotted as 0% Ni and 100% Ni in Figure 5-47 and Figure 5-50) have similar sintering shrinkages in the length and width but slightly lower shrinkages in the thickness. The 100% YSZ and 100% Ni from NiO samples show significant shrinkage while the 100% Ni from Ni samples actually expand slightly. The expansion of the 100% Ni from Ni samples can be attributed to the further oxidation of the unoxidized nickel powder still remaining after the burnout stage, as suggested by the slight weight increase of the samples after sintering.

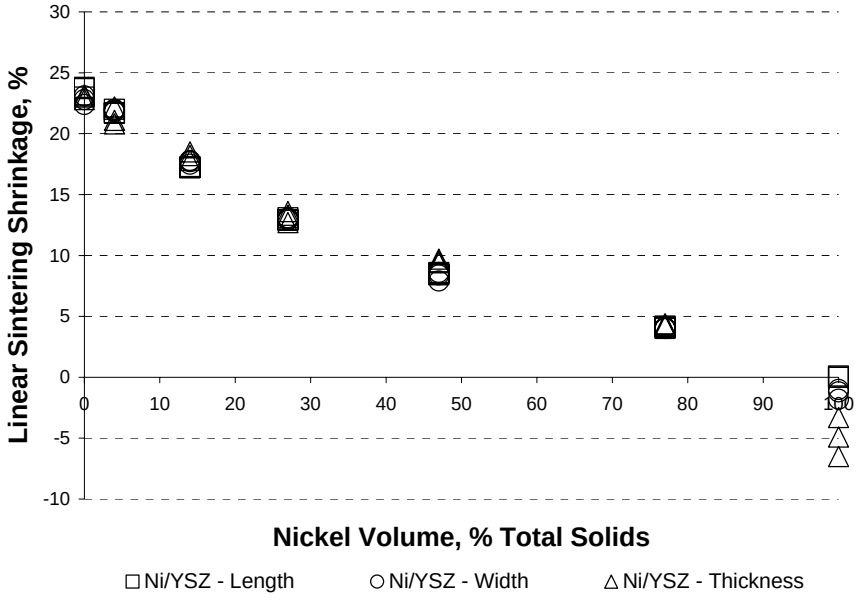

Figure 5-47: Manually measured linear sintering shrinkage from the burnout to sintered state for the length, width, and thickness of Ni/YSZ composite samples sintered in a dilatometer

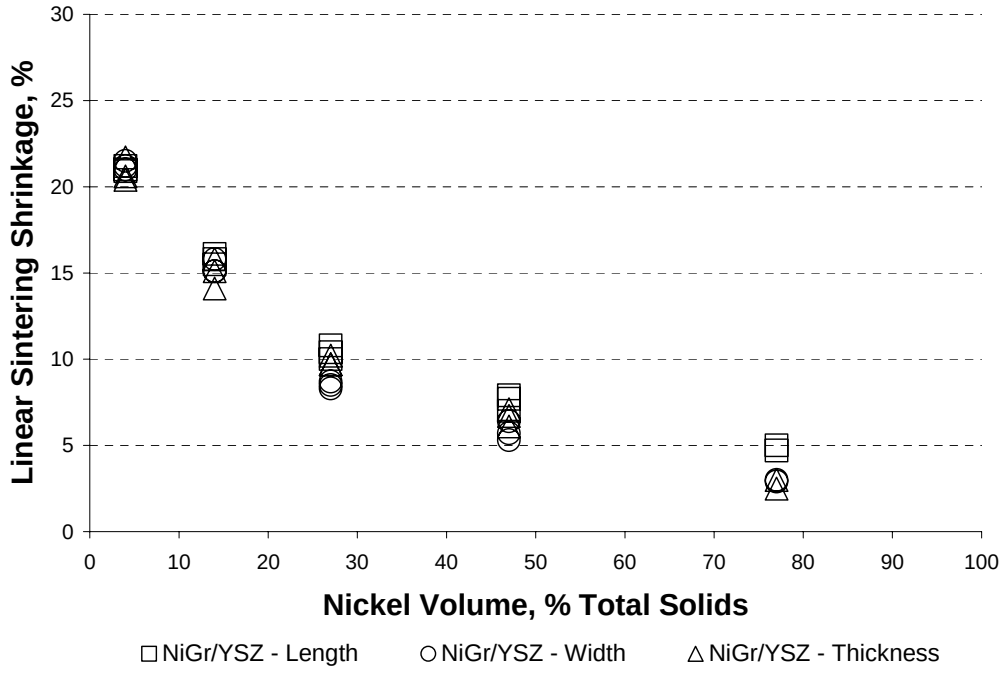

Figure 5-48: Manually measured linear sintering shrinkage from the burnout to sintered state for the length, width, and thickness of NiGr/YSZ composite samples sintered in a dilatometer

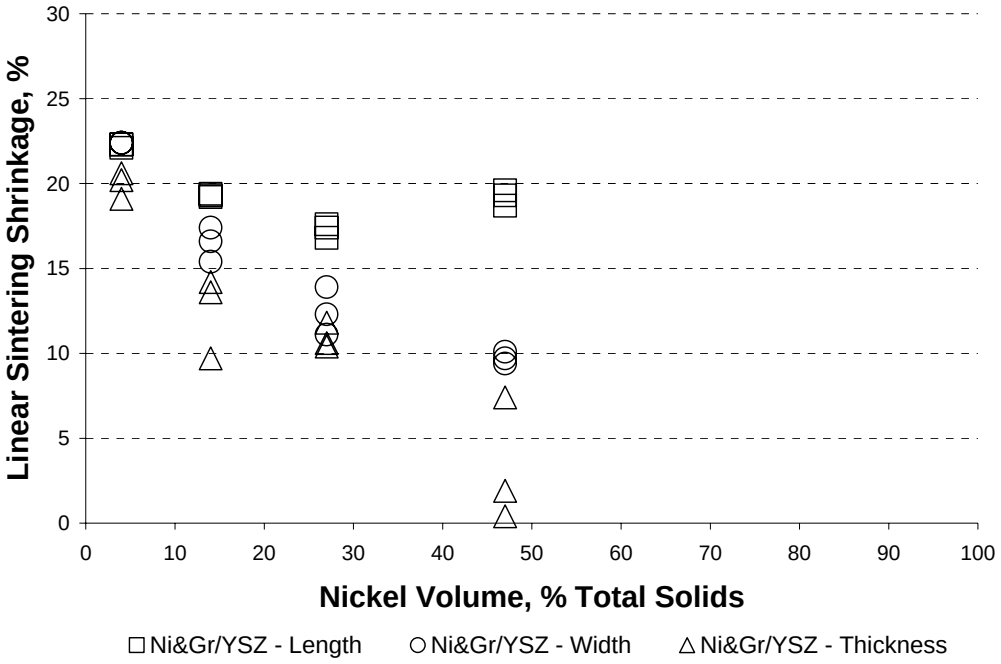

Figure 5-49: Manually measured linear sintering shrinkage from the burnout to sintered state for the length, width, and thickness of Ni&Gr/YSZ composite samples sintered in a dilatometer

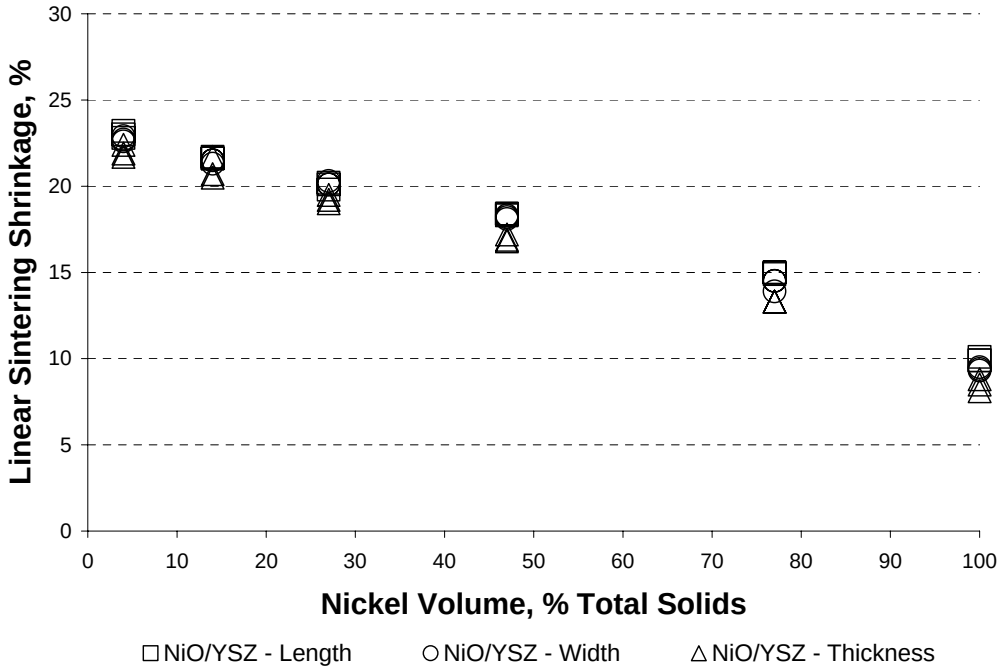

Figure 5-50: Manually measured linear sintering shrinkage from the burnout to sintered state for the length, width, and thickness of NiO/YSZ composite samples sintered in a dilatometer

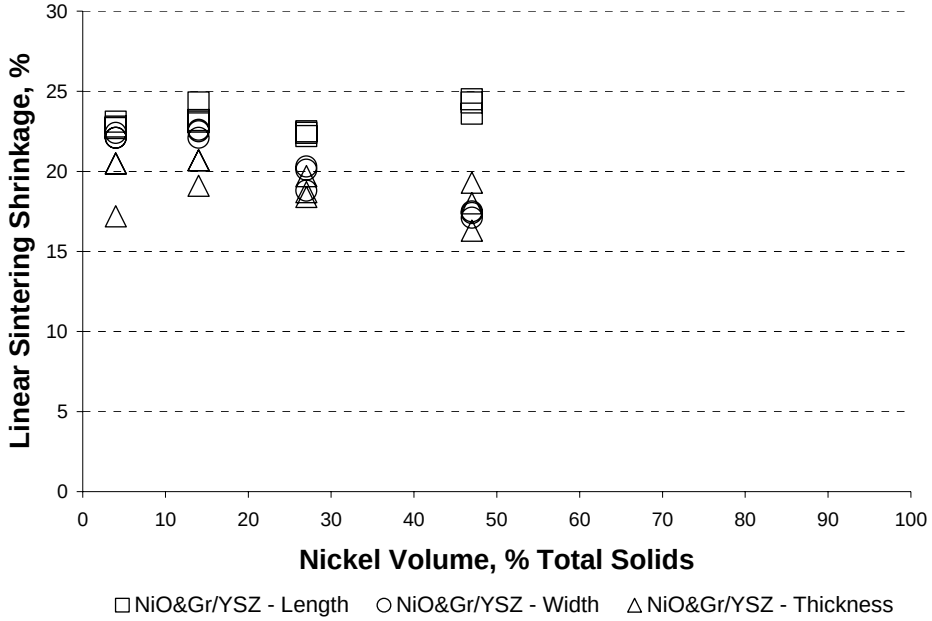

Figure 5-51: Manually measured linear sintering shrinkage from the burnout to sintered state for the length, width, and thickness of NiO&Gr/YSZ composite samples sintered in a dilatometer

Once graphite is added to the composite, the linear sintering shrinkage is more anisotropic. When graphite is added as a nickel coated particle (Figure 5-48), the linear sintering shrinkage shows a decreasing linear shrinkage with increasing nickel loading, similar to the Ni/YSZ composites, but with a wider range of linear sintering shrinkages in the three different directions. While there is a range of sintering shrinkages in each direction, the sintering behaviour remains relatively isotropic. Conversely, when graphite is added as a separate particle, the effect on the linear sintering shrinkage is more dramatic for a given direction. The Ni&Gr/YSZ (Figure 5-49) and NiO&Gr/YSZ (Figure 5-51) composites show much different linear sintering shrinkages compared with the graphite-free composites. While the graphite-free composites show a steadily decreasing "isotropic" linear sintering shrinkage with increasing nickel content, the graphite containing composites have very anisotropic linear sintering shrinkages. The Ni&Gr/YSZ composites exhibit a steadily decreasing shrinkage in the width and thickness directions with increasing nickel loading, while linear shrinkage in the length direction initially decreases with increasing nickel loading then begins to increase at 47 vol% Ni of total solids. The variability in the measurements of the Ni&Gr/YSZ composites is also much greater. On the other hand, the NiO&Gr/YSZ composites have a nearly constant linear sintering shrinkage in length direction, independent of the nickel loading, while the linear sintering shrinkage in the width and thickness are steady at low nickel contents and then decrease at nickel loadings greater than 27 vol% Ni of total solids.

The Ni&Gr-27/YSZ and NiO&Gr-27/YSZ composites tend to have a slight increasing linear sintering shrinkage in the length direction with increasing graphite loading and linear sintering shrinkages in the width and thickness directions that are nearly independent of graphite loading as illustrated in Figure 5-52 and Figure 5-53. This directional difference in sintering shrinkage leads to increasing anisotropy with increasing graphite content. At the higher nickel loadings (i.e. Ni&Gr-47/YSZ and NiO&Gr-47/YSZ), the linear sintering shrinkage also increases in the length direction but decreases in the thickness direction with increasing graphite content. This leads to a larger anisotropy

in the linear sintering shrinkage with increasing graphite loading at the higher nickel loadings. The composites made from nickel powder tend to have greater anisotropic sintering behaviour compared to the composites made from NiO.

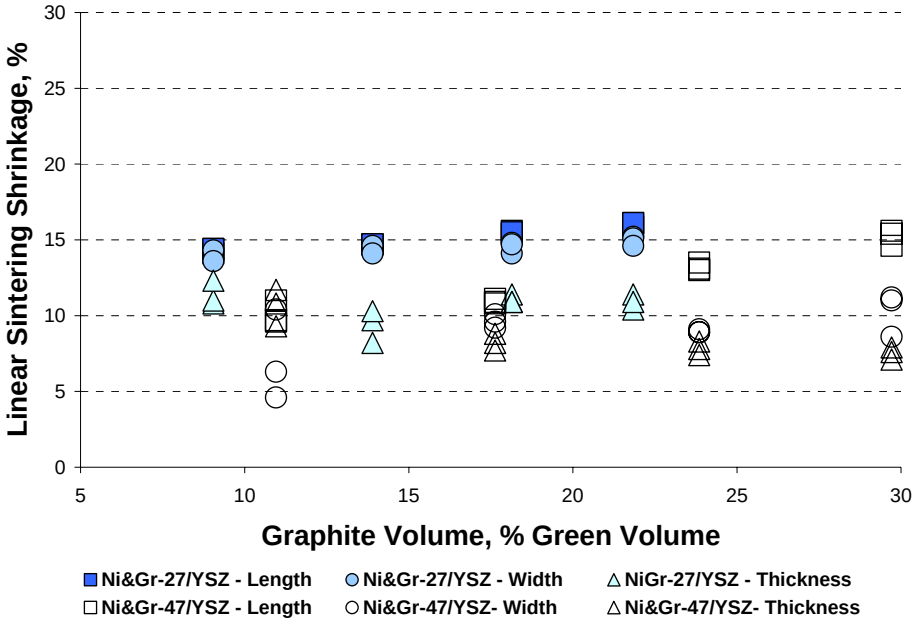

Figure 5-52: Manually measured linear sintering shrinkage from the burnout to sintered state for the length, width, and thickness of Ni&Gr-27/YSZ and Ni&Gr-47/YSZ composite samples sintered in a dilatometer

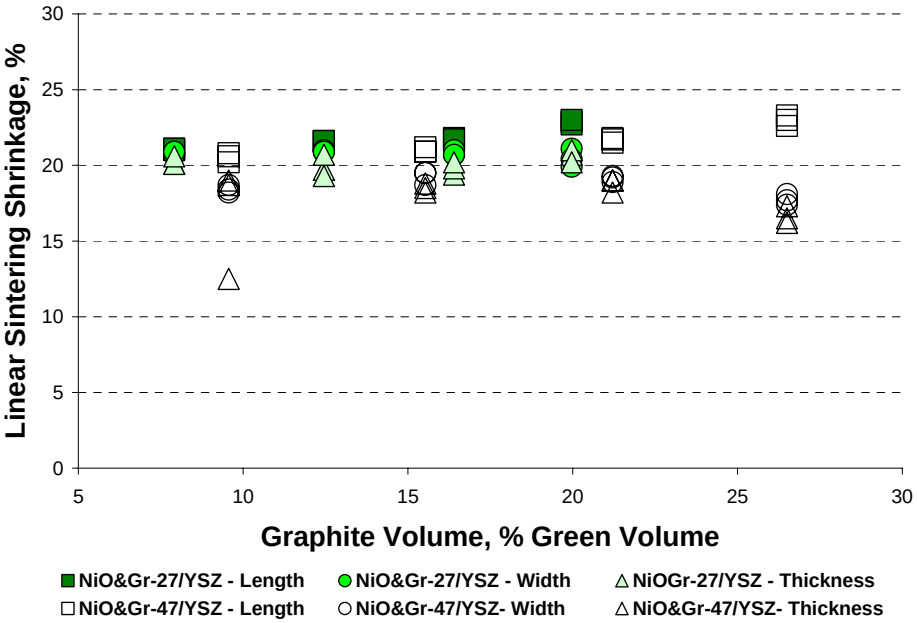

Figure 5-53: Manually measured linear sintering shrinkage from the burnout to sintered state for the length, width, and thickness of NiO&Gr-27/YSZ and NiO&Gr-47/YSZ composite samples sintered in a dilatometer

5.3.1.4 Volumetric Sintering Shrinkage

Generally, each composite type experiences some degree of volumetric shrinkage because of densification during the sintering stage. The degree of volumetric sintering shrinkage, a function of the linear dimensional sintering shrinkages, is dependent on the composite type and its nickel loading. The volumetric sintering shrinkage from the burnout stage through the sintered stage is shown for each composite type in Figure 5-54 (Ni/YSZ), Figure 5-55 (Ni&Gr/YSZ), Figure 5-56 (NiGr/YSZ), Figure 5-57 (NiO/YSZ), and Figure 5-58 (NiO&Gr/YSZ). The volumetric changes from the green state through the burnout stage are also included for reference. In addition, the volumetric shrinkages for the 100% YSZ and 100% Ni from Ni samples are plotted with the volumetric shrinkages of the Ni/YSZ composites as samples with 0% nickel (100% YSZ) and 100% nickel, but are not labelled separately. Likewise, the volumetric shrinkages of the 100% Ni from NiO samples are plotted with the volumetric shrinkage of the NiO/YSZ composites.

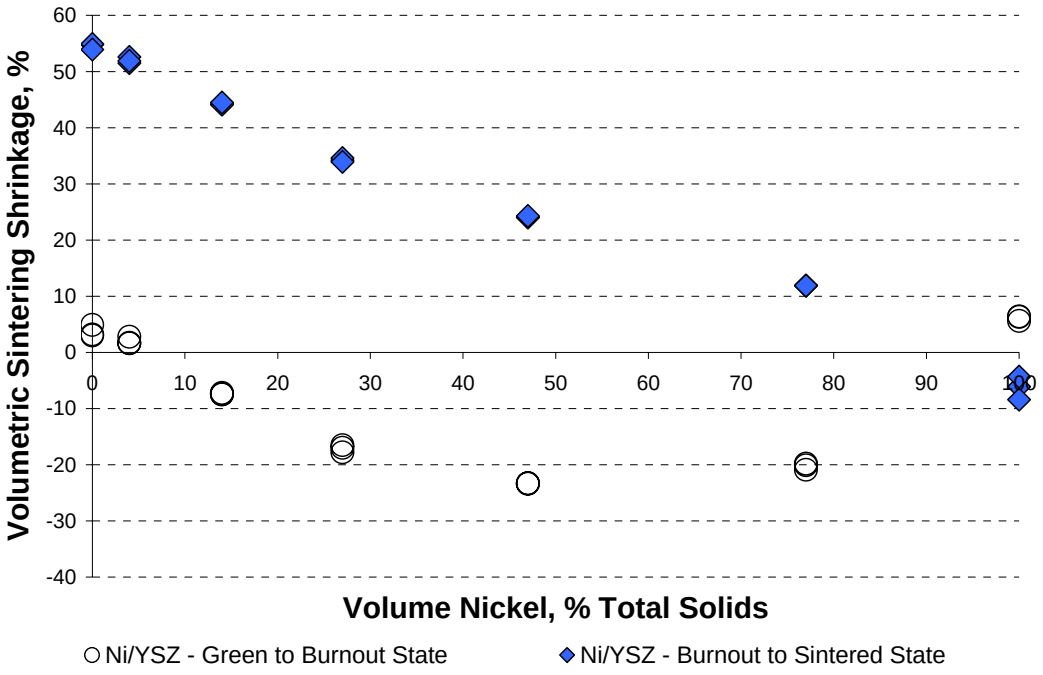

Figure 5-54: Volumetric sintering shrinkage for the Ni/YSZ composites sintered in a dilatometer after the burnout and sintering stage

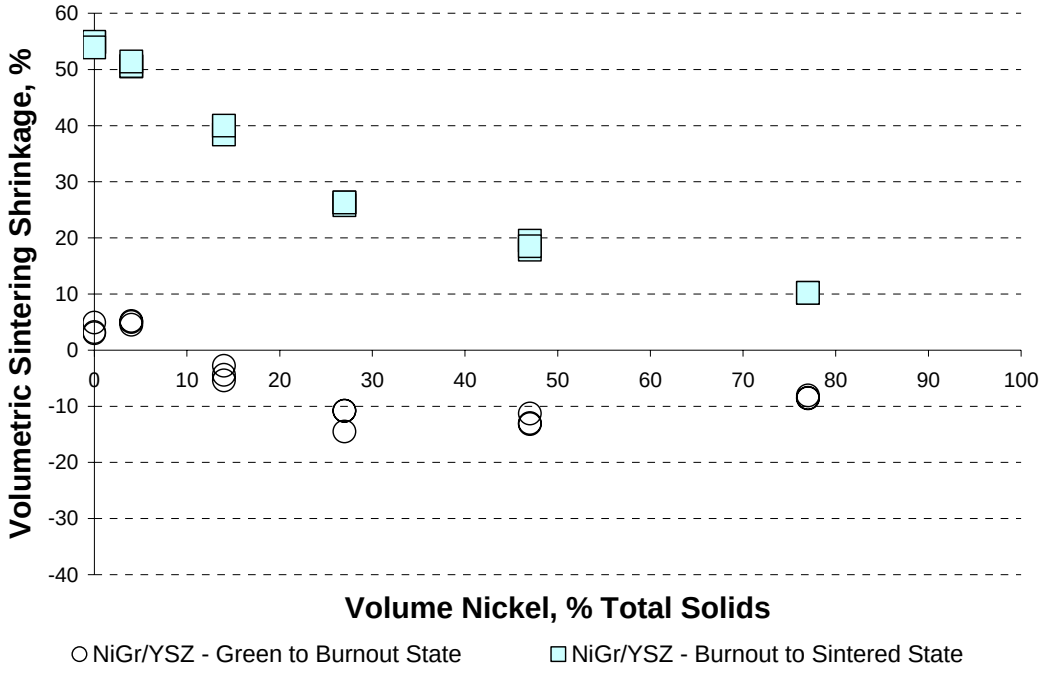

Figure 5-55: Volumetric sintering shrinkage for the NiGr/YSZ composites sintered in a dilatometer after the burnout and sintering stage

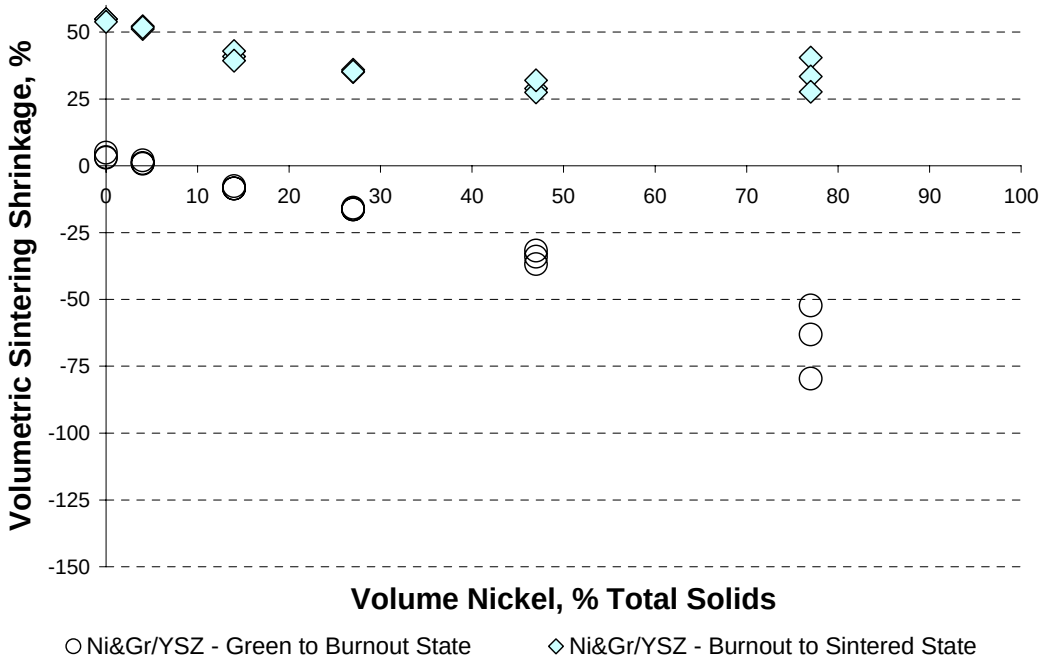

Figure 5-56: Volumetric sintering shrinkage for the Ni&Gr/YSZ composites sintered in a dilatometer after the burnout and sintering stage

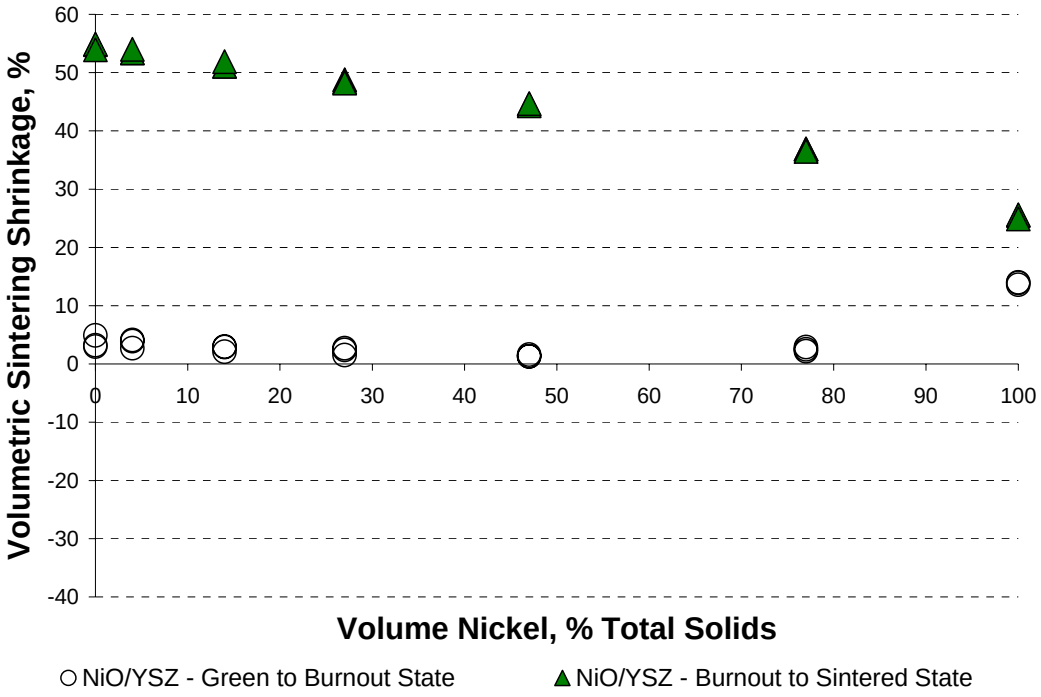

Figure 5-57: Volumetric sintering shrinkage for the NiO/YSZ composites sintered in a dilatometer after the burnout and sintering stage

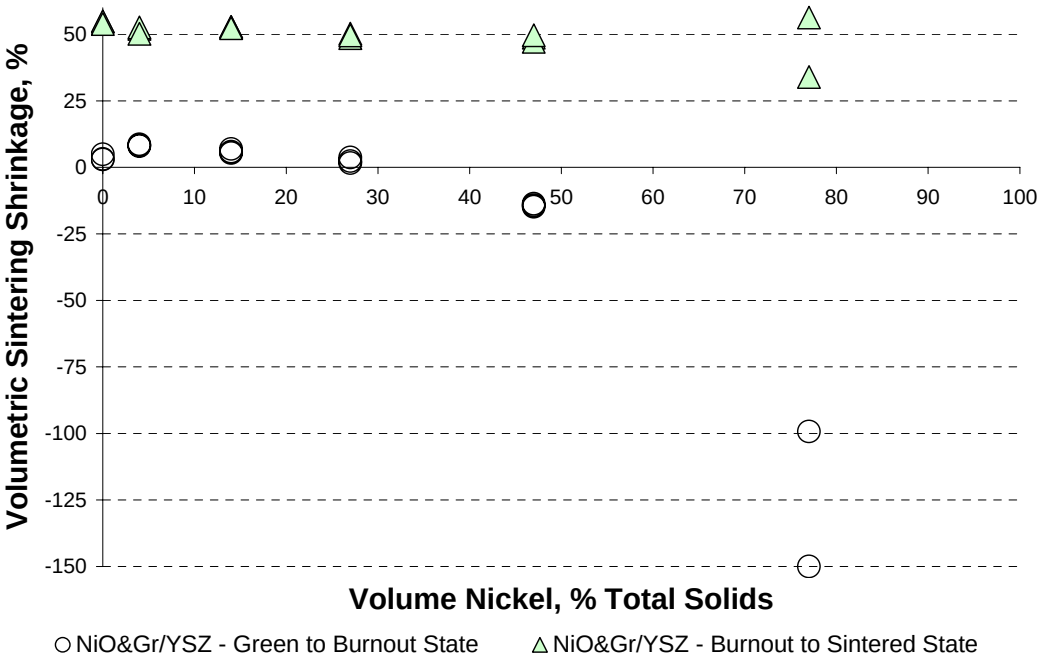

Figure 5-58: Volumetric sintering shrinkage for the NiO&Gr/YSZ composites sintered in a dilatometer after the burnout and sintering stage

From each of the above figures, it is apparent that the majority of the densification takes place during the sintering stage. During the burnout stage, very little densification occurred. In fact, the composites made from nickel powder actually grew in size. Conversely, each composite type experienced at least a 10% volumetric sintering shrinkage or higher during the sintering stage.

The extent of volumetric sintering shrinkage is very dependent on the composite composition. For each composite type, increasing the nickel content causes a decrease in the amount of volumetric sintering shrinkage. Composites created from nickel powder tend to shrink less during sintering at higher nickel loadings compared to the composites created from nickel oxide powder, as illustrated in Figure 5-54 and Figure 5-57. Moreover, the difference in volumetric sintering shrinkage for the composites made from the highest and lowest nickel loading is nearly 40% while the change in sintering shrinkage for the highest and lowest nickel oxide containing composites is only 15%. Despite the method of adding nickel to the composite, the degree of volumetric sintering shrinkage is essentially proportional to the volume of nickel present within the composite.

Graphite additions seem to have little effect on the volumetric sintering shrinkage despite the differences in the linear sintering shrinkages in the length, width, and thickness between the graphite containing composites and the graphite free composites. When examining the volumetric sintering shrinkages for the Ni&Gr-27/YSZ, Ni&Gr-47/YSZ, NiO&Gr-27/YSZ, and NiO&Gr-47/YSZ composites in Figure 5-59 and Figure 5-60, the volumetric sintering shrinkages appear relatively constant for a given nickel loading.

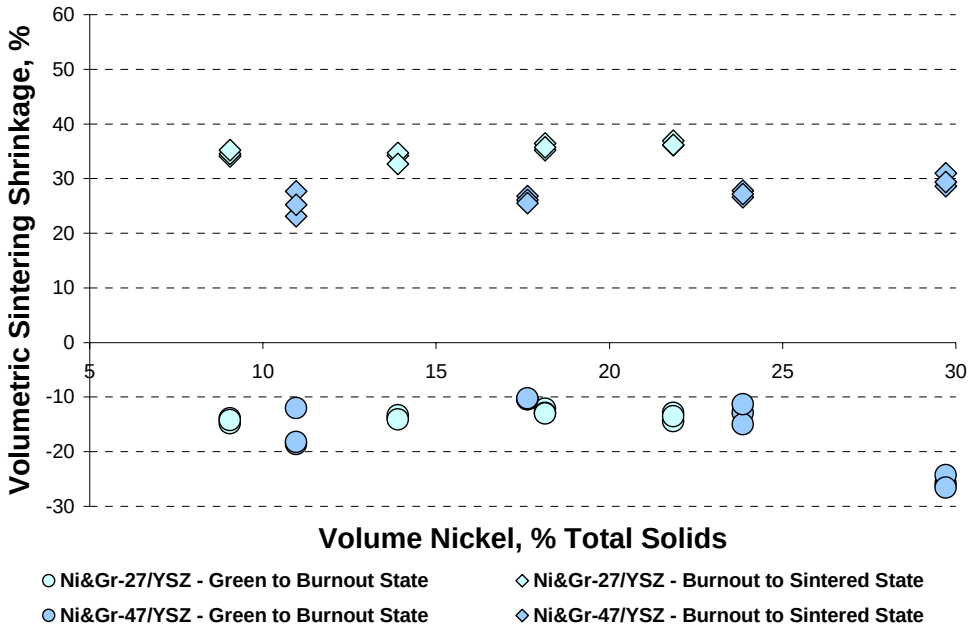

Figure 5-59: Volumetric sintering shrinkages during the burnout and sintering stages for the Ni&Gr-27/YSZ and Ni&Gr-47/YSZ composites with a fixed nickel content and varying graphite loading sintered in a dilatometer

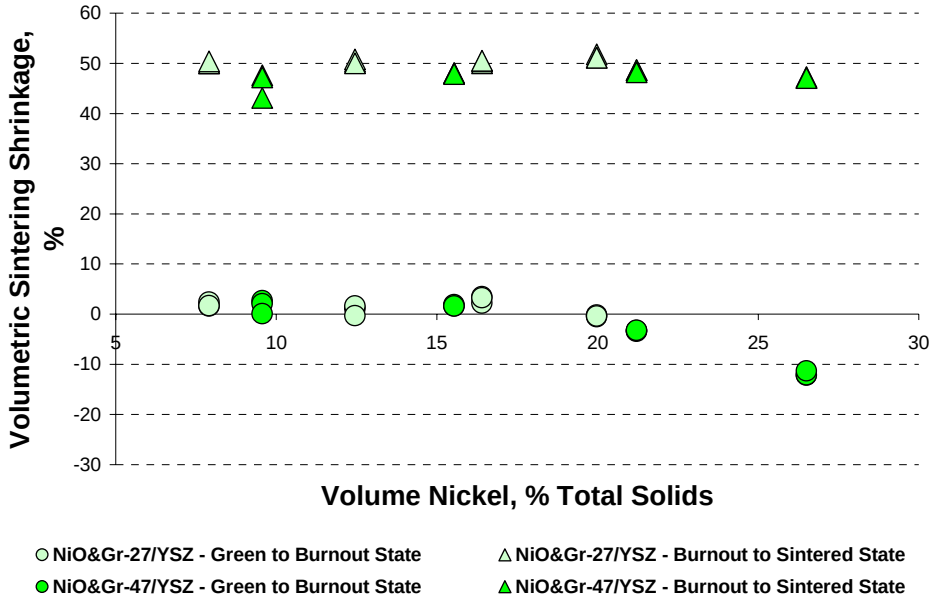

Figure 5-60: Volumetric sintering shrinkages during the burnout and sintering stages for the NiO&Gr-27/YSZ and NiO&Gr-47/YSZ composites with a fixed nickel content and varying graphite loading sintered in a dilatometer

5.3.1.5 Bulk Porosity

The amount of densification that occurs after sintering can be monitored more explicitly by measuring the relative density of each composite sample. The measured density of each composite type is divided by the expected theoretical density, assuming that all nickel present is oxidized and all graphite has burned away, to compute a relative density. The relative density for each sample of the composite types is plotted in Figure 5-61 through Figure 5-65.

As was the case for the burned out samples, increasing the graphite loading causes a substantial decrease in the relative density of each sample. Again, this is by design since the graphite is added to increase the composite porosity. As the amount of graphite in the composite increases, the relative density decreases proportionally. This is demonstrated by the relative densities of the NiO&Gr/YSZ, Ni&Gr-27/YSZ, Ni&Gr-47/YSZ, NiO&Gr-27/YSZ, and NiO&Gr-47/YSZ composites. The NiO&Gr/YSZ composites show a similar behaviour as the relative density of the composites decreases with increasing nickel content.

The NiGr/YSZ and Ni&Gr/YSZ composites however, demonstrate a non-linear relationship between nickel loading and relative density. While both composites exhibit decreasing relative density with increasing nickel loading, the change in relative density from 0 vol% Ni to 27 vol% Ni of total solids is much greater than the change in relative density from 27 vol% Ni to 77 vol% Ni of total solids.

The non-linearity of the decrease in relative density of the NiGr/YSZ and Ni&Gr/YSZ composites may be attributed to the densification behaviour of the Ni/YSZ composites. The Ni/YSZ composites tend to have decreasing relative densities to 75% of theoretical at a nickel loading of 27 vol% Ni of total solids at which point the relative density begins to increase to 90% of theoretical for the 100% Ni from Ni sample (See Figure 5-61). While graphite additions dominate the densification behaviour of

the NiGr/YSZ and Ni&Gr/YSZ composites, the increasing relative density at nickel loadings above 27 vol% Ni of total solids for composites made from nickel powder could contribute to the levelling of the relative density at the higher nickel loadings.

Lastly, the NiO/YSZ composites tend to show a very subtle increase in relative density with increasing nickel loading at lower nickel loadings. A peak relative density of approximately 93% at a volume fraction of nickel between 27 vol% Ni and 47 vol% Ni of total solids is reached before the relative density decreases again.

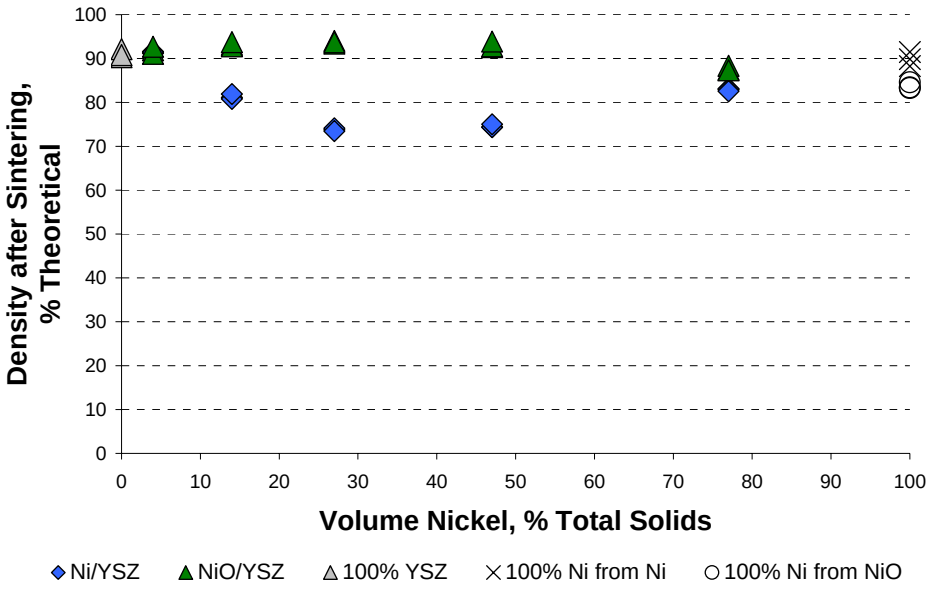

Figure 5-61: Relative density of Ni/YSZ and NiO/YSZ composites after sintering in a dilatometer

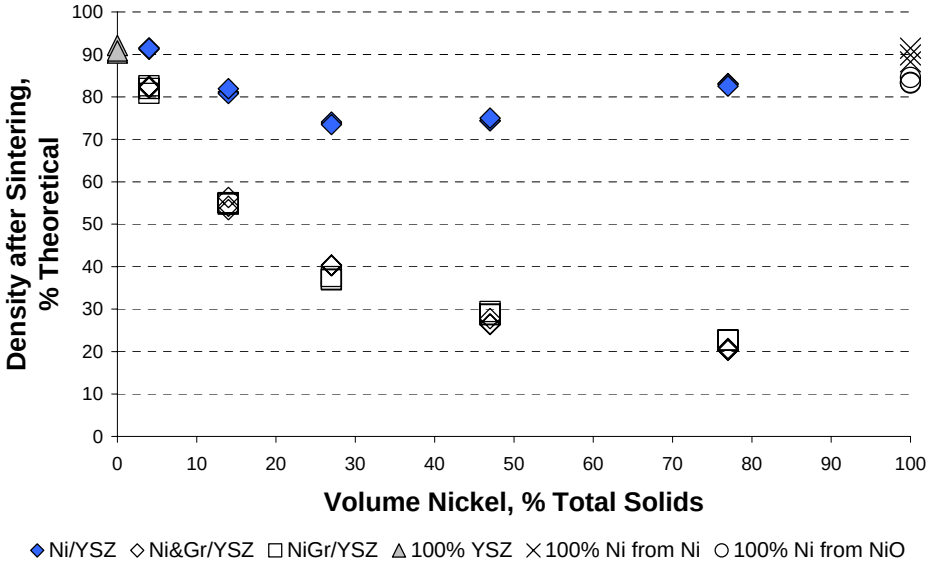

Figure 5-62: Relative density of Ni/YSZ, NiGr/YSZ, and Ni&Gr/YSZ composites after sintering in a dilatometer

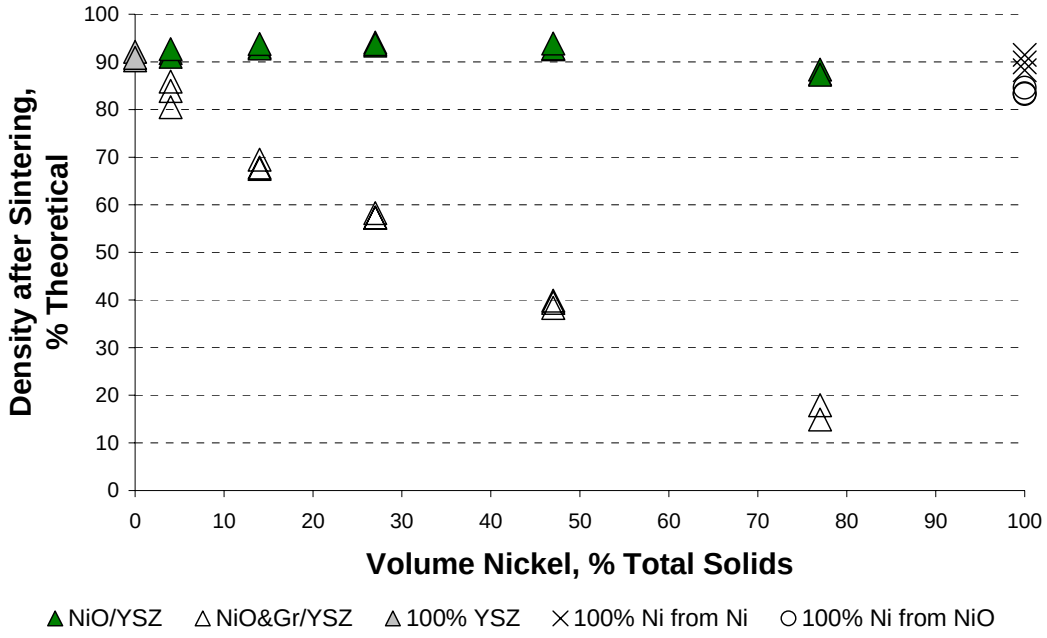

Figure 5-63: Relative density of NiO/YSZ and NiO&Gr/YSZ composites after sintering in a dilatometer

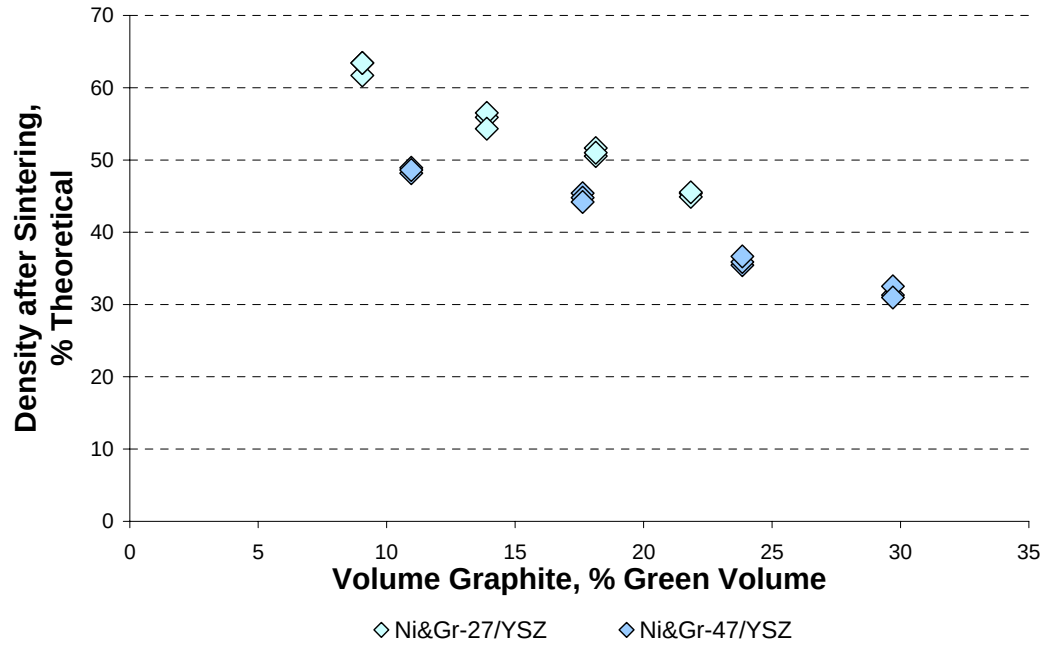

Figure 5-64: Relative density of Ni&Gr-27/YSZ, and Ni&Gr-47/YSZ composites after sintering in a dilatometer

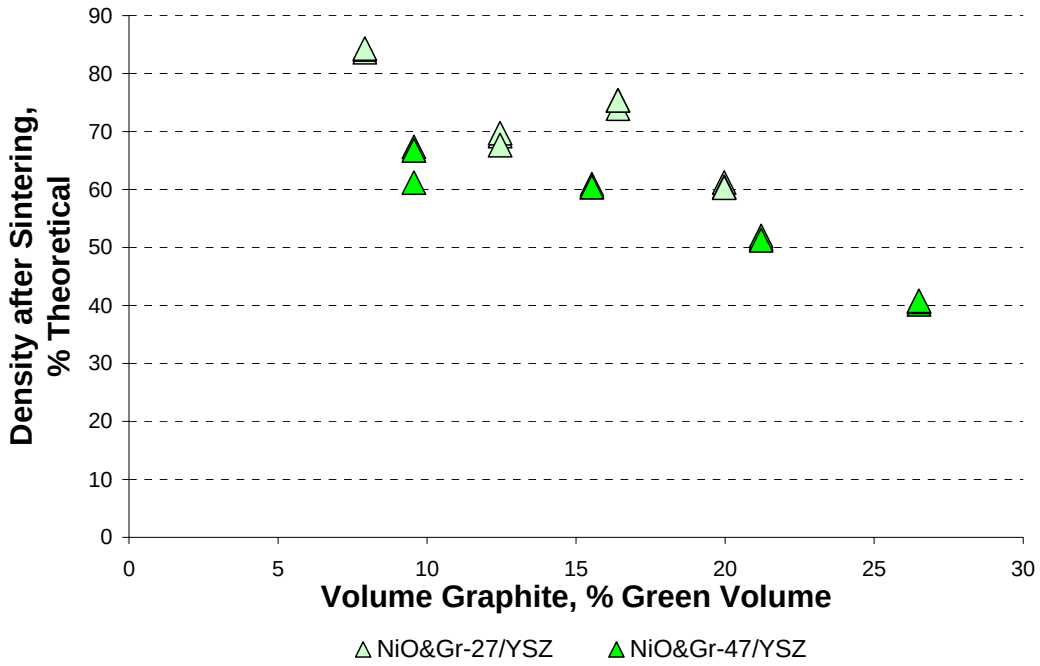

Figure 5-65: Relative density of NiO&Gr-27/YSZ, and NiO&Gr-47/YSZ composites after sintering in a dilatometer

5.3.2 Bulk Sintered Samples

In order to determine any affect sintering in the dilatometer may have on the sintering behaviour of the composites, a similar set of experiments was conducted for all samples sintered simultaneously in a box furnace. It should be noted that the samples with 4 vol% Ni of total solids were not prepared for the Ni/YSZ, NiGr/YSZ, and Ni&Gr/YSZ composites and are not included in the results for the bulk sintered samples.

5.3.2.1 Directional Linear Sintering Shrinkage

The linear sintering shrinkages, from the burnout state to the sintered state, in the length, width, and thickness directions for samples of each composite type sintered in a box furnace are shown in Appendix D. The directional linear sintering shrinkages for the dilatometer samples of each composite type have already been reported in Figure 5-47 through Figure 5-53.

Overall, the bulk sintered samples show the same linear sintering shrinkages as the samples sintered in a dilatometer with some subtle differences. First, the difference between the linear shrinkage in the length, width, and thickness directions is not as great in the bulk sintered samples compared with the dilatometer sintered samples. The linear sintering shrinkages appear to be more uniform resulting in more isotropic sintering shrinkage. In addition, the sintering shrinkage in the thickness direction tends to be highest for the bulk sintered samples while the linear sintering shrinkage in the length direction dominates the dilatometer sintered samples.

Although the Ni/YSZ, NiGr/YSZ, and NiO&Gr/YSZ composites demonstrate similar sintering shrinkages regardless of whether they are sintered in the dilatometer or a box furnace, the linear

sintering behaviour of Ni&Gr/YSZ and NiO&Gr/YSZ composites is influenced by the method of sintering. When the Ni&Gr/YSZ composites were sintered in the dilatometer, the linear sintering shrinkage in the width and thickness directions decreased with increasing nickel content compared with the sintering shrinkage in the length direction. For the bulk sintered Ni&Gr/YSZ samples, the linear sintering shrinkage still decreased with increasing nickel content but the linear sintering shrinkage was much more isotropic. Similarly, the bulk sintered NiO&Gr/YSZ samples had a more uniform, isotropic linear sintering shrinkage that was independent of the nickel loading, whereas in the dilatometer sintered samples the linear sintering shrinkage in the width and thickness tended to decrease with increasing nickel loading. As an aside, the linear sintering shrinkages for the Ni&Gr/YSZ and NiO&Gr/YSZ composites with a nickel loading of 77 vol% Ni of total solids is only presented with the bulk sintered samples as they were too fragile to sinter within the dilatometer.

Lastly, the bulk sintered Ni&Gr-27/YSZ, Ni&Gr-47/YSZ, NiO&Gr-27/YSZ, and NiO&Gr-47/YSZ composites, like the other composite samples, show similar linear sintering shrinkages as the dilatometer sintered samples, but with more isotropic linear sintering shrinkages.

5.3.2.2 Volumetric Sintering Shrinkage

Despite the differences in the linear sintering shrinkages, the volumetric sintering shrinkages for the samples bulk sintered in a box furnace are nearly identical to the volumetric sintering shrinkages of the samples sintered in the dilatometer. (See Appendix D for results) Like the dilatometer samples (Figure 5-54 to Figure 5-60), the majority of the densification takes place during the sintering stage with the degree of volumetric sintering shrinkage decreasing with increasing nickel content. Furthermore, the composites made from nickel powder tend to shrink less than the composites made from nickel oxide powder. Lastly, graphite additions appear to have little effect on the volumetric sintering shrinkage as it remains relatively constant with increasing graphite content.

5.3.2.3 Bulk Porosity

The relative density of samples of each composite type after bulk sintering is shown in Appendix D. Again, the bulk sintered samples have nearly the same relative densities as the same composite samples sintered in the dilatometer. Like the dilatometer sintered samples, the composites with increasing graphite loadings had lower relative densities, while the Ni/YSZ composites reached a minimum relative density at a nickel loading of 27 vol% Ni of total solids and the NiO/YSZ composite samples reached a maximum relative density at the same nickel loading.

5.3.2.4 Comparison between Bulk and Dilatometer Sintered Samples

To better distinguish any effects sintering in the dilatometer might have on the sintering of the composites, the volumetric sintering shrinkages from the green to the sintered state are presented for both the bulk and dilatometer sintered samples in Appendix D.

Overall, the volumetric sintering shrinkages from the green to sintered state of the bulk sintered samples shows reasonable agreement with the volumetric sintering shrinkage of the samples sintered in the dilatometer. The graphite-free composites, Ni/YSZ and NiO/YSZ composites tend to have better agreement between the two sintering shrinkages compared to the graphite containing composites. Figure 5-66 is an example of the best agreement between the two volumetric sintering shrinkages for the NiO/YSZ composite samples.

For the graphite containing composites, the volumetric sintering shrinkage of the bulk sintered samples are usually higher than the volumetric sintering shrinkage of the dilatometer sintered samples,

particularly at higher nickel contents. Figure 5-67 illustrates the difference in volumetric sintering shrinkages of the Ni&Gr/YSZ composites and is an example of the worst agreement between the two measured shrinkages.

The difference between the two volumetric shrinkages may be associated with the more isotropic dimensional linear sintering shrinkages of the bulk sintered samples. The bulk sintered samples typically have similar linear sintering shrinkages in the length and width but have a higher linear sintering shrinkage in the thickness compared to the dilatometer sintered samples. Consequently, the greater shrinkage in the thickness will result in a greater volumetric sintering shrinkage if the other linear sintering shrinkages are similar.

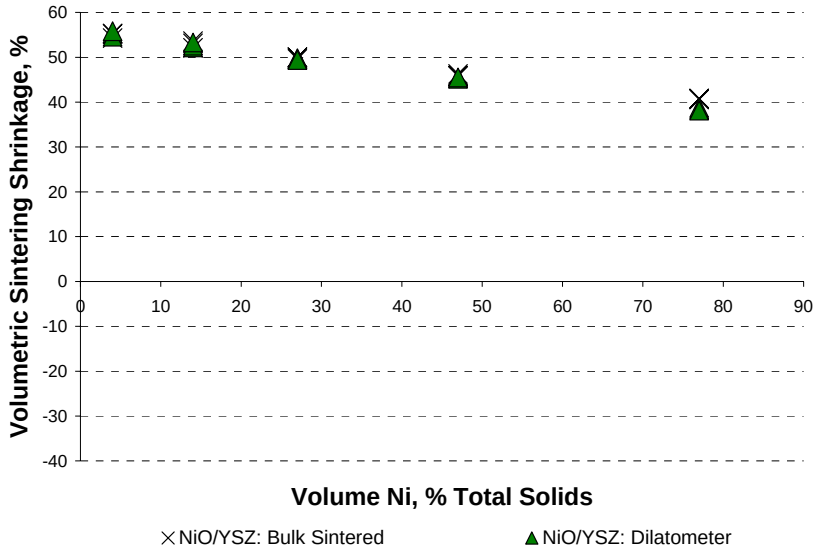

Figure 5-66: Volumetric sintering shrinkage from the green to sintered state for NiO/YSZ composite samples sintered in a box furnace or dilatometer

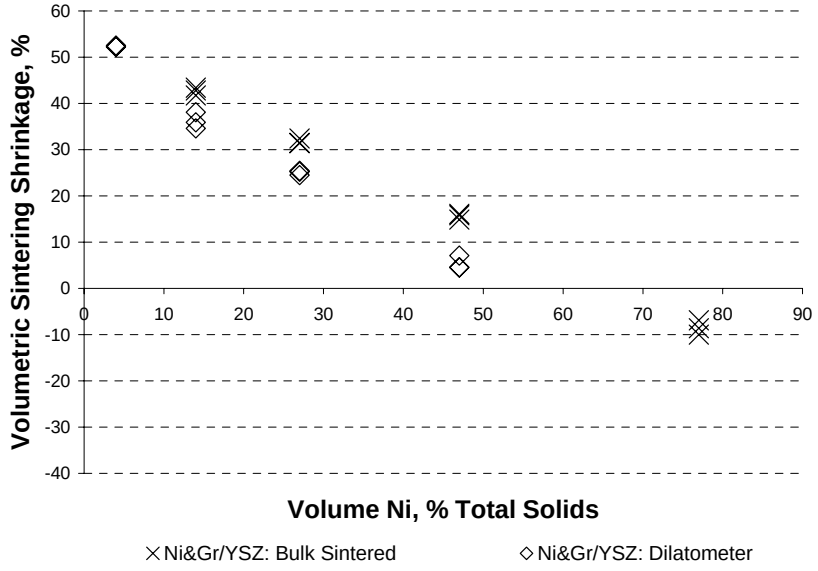

Figure 5-67: Volumetric sintering shrinkage from the green to sintered state for Ni&Gr/YSZ composite samples sintered in a box furnace or dilatometer

5.4 THE SINTERED AND REDUCED STATE

During sintering, any remaining nickel metal is transformed into nickel oxide. For the composites to be useful solid oxide fuel cell anodes, the nickel oxide must be converted back to nickel metal. The reduction of nickel oxide back to nickel metal is completed by heating the samples to 1000°C in a 10% hydrogen/90% nitrogen atmosphere and holding for one hour. Since nickel metal is denser than nickel oxide, the composites are expected to shrink slightly during reduction.

5.4.1 Dilatometer Studies

The average change in length of three samples of each composite type during the reduction stage as measured by the dilatometer is given in Figure 5-68 through Figure 5-76. The heating schedule, represented by a dashed line, is also included with the dilatometer plot. For the most part, the composite samples experience very little change in dimension during reduction. Since the linear shrinkages during reduction are on the same order of magnitude as the expected measurement variability (±0.5%), it is very difficult to draw any specific conclusions regarding the effect nickel and graphite have on the dimensional changes.

Any composites with nickel loadings less than 47 vol% Ni of total solids show virtually no change in dimension after reduction, while composites with nickel loadings 77 vol% Ni or greater show more significant linear shrinkages. For example, the 100% Ni from NiO samples shrink the most, nearly 10%, followed by the NiGr/YSZ composite with a nickel loading of 77 vol% Ni of total solids and the 100% Ni from Ni samples with linear shrinkages of approximately 3% and 2% respectively. The other composites samples have linear shrinkages that are less than 0.5%.

When examining the linear shrinkages of the Ni&Gr-27/YSZ, Ni&Gr-47/YSZ, NiO&Gr-27/YSZ, and NiO&Gr-47/YSZ composites (Figure 5-73 to Figure 5-76), it appears graphite does not significantly influence the linear shrinkage during reduction. For instance, the linear shrinkage for the Ni&Gr-47/YSZ composites with no graphite is greater than the linear shrinkage of the composites with graphite additions, and the linear shrinkages for the Ni&Gr-27/YSZ composites are nearly identical despite the differences in graphite loading.

5.4.1.1 Dilatometer Sample Measurements

A comparison between the linear sintering shrinkages as measured by the dilatometer and measured manually for each composite type may be found in Appendix E. In most cases, the agreement between the two measuring methods was very good, particularly at low nickel loadings. At higher nickel loadings, the variability in the dilatometer measured shrinkages was greater compared to the variability in the manually measured linear shrinkages. Figure 5-77, a typical example, shows the agreement between the manual and dilatometer measured linear shrinkages after reduction for the NiO/YSZ composites is reasonable.

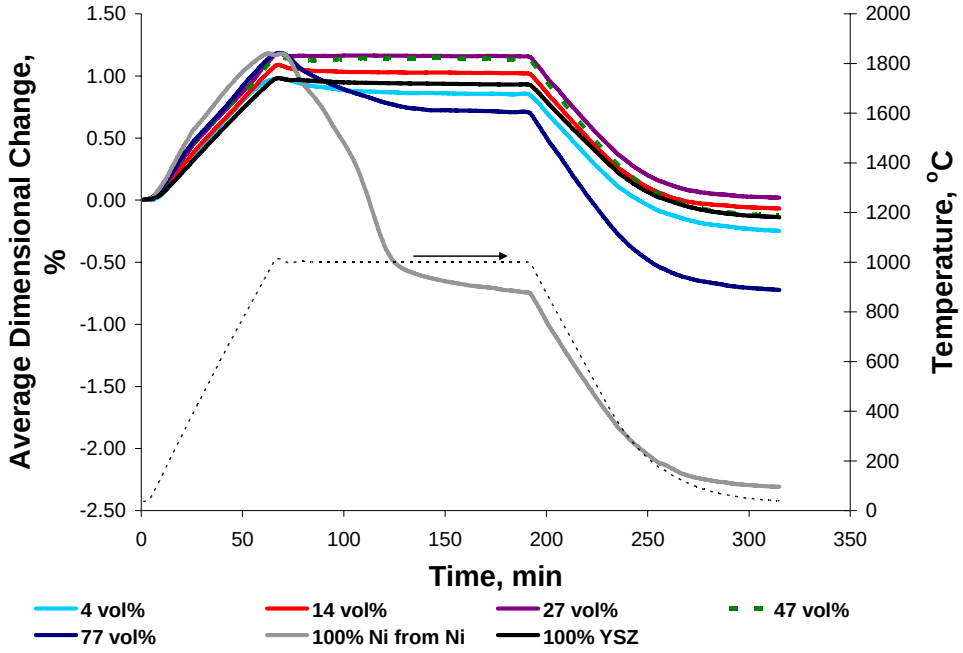

Figure 5-68: Dilatometer plots showing the average shrinkage during reduction for various Ni/YSZ composites. The nickel fractions represent the volume of nickel as a percent of total solids in the sintered and reduced state.

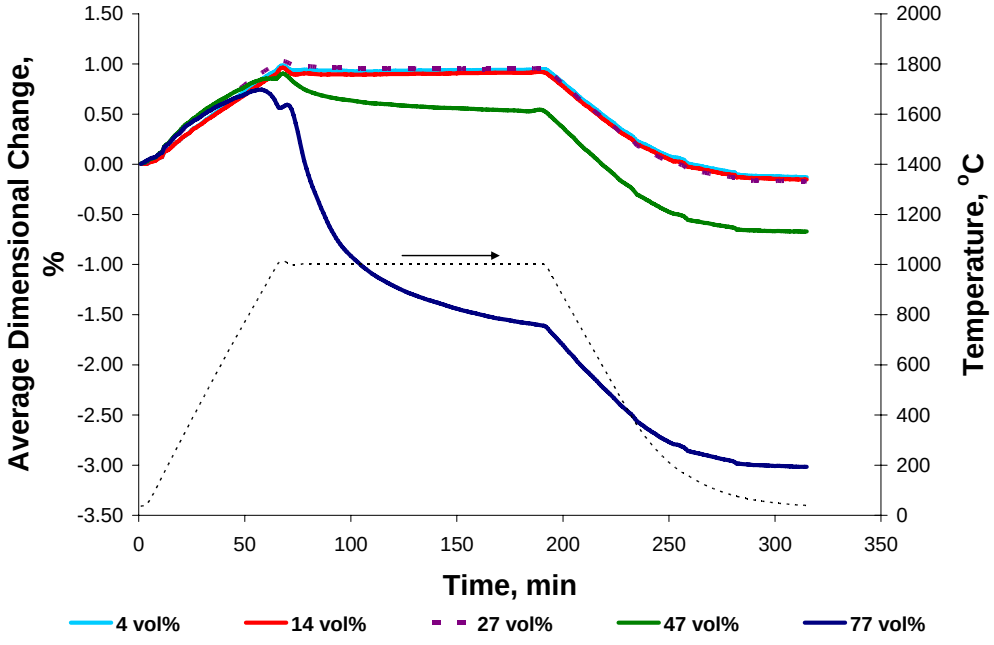

Figure 5-69: Dilatometer plots showing the average shrinkage during reduction for various NiGr/YSZ composites. The nickel fractions represent the volume of nickel as a percent of total solids in the sintered and reduced state.

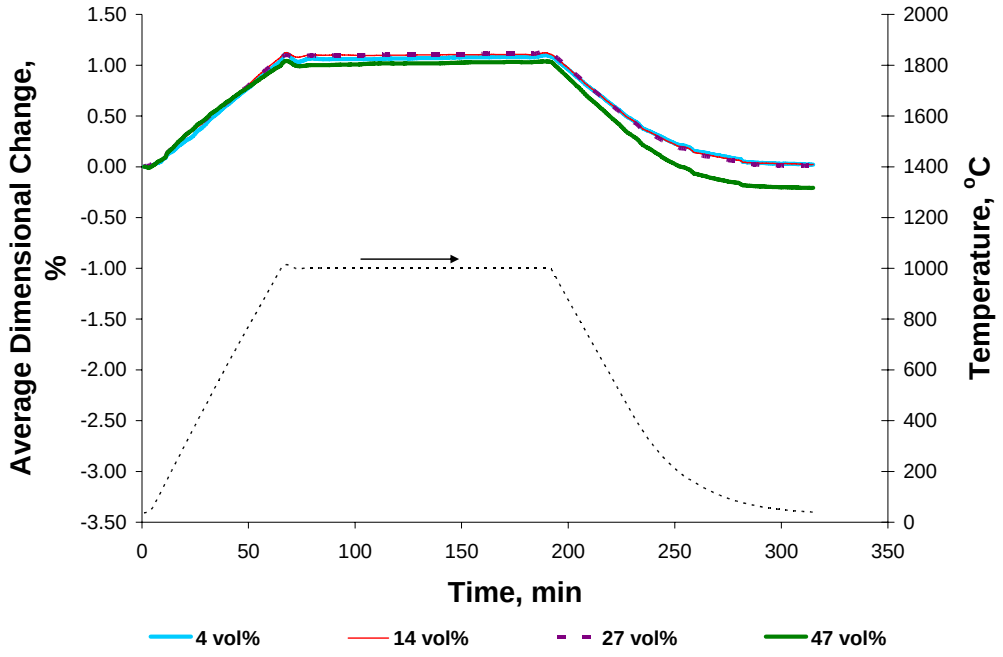

Figure 5-70: Dilatometer plots showing the average shrinkage during reduction for various Ni&Gr/YSZ composites. The nickel fractions represent the volume of nickel as a percent of total solids in the sintered and reduced state.

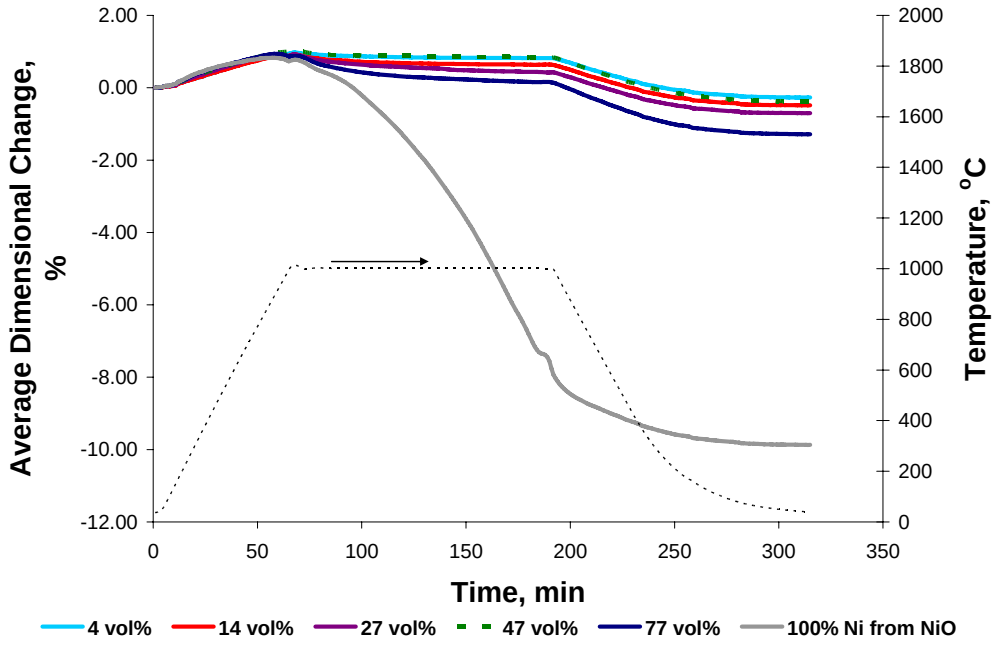

Figure 5-71: Dilatometer plots showing the average shrinkage during reduction for various NiO/YSZ composites. The nickel fractions represent the volume of nickel as a percent of total solids in the sintered and reduced state.

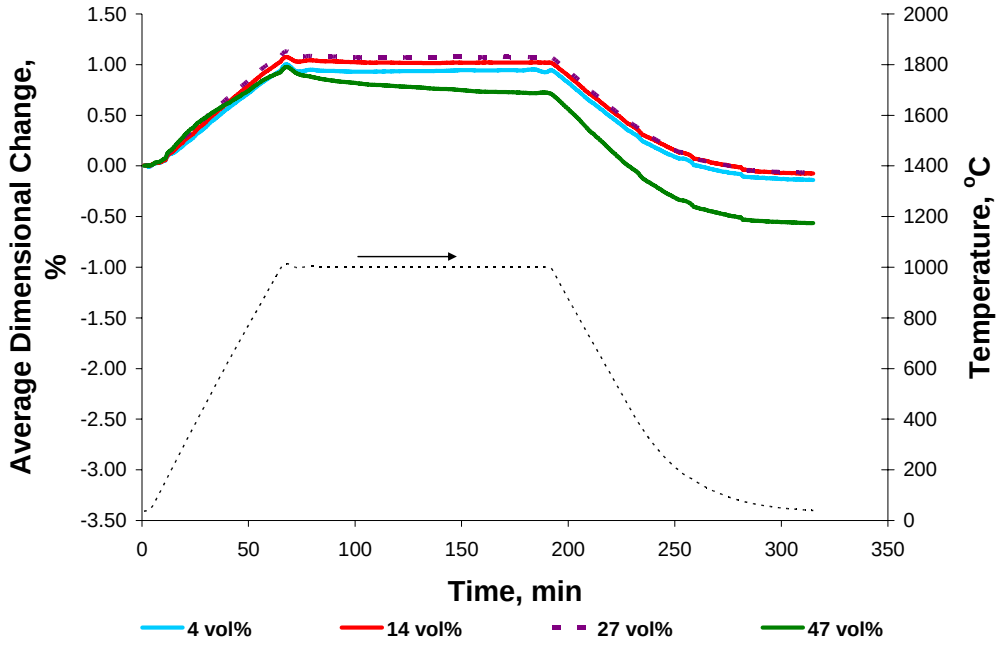

Figure 5-72: Dilatometer plots showing the average shrinkage during reduction for various NiO&Gr/YSZ composites. The nickel fractions represent the volume of nickel as a percent of total solids in the sintered and reduced state.

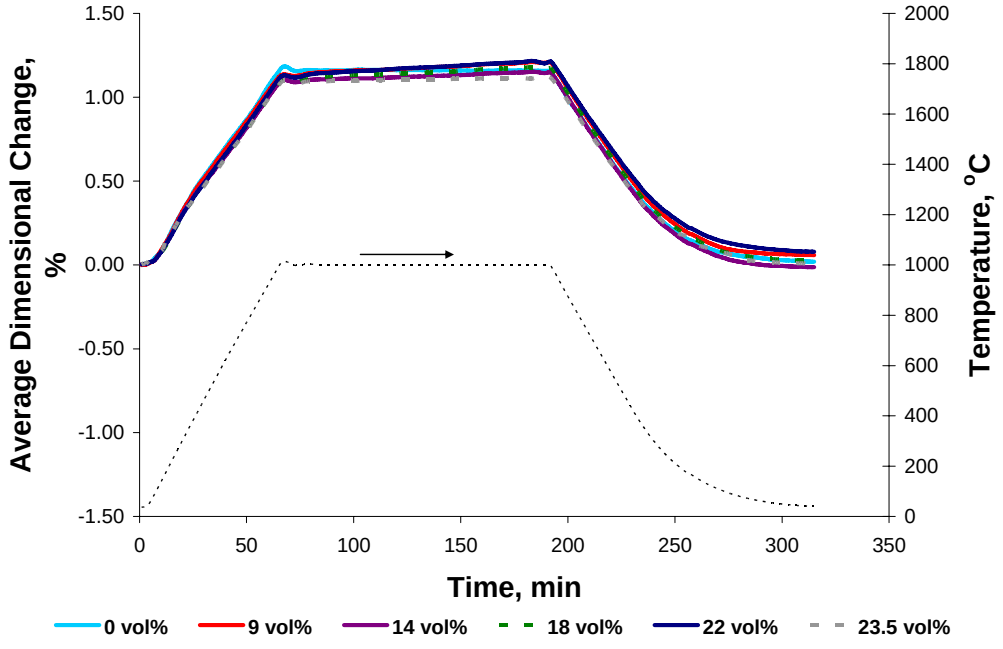

Figure 5-73: Dilatometer plots showing the average shrinkage during reduction for various Ni&Gr-27/YSZ composites. The percentages represent the graphite loading as a fraction of the dried green volume.

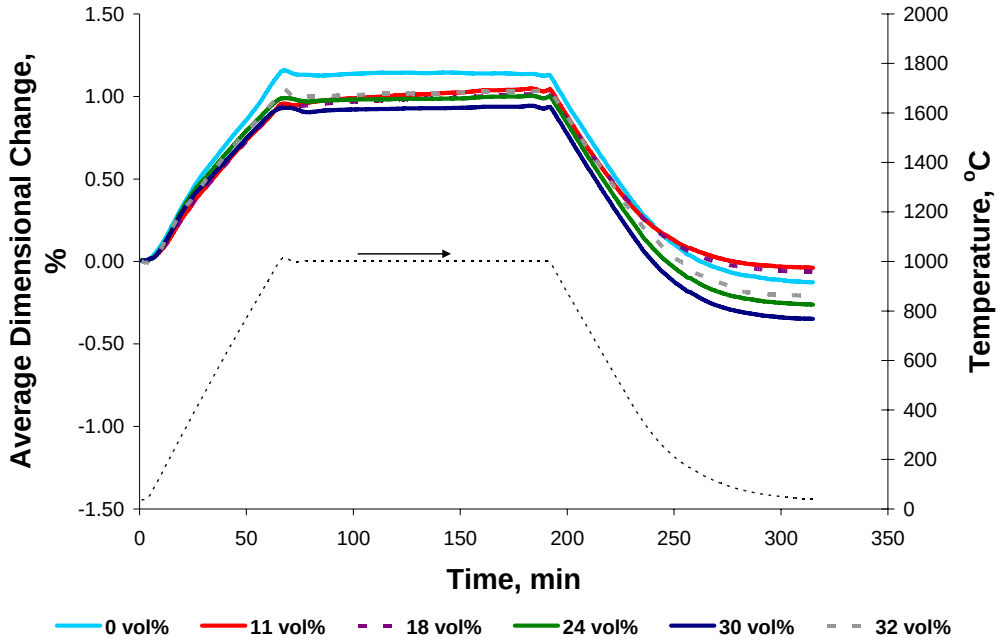

Figure 5-74: Dilatometer plots showing the average shrinkage during reduction for various Ni&Gr-47/YSZ composites. The percentages represent the graphite loading as a fraction of the dried green volume.

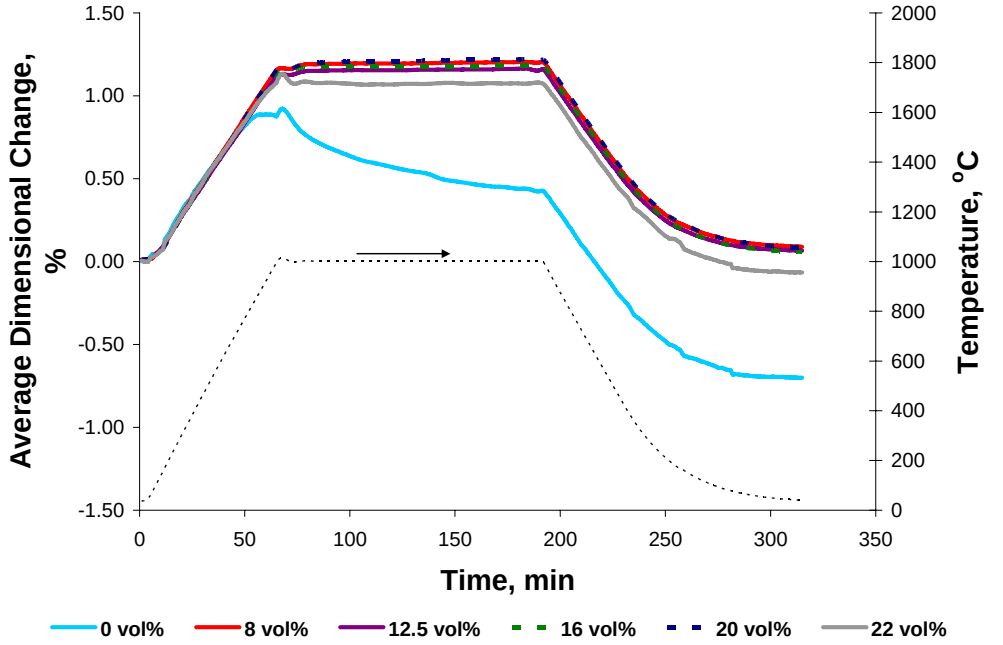

Figure 5-75: Dilatometer plots showing the average shrinkage during reduction for various NiO&Gr-27/YSZ composites. The percentages represent the graphite loading as a fraction of the dried green volume.

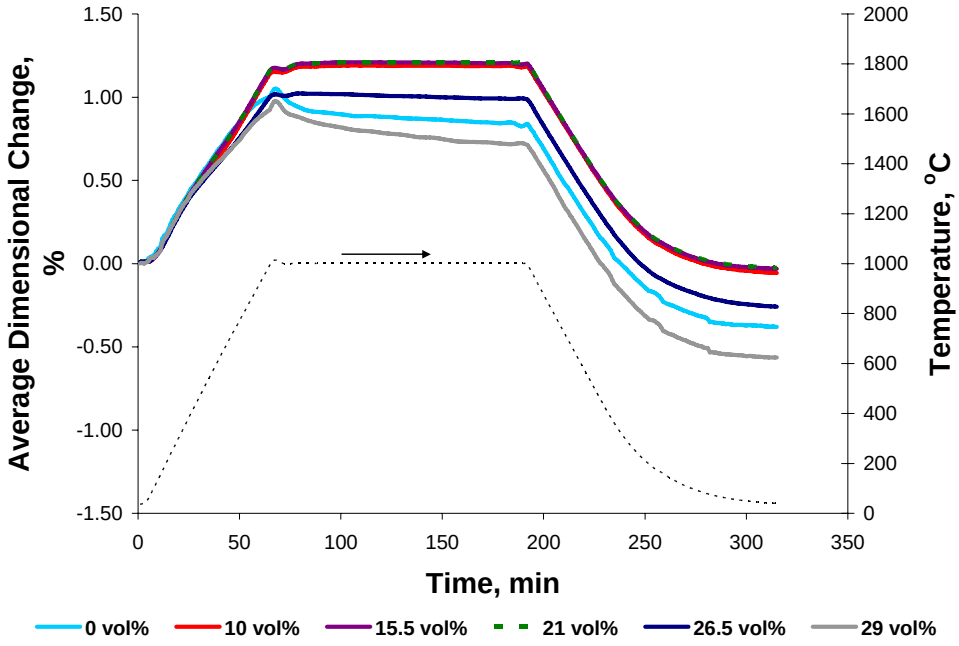

Figure 5-76: Dilatometer plots showing the average shrinkage during reduction for various NiO&Gr-47/YSZ composites. The percentages represent the graphite loading as a fraction of the dried green volume.

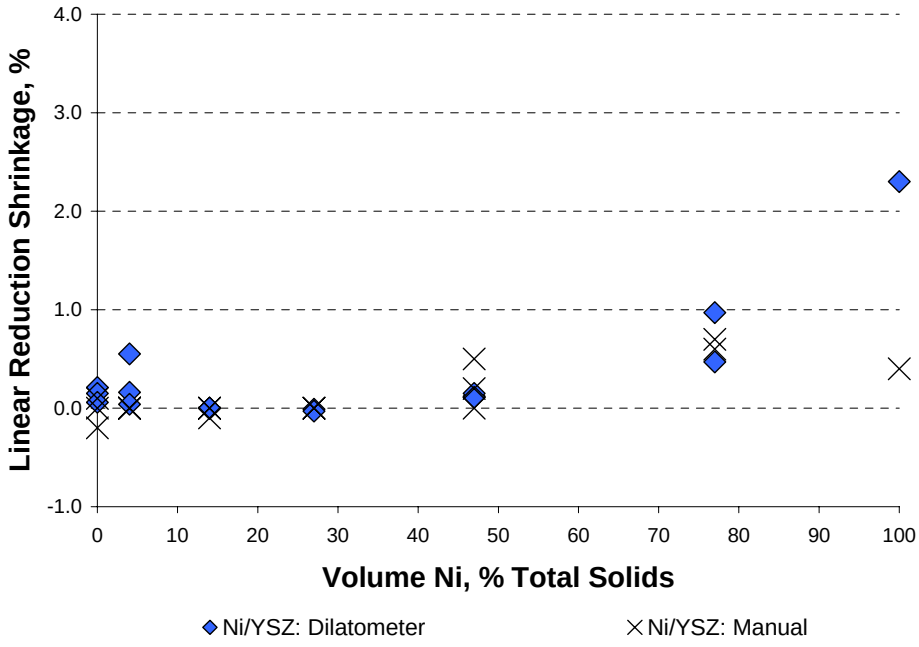

Figure 5-77: Comparison of linear reduction shrinkages in the length direction as measured manually and with a dilatometer for the Ni/YSZ composites

5.4.1.2 Dimensional Changes during Reduction

Volumetric Shrinkage during Reduction

The volumetric shrinkages from the sintered to the reduced state and the total volumetric shrinkage from the pressed green state to the final sintered & reduced state for each composite type are given in Figure 5-78 through Figure 5-84. Upon inspection of these figures, it is clear that the relative amount of volumetric shrinkage during reduction is quite small compared to the total volumetric shrinkage from the green state. With the exception of the 100% Ni from NiO sample, which shrinks over 20% during the reduction stage (See Figure 5-81), the other composite samples experience volumetric shrinkages that are consistently less than 5%, and in fact some of the graphite containing composites actually expand slightly during reduction (See Figure 5-82 to Figure 5-84).

The total volumetric shrinkage from the green state to the final sintered & reduced state is a function of all the volumetric shrinkages from the previous processing stages. Consequently, the Ni/YSZ composites show a consistent decrease in the total volumetric shrinkage with increasing nickel loading. At the lowest nickel loading, the total volumetric shrinkage is quite similar to the total volumetric shrinkage of the 100% YSZ sample. As the nickel loading increases, the total volumetric shrinkage decreases until it reaches a minimum at a nickel loading of 77 vol% Ni of total solids where the composite samples actually expand about 5%. Finally, the 100% Ni from Ni samples show only a slight total volumetric shrinkage with the majority of the shrinkage taking place during the reduction stage.

The other composite types show similar trends in that increasing nickel loading leads to a decrease in the total volumetric shrinkage. Again, the exception being the 100% Ni from NiO samples that tend to shrink as much as the lowest nickel loaded NiO/YSZ composites. Although the Ni/YSZ sample at a nickel loading of 77 vol% Ni of total solids is unique with its overall expansion, the nickel based composites (Ni/YSZ, NiGr/YSZ, and Ni&Gr/YSZ) tend to shrink significantly less compared to the nickel oxide based composites (NiO/YSZ and NiO&Gr/YSZ).

On the other hand, graphite additions appear to have little influence over the volumetric shrinkage during reduction and the total volumetric shrinkage. When examining the composites with varying graphite loadings, shown in Figure 5-83 and Figure 5-84, the total volumetric shrinkage increases slightly with increasing graphite loading and then decreases slightly at the highest graphite loading.

Linear Dimensional Shrinkage during Reduction

The linear dimensional changes after reduction for the length, width, and thickness directions are shown in Appendix E. Generally, the dimensional changes in each direction are similar and range between a shrinkage of 2% and an expansion of 2% but the majority of the composite samples have virtually no change in dimension after the reduction stage. Since the dimensional changes are on the same order of magnitude as the expected measurement variability (±0.5%), it is difficult to determine any significant trend other than the change in dimension is very slight and relatively isotropic.

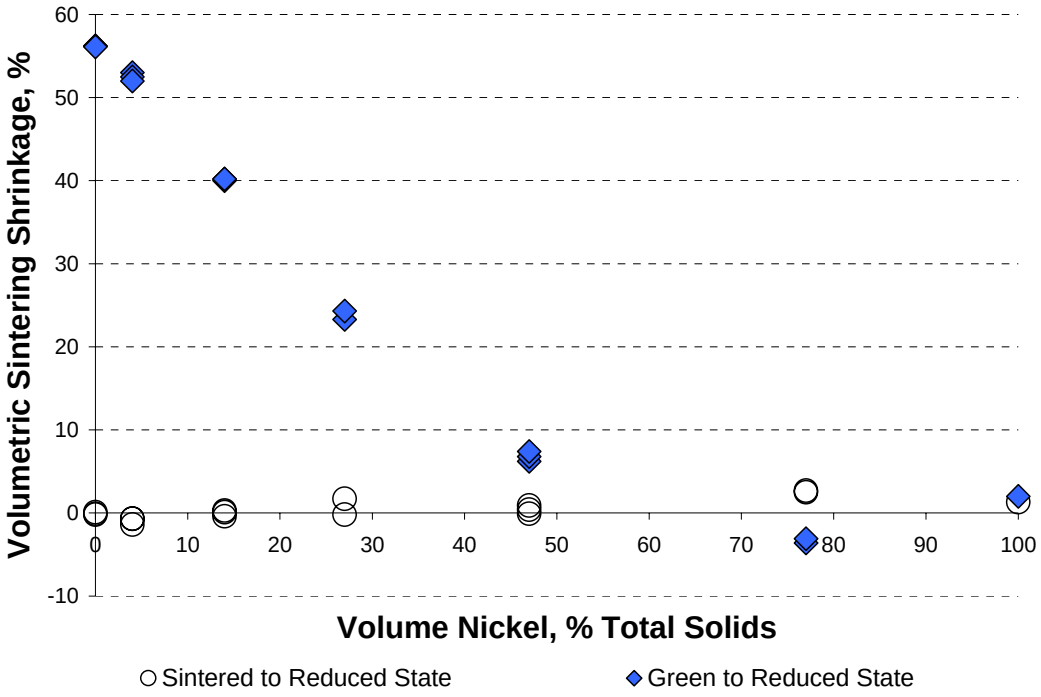

Figure 5-78: Manually measured volumetric shrinkage for the Ni/YSZ composites reduced in a dilatometer after the sintering stage and the total volumetric shrinkage from the green to the sintered & reduced state

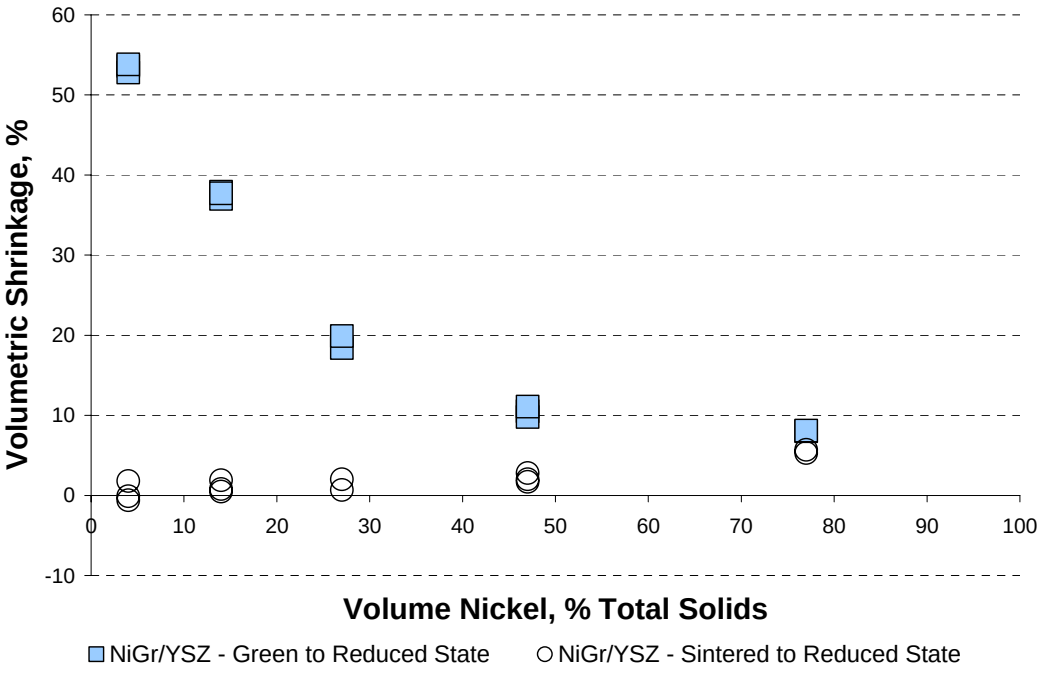

Figure 5-79: Manually measured volumetric shrinkage for the NiGr/YSZ composites reduced in a dilatometer after the sintering stage and the total volumetric shrinkage from the green to the sintered & reduced state

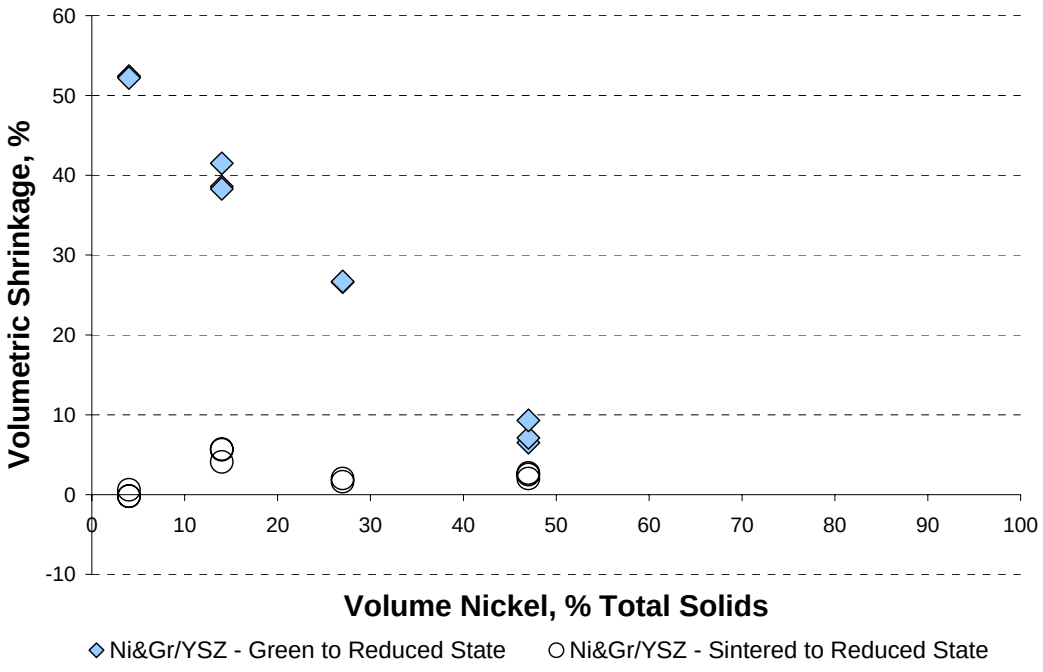

Figure 5-80: Manually measured volumetric shrinkage for the Ni&Gr/YSZ composites reduced in a dilatometer after the sintering stage and the total volumetric shrinkage from the green to the sintered & reduced state

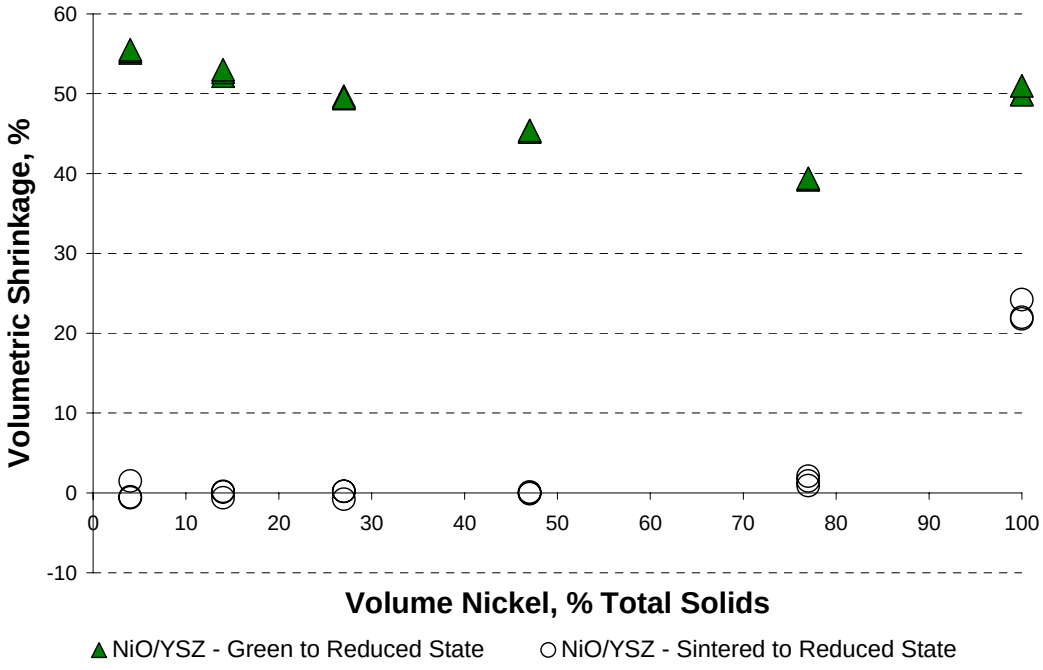

Figure 5-81: Manually measured volumetric shrinkage for the NiO/YSZ composites reduced in a dilatometer after the sintering stage and the total volumetric shrinkage from the green to the sintered & reduced state

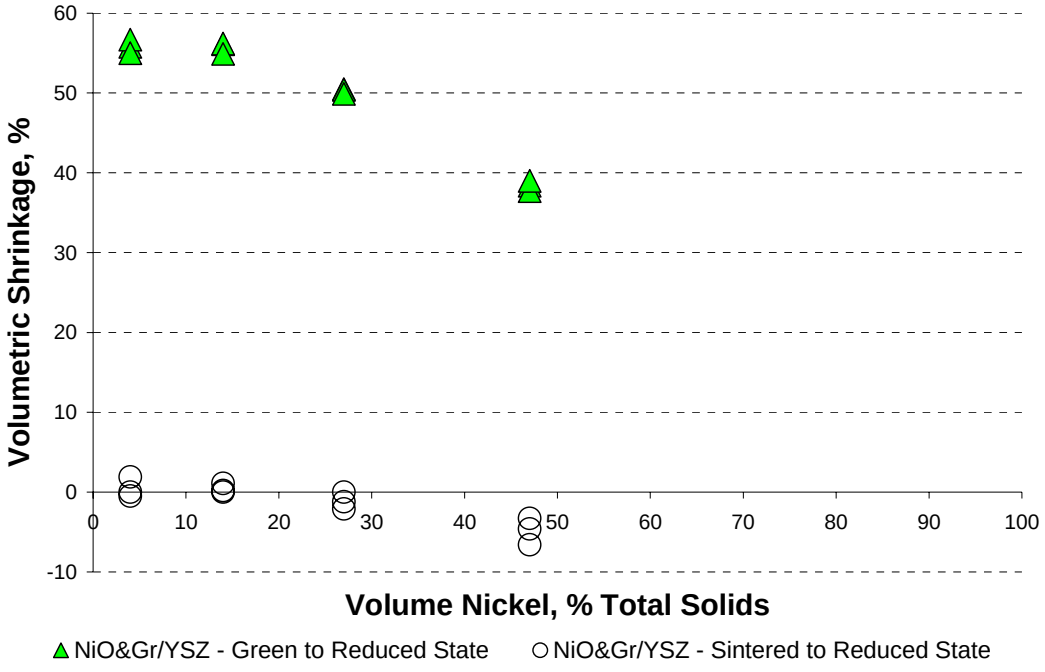

Figure 5-82: Manually measured volumetric shrinkage for the NiO&Gr/YSZ composites reduced in a dilatometer after the sintering stage and the total volumetric shrinkage from the green to the sintered & reduced state

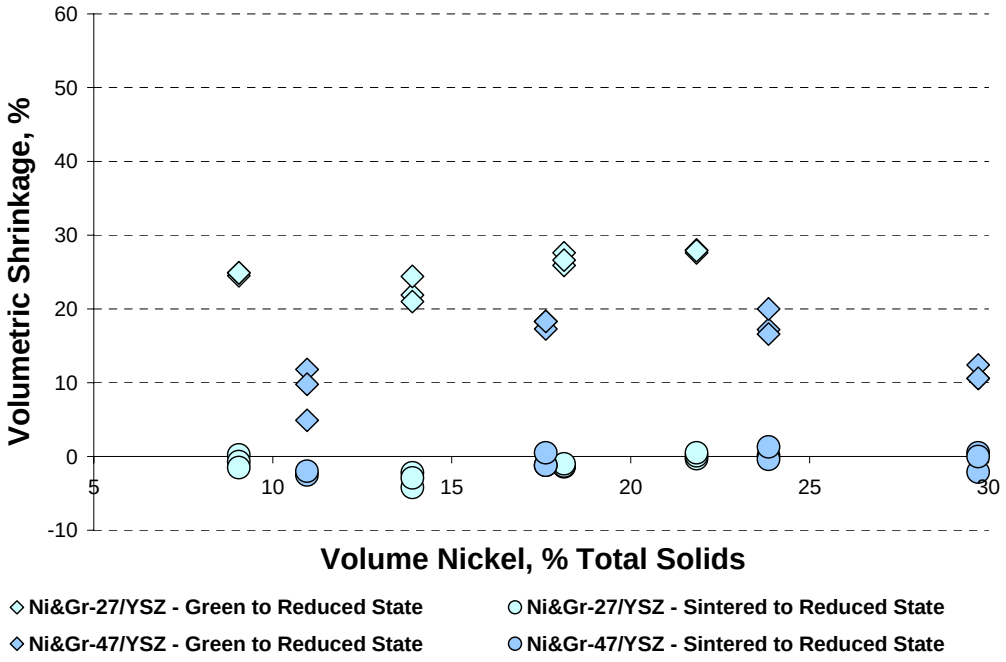

Figure 5-83: Manually measured volumetric shrinkage for the Ni&Gr-27/YSZ and Ni&Gr-47/YSZ composites reduced in a dilatometer after the sintering stage and the total volumetric shrinkage from the green to the sintered & reduced state

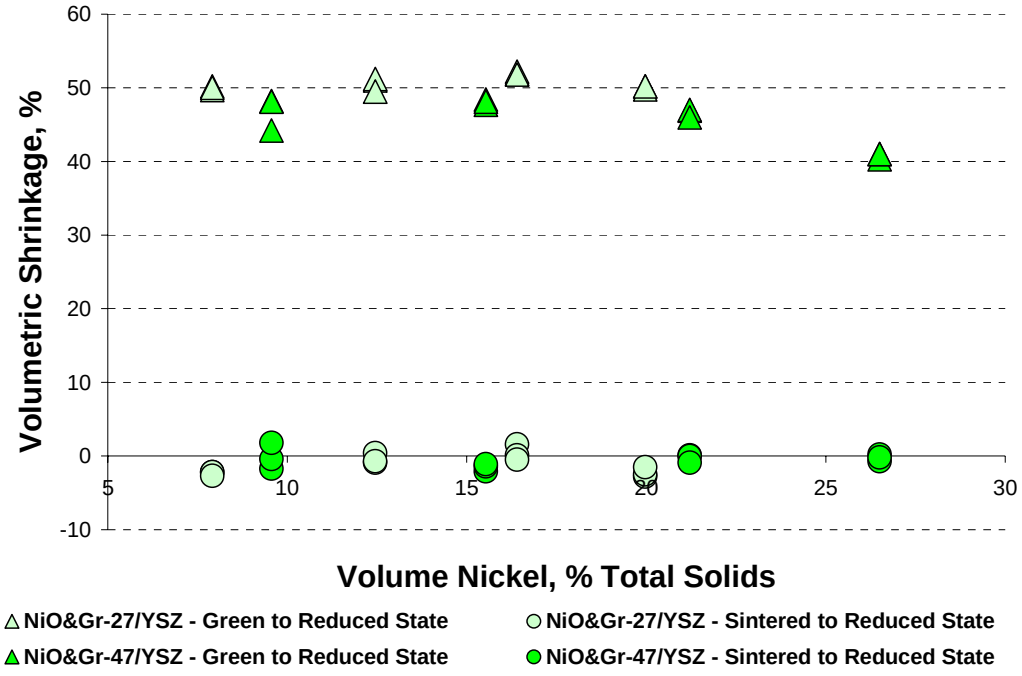

Figure 5-84: Manually measured volumetric shrinkage for the NiO&Gr-27/YSZ and NiO&Gr-47/YSZ composites reduced in a dilatometer after the sintering stage and the total volumetric shrinkage from the green to the sintered & reduced state

5.4.2 Degree of Reduction

The average degree of reduction for each of the composite types is shown in Figure 5-85 and Figure 5-86. With the exception of the 100% Ni from Ni sample, having an average reduction of 82%, the other composite types have an average reduction of nearly 100%, indicating that the reduction stage successfully reduced the nickel oxide back to nickel metal.

5.4.3 Bulk Porosity

5.4.3.1 Manual Measurement

The relative densities of each composite type are shown in Figure 5-87 through Figure 5-91. The relative density is calculated by dividing the measured density by the theoretical density of the composite assuming that the composite comprises YSZ and nickel metal only. Overall, increasing graphite and nickel loadings lead to decreasing relative densities. The relative densities of the sintered & reduced composites with nickel loadings above 27 vol% Ni of total solids are about 10% less than the relative densities of the samples after sintering. For the composites with the lowest nickel loading, the relative density is essentially unchanged after reduction and the composites with a nickel loading of 14 vol% Ni of total solids the relative density is about 5% less.

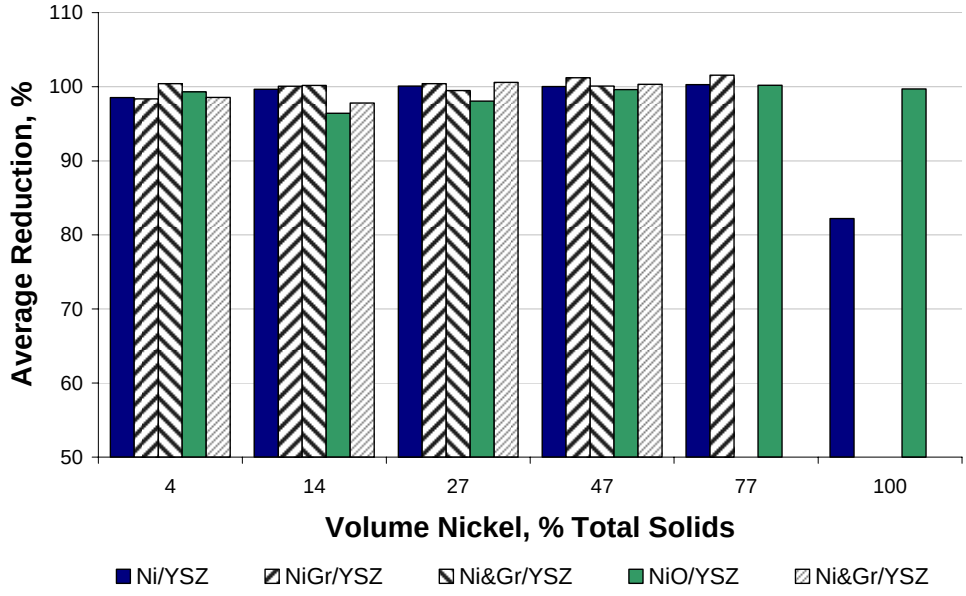

Figure 5-85: Average degree of nickel reduction for the Ni/YSZ, NiGr/YSZ, Ni&Gr/YSZ, NiO/YSZ, and NiO&Gr/YSZ composite types.

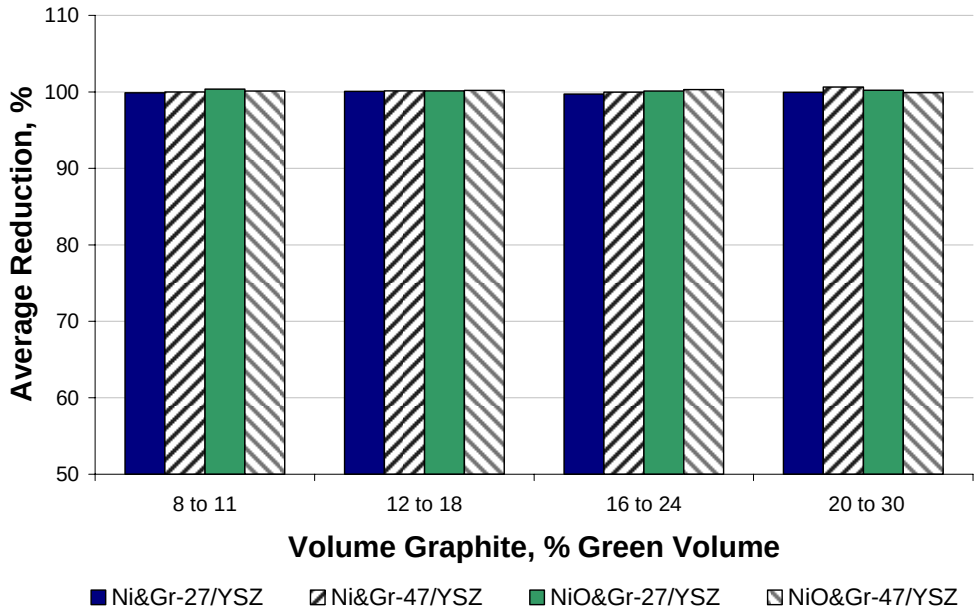

Figure 5-86: Average degree of nickel reduction for the Ni&Gr-27/YSZ, Ni&Gr-47/YSZ, NiO&Gr-27/YSZ, and NiO&Gr-47/YSZ composites. The graphite loadings are given as a range which encompasses the graphite loadings for each of the individual composites. For each composite type, the lowest graphite loading is on the left and progressively increases to the highest graphite loading on the right.

Since the porosity formed by the graphite additions is present in both the sintered and the sintered & reduced samples, the graphite containing composites show the same trends after reduction as they did before the reduction stage. The sintered & reduced samples have sintered densities of about 10% less than the samples after sintering.

After sintering, the Ni/YSZ composites showed a minimum relative density of about 75% at a nickel loading of 47 vol% Ni of total solids. Now after reduction, the Ni/YSZ composite show a minimum relative density of 55% at a nickel loading between 47 vol% and 77 vol% Ni of total solids. The relative densities of the 100% Ni from Ni and 100% Ni from NiO samples also decreases from 90% after sintering to 65% after sintering & reduction, whereas the 100% YSZ samples shows no change in relative density after sintering & reduction.

Unlike the Ni/YSZ composites, the NiO/YSZ composites show a significant decrease in the relative density after reduction compared to the relative densities after sintering. Before reduction, the NiO/YSZ composites show a nearly constant relative density of 90% independent of nickel loading, as shown in Figure 5-61. Once the reduction of the nickel oxide is complete, the relative densities of the composites show a decrease in relative density that is proportional to the nickel content of the composite. For example, the 77 vol% Ni of total solids composite samples yield a change in relative density from 90% before reduction to a relative density of 55% afterwards.

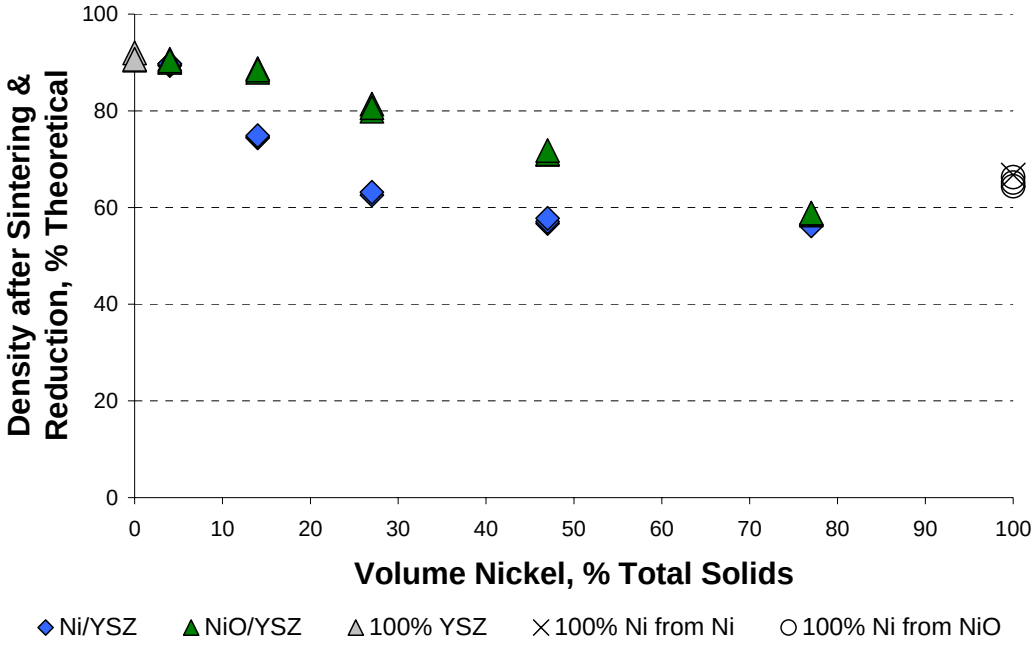

Figure 5-87: Relative density of Ni/YSZ and NiO/YSZ composites after reduction in a dilatometer

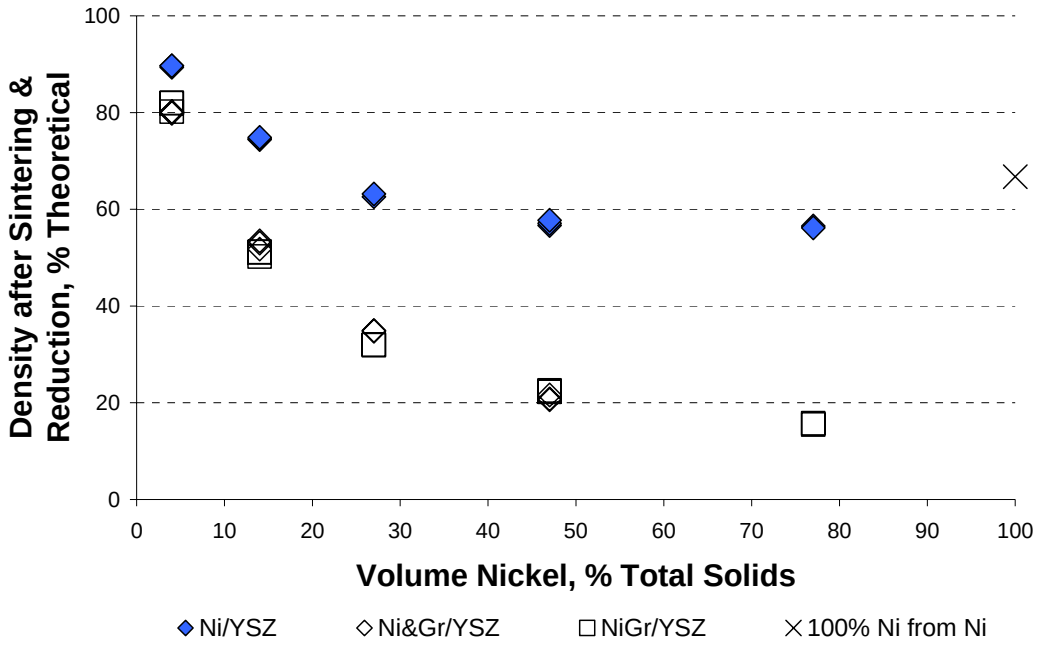

Figure 5-88: Relative density of Ni/YSZ, NiGr/YSZ, and Ni&Gr/YSZ composites after reduction in a dilatometer

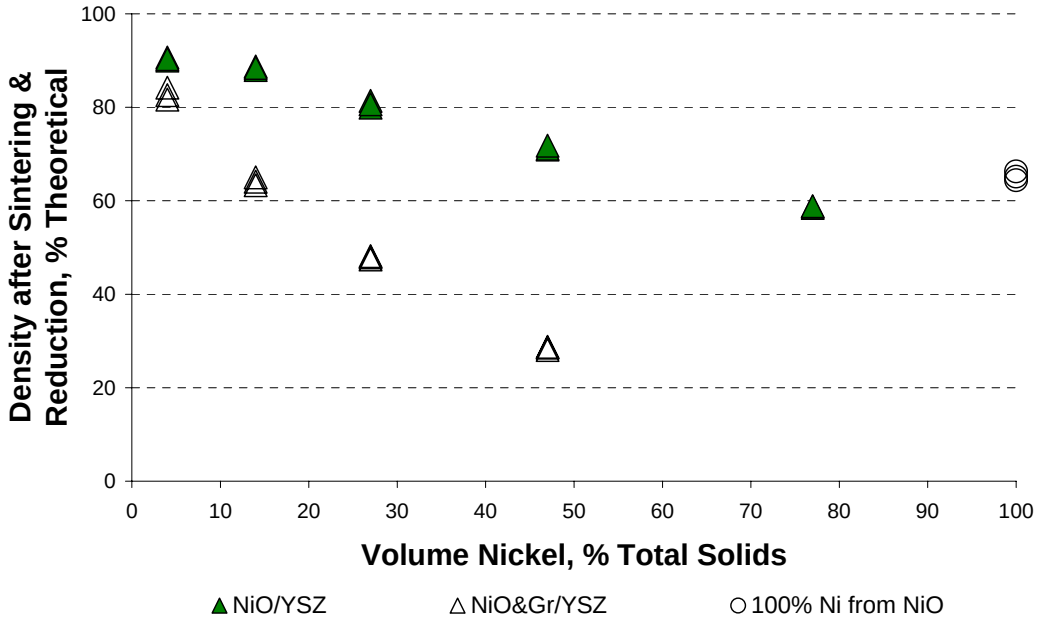

Figure 5-89: Relative density of NiO/YSZ and NiO&Gr/YSZ composites after reduction in a dilatometer

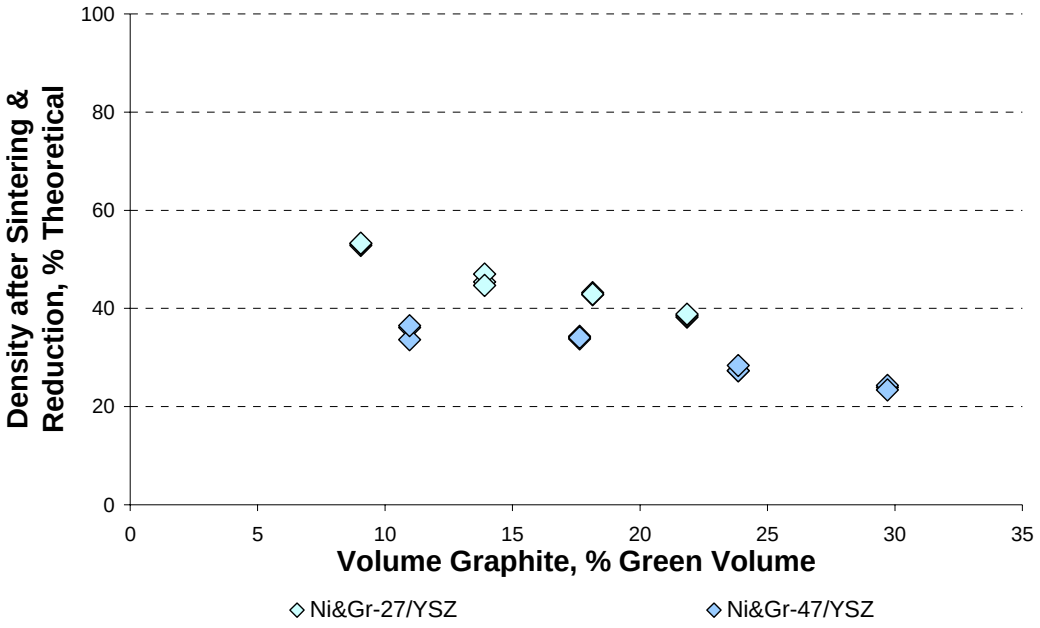

Figure 5-90: Relative density of Ni&Gr-27/YSZ and Ni&Gr-47/YSZ composites after reduction in a dilatometer

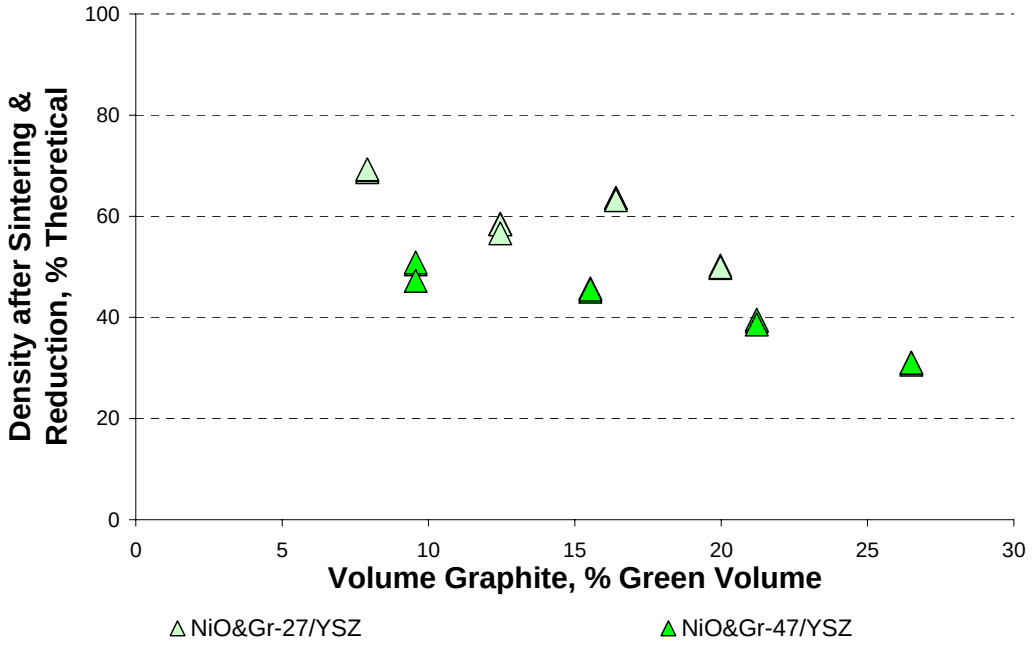

Figure 5-91: Relative density of NiO&Gr-27/YSZ and NiO&Gr-47/YSZ composites after reduction in a dilatometer

5.4.3.2 Image Analysis

Image analysis was used to estimate the bulk porosity of the composites after reduction based on back scattered scanning electron micrographs in order to compare the relative densities calculated from the measured dimensions of each composite sample. The porosity measurements from five images was averaged together to get the estimated bulk porosity of the composite. Samples of the SEM images used for image analysis are shown in Appendix F. The bulk porosity for each sample can be calculated from the relative density by using the following equation:

$$Bulk\ Porosity,\% = 100\% - Relative\ Density,\% \quad \textbf{(5-7)}$$

where the relative density of the composite as a percentage is subtracted from 100% to get the bulk porosity as a fraction of the total composite volume.

For the most part, the bulk porosities determined from image analysis are comparable but usually less than the bulk porosities calculated from the measured dimensions of the samples, as shown in Figure 5-92 through Figure 5-98. In some cases, the agreement between the two methods is quite close (See Figure 5-94); while in other cases the difference in porosity can be as much as 20% (See Figure 5-93).

The discrepancy between the two bulk porosity measurements can be attributed to the manner in which they are calculated. Bulk porosity measurements based on image analysis are dependent on the location of the image within the sample and the characteristics of the image such as magnification, brightness, and contrast. The SEM micrographs prepared for image analysis were taken from the top plane of the composite samples at a relatively low magnification of 150x. Although a portion of the surface was removed during polishing, it is still possible that the images used for analysis are influenced by the surface characteristics of the composite and may not be a true representation of the composite volume. Finally, even though care was used to select the appropriate area fractions, it was often difficult to precisely distinguish between porosity and the composite structure resulting in a less accurate estimation of the porosity. On the other hand, measuring the volume of each of the samples with callipers can lead to an exaggeration of the volume resulting in overestimation of the bulk porosity. Most likely, the true bulk porosity lies somewhere between the estimated porosities of the two methods. Lastly, it is important to note that both measurement methods show exactly the same trends with respect to the influence of nickel and/or graphite content on the bulk porosity of the composite samples.

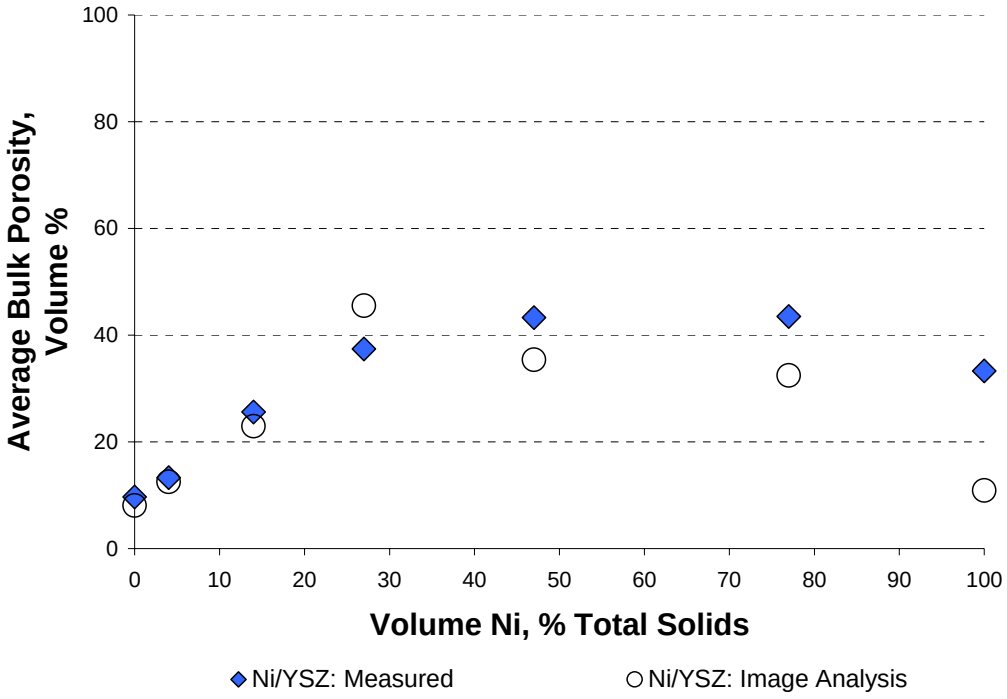

Figure 5-92: Comparison between bulk porosity as measured manually and bulk porosity determined through image analysis for Ni/YSZ composite samples

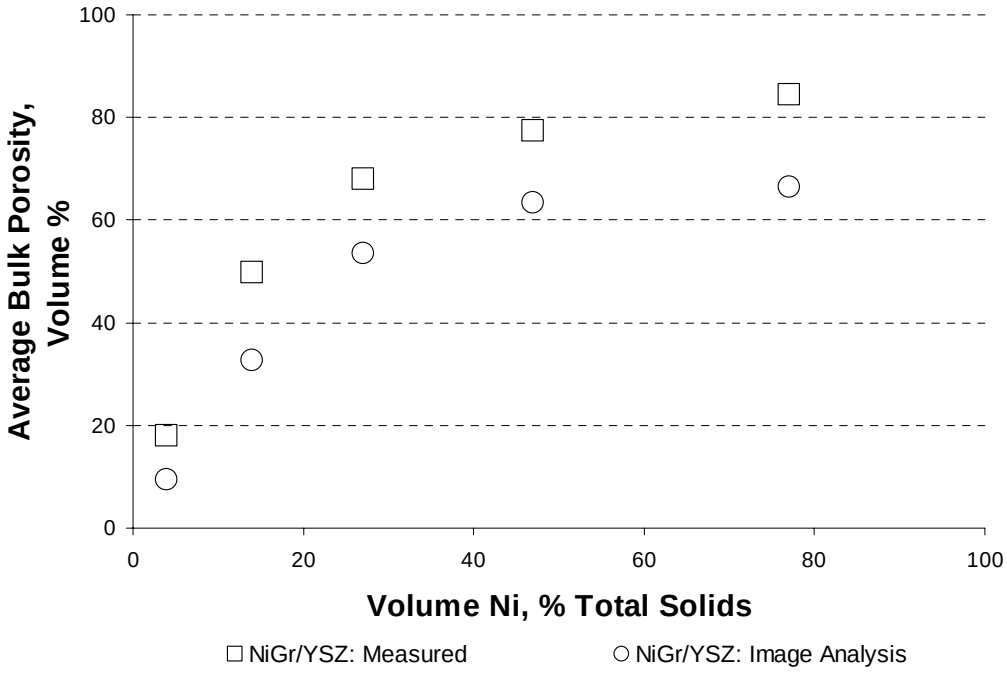

Figure 5-93: Comparison between bulk porosity as measured manually and bulk porosity determined through image analysis for NiGr/YSZ composite samples

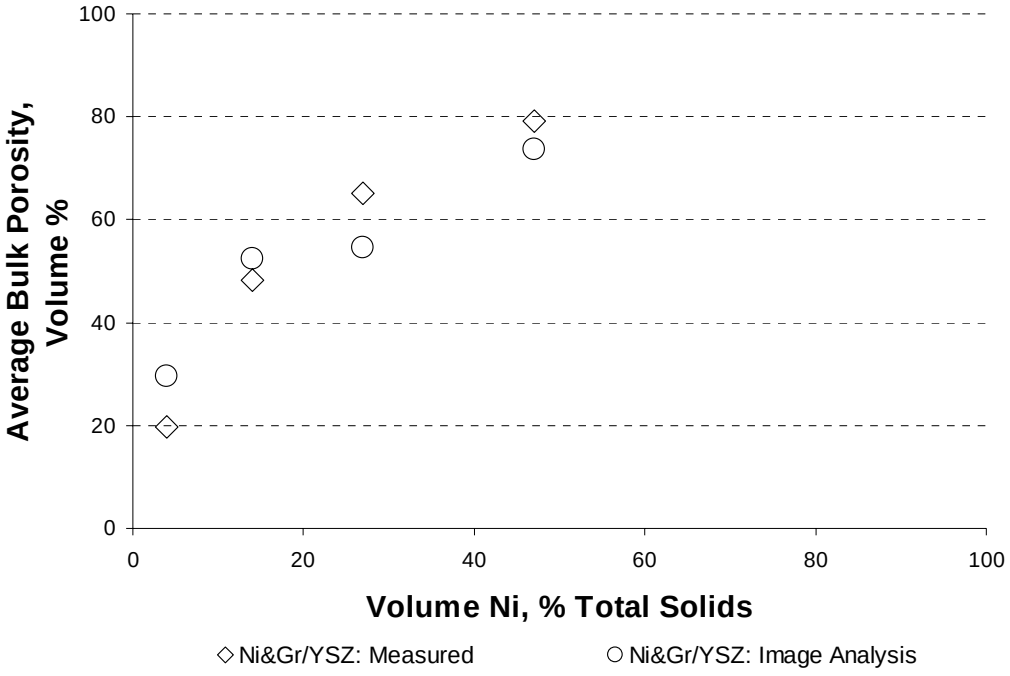

Figure 5-94: Comparison between bulk porosity as measured manually and bulk porosity determined through image analysis for Ni&Gr/YSZ composite samples

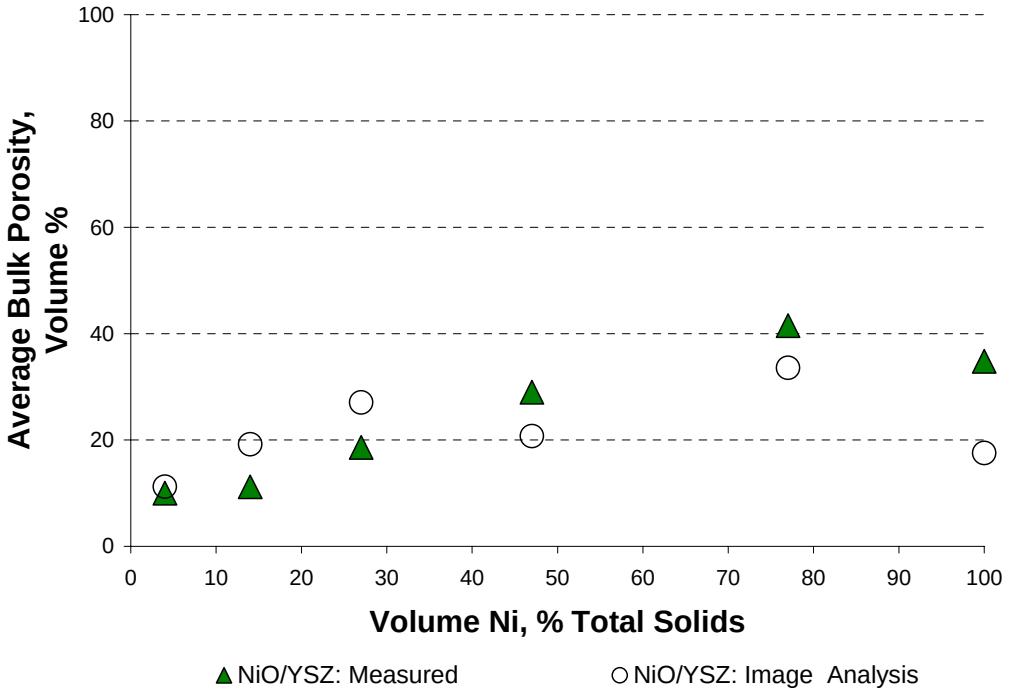

Figure 5-95: Comparison between bulk porosity as measured manually and bulk porosity determined through image analysis for NiO/YSZ composite samples

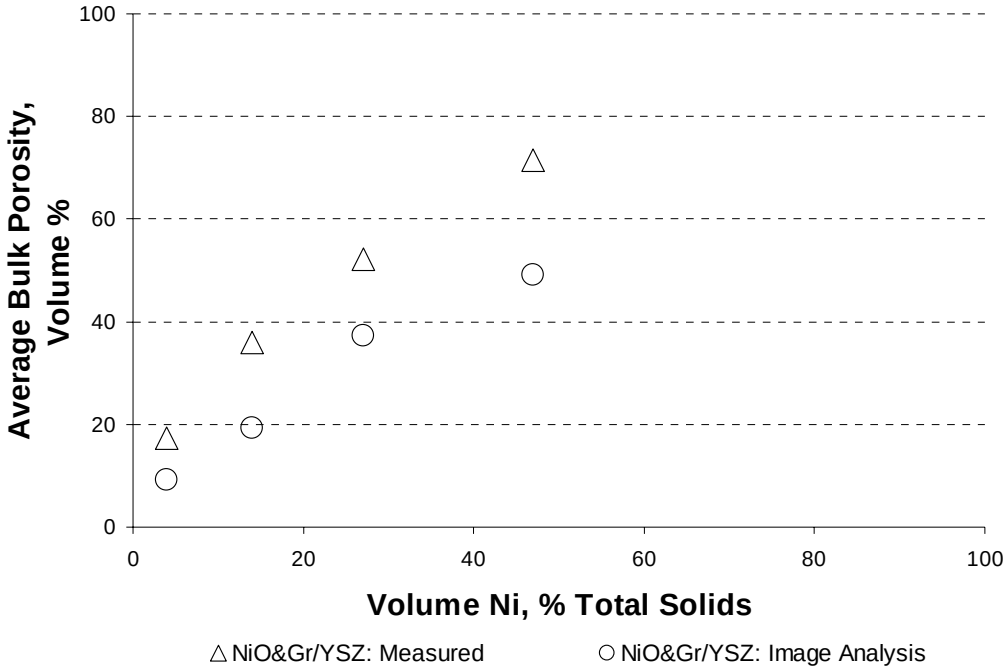

Figure 5-96: Comparison between bulk porosity as measured manually and bulk porosity determined through image analysis for NiO&Gr/YSZ composite samples

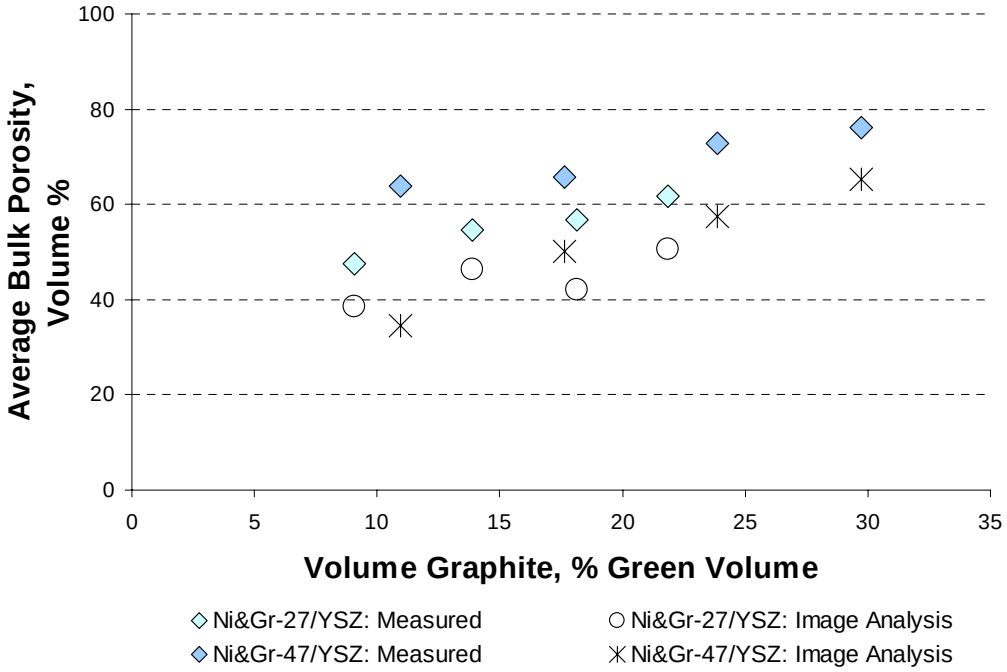

Figure 5-97: Comparison between bulk porosity as measured manually and bulk porosity determined through image analysis for Ni&Gr-27/YSZ and Ni&Gr-47/YSZ composite samples

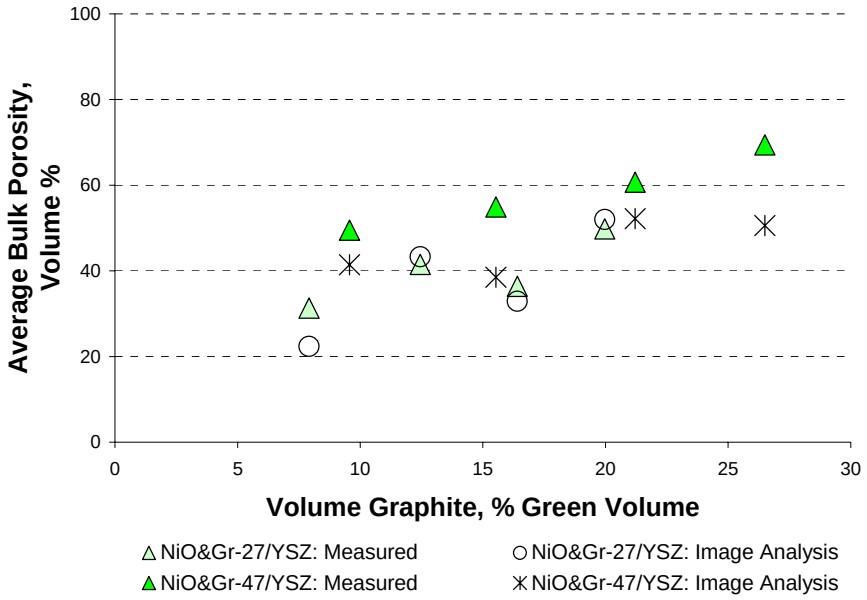

Figure 5-98: Comparison between bulk porosity as measured manually and bulk porosity determined through image analysis for NiO&Gr-27/YSZ and NiO&Gr-47/YSZ composite samples

5.5 POROUS MICROSTRUCTURES

The microstructures from each composite type experience a number of changes during the various processing stages. Similarly, the nickel loading and porosity influence the final microstructures for each of the composite types in the sintered and reduced states.

5.5.1 Evolution of Selected Microstructures during Processing

5.5.1.1 Pure Materials: YSZ, Ni, and NiO

The YSZ powder is submicron in size such that no discernable features were visible under the optical microscope in the burnout stages. During sintering, many fine pores develop, represented by the dark grey areas in Figure 5-99, as the YSZ samples increase in strength and density during sintering.

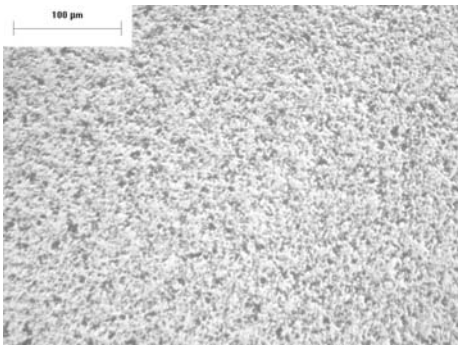

Figure 5-99: Optical micrograph of a 100% YSZ sample after sintering

The 100% Ni from Ni samples show considerable porosity (dark regions) even after the first burnout stage, as shown in Figure 5-100a, unlike the 100% YSZ samples that had a more uniform microstructure. The nickel (light regions) also appears to have a wide range of particle sizes with some very small and some very large particles present. After the second burnout, the nickel and porosity phases are more finely distributed over the cross-section. Dark grey areas are visible which indicate areas of nickel oxidation, while the light areas show that some nickel metal still exists. Once sintered, the nickel phase has oxidized substantially given its grey colour (Figure 5-100c). In addition, very large round pores have developed during sintering, showing a coarsening of the microstructure. Finally, after reduction the nickel has reverted back to its light colour signifying that the nickel oxide has indeed reduced back to nickel metal, as shown in Figure 5-100d. It is also important to note the large round pores that still remain.

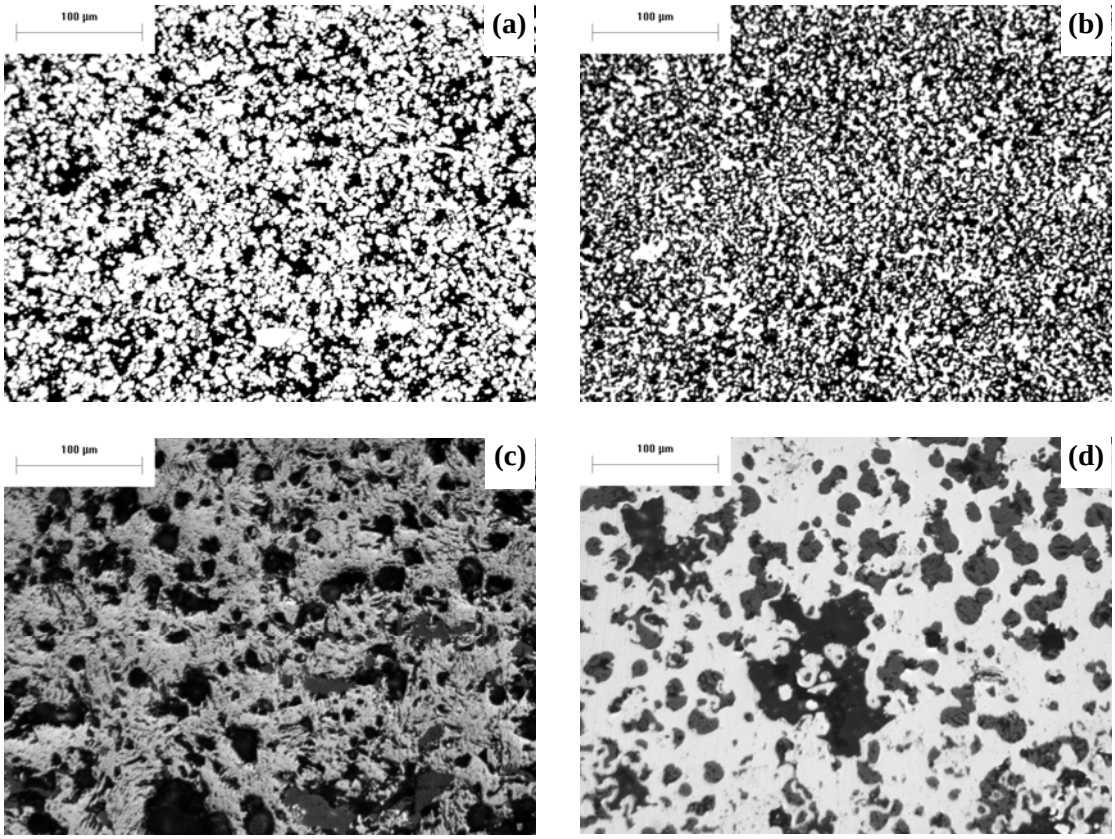

Figure 5-100: Microstructures of 100% Ni samples made from nickel powder after a) the first burnout stage, b) the second burnout stage, c) sintering, and d) reduction

The evolution of the 100% Ni from NiO sample microstructures during processing is shown in Figure 5-101. The 100% Ni from NiO samples have a very uniform microstructure after the first and second burnout stages with evidence of some small pores developing after the second burnout stage. However after sintering, larger round pores develop with the size of the pores being between the pore size of the 100% YSZ and 100% Ni from Ni samples. Interestingly, there is dramatic change in the microstructure after the reduction stage. Before reduction the pores are large and rounded, however, after reduction the pores are primarily long and thin and located along the edges of the nickel grains.

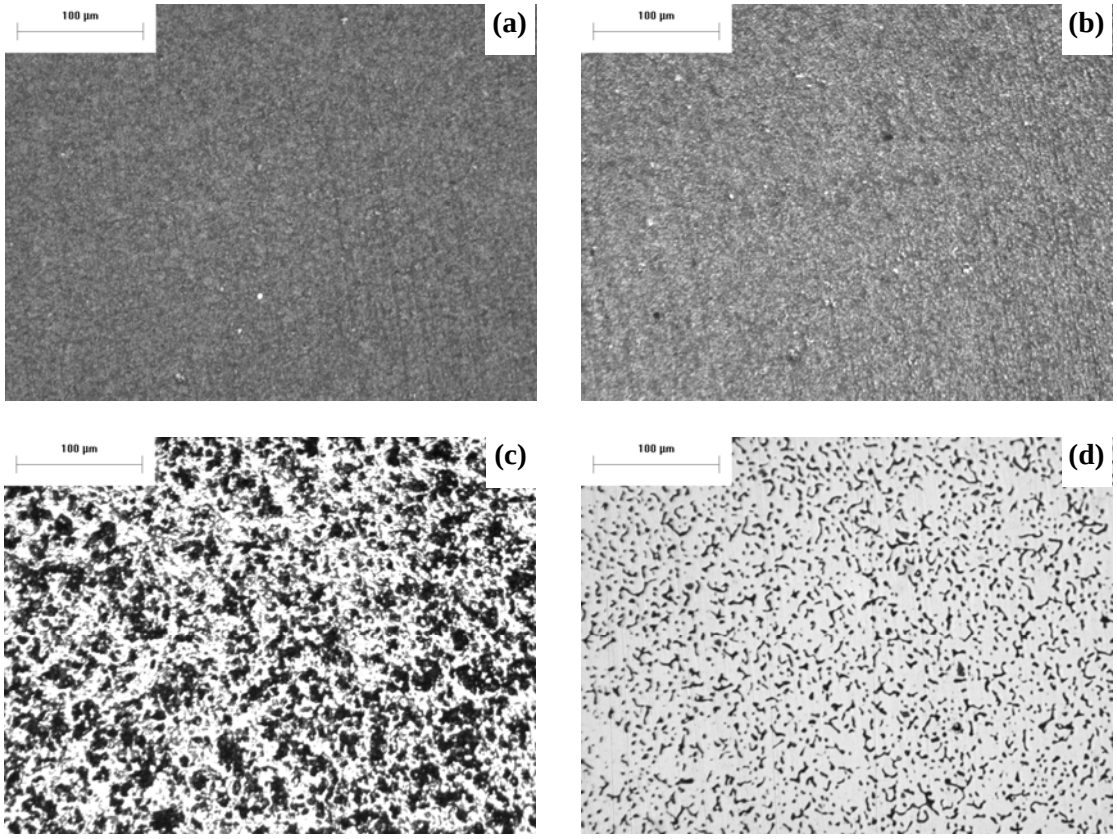

Figure 5-101: Microstructures of 100% Ni samples made from nickel oxide powder after a) the first burnout stage, b) the second burnout stage, c) sintering, and d) reduction:

5.5.1.2 Composite Microstructures

In addition to the pure materials, the evolution of the Ni/YSZ, NiGr/YSZ, Ni&Gr/YSZ, NiO/YSZ, and NiO&Gr/YSZ composite microstructures during processing were also examined. Upon inspection of the Ni/YSZ composite microstructure after the first burnout stage (Figure 5-102a), it is clear that the nickel phase (white) is well distributed amongst the YSZ phase (grey) and small pores (black). However, after the second burnout stage, the nickel turns a light grey colour indicating that the nickel has oxidized. The nickel is still well distributed with a similar particle size distribution but the porosity is less defined. Once sintering is complete, the amount of porosity has increased significantly although it is now difficult to distinguish between the nickel and YSZ phases. After reduction, the white nickel phase remains well distributed as before but there is a noticeable increase in its average particle size. In addition, the amount of porosity has increased while the YSZ phase is more discontinuous than it was after the initial burnout.

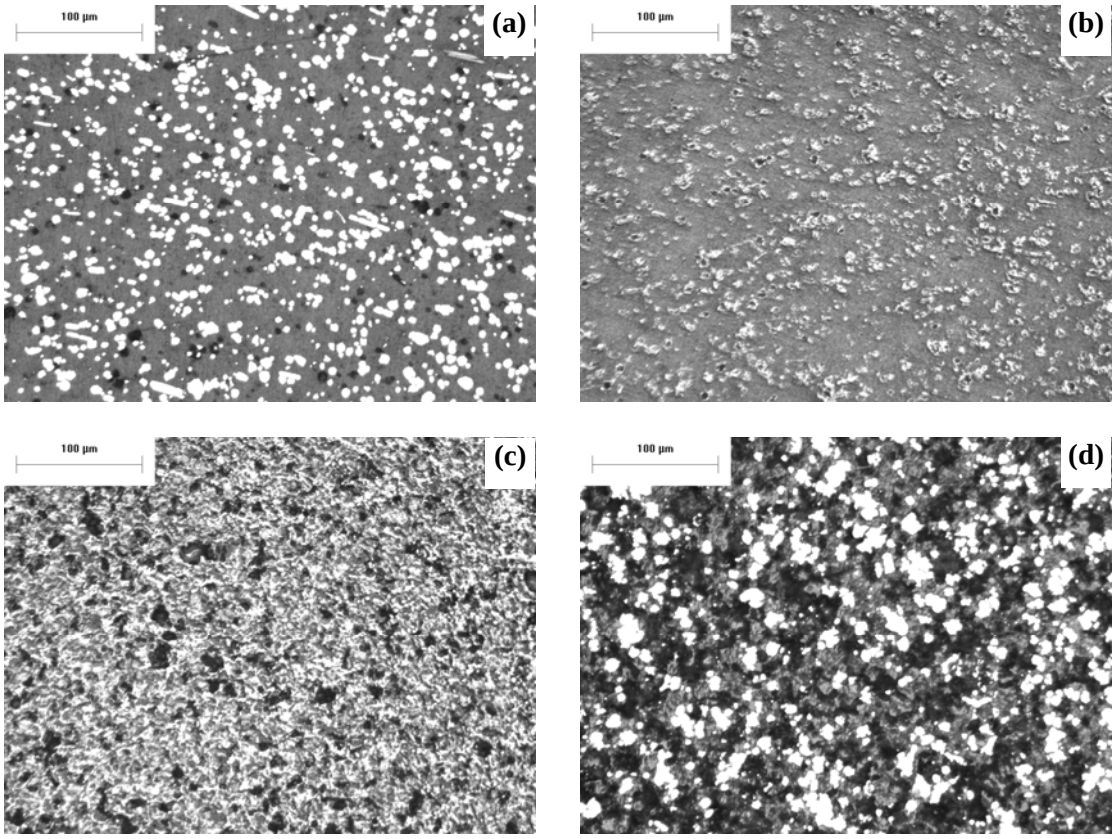

Figure 5-102: Microstructures of a Ni/YSZ composite with a nickel loading of 27 vol% Ni of total solids after a) the first burnout stage, b) the second burnout stage, c) sintering, and d) reduction

The microstructures of the NiGr/YSZ composites are quite unique compared to the other composite types since the white nickel coating clearly encircles the grey graphite cores as presented in Figure 5-103a. As was the case for the nickel in the Ni/YSZ composites, the nickel coated graphite particles are uniformly distributed throughout the YSZ matrix. A few very large pores appear after the first burnout stage but they may have formed as result of some dislodged NiGr particles during polishing. Evidence of the graphite burning away during the second burnout stage is clearly visible in Figure 5-103b where large pores exist where the graphite used to be. The amount of porosity increases further during sintering as the light grey YSZ phase shrinks in Figure 5-103c. Finally, after the nickel oxide is reduced back to nickel metal, the nickel ring structure remains visible but is more tightly packed together (Figure 5-103d). Also, the YSZ phase (light grey) appears as small agglomerates between the nickel rings and the large amount of porosity (dark grey and black regions).

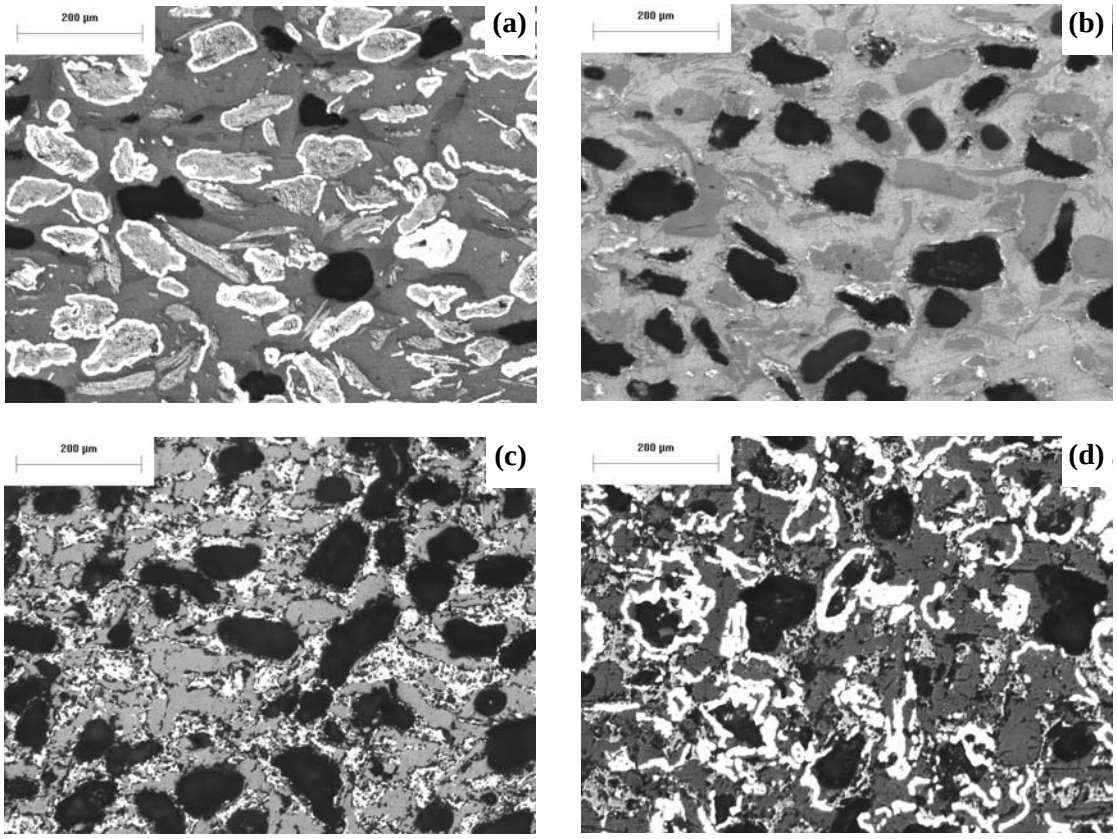

Figure 5-103: Microstructures of a NiGr/YSZ composite with a nickel loading of 27 vol% Ni of total solids after a) the first burnout stage, b) the second burnout stage, c) sintering, and d) reduction

The needle-like graphite particles are quite prominent when examining the Ni&Gr/YSZ microstructure after the first burnout stage in Figure 5-104a. Situated between the graphite particles are the evenly distributed nickel and YSZ particles with some residual porosity. The network of pores maintains the shape of the graphite particles through to the sintered & reduced state after the graphite has burned away. After sintering, the nickel has oxidized and the amount of porosity increases like the other nickel containing composites. Finally, after reduction the network of large pores is preserved, however, the nickel phase has coarsened considerably with fine ribbons of YSZ scattered amongst the large nickel clusters (Figure 5-104d).

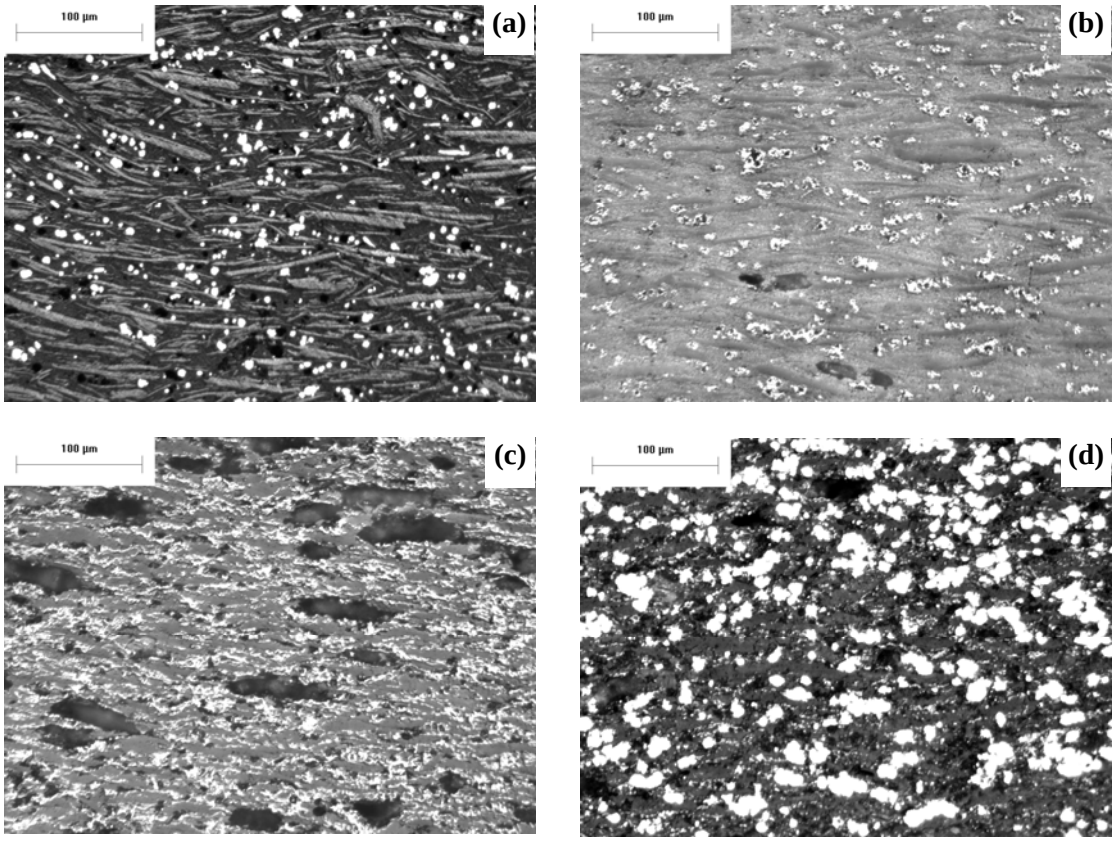

Figure 5-104: Microstructures of a Ni&Gr/YSZ composite with a nickel loading of 27 vol% Ni of total solids after a) the first burnout stage, b) the second burnout stage, c) sintering, and d) reduction

The evolution of the NiO/YSZ composite sample is quite similar to the evolution of the 100% Ni from NiO samples in the early stages, as shown in Figure 5-105. In the first and second micrographs (Figure 5-105a and Figure 5-105b), the nickel oxide powder (light grey) is distributed evenly throughout and with very little porosity. However, after sintering there is a significant increase in the amount of porosity (Figure 5-105c). After reduction, the white nickel metal phase shows that it still remains well distributed but there are a few large clusters of nickel. It is worthwhile noting that the NiO/YSZ composite microstructure in the sintered & reduced state has many more fine nickel particles and less porosity compared to the Ni/YSZ sintered & reduced microstructure (Figure 5-105d).

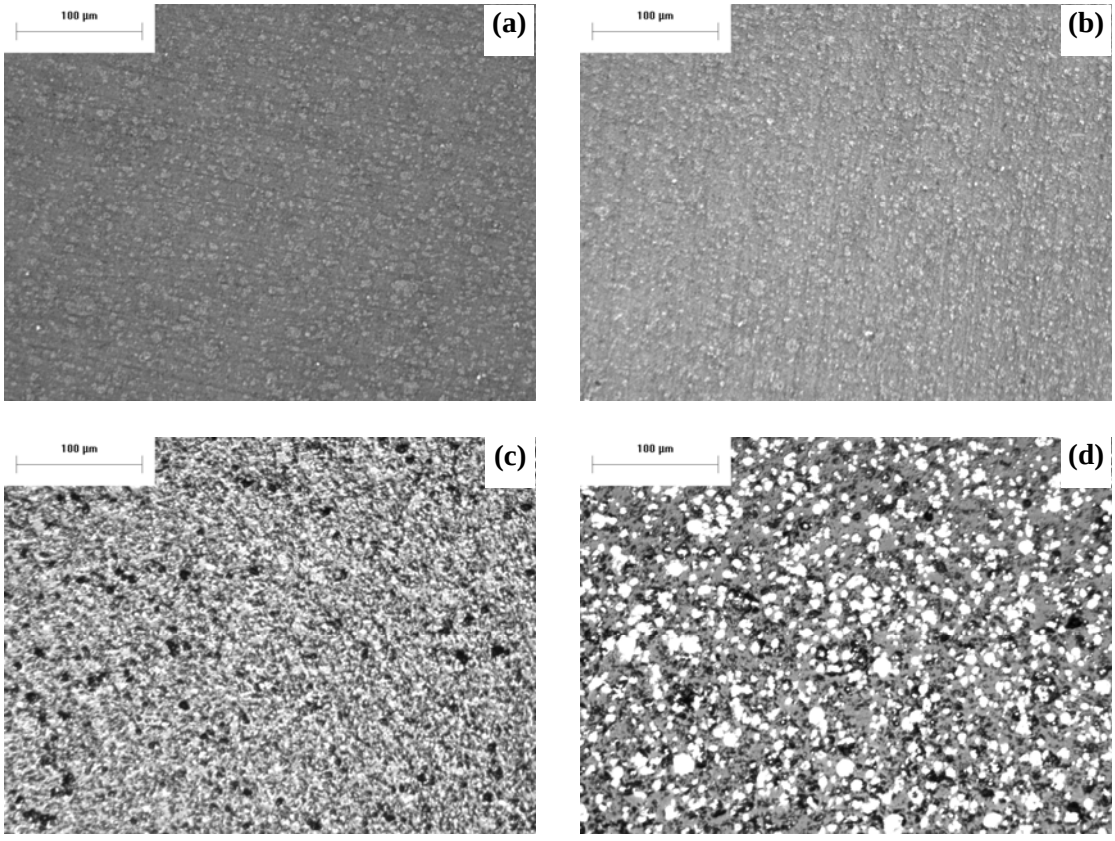

Figure 5-105: Microstructures of a NiO/YSZ composite with a nickel loading of 27 vol% Ni of total solids after a) the first burnout stage, b) the second burnout stage, c) sintering, and d) reduction

The microstructural changes during processing in the NiO&Gr/YSZ composites are nearly identical to the microstructural changes of the Ni&Gr/YSZ composites (See Figure 5-106). Like the Ni&Gr/YSZ composites, the needle-like graphite particles are clearly visible from the first burnout stage. The fine distribution of grey nickel oxide particles is also evident in Figure 5-106a. Once the graphite is burned away, the open network of pores is maintained through the subsequent processing stages. After reduction, the nickel phase has coarsened slightly but not as significantly as the Ni&Gr/YSZ composites. Small clusters of YSZ particles are also scattered throughout the microstructure, partially tracing out where the graphite used to be.

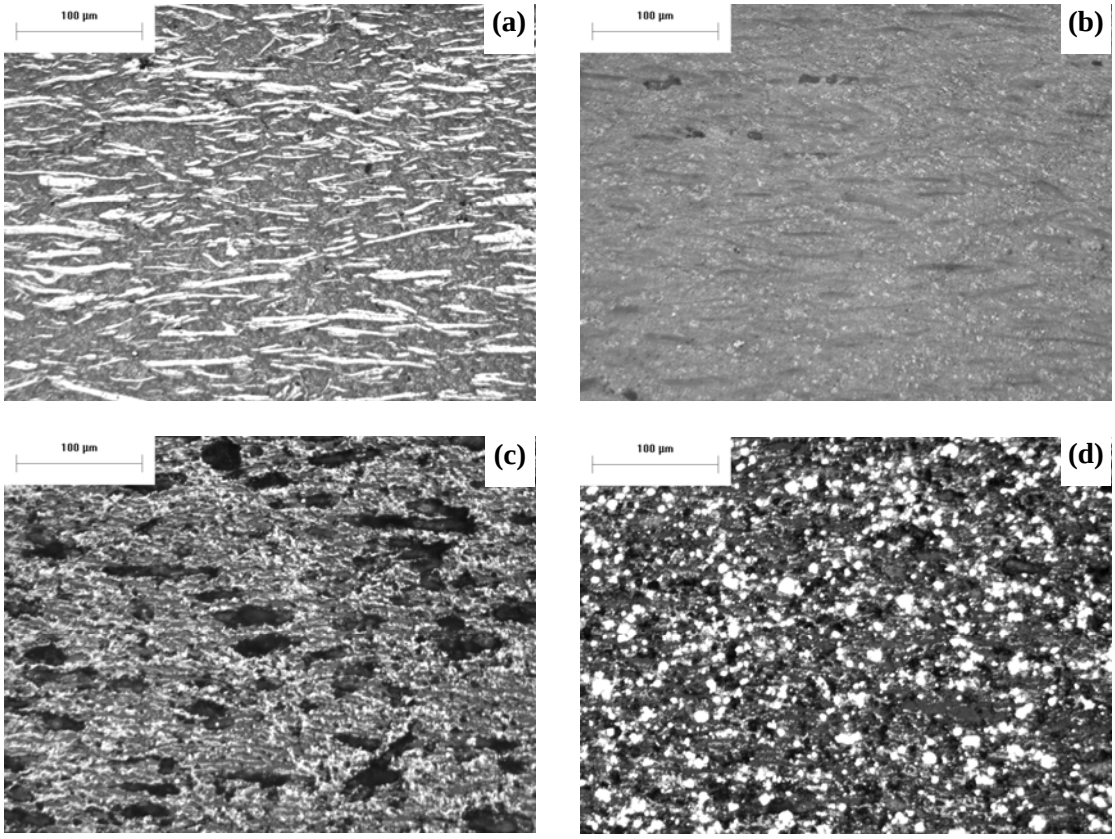

Figure 5-106: Microstructures of a NiO&Gr/YSZ composite with a nickel loading of 27 vol% Ni of total solids after a) the first burnout stage, b) the second burnout stage, c) sintering, and d) reduction

5.5.2 Reduced and Sintered Microstructures

5.5.2.1 Composites with Varying Nickel Content

Optical micrographs of each of the composite types, with varying nickel loadings, after sintering & reduction are shown in Figure 5-107 through Figure 5-111. The white, light grey, and dark grey phases in each micrograph correspond to nickel, YSZ, and porosity respectively. In general, the nickel, YSZ, and graphite phases are evenly distributed throughout each of the microstructures. However, at low nickel loadings, the YSZ is quite prominent, but as the nickel loading increases, it

becomes increasingly difficult to distinguish the YSZ phase from pores filled with the mounting epoxy.

The NiGr/YSZ composites have the most unique microstructure of the composites studied (Figure 5-108). Since the nickel is added as a coating surrounding a graphite particle, the nickel forms a ring around a pore formed after the graphite was burned away. At low nickel loadings the large nickel rings are separated by a continuous YSZ matrix, but as the nickel loading increases, the nickel rings are packed more closely together. As expected, the amount of porosity also increases with increasing nickel loading because of the concomitant increase in the graphite loading.

The differences in the Ni/YSZ and NiO/YSZ composites are much more subtle as shown in Figure 5-107 and Figure 5-110. For the NiO/YSZ composites, nickel is more finely dispersed throughout the microstructure having a smaller average particle size compared to the Ni/YSZ composites. In addition, the amount of porosity is higher in the Ni/YSZ composites leading to a more discontinuous YSZ phase. For both composites, it appears that the pore morphology changes at the highest nickel loading where they tend to be long and thin rather than the more rounded pores forming at a lower nickel content.

Finally, the addition of graphite appears to have a significant effect on the nature of the Ni&Gr/YSZ and NiO&Gr/YSZ composite microstructures, as illustrated in Figure 5-109 and Figure 5-111, since the amount of porosity increases significantly as the graphite loadings increase. At the lowest nickel loading, the pores created from the larger graphite particles are situated within the YSZ matrix and do not significantly alter the nickel distribution. However, as the nickel and graphite loadings increase, the nickel becomes more concentrated and forms much larger particles compared to the graphite-free composites. In fact, the finer nickel particles in the highest nickel loaded NiO&Gr/YSZ composites form an outline of where the graphite particle used to be. Similarly, fine ligaments of YSZ are visible as they also trace around pores at former graphite particle areas.

5.5.2.2 Composites with Varying Graphite Content

The transition from the Ni/YSZ or NiO/YSZ composite microstructures to the composite microstructures of the Ni&Gr/YSZ and NiO&Gr/YSZ composites is clearer when examining the sintered and reduced optical micrographs for the Ni&Gr-27/YSZ, Ni&Gr-47/YSZ, NiO&Gr-27/YSZ, and NiO&Gr-47/YSZ composites with varying graphite loading as shown in Figure 5-112 through Figure 5-115. For all four composite types, the transition from a graphite-free microstructure to the microstructure with the highest graphite loading is relatively the same. At the lowest graphite loading, the large pores formed from the graphite particles are evenly distributed throughout the microstructure without significantly altering the distribution of the nickel and YSZ. As the graphite loading increases, the smaller nickel and YSZ particles are forced into the spaces between the large graphite particles. As a result, the nickel and YSZ tend to cluster together forming larger sized particles surrounded by ever increasing pores, like a series of islands. The agglomeration of the nickel is much more substantial for the Ni&Gr/YSZ composites compared to the NiO&Gr/YSZ composites.

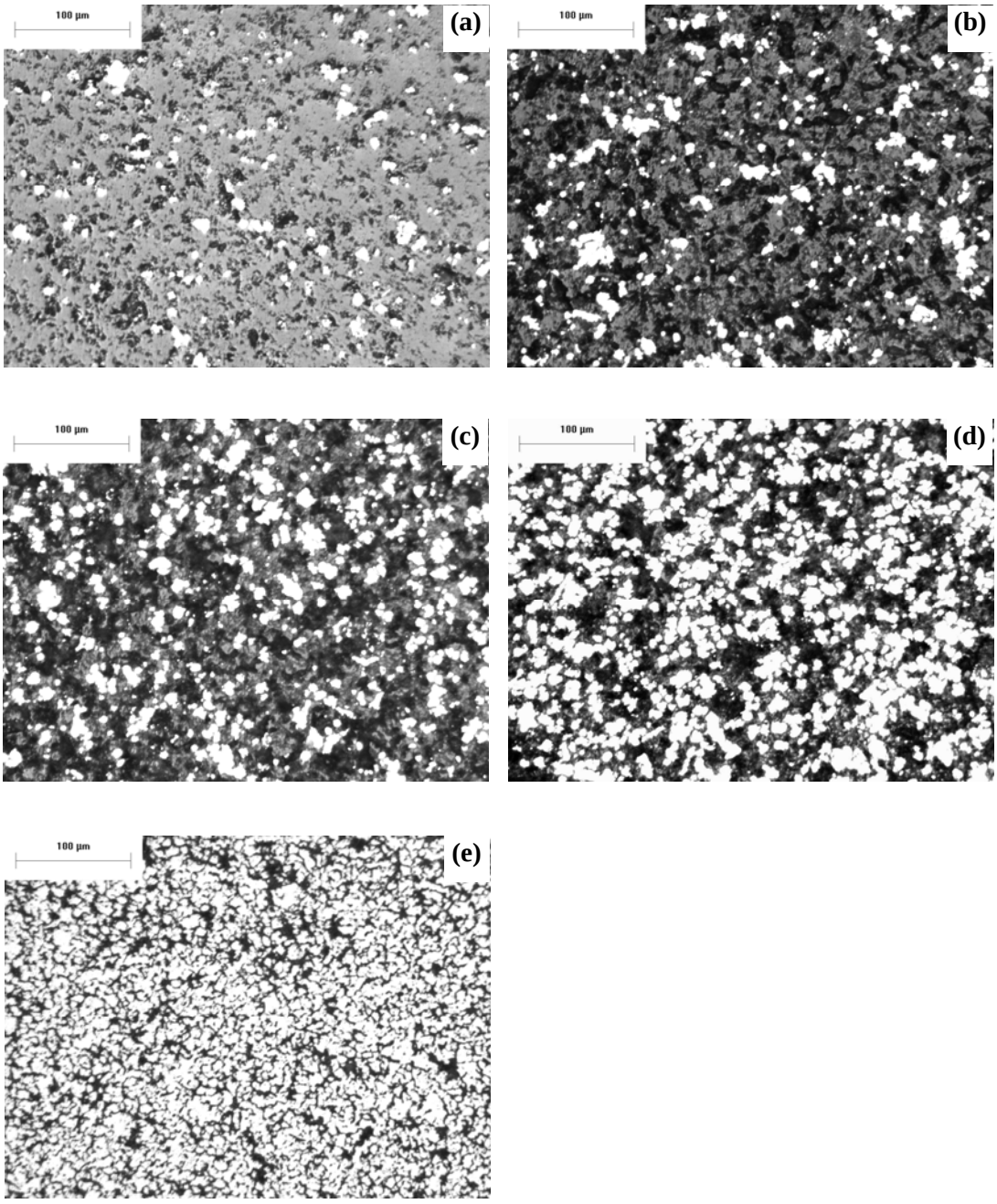

Figure 5-107: Microstructures of Ni/YSZ composites after sintering and reduction with a nickel loading of a) 4 vol% Ni, b) 14 vol% Ni, c) 27 vol% Ni, d) 47 vol% Ni, and e) 77 vol% Ni of total solids. The white, light grey, and dark regions are nickel, YSZ, and porosity respectively.

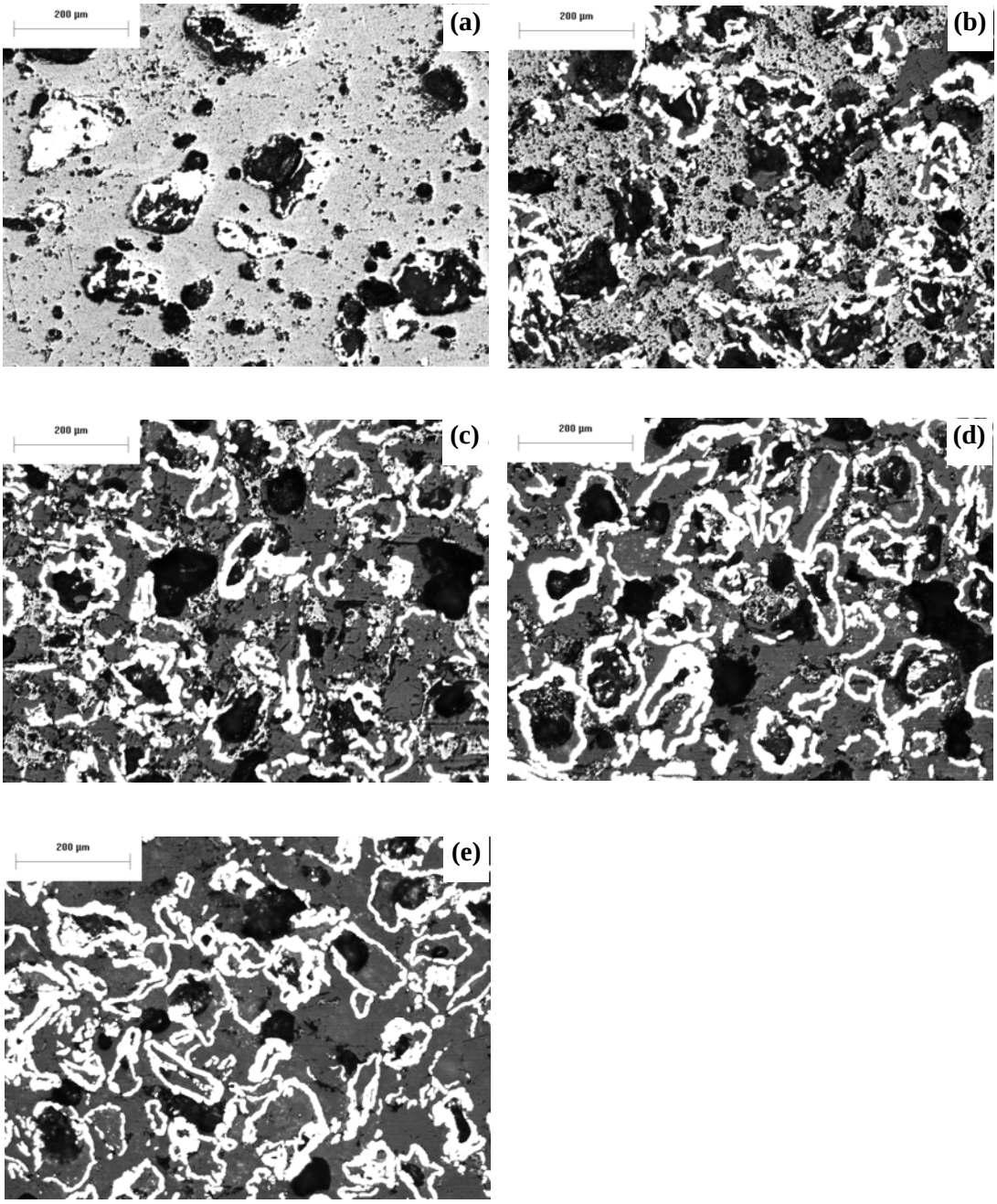

Figure 5-108: Microstructures of NiGr/YSZ composites after sintering and reduction with a nickel loading of a) 4 vol% Ni, b) 14 vol% Ni, c) 27 vol% Ni, d) 47 vol% Ni, and e) 77 vol% Ni of total solids. The white, light grey, and dark regions are nickel, YSZ, and porosity respectively.

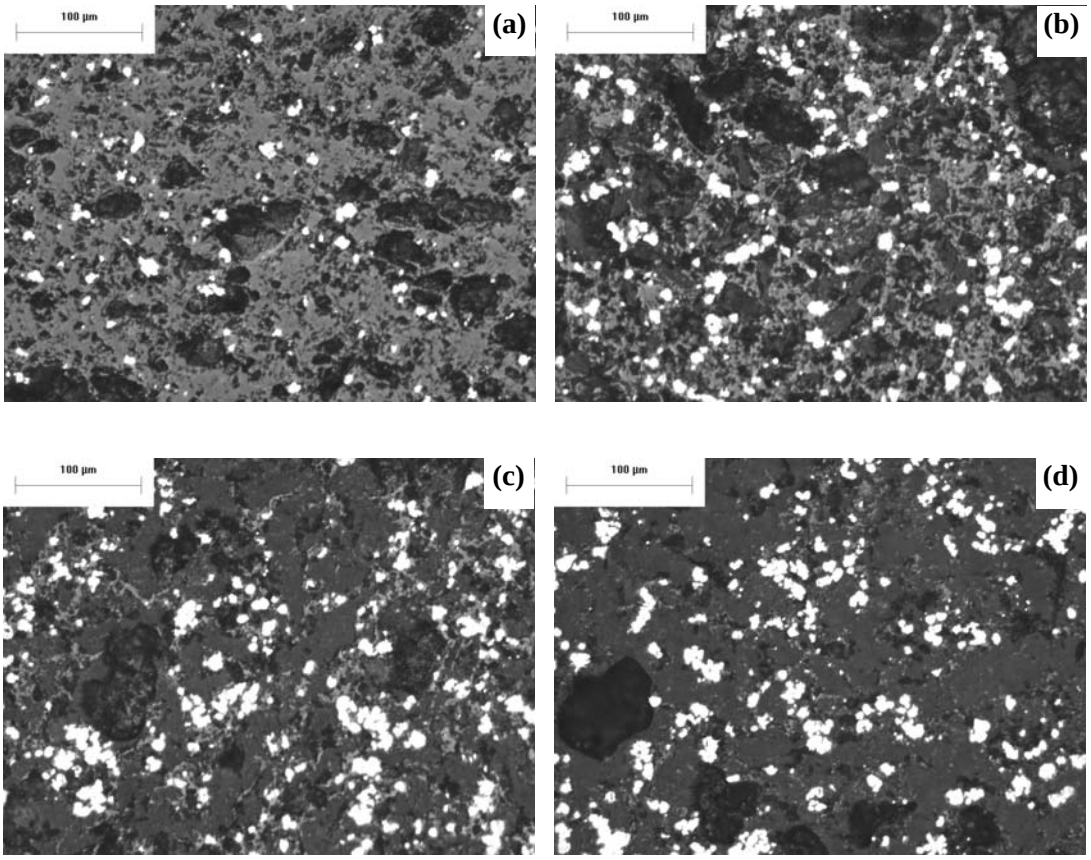

Figure 5-109: Microstructures of Ni&Gr/YSZ composites after sintering and reduction with a nickel loading of a) 4 vol% Ni, b) 14 vol% Ni, c) 27 vol% Ni, and d) 47 vol% Ni of total solids. The white, light grey, and dark regions are nickel, YSZ, and porosity respectively.

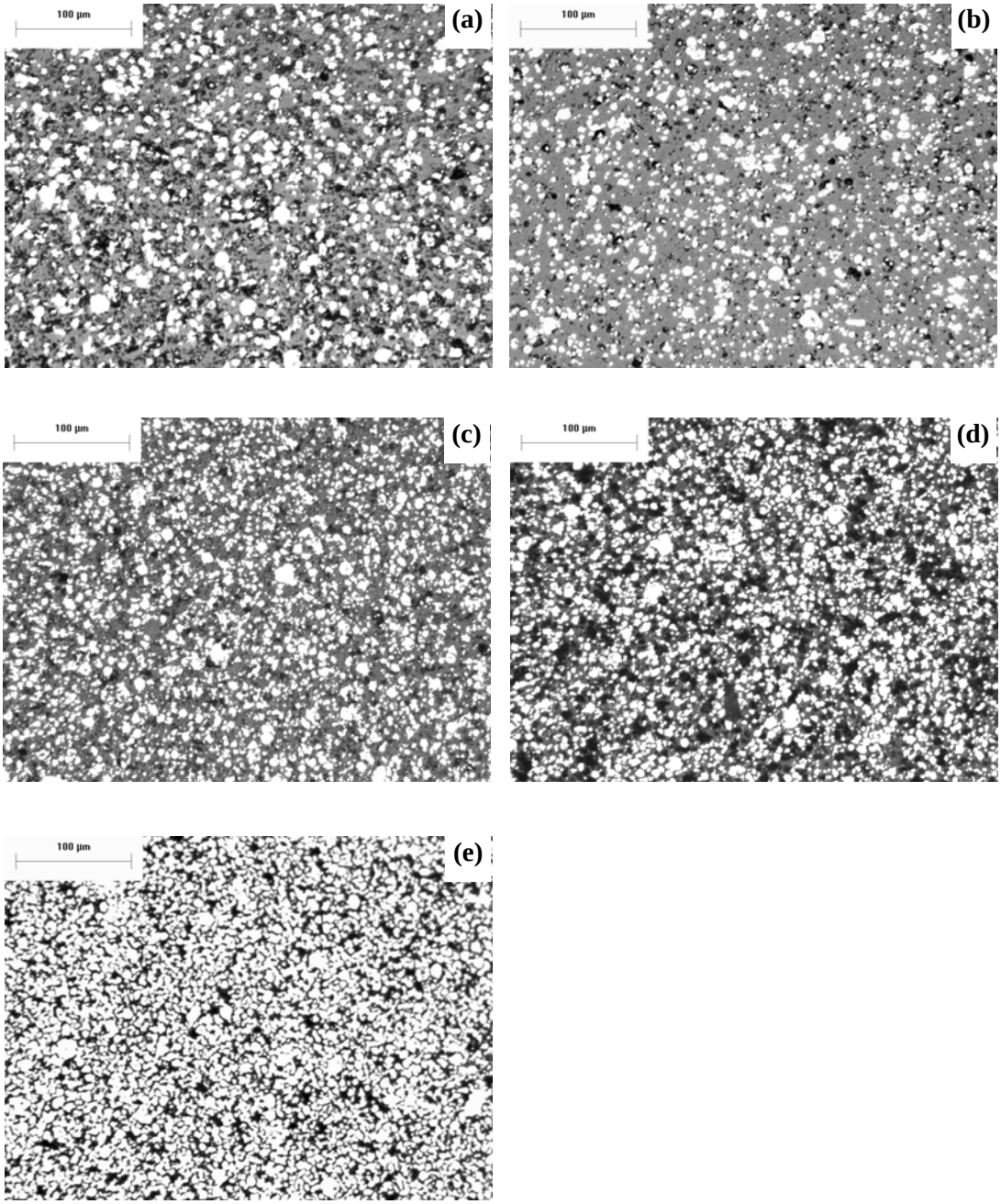

Figure 5-110: Microstructures of NiO/YSZ composites after sintering and reduction with a nickel loading of a) 4 vol% Ni, b) 14 vol% Ni, c) 27 vol% Ni, d) 47 vol% Ni, and e) 77 vol% Ni of total solids. The white, light grey, and dark regions are nickel, YSZ, and porosity respectively.

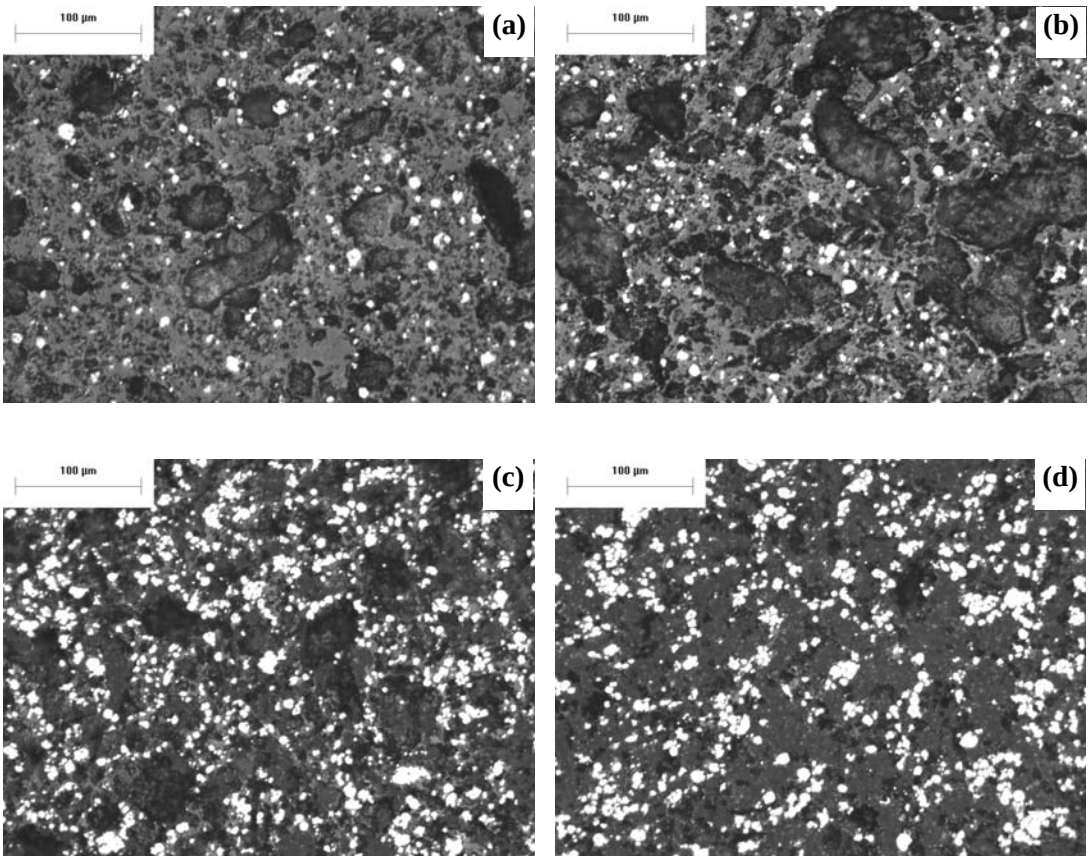

Figure 5-111: Microstructures of NiO&Gr/YSZ composites after sintering and reduction with a nickel loading of a) 4 vol% Ni, b) 14 vol% Ni, c) 27 vol% Ni, and d) 47 vol% Ni. The white, light grey, and dark regions are nickel, YSZ, and porosity respectively.

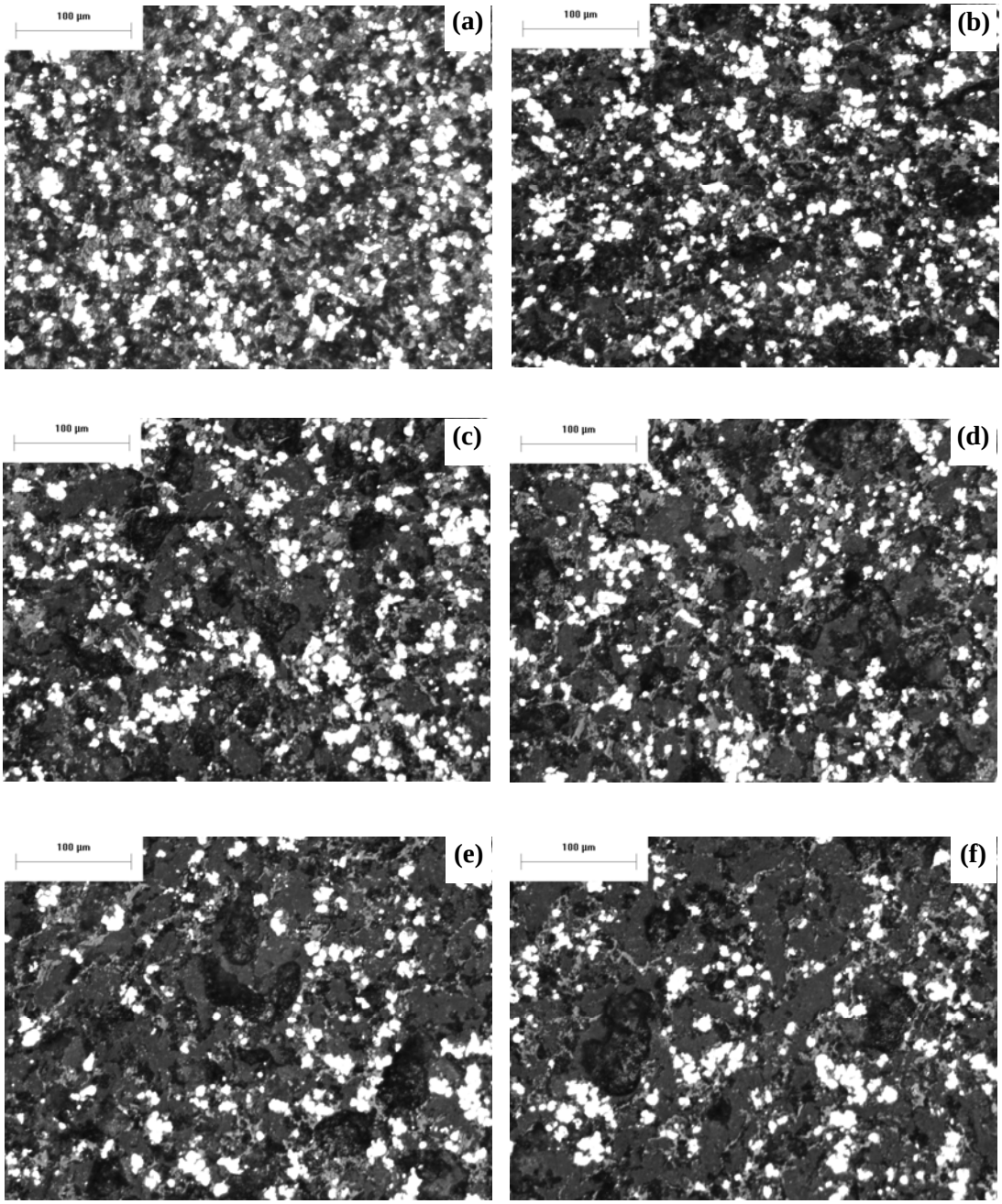

Figure 5-112: Microstructures of Ni&Gr/YSZ composites with a nickel loading of 27 vol% Ni of total solids after sintering and reduction with a graphite loading of a) 0 vol% graphite, b) 9.1 vol% graphite, c) 13.9 vol% graphite, d) 18.1 vol% graphite, e) 21.8 vol% graphite, and f) 23.5 vol% graphite as fraction of the dried green volume. The white, light grey, and dark regions are nickel, YSZ, and porosity respectively.

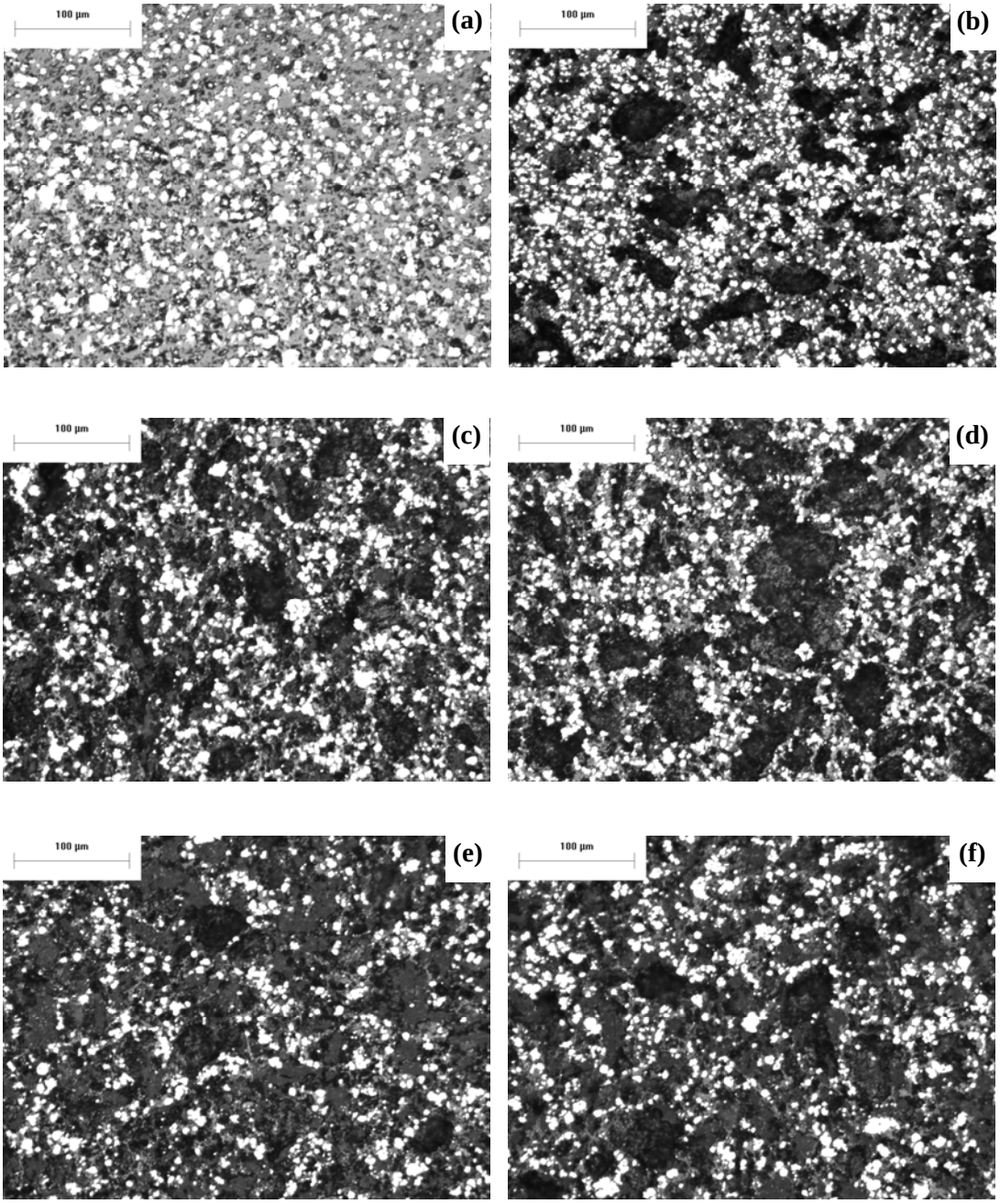

Figure 5-113: Microstructures of NiO&Gr/YSZ composites with a nickel loading of 27 vol% Ni of total solids after sintering and reduction with a graphite loading of a) 0 vol% graphite, b) 7.9 vol% graphite, c) 12.5 vol% graphite, d) 16.4 vol% graphite, e) 20 vol% graphite, and f) 21.6 vol% graphite as fraction of the dried green volume. The white, light grey, and dark regions are nickel, YSZ, and porosity respectively.

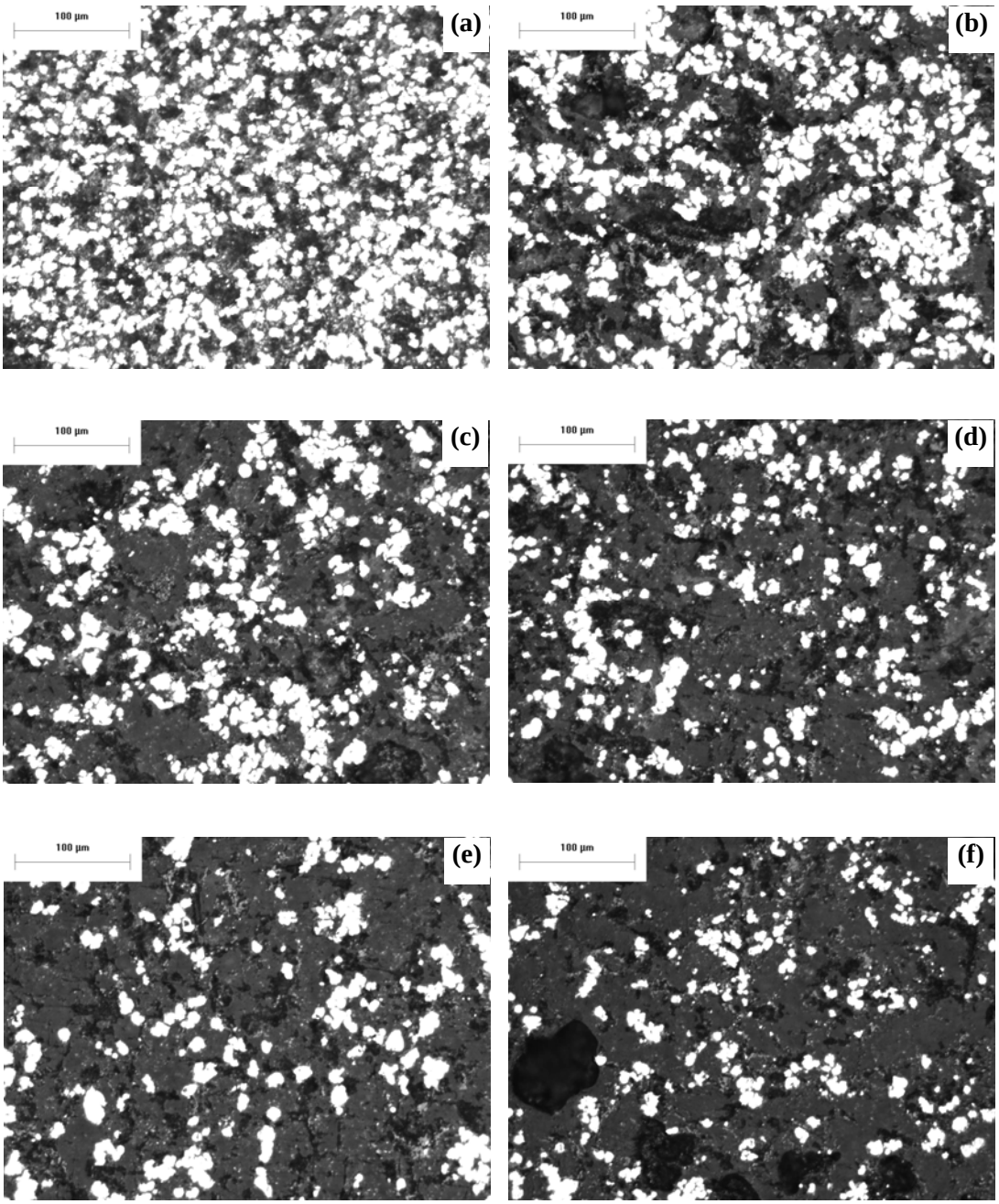

Figure 5-114: Microstructures of Ni&Gr/YSZ composites with a nickel loading of 47 vol% Ni of total solids after sintering and reduction with a graphite loading of a) 0 vol% graphite, b) 11 vol% graphite, c) 17.6 vol% graphite, d) 23.9 vol% graphite, e) 29.7 vol% graphite, and f) 31.8 vol% graphite as fraction of the dried green volume. The white, light grey, and dark regions are nickel, YSZ, and porosity respectively.

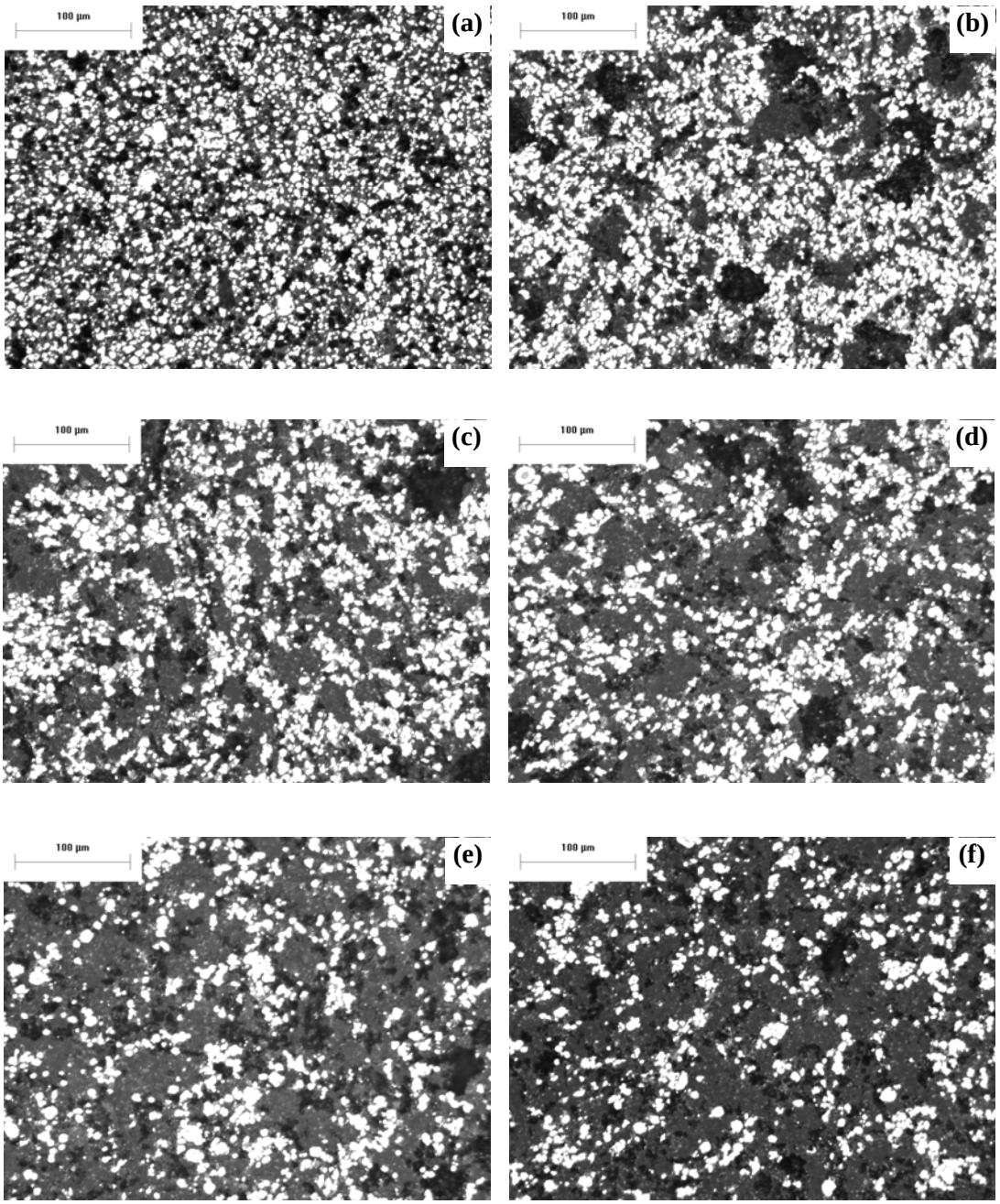

Figure 5-115: Microstructures of NiO&Gr/YSZ composites with a nickel loading of 47 vol% Ni of total solids after sintering and reduction with a graphite loading of a) 0 vol% graphite, b) 9.6 vol% graphite, c) 15.5 vol% graphite, d) 21.2 vol% graphite, e) 26.5 vol% graphite, and f) 28.6 vol% graphite as fraction of the dried green volume. The white, light grey, and dark regions are nickel, YSZ, and porosity respectively.

CHAPTER 6:
SINTERING DISCUSSION

Having presented the experimental results from the burnout, sintering, and reduction stages in Chapter 5, the results are discussed in more detail here in Chapter 6.

6.1 DIMENSIONAL CHANGES DURING BURNOUT

6.1.1 NiO/YSZ Composites

The microstructural and dimensional changes of the NiO/YSZ composites during the burnout stage are discussed first as they are the most straightforward compared to the other composite types. During the burnout stage, only the polymer material is removed, the nickel does not oxidize, and there is no graphite to eliminate. How nickel oxidation and graphite burnout affect the processing of the other composites will be discussed in the next sections.

After the burnout stages, the 100% YSZ samples show an average volumetric shrinkage of 3.7% (See Figure 5-17) which is comparable to the small volumetric shrinkages expected during the initial stages of sintering. The other NiO/YSZ composite samples also show a similar volumetric shrinkage to the 100% YSZ samples, while the 100% Ni from NiO samples shrink on average 13.8%.

According to Equation (4-4), the final sintered density is related to the green density of only the sintering species through the volumetric shrinkage. Therefore, ρ_g is the bulk green density of the YSZ, NiO, or their combination within the green body and is calculated as follows:

$$\rho_{g_{NiO/YSZ}} = \frac{m_{YSZ} + m_{NiO}}{V_g} \tag{6-1}$$

where m_{YSZ} and m_{NiO} are the mass of YSZ and NiO in the green body respectively, and V_g is the pressed green volume. In the case of the 100% YSZ, 100% Ni from NiO, and NiO/YSZ composite samples, there is no oxidation of the nickel phase during burnout. Thus, the mass of the samples after burnout is equivalent to the mass of YSZ and NiO in the green state. Applying Equation (4-4) with the new 100% YSZ green density, for example, the burnout density becomes:

$$\rho_{BO\,YSZ} = \frac{\frac{m_{BO}}{V_g}}{1 - \frac{\Delta V}{V_g}} = \frac{\frac{0.317\ g}{0.1295\ cm^3}}{1 - 0.037} = \frac{2.45}{0.963} = 2.54\ g/cm^3 \tag{6-2}$$

which is equal to the measured burnout density. By using the appropriate green density, a volumetric shrinkage does in fact lead to a small increase in relative density for the 100% YSZ samples as shown

in Table 6-1. To calculate the relative density of the 100% YSZ samples after burnout, ρ_{theoBO}, the following equation was used:

$$\rho_{theo\,BO} = \frac{\rho_{BO}}{\rho_{theo}} \times 100\% = \frac{2.54}{6.1} = 41.7\% \quad \textbf{(6-3)}$$

where ρ_{BO} is the burnout density and ρ_{theo} is the theoretical density of YSZ (6.1 g/cm^3).

Similarly, the other NiO/YSZ composite samples show a modest increase in density after burnout, as shown in Table 6-1, whereas the 100% Ni from NiO samples show a larger increase in density because of their increased volumetric shrinkage. In addition, the relative burnout densities are similar to the solid volume fractions of nickel and YSZ presented in Figure 5-12 assuming that the polymer material is converted to porosity. Since the polymer content decreases with increasing nickel loading and NiO tends to sinter more readily than YSZ, the relative density of the NiO/YSZ composites after burnout increases with increasing nickel loading.

Table 6-1: Average NiO/YSZ composite relative densities of sintering species in the green state and the burnout state

Composite	Ni Loading, Vol% Total Solids	Green Density, % Theoretical	Burnout Density, % Theoretical
100% YSZ	0	40.1	41.7
NiO/YSZ	4	41.3	42.8
	14	44.3	45.5
	27	47.5	48.5
	47	51.0	51.7
	77	54.0	55.4
100% Ni from NiO	100	53.9	62.5

The larger increase in density for the 100% Ni from NiO samples compared to the other composite samples suggests that even small YSZ additions limit the amount of NiO shrinkage during the burnout stage. A constrained sintering effect, as proposed by De Jonghe et al. [83], is revealed for the NiO/YSZ composite samples by plotting the change in density from the green to burnout states for each sample after normalizing with the change in density of the higher sintering phase (i.e. NiO). Since the plotted results deviate from the rule of mixtures prediction, as shown in Figure 6-1, the YSZ phase does indeed constrain the sintering of the nickel oxide phase during burnout.

In fact, the low sintering shrinkage of the YSZ dominates the low temperature sintering behaviour of the NiO/YSZ composites. Further evidence of the high constraining effect of the YSZ is given in Figure 5-30 where the dilatometer plots measuring the dimensional changes during the burnout stage are given. The 100% YSZ shrinks very little while the 100% Ni from NiO samples begins to shrink significantly around 750°C. Even with a nickel loading of 47 vol% Ni of total solids, the NiO/YSZ composite sample still only shrinks a small amount in a similar manner to the 100% YSZ sample.

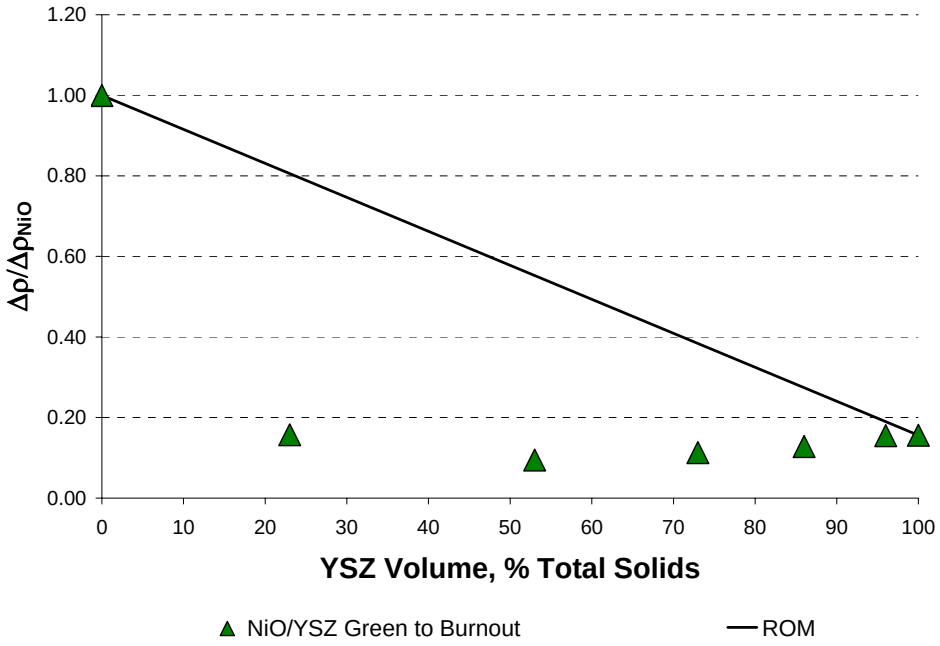

Figure 6-1: Normalized change in density from the green state to the burnout state for the NiO/YSZ composite samples based on the change in NiO density

6.1.2 Ni/YSZ Composites

The dimensional changes that the Ni/YSZ composites undergo during the burnout stage are quite different than the dimensional changes shown by the NiO/YSZ composites. Rather than showing a slight shrinkage, the Ni/YSZ composite samples actually expand during burnout (See Figure 5-17). This behaviour may be explained by considering that when nickel oxidizes it expands approximately 66% due to the lower density of nickel oxide compared to nickel metal. As plotted in Figure 6-2, an expected volumetric expansion, $\Delta V_{Ni/YSZ}/V_o$, of the Ni/YSZ composites due to the oxidation of the nickel phase can be calculated based on a simple rule of mixtures of the volumetric changes of the YSZ and nickel structures. That is:

$$\left(\frac{\Delta V}{V_o}\right)_{Ni/YSZ} = \frac{\Delta V_{YSZ}}{V_o} f_{YSZ} + \frac{\Delta V_{Ni}}{V_o} f_{Ni} \qquad \textbf{(6-4)}$$

where $\Delta V_{YSZ}/V_o$ is the change in volume of a pure YSZ tape after burnout (equal to 0.037), $\Delta V_{Ni}/V_o$ is the change in volume due only to oxidation of the nickel within the composite and assuming no sintering (equal to -0.66), and f_{YSZ} and f_{Ni} are the volume fractions of YSZ and Ni on a solids basis within the composite respectively. Note that the inherent assumption of Equation (6-4) is the YSZ within the Ni/YSZ composite shrinks in the same manner as the 100% YSZ samples. From Figure 6-2, it is clear that the Ni/YSZ composite samples with nickel loadings below 27 vol% Ni of total solids expand the predicted amount, whereas the composite samples with nickel loadings above 27 vol% Ni start to deviate from expected expansion line with the deviation increasing with higher

nickel loadings. As the nickel loading increases, the actual composite expansion deviates even further from the expected expansion line.

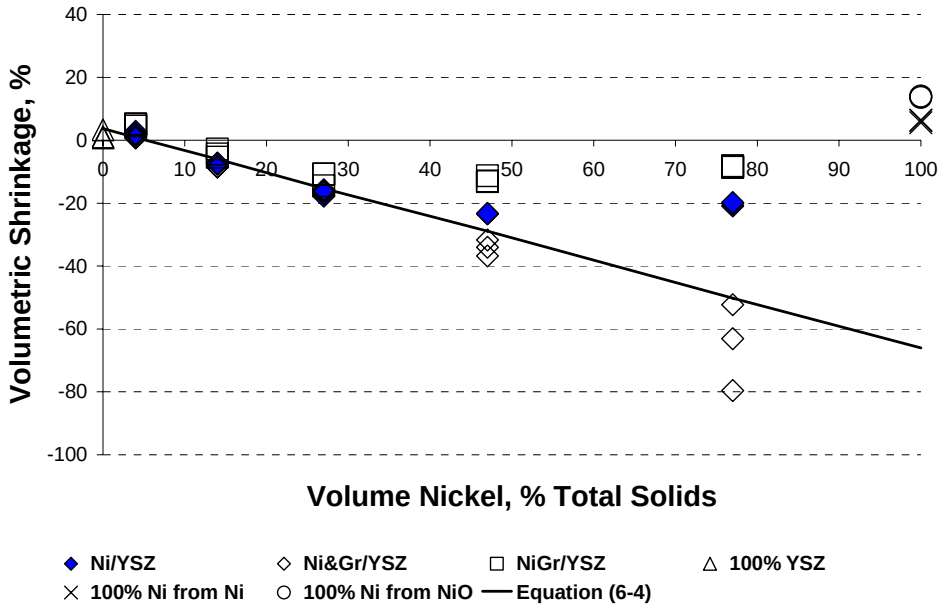

Figure 6-2: Volumetric changes for the Ni/YSZ, NiGr/YSZ and Ni&Gr/YSZ composites during burnout. The solid line indicates the expected composite expansion from the rule of mixtures prediction of Equation (6-4).

At low nickel loadings, the nickel phase is isolated into small clusters as a percolation path has not been established (as indicated by the low electrical conductivity results presented in Section 7.4). Consequently, while isolated clusters of nickel (or NiO) sinter together, they do not contribute to the overall sintering shrinkage of the sample. During oxidation however, the YSZ matrix is not able to resist the expansion of the nickel as readily and the composite samples expand. Once a percolation path is established at a nickel loading of 27 vol% Ni of total solids, the YSZ matrix cannot restrain the cumulative shrinkage of the nickel particles and the Ni/YSZ composite samples begin to deviate from the predicted expansion of composites which assumes no contributions from sintering.

The deviation from the expansion line is caused by the sintering of the nickel phase during the early stages of the burnout. From Figure 5-30, the 100% Ni from Ni samples start to shrink around 400°C and at approximately 500°C the nickel begins to oxidize. Interestingly, the dimensional change is nearly constant during the remainder of the burnout stage indicating that the linear expansion due to oxidation is offset by an equal linear shrinkage due to sintering, particularly when compared with the dimensional changes of the other composites. For the Ni/YSZ composite samples with a nickel loading of 47 vol% Ni of total solids, the deviation from the predicted expansion with no sintering of the nickel phase is small and the composite samples indeed expand significantly (See Figure 5-30). Conversely, the Ni/YSZ composite samples with a nickel loading of 77 vol% Ni show a greater deviation from the predicted expansion due to nickel oxidation and ultimately expand less than the composite samples with the lower nickel loading. Ultimately, the degree to which the composites deviate from the predicted expansion line indicates the amount of nickel (oxide) sintering that takes

place. As the nickel loading increases, the increased nickel shrinkage is sufficient to overcome a portion of the expected expansion of the nickel phase due to oxidation and for the 100% Ni from Ni samples the sintering shrinkage is so great that it actually results in an overall volumetric shrinkage.

It is important to note that the all the Ni/YSZ composites show the expected weight change during the burnout stage with the exception of the 100% Ni from Ni samples which are only partially oxidized. As a result, the actual degree of expansion due to the oxidation of nickel will be less than predicted thereby contributing to the increased shrinkage of the 100% Ni from Ni samples. The lessened amount of oxidation may be due to the oxide layer that forms on the nickel which limits the amount of oxygen diffusing into the interior of the sample. For the Ni/YSZ composites, the presence of YSZ may enhance the amount of nickel oxidation because YSZ is a good conductor of oxygen ions and higher YSZ loadings can improve the transport of oxygen to the interior of the composite. Another contributing factor is the higher relative density of the Ni/YSZ composites with higher nickel loadings (See Figure 5-32). With less porosity, air cannot penetrate the interior of the sample as easily also limiting the degree of nickel oxidation.

When comparing the densities of the Ni/YSZ composites with the NiO/YSZ composites after burnout (See Figure 5-32), it is surprising that the relative density of the Ni/YSZ composites is higher than the NiO/YSZ composites despite the fact that the Ni/YSZ composites expand during the burnout stage while the NiO/YSZ composites shrink. Since the mass of the nickel phase in the Ni/YSZ composites increases during burnout, unlike the NiO/YSZ composites, it is not possible to use Equation (4-4) to explain the change in density after burnout. However, the density changes in the Ni/YSZ composites can be understood if the balance between the expansion of the nickel as it oxidizes and any sintering shrinkage is considered. As the nickel oxidizes its volume will increase, and if the total composite volume expands, according to the rule of mixtures of Equation (6-4), then there is no net change in the composite relative density as a percentage of the theoretical density. After comparing the relative green density (calculated from the fraction of total solids in the green volume) with the relative burnout density (i.e. Equation (6-3)), the two relative densities are essentially identical for the Ni/YSZ composites with a nickel loading of 14 vol% Ni and 27 vol% Ni of total solids, as presented in Table 6-2. This suggests that the oxidation of nickel does not alter the density of the composites during burnout. For the Ni/YSZ composites with higher nickel loadings, the relative density after burnout is substantially higher than the relative green density. This corresponds to the significant deviation from the predicted rule of mixtures volumetric expansion in Figure 6-2 indicating that some sintering is taking place which contributes to the higher density. On the other hand, the increase in density for the Ni/YSZ composite with a nickel loading of 4 vol% Ni of total solids is likely due to the slight volumetric shrinkage.

Table 6-2: Average Ni/YSZ composite relative densities of the sintering species in the green state and the burnout state

Composite	Ni Loading, Vol% Total Solids	Green Density, % Theoretical	Burnout Density, % Theoretical
100% YSZ	0	40.5	41.7
Ni/YSZ	4	42.3	44.2
	14	45.0	45.6
	27	48.4	48.7
	47	53.7	56.7
	77	58.2	73.0
100% Ni from Ni	100	62.1	94.4

6.1.3 NiGr/YSZ Composites

The NiGr/YSZ composite samples show a similar increasing volumetric expansion of the composites as the Ni/YSZ composites up to a nickel loading of 27 vol% Ni of total solids (See Figure 6-2). At nickel loadings above 27 vol% Ni, the degree of expansion lessens. While the volumetric expansion for the NiGr/YSZ composite samples shows a trend similar to the Ni/YSZ composites, the magnitude of the volumetric expansion of the NiGr/YSZ composites is slightly less. This suggests that the addition of graphite with a nickel coating does not dramatically alter the volumetric changes of the composite samples during burnout.

The lower volumetric expansion, relative to the expected composite expansion due to the oxidation of nickel, may be attributed to two important factors. First, the NiGr particles tend to form a more fully connected network at lower nickel loadings compared with the Ni/YSZ composites (as evidenced by the electrical conductivity results presented in Section 7.4). Therefore, the NiGr particles may sinter together more readily contributing to a greater sintering shrinkage. Likewise, the resultant microstructure of the NiGr/YSZ composites may contribute to the reduced expansion. When the graphite burns away, the nickel is left as a hollow shell. Since this shell is weaker than a solid particle of the same size, the induced strain in the YSZ matrix due to the expansion of nickel during oxidation is lower. If the strain acting on the YSZ matrix is less, then the actual degree of expansion will also be less.

6.1.4 Composites with Separate Graphite Additions

When graphite is added as a separate particle, the resultant dimensional changes are highly dependent on the graphite loading. For the Ni&Gr/YSZ and NiO&Gr/YSZ composite samples at low graphite loadings (i.e. low nickel loadings), the volumetric change during burnout is similar to the volumetric change experienced by the graphite-free composites (i.e. Ni/YSZ and NiO/YSZ), as shown in Figure 5-18 and Figure 5-19. However, at graphite loadings greater than 20 vol% Gr in the green state (47 vol% Ni of total solids), the Ni&Gr/YSZ and NiO&Gr/YSZ composites show a volumetric expansion that deviates from the volumetric changes of the graphite-free composites, but remains closer to the expected composite expansion due to nickel oxidation as shown in Figure 6-2. At higher graphite loadings, the difference between the volumetric expansion of the graphite containing

composites and the graphite-free composites is quite extreme and actually greater than the expected expansion at the highest graphite loading.

This deviation of the volumetric expansion of the Ni&Gr/YSZ and NiO&Gr/YSZ composites from the volumetric expansion of the graphite-free composites suggests that there is a critical graphite volume fraction whereby the volumetric expansion of the composite becomes severe. There is evidence of a critical graphite loading when examining the volumetric dimensional changes of the Ni&Gr-27/YSZ, Ni&Gr-47/YSZ, NiO&Gr-27/YSZ, and NiO&Gr-47/YSZ composite samples (See Figure 5-21). For the Ni&Gr-27/YSZ and NiO&Gr-27/YSZ composite samples the volumetric changes are essentially independent of the graphite loading. Similarly, the Ni&Gr-47/YSZ and NiO&Gr-47/YSZ composite samples have volumetric changes independent of the graphite loading below 20 vol% Gr of the green volume. However at graphite volume fractions greater than 25 vol% Gr, there is a significant increase in volumetric expansion.

The sudden increase in volumetric expansion shown by the graphite containing composites is similar to the sudden increase in the electrical conductivity of a particulate composite once the critical volume fraction of conducting material is reached. Thus, the significant volumetric expansion may be connected with the percolation of the graphite powder within the green volume. When the graphite loading is low (less than 25 vol% Gr), the resultant porosity after burnout is isolated by the Ni(O)/YSZ matrix because the graphite does not form a percolating network (See Figure 5-109 and Figure 5-111). As a result, the volumetric expansion is similar for the graphite containing and graphite-free composites. However, once a graphite percolating network forms (at graphite loadings greater than 25 vol% Gr), the strength of the composite is severely compromised during burnout due to the formation of a long continuous pore network throughout the entire composite. The low composite strength in combination with the large volume of exit gases created by the removal of the graphite powder causes the composite to swell. In addition, the laminated green dilatometer samples, made from 30 layers of tape, are weakest where the laminated layers are bonded together. As a result, even a small de-lamination or de-bonding strain in each layer can cause the large thickness expansion observed for the higher graphite containing samples. In fact, the individual layers are quite prominent in the Ni&Gr/YSZ and NiO&Gr/YSZ composite samples with a nickel loading of 77 vol% Ni of total solids, as shown in Figure 5-20, suggesting that partial delamination is a source of the severe swelling.

Lastly, the change in the density of the Ni&Gr/YSZ and NiO&Gr/YSZ composites follow the same trends as the other composite types. The relative density of the Ni&Gr/YSZ and NiO&Gr/YSZ composites is slightly lower, particularly at the high nickel loadings, compared with the volume fraction of nickel and YSZ given in Figure 5-12b assuming that the polymer and graphite material is converted to porosity during burnout.

6.2 SINTERING CHARACTERISTICS

6.2.1 NiO/YSZ Composites

Generally, the purpose of the sintering stage is to improve the strength and density of the powder compacts. In achieving this aim, the compacts typically undergo a dimensional shrinkage as a result of densification. As indicated by Equation (4-3), the degree of sintering shrinkage is a function of the system geometry and physical characteristics of the material to be sintered, such as: surface energy, vacancy diffusivity, and particle size. For that reason, the sintering characteristics of one material can be quite different than the sintering characteristics of another.

From Figure 5-38, it is quite clear that the sintering characteristics of the 100% YSZ samples are different than the sintering characteristics of the 100% Ni from NiO samples, because the 100% YSZ samples shrink significantly more than the 100% Ni from NiO samples. While the smaller particle size of the YSZ will lead to greater sintering shrinkage, the inherent material properties of YSZ will also influence densification.

The differences in the low and high temperature sintering characteristics of YSZ and NiO also contribute to the disparity in the degree of sintering shrinkage. During burnout, the 100% YSZ samples sinter very little and only begin to sinter significantly around 1100°C during the sintering stage. If the 100% YSZ dilatometer plot in Figure 5-38 is compared to the grain size versus density plots depicted in Figure 4-5, the dilatometer plot shows a similar densification trend as "curve z", indicating that the 100% YSZ samples are undergoing pure densification. (To relate the two Figures, the linear shrinkage and time axes in Figure 5-38 correlate to the percent theoretical density and grain size axes respectively in Figure 4-5). On the other hand, the 100% Ni from NiO samples begin to shrink significantly at 750°C during burnout and resume sintering around 1000°C during the sintering stage. Since some of the sintering shrinkage occurs during burnout, there is less sintering shrinkage during the sintering stage. As a result, the dilatometer plot of the 100% Ni from NiO samples in Figure 5-38 is better represented by "curve y" of Figure 4-5 where some coarsening and densification are taking place simultaneously. The coarsening of the microstructure is likely due to the interrupted sintering of the 100% Ni from NiO samples.

Despite the differences in the sintering characteristics of pure YSZ and NiO materials, the NiO/YSZ composites still experience some degree of sintering shrinkage depending on the nickel loading. The composites with lower nickel loadings tend to shrink more than the composites with higher nickel loadings (See Figure 5-57). Again, the volumetric shrinkage translates into an increase in density, which is consistent with Equation (4-4). Since there is no weight change during sintering, the burnout density may be used in Equation (4-4) directly. Interestingly, the relative densities of the NiO/YSZ composite samples with nickel loadings less than 47 vol% Ni of total solids are all at least 90%, while the relative densities of the NiO/YSZ composite samples with a nickel loading of 77 vol% Ni and the 100% Ni from NiO samples are approximately 85% (See Figure 5-61). According to Equation (4-4), the volumetric sintering shrinkage will be lower for a material with a higher green density than a similar material with a lower green density if they were to sinter to the same final density. If a relative density of 90% is considered the maximum possible density that can be achieved within the NiO/YSZ composites, then the composite samples with higher nickel loadings are expected to shrink less during sintering because they have a higher initial density (See Table 6-1). This too will limit the amount of sintering shrinkage that takes place in the composites with higher nickel contents.

The change in density from the burnout to the sintered state normalized by the change in density of the 100% YSZ samples is plotted in Figure 6-3. Upon inspection of Figure 6-3, the normalized density changes in the NiO/YSZ composite samples tend to be higher than the rule of mixtures prediction suggesting that the YSZ actually acts as a sintering aid for the NiO phase during the sintering stage. However, when the total change in density, from the green state to the sintered state, is normalized with the change in density for the 100% YSZ samples, the different sintering characteristics during the relatively low temperature burnout is balanced out by the sintering characteristics of the higher temperature sintering regime such that constrained sintering does not determine the overall densification of the NiO/YSZ composites (See Figure 6-4).

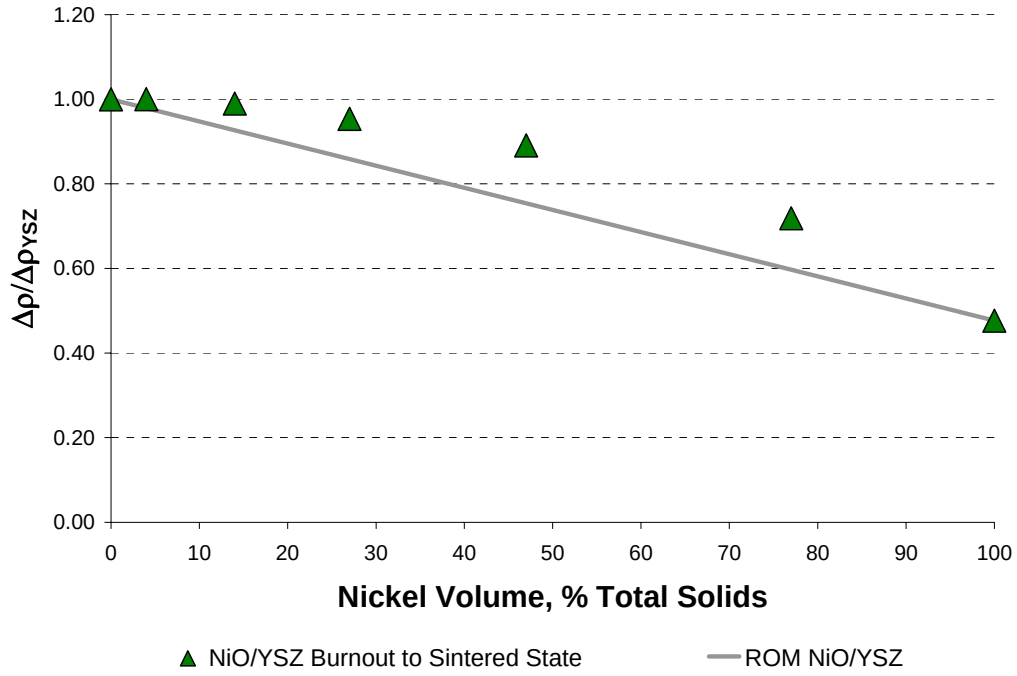

Figure 6-3: Normalized change in density from the burnout state to the sintered state for the NiO/YSZ composite samples based on the change in YSZ density

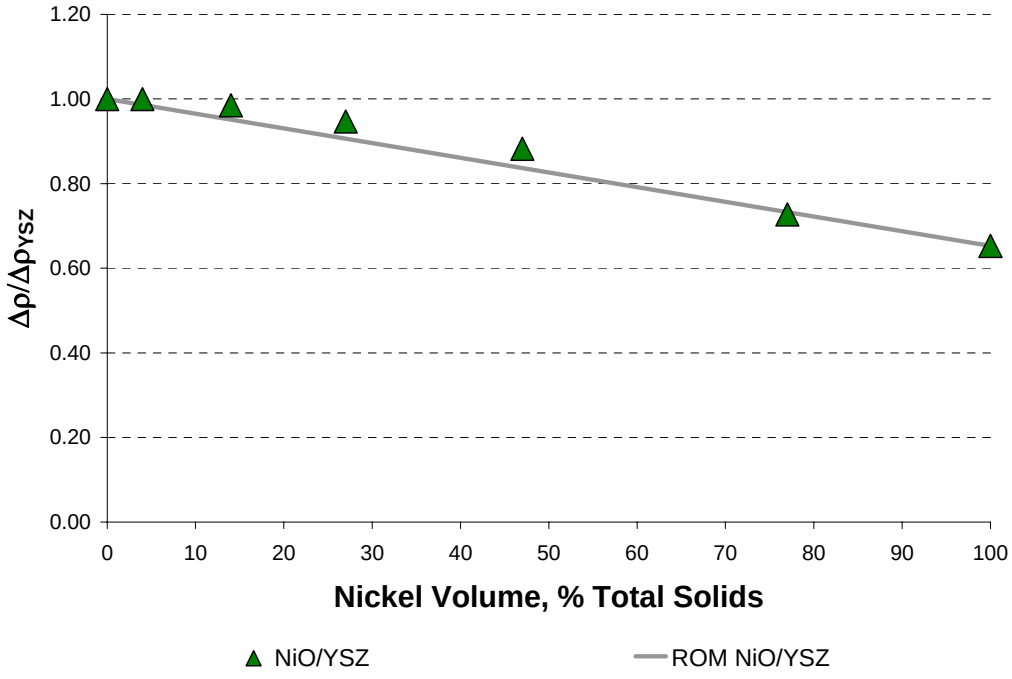

Figure 6-4: Normalized change in density from the green state to the sintered state for the NiO/YSZ composite samples based on the change in YSZ density

6.2.2 Ni/YSZ Composites

The sintering characteristics of the Ni/YSZ composite samples are different from the sintering characteristics of the NiO/YSZ composites despite the fact that both types of composites are comprised of nickel oxide after the burnout stage. The two types of composites behave differently during sintering because of the difference in the sintering characteristics of the 100% Ni from Ni and the 100% Ni from NiO samples at low temperatures during burnout. Examination of Figure 5-36 and Figure 5-38 reveals that the 100% Ni from Ni samples shrink less than the 100% Ni from NiO samples. The reason for the reduced shrinkage of the 100% Ni from Ni samples during sintering is a result of the higher sintering shrinkage during burnout. Since a greater proportion of the sintering takes place at lower temperatures, there is little shrinkage occurring during the sintering stage. In fact, the 100% Ni from Ni samples actually stop shrinking during the one hour hold time indicating that the sintering process is essentially complete under these processing conditions. The lack of densification suggests that the nickel oxide in the 100% Ni from Ni samples essentially coarsens during the sintering stage. Comparing the dilatometer plot for the 100% Ni from Ni samples (Figure 5-36) with "curve x" of Figure 4-5, confirms that the 100% Ni from Ni samples are likely coarsening.

Complicating the sintering behaviour of the 100% Ni from Ni samples however, is that they actually expand volumetrically during sintering (See Figure 5-54). The expansion of the 100% Ni from Ni samples during sintering is due to the oxidation of the approximately 14% residual nickel metal present after burnout (See Figure 5-14). Since the previously oxidized nickel appears to have sintered completely, the volumetric expansion (~7%) is similar to the expected expansion of the residual nickel metal due to oxidation.

Unlike the NiO/YSZ composites, the relative densities of the Ni/YSZ composites after sintering are not the same. In fact, the relative densities are lowest at a nickel loading of 27 vol% and 47 vol% Ni, as illustrated in Figure 5-61. The variation in the relative densities is a function of the volumetric shrinkage during sintering and the relative density of the samples after burnout (i.e. Equation (4-4)). Since the polymer content decreases with increasing nickel loading, the Ni/YSZ composites with higher nickel loadings also have a higher initial density. Even though these composites shrink less than the composites with a lower nickel loading, the combination of a high initial density and low volumetric shrinkage still results in a higher relative sintered density than the composites with moderate nickel loadings. In fact, the relative density of the 100% Ni from Ni samples actually decreases after sintering due to the small volumetric expansion.

The lower relative densities of the Ni/YSZ composite samples imply that the nickel phase may be constraining the sintering of the YSZ. Since 100% Ni from Ni samples are not fully oxidized while the other composite samples are, it is not possible to accurately compare the change in density from the burnout to sintered state to the rule of mixtures. With that said, there does appear to be a constrained sintering effect for the composites with lower nickel loadings when the change in density from the burnout to sintered states is normalized by the change in density of the YSZ, as shown in Figure 6-5. If the change in density from the green state to the sintered state normalized with the change in density of the YSZ is compared with the rule of mixtures, it is clear that constrained sintering is a real effect as shown in Figure 6-6. The constrained sintering effect likely arises from the greater sintering of the nickel during the burnout stage which then limits the amount of YSZ shrinkage that takes place during sintering.

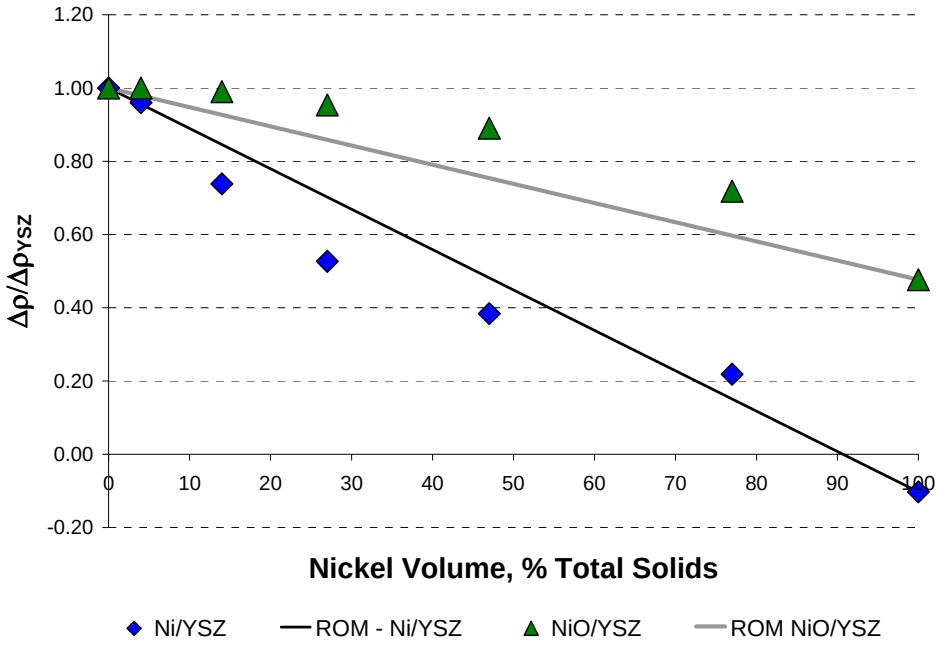

Figure 6-5: Normalized change in density from the burnout state to the sintered state for the Ni/YSZ composite samples based on the change in YSZ density. The normalized change in density from the burnout state to the sintered state for the NiO/YSZ composite samples is also included for reference.

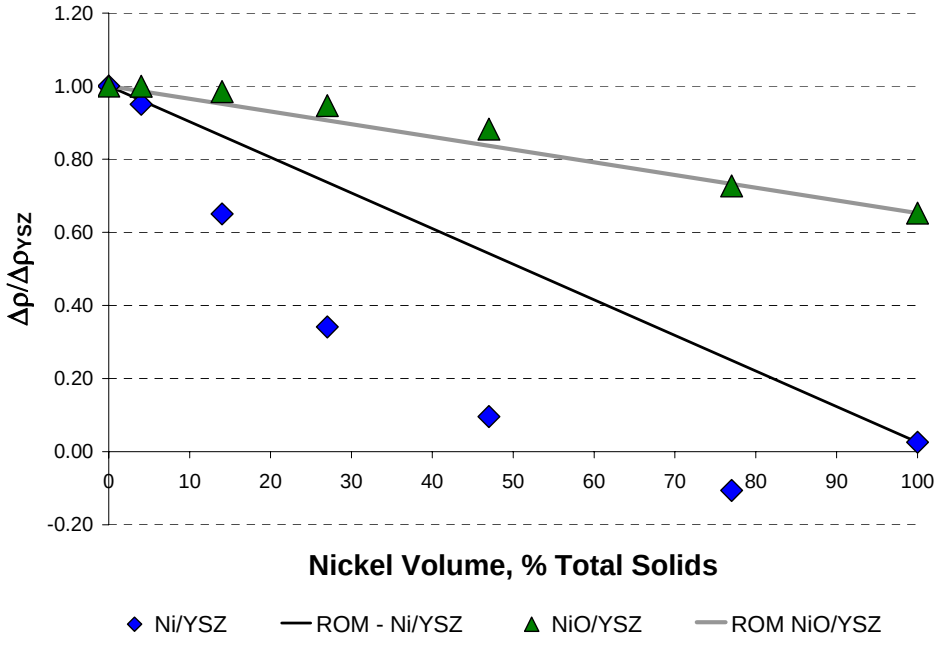

Figure 6-6: Normalized change in density from the green state to the sintered state for the Ni/YSZ composite samples. The normalized change in density from the green state to the sintered state for the NiO/YSZ composite samples is also included for reference.

6.2.3 NiGr/YSZ Composites

The NiGr/YSZ composite samples sinter in a manner that is consistent with the sintering characteristics of the Ni/YSZ composites as indicated when comparing the volumetric sintering shrinkages (Figure 5-54 and Figure 5-55) and the dilatometer plots (Figure 5-36 and Figure 5-37) of the two composite types. The NiGr/YSZ composite samples tend to have a slightly lower volumetric sintering shrinkage at moderate nickel loadings compared with the Ni/YSZ composite samples. The lower sintering shrinkage is due to the increased shrinkage of the NiGr/YSZ samples during the burnout stage. While it is difficult to compare the relative densities of the two composites due to the graphite additions, if the relative density of the NiGr/YSZ matrix is higher than the relative density of the Ni/YSZ matrix, then the volumetric shrinkage is expected to be lower during sintering.

To determine how much porosity is generated by the burnout of the graphite additions after sintering, the average bulk porosity of the NiGr/YSZ composite samples is plotted with respect to the graphite loading as a fraction of the combined YSZ, nickel oxide (due to nickel oxidation during burnout) and graphite volumes in Figure 6-7. If the graphite is solely responsible for the amount of porosity generated in the composite, then the volume fraction of graphite as a percentage of the total solids volume including the graphite should be equal to the bulk porosity. Therefore, a line denoting the expected degree of porosity if the volume of graphite added generates an equal volume of porosity, is also included in Figure 6-7. For the NiGr/YSZ composite samples, the bulk porosity is actually higher than the expected porosity due to graphite indicating that there is additional porosity in the NiGr/YSZ composite matrix. The higher bulk porosity is caused by the constrained sintering of the YSZ which prevents the nickel and YSZ matrix from sintering to its full density, and other pores formed through microcracks, layer delamination, and particle bridging voids.

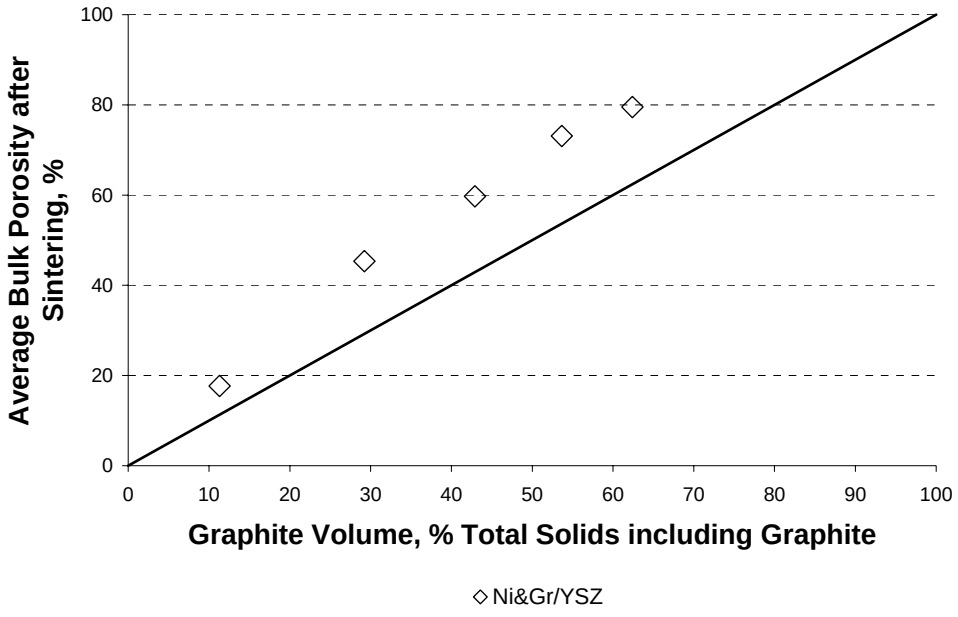

Figure 6-7: Sintered bulk porosity for the NiGr/YSZ composite samples as a function of the YSZ, nickel oxide, and graphite volumes. The line indicates the amount of porosity generated by an equal amount of graphite.

6.2.4 Graphite Containing Composites

With the exception of the increase in bulk porosity, adding graphite to the Ni/YSZ and NiO/YSZ composites has a minor effect on the sintering characteristics of the Ni&Gr/YSZ and NiO&Gr/YSZ composites. When examining the volumetric sintering shrinkages of the Ni&Gr-27/YSZ, Ni&Gr-47/YSZ, NiO&Gr-27/YSZ, and NiO&Gr-47/YSZ composite samples, plotted in Figure 5-59 and Figure 5-60, they increase slightly with increasing graphite loading. The higher volumetric shrinkage may be attributed to the lower packing density of the nickel and YSZ phases, shown in Figure 5-10 and Figure 5-11, as the amount of graphite increases. To achieve the same final density, the less tightly packed nickel and YSZ powders will shrink more during sintering than the more tightly packed composites with lower graphite loadings.

However, the dilatometer plots for the composites with varying graphite loading suggest that the linear sintering shrinkage increases more significantly with increasing graphite loading (See Figure 5-41 through Figure 5-44). In order to maintain a constant volumetric sintering shrinkage, the linear shrinkage in the thickness direction tends to be lower, thereby introducing anisotropy to the sintering of the graphite containing composites (See Figure 5-49 and Figure 5-51 through Figure 5-53). The anisotropy appears to be introduced by the dilatometer during the measurement of the sintering shrinkage since the bulk sintered samples do not exhibit the same anisotropic behaviour as shown in Appendix D (Figure D-3 and Figure D-5). Since the graphite containing composites have such low density, and thus low strength, when the push rod is placed against the composite sample, it compresses the sample slightly leading to a contraction in the length direction and an expansion in the thickness direction.

Like the NiGr/YSZ composites, the bulk porosity of the graphite containing composites after sintering increases with the amount of graphite added as shown in Figure 6-8 and Figure 6-9. For the NiO&Gr-27/YSZ composite samples, the bulk porosities follow the line denoting the expected bulk porosity due solely to the graphite additions reasonably well. Since the NiO/YSZ composite with the same nickel loading sintered to a high density, the nickel oxide and YSZ phases in the NiO&Gr-27/YSZ composites likely sintered to a similar high density as well. Likewise, the bulk porosities for the other graphite containing composite samples deviate from the line representing the porosity due to graphite since the respective graphite-free composites do not sinter to full density either. For example, the nickel based composites have higher bulk porosities due to the constrained sintering of the YSZ.

6.3 MICROSTRUCTURAL AND DIMENSIONAL CHANGES DURING REDUCTION

In order for the Ni/YSZ composites to be used as effective anodes, the nickel oxide formed during the burnout and sintering stages must be reduced back to nickel metal. In general, the composites undergo only a small degree of linear and volumetric shrinkage during reduction. Specifically, composites with a nickel loading of 47 vol% Ni of total solids or less shrink approximately 0.5% while composites with higher nickel contents (77 vol% Ni and 100 vol% Ni) shrink up to 5%. The 100% Ni from NiO samples exhibited the largest volumetric shrinkage, over 22%, which is comparable to the expected volumetric shrinkage of 25% for NiO measured by Jiang et al. [22].

A constrained sintering analysis similar to the constrained sintered effects presented in Figure 6-1, Figure 6-3, and Figure 6-4 is not possible for the reduction stage since the changes in the composite density may be due to sintering shrinkage and/or a different solids volume due to the reduction of nickel oxide to nickel metal. Nevertheless, the lower volumetric shrinkage during reduction in the lower nickel containing composites can be attributed to the constraining effects of the solid YSZ backbone that resists the change in the composite volume. The dilatometer plots measuring the linear

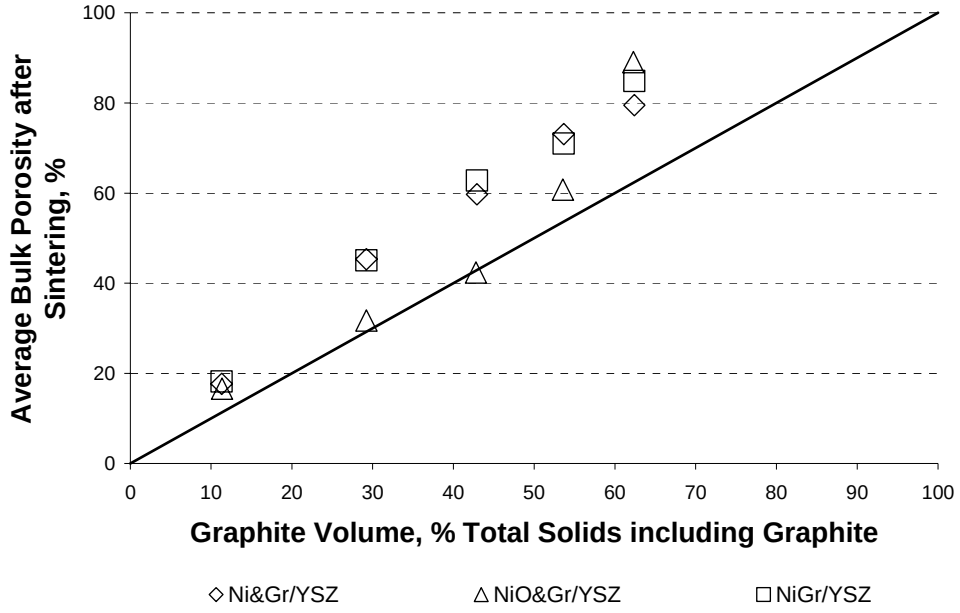

Figure 6-8: Sintered bulk porosity for the NiGr/YSZ, Ni&Gr/YSZ, and NiO&Gr/YSZ composite samples as a function of the YSZ, nickel oxide, and graphite volumes. The line indicates the amount of porosity generated by an equal amount of graphite.

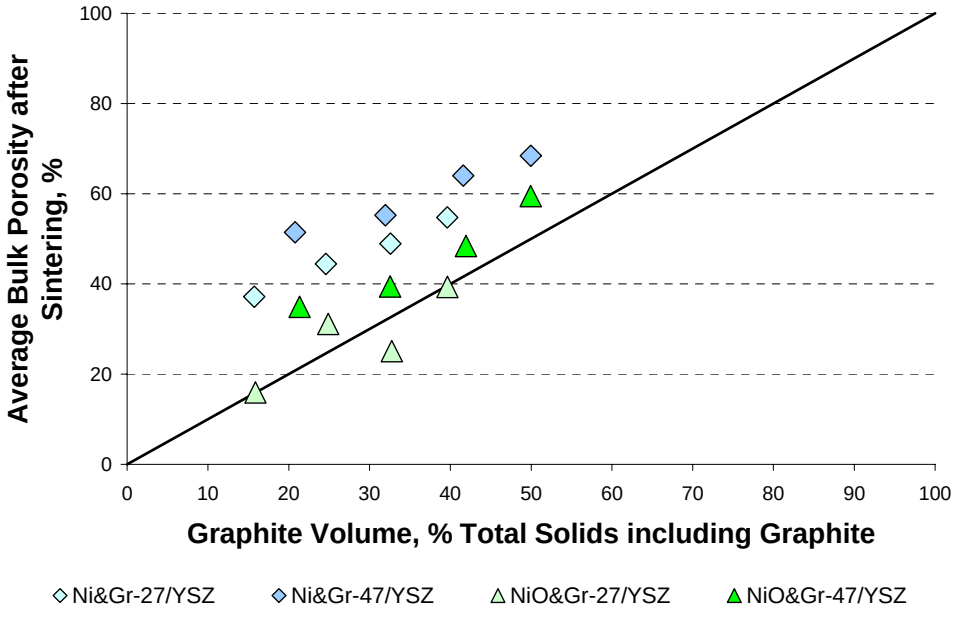

Figure 6-9: Sintered bulk porosity for the Ni&Gr-27/YSZ, Ni&Gr-47/YSZ, NiO&Gr-27/YSZ, and NiO&Gr-47/YSZ composite samples as a function of the YSZ, nickel oxide, and graphite volumes. The line indicates the amount of porosity generated by an equal amount of graphite.

shrinkage during reduction provide good examples of this effect (See Figure 5-68 through Figure 5-76). For example at low nickel loadings (less than 27 vol% Ni of total solids), the NiGr/YSZ composites have nearly identical linear shrinkages (See Figure 5-69). However, as the nickel content increases, and the amount of YSZ decreases, the linear shrinkage due to reduction also increases. This increase in linear shrinkage may be attributed to a lower stiffness of the YSZ matrix which decreases its ability to restrain the shrinkage of the nickel phase. For the graphite containing composites with high graphite loadings, the increase in shrinkage can also be caused by the dilatometer compressing the sample slightly because of the overall lower strength of the highly porous composite.

The results of this study are consistent with similar results published in the literature. Marinsek et al. found that a pure NiO sample decreased in volume by about 20% after reduction to nickel metal, while there was no volume change in the Ni/YSZ composites containing a continuous network of YSZ [29]. The continuous YSZ network was believed to resist the contraction of the nickel phase thereby limiting the composite shrinkage during reduction. Similarly, Cassidy et al. measured volumetric sintering shrinkages between 2% and 4% for Ni/YSZ composites with a nickel loading of 40 vol% Ni of total solids [38].

An important aspect of the reduction process is the resultant decrease in the relative density of the composites as nickel oxide reduces to nickel metal. For the composites tested, the decrease in density from the sintered state to the reduced state is clear after comparing Figure 5-61 through Figure 5-65 with Figure 5-87 through Figure 5-91. This decrease in density is of practical importance because it is the primary mechanism for generating porosity in conventionally processed anodes. However, continued sintering of the nickel phase during the reduction stage can also lead to a decrease in the amount of porosity generated by the reduction of nickel oxide. To evaluate this sintering contribution to the change in porosity, an upper bound for the new porosity generated by the reduction of nickel oxide may be determined by:

$$\%\ New\ Porosity = \frac{V_{NiO} - V_{Ni}}{V_{Sintered}} \times 100\% \qquad \textbf{(6-5)}$$

where the V_{NiO}, V_{Ni}, and $V_{Sintered}$ are the volumes of nickel oxide and nickel metal contained in the volume of the sintered composite sample. By using the sintered volume in Equation (6-5), it is assumed that no sintering and therefore no shrinkage takes place during the reduction stage. An indication of the relative importance of sintering shrinkage in the prevention of new porosity can be made by comparing Equation (6-5) with the experimentally measured change in porosity due to the reduction of nickel oxide. For each of the composites, the experimentally measured change in porosity can be determined from the difference between the sintered relative density and the sintered & reduced relative density. The calculated and experimentally measured amount of new porosity due to the reduction of nickel oxide is presented in Table 6-3 and Table 6-4 for each composite type. In addition, the same data for the Ni/YSZ and NiO/YSZ composites is plotted in Figure 6-10. In essentially all cases, the experimentally measured new porosity is lower than the upper bound prediction indicating that some degree of sintering shrinkage has occurred, thereby reducing the amount of new porosity. In particular, the composites with higher nickel loadings, especially the 100% Ni from Ni and 100% Ni from NiO samples, have real porosities that are significantly lower than the upper bound prediction, as shown in Figure 6-10. This suggests that sintering shrinkage reduces the amount of added porosity and is consistent with the increased volumetric shrinkage observed for these samples in Figure 5-78 and Figure 5-81.

The exceptions to the above observations are the experimentally measured porosities for the NiO&Gr/YSZ composite samples with nickel loadings of 27 vol% Ni and 47 vol% Ni of total solids are higher than the upper bound prediction. Inspection of Figure 5-82 reveals that these samples actually expand volumetrically during reduction which leads to an increase in porosity.

Table 6-3: Average estimated and measured changes in porosity due to the reduction of nickel oxide for the Ni/YSZ and NiO/YSZ composite samples

Composite	Nickel Loading	Estimated New Porosity, %	Difference between Sintered and Sintered & Reduced Relative Densities
Ni/YSZ	4	2.4	1.80
	14	7.0	6.65
	27	11.5	10.90
	47	17.9	17.42
	77	28.3	26.53
100% Ni from Ni	100	41.4	23.13
NiO/YSZ	4	2.4	1.53
	14	8.0	4.83
	27	14.6	13.08
	47	22.3	21.80
	77	29.8	29.04
100% Ni from NiO	100	33.6	18.47

Table 6-4: Average estimated and measured changes in porosity due to the reduction of nickel oxide for the NiGr/YSZ, Ni&Gr/YSZ, and NiO&Gr/YSZ composite samples

Composite	Nickel Loading	Estimated New Porosity, %	Difference between Sintered and Sintered & Reduced Relative Densities
NiGr/YSZ	4	2.2	0.41
	14	4.7	4.09
	27	5.8	5.26
	47	6.9	6.63
	77	7.8	7.07
Ni&Gr/YSZ	4	2.1	2.30
	14	4.7	1.92
	27	6.3	5.43
	47	6.6	5.89
NiO&Gr/YSZ	4	2.2	0.59
	14	6.0	4.12
	27	8.9	9.77
	47	9.5	10.74

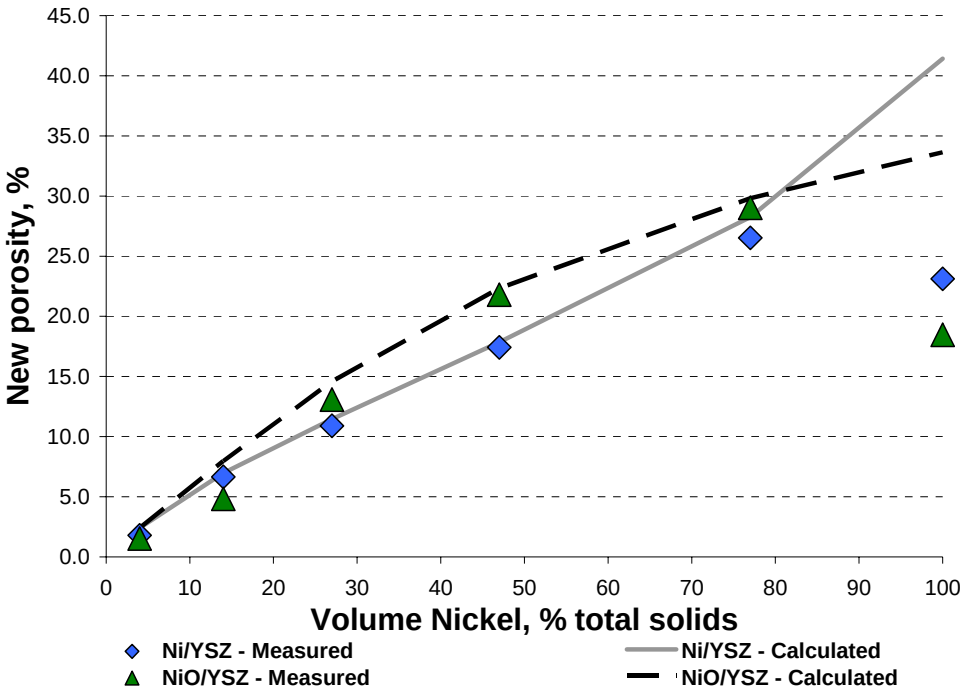

Figure 6-10: Calculated and measured new porosity in the Ni/YSZ and NiO/YSZ composites after the reduction stage. The new porosity for each composite was calculated using Equation (6-5).

6.4 FUTURE WORK

There are many variables associated with sintering such as the heating rate, sintering temperature, hold time, and sintering atmosphere. Further experiments can be carried out to determine the effect the different conditions have on the final properties of the composites. For example, sintering of the Ni/YSZ composites typically takes place between 1350°C and 1500°C at hold times ranging from one hour to several days. It would be beneficial to determine an optimum heating schedule for sintering in order to maximize the desired composite properties while minimizing the total processing time. Changing the sintering atmosphere, such as using a reducing atmosphere for sintering the Ni/YSZ composites may also prove beneficial. Similar studies can be conducted to optimize the polymer burnout schedule, the graphite burnout schedule and the reduction schedule.

In addition to changing the processing variables, altering the relative particle sizes of the nickel, nickel oxide, graphite, and YSZ particles could change the sintering characteristics of the composites investigated. By altering the particle sizes, it will be possible to determine whether the size or the materials themselves are responsible for the resultant dimensional changes after sintering.

CHAPTER 7:
ELECTRICAL CONDUCTIVITY

7.1 ELECTRICAL CONDUCTIVITY IN PURE MATERIALS

As the term suggests, electrical conductivity is a measure of how well a material conducts electricity. A good electrical conductor possesses many highly mobile electrons [73]. How easily electrons move through a material is dependent on its atomic bonding, the number of crystal lattice imperfections, and the microstructure of the material. Metals, such as nickel, are good electrical conductors while insulating materials, such as yttria-stabilized zirconia are not. The electrical conductivity of nickel (σ_{Ni}) is 146 200 S/cm while the electrical conductivity of YSZ (σ_{YSZ}) is 0.006 S/cm at 25°C [52].

The resistance to current flow through a conductor is given by the familiar form of Ohm's Law:

$$V = IR \tag{7-1}$$

where V is the voltage, I is the current, and R is the resistance in ohms (Ω). This resistance is also a function of the size, shape, and the properties of the materials within the circuit given by the equation [89]:

$$R = \frac{l}{\sigma A} \tag{7-2}$$

where l is the length of the conductor, A is the cross-sectional area, and σ is the electrical conductivity. By combining equations (7-1) and (7-2) an expression for calculating the bulk electrical conductivity of a material is given as [89]:

$$\sigma = \frac{Il}{VA} \tag{7-3}$$

Another term commonly used to describe the electrical conductivity of a material is electrical resistivity which is the reciprocal of electrical conductivity. That is, good conductors have low electrical resistivity while poor conductors have high electrical resistivity. In addition, units for electrical conductivity are commonly stated in siemens per centimetre (S/cm) while the units for resistivity are given as Ω.cm. Therefore, one siemen is equal to one Ω^{-1}.

7.2 ELECTRICAL CONDUCTIVITY IN DENSE COMPOSITES WITH CONTINUOUS PHASES

The properties of a composite material are a function of the properties of each individual material component and how they are distributed throughout the composite. For instance, a composite containing a metal (high electrical conductivity) and a ceramic (low electrical conductivity) will have a very different electrical conductivity compared to its constituent phases depending on how each phase is distributed throughout the composite. To achieve the maximum electrical conductivity, continuous parallel fibres or sheets of the high conducting phase are embedded in the low conducting matrix as shown in Figure 7-1. This upper bound, representing the best structure in terms of electrical conductivity, can be expressed as:

$$\sigma_{comp} = V_h \sigma_h + V_l \sigma_l \tag{7-4}$$

where V_h is the volume fraction of the high conducting phase, V_l is the volume fraction of the low conducting phase, and σ_{comp}, σ_h, and σ_l are the composite, high conducting phase, and low conducting phase electrical conductivities respectively.

The minimum electrical conductivity of a composite occurs when the high conducting phase is in series with the low conducting phase (See Figure 7-1). This lower bound, representing the composite structure with the lowest electrical conductivity is represented by:

$$\frac{1}{\sigma_{comp}} = \frac{V_h}{\sigma_h} + \frac{V_l}{\sigma_l} \tag{7-5}$$

It is important to note that Equations (7-4) and (7-5) assume that each phase is fully dense and continuous.

7.3 ELECTRICAL CONDUCTIVITY OF PARTICULATE COMPOSITES

For particulate composites where at least one phase is not continuous, Equations (7-4) and (7-5) are not applicable, particularly at low volume fractions of the high conducting phase or low conducting phase. More realistic models for composite electrical conductivity are based on percolation theory where discrete particles of the conducting phase are embedded in the composite volume. One model, proposed by McLachlan is given by [62]:

$$\sigma_{comp} = \sigma_h \left(\frac{V_h - V_c}{1 - V_c} \right)^t \tag{7-6}$$

for high conducting phase loadings above the percolation threshold and

$$\sigma_{comp} = \frac{\sigma_l}{\left(1 - \frac{V_h}{V_c}\right)^t}$$

(7-7)

for high conducting phase loadings below the percolation threshold where, $\sigma_{comp,}$ $\sigma_{h,}$ σ_l are the electrical conductivities of the composite, high conducting phase, and low conducting phase respectively, V_h is the volume fraction of the high conducting phase, and V_c is the critical (percolation) volume fraction for the high conducting phase as a fraction of total solids. To clarify, V_c is dependent on the geometry of the actual composite microstructure which may contain a variety of particle shapes and sizes and differs from the critical volume fraction, ϕ_c, of Equation (2-1) which corresponds to the percolation threshold associated with composites comprised of equal sized spheres. Note that Equation (7-6) simplifies to the upper bound prediction of Equation (7-4) when $V_c = 0$ (i.e. a continuous conducting phase) and t = 1. For conductivities close to the percolation threshold, the value of the parameter t typically falls between t = 1.6 and 2.0 in three dimensional systems and t = 1.0 to 1.4 in two dimensional systems [90].

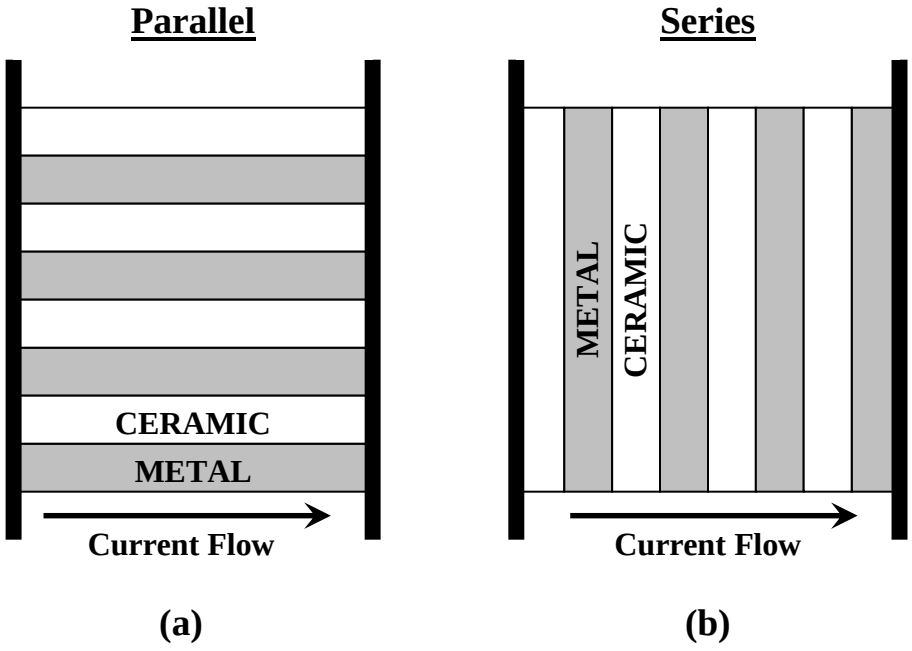

Figure 7-1: Schematic diagram illustrating the composite structure corresponding to the a) maximum electrical conductivity, and b) the minimum electrical conductivity. Each phase is assumed to be continuous and fully dense.

7.3.1 Comparison of Fibre and Particulate Composite Electrical Conductivities

To illustrate the differences between the predicted electrical conductivities of fibre composites and particulate composites, a plot of the predicted electrical conductivities from Equations (7-4) to (7-7) using nickel and YSZ as the composite materials is given in Figure 7-2. The predicted electrical conductivities of a two dimensional and a three dimensional percolating particulate composite are given in Figure 7-2 in addition to the upper and lower bound predictions of electrical conductivity for fibre composites. For the two dimensional case, the critical volume fraction $V_c = 0.45$ and $t = 1.2$ while $V_c = 0.16$ and $t = 1.8$ for the three dimensional case.

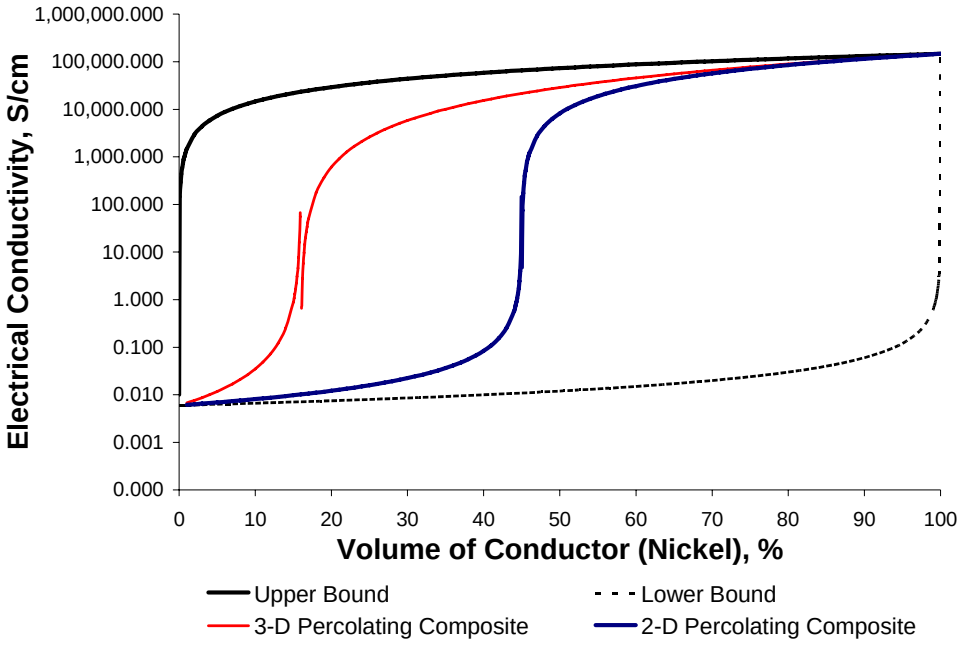

Figure 7-2: Predicted electrical conductivities from Equations (7-4) and (7-7) using the electrical conductivities of YSZ and Ni. The values for V_c and t in Equation (7-6) and (7-7) for the 2-D and 3-D examples are $V_c = 0.45$, $t = 1.2$ and $V_c = 0.16$, $t = 1.8$ respectively.

From Figure 7-2, it is clear that the predicted electrical conductivity varies significantly depending on the equation used. The upper bound prediction increases very rapidly at low volume fractions of the conducting material (nickel) since the electrical conductivity of the composite is dominated by the conductivity of the continuous imbedded fibres (i.e. $V_c = 0$). Likewise, the lower bound prediction is dominated by the low conductivity YSZ with the electrical conductivity only rising significantly at very high concentrations of the high conducting nickel phase.

The electrical conductivity in the percolating networks is a combination of both upper bound and lower bound behaviours. Below the percolation threshold, the electrical conductivity of the composite is dominated by the low conducting phase and behaves in a similar manner to the lower bound prediction since the high conducting phase does not produce a percolating network. Once the percolation threshold is reached, the high conducting phase forms a percolating network and there is a rapid increase in the electrical conductivity of the composite, similar to the behaviour predicted by the

upper bound. The percolation threshold therefore determines where this transition takes place, while the parameter t alters the shape of the curve.

The two curves representing the electrical conductivity above and below the percolation threshold overlap in Figure 7-2 because the percolation threshold represents an asymptote. Mathematically, the electrical conductivity prediction for the composite approaches infinity as the volume fraction of the conducting phase nears the percolation threshold from below. Similarly, the electrical conductivity of the composite approaches zero as the volume fraction of the conducting phase nears the percolation threshold from above [58].

7.4 ELECTRICAL CONDUCTIVITY RESULTS

The measured electrical conductivity for three composite samples with various nickel volume fractions made from Ni/YSZ and NiO/YSZ are shown in Figure 7-3. First, the electrical conductivities of the composites are plotted with respect to nickel as a fraction of the total solids (i.e. Ni and YSZ only) and then the same sample electrical conductivities are plotted with respect to nickel as a fraction of the total composite volume including porosity. Typically, electrical conductivity results from the literature are plotted with respect to nickel fractions as a percentage of total solids [19].

The effect of increasing nickel volume fraction is quite evident when examining Figure 7-3a. Clearly, the electrical conductivity results for both the Ni/YSZ and NiO/YSZ composites exhibit percolating behaviour similar to that exhibited by data from the literature (See Section 2.2). In addition, the NiO/YSZ composite samples with a nickel loading of 47 vol% Ni of total solids (62 wt% NiO) has an average electrical conductivity of 3904 S/cm which is comparable to the NiO/YSZ composite prepared by Simwonis et al. (56 wt% NiO) which has a similar electrical conductivity of 3900 S/cm at 25°C [53]. As expected, the electrical conductivity increases with greater nickel content above the critical percolating volume fraction where there is a sudden rise in electrical conductivity. For all samples below the critical percolating volume fraction, the electrical conductivity was too low to be measured by the experimental set-up and is assumed to be the same as the electrical conductivity of YSZ (0.006 S/cm).

Generally, the electrical conductivities for the composite samples made from Ni/YSZ are similar to the electrical conductivities of the samples made from NiO/YSZ as illustrated in Figure 7-3a. One noticeable difference is that composites made with Ni/YSZ have a lower critical percolating volume fraction than the NiO/YSZ composite samples. The lower critical percolating volume fraction is indicated by the Ni/YSZ samples having a measurable conductivity at a nickel fraction of 27 vol% of total solids while the NiO/YSZ samples do not.

The same trends appear when comparing the electrical conductivities of the same composite samples based on nickel as a fraction of the total composite volume, as shown in Figure 7-3b. The difference now is the Ni/YSZ composites have a lower volume fraction of nickel compared to the NiO/YSZ composite samples because the Ni/YSZ samples are generally more porous (See Figure 5-87). The opposite is true at a nickel loading of approximately 50% where the porosity is greater in the NiO/YSZ composite samples. The measured electrical conductivities for both composite types are still similar for a given nickel loading despite the difference in nickel volume fraction.

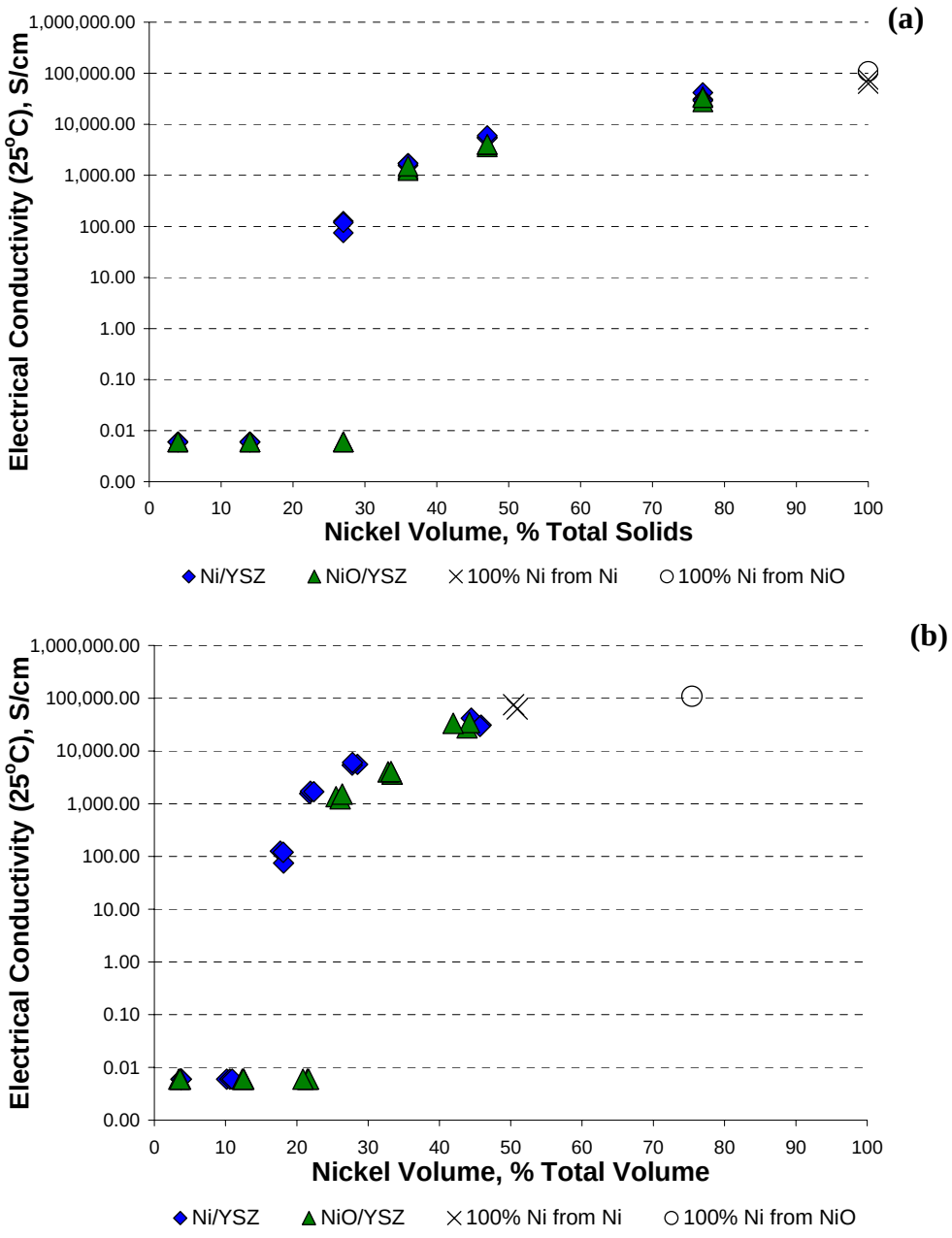

Figure 7-3: Measured electrical conductivity of composites made from Ni/YSZ and NiO/YSZ with varying nickel content based on a) nickel as a fraction of total solids, and b) nickel as a fraction of the total composite volume

The measured electrical conductivities of three samples of the Ni&Gr/YSZ and NiO&Gr/YSZ composites are plotted in Figure 7-4 along with the electrical conductivity measurements for the Ni/YSZ and NiO/YSZ composite samples. Note in this case, both the nickel and graphite loadings are increasing in the Ni&Gr/YSZ and NiO&Gr/YSZ composites according to a fixed ratio of 55 wt% nickel to 45 wt% graphite; similar to the NiGr/YSZ composites. Based on total solids, the Ni&Gr/YSZ and NiO&Gr/YSZ composites have lower electrical conductivities compared to the composite samples without graphite additions (See Figure 7-4a). The critical percolating volume fraction is also higher as the composites with graphite additions do not conduct electricity at nickel fractions below 36 vol% nickel of total solids. Note that, the Ni&Gr/YSZ and NiO&Gr/YSZ composite samples with nickel volume fractions above 47 vol% of total solids were not measured. Those composite samples were too brittle and had a tendency to break when measured because of the excess porosity associated with the higher graphite loading.

A completely different picture is presented when the electrical conductivities of the Ni&Gr/YSZ and NiO&Gr/YSZ composite samples are plotted with respect to nickel fractions based on the total composite volume (See Figure 7-4b). In fact, the Ni&Gr/YSZ and NiO&Gr/YSZ composites have superior electrical conductivities at lower nickel fractions compared to the Ni/YSZ and NiO/YSZ composites. The additional porosity in the composites made with graphite is accounted for when the electrical conductivities are plotted with respect to nickel as a fraction of the total composite volume. It is this additional porosity that causes a decrease in the expected electrical conductivity at the given nickel loading based on total solids.

The method in which nickel and graphite are added to the composite also affects the electrical conductivity as depicted in Figure 7-5. When nickel is added in the form of a coating on a graphite particle the resulting electrical conductivity is vastly superior to the electrical conductivity of composites made of separate nickel and graphite powders regardless of how the data is presented. The average electrical conductivity measurements for the NiGr/YSZ composites with nickel loadings of 27 vol% Ni (5302 S/cm) and 47 vol% Ni (14,273 S/cm) compare quite favourably with the NiGr-29 (2747 S/cm) and the NiGr-49 (11,034 S/cm) composites prepared by Corbin et al. with similar nickel loadings [39]. The NiGr/YSZ composites also have electrical conductivities that are similar to the electrical conductivities of the composites prepared by Hu et al. having the same nickel loading (26 vol% Ni = 2382 S/cm and 49.5 vol% Ni = 16,900 S/cm) using nickel coated YSZ particles [56]. It is also worth noting that the NiGr/YSZ composite samples have a much lower critical percolating volume fraction compared to the other composite types.

The effect of porosity, due to graphite additions, on the electrical conductivity of a composite is further understood when examining the electrical conductivities of the Ni&Gr-47/YSZ and NiO&Gr-47/YSZ composite samples, as given in Figure 7-6. The electrical conductivity data for the Ni&Gr-27/YSZ and NiO&Gr-27/YSZ composite samples are not presented because the nickel loading for each composite sample is below the percolation threshold, thereby making the electrical conductivity difficult to quantify.

When the electrical conductivities for the Ni&Gr/YSZ and NiO&Gr/YSZ samples are plotted with respect to nickel as a fraction of total solids, the data simply gives a range of electrical conductivities at a nickel volume fraction of 47 vol% Ni because each sample has the same nickel loading, as shown in Figure 7-6a. Consequently, no meaningful conclusions can be made about the effect of porosity due to increasing graphite additions until the electrical conductivity data is plotted with respect to nickel as a fraction of the total composite volume as in Figure 7-6b. When plotted in this manner, it is evident that the electrical conductivities of the composite samples are inversely proportional to the amount of

porosity contained in the composite. That is, as porosity increases in the composite, the electrical conductivity decreases.

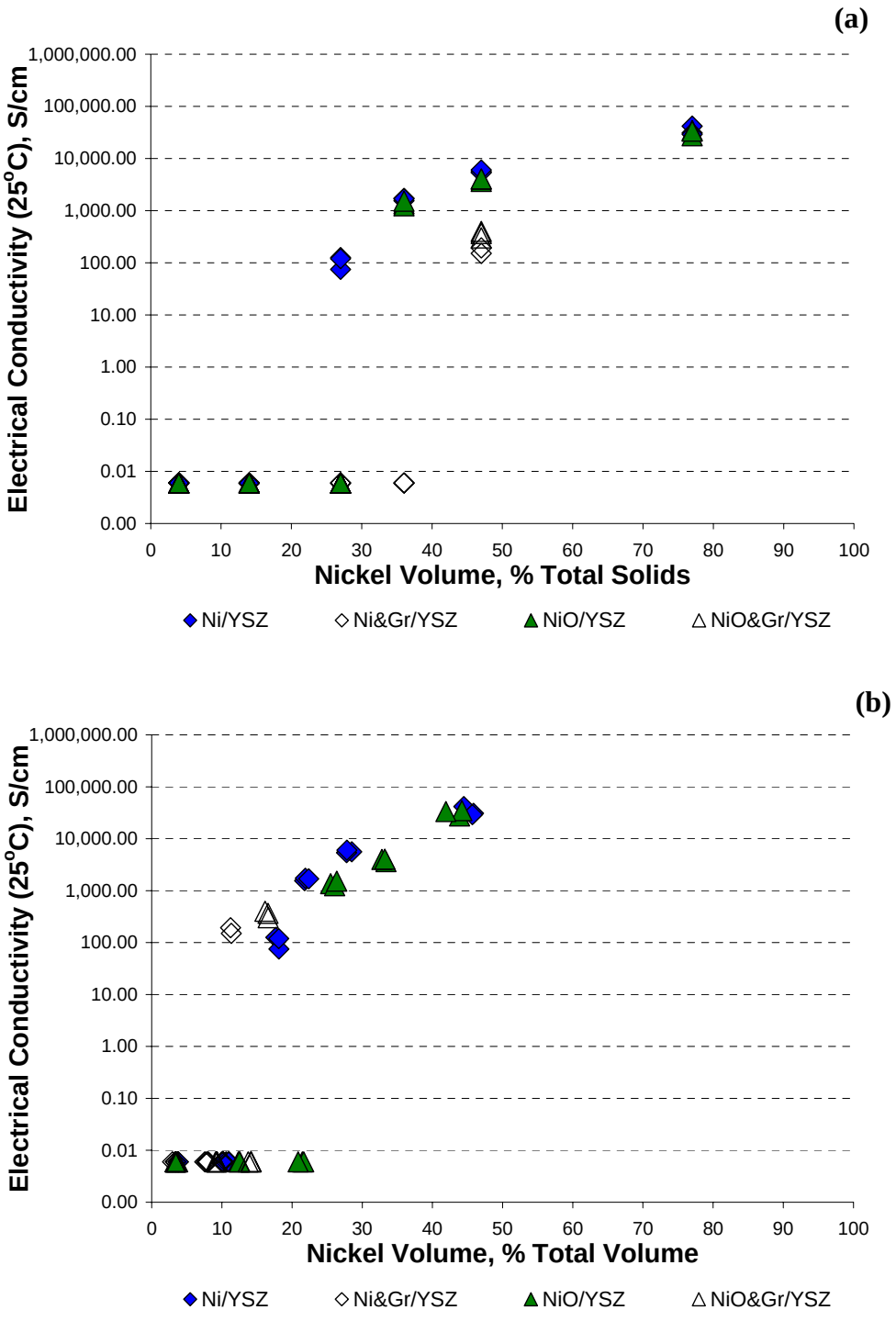

Figure 7-4: Measured electrical conductivity of composites made from Ni&Gr/YSZ and NiO&Gr/YSZ with varying nickel content based on a) nickel as a fraction of total solids, and b) nickel as a fraction of the total composite volume. (Ni/YSZ and NiO/YSZ composite sample data is included for reference.)

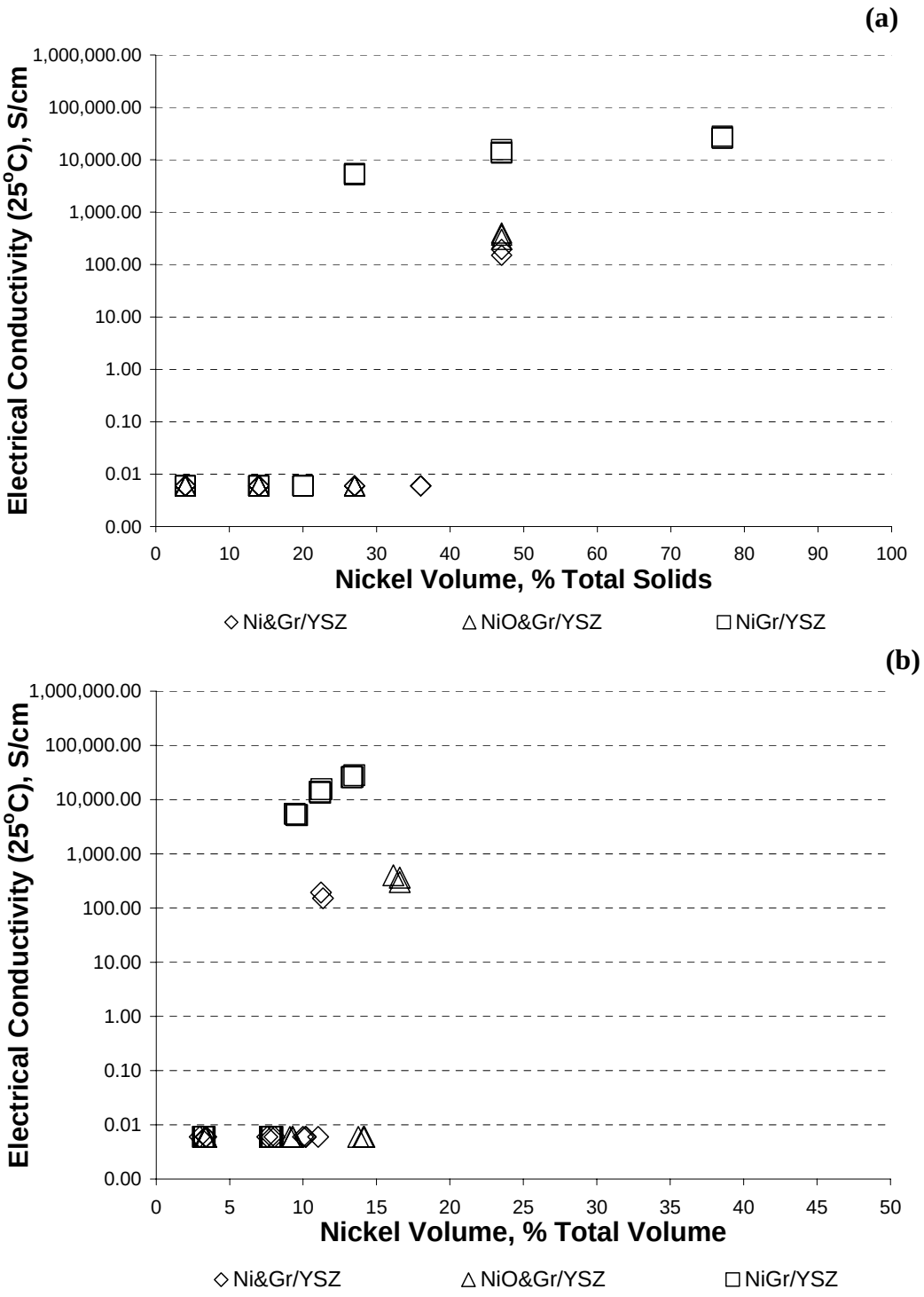

Figure 7-5: Measured electrical conductivity of composites made from NiGr/YSZ with varying nickel content based on a) nickel as a fraction of total solids, and b) nickel as a fraction of the total composite volume. (Ni&Gr/YSZ and NiO&Gr/YSZ composite sample data is included for reference.)

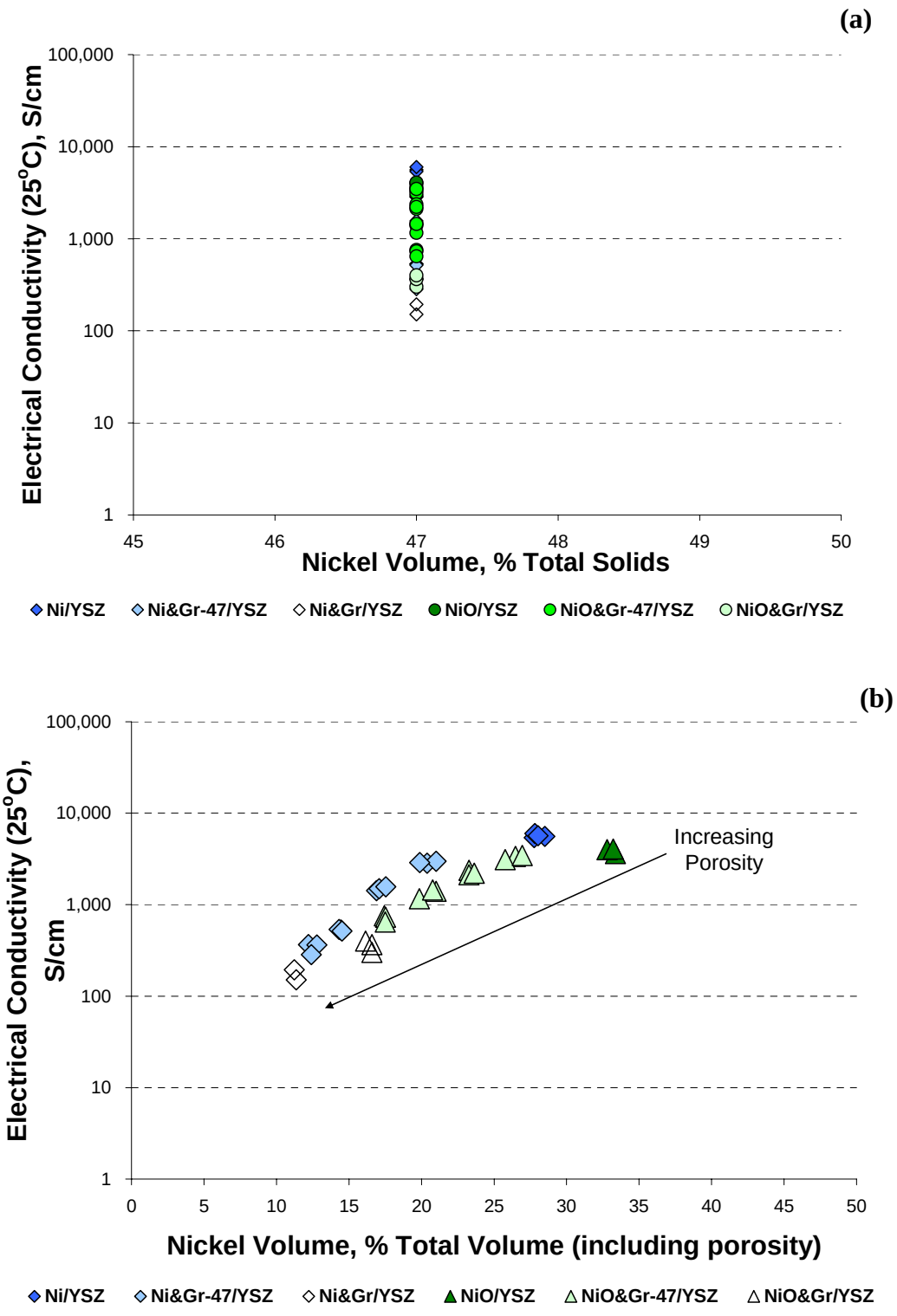

Figure 7-6: Measured electrical conductivities of Ni&Gr-47/YSZ and NiO&Gr-47/YSZ composite samples with a fixed nickel loading of 47 vol% Ni of total solids and varying graphite loadings plotted with respect to a) nickel as a fraction of total solids, and b) nickel as a fraction of the total composite volume. Electrical conductivity results for composite samples made from Ni/YSZ and NiO/YSZ with a similar nickel loading are also included for reference.

7.5 ELECTRICAL CONDUCTIVITY DISCUSSION

7.5.1 Composites with No Added Graphite

The electrical conductivity results for each of the composite types are plotted again in Figure 7-7 with respect to nickel as a fraction of the total solids. However, this time the upper bound represented by Equation (7-4) is also included:

$$\sigma_{comp} = V_h \sigma_h + V_l \sigma_l \tag{7-4}$$

This upper bound represents the maximum possible electrical conductivity that can be achieved in a composite where each phase is continuous and pore free (i.e. the parallel microstructure of Figure 7-1a). From Figure 7-7, the 100% Ni from Ni and 100% Ni from NiO samples have electrical conductivities that approach the expected maximum electrical conductivity. Conversely, the Ni/YSZ and NiO/YSZ composites have electrical conductivities that are much lower than the upper bound prediction, particularly at nickel loadings below 30 vol% Ni of total solids. However, above 30 vol% Ni of total solids, the electrical conductivity nears the upper bound prediction as the nickel volume increases. This suggests that, compared to a Ni/YSZ composite that is continuous and pore free, the electrical conductivity of the Ni/YSZ and NiO/YSZ composites can be improved significantly, particularly at lower nickel volume fractions. (Note: the electrical conductivity data for the other composite types will be discussed in more detail in the following sections.)

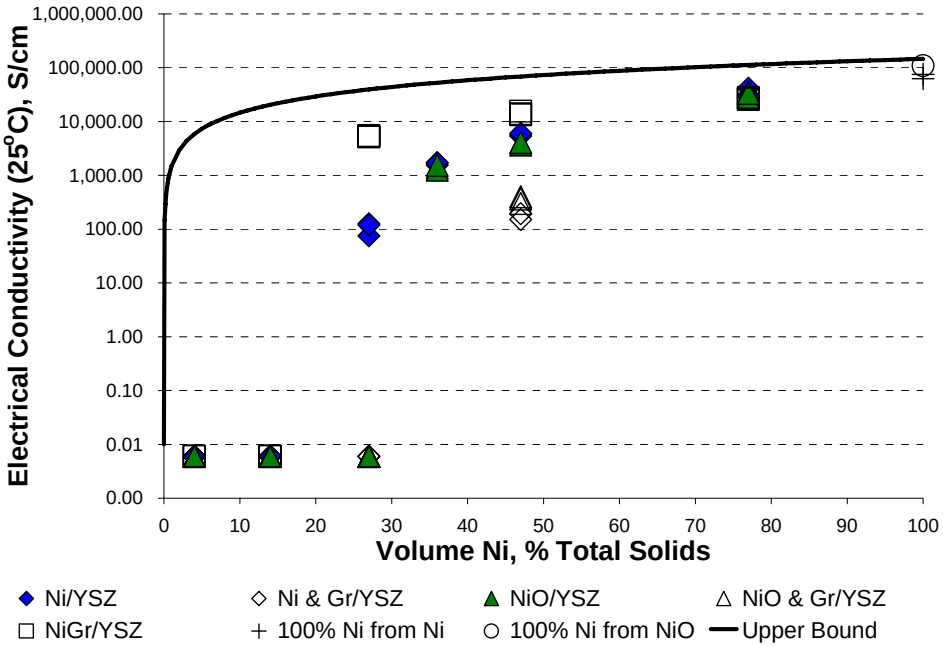

Figure 7-7: Electrical conductivity of Ni/YSZ, NiO/YSZ, Ni&Gr/YSZ, NiO&Gr/YSZ, and NiGr/YSZ composite samples with varying nickel content based on nickel as a fraction of total solids. The upper bound is given by Equation (7-4).

It is difficult to compare the composite electrical conductivity to the predicted electrical conductivity from the upper bound presented in Equation (7-4) because each composite sample has some degree of porosity (See Figure 5-87) which is not accounted for when conductivities are plotted with respect to the nickel loading as a volume fraction of total solids. For example, the 100% Ni sample made from Ni powder (100% Ni from Ni) and the 100% Ni sample made from NiO powder (100% Ni from NiO) have lower than expected electrical conductivities compared to the upper bound of Equation (7-4) (i.e. 69,000 S/cm and 109,000 S/cm respectively compared to the theoretical value of 146,200 S/cm). The lower electrical conductivities of both of these materials are due to the residual porosity.

Since electrical conductivity is a material property, the only way to improve the electrical conductivity of the pure nickel samples is to decrease the amount of porosity in each sample. Given that some porosity is necessary for an effective SOFC anode, eliminating porosity entirely is not an option for improving the composite electrical conductivity. Therefore, an improved estimation of the maximum electrical conductivity for a porous composite is represented by:

$$\sigma_{comp} = v_h \sigma_h + v_l \sigma_l + v_{pore} \sigma_{pore} \tag{7-8}$$

where v_h, v_l, and v_{pore} are now the volume fractions of the high conductivity phase, the low conductivity phase, and porosity as a fraction of the total composite volume respectively. Since air is a poor electrical conductor, the electrical conductivity of the porous phase, σ_{pore}, is assumed to be zero.

When taking porosity into account (i.e. by plotting the nickel volume as a fraction of the total composite volume in Figure 7-8), the 100% Ni from Ni and 100% Ni from NiO samples actually have an electrical conductivity that approaches the conductivity of pure nickel with a similar level of porosity as predicted by the new upper bound of Equation (7-8). The improved agreement between the new upper bound which includes porosity and the 100% Ni from Ni and 100% Ni from NiO sample conductivities is depicted in Figure 7-8 where the electrical conductivity results for the different composite types are re-plotted with respect to nickel as a fraction of the total volume. Similarly, the Ni/YSZ and NiO/YSZ composites with the highest nickel loading show electrical conductivities that approach the new upper bound indicating that these composites have nearly the optimal electrical conductivity for their respective porosity levels, unlike the composite samples with lower nickel loadings.

While the new upper bound accounts for the effect of porosity on electrical conductivity, it still assumes that each phase is continuous. For particulate composites, like the Ni/YSZ and NiO/YSZ composites, this is not true. Below the percolation threshold, the nickel is isolated by the surrounding YSZ matrix resulting in a very low electrical conductivity. As the nickel volume increases, the number of nickel particles in contact with each other also increases until a percolation path is formed. However just above the percolation threshold, there are a number of nickel clusters that may exist as "dead ends" or are simply not part of the percolation path (See Figure 2-2) and do not contribute to the electrical conductivity of the composite. As the nickel volume fraction is further increased, more and more clusters become part of the percolating path until eventually the nickel is fully connected and continuous. At this point, the porous composite has an electrical conductivity that is similar to the electrical conductivity predicted by the upper bound of Equation (7-8). This behaviour is exhibited by the electrical conductivity results for the Ni/YSZ and NiO/YSZ composites plotted in Figure 7-8. At nickel volume fractions below 20 vol% Ni of the total volume, the electrical conductivity of the Ni/YSZ and NiO/YSZ composites is very low. When the nickel volume fraction is between 20 vol%

and 40 vol%, the critical percolating volume fraction is surpassed and the electrical conductivity increases significantly as the nickel becomes fully connected, like the composite samples with nickel loadings of 45 vol% Ni of the total volume.

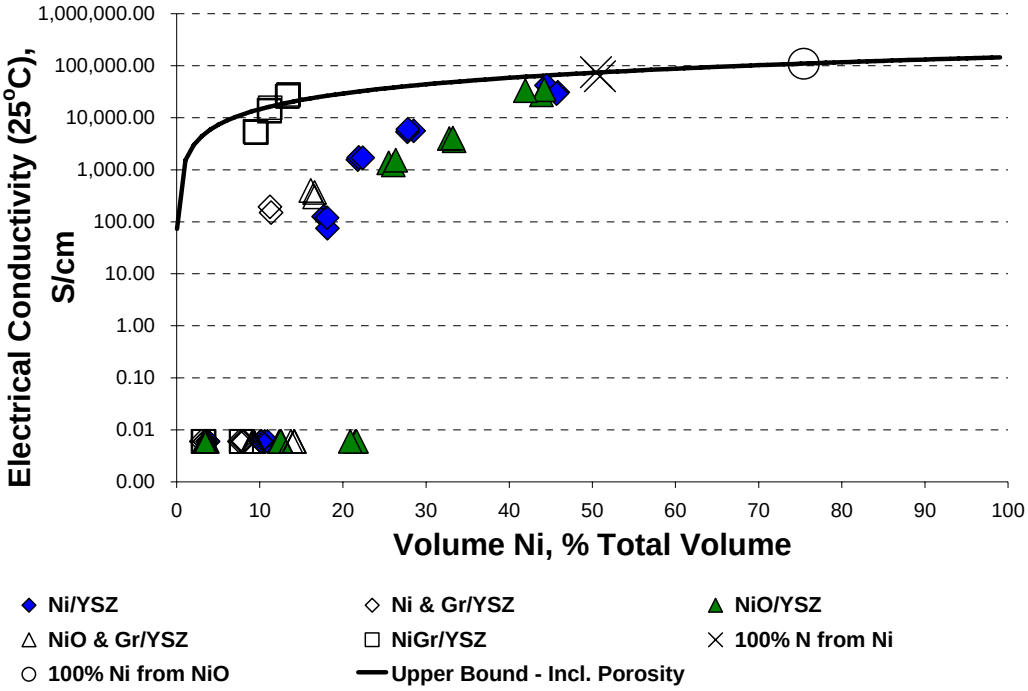

Figure 7-8: Electrical conductivity of Ni/YSZ, NiO/YSZ, Ni&Gr/YSZ, NiO&Gr/YSZ, and NiGr/YSZ composite samples with varying nickel content based on nickel as a fraction of the total composite volume in addition to the electrical conductivities of the 100% Ni from Ni and 100% Ni from NiO samples. The upper bound including porosity is given by Equation (7-8).

By using McLachlan's model for nickel loadings above the percolation threshold (i.e. Equation (7-6)), further comparisons of the average electrical conductivities of the various composite types are possible. A reasonable fit of McLachlan's model to the Ni/YSZ and NiO/YSZ composite electrical conductivity data is shown in Figure 7-9. From this model, the Ni/YSZ composites are superior electrical conductors to the NiO/YSZ composites because they have a lower critical volume fraction ($V_c = 0.175$, $t = 1.5$) versus ($V_c = 0.27$, $t = 1.0$) for the NiO/YSZ composites. That is, for a particular nickel loading above the Ni/YSZ composite percolation threshold the electrical conductivity is expected to be higher, compared to the electrical conductivity of the NiO/YSZ composites, because the nickel phase tends to be better connected.

The differences in the electrical conductivities between the Ni/YSZ and NiO/YSZ composites can be better understood by examining the changes in the microstructure from the green state to the sintered & reduced state. In order for a composite to have meaningful electrical conductivity, a nickel percolation network must be established in the green state. If the nickel loading in the composite is below the critical volume fraction ($\phi_c = 16\%$) then nickel clusters are isolated from one another and cannot sinter together to form a percolating network. Conversely, if the nickel loading is above the critical volume fraction then the nickel particles will sinter together and form a more highly connected nickel phase.

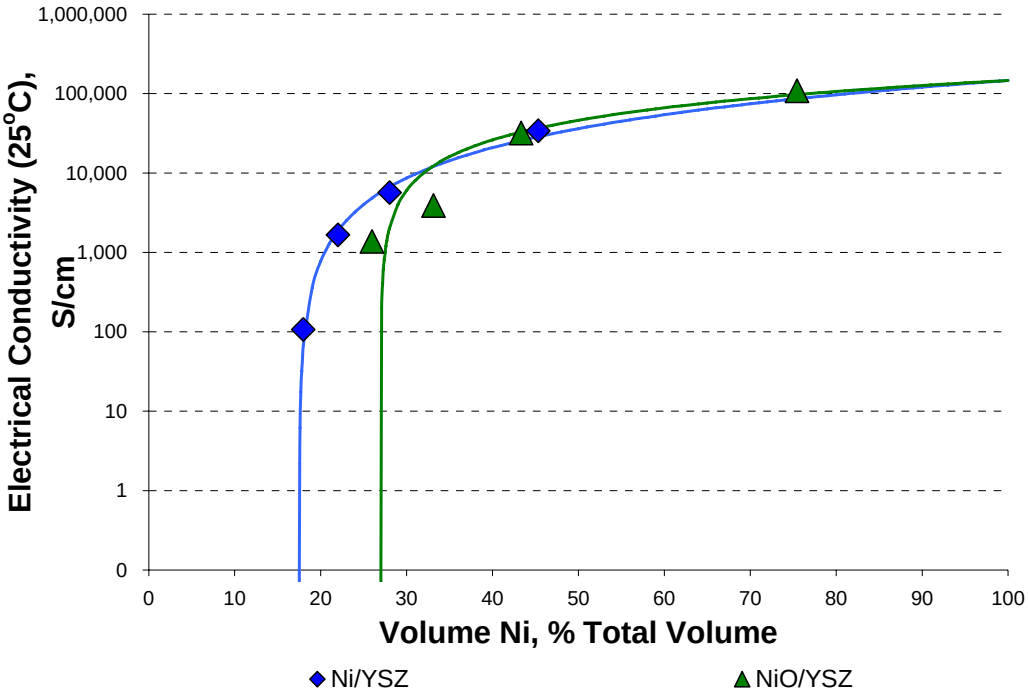

Figure 7-9: Average electrical conductivity as a function of nickel volume percent of total volume. The solid lines represent the fit of McLachlan's model (Equation (7-6)) to the Ni/YSZ, NiO/YSZ, and NiGr/YSZ electrical conductivity data.

The bulk packing density (Equation (5-3)) can be modified to calculate the bulk packing of the nickel (oxide) particles by dividing the nickel (oxide) volume by the total green volume. That is:

$$\rho_c^b = \frac{Volume\ of\ Ni(O)}{V_T - Volume\ of\ PFA} \times 100\% \qquad \textbf{(7-9)}$$

Since no pore forming agents are added to the Ni/YSZ and NiO/YSZ composites, the Volume of PFA is zero. The results of this calculation for the Ni/YSZ composites using the measured nickel volumes and the measured nickel oxide volumes in the green state for the NiO/YSZ composites are plotted in Figure 7-10.

The nickel (oxide) bulk packing density predictions compare favourably to the electrical conductivity results of Figure 7-7 and Figure 7-8 where the composites below a nickel loading of 14 vol% Ni of total solids do not conduct electricity and the composites with a nickel loading above 47 vol% Ni do. The only discrepancies between the predictions of Figure 7-10 and the measured electrical conductivities are the Ni/YSZ composites at a nickel loading of 27 vol% Ni of total solids have a significant electrical conductivity despite not reaching the critical volume fraction of nickel in the green state, while the NiO/YSZ composites with a similar nickel loading do not conduct electricity despite having a nickel oxide loading above 16% of the total composite volume.

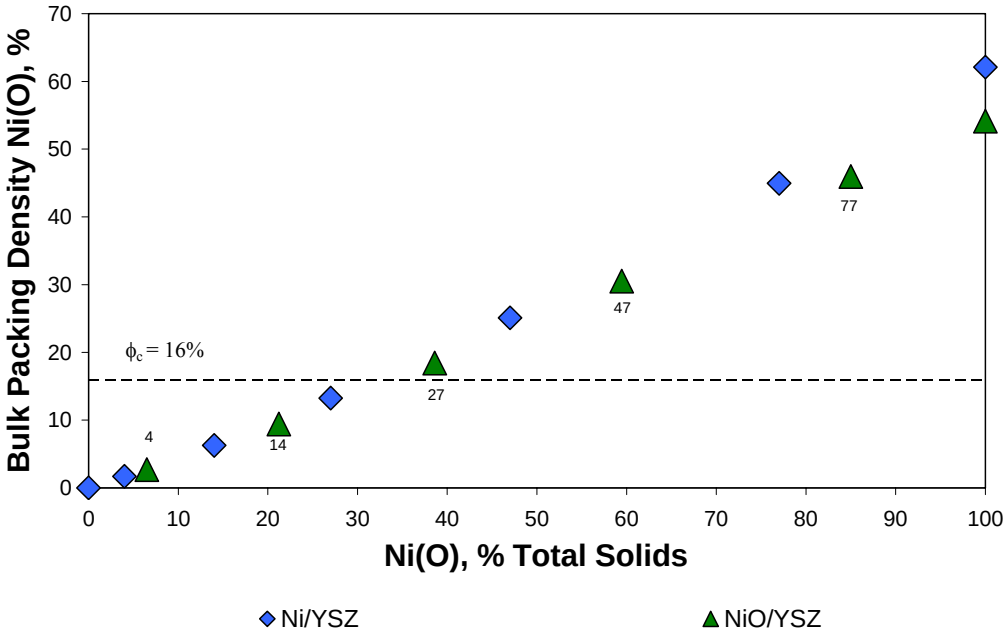

Figure 7-10: The nickel and nickel oxide bulk packing densities are calculated for the Ni/YSZ and NiO/YSZ composites. The numbers under the NiO/YSZ composite data points represent the equivalent nickel loading as a fraction of total solids and the dashed line represents the critical volume fraction for percolation.

The differences in the predicted electrical conductivity for the Ni/YSZ and NiO/YSZ composites at a nickel loading of 27 vol% can be attributed to the oxidation and reduction of the nickel phase during the burnout and reduction stages. In the green state, the volume fraction of nickel in the Ni/YSZ composite is lower than the volume fraction of nickel oxide powder in the NiO/YSZ composite. However, in the oxidized state, the volume of nickel oxide may be sufficient to form a percolating network in the Ni/YSZ composite thus allowing neighbouring nickel oxide particles to sinter together during the sintering stage and improve inter-particle contact. The NiO/YSZ composites on the other hand have limited volumetric shrinkage during the burnout stage due to the constraining effect of the YSZ powder and the strength of the particle-to-particle contact is diminished (See Figure 6-1). During the reduction stage, the volume of nickel decreases. Since the reduction of the nickel volume is restrained by the YSZ phase, poorly connected nickel oxide particles may detach from one another as they shrink. For the NiO/YSZ particles, generally having a less connected nickel network compared to the Ni/YSZ composites (See Figure 7-7), the reduction of the nickel oxide may cause the percolating network to fracture. (Evidence of this effect is given in Appendix G, where the percolation threshold and electrical conductivity of NiO/YSZ and Ni&Gr/YSZ composites changed depending on the degree of nickel reduction.) Conversely, the contacts between the nickel particles in the Ni/YSZ composite may have adequate strength to withstand the change in volume as the nickel reverts back to its original state. With enough bonding between the nickel particles, the nickel percolation network is maintained and the composite conducts electricity.

7.5.2 NiGr/YSZ Composites

When examining the electrical conductivity of the NiGr/YSZ composites presented in Figure 7-7, it appears as though the electrical conductivity is slightly higher than the electrical conductivities of the Ni/YSZ and NiO/YSZ composites at nickel loadings above 45 vol% Ni of total solids, and is significantly higher at a nickel loading of 27 vol% Ni of total solids. However, when porosity is accounted for, the electrical conductivity of the NiGr/YSZ composites is far superior to the other composite types, as shown in Figure 7-8, even though the porosity is significantly higher in the NiGr/YSZ composites (See Figure 5-88). Once the nickel percolation threshold is reached, the electrical conductivity of the NiGr/YSZ composite samples quickly approaches the electrical conductivity predicted by the upper bound of Equation (7-8) indicating that the nickel forms a fully connected 3-D network.

In the green state, nickel is present as a continuous coating on a graphite core. However during subsequent processing, the graphite core is removed but the nickel shell remains (See Figure 5-108). Since the nickel forms a continuous shell, it is able to occupy a larger "effective" volume (i.e. the nickel volume plus the volume of the former graphite core), compared to a solid nickel particle with the same mass, while still effectively conducting electricity. Furthermore, the porosity created by the graphite is encapsulated by the nickel shell minimizing the disruption to the nickel phase.

As a result, less nickel is required to occupy a given composite volume when NiGr particles are used instead of similar sized solid particles thus reducing the critical percolation volume fraction. The lower critical percolation volume fraction, despite the larger NiGr particle size (d_{avg} = 133 μm), is evident when examining Figure 7-11 where the electrical conductivity data for the NiGr/YSZ composites is plotted with respect to the actual nickel volume and the corresponding effective nickel volume as a percentage of total solids. That is, the electrical conductivity data for the NiGr/YSZ composites is plotted with the actual volume fraction of nickel and the predicted volume fraction of nickel if solid particles of similar size to the NiGr particles were used. Clearly, using larger sized solid particles leads to the greatest critical percolating volume fraction.

For comparison, McLachlan's model is also fit to the NiGr/YSZ composite electrical conductivity data (V_c = 0.08, t = 0.7), shown in Figure 7-12. Again, the NiGr/YSZ composites demonstrate the best electrical conductivity results having the lowest critical percolation volume fraction and high electrical conductivities at low nickel volume fractions compared to the Ni/YSZ and NiO/YSZ composites.

7.5.3 Composites with Separate Graphite Additions

Upon inspection of Figure 7-4 and Figure 7-6, the graphite containing composites (Ni&Gr/YSZ and NiO&Gr/YSZ) show inferior electrical conductivities compared to the graphite-free Ni/YSZ and NiO/YSZ composites at comparable nickel loadings. The Ni&Gr/YSZ composites do not conduct electricity until the nickel loading reaches 47 vol% Ni of total solids, whereas the Ni/YSZ composites begin to conduct at a nickel loading of 27 vol% Ni. Even at a nickel loading of 47 vol% Ni, the electrical conductivity of the Ni&Gr/YSZ composites is much lower than the electrical conductivity of the Ni/YSZ composite with the same nickel content. Similarly, the NiO&Gr/YSZ and NiO/YSZ composites both conduct electricity at nickel loadings of at least 47 vol% Ni but the electrical conductivity of the NiO&Gr/YSZ composites is much lower. From these results, it appears that increasing the composite porosity by adding graphite reduces the composite electrical conductivity and increases the percolation threshold.

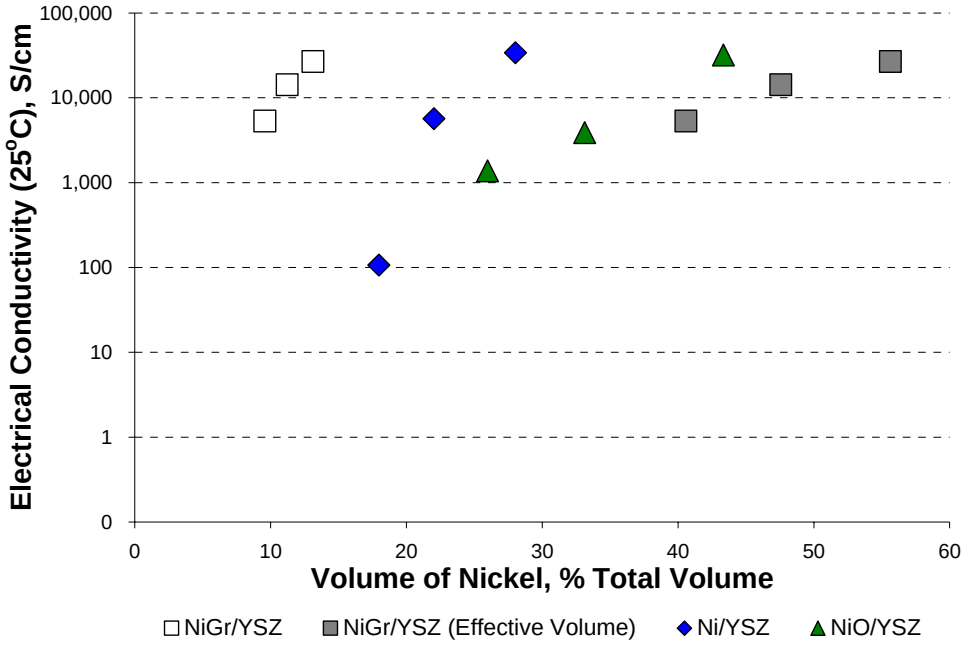

Figure 7-11: Electrical conductivity of Ni/YSZ composites in comparison to the effective nickel volume. Data for the Ni/YSZ and NiO/YSZ composites are included for reference.

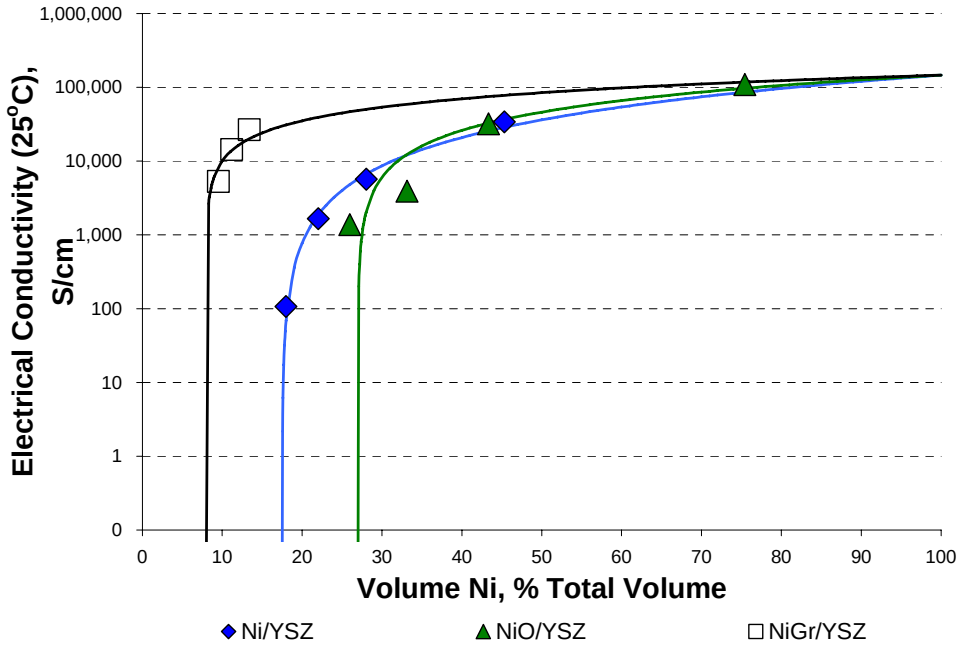

Figure 7-12: Average electrical conductivity as a function of nickel volume percent of total volume. The solid lines represent the fit of McLachlan's model (Equation (7-6)) to the Ni/YSZ, NiO/YSZ, and NiGr/YSZ electrical conductivity data.

The percolation of conductive nickel particles through a porous composite is established by the dispersion of the powders in the green state. Therefore, a conceptual model representing the composite microstructure in the green tape, shown in Figure 7-13, is useful in explaining the electrical conductivity results presented in Figure 7-4 and Figure 7-6. Figure 7-13a depicts the particle packing arrangement of equally sized spherical powders for a Ni/YSZ composite with no graphite additions. Also included in Figure 7-13 is a single percolating path of nickel that leads to electrical conduction indicating that this structure has a nickel loading just above the critical percolation threshold.

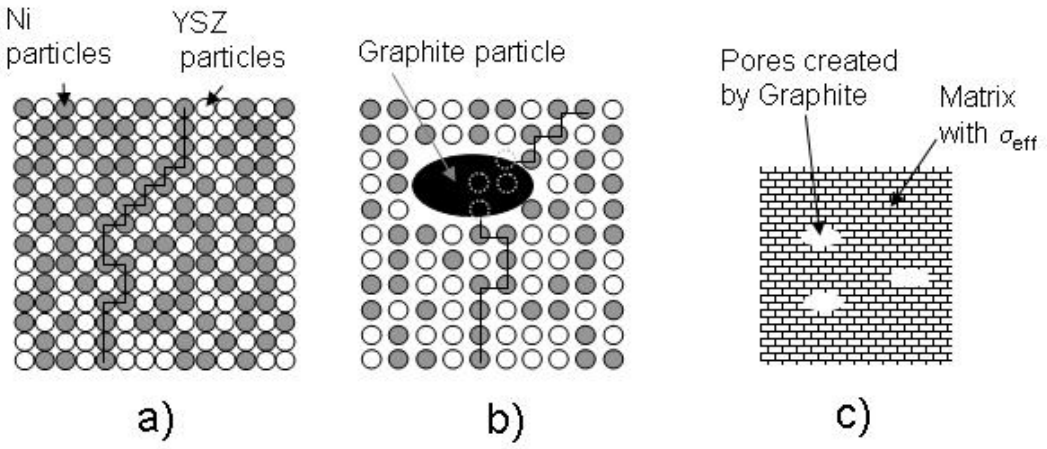

Figure 7-13: Conceptual model depicting the green microstructure of a) Ni/YSZ composite, b) Ni&Gr/YSZ composite, and c) a fully sintered and reduced Ni&Gr/YSZ composite

The influence of graphite additions on the Ni/YSZ composite structure can be visualized in the following manner. When graphite is added to the graphite-free Ni/YSZ composite structure (See Figure 7-13b) a small volume of the "matrix" or effective medium consisting of the nickel and YSZ particles is removed and replaced by the graphite particle. With this approach, when the graphite particles are much larger (d_{avg} = 77 μm) than the nickel and YSZ powders (d_{avg} = 17.7 μm and d_{avg} = 1.74 μm respectively), it is reasonable to assume that the packing of the nickel and YSZ is unaffected. However as described in Section 5.1.4, additional binder and plasticizer is added with the graphite powder when preparing the tape casting slurries. This extra polymer material distributes itself throughout the Ni/YSZ structure thereby diluting the packing density of the nickel and YSZ particles as indicated schematically in Figure 7-13b and plotted in Figure 5-8 and Figure 5-10.

Like the Ni/YSZ and NiO/YSZ composites, the bulk packing density of the nickel (oxide) phase can be calculated using Equation (7-9) and the results are plotted in Figure 7-14 and Figure 7-15. Clearly the addition of graphite reduces the bulk packing density of the nickel and nickel oxide phases. Consequently, the Ni/YSZ composites with a nickel loading of 27 vol% Ni of total solids are no longer able to conduct electricity once graphite is added. Since more nickel is required to form a percolating network within the Ni&Gr/YSZ composites, the percolation threshold increases. It should be noted that the Ni&Gr-47/YSZ composites still show a significant electrical conductivity, despite having a nickel bulk packing density below 16%, because of the oxidation and reduction of the nickel phase during the burnout and reduction stages as described in Section 7.5.1.

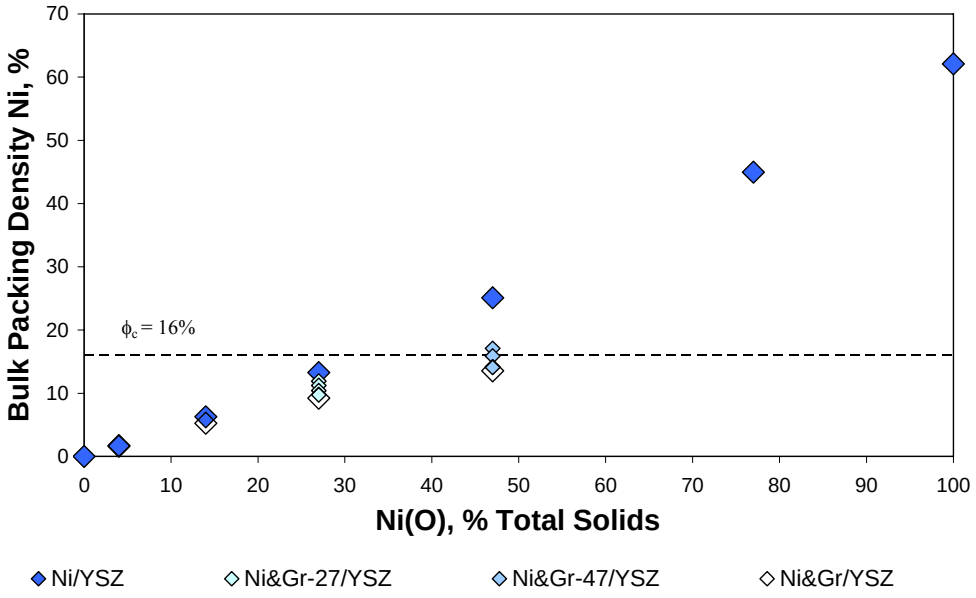

Figure 7-14: The nickel bulk packing densities are calculated for the Ni/YSZ, Ni&Gr/YSZ, Ni&Gr-27/YSZ, and Ni&Gr-47/YSZ composites. The dashed line represents the critical volume fraction for percolation.

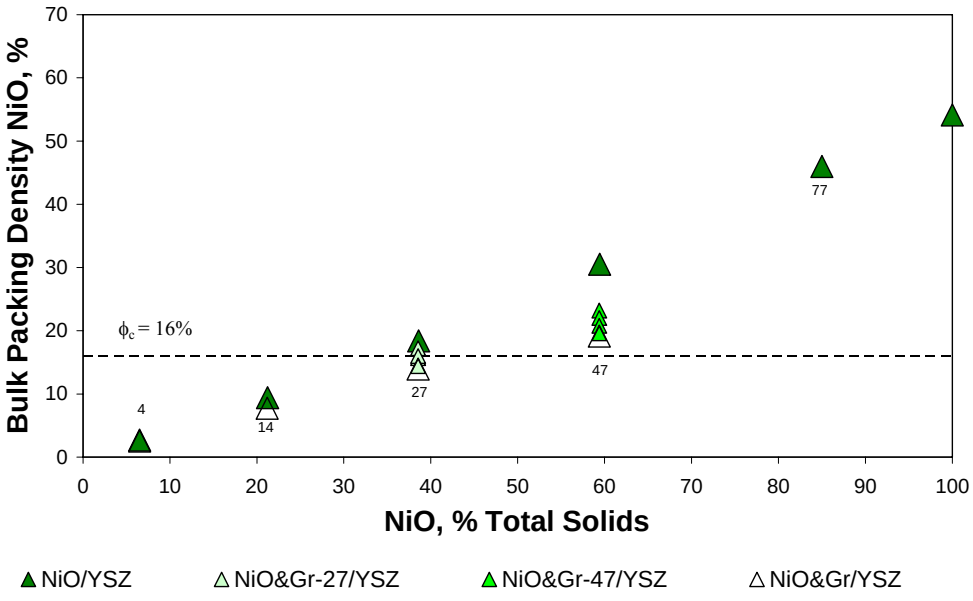

Figure 7-15: The nickel oxide bulk packing densities are calculated for the NiO/YSZ, NiO&Gr/YSZ, NiO&Gr-27/YSZ, and NiO&Gr-47/YSZ composites. The numbers under the NiO /YSZ composite data points represent the equivalent nickel loading as a fraction of total solids and the dashed line represents the critical volume fraction for percolation.

In addition to the dilution of the nickel phase due to the addition of graphite, the reduction in electrical conductivity in the Ni&Gr/YSZ and NiO&Gr/YSZ composites may be attributed to the graphite interrupting or preventing the formation of a percolating network, as illustrated in Figure 7-13b. As more graphite is added, more percolating paths may be interrupted and the electrical conductivity of the composite decreases. To document the importance of this effect, a calculation of an upper bound electrical conductivity can be compared to the experimentally determined electrical conductivity.

An upper bound for the composite structure of Figure 7-13b can be developed by first considering the graphite-free Ni/YSZ composite as an "effective medium" with a particular electrical conductivity, σ_{eff}, associated with its nickel content. For example, the Ni/YSZ composite with a nickel loading of 47 vol% Ni of total solids has a measured electrical conductivity of 5668 S/cm. It is important to note that this composite is also 40% porous due to incomplete sintering and the reduction of nickel oxide to nickel metal. (See Figure 5-107 for the sintered and reduced microstructure). However, adding graphite to the composite structure creates larger scale porosity that is dispersed throughout the effective medium as shown in Figure 7-13c. Although it is difficult to image this porosity, particularly at higher graphite loadings, the best example of this dispersion of porosity is given in Figure 5-112 through Figure 5-115. The upper bound of a porous composite structure due to graphite additions is calculated as:

$$\sigma_{comp} = V_{eff}\sigma_{eff} + V_{pore}\sigma_{pore} \qquad \textbf{(7-10)}$$

where σ_{comp}, σ_{eff}, and σ_{pore} are the electrical conductivities of the porous composite, effective medium (or matrix), and pores created by the graphite respectively, and V_{eff} and V_{pore} are the volume fractions of the effective medium and porosity. Assuming $\sigma_{pore} = 0$ and $V_{eff} = (1-V_{pore})$, Equation (7-10) simplifies to:

$$\sigma_{comp} = (1 - V_{pore})\sigma_{eff} \qquad \textbf{(7-11)}$$

The inherent assumption of Equations (7-10) and (7-11) is the addition of graphite (and the pores it creates) does not influence the packing arrangement of the particles within the Ni/YSZ matrix or reduce the contribution of the nickel phase to the total percolating network despite the elimination of some nickel (and YSZ) from the total bulk composite volume.

Other upper bound predictions for the electrical conductivity of porous solids, proposed by other researchers, may be generalized as follows [91,92,93]:

$$\sigma_{comp} = (1 - V_{pore})^{x}\sigma_{eff} \qquad \textbf{(7-12)}$$

where the exponent, x, can range from 1.5 to 3. Equation (7-12) is also based on the same assumption regarding the percolation of the nickel phase within the remaining effective medium as Equations (7-10) and (7-11).

More recently, Wu and Liu [93] developed a model that attempts to account for the effect porosity has on the continuity of the conducting phase. The model, given by Equation (7-13), is based on a composite having three phases: a low conductivity phase (phase 1), a high conductivity phase (phase 2), and porosity (phase 3), and predicts the influence porosity has on the percolation threshold in addition to the electrical conductivity of the composite beyond this threshold:

$$\sigma_{comp} = \frac{F_1 + \sqrt{(F_1^2 + F_2)}}{4} \tag{7-13}$$

where

$$F_1 = 3(p_1\sigma_1 + p_2\sigma_2) - (\sigma_1 + \sigma_2)$$

$$F_2 = 4\sigma_1\sigma_2\left[3(p_1 + p_2) - 1\right]$$

with p_1, σ_1 and p_2, σ_2 representing the volume fractions and electrical conductivity of the low and high electrically conducting phases respectively and with $p_1 + p_2 + p_3 = 1$ where p_3 is the volume fraction of porosity. It should be noted that Wu and Liu indicate that this equation is valid when p_3 is less than 0.66.

The composite electrical conductivities as predicted by Equation (7-11) through Equation (7-13) are plotted in Figure 7-16 along with the experimentally measured electrical conductivities for the Ni&Gr-47/YSZ series of composites with respect to the increase in porosity due to graphite additions. It is important to note the distinction between ($1\text{-}V_{pore}$), in Figure 7-16 (and Figure 7-17), and p_3 in Equation (7-13). The term ($1\text{-}V_{pore}$) represents the increase in porosity from the addition of graphite to the "effective medium" or graphite-free composite (i.e. Ni/YSZ), whereas p_3 represents the total composite porosity. In order for Equation (7-13) to be valid, the porosity in the graphite-free composite plus the additional porosity from the graphite additions must not exceed 0.66 meaning ($1-V_{pore}$) must be greater than 0.34. For the Ni&Gr-47/YSZ composites, Equation (7-13) can only be calculated for the composites with a graphite loading less than 18 vol% Gr in the green volume otherwise the total composite porosity will exceed 66%.

Clearly the measured electrical conductivities are much lower than the upper bound predictions of Equations (7-11) and (7-12). This indicates that graphite additions indeed reduce the degree of percolation of the nickel phase within the composite matrix as illustrated in Figure 7-13b. However, this effect is not as pronounced as that predicted by Wu and Liu where none of the Ni&Gr-47/YSZ composites are expected to exceed the nickel percolation threshold. The overestimation of the porosity effects on the continuity of the nickel phase is likely associated with the scale of the porosity compared to the size of the low conducting and high conducting phases. Wu and Liu's model represents the composite as a three-dimensional array of electrical resistors that does not consider the shape and size of the composite phases but assumes that the phases are randomly and evenly distributed throughout the composite. Since the larger scale porosity produced by the graphite minimizes the disruption of the smaller sized nickel particles, the composite electrical conductivity predicted by Wu and Liu's model (based on similar sized conducting and porous phases) represents a lower bound.

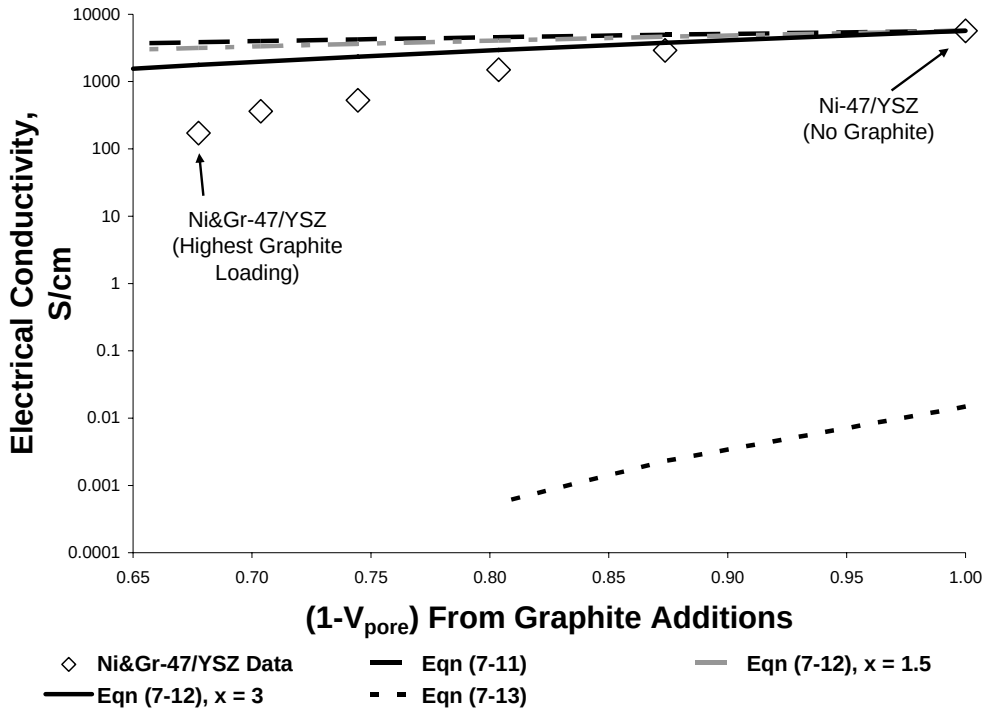

Figure 7-16: Measured electrical conductivity data for the Ni&Gr-47/YSZ composites and the corresponding electrical conductivity predictions based on Equation (7-11) through Equation (7-13).

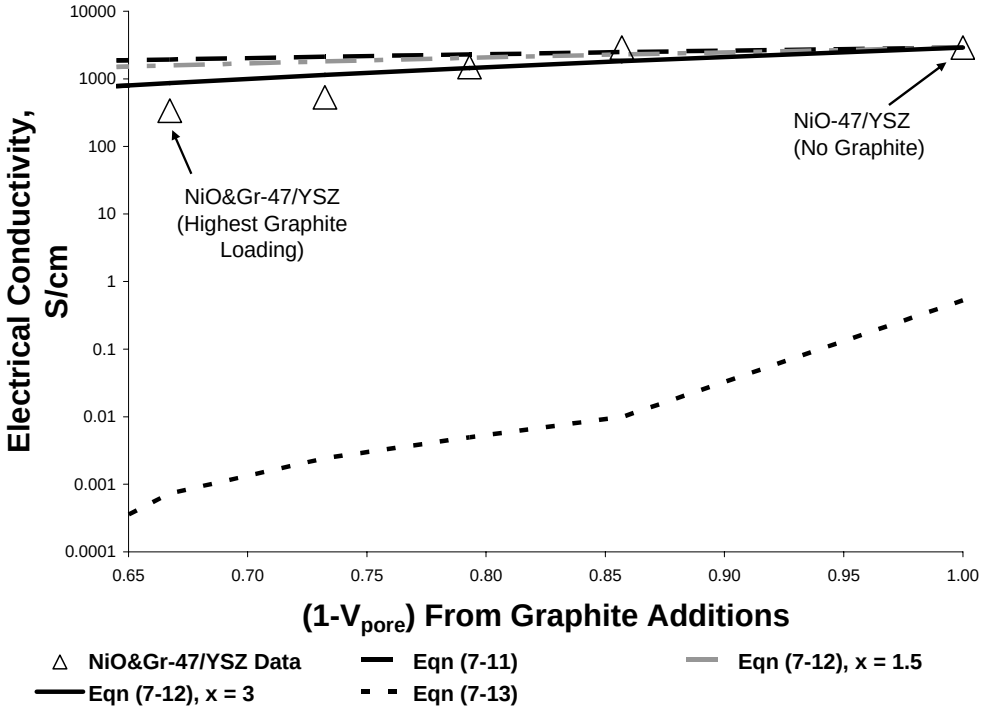

Figure 7-17: Measured electrical conductivity data for the NiO&Gr-47/YSZ composites and the corresponding electrical conductivity predictions based on Equation (7-11) through Equation (7-13).

Similar results are obtained when the above analysis is repeated for the NiO&Gr-47/YSZ composites, as shown in Figure 7-17. Since the total porosity of the NiO&Gr-47/YSZ composites does not exceed 65%, it possible to plot a wider range of electrical conductivity predictions using Equation (7-13). Unlike the Ni&Gr-47/YSZ composites, the electrical conductivity data for the NiO&Gr-47/YSZ composites better matches the upper bound predictions, particularly at lower porosity levels.

7.6 FUTURE EXPERIMENTS

It is important to note that the electrical conductivity results presented are dependent on the microstructures of the composites tested. The evolution of the microstructure is a function of the tape casting formulation, the nature of the particles used, and the burnout, sintering, and reduction heat treatments. Altering the heating schedules during burnout, sintering, or reduction may lead to a better understanding of how the processing stages affect the electrical conductivity Further improvements and insights into the electrical conductivity of porous composites may be achieved by altering some of the processing methods, specifically the types of particles used.

Currently, the YSZ powders are much finer than the nickel and nickel oxide powders. If the nickel and YSZ powders were more similar in size, the critical percolation volume fraction may be further reduced. This could lead to a further reduction in the amount of nickel required for adequate electrical conductivities in SOFC anodes. Similarly, using smaller NiGr particles or nickel powders with different shapes and morphologies, may lead to further improvements in the electrical conductivity of the composites.

Another significant area of research is related to the impact porosity has on the electrical conductivity. In this investigation, the graphite powders used to generate porosity were much larger than the nickel and YSZ powders. This leads to a dilution of the nickel and YSZ powders resulting in a decrease in the electrical conductivity and percolation threshold. Experiments could be conducted, using smaller graphite particles, to see if the size of the graphite particles added has a significant effect on the percolation and electrical conductivity characteristics of the composites. In addition, other pore forming agents, such as cornstarch and rice starch, could be investigated to determine their influence on the electrical conductivity.

CHAPTER 8:
COMPOSITE THERMAL EXPANSION BEHAVIOUR

8.1 THERMAL EXPANSION OF PURE MATERIALS

Typically, when a pure material is heated it is expected to expand due to the increased thermal energy of its atoms. As the internal temperature of the material rises, the average distance between atoms also grows causing an overall increase in the dimensions of the material. How much the material expands depends on the strength of its atomic bonds and its crystal structure. Generally metals and polymers, having relatively weak atomic bonds, will expand more readily when heated compared to ceramics which have stronger atomic bonds.

The expected degree of thermal expansion for a given material is expressed as a linear coefficient of thermal expansion, α. The coefficient of thermal expansion (CTE) is related to the change in the dimensions of the material and temperature as follows:

$$\alpha = \frac{l_f - l_o}{l_o(T_f - T_o)} = \frac{\Delta l}{l_o \Delta T} \qquad \textbf{(8-1)}$$

where l_o and l_f are the initial and final dimensions, and T_o and T_f are the initial and final temperatures [94]. It is important to note that the CTE for a given material may vary depending on the temperature conditions. Consequently, CTE values are given as an equation or quoted for a particular temperature range [94]. The coefficient of thermal expansion for nickel from 20°C to 900°C is 16.3 x 10^{-6} 1/K and the CTE for yttria-stabilized zirconia is 10.2 x 10^{-6} 1/K for a wide temperature range [24]. Other CTE values for YSZ, between 7.6 x 10^{-6} 1/K to 11.4 x 10^{-6} 1/K, are also given in the literature for unspecified compositions of yttria [66].

8.2 THERMAL EXPANSION OF COMPOSITES

The thermal expansion of a composite is quite different from the thermal expansion behaviour of a pure material because of the thermally induced stresses that develop when the constituent materials are joined together. For example, when a high CTE material is bonded to a low CTE material and heated together, as shown in Figure 8-1, the low CTE material constrains the normally large expansion of the high CTE material. This constraint of the materials induces a compressive stress within the high CTE material in addition to a tensile stress in the low CTE material. The magnitude of the thermally induced stresses is related to the operating temperature, the difference in the CTEs of the constituent materials, their proportions, and their elastic properties. If the thermal stresses are too great – due to a significant CTE mismatch – then the composite may crack and ultimately fail. For this reason, it is important to design the composite with materials having similar CTEs, particularly at extreme temperatures, to prevent premature failure of the composite due to thermal fatigue.

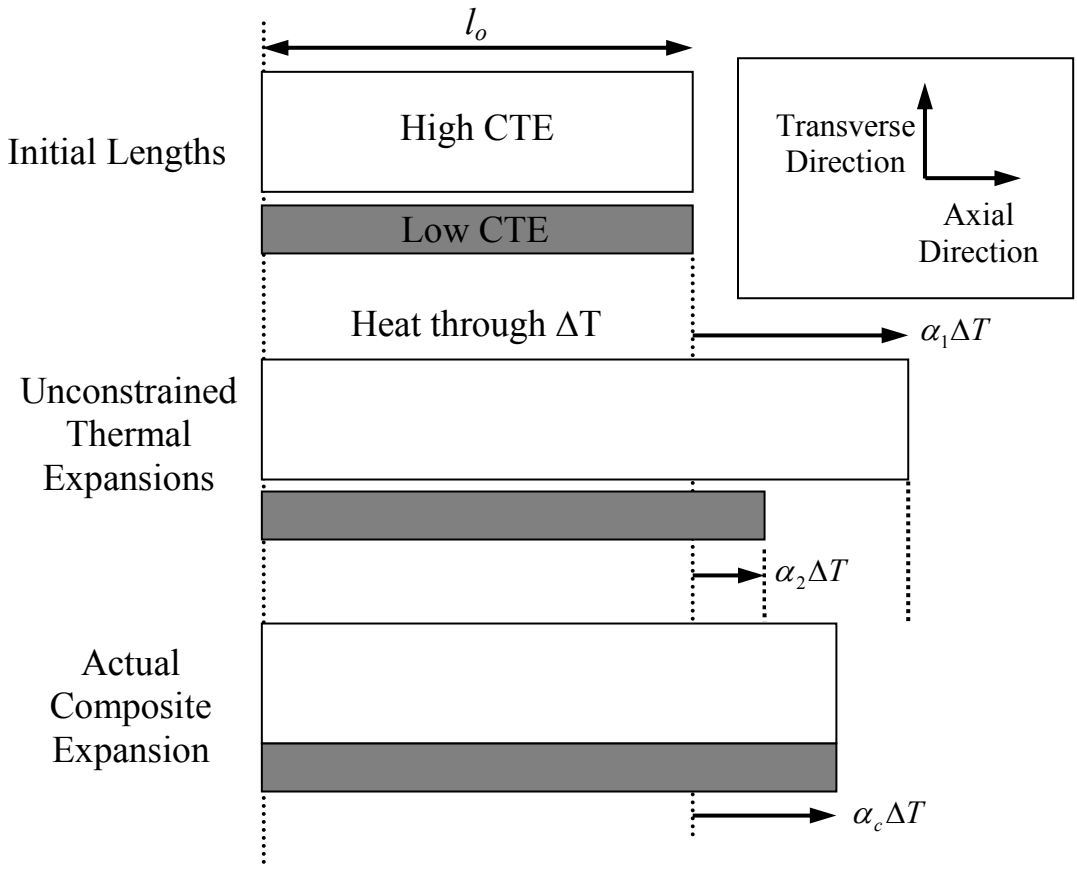

Figure 8-1: Schematic diagram depicting the thermal expansion of a composite and its unconstrained constituent materials in the axial direction [95]

From the induced thermal stresses and resultant thermal strains, the linear coefficient of thermal expansion of a composite in the axial direction, α^{ax}_c, (i.e. parallel to the direction shown in Figure 8-1) may be predicted by [95]:

$$\alpha_c^{ax} = \frac{\alpha_1 V_1 E_1 + \alpha_2 V_2 E_2}{V_1 E_1 + V_2 E_2} \tag{8-2}$$

where α, E, V, are the linear coefficient of thermal expansion, elastic modulus, and the volume fraction of materials 1 and 2 comprising the composite.

Similarly, the coefficient of thermal expansion in the transverse direction, α^{tr}_c, (i.e. perpendicular to the direction shown in Figure 8-1) as proposed by Schapery may be predicted by [96]:

$$\alpha_c^{tr} = \alpha_1 V_1 (1 + \nu_1) + \alpha_2 V_2 (1 + \nu_2) - \alpha_c^{ax} \nu_{12c} \tag{8-3}$$

where ν_1 and ν_2 are the Poisson ratios for material 1 and 2 respectively, α^{ax}_c is calculated from Equation (8-2), and the Poisson ratio, ν_{12}, is determined by a rule of mixtures for the Poisson ratios of the constituent materials. The linear coefficient of thermal expansion predicted by Equation (8-2) generally represents a lower bound on the CTE of the composite while Equation (8-3) represents an upper bound.

For pure porous materials, the CTE will be the same as the CTE of the fully dense material [95]. This is evident when calculating the CTE of the porous "composite" using Equation (8-2) (i.e. a composite made from pure material and pores). The composite CTE collapses to the CTE of the pure phase when the porosity stiffness is set to zero since pores do not have any stiffness.

Similarly, the upper and lower bounds of the composite CTE will differ considerably depending on the disparity between the elastic moduli and the Poisson ratios for each of the constituent materials. For instance, the CTE of a carbon/epoxy composite composed of varying amounts of carbon fibre (α = -0.7 x 10^{-6} 1/K, E = 380 GPa, and ν = 0.2) and epoxy (α = 60 x 10^{-6} 1/K, E = 4.5 GPa, ν = 0.39) is shown in Figure 8-2 [95]. Since the carbon fibre is significantly stiffer than the epoxy resin, thus increasing the constraining effect on the epoxy matrix, the axial CTE of the carbon/epoxy composite is dominated by the CTE behaviour of the carbon fibre. Similarly, the increased constraint of the epoxy matrix yields an increase in the transverse composite CTE.

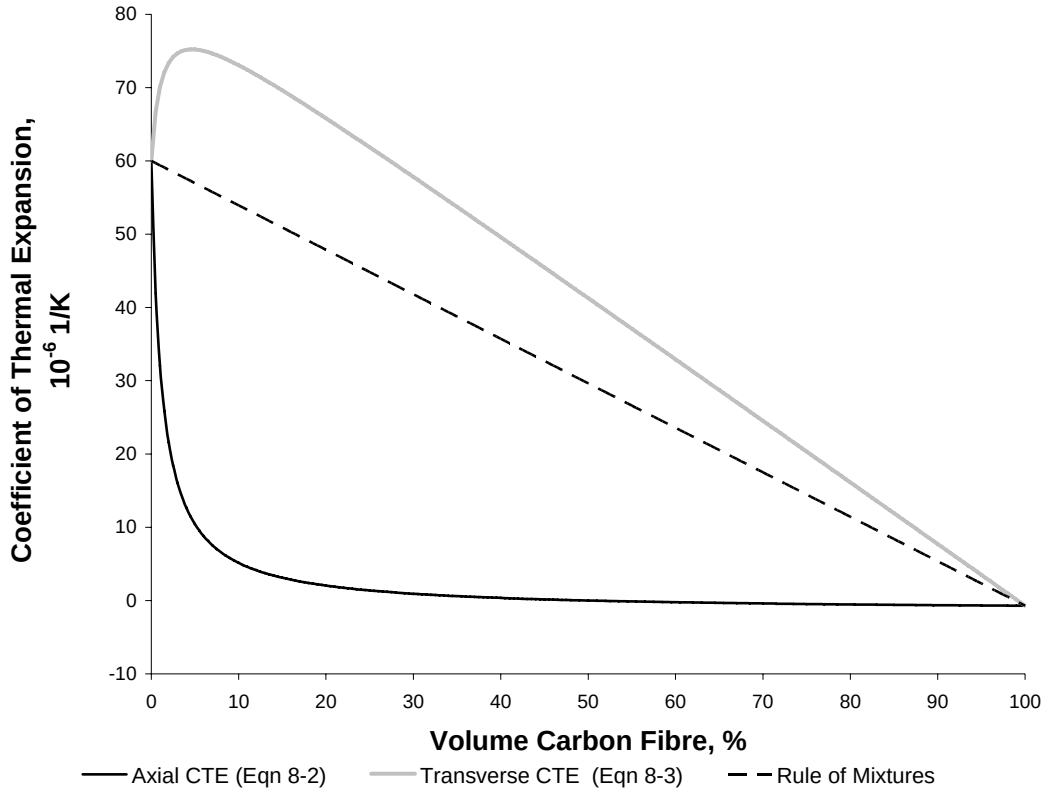

Figure 8-2: Predicted CTE behaviour of a carbon/epoxy composite based on Equations (8-2), (8-3), and the rule of mixtures prediction

On the other hand, the difference between the predicted composite CTEs in the axial and transverse directions for an aluminum/E-glass composite is quite minor, as illustrated in Figure 8-3, since aluminum (α = 25 x 10^{-6} 1/K, E = 70 GPa, ν = 0.33) and E-glass (α = 4.9 x 10^{-6} 1/K, E = 76 GPa, ν = 0.22) have similar elastic moduli [95]. The bowing out of the predicted upper and lower CTE bounds from the rule of mixtures prediction can be attributed to the differences in the Poisson ratios of the aluminum and E-glass.

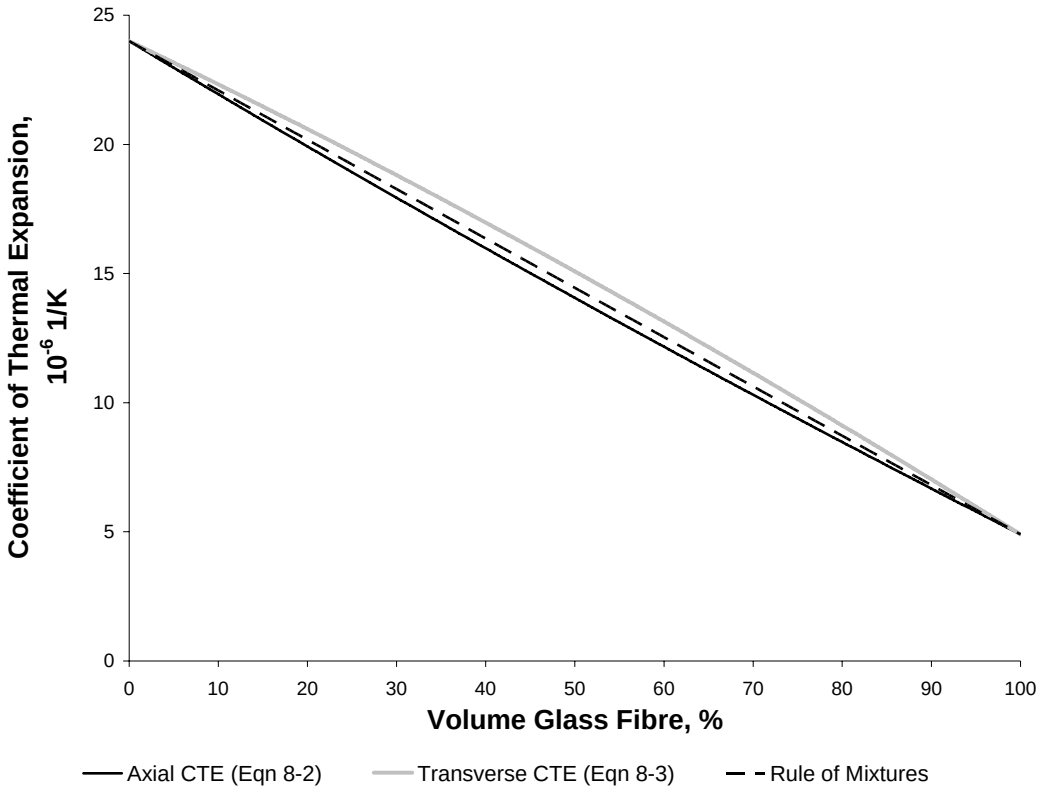

Figure 8-3: Predicted CTE behaviour of an aluminum/E-glass composite based on Equations (8-2), (8-3), and the rule of mixtures prediction

In fact, the rule of mixtures may be used to predict the coefficient of thermal expansion of a composite when the elastic modulus and Poisson ratio of the constituent materials are the same, as illustrated in Figure 8-4 [97]. Since the elastic properties of nickel (E = 197 GPa, ν = 0.31) and YSZ (E = 200 GPa, ν = 0.32) are nearly identical, it is reasonable to use the rule of mixtures to predict the CTE of Ni/YSZ composites as follows [66,98,99]:

$$\alpha_c = \alpha_{Ni} V_{Ni} + \alpha_{YSZ} V_{YSZ} \qquad \textbf{(8-4)}$$

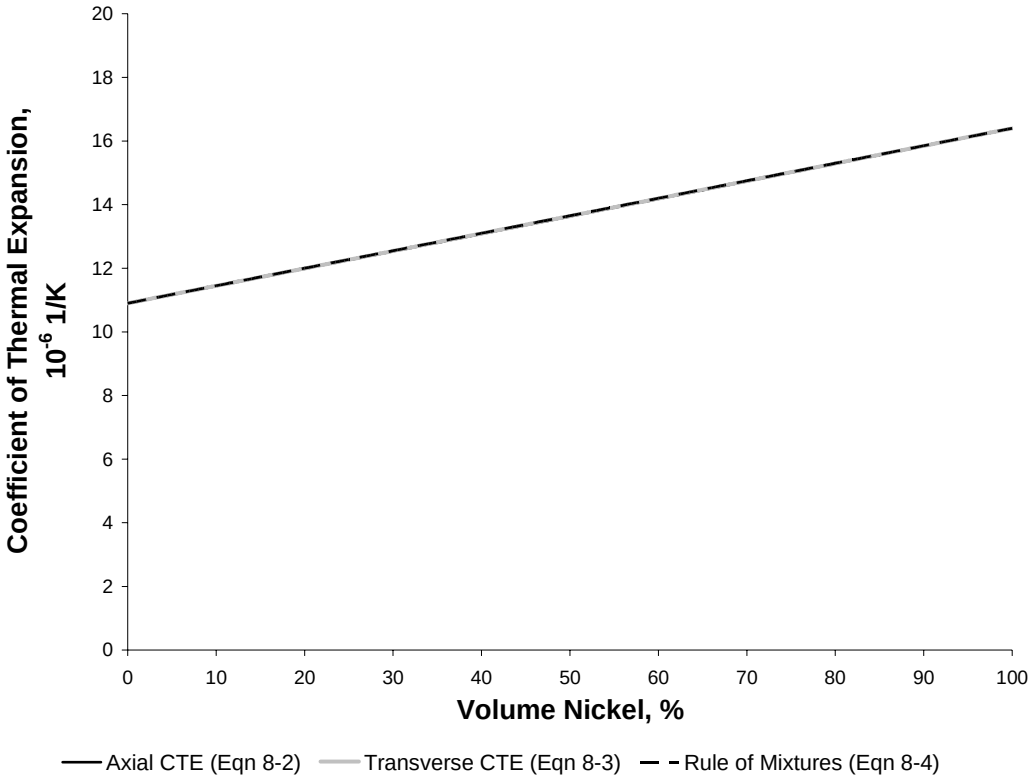

Figure 8-4: Predicted CTE behaviour of a nickel/YSZ composite based on Equations (8-2), (8-3), and (8-4)

8.3 THERMAL EXPANSION RESULTS

In order to measure the coefficient of thermal expansion of a sample of each composite type it was placed in a dilatometer and heated to 950°C at 10°C/min in a 10% hydrogen - 90% nitrogen atmosphere. To ensure a proper measurement, several heating cycles were repeated until a thermal expansion measurement matched the previous measurement. The "corrected" thermal expansion measurements for a 100% YSZ, 100% Ni from Ni, 100% Ni from NiO, and a Ni/YSZ composite with a nickel loading of 27 vol% Ni are plotted in Figure 8-5 through Figure 8-8. Typically, 3 to 7 cycles were needed to produce a repeatable measurement.

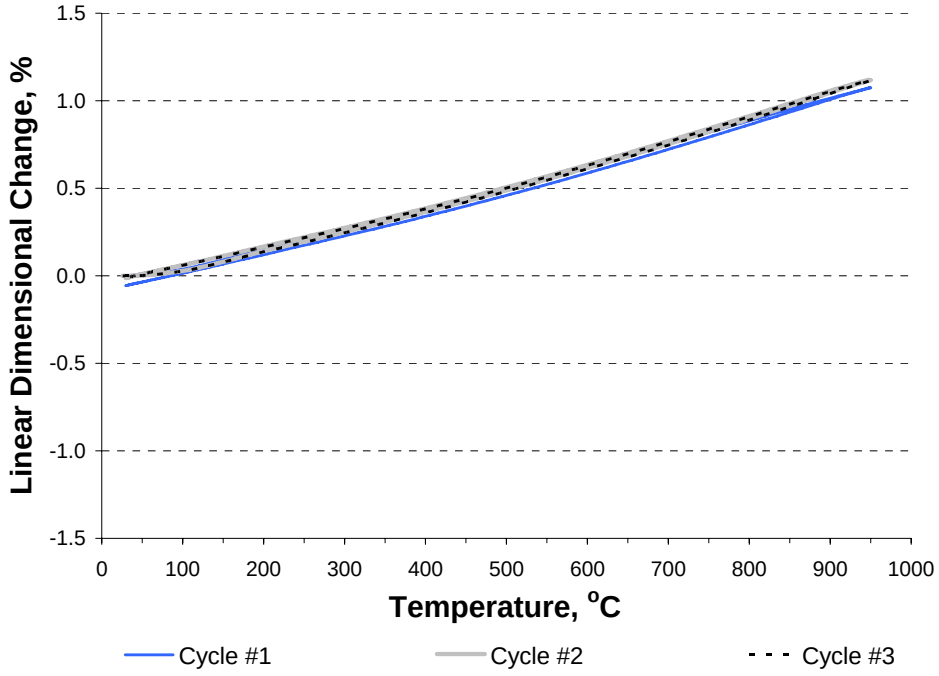

Figure 8-5: Thermal expansion plots of a 100% YSZ sample plotted with respect to temperature after several trials as measured by a dilatometer

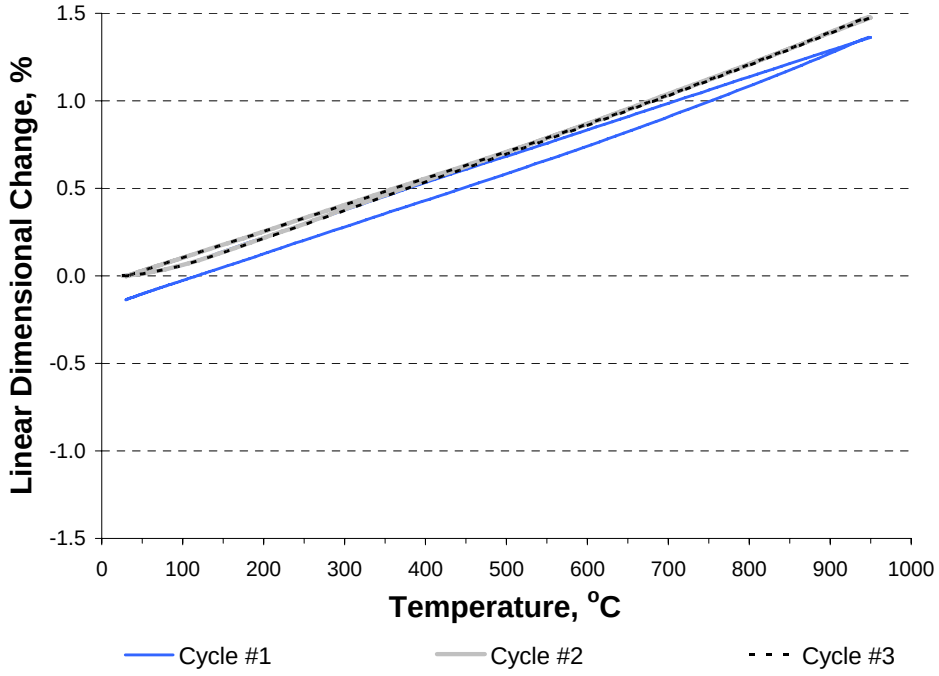

Figure 8-6: Thermal expansion plots of a 100% Ni from Ni sample after several trials as measured by a dilatometer

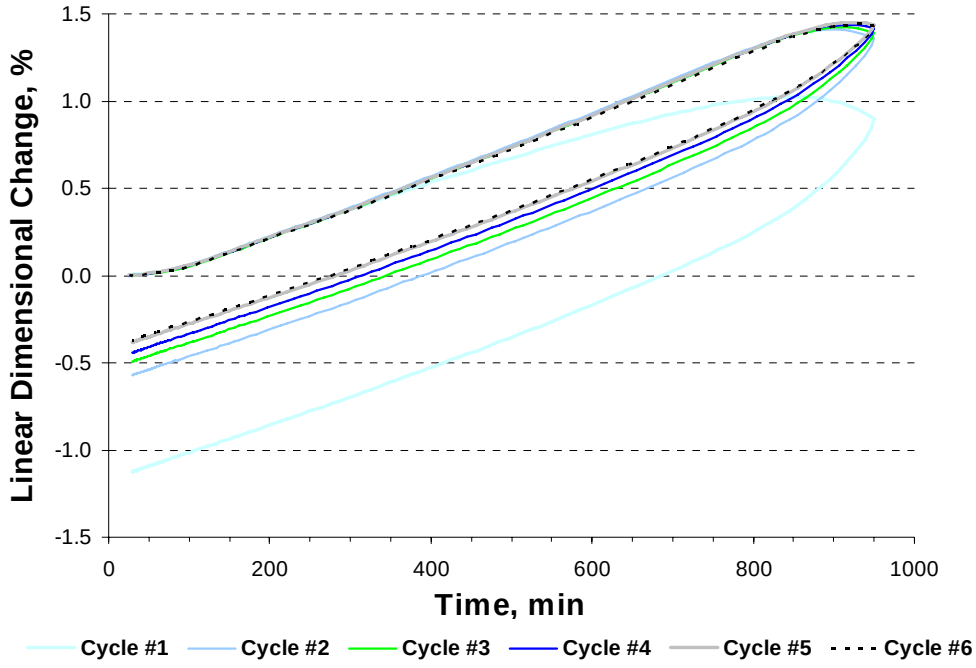

Figure 8-7: Thermal expansion plots of a 100% Ni from NiO sample after several trials as measured by a dilatometer

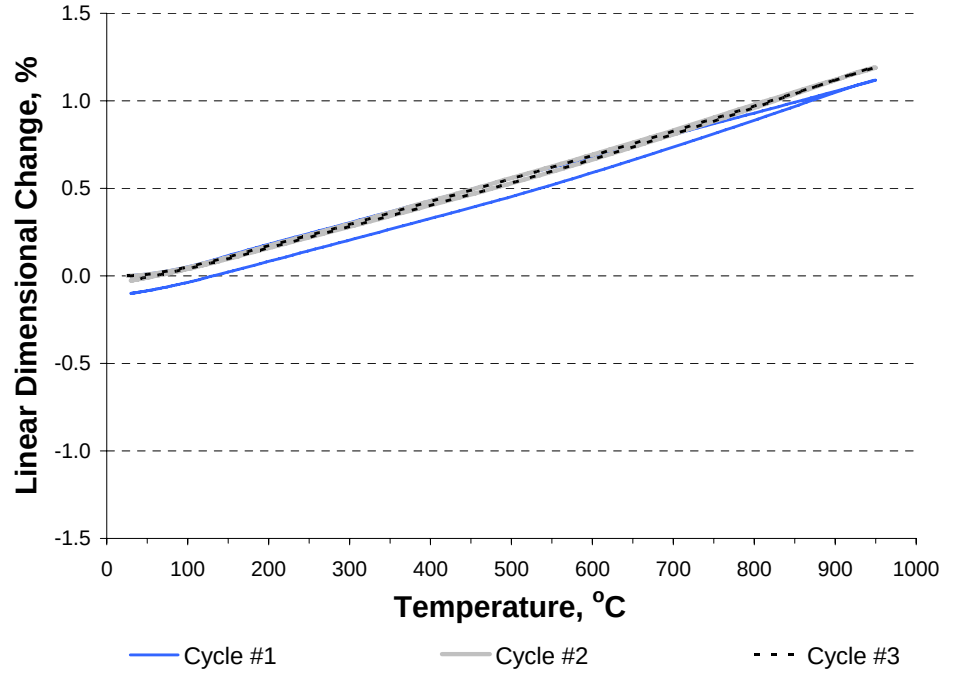

Figure 8-8: Thermal expansion plots of a Ni/YSZ sample with 27 vol% Ni of total solids after several trials as measured by a dilatometer. All other Ni/YSZ composite types showed similar behaviour with no hysteresis present after 3 to 5 cycles.

In general, the 100% YSZ, 100% Ni from Ni, and Ni/YSZ composite samples demonstrate the same thermal expansion tendencies. During the first heating cycle, the degree of expansion is not as great as subsequent cycles. Furthermore, there is a slight hysteresis upon cooling during the first cycle that is likely associated with the samples settling in the dilatometer, although the shrinkage may also be attributed to some residual sintering and/or nickel reduction. After the first heating cycle, the cooling hysteresis is negligible and the remaining thermal expansion measurements follow an identical path.

In contrast, the 100% Ni from NiO samples show a continued hysteresis during cooling for all six cycles. During the first heating cycle, the 100% Ni from NiO sample experiences a noticeable decrease in length from 900°C to 950°C, rather than the steady increase in length shown by the other samples (See Figure 8-7). Once the first cycle is complete, the 100% Ni from NiO has shrunk in length by over 1%. When heated again, the 100% Ni from NiO sample shows a levelling of the thermal expansion between 900°C and 950°C with each additional heating cycle and a gradual reduction in the amount of hysteresis during cooling to room temperature. Despite the final two cycles overlapping, there is still a significant amount of hysteresis when compared with the other composite samples. Although, some of the hysteresis may be attributed to the sample settling in the dilatometer and possibly some nickel reduction, the significant drop and subsequent levelling in the thermal expansion of the 100% Ni from NiO sample above 900°C suggests that some sintering is taking place.

Once suitable thermal expansion measurements were taken for each composite type, the linear coefficient of thermal expansion was calculated from Equation (8-1) using the thermal analysis software package delivered with the dilatometer. The linear coefficient of thermal expansion from 30°C to 950°C for each composite sample was determined by averaging the CTEs calculated from each of the two repeatable thermal expansion measurements. The final CTE results for each composite type are shown in Figure 8-9 through Figure 8-11 along with the predicted CTE from the rule of mixtures (ROM). To calculate the ROM, the measured CTE from a 100% YSZ sample (α_{YSZ} = 11.8 x 10^{-6} 1/K) and a 100% Ni from Ni sample (α_{Ni} = 16.2 x 10^{-6} 1/K) were used which are in reasonable agreement with the CTE values published in the literature. The measured CTE of a 100% Ni from NiO sample (α = 15.6 x 10^{-6} 1/K) is slightly lower than the published value despite it also consisting of pure nickel due to the persistent sintering effect observed above 800°C in Figure 8-7.

Overall, each of the composite samples demonstrated an increase in the measured CTE with increasing nickel content. The NiGr/YSZ composites, having the lowest CTE for a given nickel loading, show measured CTEs with the best agreement with the CTE predicted by the ROM. Conversely, the Ni&Gr/YSZ composites show the worst agreement because they have measured CTEs that are significantly higher than the ROM prediction. Moreover, the Ni&Gr/YSZ composites show the highest CTE of all the composite types for comparable nickel loadings. For the Ni/YSZ composite samples, the measured CTE tends to be slightly higher than the CTE predicted from the ROM for each nickel loading. The NiO/YSZ composites, on the other hand, show good agreement with the ROM below 20 vol% Ni of total solids but then show similar CTE values to the Ni/YSZ composite samples above this nickel loading. The CTE values are also in agreement with those published in the literature (See Section 2.3). Lastly, the NiO&Gr/YSZ composites have measured CTEs that tend to vary above and below the ROM prediction. It should also be noted that the thermal expansion behaviour of Ni&Gr/YSZ and NiO&Gr/YSZ composites with a nickel loading of 77 vol% Ni of total solids were not measured as they were too fragile because of their high porosity.

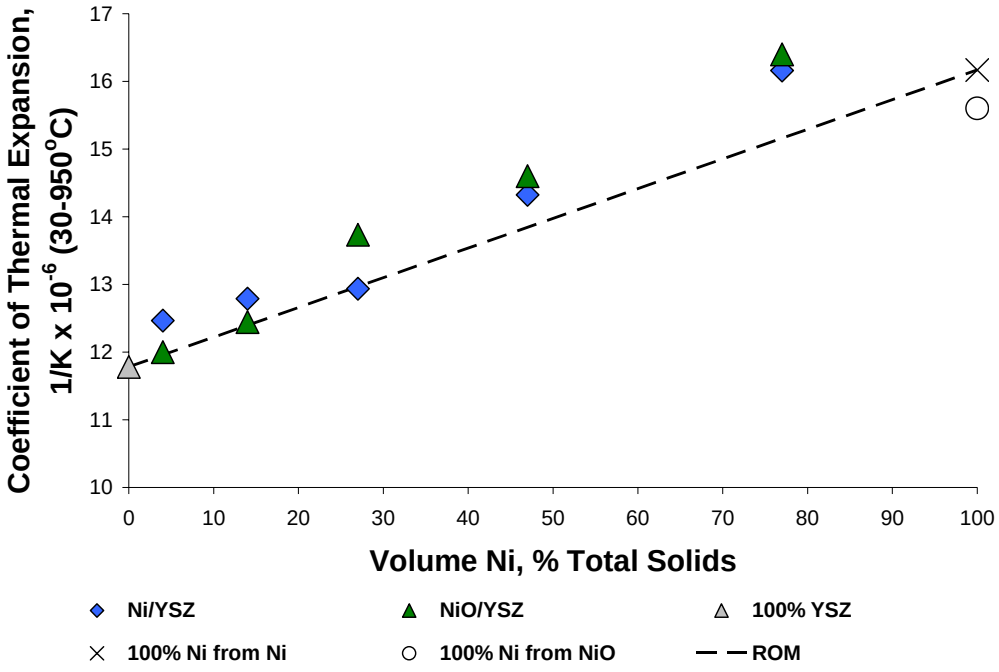

Figure 8-9: Linear coefficient of thermal expansion from 30ºC to 950ºC for Ni/YSZ and NiO/YSZ composite samples as a function of nickel volume percent of total solids. The dashed line represents the predicted CTE from the rule of mixtures (ROM).

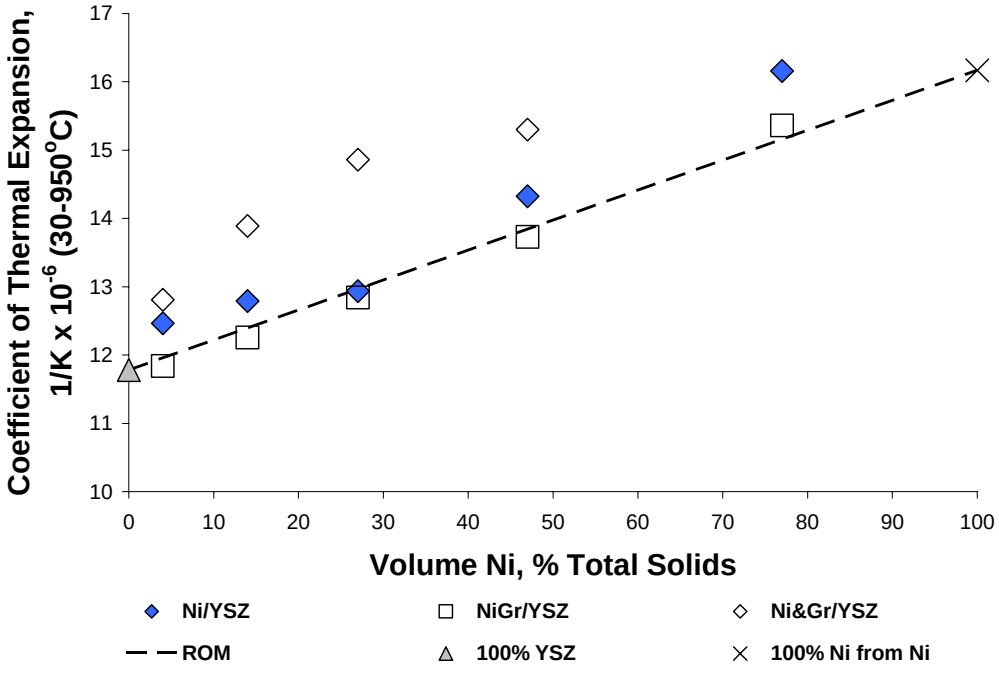

Figure 8-10: Linear coefficient of thermal expansion from 30ºC to 950ºC for Ni/YSZ, NiGr/YSZ, and Ni&Gr/YSZ composite samples as a function of nickel volume percent of total solids. The dashed line represents the predicted CTE from the rule of mixtures (ROM).

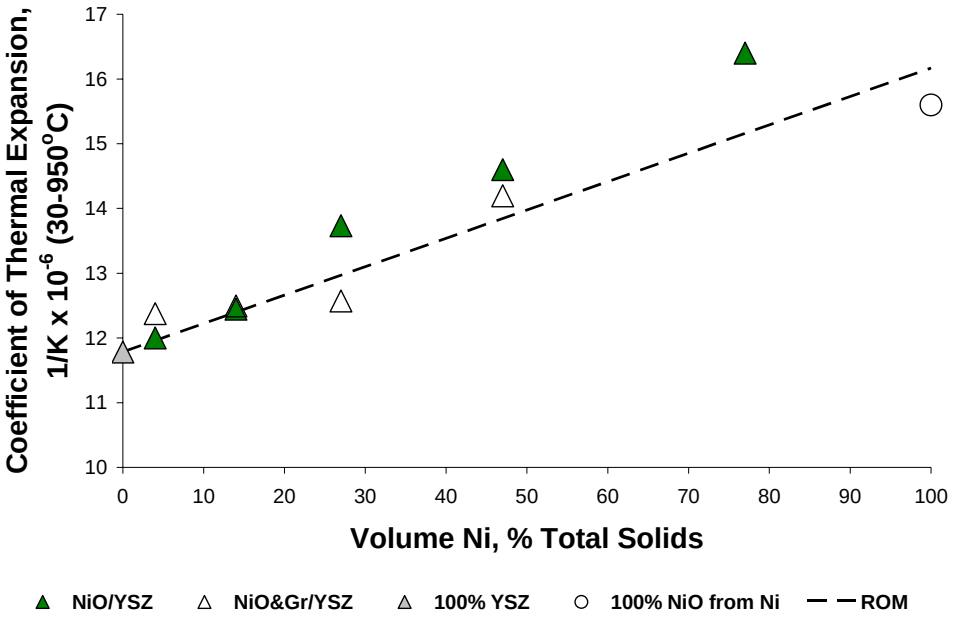

Figure 8-11: Linear coefficient of thermal expansion from 30ºC to 950ºC for NiO/YSZ and NiO&Gr/YSZ composite samples as a function of nickel volume percent of total solids. The dashed line represents the predicted CTE from the rule of mixtures (ROM).

While the effect nickel has on the thermal expansion behaviour of each of the composites is clear, porosity seems to have little effect on the CTE of a composite when examining the CTE of the Ni&Gr-27/YSZ, Ni&Gr-47/YSZ, NiO&Gr-27/YSZ, and NiO&Gr-47/YSZ composite samples, shown in Figure 8-12. For the composites with a nickel loading of 27 vol% Ni of total solids and the NiO&Gr-47/YSZ composites, the CTE is essentially constant. Conversely, the Ni&Gr-47/YSZ composites show an increase in the CTE (13 x 10^{-6} 1/K to 14.5 x 10^{-6} 1/K) at graphite loadings above 20 vol% of the green volume.

The coefficients of thermal expansion of each of the composites with the fixed nickel loadings and varying graphite content may not change significantly with increased porosity because of the very large pores created by the graphite. If the pores are excessively large, relative to the composite powders, the resultant microstructure may still have the same thermal expansion behavior as a similar fully dense composite because the constituent phases are still continuous. That is, the porosity is not associated with any individual phase and simply displaces the existing material without significantly disrupting the microstructure.

To examine the effects smaller pore sizes have on the thermal expansion behaviour of Ni/YSZ composites, particularly in the YSZ phase, another series of composites were created from the formulations for the NiGr/YSZ composites with increasing amounts of cornstarch added as a pore forming agent (PFA). Three NiGr/YSZ composites with a nickel loading of 27 vol% Ni of total solids (NiGr-27/YSZ) and three NiGr/YSZ composites with a nickel loading of 47 vol% Ni of total solids (NiGr-47/YSZ) were created with each composite having a different cornstarch loading ranging from 7 vol% to 30 vol% of the green volume. The volume fractions of graphite, cornstarch and total PFA is given in Table 8-1 for each composite, while the formulations used to prepare the composites are given in Appendix B.

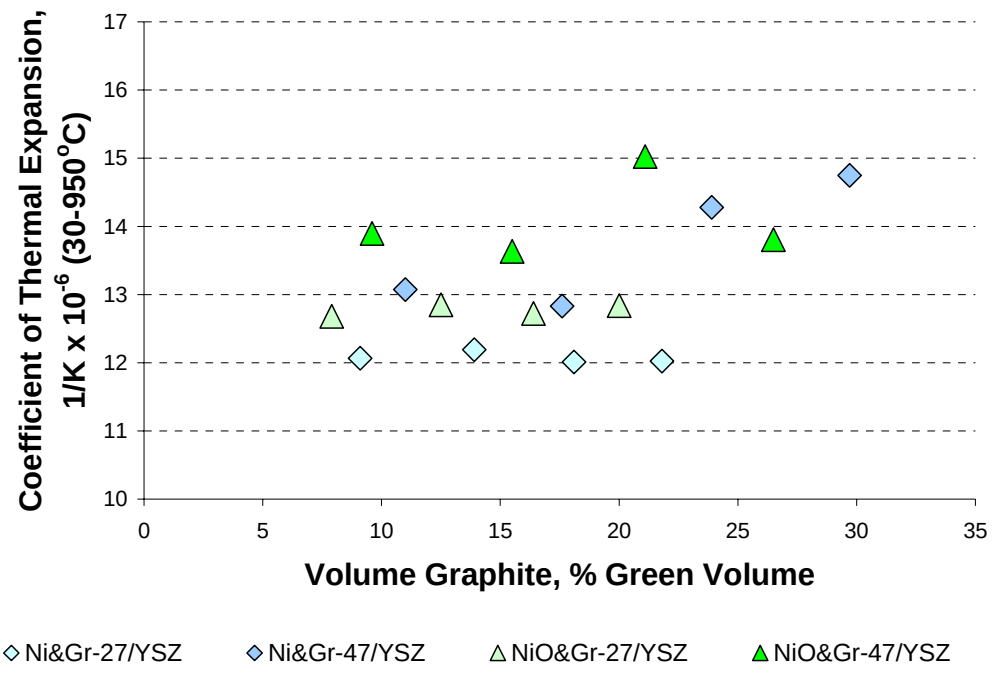

Figure 8-12: Linear coefficient of thermal expansion from 30ºC to 950ºC for Ni&Gr-27/YSZ, Ni&Gr-47/YSZ, NiO&Gr-27/YSZ, and NiO&Gr-47/YSZ composite samples as a function of graphite volume percent of the green volume.

Table 8-1: Pore Forming Agent Loadings for the new NiGr-27/YSZ and NiGr-47/YSZ composites

Composite	Volume Nickel (vol% Total Solids)	Volume PFA (vol% Green Volume)		
		Graphite (from NiGr powder)	Cornstarch	Total PFA
NiGr-27/YSZ	27	18.5	8.9	27.0
	27	15.8	17.9	33.7
	27	11.9	31.3	43.2
NiGr-47/YSZ	47	24.9	7.0	31.9
	47	22.0	14.5	36.5
	47	17.5	27.0	44.5

Optical micrographs of the new composite structures in the sintered & reduced state are presented in Figure 8-13 and Figure 8-14 for the NiGr-27/YSZ and NiGr-47/YSZ composites with added cornstarch. From the micrographs, it is evident that the smaller cornstarch powder successfully generated more porosity in the YSZ phase in addition to a few very large pores. The additional porosity in the YSZ is a result of the greater mixing between the cornstarch powder and YSZ as these powders are much smaller than the NiGr powders. The sintered and reduced micrographs for the NiGr/YSZ composites with no added starch are also included for reference in Figure 8-13 and Figure 8-14.

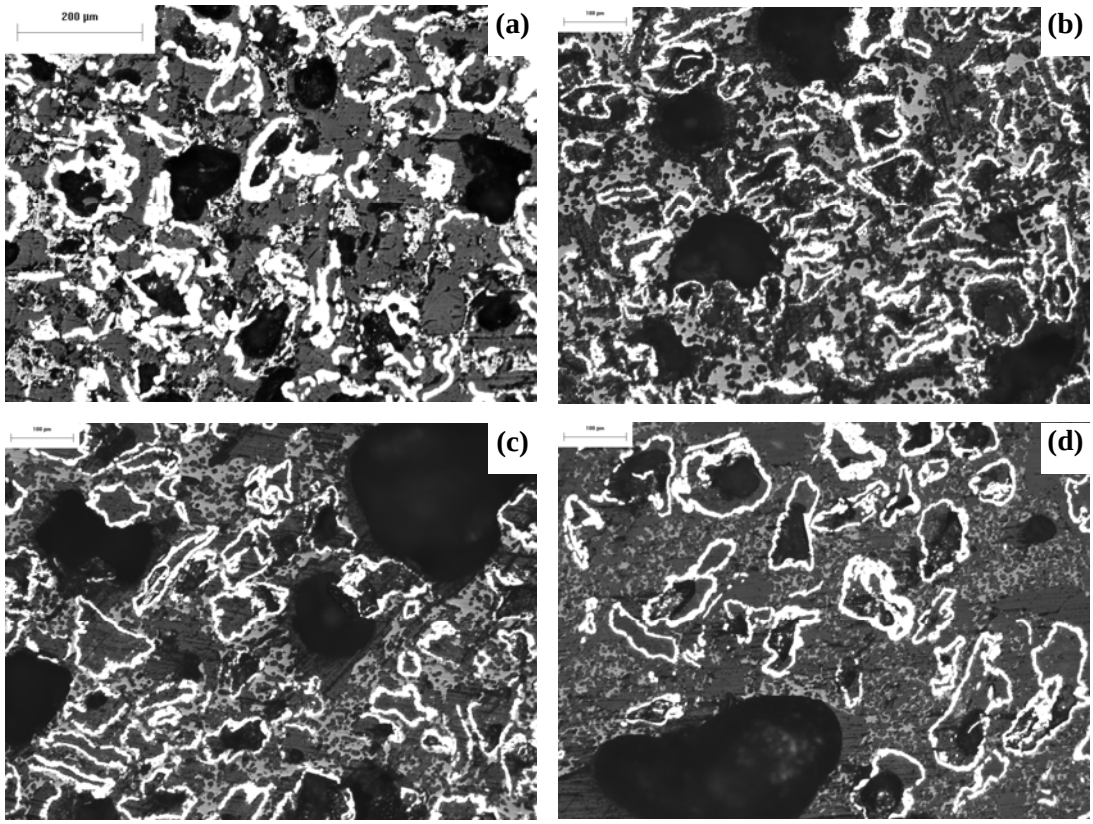

Figure 8-13: Optical micrographs of NiGr/YSZ composites in the sintered & reduced state with a nickel loading of 27 vol% of total solids and a cornstarch loading of a) 0 vol% (i.e. no added starch), b) 8.9 vol%, c) 17.9 vol%, and d) 31.3 vol% of the green volume

After determining the CTE for the NiGr/YSZ composites with added cornstarch, shown in Figure 8-15, it is clear that increasing the amount of pore forming agents, specifically the cornstarch, causes an increase in the composite CTE.

It is important to note that some of the thermal expansion measurements were taken at different times and with different silica sample holders. During the course of an unrelated experiment, the original silica sample holder used to measure the thermal expansion of the majority of the composite samples was damaged. Consequently, the coefficient of thermal expansion for the Ni&Gr-27/YSZ, Ni&Gr-47/YSZ, and NiGr/YSZ with starch composite samples was measured using the new silica sample holder. Comparison of the NiO&Gr-47/YSZ composite CTEs using the old and new sample holder shows that the new sample holder tends to have lower CTE measurement readings compared to the old sample holder. It is for this reason, that the CTE measurements for the NiGr/YSZ with starch, the Ni&Gr-27/YSZ, and Ni&Gr-47/YSZ composite samples are inconsistent with the CTE data in Figure 8-10.

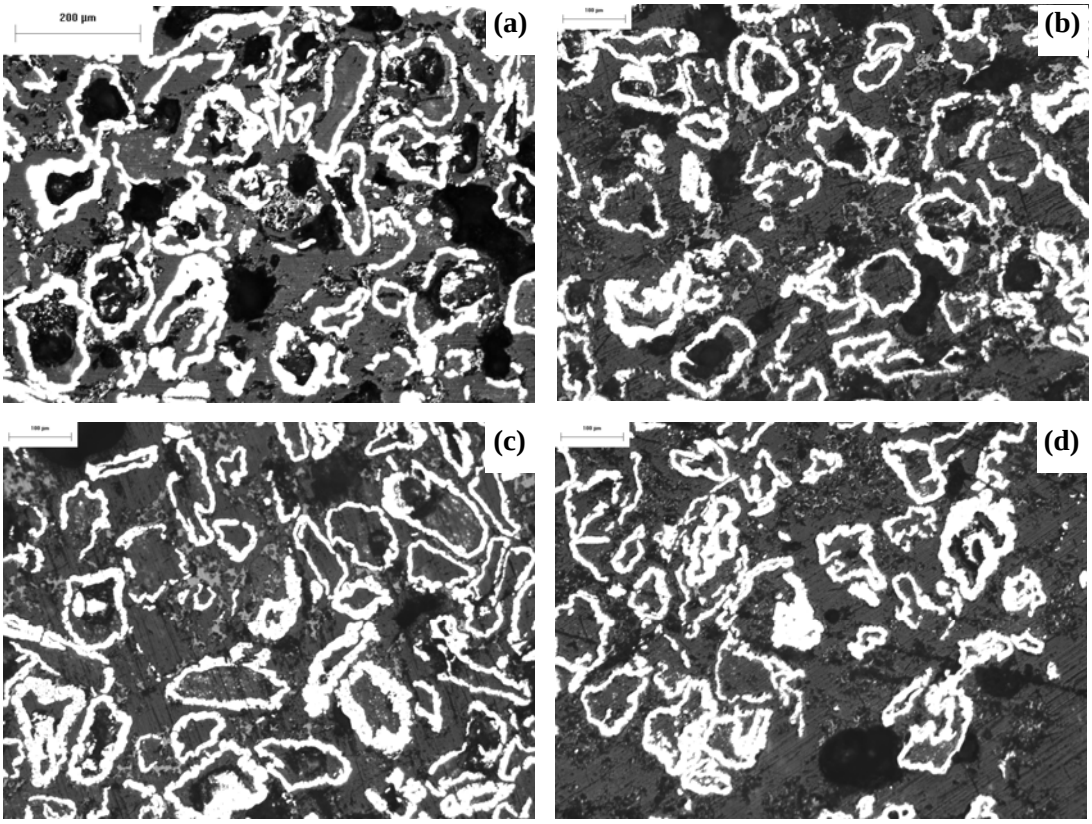

Figure 8-14: Optical micrographs of NiGr/YSZ composites in the sintered & reduced state with a nickel loading of 47 vol% of total solids and a cornstarch loading of a) 0 vol% (i.e. no added starch), b) 7 vol%, c) 14.5 vol%, and d) 27 vol% of the green volume

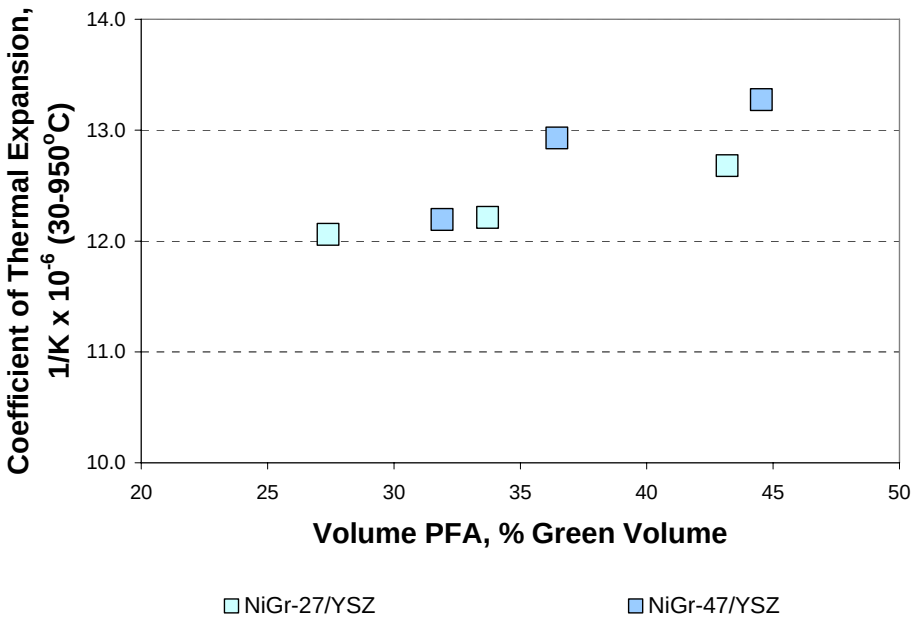

Figure 8-15: Linear coefficient of thermal expansion from 30ºC to 950ºC for NiGr-27/YSZ and NiGr-47/YSZ composite samples with increasing cornstarch loading plotted with respect to the volume fraction of pore forming agent (PFA) as a percentage of the green volume.

8.4 COMPOSITE THERMAL EXPANSION DISCUSSION

According to Equations (8-2) and (8-3), the axial and transverse composite CTE predictions will coincide with the rule of mixtures prediction if the elastic modulus and Poisson ratio for the constituent materials are the same. For dense nickel and YSZ this holds true and the rule of mixtures should be a good estimate of the composite CTE (i.e. Figure 8-4).

However, upon inspection of the CTE results for the composites tested, with the exception of the NiGr/YSZ composites, the measured CTE tends to be higher than the ROM prediction (Figure 8-9 through Figure 8-11). This deviation from the ROM CTE prediction may indicate that the elastic properties of the nickel and YSZ are not actually the same. As illustrated by the carbon/epoxy composite example (Figure 8-2), the deviation from the ROM CTE prediction may be attributed to the differences in the elastic modulus of the two constituent materials.

To test this hypothesis, the measured coefficients of thermal expansion for the Ni/YSZ, NiO/YSZ, and NiO&Gr/YSZ composites, and the Ni/YSZ, NiGr/YSZ, and Ni&Gr/YSZ composites are plotted again in Figure 8-16 and Figure 8-17 respectively along with the axial, transverse, and rule of mixtures CTE predictions. In order to best fit the axial CTE prediction with the Ni/YSZ and NiO/YSZ CTE data in Figure 8-16 and the Ni&Gr/YSZ data in Figure 8-17, the ratio between the elastic modulus for nickel and YSZ was altered. Similarly, the transverse CTE was calculated using the same elastic modulus ratio for each set of data. The best fit for the Ni/YSZ and NiO/YSZ data occurs when the ratio of the nickel elastic modulus to the YSZ elastic modulus is 2:1, whereas the ratio is 5.5:1 in order to fit the axial CTE prediction to the Ni&Gr/YSZ CTE data. Since the elastic modulus ratios for the two data sets are not equal to one, the elastic modulus of the nickel and YSZ are no longer equal and the CTE data is expected to deviate from the ROM prediction. Upon inspection of Figure 8-16 and

Figure 8-17, it is evident that the measured CTE of each composite generally falls within the bounds of the axial and transverse CTE predictions.

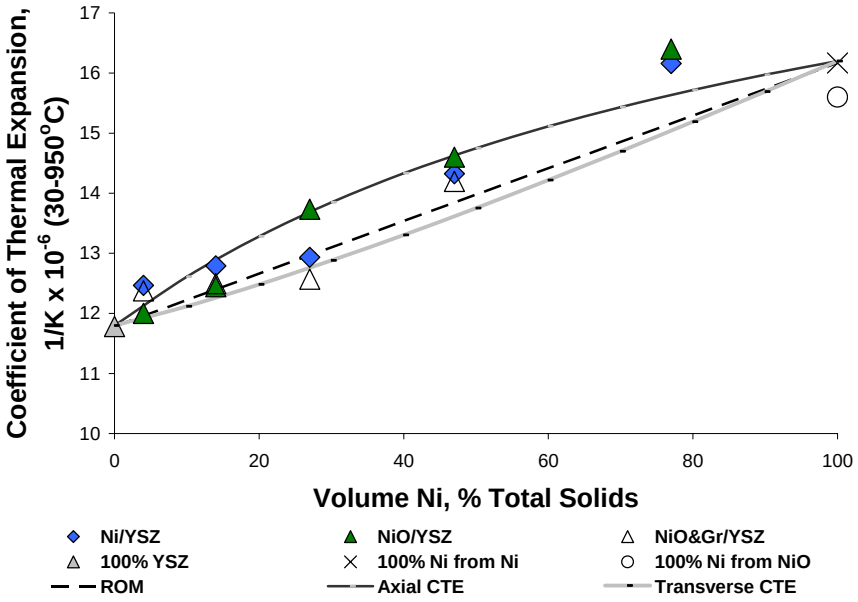

Figure 8-16: Linear coefficient of thermal expansion from 30ºC to 950ºC for Ni/YSZ, NiO/YSZ and NiO&Gr/YSZ composite samples as a function of nickel volume percent of total solids. In addition, the axial, transverse, and rule of mixtures (ROM) CTE predictions represented by Equations (8-2), (8-3), and (8-4) are also included.

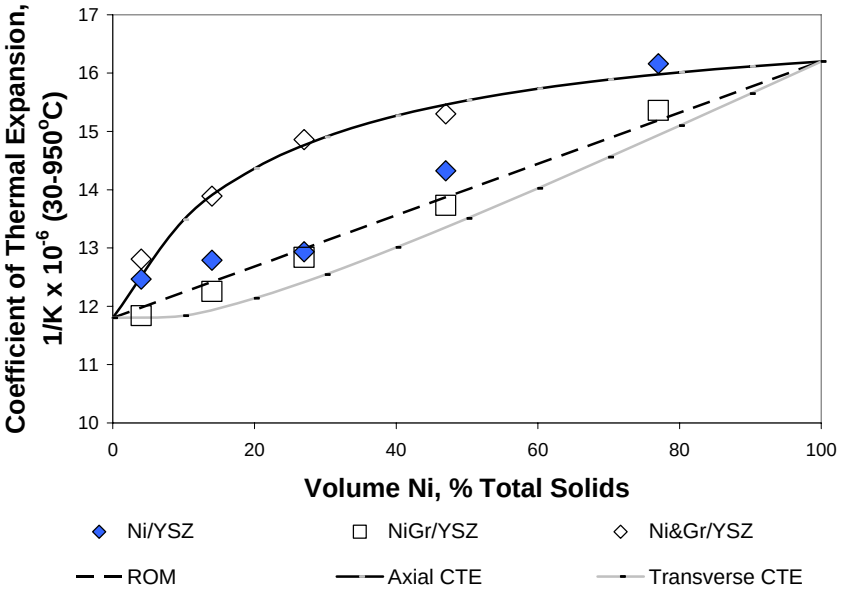

Figure 8-17: Linear coefficient of thermal expansion from 30ºC to 950ºC for Ni/YSZ, NiGr/YSZ, and Ni&Gr/YSZ composite samples as a function of nickel volume percent of total solids. In addition, the axial, transverse, and rule of mixtures (ROM) CTE predictions represented by Equations (8-2), (8-3), and (8-4) are also included.

The change in the elastic modulus for each phase may be attributed to varying porosity levels in each phase since the elastic modulus of a material decreases with increasing porosity [100,101,102]. While several models have been proposed to describe how porosity affects the elastic modulus of a material, the Sprigg's equation is one of the more straightforward corrections [100,102]:

$$E = E_o exp(-bP) \quad \textbf{(8-5)}$$

where E is the elastic modulus of the porous material, E_o is the elastic modulus of the fully dense material, b is an empirical constant, and P is the bulk porosity of the sample. Since the composites tested in this investigation are porous, it is plausible that the elastic modulus of the nickel and YSZ phases vary depending on the nature and distribution of the porosity. Consequently, any differences between the elastic modulus of the nickel and YSZ phases will cause the axial and transverse CTE predictions to deviate from the ROM CTE prediction as well.

The CTE of the porous Ni/YSZ composites will deviate from the ROM prediction depending on how the porosity is distributed throughout the composite, as illustrated in Figure 8-18. When the composite phases are continuous and fully dense, the composite CTE can be predicted by α^{ax}_c. However, the degree of thermal expansion will change when porosity is distributed throughout a single phase of the composite. For example, when porosity is concentrated in the high CTE phase (Figure 8-18b), the composite expands less than the fully dense composite because the dense low CTE material easily restrains the expansion of the porous high CTE phase which now has a lower stiffness. Likewise, the thermal expansion of a composite with porosity concentrated in the low CTE phase (Figure 8-18c) will expand more than the dense composite because the low CTE material, having a lower stiffness, does not resist the thermal expansion of the high CTE material as readily. Lastly, the thermal expansion of a composite with similar porosities in each phase will have a similar CTE to the fully dense composite provided that the ratio between the elastic modulus of each phase remains the same.

By adding cornstarch to the NiGr/YSZ composites, it effectively increased the porosity of the YSZ phase. As a result, the CTE of the composites increased with higher cornstarch loadings because of the greater porosity in the YSZ phase. Similarly, the Ni&Gr/YSZ composites have a higher CTE than the rule of mixtures prediction because of the relatively large nickel particles having little porosity, thus maintaining a high stiffness, compared to the more finely distributed YSZ phase which would have a lower stiffness.

8.5 FUTURE WORK

In order to better ascertain the influence porosity has on the coefficient of thermal expansion of Ni/YSZ composites, another series of experiments can be carried out where the porosity size and distribution is varied. For example, a series of porous Ni/YSZ composites could be created using the smaller sized cornstarch powders. Also, repeating the CTE measurements for a greater number of samples would help determine the degree of variability in the measurements.

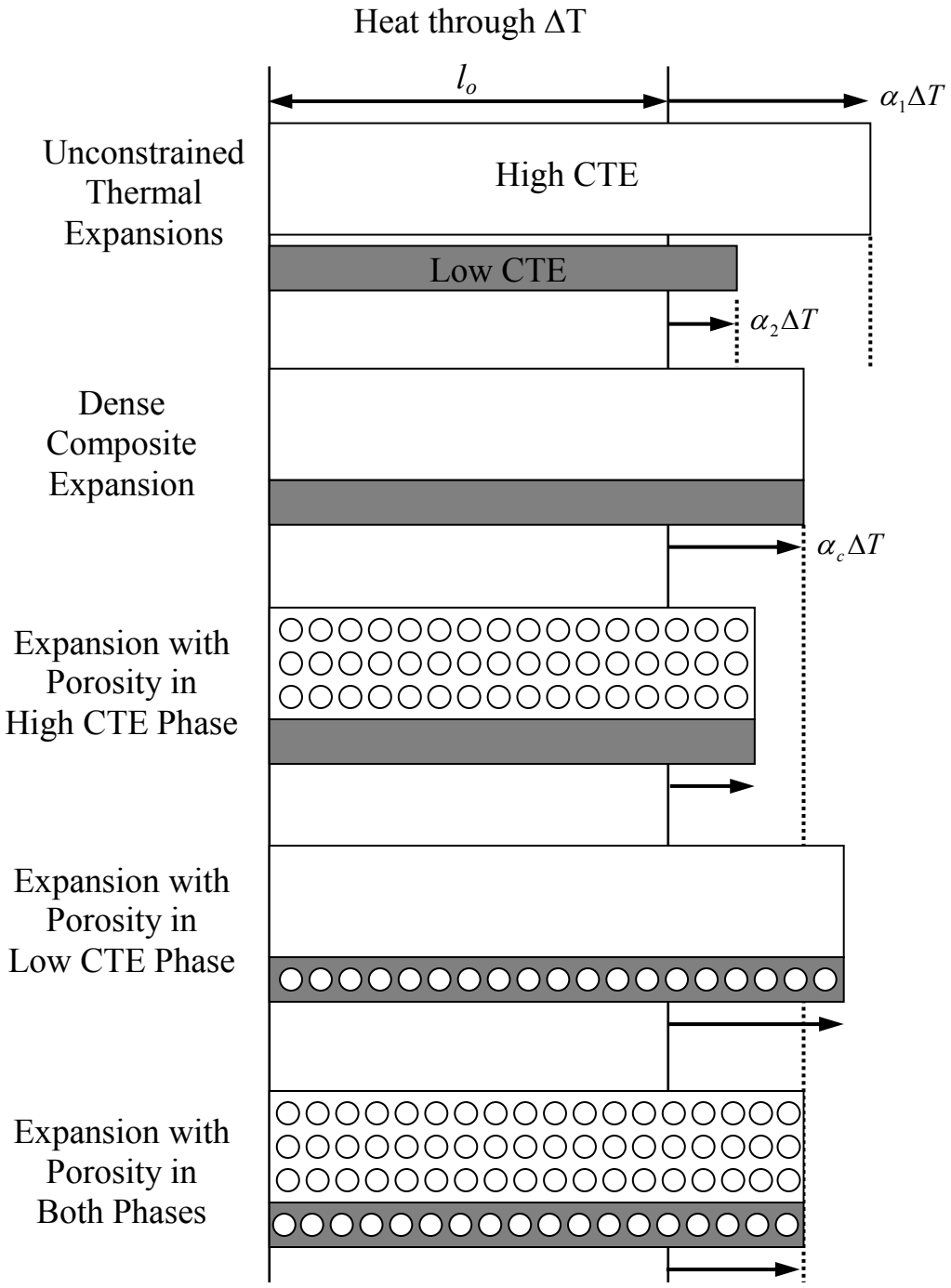

Figure 8-18: Schematic diagram depicting the thermal expansion of a porous composite where the porosity is concentrated in each individual phase and evenly distributed

CHAPTER 9:
CONCLUSIONS AND RECOMMENDATIONS

9.1 SINTERING CHARACTERISTICS

9.1.1 Nickel Oxide Additions

During the burnout stage, the volumetric shrinkage of the NiO/YSZ composites is similar to the volumetric shrinkage of the 100% YSZ samples which is less than 5%. Conversely, the 100% Ni from NiO samples shrink approximately 14%. The lower shrinkage of the NiO/YSZ composites is due to the significant constrained sintering of the NiO phase by the YSZ additions. After burnout, the density of the NiO/YSZ composites increases with higher nickel loadings and subsequent lower polymer content.

After sintering, the 100% YSZ samples shrink the most (55% by volume) while the 100% Ni from NiO samples shrink the least (25% by volume). The difference in the sintering shrinkage can be attributed to the differences in the sintering characteristics of the two materials and the additional shrinkage of the nickel oxide during the burnout stage. Therefore, the amount of isotropic shrinkage decreases as the nickel content increases. Once sintered, the NiO/YSZ composites with nickel loadings less than 47 vol% Ni of total solids have a relative density of 90% whereas the NiO/YSZ composites with higher nickel loadings have a relative density of only 85%. Finally, it was concluded that constrained sintering is not significant, considering the total change in density for the NiO/YSZ composites from the green to the sintered state.

9.1.2 Nickel Additions

The sintering characteristics of the Ni/YSZ composites are dramatically altered when using nickel powder rather than nickel oxide powder. After the burnout stage, the Ni/YSZ composites actually swell due to the oxidation of nickel. When nickel metal oxidizes (at 500°C), it experiences a volumetric expansion of 66%. The Ni/YSZ composites with nickel loadings less than 27 vol% Ni of total solids expand an amount that is equal to the full expansion of the nickel phase. At nickel loadings above 27 vol% Ni, some nickel sintering occurs causing the expansion of the composites to be less than the expected full expansion of the nickel phase. The shrinkage due to sintering is more prevalent at higher nickel loadings because a percolating path of nickel is better established and the shrinkage is not easily restrained by the YSZ matrix. While the 100% Ni samples are not completely oxidized during burnout, the degree of sintering shrinkage is sufficient enough to overcome the nickel expansion due to oxidation resulting in an overall volumetric shrinkage of 6%. Once burnout is completed, the relative density of the Ni/YSZ composites increases with higher nickel contents. This increase is more significant at higher nickel loadings, compared with the NiO/YSZ composites, despite a net expansion of the nickel phase because the volume increase due to nickel oxidation is counter balanced by a sintering shrinkage.

Upon sintering, the Ni/YSZ composites shrink less than the NiO/YSZ composites at the same nickel loading with the amount of sintering shrinkage being proportional to the nickel content. The lower isotropic sintering shrinkage of the Ni/YSZ composites is a result of the greater sintering that takes

place during the burnout stage and the resultant constrained sintering of the YSZ phase from the green state to the sintered state. Although the samples are expected to shrink during sintering, the 100% Ni from Ni samples expand (6% by volume from the burnout state to the sintered state) because of the oxidation of the residual nickel metal. Lastly, the bulk densities of the Ni/YSZ composites are lowest at nickel loadings of 27 vol% Ni and 47 vol% Ni and the bulk density of the 100% Ni from Ni samples decreases after sintering.

In conclusion, using nickel metal as an additive to tape cast Ni/YSZ anodes has a larger impact on the sintering characteristics of these composites compared with anodes made from nickel oxide powder. For instance, nickel oxide sinters less, and at a lower temperature, than the YSZ phase. Consequently, there is a modest reduction in the sintering shrinkage (and therefore densification) of the NiO/YSZ composites with increasing nickel oxide loading which follows a simple additive rule of mixtures. Conversely, the oxidation of the nickel phase during burnout at temperatures less than 1000°C introduces a volumetric expansion. At higher nickel loadings the volumetric expansion decreases because of sintering shrinkage, but still results in an overall expansion. Upon subsequent sintering, the Ni/YSZ composites shrink but to a lesser extent compared with the NiO/YSZ composites. The lower sintering shrinkage of the Ni/YSZ composites is associated with the lower sinterability of the oxidized nickel phase and the higher composite relative densities after burnout. An analysis of the changes in density during burnout and sintering indicate that the oxidized nickel phase imparts an apparent constraining effect on the YSZ phase resulting in overall lower densification and dimensional changes compared with the NiO/YSZ composites. Once sintered, the Ni/YSZ and NiO/YSZ composites behave similarly during reduction with the Ni/YSZ composites having a lower relative density after reduction because of the lower initial density after sintering.

The constrained sintering effect caused by nickel additions may increase the difficulty of co-sintering an anode made from nickel metal and YSZ with a YSZ electrolyte. Therefore, processing methods that involve screen printing the Ni/YSZ composite anodes onto previously sintered dense electrolytes may be the preferred technique.

9.1.3 Nickel Coated Graphite Additions

The NiGr/YSZ composites behave in a similar manner to the Ni/YSZ composites during the burnout and sintering stages. After burnout, the NiGr/YSZ composites swell because of the oxidation of nickel. At low nickel loadings (less than 27 vol% Ni of total solids), there is no composite shrinkage as a result of the sintering of the nickel phase, and therefore the composites expand an amount equal to the expected expansion of the nickel after oxidation. At nickel loadings above 27 vol% Ni, some sintering occurs and the composites expand less than the full expansion of the nickel phase after oxidation. The degree of volumetric shrinkage after sintering is slightly lower than the Ni/YSZ composites, although the shrinkage is anisotropic because of the removal of the graphite. Hence, the NiGr/YSZ composites tend to shrink less in the thickness direction compared to the length and width directions. Lastly, it was found that the bulk porosity of the NiGr/YSZ composites is higher than the volume of graphite added. The additional porosity can be attributed to the constrained sintering of the matrix material, microcracks, delamination of the layers, and particle bridging voids. Like the Ni/YSZ composites, the NiGr/YSZ anodes will exhibit the same challenges in terms of co-sintering and may be better suited to screen printing methods.

9.1.4 Graphite Additions

When graphite is added to the nickel and nickel oxide based composites, the sintering characteristics of the composites at low graphite loadings during burnout are not significantly altered. However, if the graphite loading exceeds 20 vol% graphite of the pressed green volume, the volumetric change begins to deviate from the volumetric change of the graphite-free composites after burnout, and at a graphite loading of over 25 vol% the volumetric expansion is extreme (greater than 100%). The increased expansion with higher graphite loadings corresponds to the formation of a graphite percolation network which ultimately weakens the composite and does not resist the composite expansion in the thickness direction as the exit gases are drawn upward.

During sintering, the presence of graphite increases the volumetric shrinkage of the composites slightly because of the lower packing density of the nickel (oxide) and YSZ matrix. When measuring the linear sintering shrinkage with the dilatometer, the sintering shrinkage in the length direction is greater than the sintering shrinkage in the thickness direction leading to anisotropic sintering. However, the anisotropy is less pronounced when the samples are bulk sintered in a box furnace. As was the case for the NiGr/YSZ composites, the amount of porosity generated in the composites is greater than the volume of added graphite and the additional porosity can be attributed to the matrix not sintering to full density.

Lastly, this study showed that adding graphite to a green tape is an effective way of introducing additional porosity into a sintered and reduced anode structure. The graphite loading can be adjusted such that it does not significantly impact the dimensional changes during burnout, sintering, or reduction while introducing up to an additional 40% porosity. Anode structures with total porosity levels of up to 70% can be processed using this approach; however, porosity levels beyond 70% are associated with considerable swelling in the thickness direction during burnout.

9.1.5 Reduction

When nickel oxide is reduced to nickel metal, the volume decreases. However, after reduction there is little dimensional change (less than 5% by volume) in the composites containing a rigid YSZ network regardless of how the composites were made. Conversely, the 100% Ni from NiO samples shrink as much as 22% by volume. The 100% Ni from Ni samples do not shrink as much as the 100% Ni from NiO samples since the nickel oxide was not completely reduced. Generally, the increase in porosity from the sintered state to the reduced state is on the same order of magnitude as the theoretical increase in porosity for each composite type, although at higher nickel loadings continued sintering during reduction leads to some shrinkage and lower porosity levels.

9.2 ELECTRICAL CONDUCTIVITY

9.2.1 Nickel and Nickel Oxide Additions

The electrical conductivity of a fully dense pure material is greater than the electrical conductivity of the same material with porosity. Consequently, it is important to state the volume fraction of the conducting material as a percentage of the total volume including porosity, rather than the volume fraction as a percentage of total solids when reporting electrical conductivity data.

The electrical conductivity of the Ni/YSZ and NiO/YSZ composites both show classic percolation behaviour. At nickel volume fractions of less than 20% of the total volume there is insufficient nickel to form a percolating network and the composite electrical conductivity is low. At nickel volume

fractions between 20 vol% Ni and 40 vol% Ni, the percolating nickel network is building and the electrical conductivity increases until a fully connected nickel network is established at nickel loadings greater than 40 vol% Ni of the total composite volume.

The electrical conductivity of the Ni/YSZ composites is slightly better than the electrical conductivity of the NiO/YSZ composites at a given nickel loading. The critical percolation volume fraction for the Ni/YSZ composites is 17.5 vol% Ni compared to 27 vol% Ni for the NiO/YSZ composites. The higher electrical conductivity for the Ni/YSZ composites may be attributed to the better particle-to-particle contact between nickel particles which develops during the burnout and sintering stages as a result of nickel oxidation. Porosity levels of mixtures above the percolation threshold are in the range of 30% to 40% with higher porosities produced in the Ni/YSZ composites.

9.2.2 Nickel Coated Graphite Additions

The electrical conductivity of the NiGr/YSZ composites is far superior to the electrical conductivity of the other composite types despite the higher degree of porosity (i.e. up to 85% porosity). Since the porosity is contained within the nickel shell, formed when the graphite core is burned away, the nickel percolation path is not disrupted. In addition, once the percolating network forms (at a critical percolation volume fraction of 0.08), the nickel becomes fully connected rather quickly.

In conclusion, the addition of nickel coated graphite into an anode tape is an effective way to increase the electrical conductivity at low nickel loadings while also introducing significant amounts of porosity.

9.2.3 Graphite Additions

The electrical conductivity of the Ni&Gr/YSZ and NiO&Gr/YSZ composites is inferior to the electrical conductivity of the graphite-free composites at similar nickel loadings. When graphite is added to the composite as a separate particle, the additional polymer used to create the composite redistributes itself throughout the green composite structure thereby reducing the packing density of the nickel and YSZ powders. It was discovered that if the nickel phase does not form a percolating network in the green state, then it will not easily sinter together to form a robust percolating network in the sintered & reduced state. (One exception is the Ni&Gr/YSZ composite with a nickel loading of 27 vol% Ni of total solids. In the green state, the nickel does not form a percolating network but is able to form a percolating network after the nickel oxidizes during the burnout stage.) Consequently, if more nickel is required to form a percolating network in the green state then the percolation threshold increases. Furthermore, the electrical conductivity of the composites is further reduced when the graphite particles interrupt the nickel percolation network. In this investigation, the size of the graphite particles is relatively large compared with the nickel and YSZ powders, and as a result, are not expected to significantly alter the packing of the solid powders. However, when comparing the electrical conductivity results of the Ni&Gr-47/YSZ and NiO&Gr-47/YSZ composites with a lower bound prediction that assumes that the same degree of porosity is evenly distributed throughout the composite, the electrical conductivity of the lower bound is considerably lower. This suggests that smaller scale porosity may further decrease the electrical conductivity of the composites. Therefore, to avoid a substantial decrease in the electrical conductivity of an anode, the amount of porosity generated by the addition of separate graphite particles should be minimized because even small graphite additions lowers the electrical conductivity.

9.3 THERMAL EXPANSION BEHAVIOUR

Nickel has a higher coefficient of thermal expansion (16.3 x 10^{-6} 1/K) compared to YSZ (10.2 x 10^{-6} 1/K) and since nickel and YSZ have a similar modulus of elasticity and Poisson's ratio, the CTE is expected to follow the rule of mixtures. However, it was determined that by introducing porosity into a particular phase of a Ni/YSZ, its elastic properties will change, and cause the CTE prediction for the composite to deviate from the rule of mixtures. Since the NiGr/YSZ composites follow the rule of mixtures CTE prediction, the porosity within the composite must be evenly distributed throughout the YSZ and Ni phases. On the other hand, when cornstarch was added to the NiGr/YSZ composites, the CTE increased because of the higher porosity within the YSZ matrix. Similarly, the CTE of the Ni/YSZ and NiO/YSZ composites tends to be slightly higher than the rule of mixtures prediction because of the higher degree of porosity in the YSZ phase. This was established by fitting the axial CTE prediction with the measured CTE data for both composite types and finding that the ratio of the nickel elastic modulus to the YSZ elastic modulus was 2 to 1. Likewise, the measured CTE of the Ni&Gr/YSZ composites was substantially higher than the rule of mixtures because of the increased porosity in the YSZ phase. This was confirmed when the fitted nickel to YSZ elastic modulus ratio was 5.5 to 1. Therefore, by controlling the distribution of porosity in an individual phase, it is possible to alter the CTE of a Ni/YSZ composite form the rule of mixtures prediction. This can prove valuable when trying to match the CTE of each of the fuel cell components to each other.

9.4 RECOMMENDATIONS

When preparing the Ni/YSZ composites for this investigation, a number of the process variables were held constant in order to isolate the effects nickel distribution and porosity have on the composite properties. With this new understanding of how to manipulate the composite properties, it is possible to expand this area of research by altering some of the previously fixed process variables. For example, the relative particle sizes for each of the constituent materials may have a substantial effect on the packing and distribution of the materials within the composite. As a result, it is recommended that a similar set of experiments be repeated with smaller nickel coated graphite particles and smaller graphite particles in order to ascertain if the measured composite properties are a function of particle size. For instance, smaller nickel coated graphite particles may lead to improved electrical conductivity whereas smaller graphite particles may further disrupt the packing of the nickel and YSZ, thus altering the sintering characteristics and electrical conductivity of composite. In addition, non-spherical nickel morphologies such as feathery particles, fibres, or foams could be investigated.

Other areas of future investigation include improving the distribution of porosity within the nickel and YSZ phases to better establish its effect on the thermal expansion behaviour of porous Ni/YSZ composites, altering the sintering temperature and heating schedule to determine how temperature affects composite sintering characteristics, and the dimensional changes during the low temperature polymer burnout.

In terms of fuel cell applications, the reduced sinterability of the nickel additions may be beneficial in improving the long term stability of the anode because the nickel is less likely to continue to sinter during fuel cell operation compared with the NiO/YSZ composites. Similarly, oxidation-reduction resistance may be higher in the Ni/YSZ composites since the nickel oxidizes during anode processing. Experiments examining the long-term stability of the anode, the oxidation-reduction resistance, thermal cycling stability, and electrochemical performance are all worthwhile in order to determine what composite anode structures are best suited for solid oxide fuel cell applications.

Appendix A:

POWDER SIZE CHARACTERIZATION

The particle size analysis for the YSZ, nickel, nickel coated graphite, and nickel oxide particles is given in the following figures:

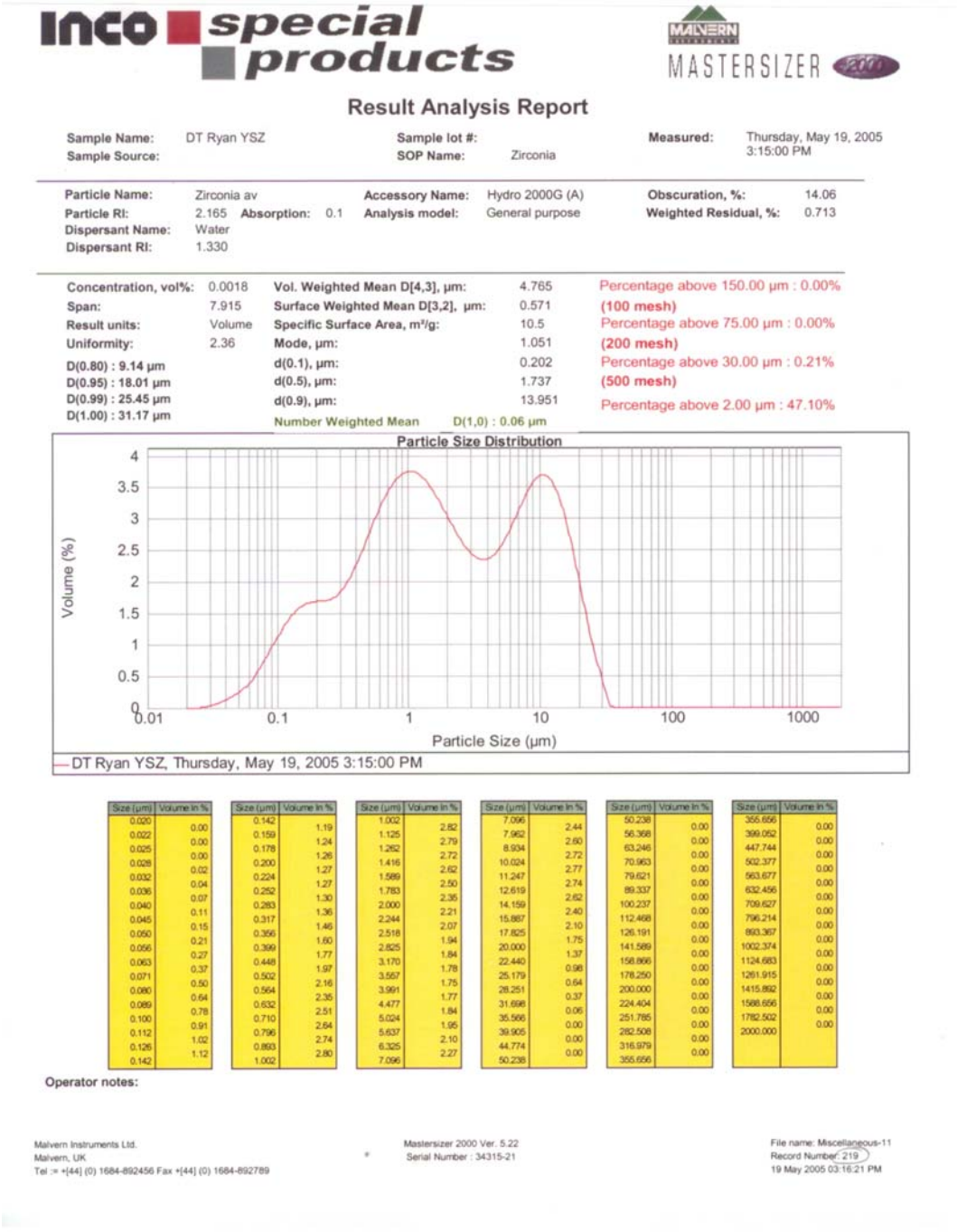

Figure A-1: YSZ particle size result analysis report

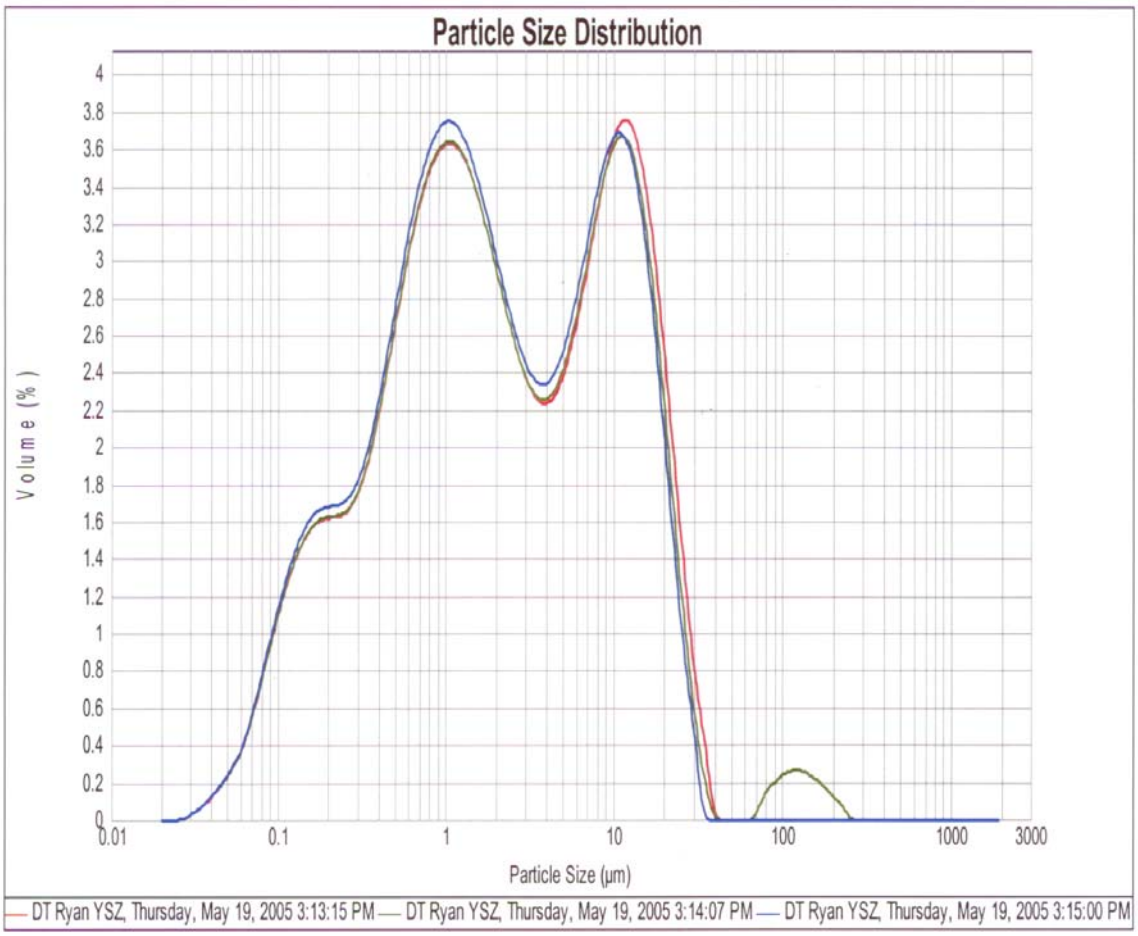

Figure A-2: YSZ particle size distribution

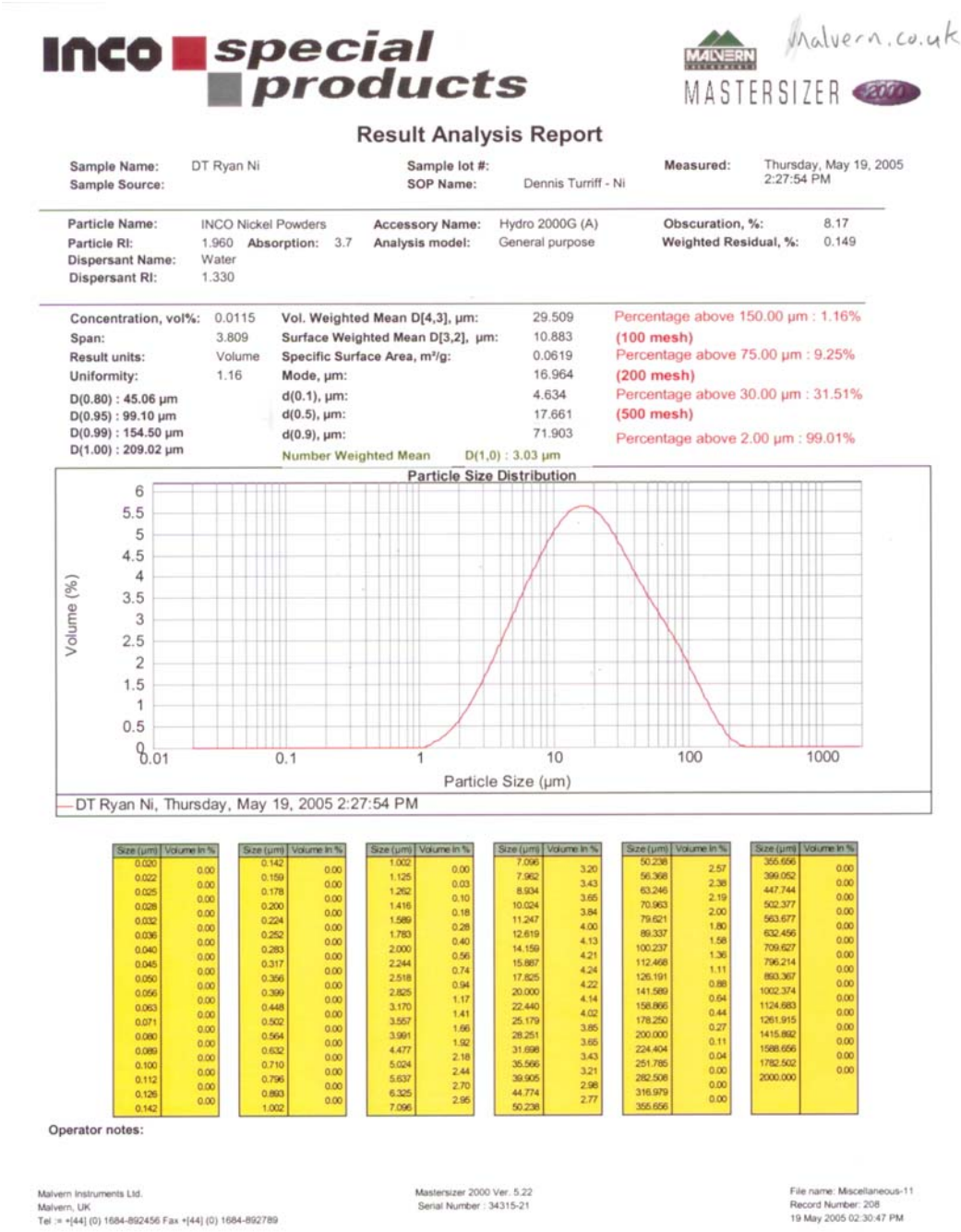

INCO special products

Malvern.co.uk

MASTERSIZER 2000

Result Analysis Report

Sample Name: DT Ryan Ni
Sample Source:
Sample lot #:
SOP Name: Dennis Turriff - Ni
Measured: Thursday, May 19, 2005 2:27:54 PM

Particle Name: INCO Nickel Powders
Particle RI: 1.960 Absorption: 3.7
Dispersant Name: Water
Dispersant RI: 1.330
Accessory Name: Hydro 2000G (A)
Analysis model: General purpose
Obscuration, %: 8.17
Weighted Residual, %: 0.149

Concentration, vol%: 0.0115
Span: 3.809
Result units: Volume
Uniformity: 1.16

D(0.80) : 45.06 µm
D(0.95) : 99.10 µm
D(0.99) : 154.50 µm
D(1.00) : 209.02 µm

Vol. Weighted Mean D[4,3], µm: 29.509
Surface Weighted Mean D[3,2], µm: 10.883
Specific Surface Area, m²/g: 0.0619
Mode, µm: 16.964
d(0.1), µm: 4.634
d(0.5), µm: 17.661
d(0.9), µm: 71.903
Number Weighted Mean D(1,0) : 3.03 µm

Percentage above 150.00 µm : 1.16%
(100 mesh)
Percentage above 75.00 µm : 9.25%
(200 mesh)
Percentage above 30.00 µm : 31.51%
(500 mesh)
Percentage above 2.00 µm : 99.01%

Particle Size Distribution

Volume (%)

Particle Size (µm)

DT Ryan Ni, Thursday, May 19, 2005 2:27:54 PM

Size (µm)	Volume In %
0.020	0.00
0.022	0.00
0.025	0.00
0.028	0.00
0.032	0.00
0.036	0.00
0.040	0.00
0.045	0.00
0.050	0.00
0.056	0.00
0.063	0.00
0.071	0.00
0.080	0.00
0.089	0.00
0.100	0.00
0.112	0.00
0.126	0.00
0.142	0.00

Size (µm)	Volume In %
0.142	0.00
0.159	0.00
0.178	0.00
0.200	0.00
0.224	0.00
0.252	0.00
0.283	0.00
0.317	0.00
0.356	0.00
0.399	0.00
0.448	0.00
0.502	0.00
0.564	0.00
0.632	0.00
0.710	0.00
0.796	0.00
0.893	0.00
1.002	0.00

Size (µm)	Volume In %
1.002	0.00
1.125	0.03
1.262	0.10
1.416	0.18
1.589	0.28
1.783	0.40
2.000	0.56
2.244	0.74
2.518	0.94
2.825	1.17
3.170	1.41
3.557	1.66
3.991	1.92
4.477	2.18
5.024	2.44
5.637	2.70
6.325	2.95
7.096	

Size (µm)	Volume In %
7.096	3.20
7.962	3.43
8.934	3.65
10.024	3.84
11.247	4.00
12.619	4.13
14.159	4.21
15.887	4.24
17.825	4.22
20.000	4.14
22.440	4.02
25.179	3.85
28.251	3.65
31.698	3.43
35.566	3.21
39.905	2.98
44.774	2.77
50.238	

Size (µm)	Volume In %
50.238	2.57
56.368	2.38
63.246	2.19
70.963	2.00
79.621	1.80
89.337	1.58
100.237	1.36
112.468	1.11
126.191	0.88
141.589	0.64
158.866	0.44
178.250	0.27
200.000	0.11
224.404	0.04
251.785	0.00
282.508	0.00
316.979	0.00
355.656	

Size (µm)	Volume In %
355.656	0.00
399.052	0.00
447.744	0.00
502.377	0.00
563.677	0.00
632.456	0.00
709.627	0.00
796.214	0.00
893.367	0.00
1002.374	0.00
1124.683	0.00
1261.915	0.00
1415.892	0.00
1588.656	0.00
1782.502	0.00
2000.000	

Operator notes:

Malvern Instruments Ltd.
Malvern, UK
Tel := +[44] (0) 1684-892456 Fax +[44] (0) 1684-892789

Mastersizer 2000 Ver. 5.22
Serial Number : 34315-21

File name: Miscellaneous-11
Record Number: 208
19 May 2005 02:30:47 PM

Figure A-3: Ni particle size result analysis report

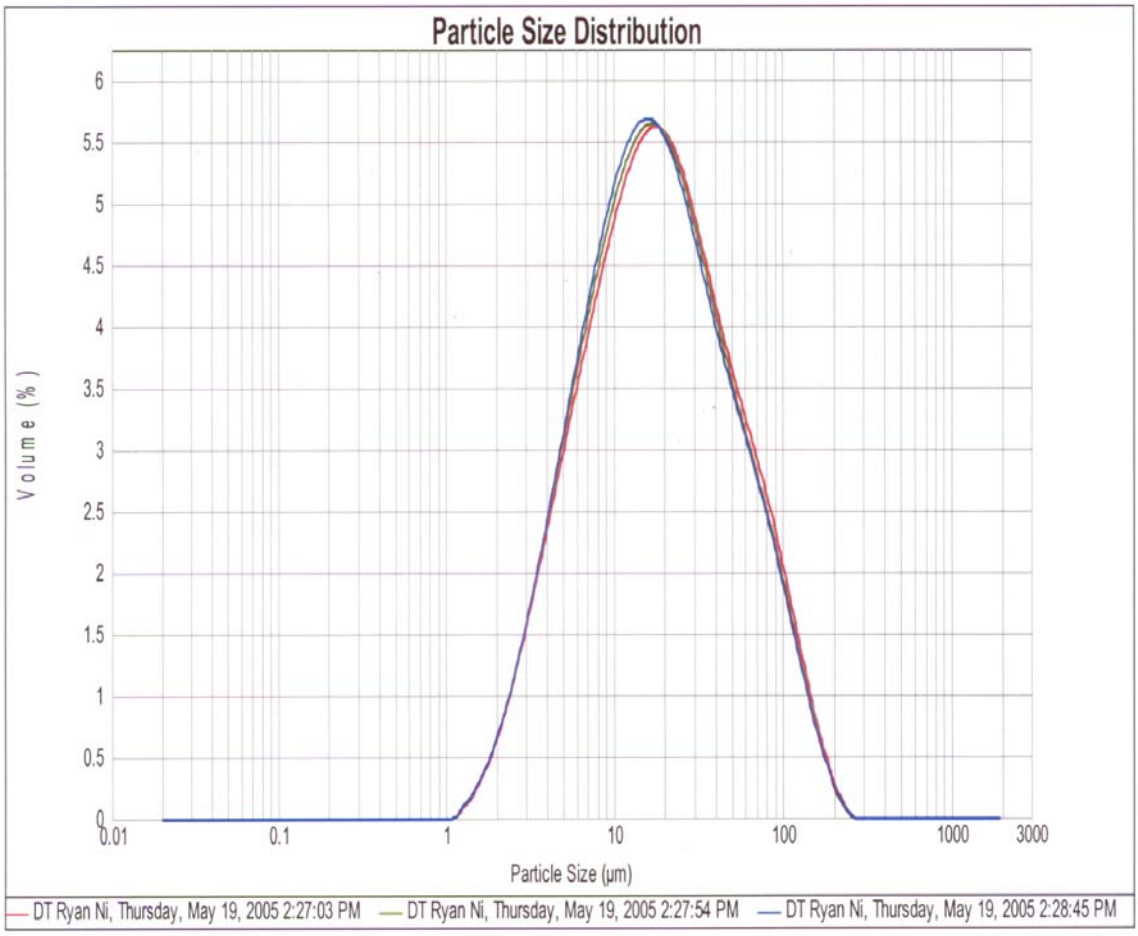

Figure A-4: Ni particle size distribution

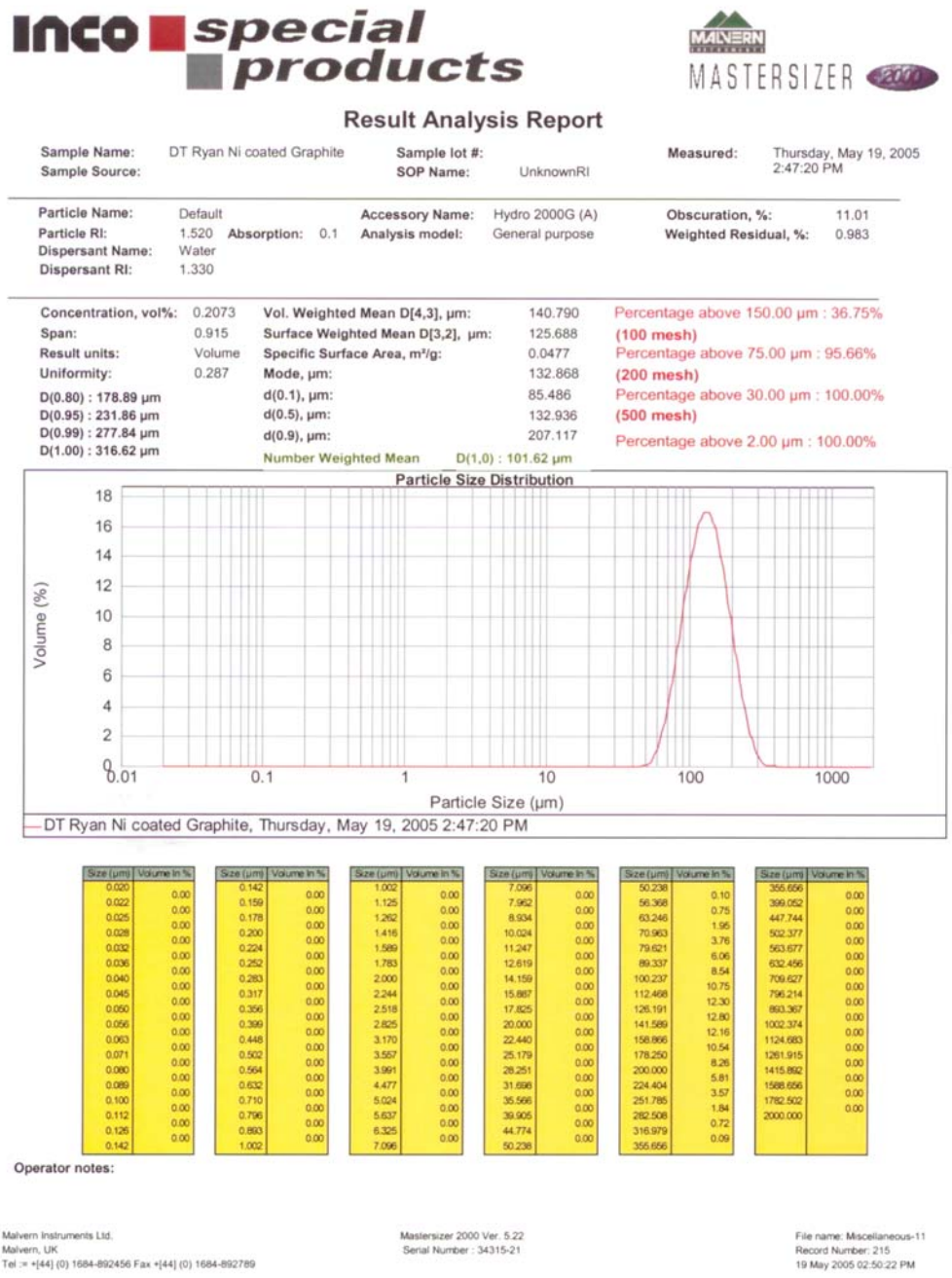

INCO special products

MALVERN MASTERSIZER 2000

Result Analysis Report

Sample Name: DT Ryan Ni coated Graphite
Sample Source:
Sample lot #:
SOP Name: UnknownRI
Measured: Thursday, May 19, 2005 2:47:20 PM

Particle Name: Default
Particle RI: 1.520 Absorption: 0.1
Dispersant Name: Water
Dispersant RI: 1.330
Accessory Name: Hydro 2000G (A)
Analysis model: General purpose
Obscuration, %: 11.01
Weighted Residual, %: 0.983

Concentration, vol%: 0.2073
Span: 0.915
Result units: Volume
Uniformity: 0.287
D(0.80) : 178.89 µm
D(0.95) : 231.86 µm
D(0.99) : 277.84 µm
D(1.00) : 316.62 µm

Vol. Weighted Mean D[4,3], µm: 140.790
Surface Weighted Mean D[3,2], µm: 125.688
Specific Surface Area, m²/g: 0.0477
Mode, µm: 132.868
d(0.1), µm: 85.486
d(0.5), µm: 132.936
d(0.9), µm: 207.117
Number Weighted Mean D(1,0) : 101.62 µm

Percentage above 150.00 µm : 36.75%
(100 mesh)
Percentage above 75.00 µm : 95.66%
(200 mesh)
Percentage above 30.00 µm : 100.00%
(500 mesh)
Percentage above 2.00 µm : 100.00%

Particle Size Distribution

Volume (%)

Particle Size (µm)

DT Ryan Ni coated Graphite, Thursday, May 19, 2005 2:47:20 PM

Size (µm)	Volume In %
0.020	0.00
0.022	0.00
0.025	0.00
0.028	0.00
0.032	0.00
0.036	0.00
0.040	0.00
0.045	0.00
0.050	0.00
0.056	0.00
0.063	0.00
0.071	0.00
0.080	0.00
0.089	0.00
0.100	0.00
0.112	0.00
0.126	0.00
0.142	0.00

Size (µm)	Volume In %
0.142	0.00
0.159	0.00
0.178	0.00
0.200	0.00
0.224	0.00
0.252	0.00
0.283	0.00
0.317	0.00
0.356	0.00
0.399	0.00
0.448	0.00
0.502	0.00
0.564	0.00
0.632	0.00
0.710	0.00
0.796	0.00
0.893	0.00
1.002	0.00

Size (µm)	Volume In %
1.002	0.00
1.125	0.00
1.262	0.00
1.416	0.00
1.589	0.00
1.783	0.00
2.000	0.00
2.244	0.00
2.518	0.00
2.825	0.00
3.170	0.00
3.557	0.00
3.991	0.00
4.477	0.00
5.024	0.00
5.637	0.00
6.325	0.00
7.096	0.00

Size (µm)	Volume In %
7.096	0.00
7.962	0.00
8.934	0.00
10.024	0.00
11.247	0.00
12.619	0.00
14.159	0.00
15.887	0.00
17.825	0.00
20.000	0.00
22.440	0.00
25.179	0.00
28.251	0.00
31.698	0.00
35.566	0.00
39.905	0.00
44.774	0.00
50.238	0.00

Size (µm)	Volume In %
50.238	0.10
56.368	0.75
63.246	1.95
70.963	3.76
79.621	6.06
89.337	8.54
100.237	10.75
112.468	12.30
126.191	12.80
141.589	12.16
158.866	10.54
178.250	8.26
200.000	5.81
224.404	3.57
251.785	1.84
282.508	0.72
316.979	0.09
355.656	

Size (µm)	Volume In %
355.656	0.00
399.052	0.00
447.744	0.00
502.377	0.00
563.677	0.00
632.456	0.00
709.627	0.00
796.214	0.00
893.367	0.00
1002.374	0.00
1124.683	0.00
1261.915	0.00
1415.892	0.00
1588.656	0.00
1782.502	0.00
2000.000	

Operator notes:

Malvern Instruments Ltd.
Malvern, UK
Tel := +[44] (0) 1684-892456 Fax +[44] (0) 1684-892789

Mastersizer 2000 Ver. 5.22
Serial Number : 34315-21

File name: Miscellaneous-11
Record Number: 215
19 May 2005 02:50:22 PM

Figure A-5: NiGr particle size result analysis report

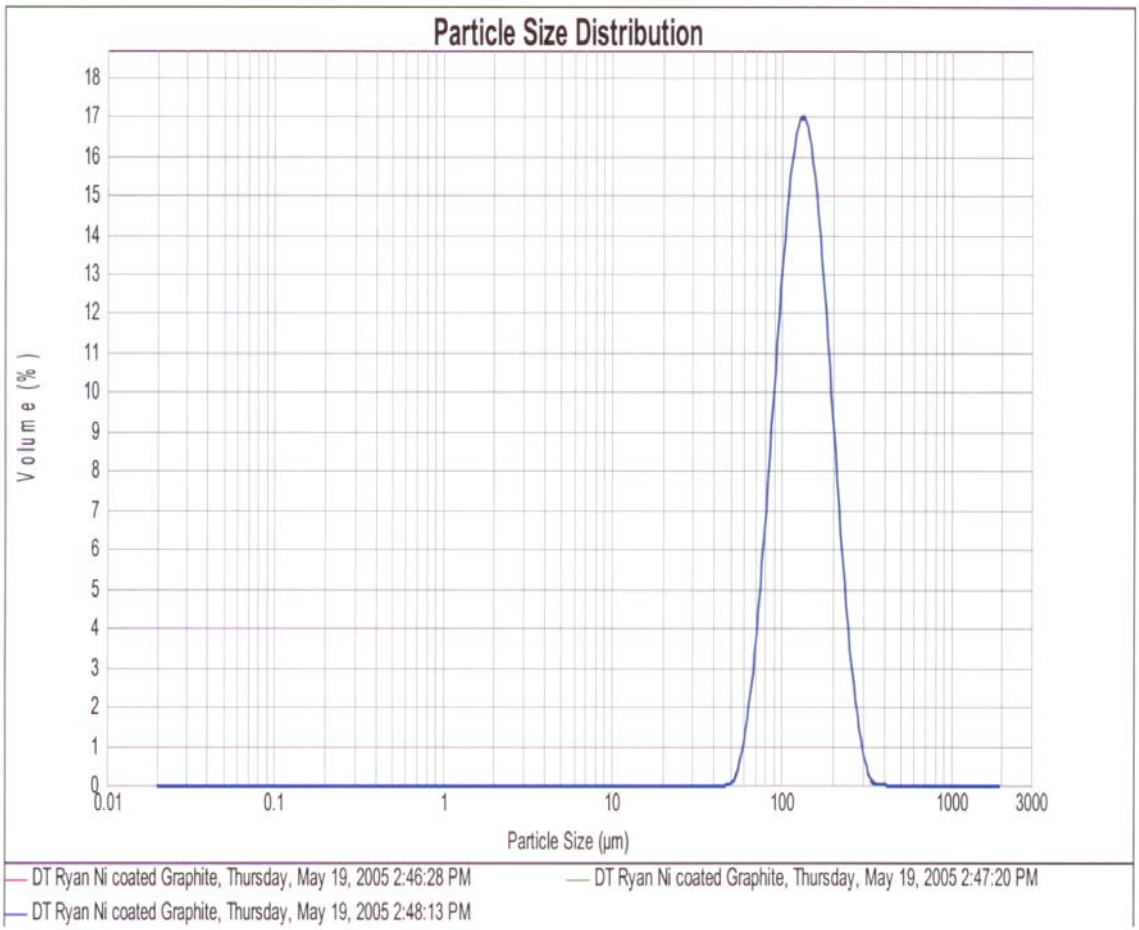

Figure A-6: NiGr particle size distribution

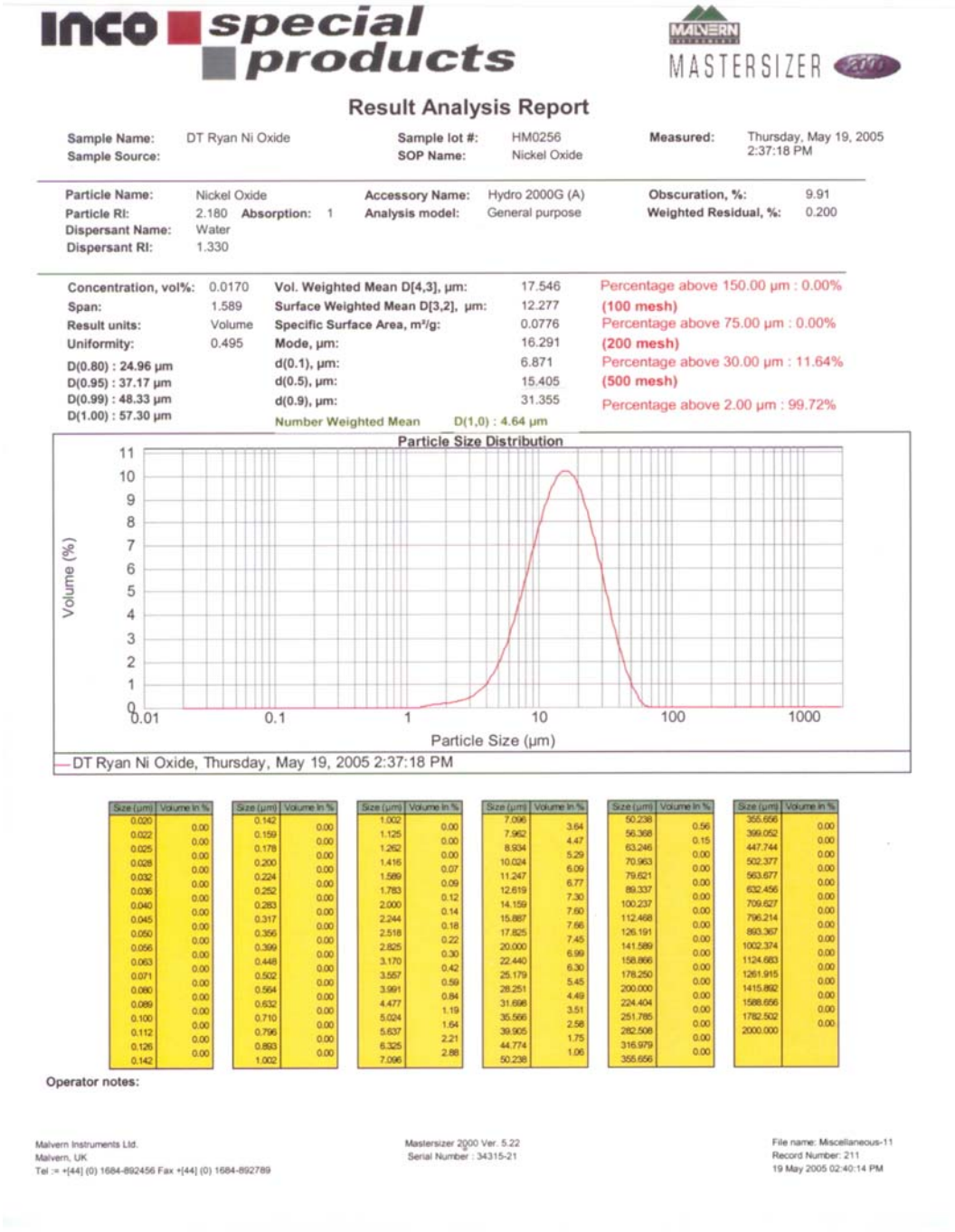

inco special products

MALVERN MASTERSIZER

Result Analysis Report

Sample Name:	DT Ryan Ni Oxide	**Sample lot #:**	HM0256	**Measured:**	Thursday, May 19, 2005 2:37:18 PM
Sample Source:		**SOP Name:**	Nickel Oxide		

Particle Name:	Nickel Oxide	**Accessory Name:**	Hydro 2000G (A)	**Obscuration, %:**	9.91
Particle RI:	2.180 **Absorption:** 1	**Analysis model:**	General purpose	**Weighted Residual, %:**	0.200
Dispersant Name:	Water				
Dispersant RI:	1.330				

Concentration, vol%:	0.0170	**Vol. Weighted Mean D[4,3], µm:**	17.546	Percentage above 150.00 µm : 0.00%
Span:	1.589	**Surface Weighted Mean D[3,2], µm:**	12.277	**(100 mesh)**
Result units:	Volume	**Specific Surface Area, m²/g:**	0.0776	Percentage above 75.00 µm : 0.00%
Uniformity:	0.495	**Mode, µm:**	16.291	**(200 mesh)**
D(0.80) : 24.96 µm		**d(0.1), µm:**	6.871	Percentage above 30.00 µm : 11.64%
D(0.95) : 37.17 µm		**d(0.5), µm:**	15.405	**(500 mesh)**
D(0.99) : 48.33 µm		**d(0.9), µm:**	31.355	Percentage above 2.00 µm : 99.72%
D(1.00) : 57.30 µm		**Number Weighted Mean**	**D(1,0) : 4.64 µm**	

Size (µm)	Volume In %	Size (µm)	Volume In %	Size (µm)	Volume In %	Size (µm)	Volume In %	Size (µm)	Volume In %	Size (µm)	Volume In %
0.020	0.00	0.142	0.00	1.002	0.00	7.096	3.64	50.238	0.56	355.656	0.00
0.022	0.00	0.159	0.00	1.125	0.00	7.962	4.47	56.368	0.15	399.052	0.00
0.025	0.00	0.178	0.00	1.262	0.00	8.934	5.29	63.246	0.00	447.744	0.00
0.028	0.00	0.200	0.00	1.416	0.07	10.024	6.09	70.963	0.00	502.377	0.00
0.032	0.00	0.224	0.00	1.589	0.09	11.247	6.77	79.621	0.00	563.677	0.00
0.036	0.00	0.252	0.00	1.783	0.12	12.619	7.30	89.337	0.00	632.456	0.00
0.040	0.00	0.283	0.00	2.000	0.14	14.159	7.60	100.237	0.00	709.627	0.00
0.045	0.00	0.317	0.00	2.244	0.18	15.887	7.66	112.468	0.00	796.214	0.00
0.050	0.00	0.356	0.00	2.518	0.22	17.825	7.45	126.191	0.00	893.367	0.00
0.056	0.00	0.399	0.00	2.825	0.30	20.000	6.99	141.589	0.00	1002.374	0.00
0.063	0.00	0.448	0.00	3.170	0.42	22.440	6.30	158.866	0.00	1124.683	0.00
0.071	0.00	0.502	0.00	3.557	0.59	25.179	5.45	178.250	0.00	1261.915	0.00
0.080	0.00	0.564	0.00	3.991	0.84	28.251	4.49	200.000	0.00	1415.892	0.00
0.089	0.00	0.632	0.00	4.477	1.19	31.698	3.51	224.404	0.00	1588.656	0.00
0.100	0.00	0.710	0.00	5.024	1.64	35.566	2.58	251.785	0.00	1782.502	0.00
0.112	0.00	0.796	0.00	5.637	2.21	39.905	1.75	282.508	0.00	2000.000	0.00
0.126	0.00	0.893	0.00	6.325	2.88	44.774	1.06	316.979	0.00		
0.142	0.00	1.002	0.00	7.096		50.238		355.656	0.00		

Operator notes:

Malvern Instruments Ltd.
Malvern, UK
Tel := +[44] (0) 1684-892456 Fax +[44] (0) 1684-892789

Mastersizer 2000 Ver. 5.22
Serial Number : 34315-21

File name: Miscellaneous-11
Record Number: 211
19 May 2005 02:40:14 PM

Figure A-7: NiO particle size result analysis report

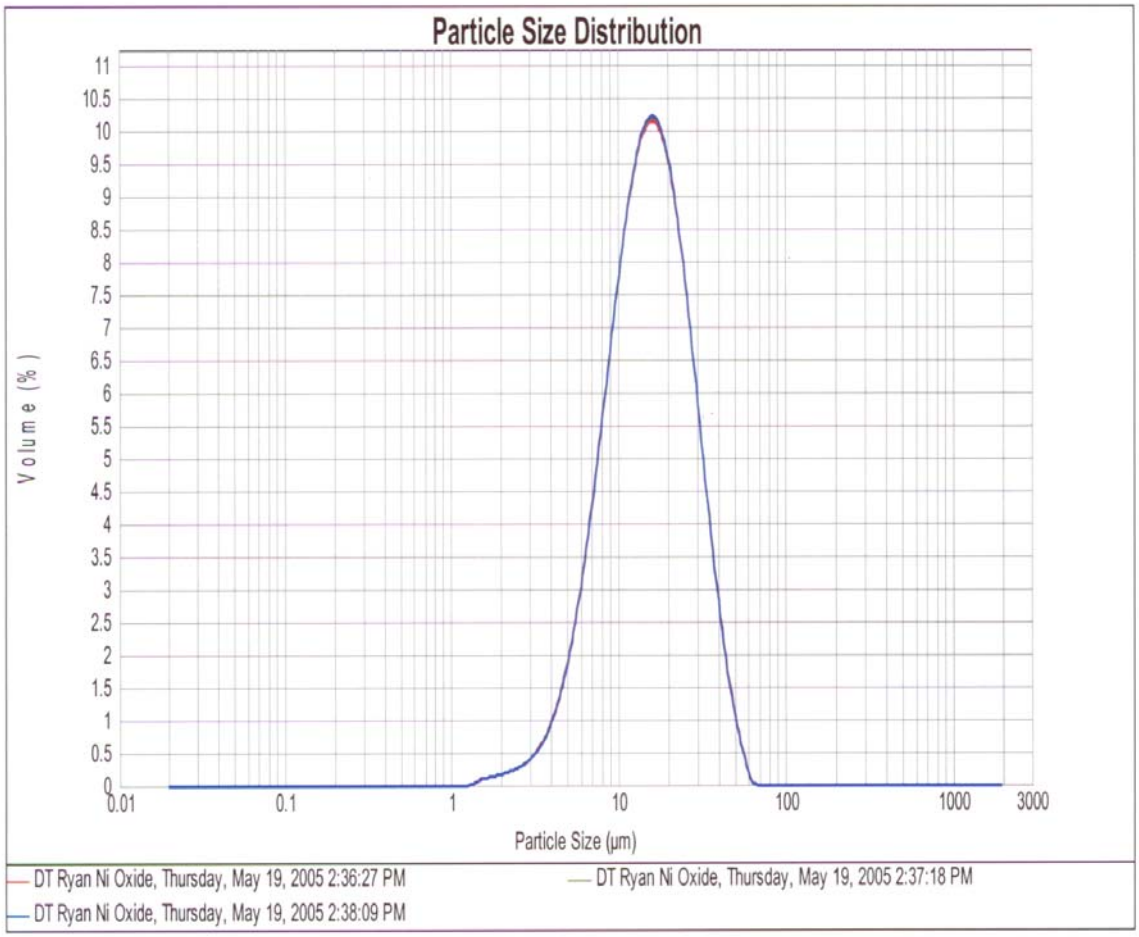

Figure A-8: NiO particle size distribution

Appendix B:
TAPE CASTING FORMULATIONS

The tape casting formulations used to create each composite type are given in the following tables:

Table B-1: Ni/YSZ composite tape casting formulations

Ni Loading (vol% total solids)	Material Mass (g)							
	YSZ	Ni	Graphite	NiGr	Ethanol	Toluene	Fish Oil	Polymer Solution
0	45.75	0.00	0	0	7.02	10.29	1.00	18.70
4	43.12	2.63	0	0	6.67	9.78	0.95	17.30
14	37.02	8.73	0	0	5.97	8.75	0.85	14.49
27	29.51	16.24	0	0	5.27	7.72	0.75	11.69
47	20.04	25.71	0	0	4.56	6.69	0.65	8.88
77	7.68	38.07	0	0	3.86	5.66	0.55	6.07
100	0.00	45.75	0	0	3.51	5.14	0.50	4.67

Table B-2: NiGr/YSZ composite tape casting formulations

Ni Loading (vol% total solids)	Material Mass (g)							
	YSZ	Ni	Graphite	NiGr	Ethanol	Toluene	Fish Oil	Polymer Solution
0	45.75	0	0	0.00	7.02	10.29	1.00	18.70
4	41.18	0	0	4.57	6.95	10.19	0.99	19.32
14	32.02	0	0	13.73	6.81	9.98	0.97	20.57
27	22.87	0	0	22.88	6.67	9.78	0.95	21.82
47	13.73	0	0	32.02	6.53	9.57	0.93	23.06
77	4.57	0	0	41.18	6.39	9.36	0.91	24.31
100	0.00	0	0	45.75	6.32	9.26	0.90	24.93

Table B-3: Ni&Gr/YSZ composite tape casting formulations

Ni Loading (vol% total solids)	Material Mass (g)							
	YSZ	Ni	Graphite	NiGr	Ethanol	Toluene	Fish Oil	Polymer Solution
0	45.75	0.00	0.00	0	7.02	10.29	1.00	18.70
4	41.18	2.51	2.06	0	7.72	11.32	1.10	18.23
14	32.02	7.55	6.18	0	9.13	13.38	1.30	17.30
27	22.87	12.58	10.30	0	10.53	15.44	1.50	16.37
47	13.73	17.61	14.41	0	11.93	17.49	1.70	15.43
77	4.57	22.65	18.53	0	13.34	19.55	1.90	14.50
100	0	25.16	20.59	0	14.04	20.58	2.00	14.03

Table B-4: NiO/YSZ composite tape casting formulations

Ni Loading (vol% total solids)	Material Mass (g)							
	YSZ	NiO	Graphite	NiGr	Ethanol	Toluene	Fish Oil	Polymer Solution
0	45.75	0.00	0	0	7.02	10.29	1.00	18.70
4	42.45	3.30	0	0	6.85	10.03	0.98	17.53
14	35.18	10.57	0	0	6.50	9.52	0.93	15.19
27	26.90	18.85	0	0	6.15	9.01	0.88	12.85
47	17.37	28.38	0	0	5.80	8.50	0.83	10.51
77	6.26	39.49	0	0	5.45	7.99	0.78	8.17
100	0.00	45.75	0	0	5.27	7.73	0.75	7.00

Table B-5: NiO&Gr/YSZ composite tape casting formulations

Ni Loading (vol% total solids)	Material Mass (g)							
	YSZ	NiO	Graphite	NiGr	Ethanol	Toluene	Fish Oil	Polymer Solution
0	45.75	0.00	0	0	7.02	10.29	1.00	18.70
4	40.57	3.15	2.03	0	7.72	11.32	1.10	18.23
14	30.64	9.20	5.91	0	9.13	13.38	1.30	17.30
27	21.27	14.91	9.57	0	10.53	15.44	1.50	16.37
47	12.42	20.29	13.03	0	11.93	17.49	1.70	15.43
77	4.02	25.41	16.32	0	13.34	19.55	1.90	14.50
100	0.00	27.86	17.89	0	14.04	20.58	2.00	14.03

Table B-6: Ni&Gr-27/YSZ composite tape casting formulations with a nickel loading of 27 vol% Ni of total solids and varying graphite content

Graphite Loading (green vol%)	Material Mass (g)							
	YSZ	Ni	Graphite	NiGr	Ethanol	Toluene	Fish Oil	Polymer Solution
0	29.51	16.24	0.00	0	5.27	7.72	0.75	11.69
9.05	27.73	14.93	3.09	0	6.84	10.03	0.98	13.09
13.90	26.39	14.21	5.15	0	7.90	11.58	1.13	14.03
18.14	25.05	13.49	7.21	0	8.95	13.12	1.28	14.96
21.84	23.71	12.77	9.27	0	10.00	14.66	1.43	15.90
23.49	22.87	12.58	10.30	0	10.53	15.44	1.50	16.37

Table B-7: Ni&Gr-47/YSZ composite tape casting formulations with a nickel loading of 47 vol% Ni of total solids and varying graphite content

Graphite Loading (green vol%)	Material Mass (g)							
	YSZ	Ni	Graphite	NiGr	Ethanol	Toluene	Fish Oil	Polymer Solution
0	20.04	25.71	0.00	0	7.02	10.29	1.00	18.70
10.96	18.23	23.20	4.32	0	9.13	13.38	1.30	17.30
17.63	16.96	21.59	7.20	0	10.53	15.44	1.50	16.37
23.85	15.69	19.97	10.09	0	11.93	17.49	1.70	15.43
29.71	14.42	18.36	12.97	0	13.34	19.55	1.90	14.50
31.80	13.73	17.61	14.41	0	14.04	20.58	2.00	14.03

Table B-8: NiO&Gr-27/YSZ composite tape casting formulations with a nickel loading of 27 vol% Ni of total solids and varying graphite content

Graphite Loading (green vol%)	Material Mass (g)							
	YSZ	NiO	Graphite	NiGr	Ethanol	Toluene	Fish Oil	Polymer Solution
0	26.90	18.85	0.00	0	6.15	9.01	0.88	12.85
7.91	25.21	17.67	2.87	0	7.46	10.94	1.06	13.90
12.45	24.09	16.88	4.79	0	8.34	12.22	1.19	14.61
16.40	22.96	16.09	6.70	0	9.21	13.51	1.31	15.31
19.97	21.84	15.30	8.61	0	10.09	14.79	1.44	16.01
21.60	21.27	14.91	9.57	0	10.53	15.44	1.50	16.37

Table B-9: NiO&Gr-47/YSZ composite tape casting formulations with a nickel loading of 47 vol% Ni of total solids and varying graphite content

Graphite Loading (green vol%)	Material Mass (g)							
	YSZ	NiO	Graphite	NiGr	Ethanol	Toluene	Fish Oil	Polymer Solution
0	17.37	28.38	0.00	0	7.02	10.29	1.00	18.70
9.56	15.90	25.94	3.91	0	9.13	13.38	1.30	17.30
15.53	14.91	24.33	6.52	0	10.53	15.44	1.50	16.37
21.21	13.92	22.71	9.12	0	11.93	17.49	1.70	15.43
26.50	12.93	21.09	11.73	0	13.34	19.55	1.90	14.50
28.60	12.42	20.29	13.03	0	14.04	20.58	2.00	14.03

Table B-10: NiGr-27/YSZ composite tape casting formulations with a nickel loading of 27 vol% Ni of total solids and varying cornstarch content

Graphite Loading (green vol%)	Material Mass (g)							
	YSZ	NiO	Graphite	NiGr	Ethanol	Toluene	Fish Oil	Polymer Solution
0	17.37	28.38	0.00	0	7.02	10.29	1.00	18.70
9.56	15.90	25.94	3.91	0	9.13	13.38	1.30	17.30
15.53	14.91	24.33	6.52	0	10.53	15.44	1.50	16.37
21.21	13.92	22.71	9.12	0	11.93	17.49	1.70	15.43
26.50	12.93	21.09	11.73	0	13.34	19.55	1.90	14.50
28.60	12.42	20.29	13.03	0	14.04	20.58	2.00	14.03

Table B-11: NiGr-47/YSZ composite tape casting formulations with a nickel loading of 47 vol% Ni of total solids and varying cornstarch content

Graphite Loading (green vol%)	Material Mass (g)							
	YSZ	NiO	Graphite	NiGr	Ethanol	Toluene	Fish Oil	Polymer Solution
0	17.37	28.38	0.00	0	7.02	10.29	1.00	18.70
9.56	15.90	25.94	3.91	0	9.13	13.38	1.30	17.30
15.53	14.91	24.33	6.52	0	10.53	15.44	1.50	16.37
21.21	13.92	22.71	9.12	0	11.93	17.49	1.70	15.43
26.50	12.93	21.09	11.73	0	13.34	19.55	1.90	14.50
28.60	12.42	20.29	13.03	0	14.04	20.58	2.00	14.03

Appendix C:
DILATOMETER SINTERING RESULTS

Dilatometer Sample Measurements

The dimensions of each of three samples were measured before and after sintering within the dilatometer. The overall linear sintering shrinkages in the length direction as measured by the dilatometer and by hand are shown in the following figures for each of the composite types.

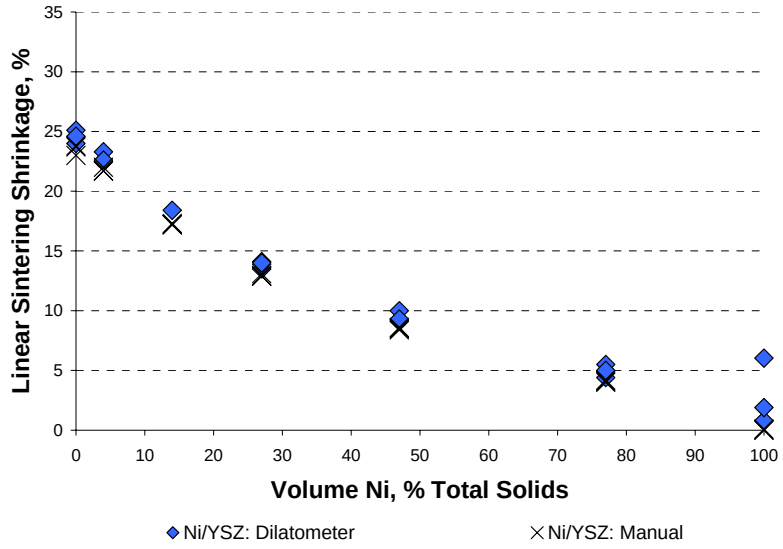

Figure C-1: Comparison of linear sintering shrinkages as measured manually and with a dilatometer for the Ni/YSZ composites

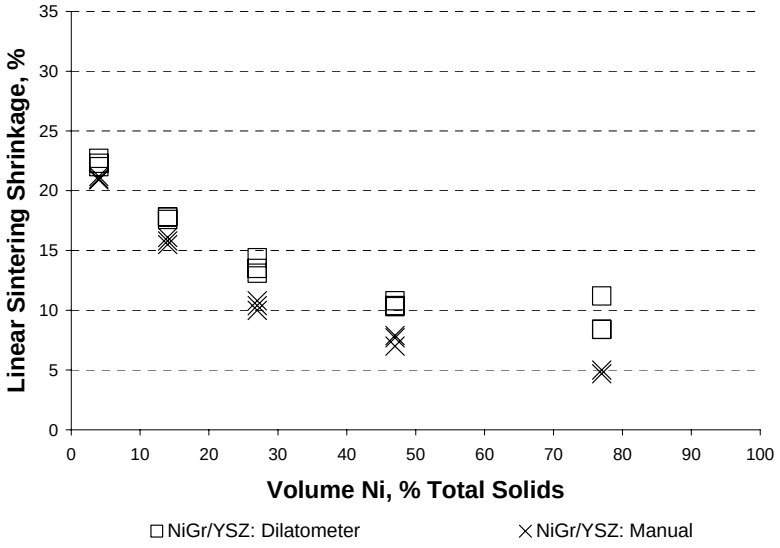

Figure C-2: Comparison of linear sintering shrinkages as measured manually and with a dilatometer for the NiGr/YSZ composites

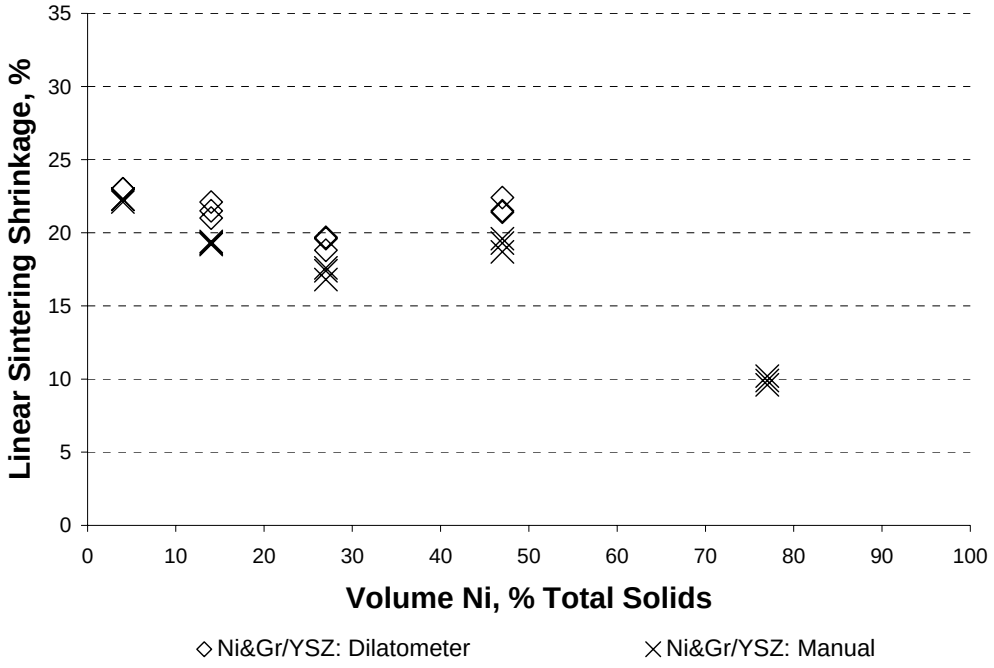

Figure C-3: Comparison of linear sintering shrinkages as measured manually and with a dilatometer for the Ni&Gr/YSZ composites

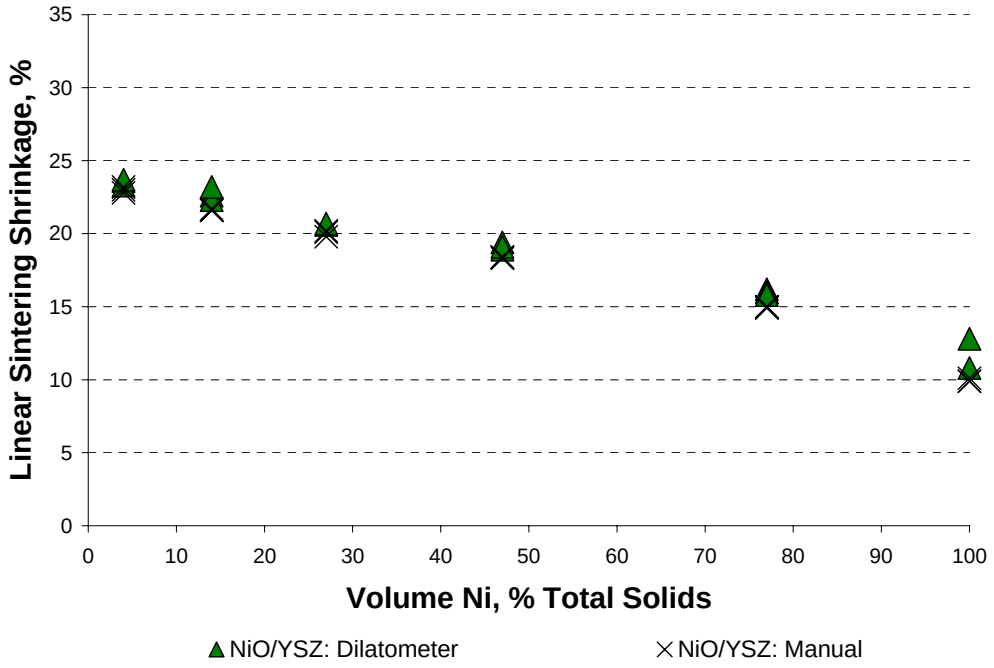

Figure C-4: Comparison of linear sintering shrinkages as measured manually and with a dilatometer for the NiO/YSZ composites

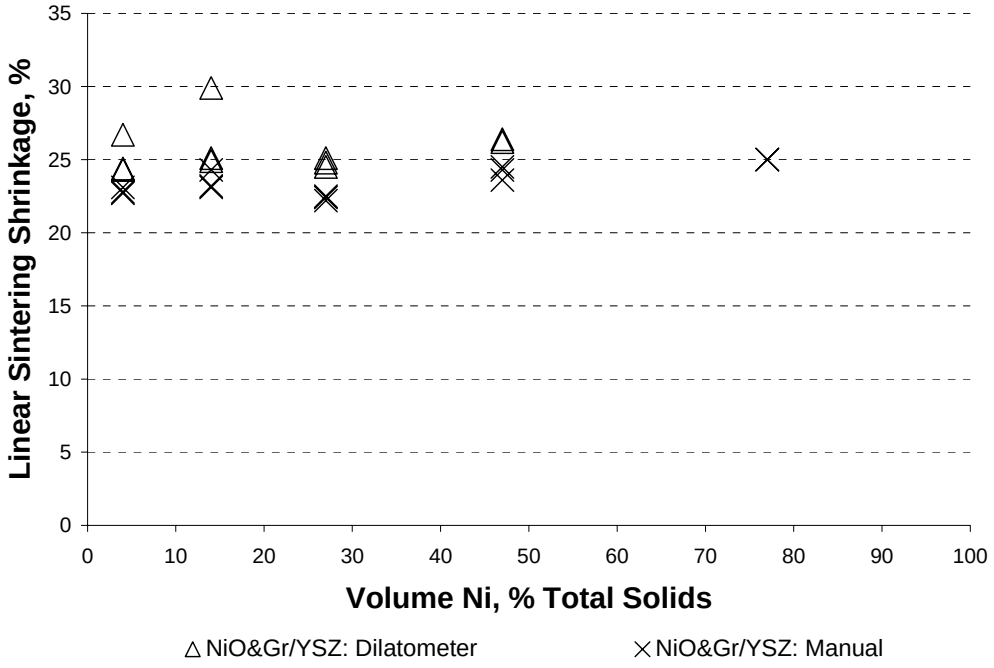

Figure C-5: Comparison of linear sintering shrinkages as measured manually and with a dilatometer for the NiO&Gr/YSZ composites

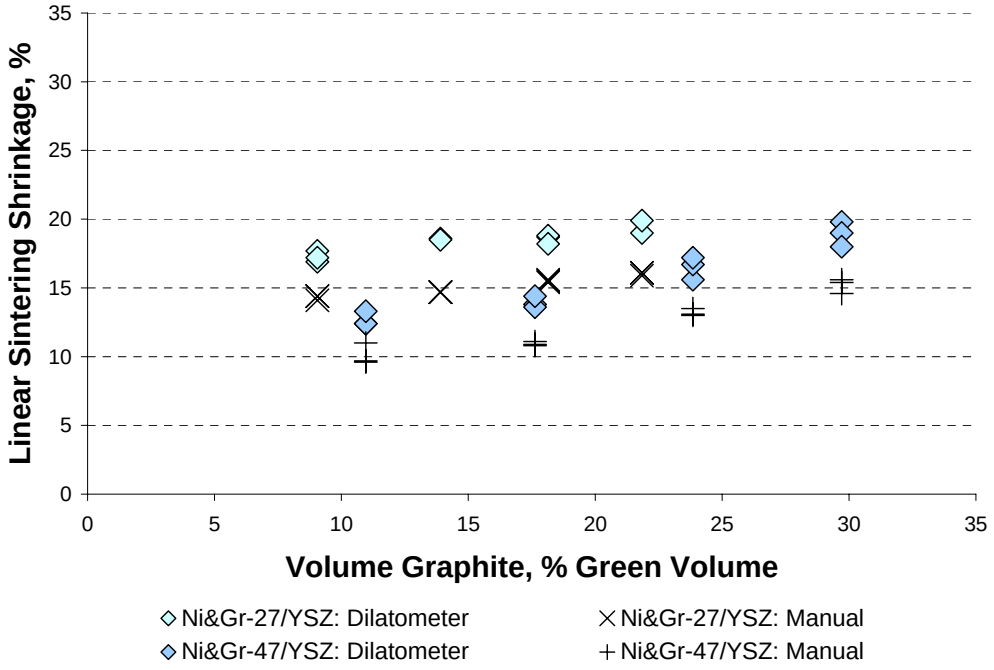

Figure C-6: Comparison of linear sintering shrinkages as measured manually and with a dilatometer for the Ni&Gr-27/YSZ and Ni&Gr-47/YSZ composites

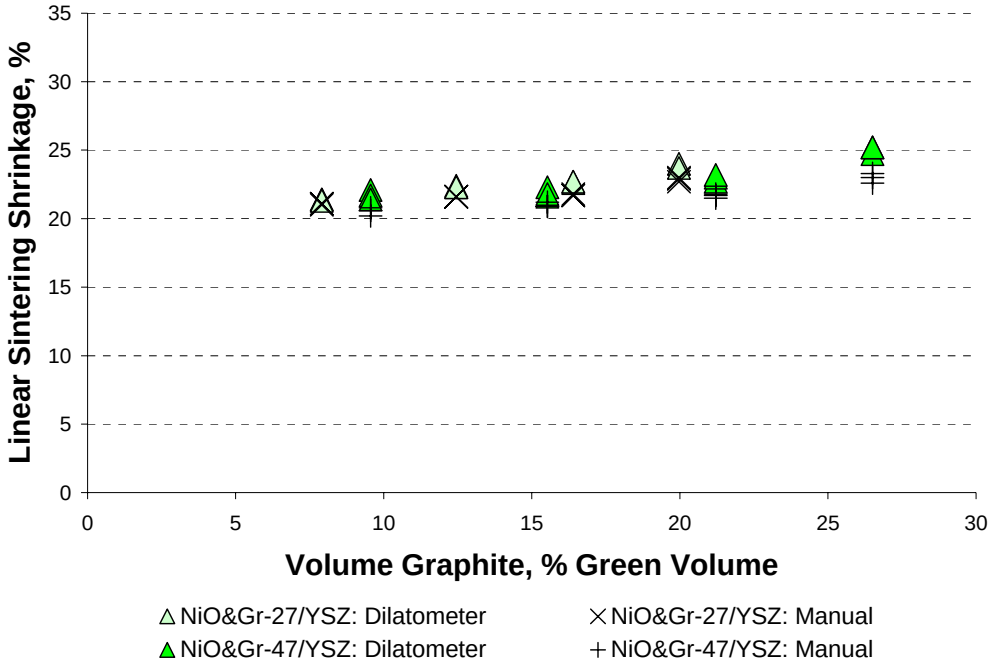

Figure C-7: Comparison of linear sintering shrinkages as measured manually and with a dilatometer for the NiO&Gr-27/YSZ and NiO&Gr-47/YSZ composites

Appendix D:
BULK SINTERING RESULTS

The linear dimensional shrinkages, volumetric shrinkages, and bulk porosity results after bulk sintering in a box furnace are presented in this Appendix.

Linear Dimensional Shrinkage after Bulk Sintering

The volumetric sintering shrinkage results after bulk sintering are presented for each composite type in the following Figures:

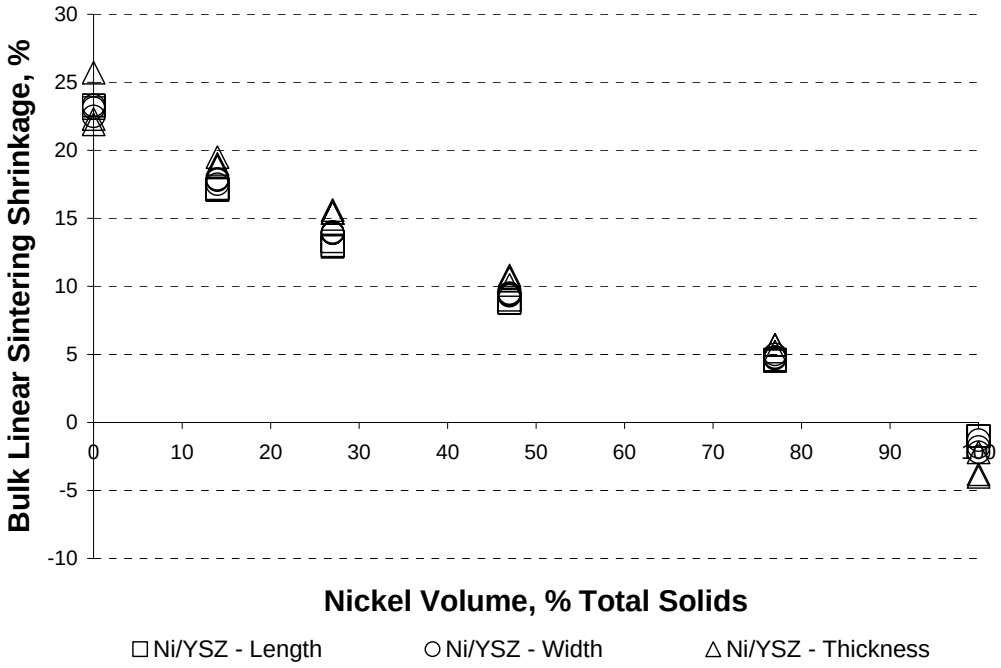

Figure D-1: Linear sintering shrinkage from the burnout to sintered state for the length, width, and thickness of Ni/YSZ composite samples sintered in a box furnace

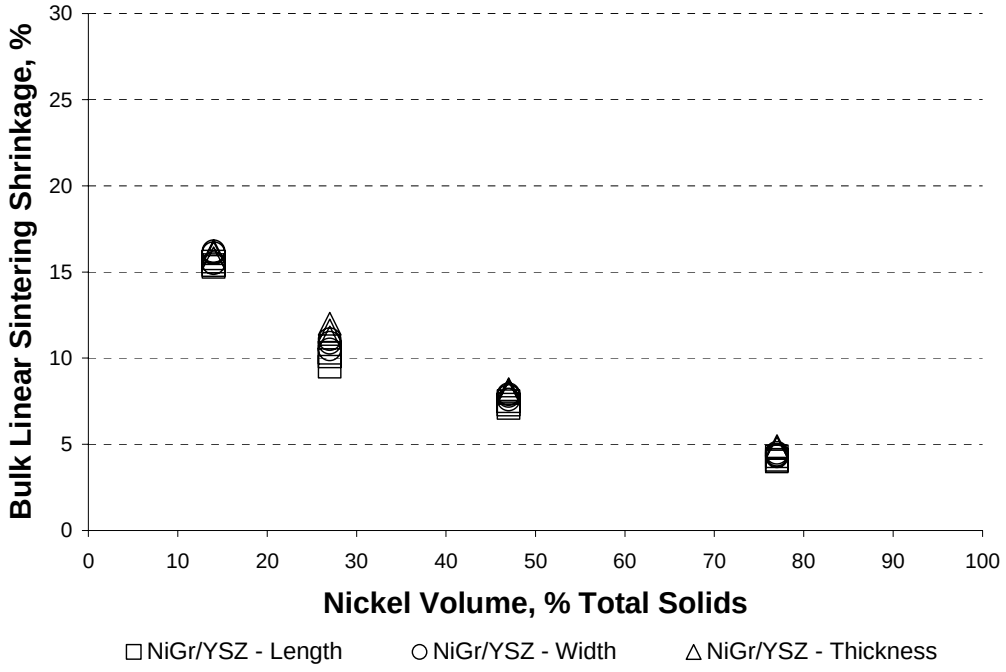

Figure D-2: Linear sintering shrinkage from the burnout to sintered state for the length, width, and thickness of NiGr/YSZ composite samples sintered in a box furnace

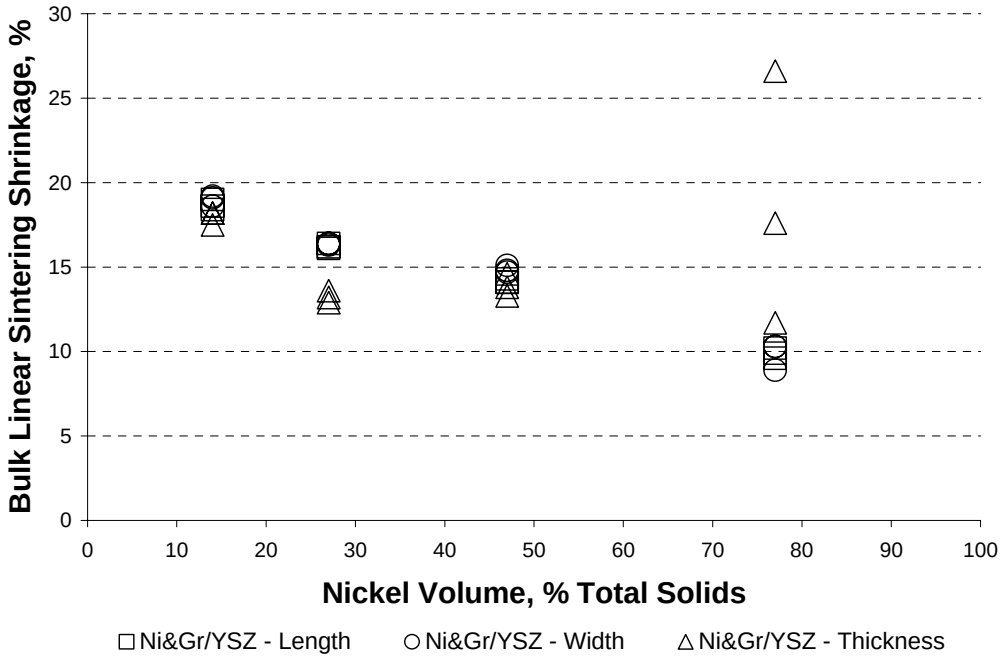

Figure D-3: Linear sintering shrinkage from the burnout to sintered state for the length, width, and thickness of Ni&Gr/YSZ composite samples sintered in a box furnace

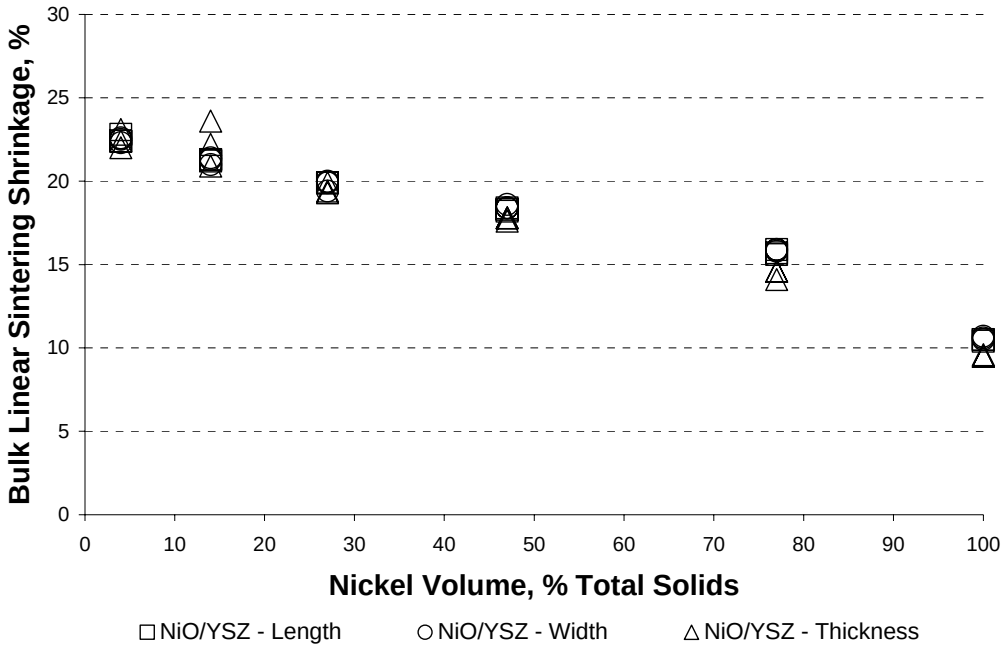

Figure D-4: Linear sintering shrinkage from the burnout to sintered state for the length, width, and thickness of NiO/YSZ composite samples sintered in a box furnace

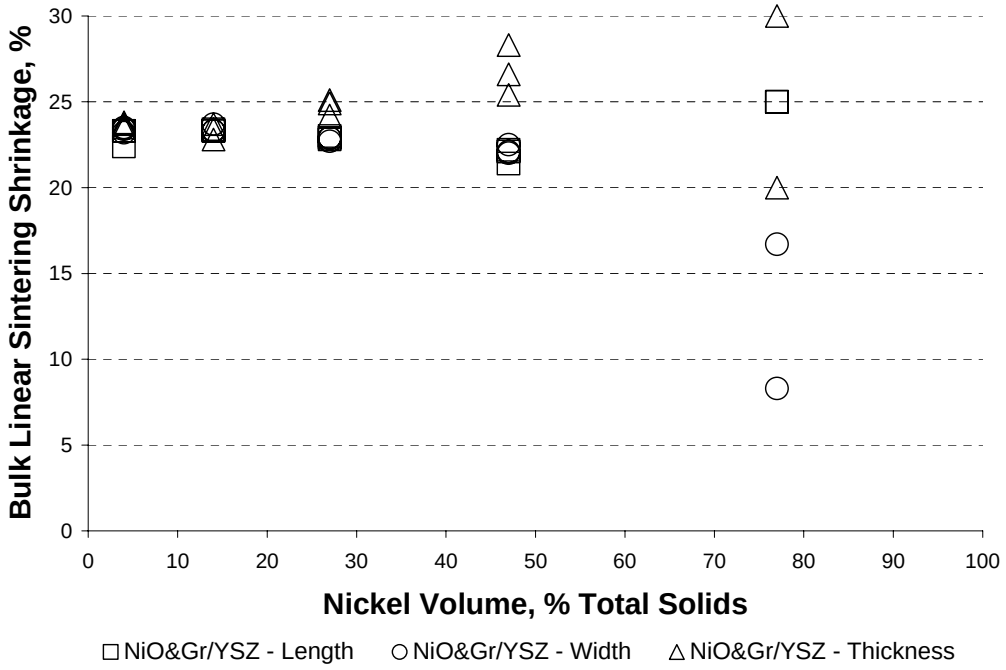

Figure D-5: Linear sintering shrinkage from the burnout to sintered state for the length, width, and thickness of NiO&Gr/YSZ composite samples sintered in a box furnace

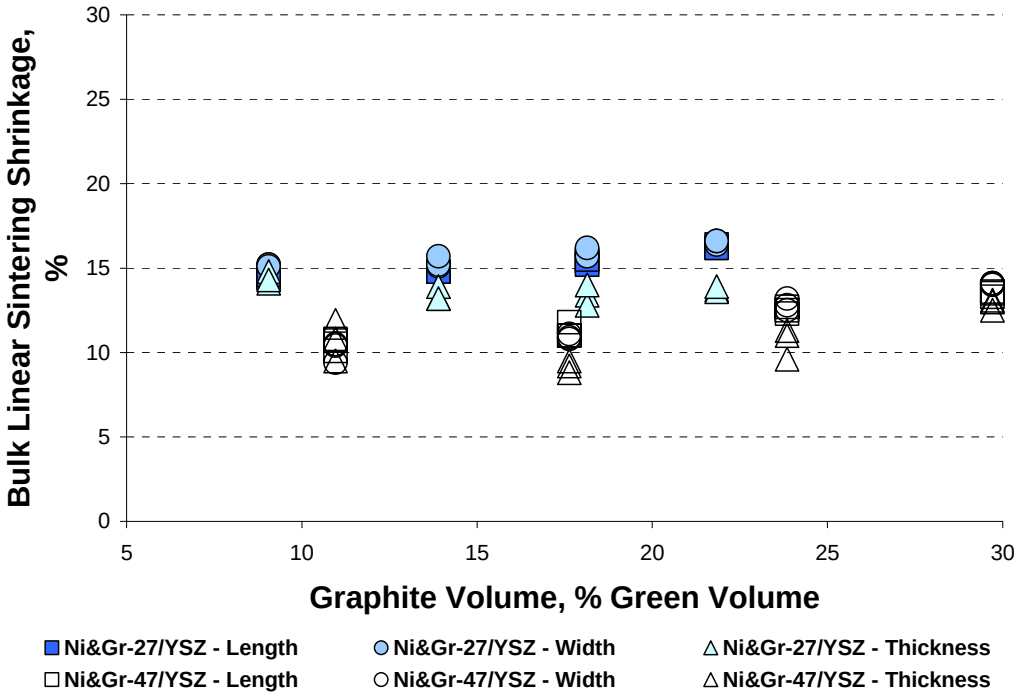

Figure D-6: Linear sintering shrinkage from the burnout to sintered state for the length, width, and thickness of Ni&Gr-27/YSZ and Ni&Gr-47/YSZ composite samples sintered in a box furnace

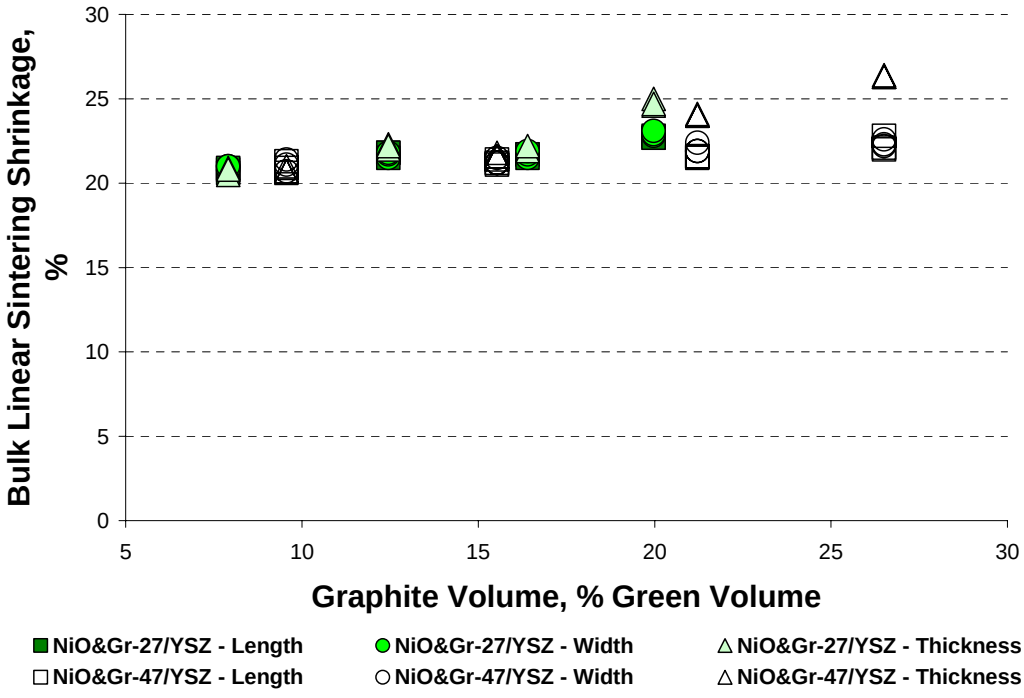

Figure D-7: Linear sintering shrinkage from the burnout to sintered state for the length, width, and thickness of NiO&Gr-27/YSZ and NiO&Gr-47/YSZ composite samples sintered in a box furnace

Volumetric Sintering Shrinkage after Bulk Sintering

The volumetric sintering shrinkage results after bulk sintering are presented for each composite type in the following Figures:

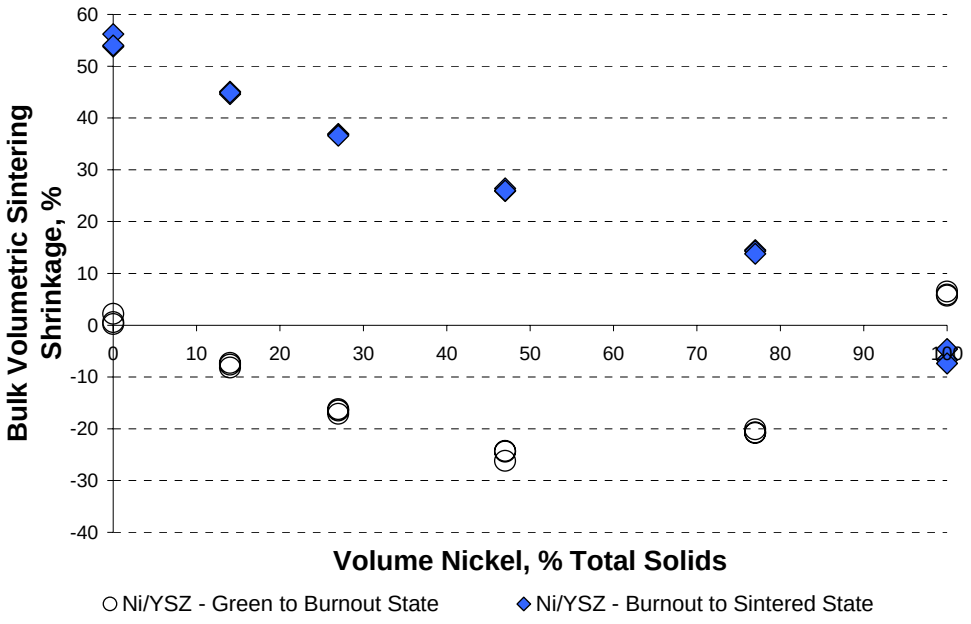

Figure D-8: Volumetric sintering shrinkage for the Ni/YSZ composites sintered in a box furnace after the burnout and sintering stage

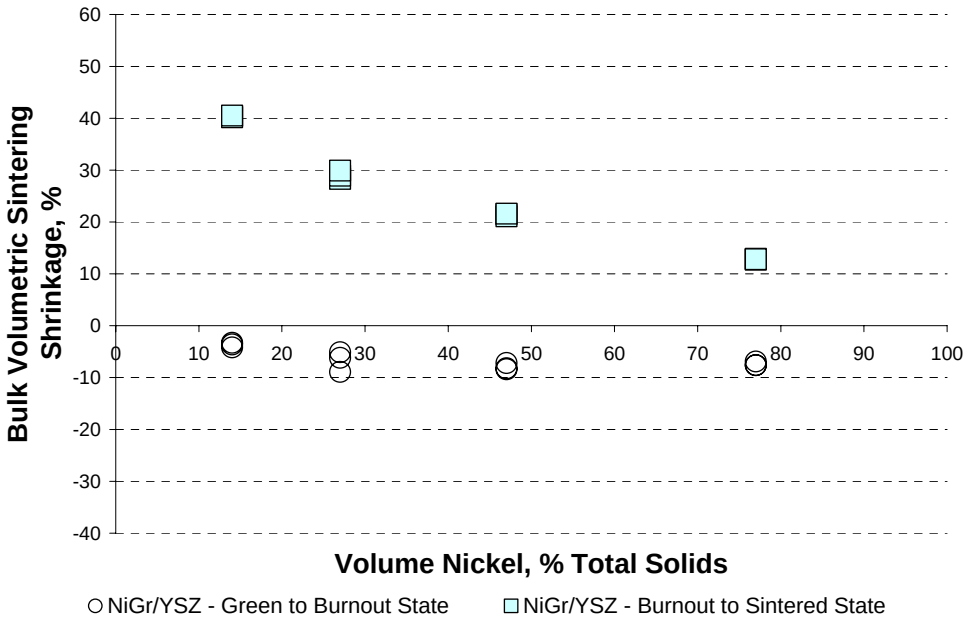

Figure D-9: Volumetric sintering shrinkage for the NiGr/YSZ composites sintered in a box furnace after the burnout and sintering stage

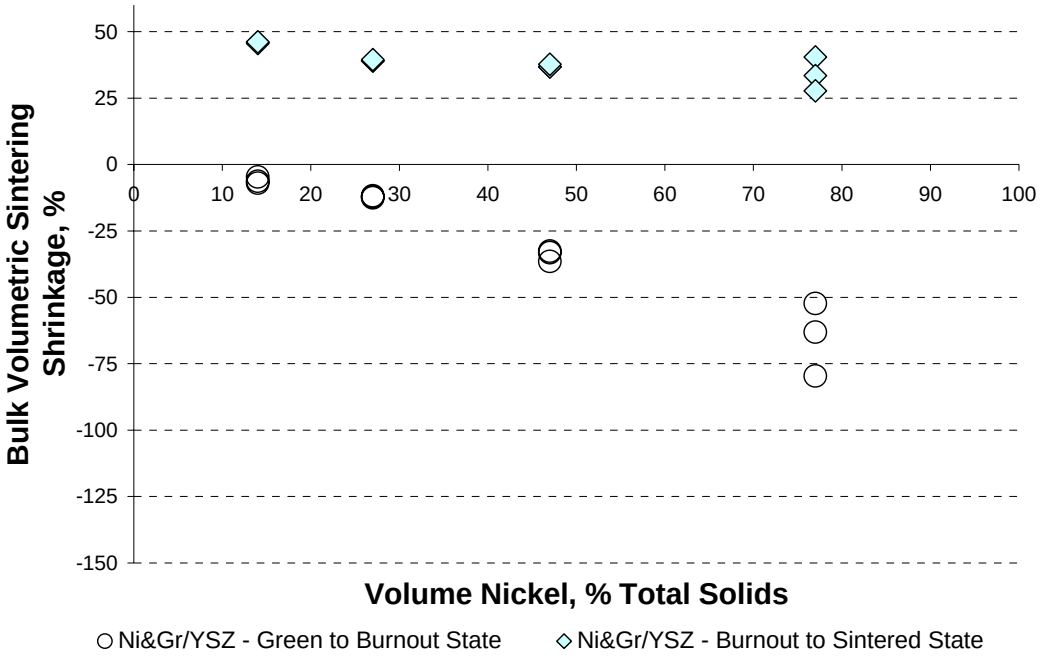

Figure D-10: Volumetric sintering shrinkage for the Ni&Gr/YSZ composites sintered in a box furnace after the burnout and sintering stage

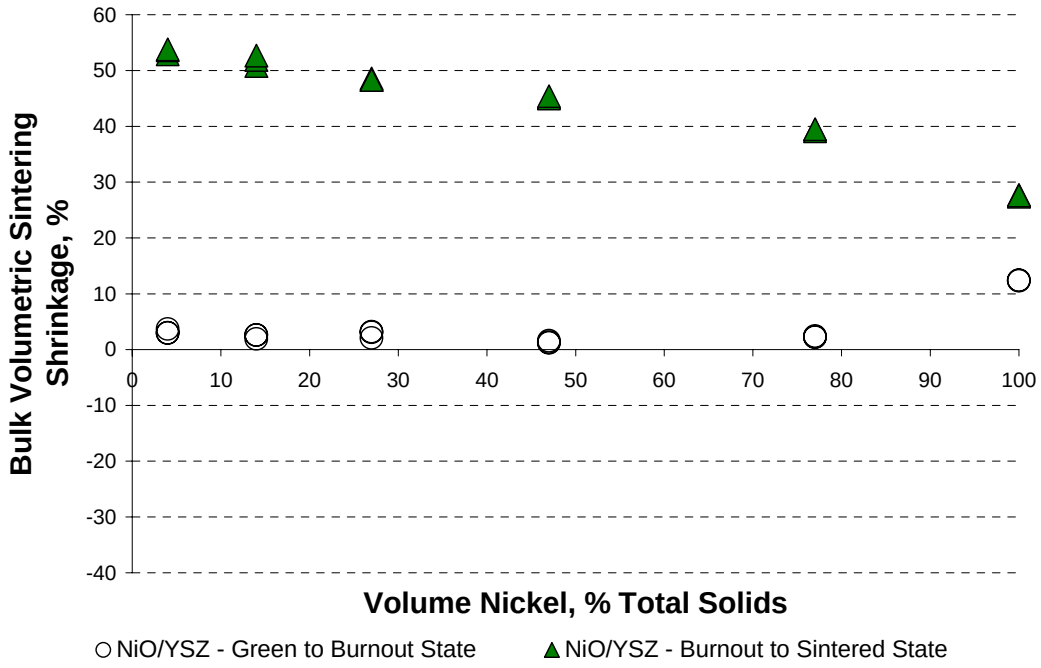

Figure D-11: Volumetric sintering shrinkage for the NiO/YSZ composites sintered in a box furnace after the burnout and sintering stage

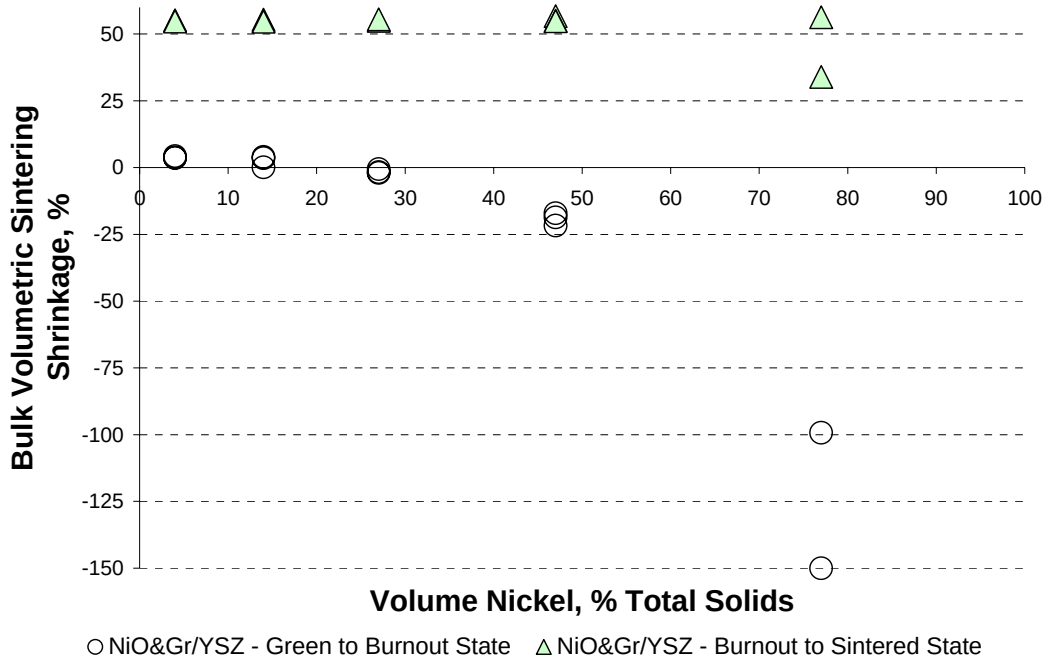

Figure D-12: Volumetric sintering shrinkage for the NiO&Gr/YSZ composites sintered in a box furnace after the burnout and sintering stage

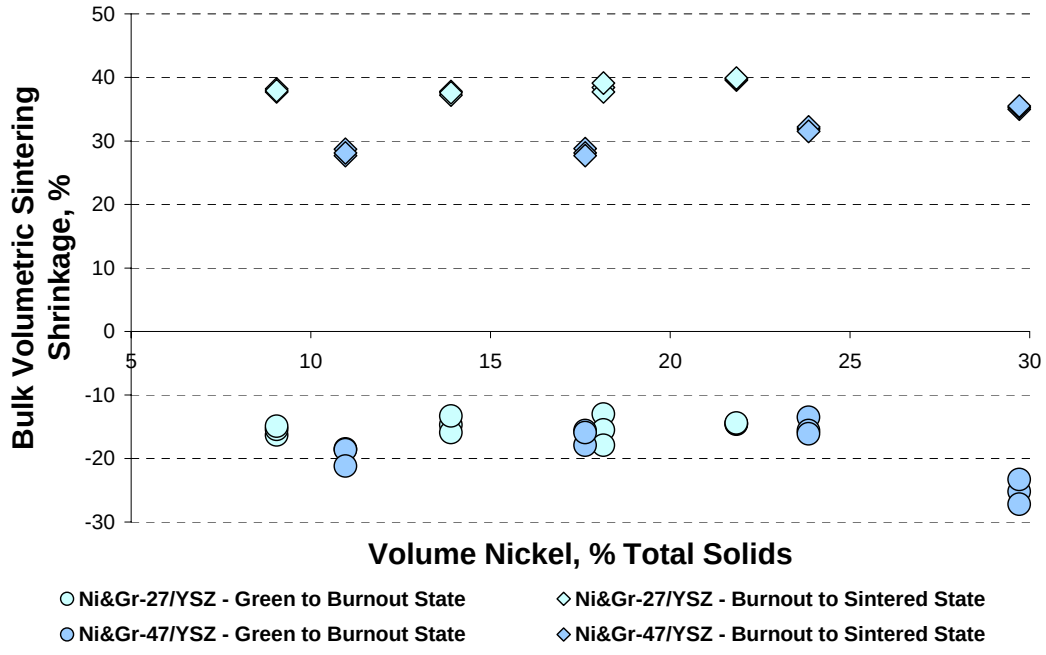

Figure D-13: Volumetric sintering shrinkages during the burnout and sintering stages for the Ni&Gr-27/YSZ and Ni&Gr-47/YSZ composites with a fixed nickel content and varying graphite loading sintered in a box furnace

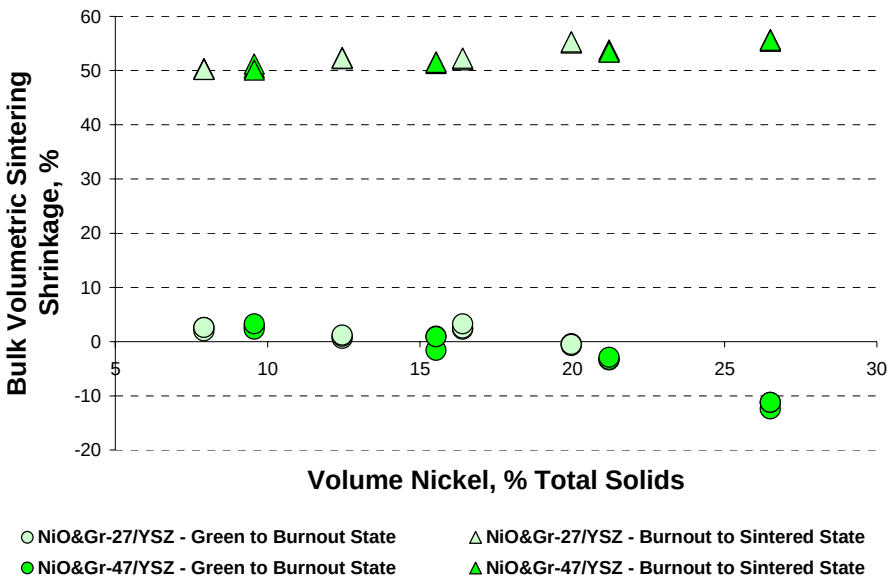

Figure D-14: Volumetric sintering shrinkages during the burnout and sintering stages for the NiO&Gr-27/YSZ and NiO&Gr-47/YSZ composites with a fixed nickel content and varying graphite loading sintered in a box furnace

Relative Composite Density after Bulk Sintering

The relative density results after bulk sintering for each composite type is presented in the following Figures:

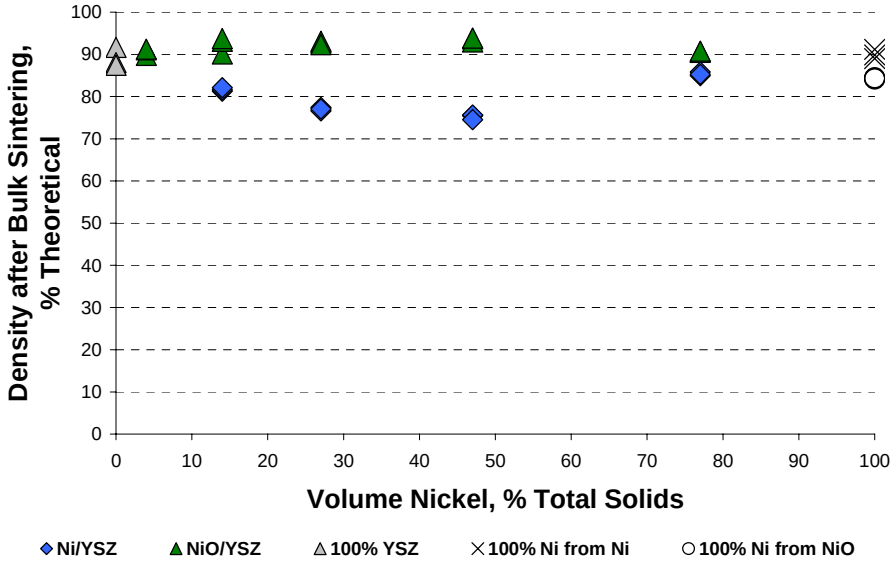

Figure D-15: Relative density of Ni/YSZ and NiO/YSZ composites after sintering in a box furnace

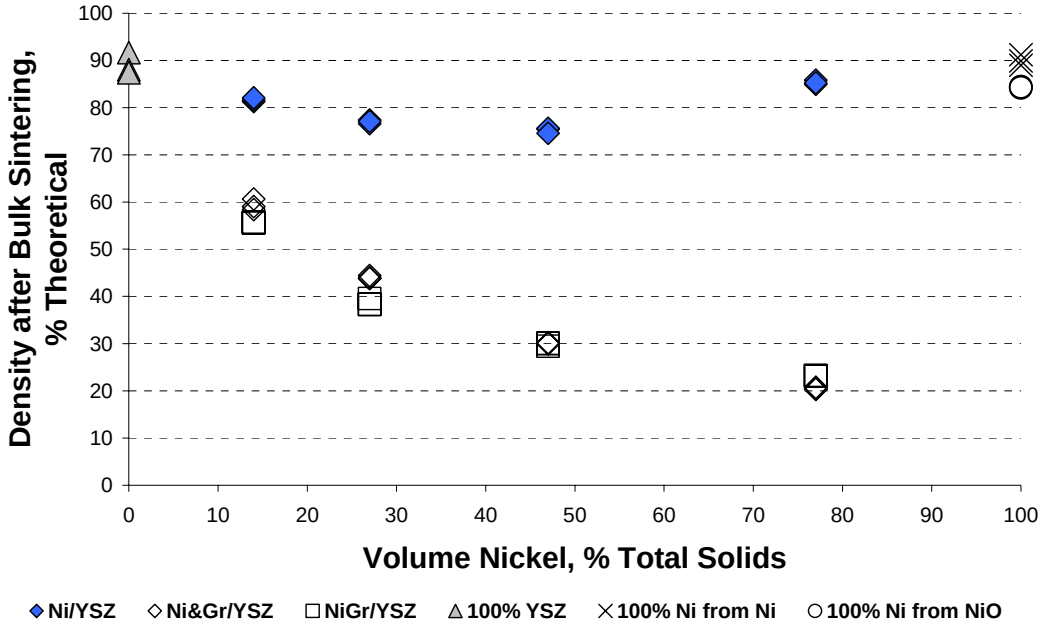

Figure D-16: Relative density of Ni/YSZ, NiGr/YSZ, and Ni&Gr/YSZ composites after sintering in a box furnace

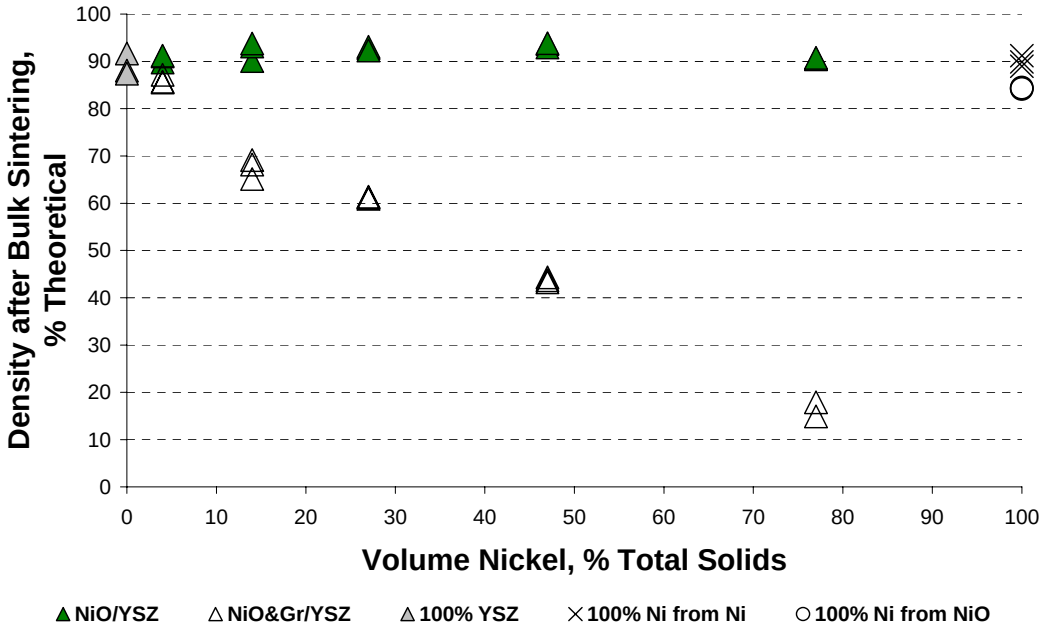

Figure D-17: Relative density of NiO/YSZ and NiO&Gr/YSZ composites after sintering in a box furnace

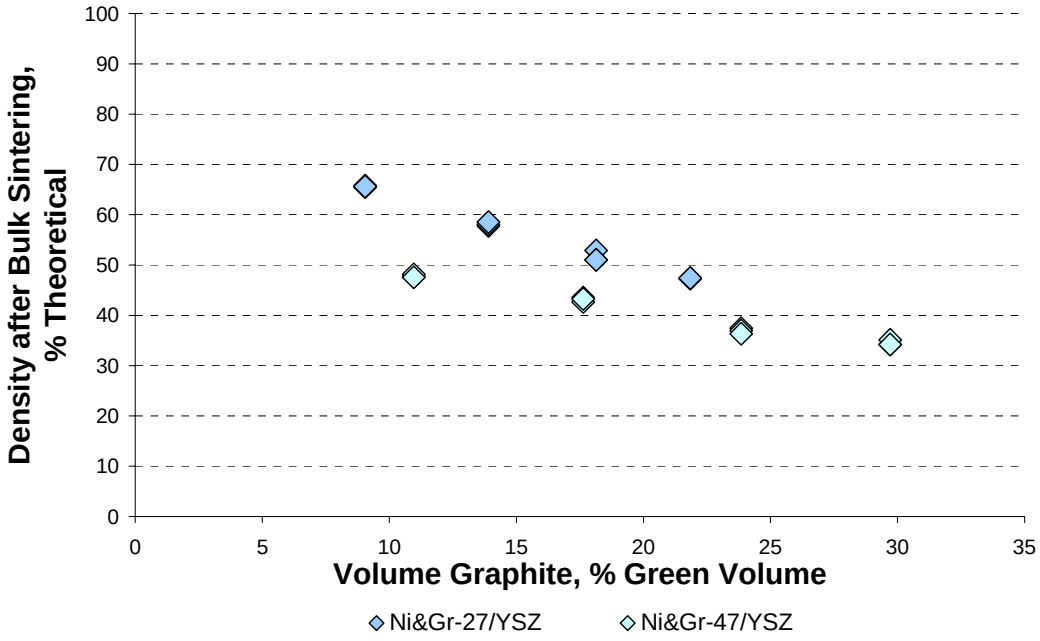

Figure D-18: Relative density of Ni&Gr-27/YSZ, and Ni&Gr-47/YSZ composites after sintering in a box furnace

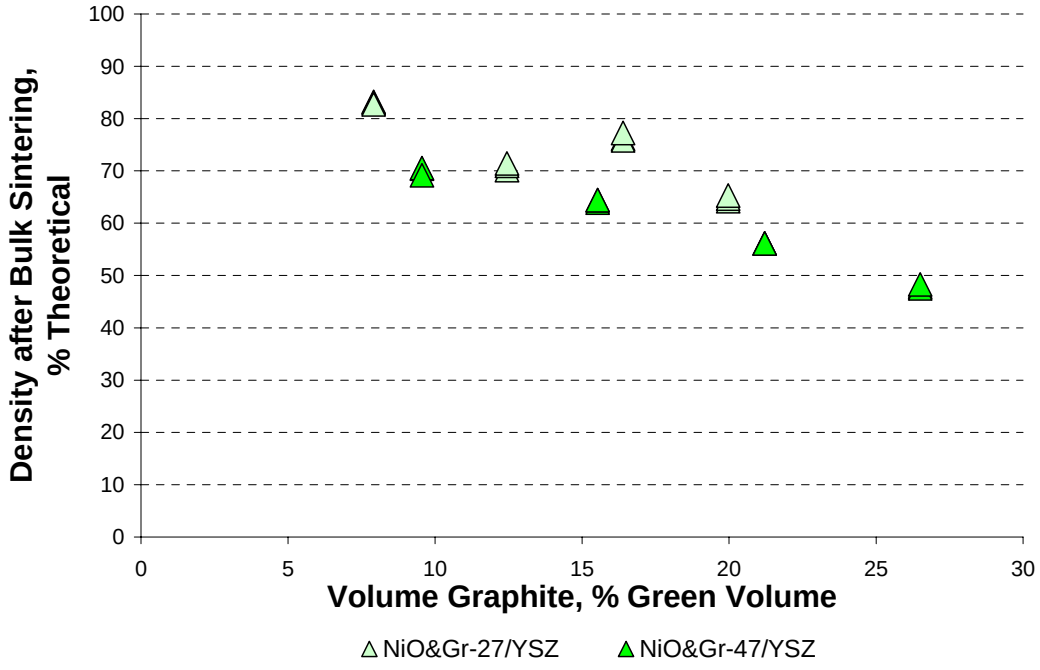

Figure D-19: Relative density of NiO&Gr-27/YSZ, and NiO&Gr-47/YSZ composites after sintering in a box furnace

Comparison between Bulk and Dilatometer Sintered Samples

To better distinguish any effects that sintering in the dilatometer might have on the sintering of the composites, the volumetric sintering shrinkages from the green to the sintered state are given for both the bulk and dilatometer sintered samples in the following Figures:

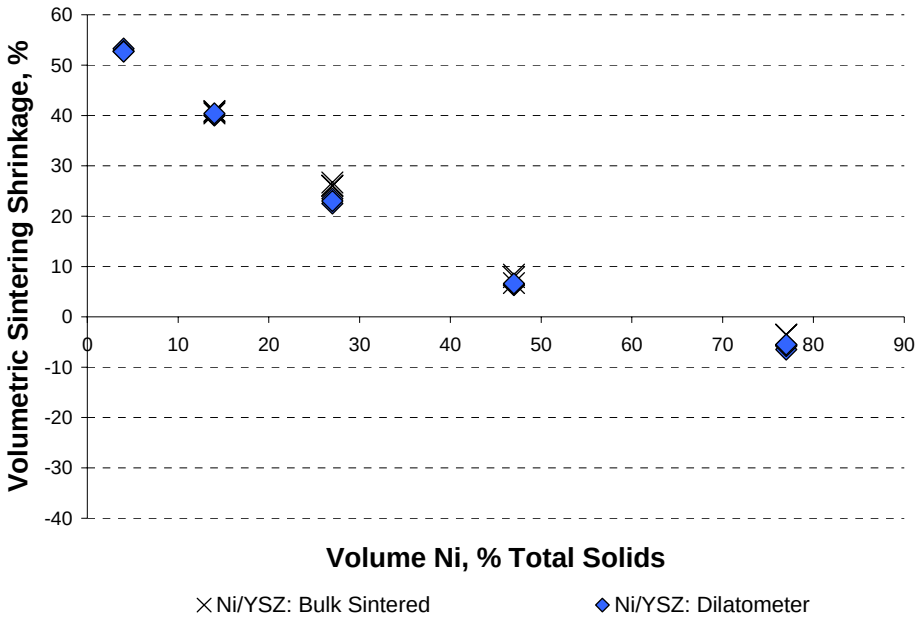

Figure D-20: Volumetric sintering shrinkage from the green to sintered state for Ni/YSZ composite samples sintered in a box furnace or dilatometer

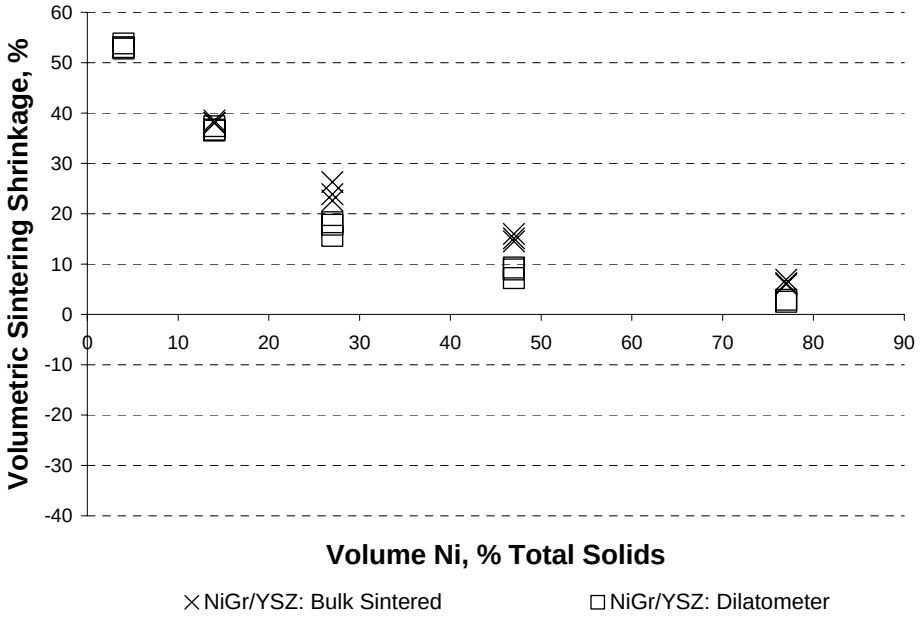

Figure D-21: Volumetric sintering shrinkage from the green to sintered state for NiGr/YSZ composite samples sintered in a box furnace or dilatometer

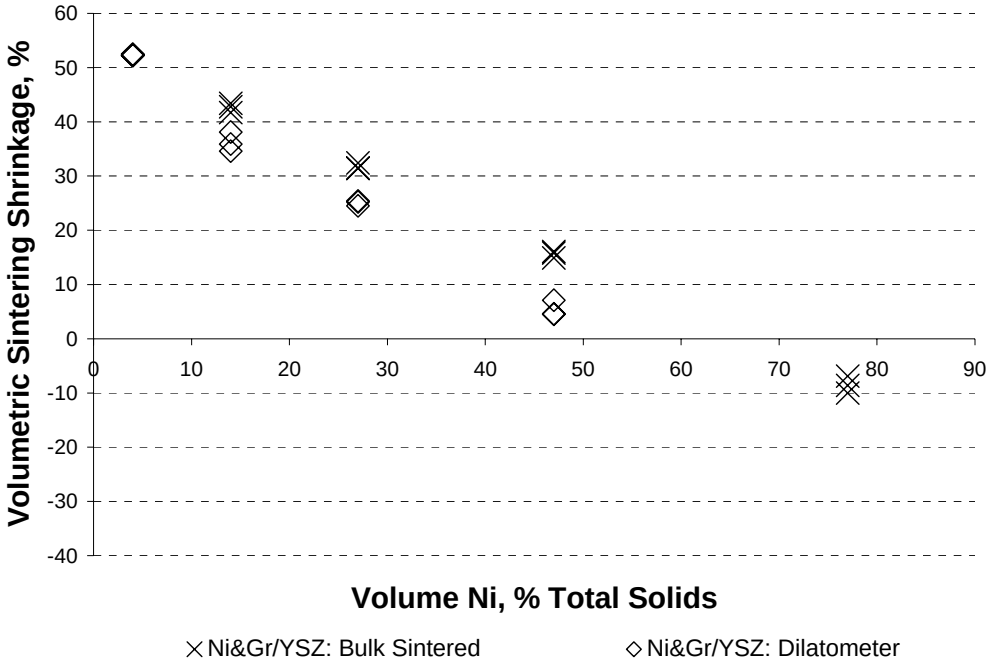

Figure D-22: Volumetric sintering shrinkage from the green to sintered state for Ni&Gr/YSZ composite samples sintered in a box furnace or dilatometer

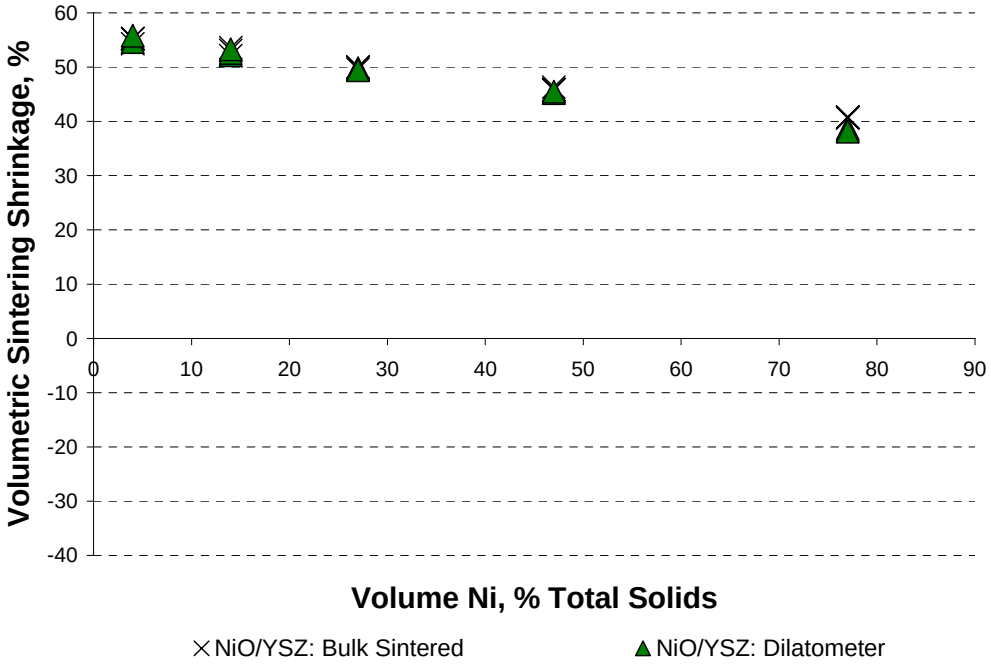

Figure D-23: Volumetric sintering shrinkage from the green to sintered state for NiO/YSZ composite samples sintered in a box furnace or dilatometer

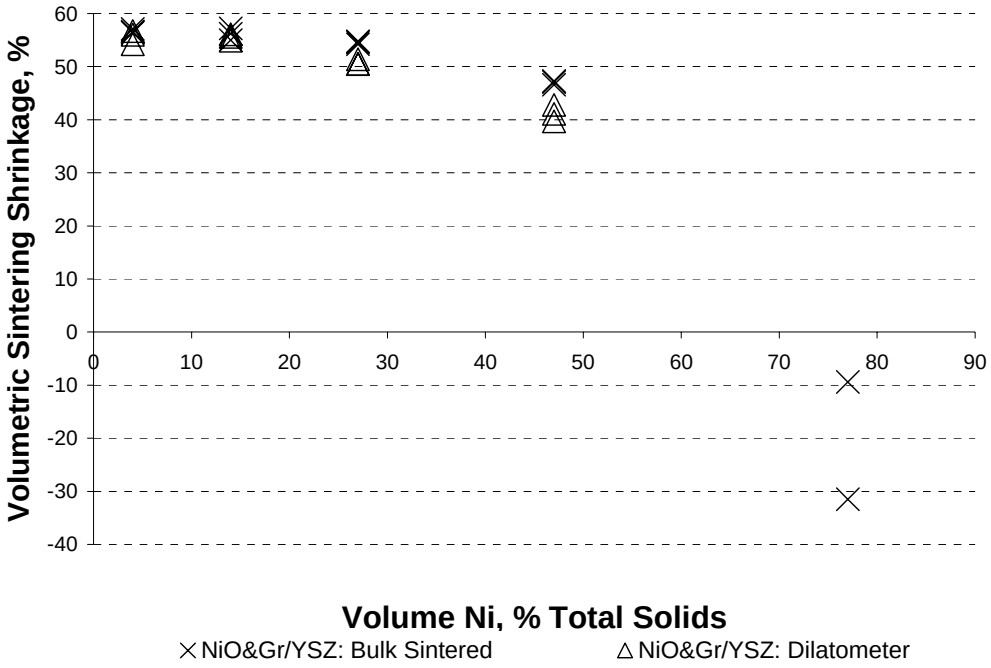

Figure D-24: Volumetric sintering shrinkage from the green to sintered state for NiO&Gr/YSZ composite samples sintered in a box furnace or dilatometer

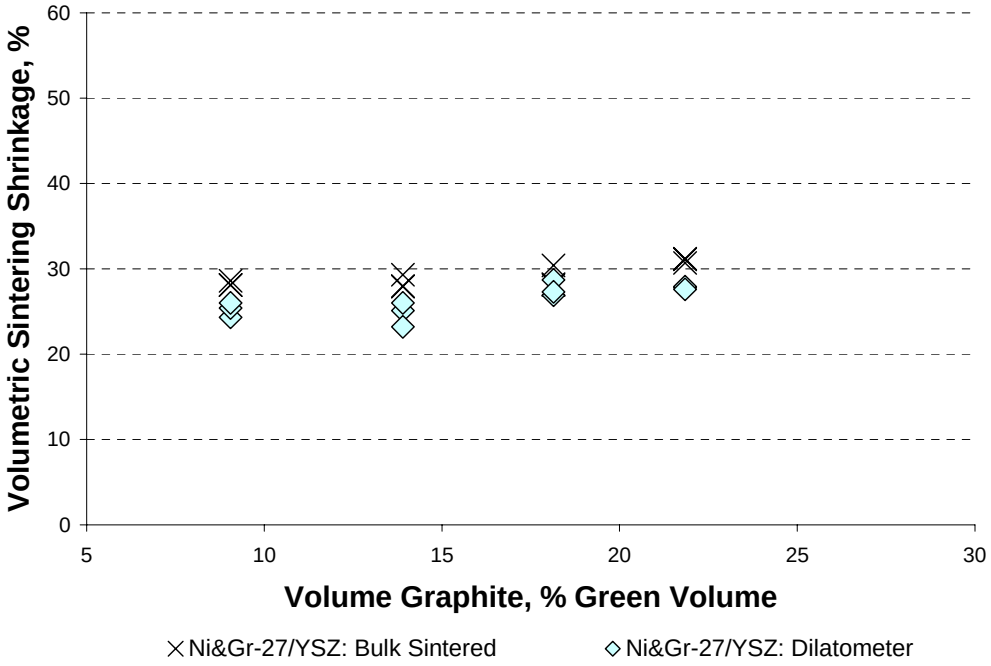

Figure D-25: Volumetric sintering shrinkage from the green to sintered state for Ni&Gr-27/YSZ composite samples sintered in a box furnace or dilatometer

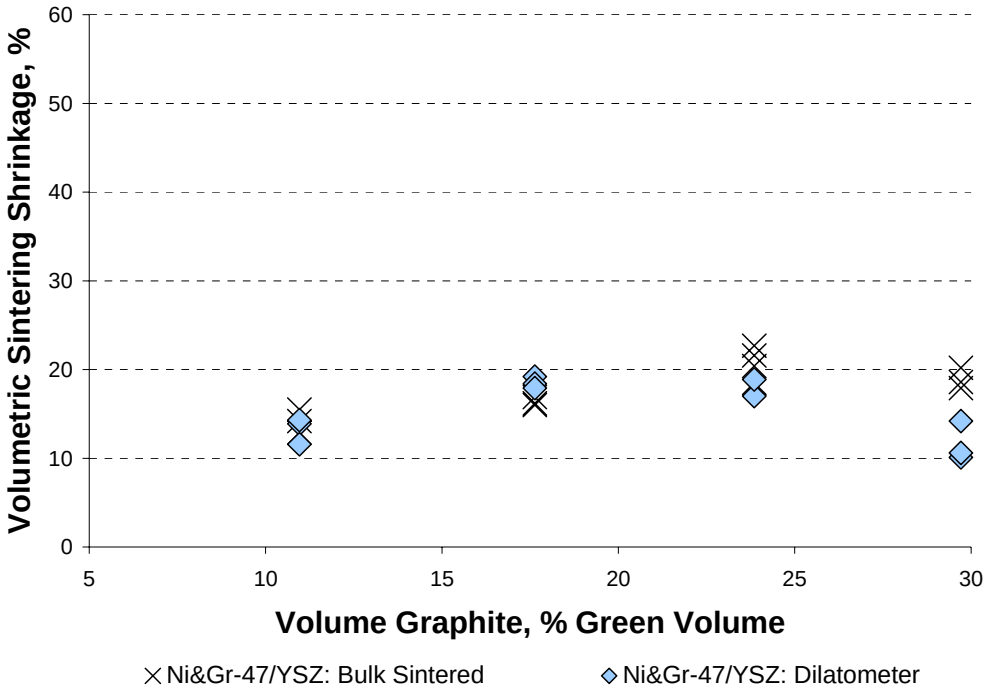

Figure D-26: Volumetric sintering shrinkage from the green to sintered state for Ni&Gr-47/YSZ composite samples sintered in a box furnace or dilatometer

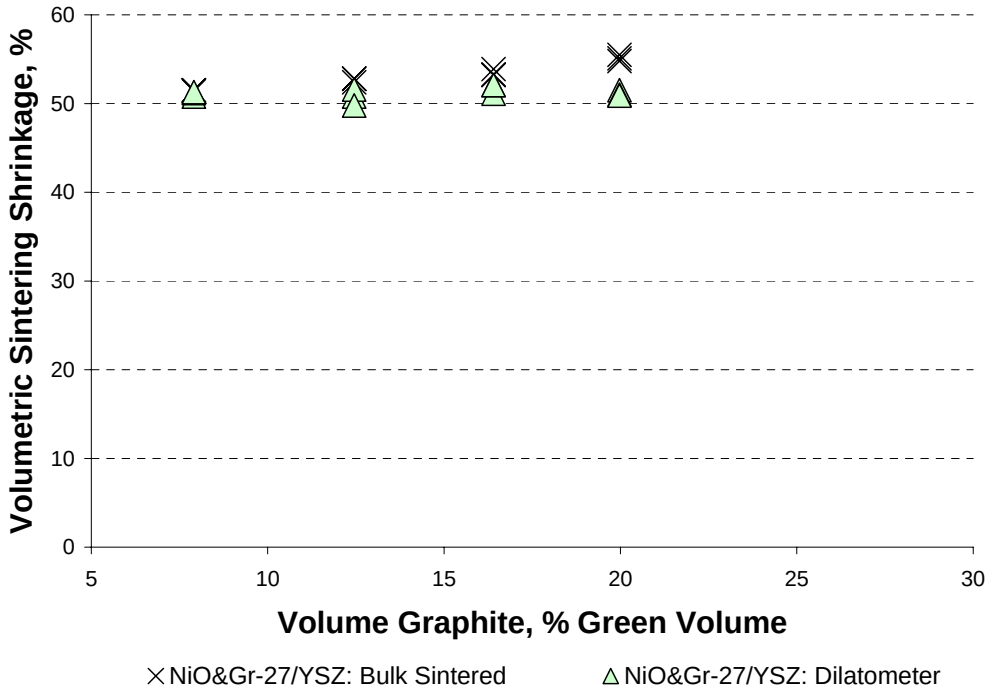

Figure D-27: Volumetric sintering shrinkage from the green to sintered state for NiO&Gr-27/YSZ composite samples sintered in a box furnace or dilatometer

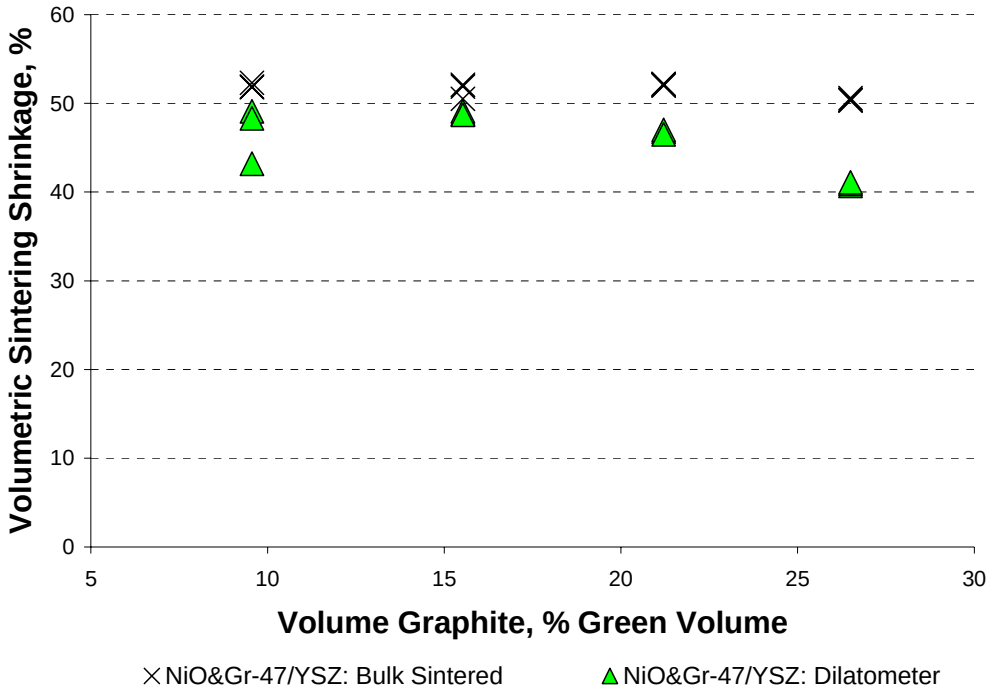

Figure D-28: Volumetric sintering shrinkage from the green to sintered state for NiO&Gr-47/YSZ composite samples sintered in a box furnace or dilatometer

Appendix E:

DILATOMETER REDUCTION RESULTS

Dilatometer Sample Measurements

The dimensions of each of three samples were measured before and after reduction within the dilatometer. The overall linear dimensional shrinkages after reduction in the length direction as measured by the dilatometer and by hand are shown in the following Figures for each of the composite types:

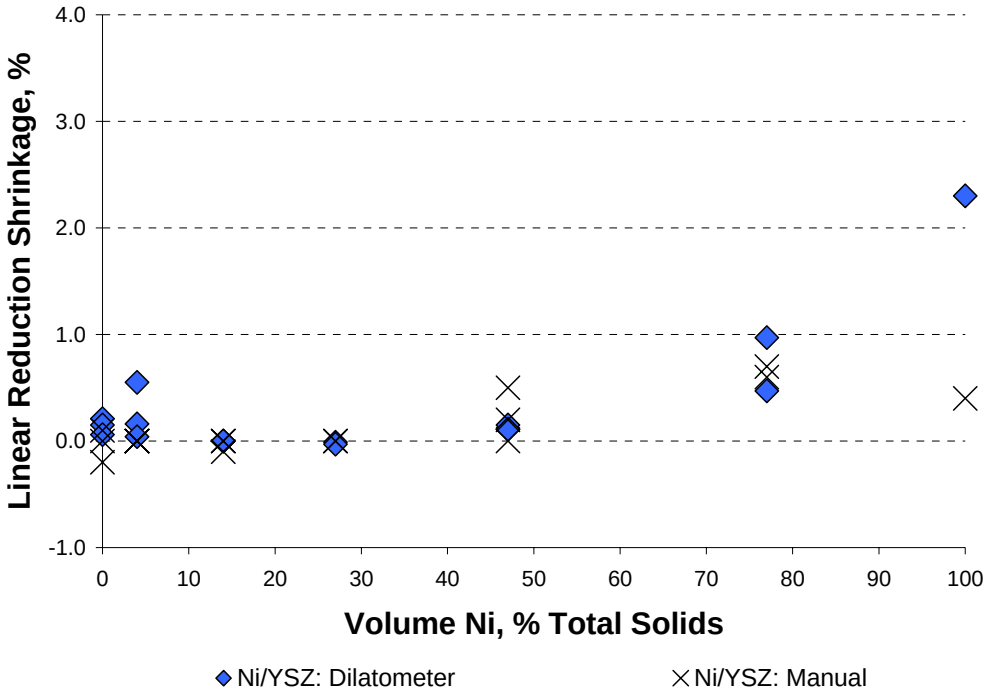

Figure E-1: Comparison of linear reduction shrinkages for the Ni/YSZ composites in the length direction as measured with a dilatometer and manually

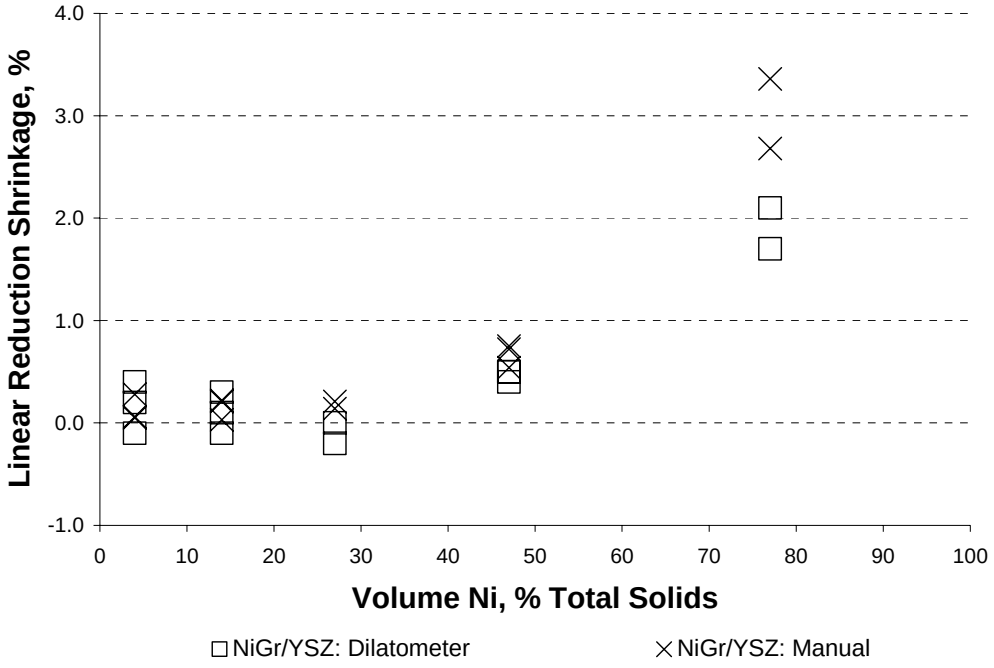

Figure E-2: Comparison of linear reduction shrinkages for the NiGr/YSZ composites in the length direction as measured with a dilatometer and manually

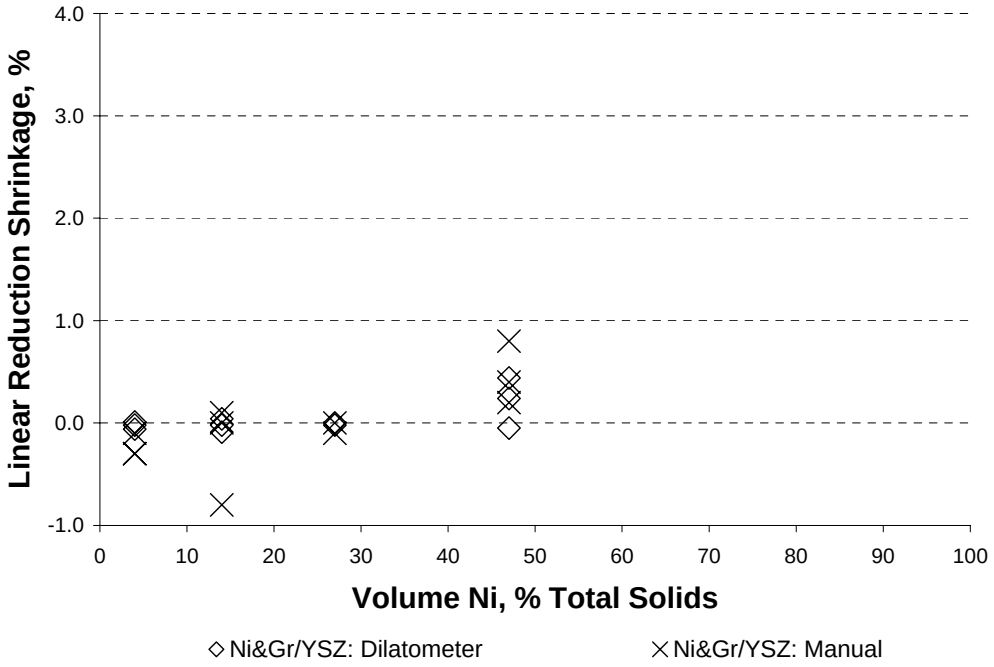

Figure E-3: Comparison of linear reduction shrinkages for the Ni&Gr/YSZ composites in the length direction as measured with a dilatometer and manually

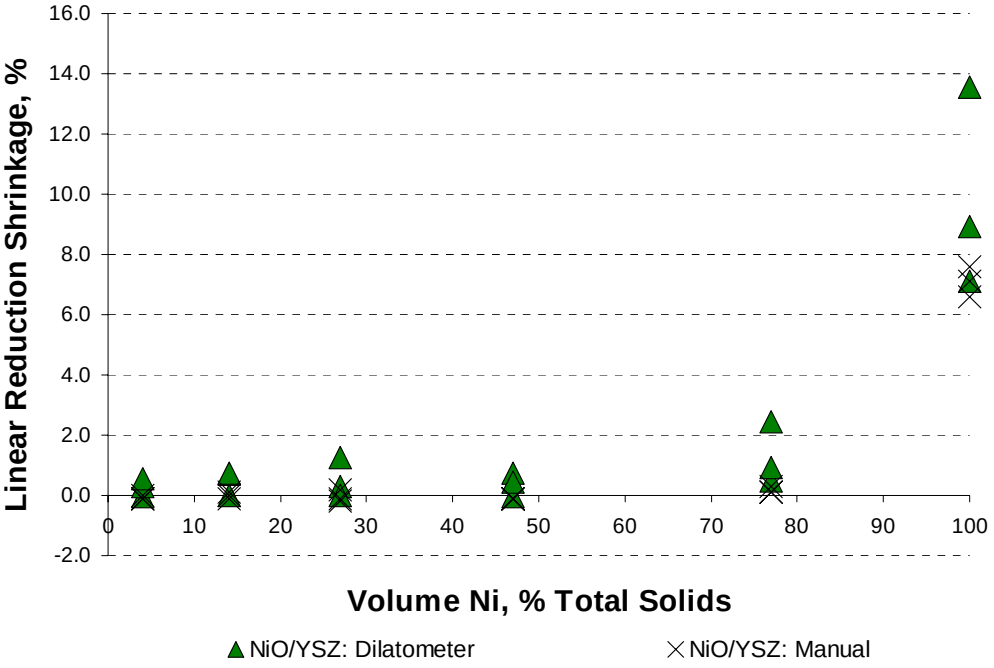

Figure E-4: Comparison of linear reduction shrinkages for the NiO/YSZ composites in the length direction as measured with a dilatometer and manually

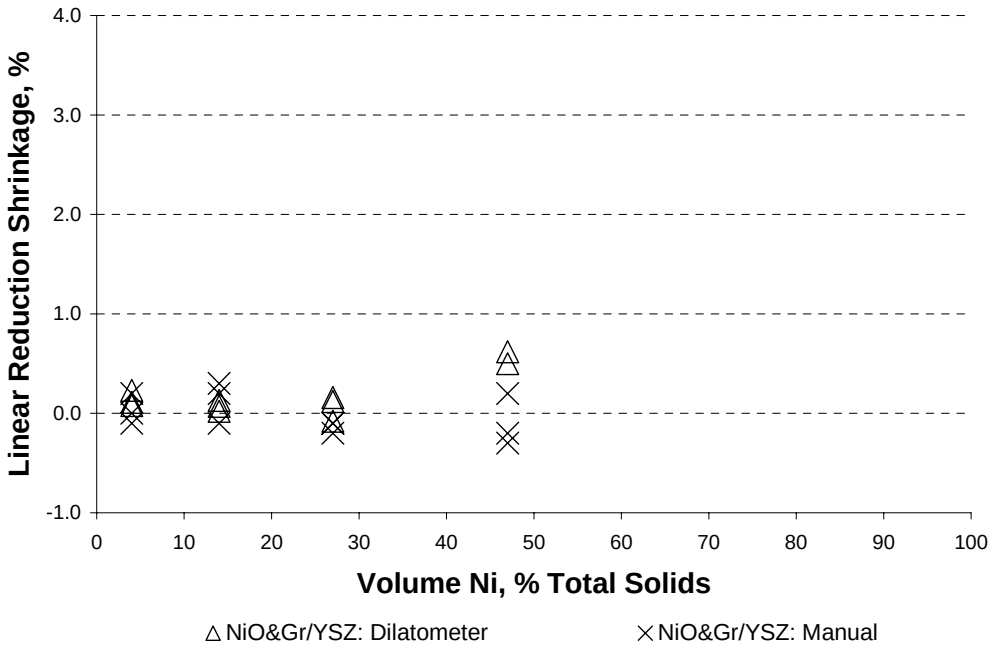

Figure E-5: Comparison of linear reduction shrinkages for the NiO&Gr/YSZ composites in the length direction as measured with a dilatometer and manually

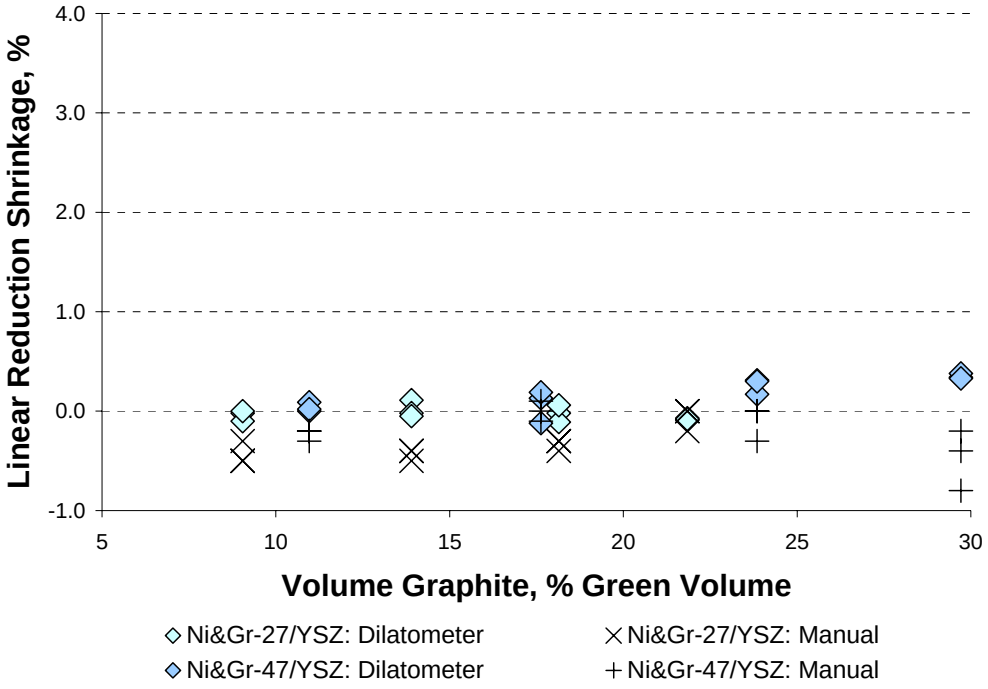

Figure E-6: Comparison of linear reduction shrinkages for the Ni&Gr-27/YSZ and Ni&Gr-47/YSZ composites in the length direction as measured with a dilatometer and manually

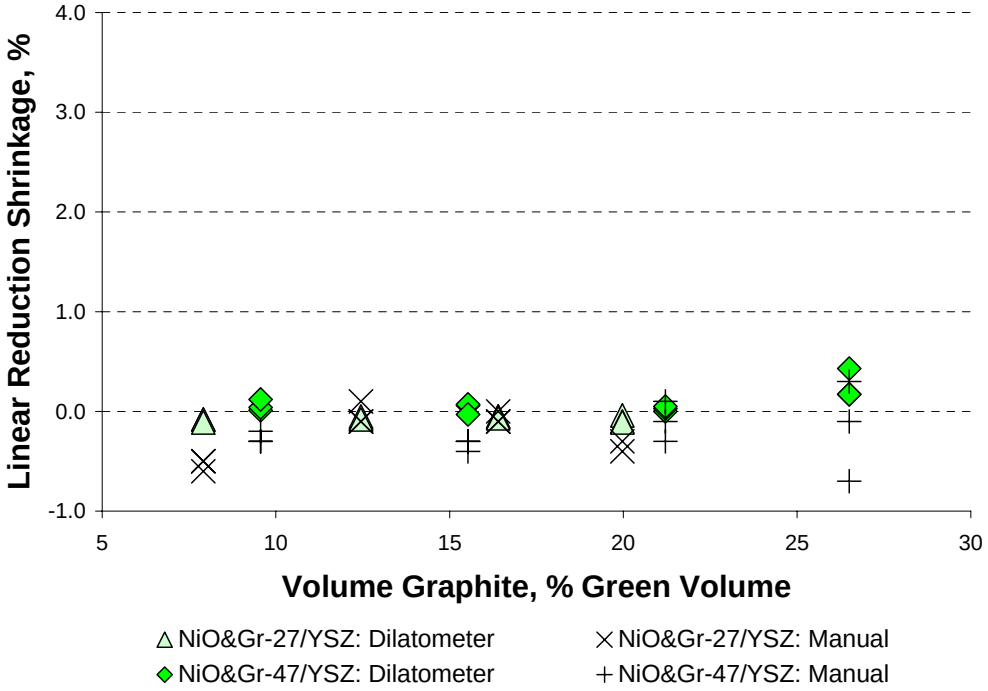

Figure E-7: Comparison of linear reduction shrinkages for the NiO&Gr-27/YSZ and NiO&Gr-47/YSZ composites in the length direction as measured with a dilatometer and manually

Linear Dimensional Shrinkage after Reduction

The linear dimensional shrinkage results after reduction are presented for each composite type in the following Figures:

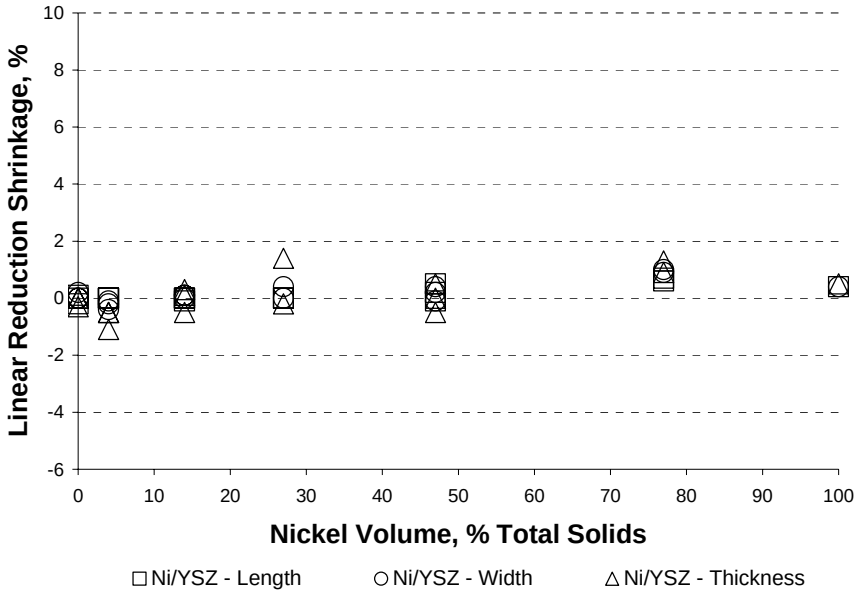

Figure E-8: Linear shrinkage from the sintered to the sintered & reduced state for the length, width, and thickness of Ni/YSZ composite samples reduced in a dilatometer

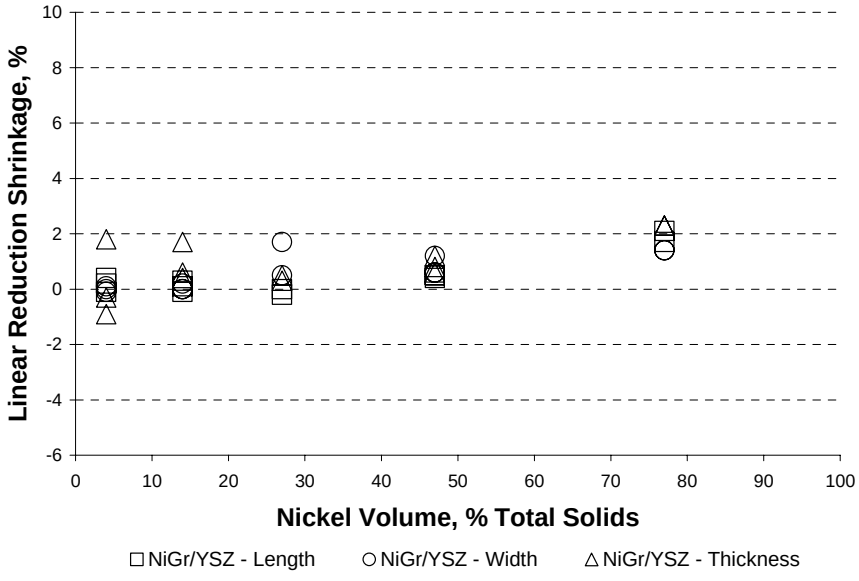

Figure E-9: Linear shrinkage from the sintered to the sintered & reduced state for the length, width, and thickness of NiGr/YSZ composite samples reduced in a dilatometer

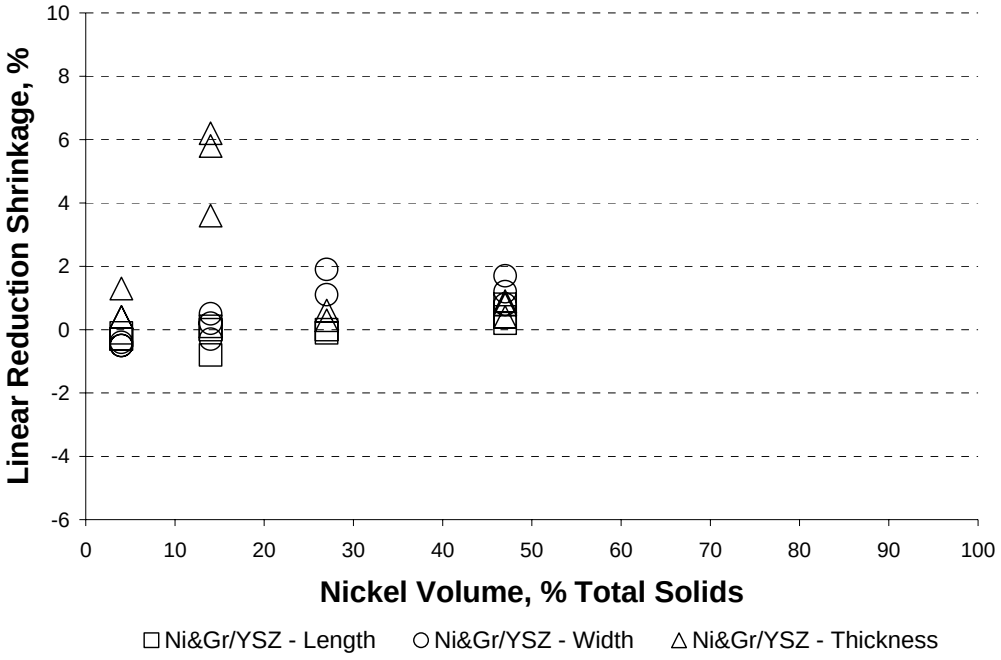

Figure E-10: Linear shrinkage from the sintered to the sintered & reduced state for the length, width, and thickness of Ni&Gr/YSZ composite samples reduced in a dilatometer

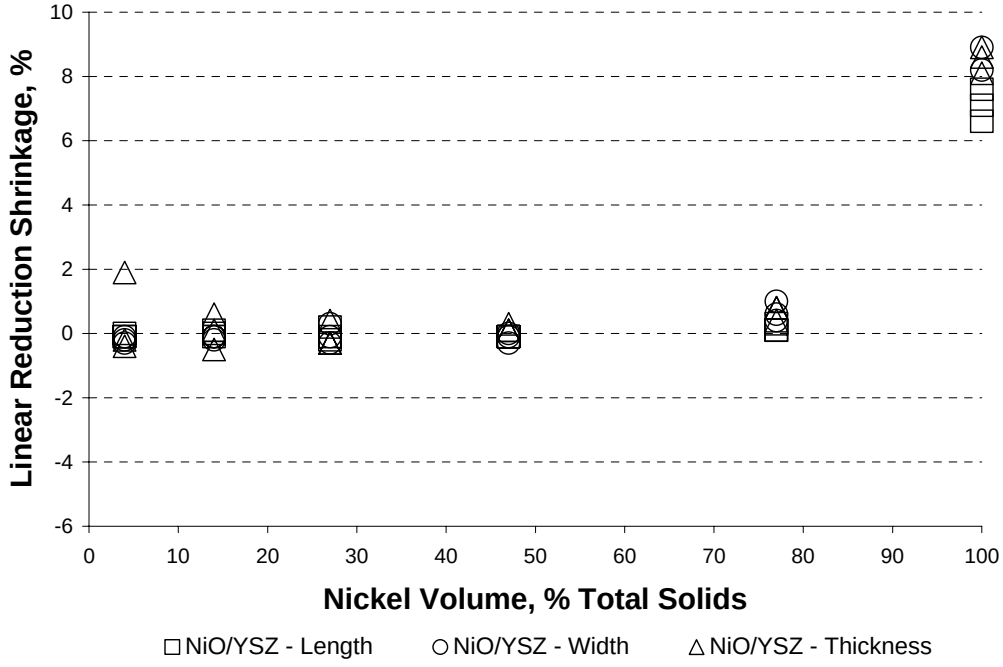

Figure E-11: Linear shrinkage from the sintered to the sintered & reduced state for the length, width, and thickness of NiO/YSZ composite samples reduced in a dilatometer

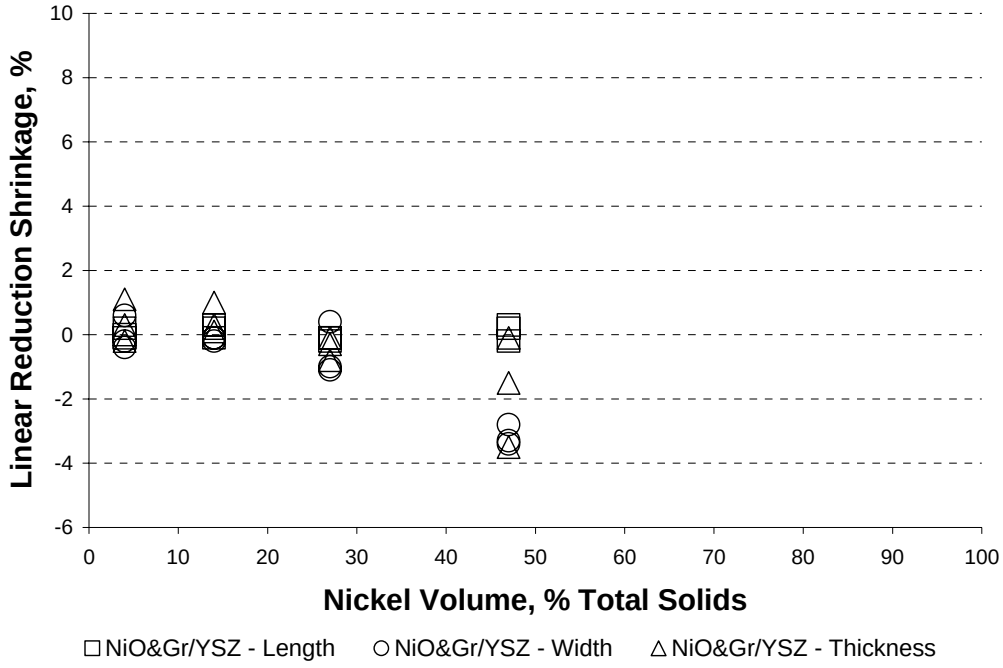

Figure E-12: Linear shrinkage from the sintered to the sintered & reduced state for the length, width, and thickness of NiO&Gr/YSZ composite samples reduced in a dilatometer

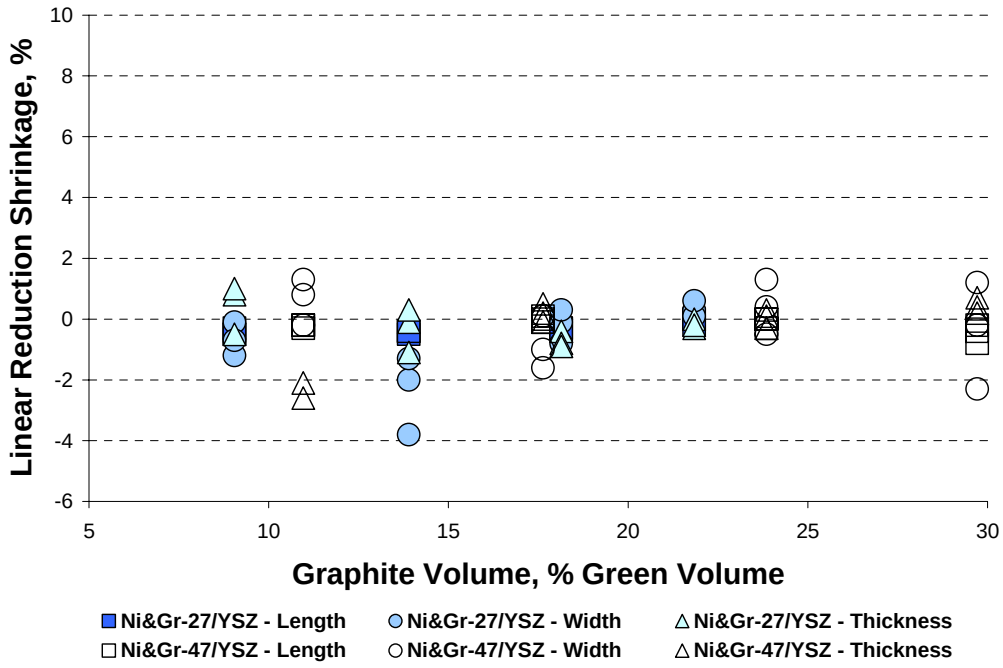

Figure E-13: Linear shrinkage from the sintered to the sintered & reduced state for the length, width, and thickness of Ni&Gr-27/YSZ and Ni&Gr-47/YSZ composite samples reduced in a dilatometer

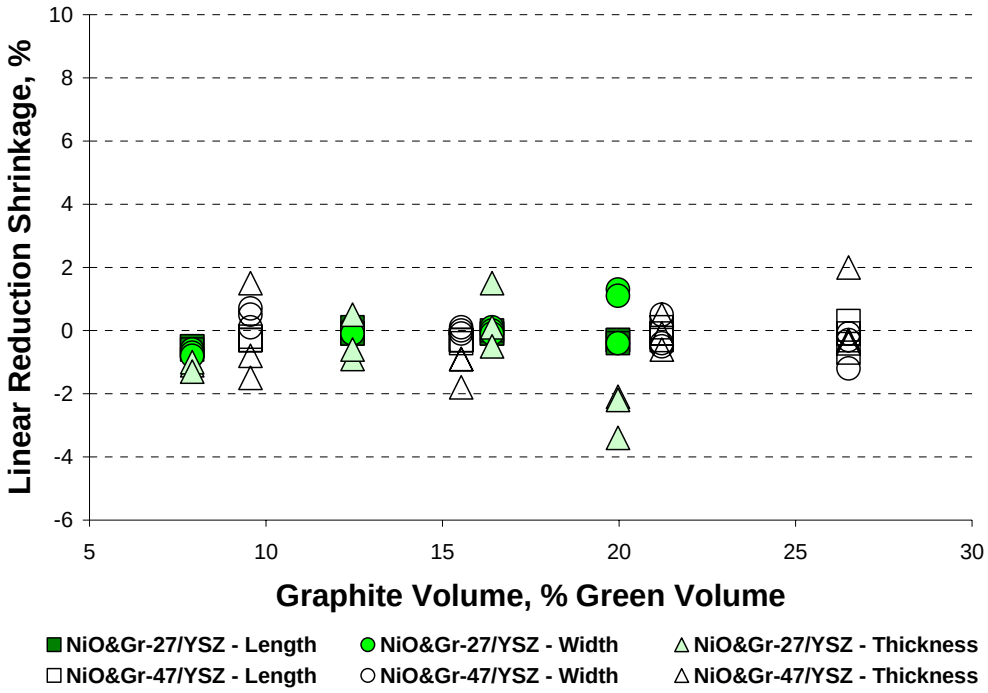

Figure E-14: Linear shrinkage from the sintered to the sintered & reduced state for the length, width, and thickness of NiO&Gr-27/YSZ and NiO&Gr-47/YSZ composite samples reduced in a dilatometer

Appendix F:
IMAGE ANALYSIS SEM MICROGRAPHS

Image Analysis SEM Micrographs

The scanning electron backscatter images used for calculating the bulk porosity of the various composites through image analysis are presented in the following Figures:

Monolithic Tapes

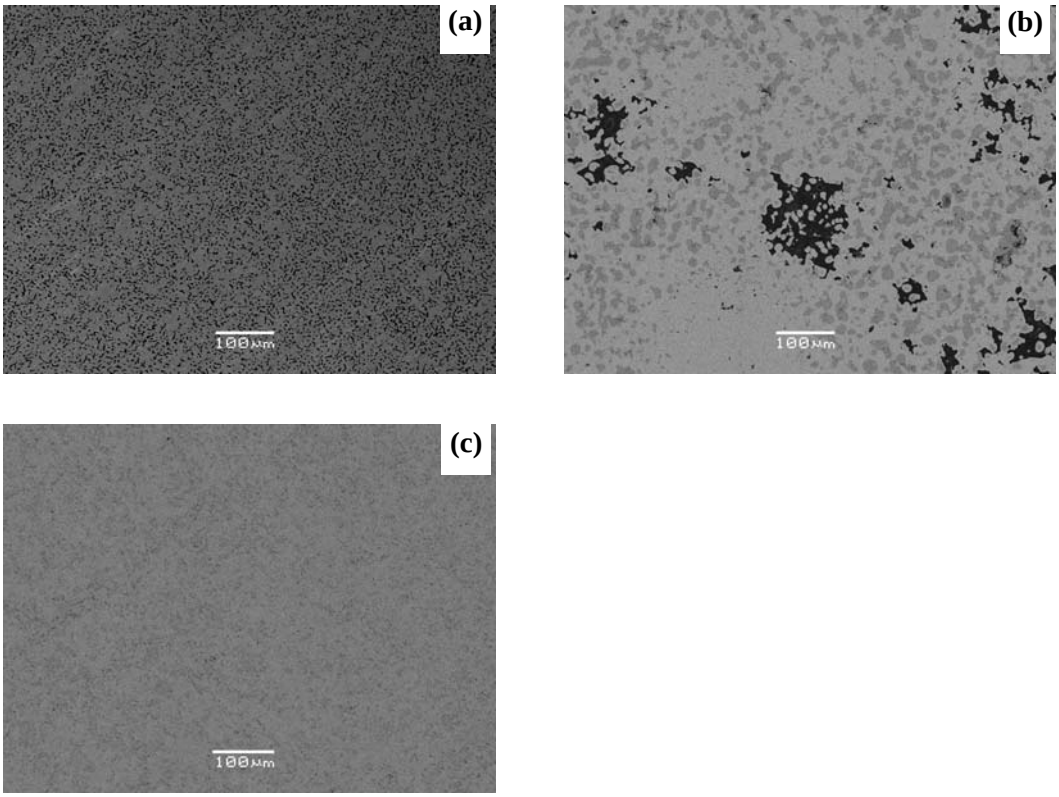

Figure F-1: SEM backscattered electron micrographs of a) 100% YSZ after sintering, b) 100% Ni from Ni after sintering and reduction, and c) 100% Ni from NiO after sintering and reduction

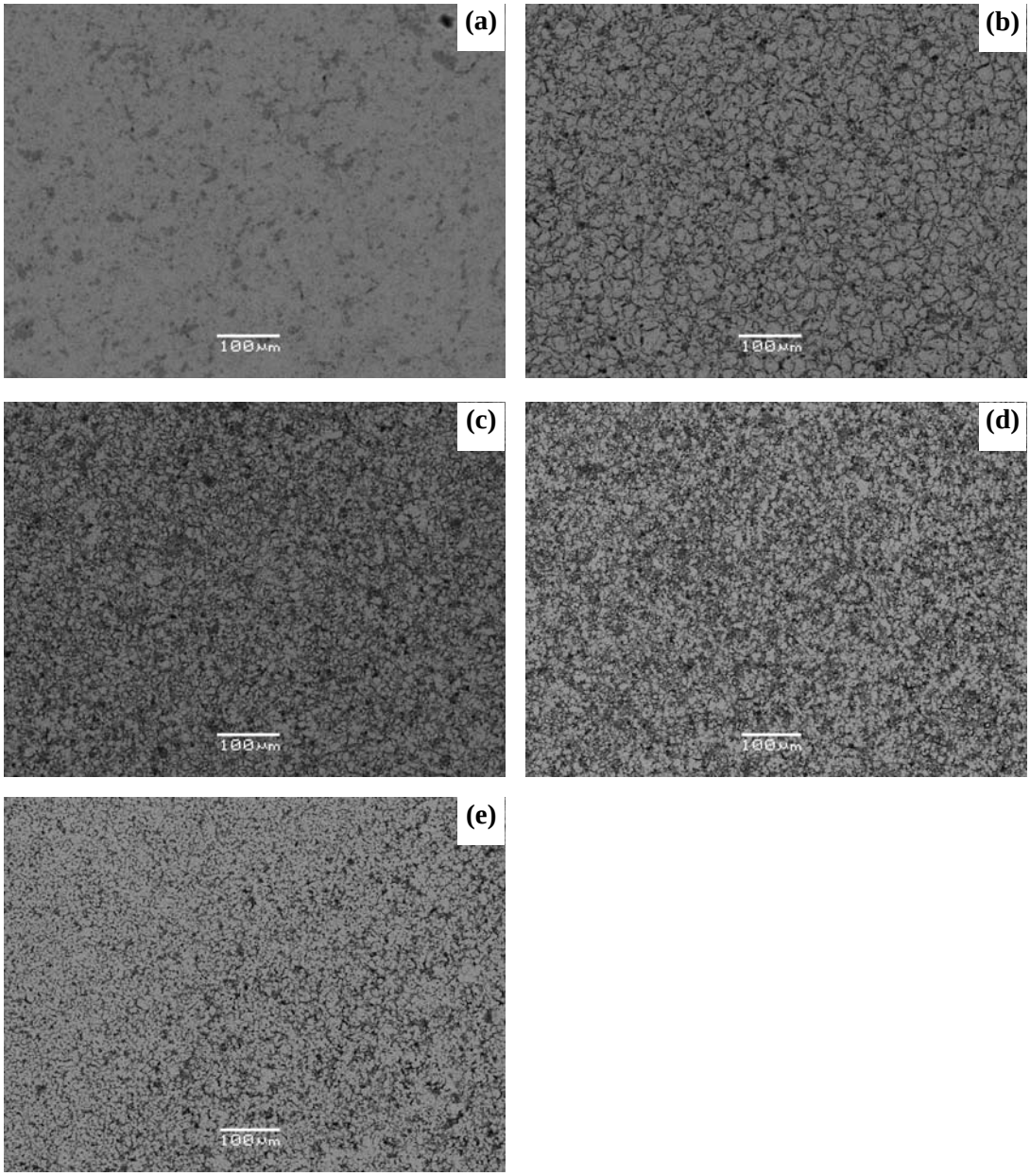

Figure F-2: SEM backscattered electron micrographs of Ni/YSZ composites after sintering and reduction with a nickel loading of a) 4 vol% Ni, b) 14 vol% Ni, c) 27 vol% Ni, d) 47 vol% Ni, and e) 77 vol% Ni of total solids

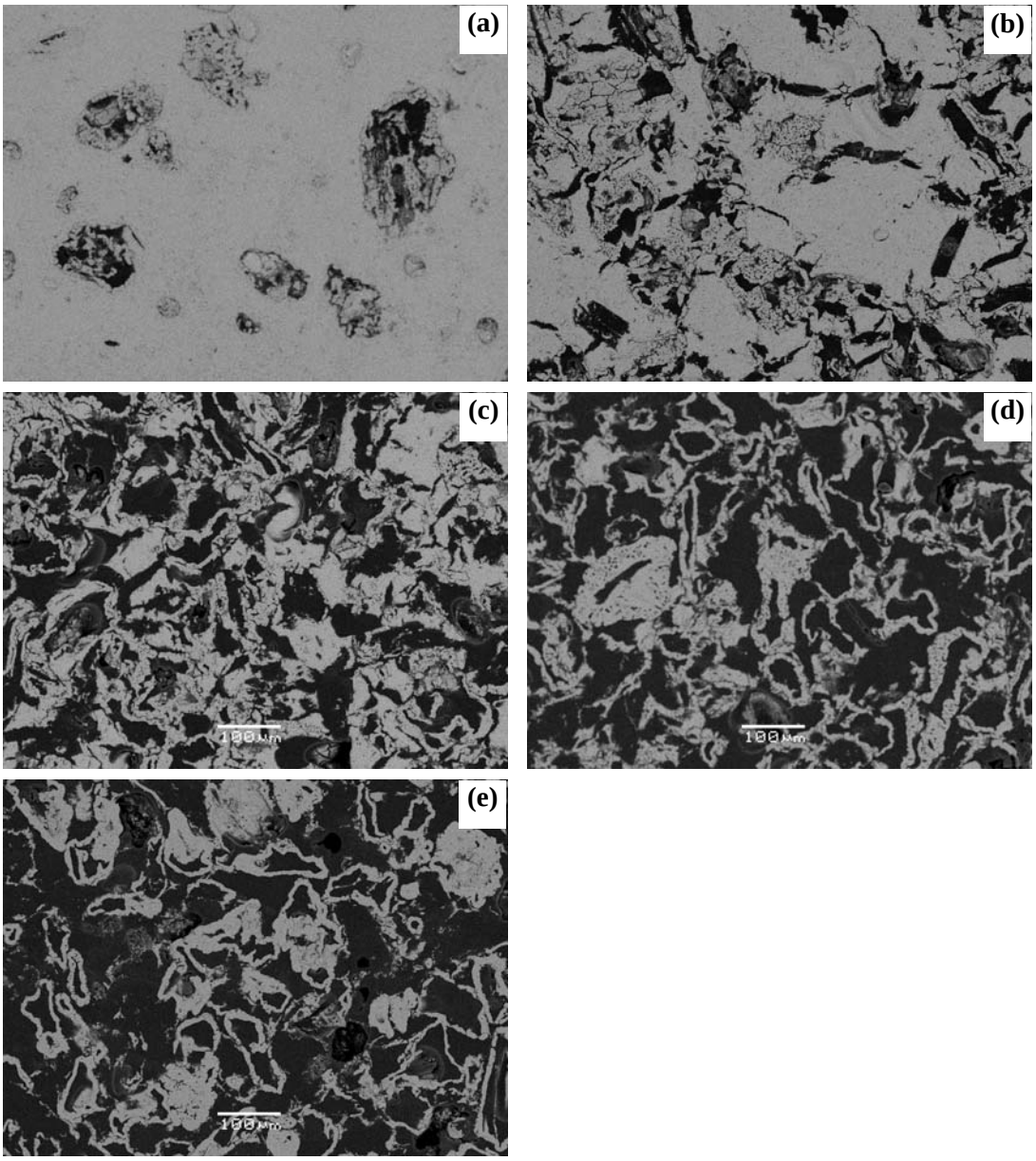

Figure F-3: SEM backscattered electron micrographs of NiGr/YSZ composites after sintering and reduction with a nickel loading of a) 4 vol% Ni, b) 14 vol% Ni, c) 27 vol% Ni, d) 47 vol% Ni, and e) 77 vol% Ni of total solids

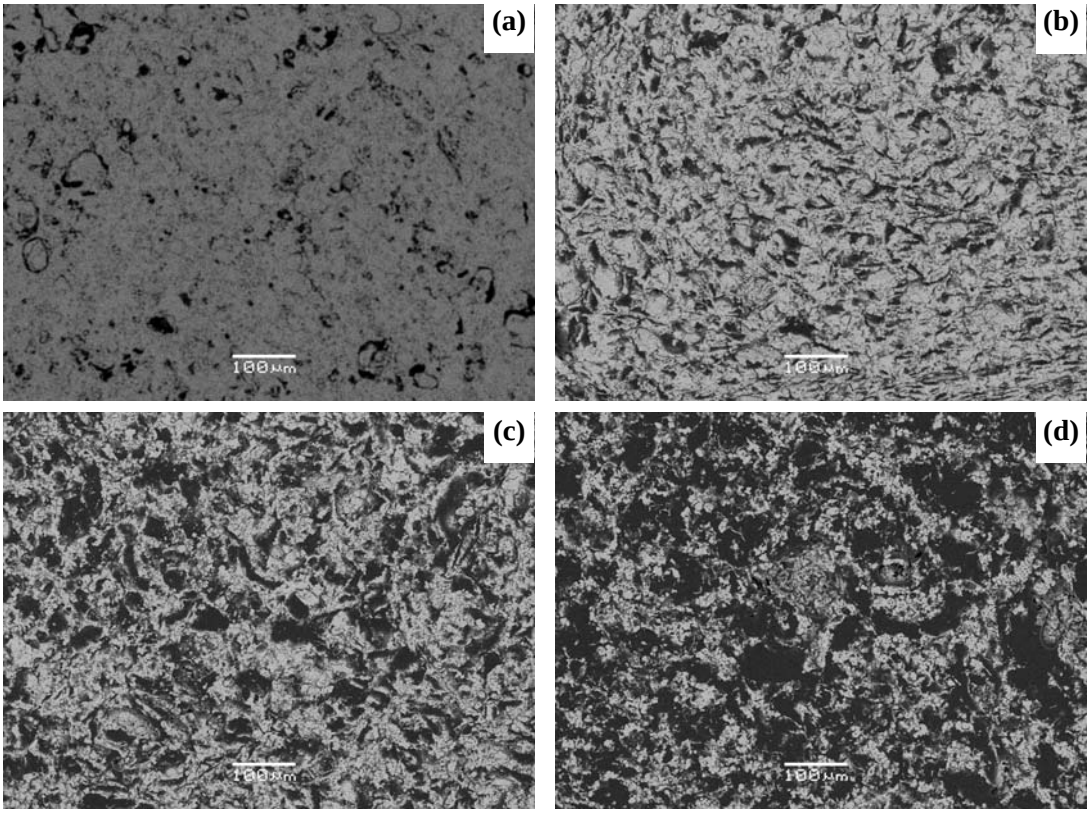

Figure F-4: SEM backscattered electron micrographs of Ni&Gr/YSZ composites after sintering and reduction with a nickel loading of a) 4 vol% Ni, b) 14 vol% Ni, c) 27 vol% Ni, and d) 47 vol% Ni of total solids

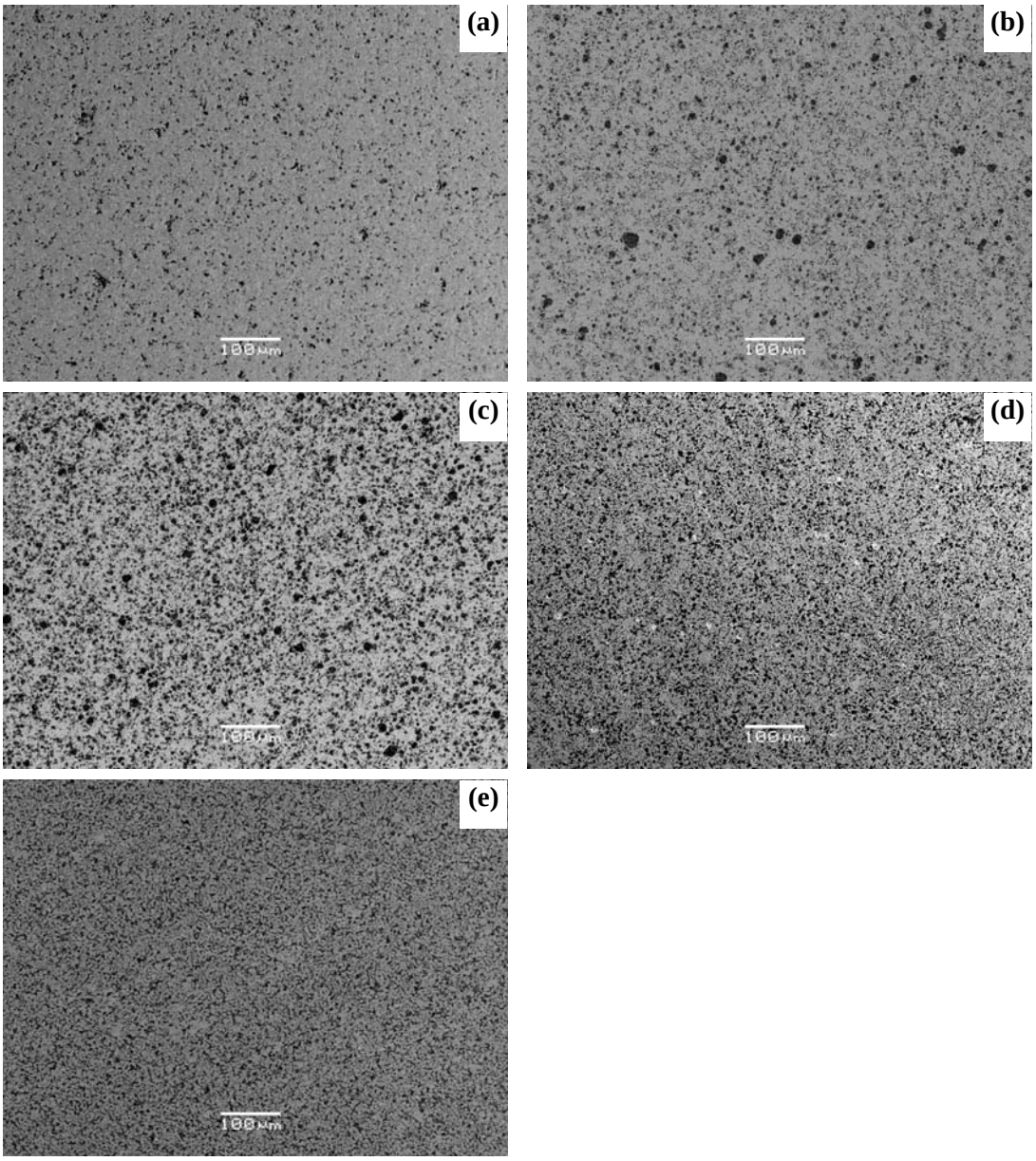

Figure F-5: SEM backscattered electron micrographs of NiO/YSZ composites after sintering and reduction with a nickel loading of a) 4 vol% Ni, b) 14 vol% Ni, c) 27 vol% Ni, d) 47 vol% Ni, and e) 77 vol% Ni of total solids

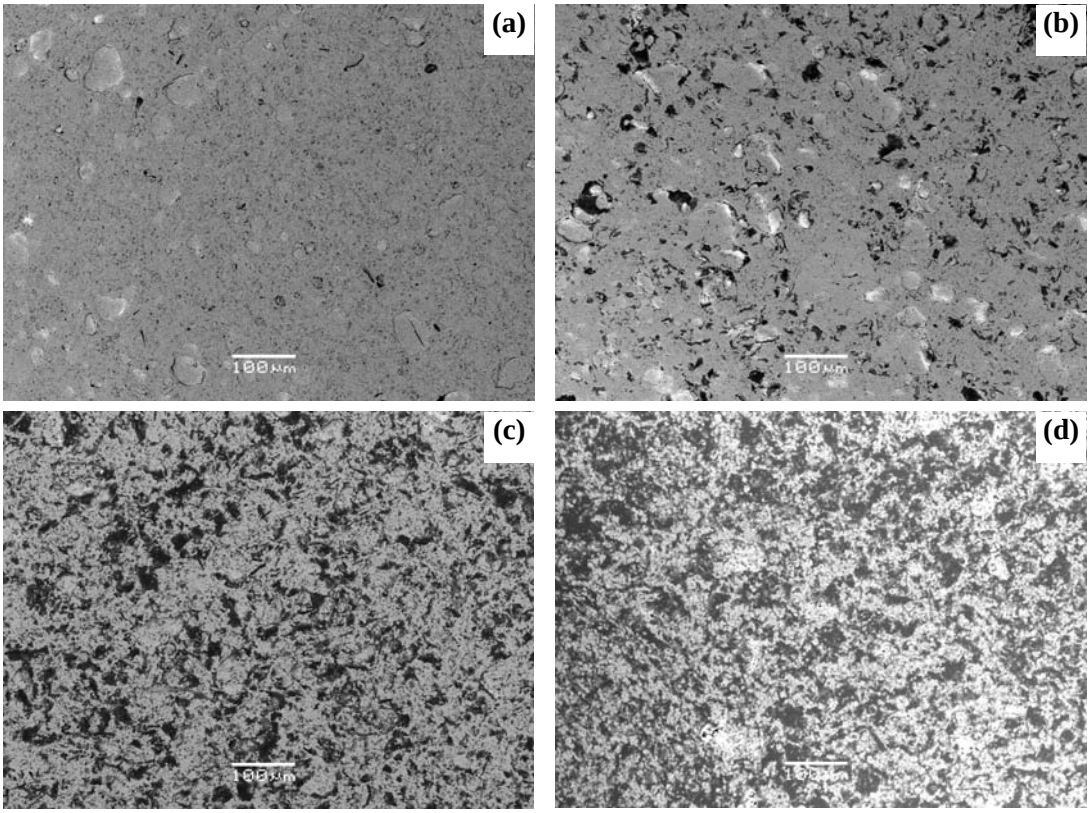

Figure F-6: SEM backscattered electron micrographs of NiO&Gr/YSZ composites after sintering and reduction with a nickel loading of a) 4 vol% Ni, b) 14 vol% Ni, c) 27 vol% Ni, and d) 47 vol% Ni of total solids

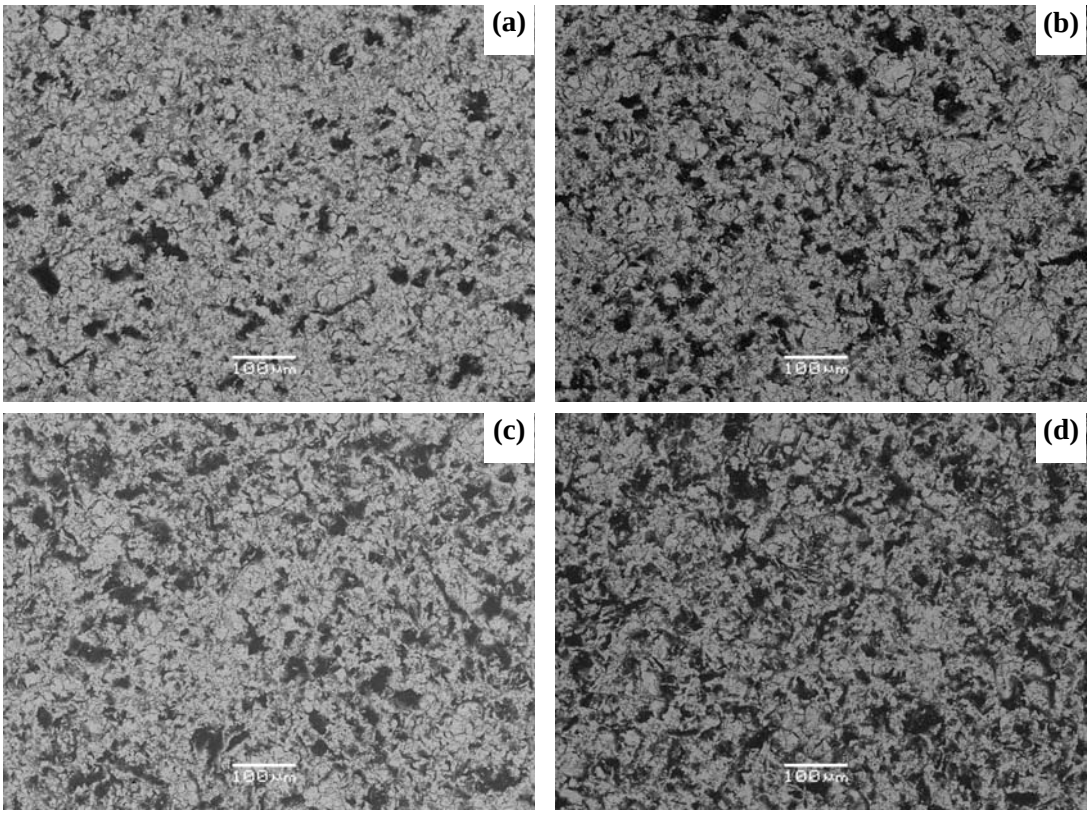

Figure F-7: SEM backscattered electron micrographs of Ni&Gr-27/YSZ composites with a nickel loading of 27 vol% Ni of total solids after sintering and reduction with a graphite loading of a) 9.1 vol% graphite, b) 13.9 vol% graphite, c) 18.1 vol% graphite, and d) 21.8 vol% graphite as fraction of the dried green volume

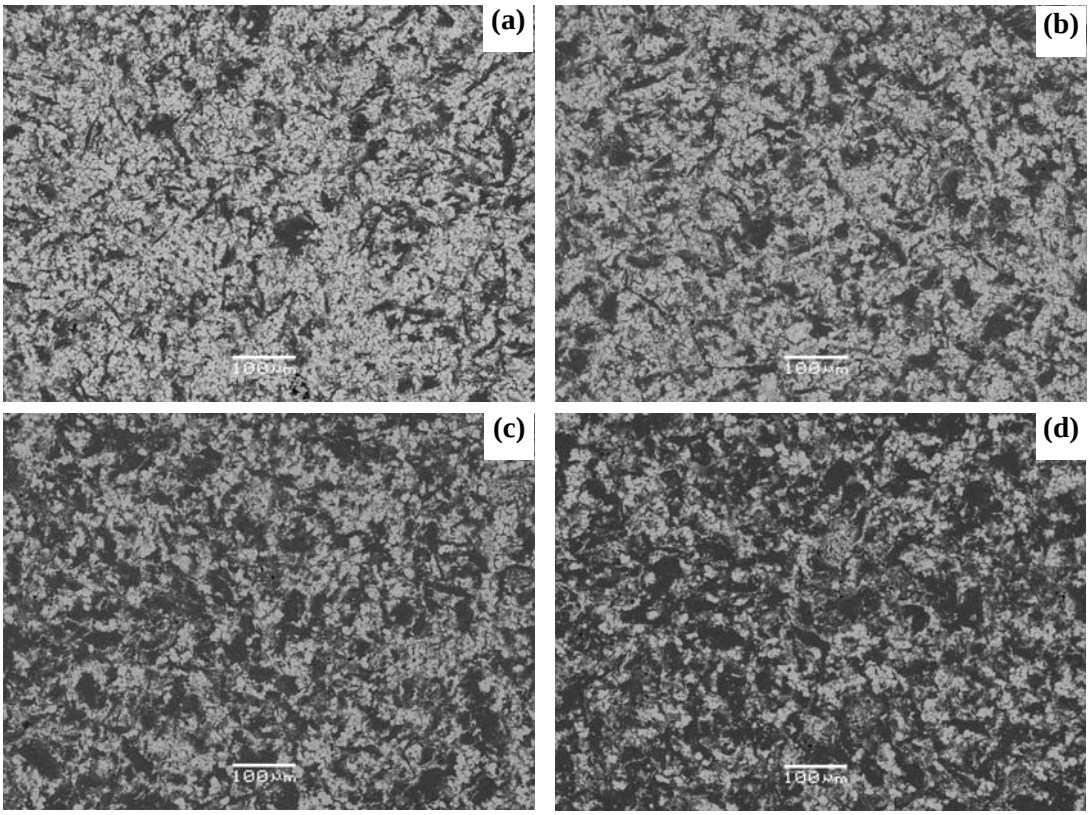

Figure F-8: SEM backscattered electron micrographs of NiO&Gr-27/YSZ composites with a nickel loading of 27 vol% Ni of total solids after sintering and reduction with a graphite loading of a) 7.9 vol% graphite, b) 12.5 vol% graphite, c) 16.4 vol% graphite, and d) 20 vol% graphite as fraction of the dried green volume

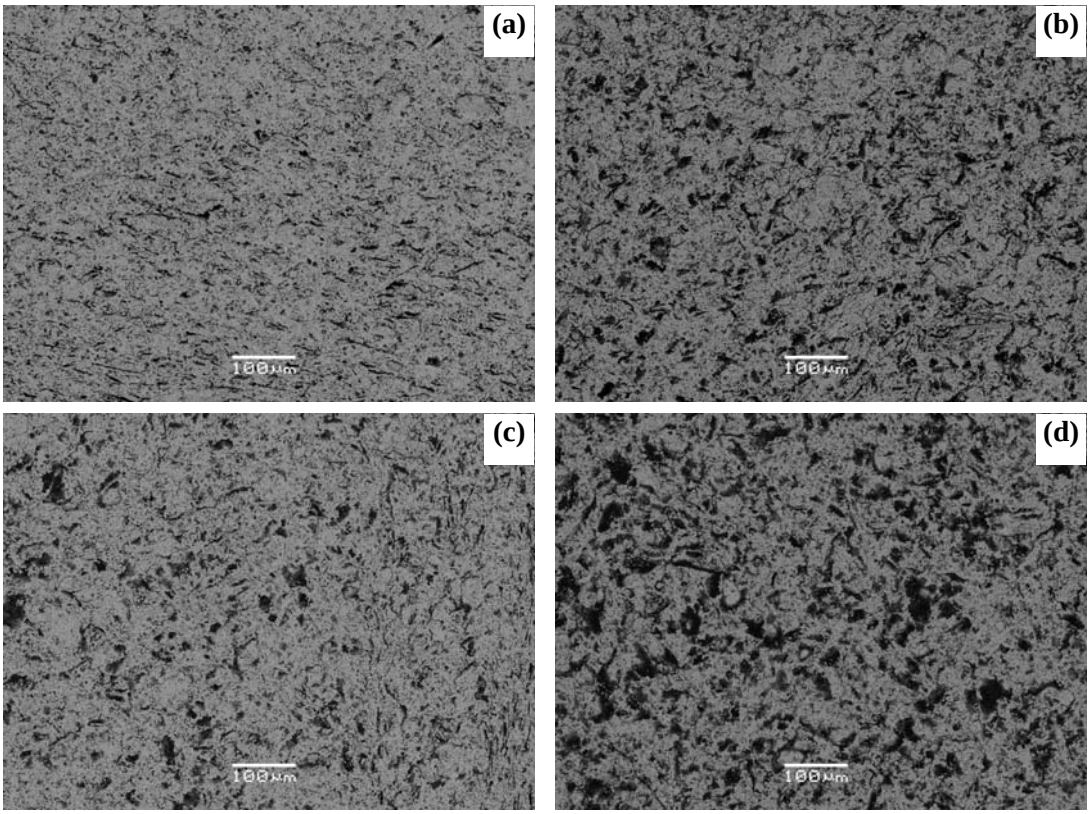

Figure F-9: SEM backscattered electron micrographs of Ni&Gr-47/YSZ composites with a nickel loading of 47 vol% Ni of total solids after sintering and reduction with a graphite loading of a) 11 vol% graphite, b) 17.6 vol% graphite, c) 23.9 vol% graphite, and d) 29.7 vol% graphite as fraction of the dried green volume

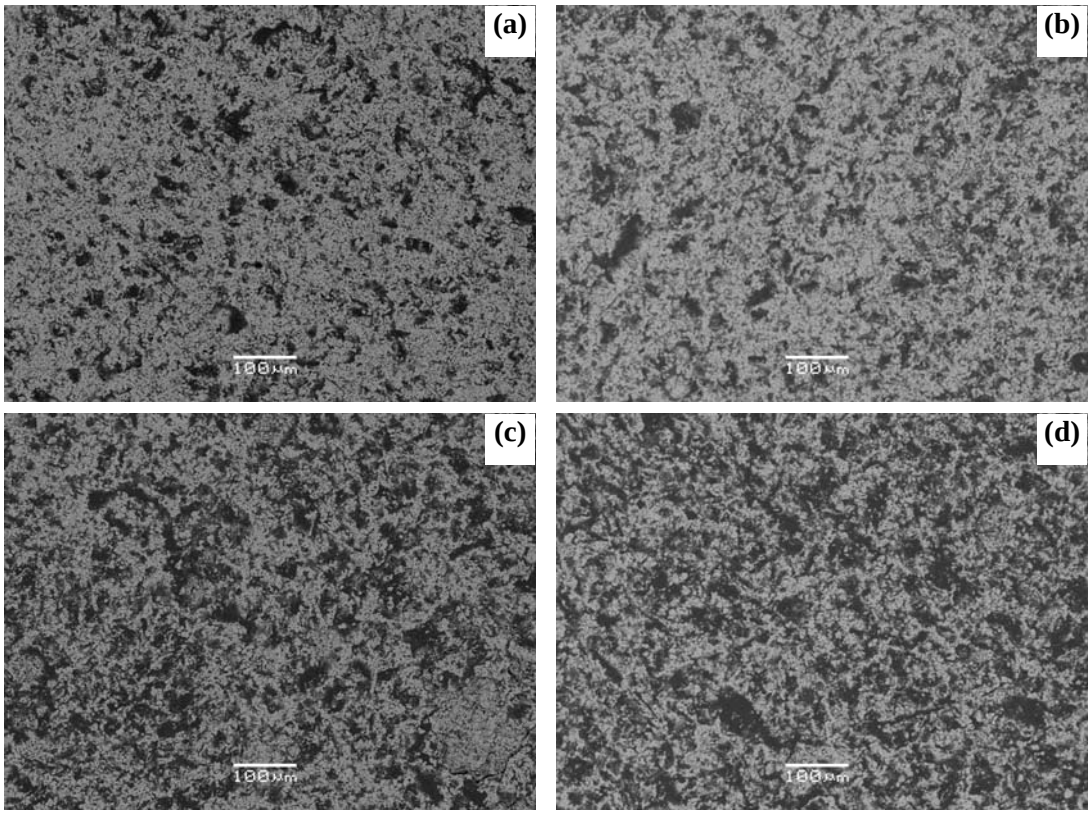

Figure F-10: SEM backscattered electron micrographs of NiO&Gr-47/YSZ composites with a nickel loading of 47 vol% Ni of total solids after sintering and reduction with a graphite loading of a) 9.6 vol% graphite, b) 15.5 vol% graphite, c) 21.2 vol% graphite, and d) 26.5 vol% graphite as fraction of the dried green volume

Appendix G:

ELECTRICAL CONDUCTIVITY AND %-REDUCTION

During the burnout and sintering stages, nickel transforms into nickel oxide. Due to the low electrical conductivity of nickel oxide, it must be reduced back into nickel metal to achieve any significant conductivity. To maximize the electrical conductivity, the nickel should be fully reduced.

Initially, the bulk reduced composite samples for electrical conductivity testing were held for two hours in a 7% hydrogen and 93% nitrogen atmosphere at 1000°C. Upon visual inspection and calculating the degree of reduction from Equation (3-1), it was apparent that the composites made from Ni&Gr/YSZ and NiO/YSZ were not fully reduced after the first reduction step. A second reduction step whereby the samples were heated to 1000°C and held for an additional three hours was added to further reduce the samples. The degree of reduction and the electrical conductivity before and after the second reduction step for the Ni&Gr/YSZ and NiO/YSZ composites is shown in Table 9-1. The electrical conductivity of the composites after the second reduction step is significantly higher than after the first reduction attempt. It is interesting to note however, that the Ni&Gr/YSZ and NiO/YSZ composites with a nickel loading of 27 vol% Ni of total solids, no longer conduct electricity after the second reduction stage. The samples that have a %-reduction greater than 100% may have lost some material during processing resulting in a greater than expected weight loss.

Table 9-1: Change in Electrical Conductivity with Reduction Stages

Composite	Nickel Volume, % Total Solids	1st Reduction (2 hrs @ 1000°C)		2nd Reduction (3 hrs @ 1000°C)	
		% Reduction	Electrical Conductivity S/cm	% Reduction	Electrical Conductivity S/cm
Ni&Gr/YSZ	27	95	6	102	-
	47	91	62	104	172
NiO/YSZ	27	93	13	101	-
	47	88	356	101	3904
	77	83	1127	102	31,917
100% Ni from NiO	100	82	1736	100	108,849

The reason for the increase in electrical conductivity is not only associated with the greater percentage of nickel present but also the nature of the particle to particle contact between the nickel/nickel oxide particles. Since nickel is denser than nickel oxide, the nickel oxide particles will shrink and sinter together during reduction. Early in the reduction process, a thin nickel coating will be present on a nickel oxide core. This composite particle is still sufficiently large enough to maintain contact with adjacent particles but is now able to conduct electricity. As the reduction of the nickel oxide progresses, the composite particles shrink and begin to lose contact with the adjacent particles. The electrical conductivity of the composite is highest when there is sufficient nickel to conduct electricity and the particles have not separated [52].

This reduction in contact between particles at higher nickel loadings does not affect the electrical conductivity of the composite as dramatically as it does when nickel loadings are near the percolation threshold. If too many particles lose contact with each other, the percolating network may be destroyed and the composite will no longer conduct electricity. This appears to be the case for the Ni&Gr/YSZ and NiO/YSZ composites at a nickel loading of 27 vol% Ni of total solids where the first reduction stage provided a low conducting path through the partial reduction of nickel oxide. Upon further reduction, the percolation network was destroyed, thus preventing the composites from conducting electricity.

The integrity of the percolation network within the composite is critical in determining the long-term stability of a solid oxide fuel cell. A portion of the composite will become electrochemically inactive if it is unable to conduct electricity. Areas of the composite may no longer conduct electricity if they lose connection to the spanning cluster or become part of a dead-end cluster due to poor particle-to-particle contact within the nickel phase. In the extreme case, the entire composite stops conducting electricity because the spanning cluster is broken into small finite clusters. To avoid this problem a sufficient amount of nickel is required to maintain the integrity of the percolating network.

At higher nickel contents, there is sufficient nickel present to maintain the percolating network. Furthermore, nickel particles in contact sinter together to further enhance the connection between particles. While some nickel particles lose contact with one another due to reduction, other particles are becoming more rigidly bound. Consequently, the electrical conductivity is quite high as in the NiO/YSZ composites at higher nickel loadings.

REFERENCES

1. N. Q. Minh and T. Takahashi, Science and Technology of Ceramic Fuel Cells, Elsevier, Amsterdam, 1995.
2. Nguyen Q. Minh, "Ceramic Fuel Cells", J. the American Ceramic Society, Vol. 76, No. 3, 1993, 563-588.
3. L. J. M. J. Blomen and M. N. Mugerwa, Fuel Cell Systems, Plenum Press, New York (1993).
4. W.Z. Zhu and S.C. Deevi, "A review on the status of anode materials for solid oxide fuel cells," Materials Science and Engineering, A362 (2003) 228-239.
5. M. Mogensen, and S. Skaarup, "Kinetic and geometric aspects of solid oxid fuel cell electrodes," Solid State Ionics, 86-88 (1996) 1151-1160.
6. B. de Boer, M. Gonzalez, H.J.M. Bouwmeester, and H. Verweij, "The effect of the presence of fine YSZ particles on the performance of porous nickel electrodes," Solid State Ionics, 127 (2000) 269-276.
7. M. Juhl, S. Primdahl, C. Manon, and M. Mogensen, "Performance/structure correlation for composite SOFC cathodes," J. of Power Sources, 61 (1996) 173-181.
8. S.H. Chan, K.A. Khor, and Z.T. Xia, "A complete polarization model of a solid oxide fuel cell and its sensitivity to the change of cell component thickness," J. Power Sources, 93 (2001) 130-140.
9. X. Li, ME 751 Winter 2001 Lecture Notes, University of Waterloo, Waterloo, ON, (2001).
10. D. A. Jones, Principles and Prevention of Corrosion, 2nd Ed., Prentice Hall, Upper Saddle River, NJ, 1996.
11. K. B. Oldham and J. C. Myland, Fundamentals of Electrochemical Science, Academic Press, San Diego, 1994.
12. A.V. Virkar, J. Chen, C.W. Tanner, and J. Kim, "The role of electrode microstructure on activation and concentration polarizations in solid oxide fuel cells," Solid State Ionics, 131 (2000) 189-198.
13. P. Singh and N.Q. Minh, "Solid Oxide Fuel Cells: Technology Status," Int'l Journal of Applied Ceramic Technology, 1 [1], 5-14, (2004).
14. B.C.H. Steele, "Materials for IT-SOFC stacks, 35 years R&D: the inevitability of gradualness?," Solid State Ionics 134 (2000) 3-20.
15. J. Holc, D Kuscer, M. Hrovat, S. Bernik, and D. Kolar, "Electrical and microstructural characterization of $(La_{0.8}Sr_{0.2})(Fe_{1-x}Al_x)O_3$ and $(La_{0.8}Sr_{0.2})(Mn_{1-x}Al_x)O_3$ as possible SOFC cathode materials," Solid State Ionics 95 (1997) 259-268.
16. M.J.L. Ostergard, C. Clausen, C. Bagger, and M. Mogensen, "Manganite-zirconia composite cathodes for SOFC: Influence of structure and composition," Electrochemical Acta, Vol. 40, No. 12, 1971-1981 (1995).
17. M. Hrovat, N. Katsarakis, K. Reichmann, S. Bernik, D. Kuscer, and J. Holc, "Characterization of $LaNi_{1-x}Co_xO_3$ as a possible SOFC cathode material," Solid State Ionics, 83 (1996) 99-105.

18. R. Chiba, F. Yoshimura, and Y. Sakurai, "An investigation of $LaNi_{1-x}Fe_xO_3$ as a cathode material for solid oxide fuel cells," Solid State Ionics, 124 (1999) 281-288.

19. S.P Jiang, and S.H. Chan, "A review of anode materials development in solid oxide fuel cells," J. Material Science, 39 (2004) 4405-4439.

20. J. Van herle, R. Ihringer, R. Vasquez Cavieres, L. Constantin, and O. Bucheli, "Anode supported solid oxide fuel cells with screen printed cathodes," J. European Ceramic Society, 21 (2001) 1855-1859.

21. A. Atkinson, S. Barnett, R.J. Gorte, J.T.S. Irvine, A.J. McEvoy, M. Mogensen, S.C. Singhal, J. Vohs, "Advanced anodes for high-temperature fuel cells," Nature Materials, Vol 3. January 2004 17-27.

22. S.P. Jiang, S.H. Chan, "Development of Ni/Y_2O_3-ZrO_2 cermet anodes for solid oxide fuel cells," Materials Science and Technology, September 2004 Vol 20, 1109-1118.

23. K.C. Wincewicz, and J.S. Cooper, "Taxonomies of SOFC material and manufacturing alternatives," J. Power Sources, 140 (2005) 280-296.

24. E.A. Brandes and G.B. Brook (eds.), Smithells Metals Reference Book, 7th Ed. Butterworth Heinemann Ltd., Oxford, U.K., 1992.

25. S.P.S. Badwal, "Stability of solid oxide fuel cell components," Solid State Ionics, 143 (2001) 39-46.

26. S.C. Singhal, "Advanced in solid oxide fuel cell technology," Solid State Ionics, 135 (2000) 305-313.

27. B.C.H. Steele, "Material Science and engineering: The enabling technology for the commercialization of fuel cell systems," J. Materials Science, 36 (2001) 1053-1068.

28. T. Fukui, S. Ohara, M. Naito, and K. Nogi, "Performance and stability of SOFC anodes fabricated from NiO/YSZ composite particles," J. European Ceramic Society, 23 (2003) 2963-2967.

29. M. Marinsek, K. Zupan, and J. Macek, "Preparation of Ni-YSZ composite materials for solid oxide fuel cell anodes by the gel-precipitation method," J. Power Sources, 86 (2000) 383-389.

30. T. Fukui, K. Murata, S. Ohara, H. Abe, M. Naito, and K. Nogi, "Morphology control of Ni-YSZ cermet anode for lower temperature operation of SOFCs," J. Power Sources, 125 (2004) 17-21.

31. D. Simwonis, H. Thulen, F.J. Dias, A. Naoumidis, and D. Stover, "Properties of Ni/YSZ porous cermets for SOFC anode substrates prepared by tape casting and coat-mix process," J. Materials Processing Technology, 92-93 (1999) 107-111.

32. H. Ohrui, T. Matsushima, and T. Hirai, "Performance of a solid oxide fuel cell fabricated by co-firing," J. Power Sources, 71 (1998) 185-189.

33. I. Zhitomirsky and A. Petric, "Electrophoretic deposition of ceramic materials for fuel cell applications," J. European Ceramic Society, 20 (2000) 2055-2061.

34. H. Koide, Y. Someya, T. Yoshida, and T. Maruyama, "Properties of Ni/YSZ cermet as anode for SOFC," Solid State Ionics, 132 (2000) 253-260.

35. T.L. Wen, D. Wang, M. Chen, H. Tu, Z. Lu, Z. Zhang, H. Nie, and W. Huang, "Material research for planar SOFC stack," Solid State Ionics, 148 (2002) 513-519.

36. S. Ramanathan, K.P. Krishnakumar, P.K. De, and S. Barerjee, "Powder dispersion and aqueous tape casting of YSZ-NiO composite," J. Materials Science, 39 (2004) 3339-3344.

37. J.W. Stevenson, K.D Meinhardt, S.P. Simner, C.F. Habeger, and N.L. Canfield, "Fabrication and testing of anode-supported SOFC," Conference: Fuel cells--powering the 21st Century. 2000 Fuel Cell Seminar, Portland, OR (US), 10/30/2000--11/02/2000; published Feb 28, 2001.

38. M. Cassidy, G. Lindsay, and K. Kendall, "The reduction of nickel-zirconia cermet anodes and the effects on supported thin electrolytes," J. Power Sources, 61 (1996) 189-192.

39. S.F. Corbin and X. Qiao, "Development of solid oxide fuel cell anodes using metal-coated pore forming agents," J. American Ceramic Society, 86 [3] 401-406 (2003).

40. R.E. Mistler, "Tape Casting: Past, Present, Potential", Ceramic Bulletin, 77 [10], 82-86, (1998).

41. R.E. Mistler, "The principles of tape casting and tape casting applications," in Chapter 5 of Ceramic Processing, (eds. R.A. Terpstra, P.P.A.C. Pex, and A.H. de Vries.) Chapman & Hall, London, 1995.

42. R.E. Mistler, "Tape Casting: The Basic Process for Meeting the Needs of the Electronics Industry", Ceramic Bulletin, 69 [6], 1022-1026, (1990).

43. R.E. Mistler, R.B. Runk, and D.J. Shanefield. "Tape Casting of Ceramics", Ceramic Fabrication Before Firing (eds. G.Y. Onoda and L.L. Hench), Wiley, New York, p. 411-448, 1978.

44. D.W. Richerson, Modern Ceramic Engineering, 2nd Ed., Ch. 10, Marcel Dekker Inc, New York (1992).

45. S. F. Corbin and P. Apte, "Engineered porosity via tape casting, lamination, and the percolation of pyrolyzable particulates," J. American. Ceramic Society, 82 [7] 1693-1701 (1999).

46. S.F. Corbin, J. Lee and X. Qiao, "Influence of green formulation and pyrolyzable particulates on the porous microstructure and sintering characteristics of tape cast ceramics", J. American Ceramic Society 84 [1], 41-47, (2001).

47. J.H. Lee, J.W. Heo, D.S. Lee, J. Kim, G.H. Kim, H.W. Lee, H.S. Song, and J.H. Moon, "The impact of anode microstructure on the power generating characteristics of SOFC," Solid State Ionics, 158 (2003) 225-232.

48. J.J. Haslam, A. Pham, B.W. Chung, J.F. DiCarlo, and R.S. Glass, "Effects of the use of pore formers on performance of an anode supported solid oxide fuel cell," J. American Ceramic Society, 88 [3] 513-518 (2005).

49. J.W. Moon, H.J. Hwang, M. Awano, and K. Maeda, "Preparation of NiO-YSZ tubular support with radially aligned pore channels," Materials Letters 57 (2003) 1428-1434.

50. Y.J. Leng, S.H. Chan, K.A. Khor, S.P. Jiang, and P. Cheang, "Effect of characteristics of Y2O3/ZrO2 powders on fabrication of anode-supported solid oxide fuel cells," J. Power Sources, 117 (2003) 26-34.

51. T. Matsushima, H. Ohrui, and T. Hirai, "Effects of sinterability of YSZ powder and NiO content on characteristics of Ni-YSZ cermets," Solid State Ionics, 111 (1998) 315-321

52. D.W. Dees, T.D. Claar, T.E. Easler, D.C. Fee and F.C. Mrazek, "Conductivity of porous Ni/ZrO_2-Y_2O_3 cermets," J. Electrochemistry Society, 134 (1987) 2141.

53. D. Simwonis, F. Tietz, and D. Stover, "Nickel coarsening in annealed Ni/8YSZ anode substrates for solid oxide fuel cells," Solid State Ionics, 132 (2000) 241-251.

54. J.H. Lee, H. Moon, H.W. Lee, J. Kim, J.D. Kim, and K.H. Yoon, "Quantitative analysis of microstructure and its related electrical property of SOFC anode, Ni-YSZ cermet," Solid State Ionics, 148 (2002) 15-26.

55. X. Li, "Principles of Fuel Cells," Ch. 9, p 477-505, Taylor and Francis Group: New York, 2006.

56. W. Hu, H. Guan, X. Sun, S. Li, M. Fukumoto, and I. Okane, "Electrical and thermal conductivities of nickel-zirconia cermets," J. American Ceramic Society, 81 [8] 2209-12 (1998).

57. J.H. Lee, J.W. Heo, D.S. Lee, J. Kim, G.H. Kim, H.W. Lee, H.S. Song, and J.H. Moon, "The impact of anode microstructure on the power generating characteristics of SOFC," Solid State Ionics, 158 (2003) 225-232.

58. R. Zallen, The Physics of Amorphous Solids, John Wiley and Sons, Toronto, 1983.

59. R. Zallen, "Percolation a Model for All Seasons," p 3-16 in Annals of the Israel Physical Society, Percolation Structures and Processes, Vol. 5. G. Deutscher, R. Zallen, and J Adler eds., Israel Physical Society, Jerusalem, Israel, 1983.

60. D. Stauffer, A. Aharony, Introduction to Percolation Theory, Taylor & Francis, Washington, 1992.

61. J. Kovacik, "Electrical conductivity of two-phase composite material," Scripta Materialia, Vol. 39, No. 2, pp. 153-157, 1998.

62. D. S. McLachlan, M. Blaszkiewicz, and R. E. Newnham, "Electrical Resistivity of Composites", J. American Ceramic Society, Vol. 73, No. 8, 1990, 2187-2203.

63. A. Malliaris, and D.T. Turner, "Influence of particle size on the electrical resistivity of compacted mixtures of polymeric and metallic powders," J. Applied Physics, Vol. 42, No. 2, p. 614-618, 1971.

64. F. Carmona, R. Canet, and P. Delhaes, "Piezoresistivity of heterogeneous solids," J. Applied Physics, Vol. 61, No. 7, pp. 2250-2257, 1987.

65. M. Mori, T. Yamamoto, H. Itoh, H. Inaba, and H. Tagawa, "Thermal expansion of nickel-zirconia anodes in solid oxide fuel cells during fabrication and operation," J. Electrochemical Society Vol. 145, No. 4, p. 1374-1381, (1998).

66. W. Hu, H. Guan, X. Sun, and S. Li, "Thermal expansion behaviour of ZrO_2-Y_2O_3-Ni cermets," Materials Letters, 32 (1997) 59-62.

67. A.C. Muller, D. Herbstritt, and E. Ivers-Tiffee, "Development of a multilayer anode for solid oxide fuel cells," Solid State Ionics, 152-153 (2002) 537-542.

68. Y.L. Shen, “Combined effects of microvoids and phase contiguity on the thermal expansion of metal-ceramic composites,” Materials Science and Engineering, A237, (1997) 102-108.

69. Y-L. Shen, “Thermal expansion of metal-ceramic composites: a three-dimensional analyss,” Materials Science and Engineering A252 (1998) 269-275.

70. Q. Yang, D. Charles, S. Metcalfe, E. Wasmund, and L. Penny, “New additives for nickel electrode batteries,” Technical Papers, INCO Special Products, June 16, 2005.

71. Personal Communication, Dr. Stephen Corbin, Department of Mechanical Engineering, University of Waterloo, Waterloo, ON, April 2006.

72. Personal Communication, Brian Ellis Graduate Student, Department of Chemistry, University of Waterloo, Waterloo, ON, July 2005.

73. D.R. Askeland, “The Science and Engineering of Materials” 3rd S.I. Edition, Ch 18, p 618-671, Chapman & Hall: New York, 1996.

74. Netzsch Instruments, “Operating Instructions: Dilatometer, Dil 402C, Operating Manual, 1999.

75. M. Barsoum, Fundamentals of Ceramics, Ch. 10, McGraw-Hill, New York, 1997.

76. J.S. Reed, Principles of Ceramics Processing, 2nd ed. John Wiley & Sons, Inc., Toronto, p. 597, 1995.

77. H.E. Exner and E. Arzat, “Sintering Processes,” Chapter 30, from Physical Metallurgy, 3rd revised and enlarged edition, R.W. Cahn and P. Haasen, eds. Elsevier Science Publishers BV, 1983.

78. R.L. Coble, “Effects of Particle-Size Distribution in Initial-Stage Sintering”, J. American Ceramic Society, 56 (1973) 461.

79. M.B. Waldron and B.L. Daniell, Sintering, Chapter 1, Heyden & Son Ltd., London, 1978.

80. H.J. Edrees, A.C. Smith, and A. Hendry, “A rule-of-mixtures model for sintering of particulate-reinforced ceramic-matrix composites,” J. European Ceramic Society, 18 (1998) 275-278.

81. M.Y. Chu, M.N. Rahaman and L.C. De Jonghe, “Effect of Heating Rate on Sintering and Coarsening”, J. American Ceramic Society, 74 [6], 1217-1225, (1991).

82. M.N. Rahaman, and L.C. De Jonghe, “Sintering of Ceramic Particulate Composites: Effect of Matrix Density”, J. American Ceramic Society, 74 [2], 433-436, (1991).

83. L.C. De Jonghe, M.N. Rahaman and C.H. Hsueh, “Transient Stresses in Bimodal Compacts During Sintering”, Acta Metall., 34, (7), 1467-1471, (1986).

84. R.E. Dutton and M.N. Rahaman, “Sintering, Creep, and Electrical Conductivity of Model Glass-Matrix Composites”, J. American Ceramic Society, 75 [8], 2146-2154, (1992).

85. M.N. Rahaman and L.C. De Jonghe, “Effect of Rigid Inclusions on the Sintering of Glass Powder Compacts”, J. American Ceramic Society, 70 [12], C348-C351, (1987).

86. M.N. Rahaman and L.C. De Jonghe, “Sintering of Particulate Composites under a Uniaxial Stress”, J. American Ceramic Society, 73 [3], 602-606, (1993).

87. R.K. Bordia and G.W. Scherer, “On Constrained Sintering-III. Rigid Inclusions”, Acta Metall., 36 (7), (1988) 2411-2416.

88. J.P. Neumann, T. Zhong, and Y.A Chang, "NiO Binary Phase Diagram," ASM Handbook, Vol. 3, p. 2-312, H. Baker ed. ASM International, Materials Park, Ohio, 1992.

89. David Adler, "Electrical Transport: General Concepts" in Electrical Conductivity in Ceramics and Glass, N.M. Tallon ed., p 1-33, Marcel Dekker Inc.: New York, 1974.

90. G. Deutscher, A. Kapitulnik, and M. Rappaport, "Percolation in Metal-Insulator Systems" p. 207-228 in Annals of the Israel Physical Society, Percolation Structures and Processes, Vol. 5. G. Deutscher, R. Zallen, and J Adler eds., Israel Physical Society, Jerusalem, Israel, 1983.

91. C.E. Baumgartner, R.H. Arendt, C.D. Iacovangelo, and B.R. Karas, "Molten carbonate fuel cell cathode materials study," J. Electrochemical Society, October 1984, Vol. 131, No. 10, 2217-2221.

92. M.P. Anderson and S. Ling, "Computer simulation of transport in thin-films," J. Electronic Materials, 19 (1990) 1161.

93. Z. Wu and M. Liu, "Modelling of ambipolar transport properties of composite mixed ionic-electronic conductors," Solid State Ionics, 93 (1997) 65-84.

94. D.R. Askeland, "The Science and Engineering of Materials" 3rd S.I. Edition, Ch 21, p. 728-742, Chapman & Hall: New York, 1996.

95. D. Hull and T.W. Clyne. Introduction to Composite Materials, 2nd ed. Cambridge University Press, Cambridge, 1996.

96. R.A. Schapery, "Thermal expansion coefficients of composite materials based on energy principles," J. Composite Materials, 2, 380, (1968).

97. R. Taylor, "Thermophysical Properties" pp 530 - 548, International Encyclopedia of Composites, Vol. 5, S.M. Lee, Ed., VCH Publishers, New York, 1991.

98. W.D. Callister, Jr., Materials Science and Engineering: An Introduction, 3rd ed., John Wiley & Sons, Inc., Toronto , 1994.

99. Advanced Materials & Processes, Vol 159, No. 12, ASM International, Materials Park, Ohio, 2001.

100. R.M. Spriggs, "Expression for effect of porosity on elastic modulus of polycrystalline refractory materials, particularly aluminum oxide," J. American Ceramic Society, Vol. 44, No. 12, p. 628-629, (1961).

101. M. Mori, T. Yamamoto, H. Itoh, H. Inaba, and H. Tagawa, J. Electrochem. Soc. Vol. 145, No. 4, p. 1374-1381, (1998).

102. M. Radovic and E. Lara-Curzio, J. American Ceramic Society, Vol. 87, No. 12, p. 2242-2246, (2004).